Vol. 59, No. 3 / 2019

e: ISSN 2068 – 2239
p: ISSN 2068 – 4215

# INMATEH – AGRICULTURAL ENGINEERING

SEPTEMBER - DECEMBER

# Editorial

The National Institute of Research-Development for Machines and Installations designed to Agriculture and Food Industry - INMA Bucharest has the oldest and most prestigious research activity in the field of agricultural machinery and mechanizing technologies in Romania.

**Short History**

- In 1927, the first research **Center for Agricultural Machinery** in Agricultural Research Institute of Romania - ICAR (Establishing Law was published in O.D. no. 97/05.05.1927) was established;
- In 1930, was founded **The Testing Department of Agricultural Machinery and Tools** by transforming Agricultural Research Centre of ICAR - that founded the science of methodologies and experimental techniques in the field (Decision no. 2000/1930 of ICAR Manager - GHEORGHE IONESCU ŞIŞEŞTI);
- In 1952, was established the Research Institute for Mechanization and Electrification of Agriculture - ICMA Bănеasa, by transforming the Department of Agricultural Machines and Tools Testing;
- In 1979, the Research Institute of Scientific and Technological Engineering for Agricultural Machinery and Tools – ICSITMUA was founded - subordinated to Ministry of Machine Building Industry - MICM, by unifying ICMA subordinated to MAA with ICPMA subordinated to MICM;
- In 1996 the National Institute of Research-Development for Machines and Installations designed to Agriculture and Food Industry – INMA was founded – according to G.D. no.1308/25.11.1996, by reorganizing ICSITMUA, G.D no. 1308/1996 coordinated by the Ministry of Education and Research G.D. no. 823/2004;
- In 2008 INMA has been accredited to carry out research and developing activities financed from public funds under G.D. no. 551/2007, Decision of the National Authority for Scientific Research - ANCSno. 9634/2008.

As a result of widening the spectrum of communication, dissemination and implementation of scientific research results, in 2000 was founded the institute magazine, issued under the name of SCIENTIFIC PAPERS **(INMATEH)**, ISSN 1583 – 1019.

Starting with volume 30, no. 1/2010, the magazine changed its name to **INMATEH - Agricultural Engineering**, appearing both in print format (ISSN 2068 - 4215), and online (ISSN online: 2068 - 2239). The magazine is bilingual, abstract being published in native language and English, with a rhythm of three issues / year: January-April, May-August, September-December and is recognized by CNCSIS – with $B^+$ category. Published articles are from the field of AGRICU LTURAL ENGINEERING: technologies and technical equipment for agriculture and food industry, renewable energy, machinery testing, environment, transport in agriculture etc. and are evaluated by specialists inside the country and abroad, in mentioned domains.

Technical level and performance processes, technology and machinery for agriculture and food industry increasing, according to national requirements and European and international regulations, as well as exploitation of renewable resources in terms of efficiency, life, health and environment protection represent referential elements for the magazine „**INMATEH - Agricultural Engineering**".

We are thankful to all readers, publishers and assessors.

Editor in chief,

Ph. D. Eng. **Vladut Nicolae-Valentin**

**In the present, *INMATEH - Agricultural Engineering* journal is indexed in the next international databases:**
ELSEVIER /SciVerse SCOPUS, CLARIVATE ANALYTICS' WEB OF SCIENCE- Emerging Sources Citation Index (ESCI), ULRICHS Web: Global Serials Directory, CABI, SCIPIO, Index COPERNICUS International, EBSCO Publishing, Elektronische Zeitschriftenbibliothek

**INMATEH - Agricultural Engineering**
**vol. 59, no.3 / 2019**
NATIONAL INSTITUTE OF RESEARCH-DEVELOPMENT FOR MACHINES AND INSTALLATIONS DESIGNED TO AGRICULTURE AND FOOD INDUSTRY - INMA Bucharest
6 Ion Ionescu de la Brad Blvd., sector 1, Bucharest

Three issues per year,
e-ISSN: 2068 – 2239
p ISSN: 2068 – 4215

Edited by: INMA Bucharest

# CONTENT

# EXPERIMENTAL STUDIES AND NUMERICAL SIMULATION OF SPEED MODES OF AIR ENVIRONMENT IN A POULTRY HOUSE

/

# ЕКСПЕРИМЕНТАЛЬНЕ ДОСЛІДЖЕННЯ ТА ЧИСЕЛЬНЕ МОДЕЛЮВАННЯ ШВИДКІСНИХ РЕЖИМІВ ПОВІТРЯНОГО СЕРЕДОВИЩА В ПТАШНИКУ

**Trokhaniak V.I.[1)], Rutylo M. I.[2)], Rogovskii I.L.[1)], Titova L.L.[1)], Luzan O. R.[3)], Bannyi O.O. [1)] [1]**

[1)] National University of Life and Environmental Sciences of Ukraine;

[2)] Ternopil Volodymyr Hnatiuk National Pedagogical University, Ukraine

[3)] Central Ukrainian National Technical University, Ukraine

*Tel: +380673513082; E-mail: Trohaniak.v@gmail.com*

*DOI: 10.35633/INMATEH-59-01*

***Keywords***: *numerical simulation, heat- and mass-exchange, range of control, poultry house, system performance.*

**ABSTRACT**

*Due to the range of indeterminate factors that influence energy consumption and quality indicators of the air medium while providing the necessary conditions for poultry management, the use of analytical methods for determining the patterns of heat-, mass- and energy-exchange processes happening there is not sufficient enough and additional experimental research is required.*

*For that purpose, numerical simulation and experimental investigations on the performance of the environment support system in a typical broiler poultry house according to technological conditions have been conducted. In the course of the experiment, quality indicators of the air medium and the process energy performance have been determined.*

**РЕЗЮМЕ**

*У зв'язку із невизначеністю ряду факторів, що впливають на витрати енергії та якісні показники повітряного середовища під час забезпечення необхідних умов утримання птиці, застосування аналітичних методів виявлення закономірностей тепло-, масо- та енергообмінних процесів, які там відбуваються, є недостатнім і додатково вимагає проведення експериментальних досліджень.*

*З цією метою нами проведено чисельне моделювання та експериментальні дослідження функціонування системи забезпечення мікроклімату у типовому пташнику-бройлернику на відповідність технологічним вимогам. Під час їх виконання досліджено якісні показники повітряного середовища та енергетику процесу.*

## INTRODUCTION

Papers of *Blanes-Vidal V. et.al., (2008), Bustamante E. et.al., (2017)* cover computational fluid dynamics (CFD) simulation of the flows of air and heat-mass exchange in a poultry house, where there is side system of ventilation used. The authors *Blanes-Vidal V. et. al., (2008); Bustamante E. et.al. (2017)* believe that the method of side mechanical system of ventilation is more effective compared to other methods and make it possible to reduce heat stress and increase productivity of summer poultry raising. As a result of numerical simulation presented in *(Blanes-Vidal V. et.al. (2008); Bustamante E. et.al. (2017)*, the distribution of velocities, pressures and temperatures of the air flow in poultry houses for a side system of ventilation have been obtained. The results of numerical simulation have been compared to the data obtained from experimental studies; here the difference between them does not exceed 12%.

The paper of *Zajicek M. and Kic P. (2012)* presents the CFD solution of miscellaneously improved cases for the various flow and shape configurations of the broiler house. Effects of the transversal and longitudinal ventilation are combined with the changes of inlet air streams directions and also with the different cross-section shaping obtained using curtains.

[1] *Trokhaniak V.I., Assoc. Prof. Ph.D. Eng.; Rutylo M. I., Assoc. Prof. Ph.D. Eng.; Rogovskii I.L., Prof. Ph.D. Eng.; Titova L.L., Assoc. Prof. Ph.D. Eng.; Luzan O. R., Senior Lecturer Ph.D. Eng.; Bannyi O.O., Assoc. Prof. Ph.D. Eng.*

Papers of *Gorobets V.G. et al. (2018); Gorobets V.G. et al. (2018)* covers the system of cooling the outside air with the help of heat exchange apparatuses of special design *(Gorobets V.G. et al. 2019)*, in which water from subterranean wells is used as a cooler. Mathematical simulation of the processes of heat and mass transfer during air ventilation in the poultry houses, where the location of ventilation equipment is changed height wise, has been conducted. As a result of numerical simulation, the fields of velocities, temperatures and pressures in a poultry building have been obtained.

The developed CFD model *(Fidaros D. et al. 2018)* is validated against measurements of temperature (16 points) and air velocity (6 points). According to the simulation results, it is drawn the conclusion that the vertical temperature gradient should be taken into account when the operational sensors for the cooling devices are positioned inside the chamber since there is a deviation higher than 2°C between the air content above and among the birds. Also, various combinations of the available five fans, operating in two possible modes of the examined poultry chamber are studied in order to assess their effect to the internal microclimate. The operation of two or three central fans is proven to be the optimum choice in terms of temperature, ventilation and air velocity. The operation of only one fan fails to preserve the required temperature, while the operation of more than three fans does not improve the ventilation rates.

Based on the conducted analysis, the main drawbacks of numerical simulation in greenhouses have been determined *(Trokhaniak V. and Klendii O., 2018)*. Numerical simulation of the processes of hydrodynamics and heat-mass exchange, that take place within the limits of commercial-scale greenhouses, has been conducted.

*Pourvosoghi N. et al. (2018)* focused on evaluation and numerical analysis of the influence of differential pressure (20, 30 and 40 Pa) and fan activation scenarios on indoor air velocity and temperature distribution in a poultry house. Results showed that air velocity tends to be maximum toward the centre of the cross-section of the house and minimum near the floor next to the side walls. Furthermore, it is elucidated that considerable thermal discomfort for chickens is likely due to temperature variation at the proximity to the exhaust fans.

Maintaining proper environment in hen house by mechanical ventilation is essential for the production. In order to fully mix the cold inlet air in winter with room air, the free space beneath ceiling of hen house is normally large. However, in summer, such a design is not optimal for tunnel ventilation where air is drawn into one end of the house and exhausted at the other end, i.e., a large portion of the ventilation air would pass through the free space under ceiling instead of caged-hen occupied zone (CZ), which leads to reduced air speed in CZ as well as wind chill effect. To solve this problem, application of deflectors beneath the ceiling was investigated by CFD simulations. To assess the effect of deflectors *(Cheng, Q.Y. et al. 2018)*, the indoor air speed and distribution with deflectors were compared to those without deflectors. The effects of heights (0.4 m, 0.55 m, 0.7 m, 0.85 m and 1 m) and intervals (6 m, 9 m, 12 m, 15 m and 18 m) of deflectors on air speed and distribution in CZ were analyzed. The CZ was modelled as porous media in simulations to reduce mesh numbers.

*Rojano F. et al., (2019),* propose a three-dimensional modelling tool that uses CFD. External and internal climate and the sensible and latent heat emitted by the hens were included in the model in accordance with the principles that govern heat and mass transport, momentum and radiative energy. Experimental data were used in the proposed 3D CFD model to predict the internal climate, considering a time series when wind blew perpendicular to the ridgeline. A period of 3h30min, occurring under a stable wind direction was replicated, resulting in an overall RMSE of 1 degrees C and 1 g [$H_2O$] kg [dry air] for temperature and absolute humidity, respectively. In addition, the coefficient of variation indicated that the experimental data pertaining to the internal climate showed less overall variability than did predicted data.

A calculation method of the characteristics of compensated asynchronous machines taking into account the change of the magnetizing contour resistance is presented. The advantages of compensated asynchronous motors and compensated asynchronous generators are determined. Recommendations as to their effective practical use are given *(Mishin V.I. et al. 2016)*.

To ensure stable joint operation of asynchronous machines in an autonomous system under extreme conditions, separation of excitation capacitances and their distribution between branches of a unified electric circuit that are separate for the motor and the generator and not interrelated by the condition of the voltage resonance are proposed using an isolated induction generator with internal capacitive excitation *(Mishin V.I. et al. 2013)*.

## MATERIALS AND METHODS

The investigations were conducted on one of the poultry farms in Ternopil region (Public Company “Ptakhofabryka Ternopilska”, Company “Skalat-Produkt”) in a poultry building for raising broiler chicken (10 thousand heads) with floor housing on a deep wood chips litter during a transient period (February-March).

In order to determine the behaviour and the dynamics of temperature change in a poultry building, the measurement of the indicated parameters was conducted immediately during the technological process. During this period the average temperature of the atmospheric air was +4°C, the value of ventilation air exchange was 0.8–1.1 $m^3$/h per 1 kg bird body weight.

In a standard building (12×76 m) there are 5 rows of technological equipment located. The investigations were conducted during the operation of heating-ventilation system. The maintenance of the predetermined temperature was conducted by means of the equipment set of "Climate-4" type (Airstream Ventilation Systems, Big Dutchman) (with 10 extractor type fans (VO-7.1) and 5 fresh air fans (VO-5.6) with electric motors P = 0.37 kW.

Spatial temperature distribution was investigated at the level of bird location (0.3 m from the floor level) at 27 points of the building (Figure 1).

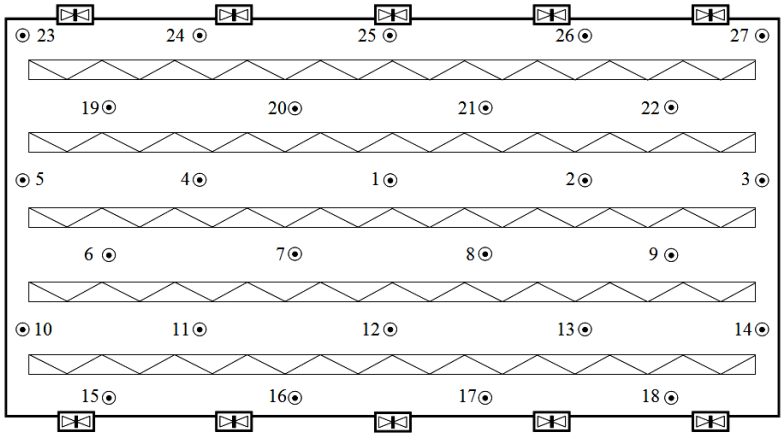


**Fig. 1 - Location schematic of experimental measurements points**

Mathematical simulation of hydrodynamic processes and the processes of heat transfer in a poultry house was conducted. For this purpose, the CFD based on ANSYS Fluent software package was used. The mathematical model is based on Navier-Stokes equations *(Khmelnik S.I., 2018)* and energy transfer equation for convective currents. Spalarta-Allmarasa turbulence model *(Spalart P.R. and Rumsey C.L., 2007; Allmaras S.R. et.al., 2012; Bailly C. and Comte-Bello G., 2015)* and Discrete Ordinates radiation model (DO) *(ANSYS, 2017)* were used in the calculations.

Figure 2 a presents boundary conditions at the "inlet" and the "outlet" and Figure 2 b shows "symmetry" and "wall", which were predetermined for conducting numerical simulation in a poultry house.

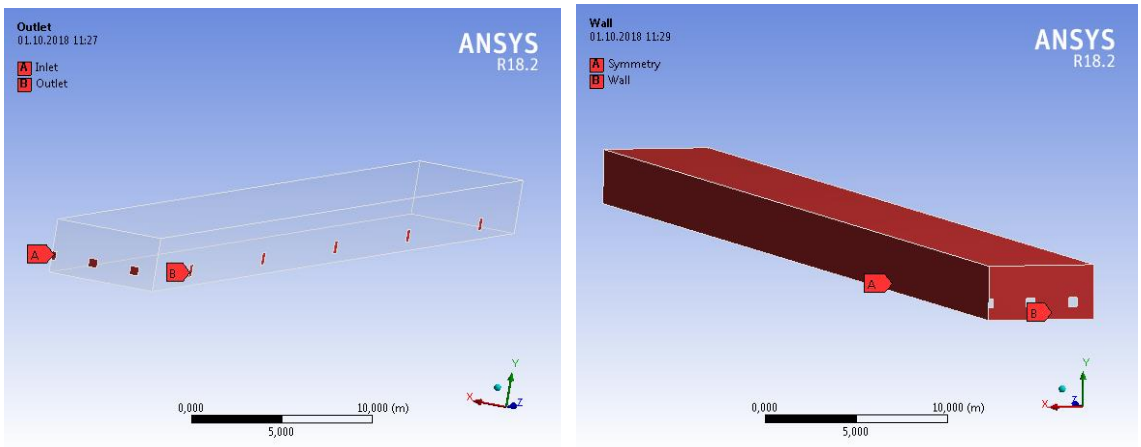


a) b)

**Fig. 2 - Boundary conditions in a poultry house:**

*a) – "inlet" and "outlet"; b) – "symmetry" and "wall"*

At the boundary “inlet” the mass air flow was predetermined to be 5.555 kg/s with the temperature of +4°C. The walls and the floor were made of keramzite concrete 0.4 m in thickness. At the boundary "wall" the temperature of the outside air was preset to be +4°C, taking into account DO radiation model. In the poultry building there were birds kept with floor housing, which is the source of heat generation of +41°C.

**RESULTS**

According to the investigation results, temperature fields (Figure 3) that present the pattern of its distribution in a poultry house during a raising cycle have been built. The significant extremums presented in the graphs (30 and 21°C, see Figure 3) indicate the exceedance of zoo-hygienic norms for the parameters of the air medium (26 – 28°C at the beginning of a cycle and 16 – 19°C beginning from the 5th week) generated by the presence of heat sources (birds' heat production), which caused its local increase and non-uniformity of temperature and gas distribution in a building.

Since the divergence of the technological parameters was determined at the beginning of a poultry raising cycle, it can be assumed that the causes of these phenomena could be the imperfection of the existing system of heating-ventilation equipment control as well as the openings in the structures of a building and the baffle systems of ventilation devices.

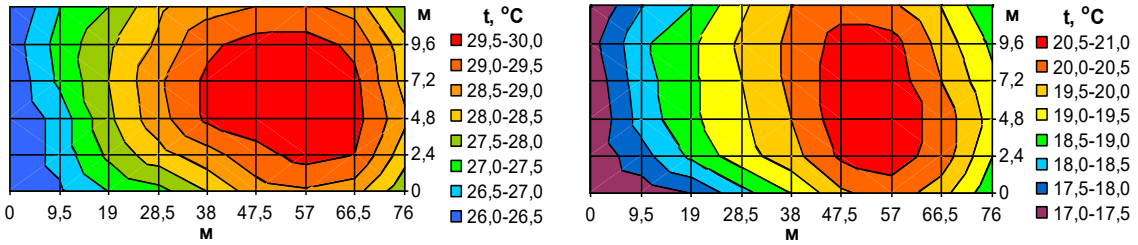


**Fig. 3 - Temperature distribution in a poultry building during a poultry raising cycle**

*a) – day 14; b) – day 42*

According to the results of the measurements, statistical analysis has been conducted and the graphs of the distribution of root-mean square deviations and error dispersions of the controlled variables have been built in order to make a comparison with the specified parameters according to X (length), Y (width) coordinates of displacement (Figure 4).

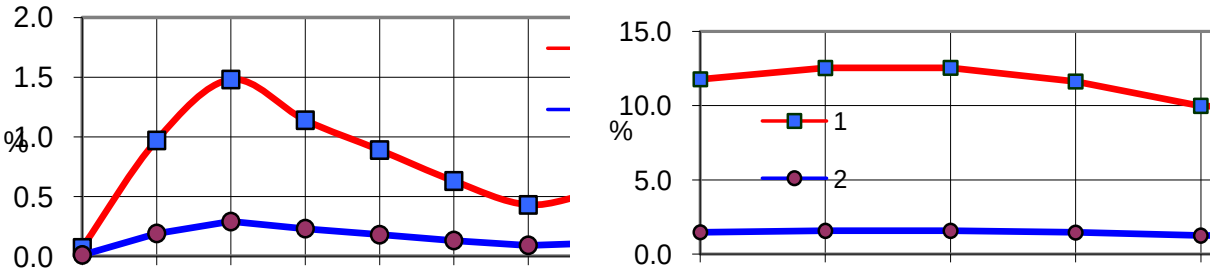


**Fig. 4 - Root-mean square deviations and error dispersions of temperature distributions**

*(1, 2) according to X, Y coordinates of displacement*

Based on the results of the experimental investigations and the production inspection of the quality indicators of the air medium in a poultry house, numerical mathematical simulation has been conducted in order to evaluate the validity degree of the obtained results.

Finite element method (FEM) was used in the numerical calculation of hydrodynamics and heat transfer problems. Figure 5 presents the FEM mesh built in ANSYS Meshing mesh generator based on Workbench framework by means of "CutCell" method. The minimum size of the boundary is equal to 0.05 m and the maximum one is 0.4 m. According to "Orthogonal Quality" criteria, the quality of the mesh is 0.75.

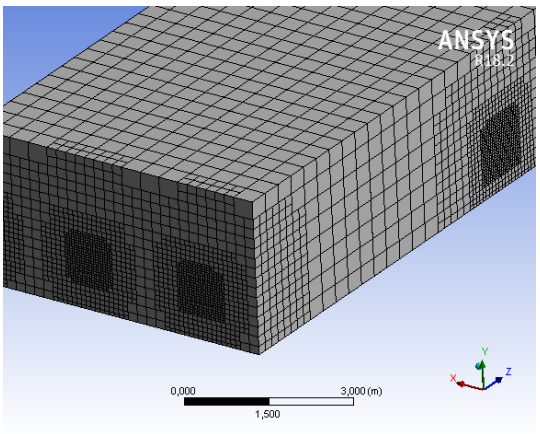


**Fig. 5 - Finite-element mesh generation**

Figure 6 and Figure 7 present the results of the numerical simulation for a half of the poultry building of the specified design. Figure 6 shows that higher temperature is observed in the center of a poultry building. It is shown that temperature distribution in a poultry building is within the limits from +24 to +31°C (see Figure 6). Figure 7 presents the distribution of the temperature field in a poultry house at the distance of 15, 30, 45 and 60 m from extractor type fans. As expected, in the transient period of the year, the air being +4°C is concentrated near the flooring of a poultry house. At a height of 0.8 m near the birds the temperature is +17°C, which meets the norms.

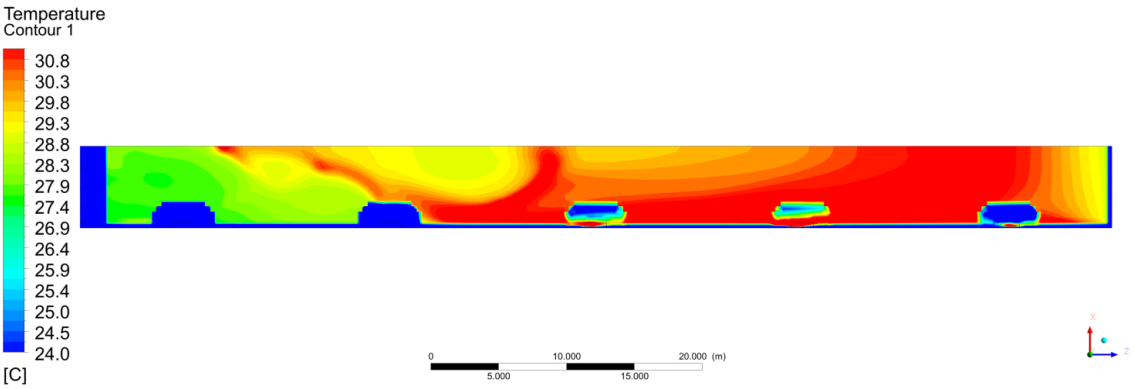


**Fig. 6 - Temperature field in a poultry house ranging from +24 to +31°C at a height of 0.3 m from the floor level along xz axis**

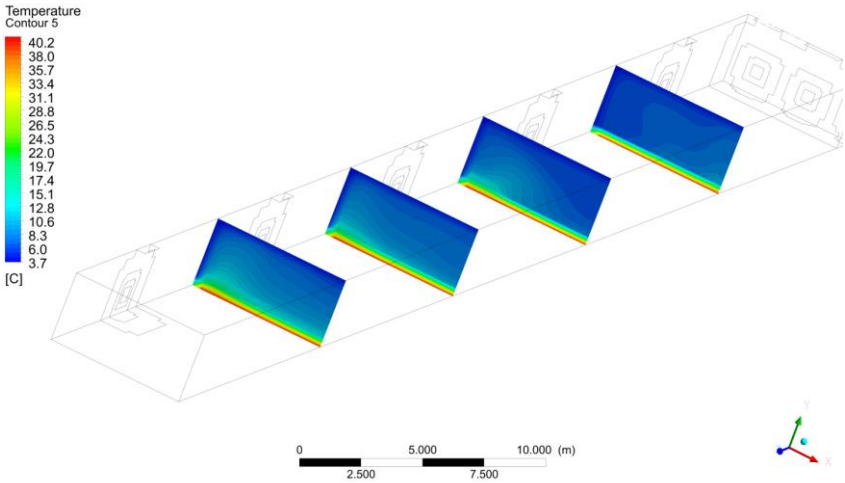


**Fig. 7 - Temperature field in a poultry house at a distance 15, 30, 45 and 60 m from extractor type fans along xy axis**

The graphs in Fig.8 characterize air temperature distributions along the length of the building and the ones obtained as a result of the numerical simulation and the experimental investigations (see Fig.3 a) at a distance of 2.4 m (see Fig.8 a) and 4.8 m (see Fig.8 b). The deviation of the results does not exceed 6.5%.

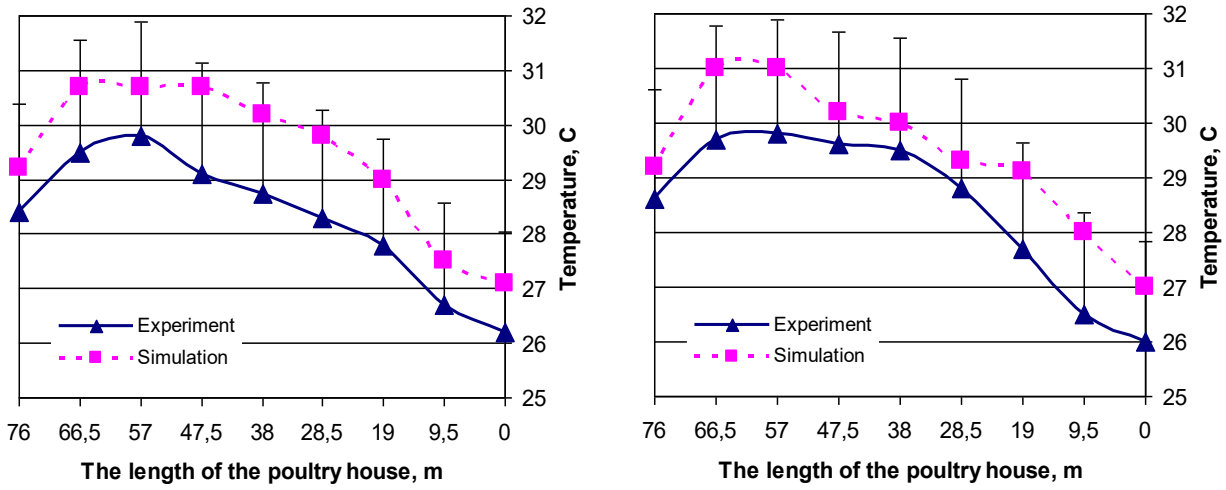


**Fig. 8 - Air temperature distribution along the length of a building from the side wall of a poultry house**

*a) – 2.4 m; b) – 4.8 m*

The ventilation system is controlled in terms of providing the predetermined temperature and gas concentration ($NH_3$). Under these conditions, depending on the balance of the inside and outside temperature, the efficiency of the ventilation system (VS) ranges from nominal (the maximum) $L_n$ to the minimum $L_{min}$. The values of the outside temperatures $T_{max}$ and $T_{min}$ correspond to these values – the beginnings of cooling and heating seasons, when inside temperature control is determined by the nominal or the minimum values of air exchange, respectively:

$$n^* = \frac{1}{L_n}\left[\frac{1}{\gamma c}\left(\frac{q_\Sigma(t)}{T_{in}-T} - \left(k_j F_j\right)_\Sigma\right)\right] \quad (1)$$

As already noted, the range of $VS$ efficiency control should be from $L_{min}$ to $L_{max}$ at the change of outside temperatures from $T_{min}$ to $T_{max}$ that are determined from heat-balance equations reduced to the following form:

$$T_{\min} = T_{in} - \frac{q_\Sigma(t)}{\gamma c L_{\min} + \left(k_j F_j\right)_\Sigma};\ T_{\max} = T_{in} - \frac{q_\Sigma(t)}{\gamma c L_{\max} + \left(k_j F_j\right)_\Sigma}$$

Current ventilator efficiency values are determined by means of processing hourly data on the temperature of the outside air taken from data books. For a certain period of time, let us determine the number of hours of temperature duration within the range of $T_{max} - T_{min}$ at a pitch of 1°C. The minimum $VS$ efficiency is determined with the condition of $NH_3$ emission depending on the age of birds $L_{min} = f(t)$.

In the temperature range of $T_{max} - T_{min}$ with the pitch of 1°C, according to the formula (1), $VS$ running time with its correspondent efficiency is obtained. Running time with nominal efficiency is equal to the temperature duration of more than $T_{max}$ and running time with the minimum efficiency – less than $T_{min}$. As a result of adding time intervals with the same efficiency based on the obtained data, it follows that VS running time in a nominal mode is about 15% of the total operating time and $VS$ running time with the minimum velocity – 7%. The rest of the time – 78% – ventilators operate with the controlled efficiency.

In order to calculate energy consumption for heating a poultry house, firstly, it is necessary to determine the beginning of a bird raising period, since cycle distribution during a year greatly influences the overall energy consumption. According to the investigation data and the methodology presented in *(Ivanova V. M., 1987; Shutka O.V. and Sukach S.V., 2010)*, cycle arrangement in a row is determined. Thus, the beginning of a raising period, which falls on the first days of November, corresponds to rational cycle distribution, at which heat energy saving up to 15% is provided.

According to the data covered above and having assumed that, currently, the minimum period of broiler raising is equal to 43 days and 9 days of sanitary period, 7 raising cycles are obtained under the condition of their optimal arrangement. According to climatological reference books, graphs of distribution of the average monthly air temperature and the change of the inside temperature in a poultry house within every raising cycle in the selected area (climatic zone) are built.

The energy consumed by heat-producing equipment of a broiler farm is calculated according to the heat balance equation:

$$Q = \int_{t_П}^{t_K} \left[ \left( k_j F_j + \gamma c L_{\min}(t) \right) \left( T_{in} - T_{out} \right) - q_{\Sigma}(t) \right] dt \quad (2)$$

While determining energy consumption during a cycle, when the preset temperature of the inside air is changed according to the birds' age, variable values in the expression (2) are $T_{in}$ and $T_{out}$ and after a 30-day age – only $T_{out}$. In order to simplify further calculations and transformations, let us set the constants:

$$\alpha = \left( k_j F_j + \gamma c L_{\min}(t) \right); \; b = T_{\max\_in} - T_{\min\_out}; \; c = Q_{T_{in}} + Q_T - Q_{out} \quad (3)$$

where $T_{max\_in}$ – inside air temperature during bird placing; $T_{min\_out}$ – minimum temperature of the outside air.

For the first and the last cycles of raising, in case of linear approximation of outside temperature distribution, $T_{min} = T_{max}$'.

Having substituted (3) into (2), for the first cycle we obtain:

$$Q = \int_{t_{ny}}^{t_{ny}+\tau} \left[ \alpha \left( b - r\left( t - t_{ny} \right) + gt \right) - c \right] dt \quad (4)$$

where $\tau$ – duration of the period of raising at changeable air temperature, twenty-four hours; $t_{ny}$ – the beginning of broiler raising cycle, calendar day; $r$, $g$ – constant coefficients of linear functions.

Having integrated and simplified the expression (4), we obtain:

$$Q = \tau \left[ \alpha \left( b + gt_{ny} - \frac{(r-g)\tau}{2} \right) - c \right] \quad (5)$$

Analogically, we obtain the dependence for calculating energy demand in the last raising cycle:

$$Q = \tau \left[ \alpha \left( b - gt_{ny} - \frac{(r+g)\tau}{2} \right) - c \right] \quad (6)$$

The number of twenty-four hours $\tau$, during which it is necessary to heat the air, can be determined by differentiating the expressions (5) and (6). As a result, we obtain:

$$n_1 = \frac{\alpha\left( b + gt_{ny} \right) - c}{\alpha\left( r - g \right)}; \; n_1 = \frac{\alpha\left( b - gt_{ny} \right) - c}{\alpha\left( r + g \right)} \quad (7)$$

For the cycles of raising, in which the approximation of the outside temperatures causes significant errors, their distribution should be presented in the form of a quadratic dependence

$$T_{out} = T_{\min.av} + kt^2 \quad (8)$$

where $T_{min.av}$ – the minimum average air temperature, which is typical of this area; $k$ – constant coefficient of the parabolic function of temperature distribution.

From the expressions (2) and (8) we obtain the equation for calculation the necessary amount of heat from the 2nd to the 6th cycle of raising:

$$Q_{(2-6)} = \int_{t_{ny}}^{t_{ny}+\tau} \left[ \alpha \left( b' - r\left( t - t_{ny} \right) + kt^2 \right) - c \right] dt \quad (9)$$

where $b' = T_{max\_in} - T_{min\_out}$ – the difference between the maximum inside temperature and the minimum (average monthly in the coldest period) outside temperature, ºC.

After integration and transformation, we obtain:

$$Q_{(2-6)} = \tau \left[ \alpha \left( b - \frac{rt}{2} - kt_{ny}^2 - kt_{ny}\tau \frac{k\tau^2}{2} \right) - c \right] \quad (10)$$

In order to calculate heat demand according to the formula (10), it is necessary to substitute the correspondent to a certain cycle values of $t_{ny}$, which characterize the time of chicken placement, in it. This is the value that significantly influences heat energy consumption.

Based on the analysis and generalization of the investigation results on the fields distribution of air medium technological parameters in a poultry house, the function of the required air exchange is obtained

and it determined the minimum volume of fresh air (m³) and, correspondingly, the minimum artificial ventilation heat exchange in order to create the optimal microclimate conditions according to $NH_3$ content, which provides the minimum heat energy consumption for medium heating:

$$G = 24k\int_a^b q(i_{NH_3})di \tag{11}$$

where $k$ – the number of twenty-four hours in the cycles of broiler raising during the period under study; $q(i_{NH3})$ – functional dependence of the minimum necessary air exchange depending on the bird's age (from $i = a$ to $i = b$), m³/h.

The amount of heat (J) required for heating the incoming air is determined as follows:

$$Q = c\rho G(T_{in.av} - T_{out.av}) \tag{12}$$

where $c$ – specific heat capacity of dry air, J/(kg·K); $\rho$ – air density, kg/m³; $T_{in.av}$ – average inside air temperature, °K; $T_{out.av}$ – average outside air temperature, °K.

From the expressions (11), (12) we obtain the equation necessary to determine the required amount of heat to provide the preselected temperature in a poultry house during air exchange according to $NH_3$ content:

$$Q = 24kc\rho(T_{in.av} - T_{out.av}) \cdot \int_a^b q(i_{NH_3})di \tag{13}$$

Heat consumption for heating the incoming air is determined by the range of ventilation system efficiency control, which was chosen with the condition of providing the maximum required demand of poultry for fresh air (m³/h):

$$L_{max} = L_n = nq_{max}m_{max} \tag{14}$$

where $n$ – the number of heads in a poultry house, unit; $q_{max}$ – summer norm of air exchange per 1 kg of body weight, m³/h; $m_{max}$ – weight of one bird at the end of a raising period, kg.

According to the technological conditions, the maximum control range of $D$ in order to provide the necessary air exchange $L_{min}(i)$ in poultry houses for young broilers should be 1:80, while the existing ventilation systems provide the maximum range of efficiency control about 1:10, its minimum limit corresponds to the value of $L_{max}(i)$ (Figure 9).

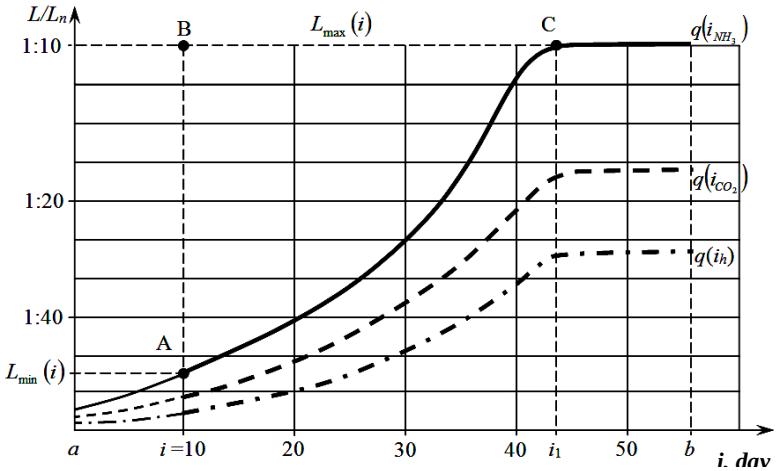


**Fig. 9 - Relative dependences of air exchange values on the birds' age in winter and transient periods of the year**

*according to ammonia $q(i_{NH3})$ content, carbon dioxide $q(i_{CO2})$ content and excess water $q(i_h)$*

According to the control range of the frequency of ventilator rotation, the calculation of the minimum value of air exchange (m³/h) is conducted according to the formula:

$$L_{min} = L_n D \tag{15}$$

The figure below (see Figure 9) presents the graphs of the relative dependences of the required efficiency $L$ of a ventilation system, according to the current birds' need for fresh air $q(i)$, on the age and the content of harmful substances.

The obtained results show that beginning from the moment of exhaust ventilation operation i = 10 and to the birds' age $i = i_1$ (43 day), there is overconsumption of the air ($m^3$), which is heated to the poultry house temperature. In the adjusted scale, it is determined by the area of the ABC plot (see Figure 9) as the difference of the integrals $L_{max}(i)$ and $q(i_{NH3})$ within the interval $i - i_1$:

$$G = L_{\max} \int_{i}^{i_1} di - \int_{i}^{i_1} q(i_{NH_3}) di \tag{16}$$

From the equations (12) and (16) we obtain the value of heat energy overconsumption (J), which is caused by insufficient range of ventilation system control:

$$\Delta Q = c\rho(T_{in.av} - T_{out.av}) \left( L_{\max} \int_{i}^{i_1} di - \int_{i}^{i_1} q(i_{NH_3}) di \right) \tag{17}$$

Thus, the investigation results presented above prove that specific heat and electric energy consumption can be decreased by means of extending the range of ventilation system control (not less than 1:50) with the help of variable-frequency asynchronous electric drive with adaptive control system, which is based on the analysis of microclimatic parameters of the air medium in poultry houses.

## CONCLUSIONS

Based on the conducted research, it is possible to draw the following conclusions:

Numerical simulation of the processes of heat and mass transfer of the ventilated air in a poultry house in order to verify the results has been conducted together with the experimental investigations. According to the investigation results, with the help of ANSYS Fluent software, 3D temperature fields in a poultry house have been obtained;

Energy consumption and quality characteristics of the environment support technology depend heavily on the organization of the speed range of technological equipment;

The solution of the stated problems makes it possible to decrease energy consumption of the environment support technology during broilers raising, increase the quality of the air medium in poultry houses, reduce feed consumption and the loss of poultry stock and, as a result, increase economic efficiency of the production process and the quality of the finished product.

## REFERENCES


[1] Allmaras S.R., Johnson F.T., Spalart P.R., (2012), Modifications and Clarifications for the Implementation of the Spalart-Allmaras Turbulence Model, *7th International Conference on Computational Fluid Dynamics*, pp. 9-13, Big Island/Hawaii;

[2] ANSYS, (2017), *ANSYS Fluent Theory Guide*. Release 18.2, Published in the USA, 832 p.;

[3] Bailly C., Comte-Bello G., (2015), *Turbulence. Series: Experimental Fluid Mechanics*, Springer International Publishing, 360 p., Heidelberg/Germany;

[4] Blanes-Vidal V., Guijarro E., Balasch S., Torres A.G., (2008), Application of computational fluid dynamics to the prediction of airflow in a mechanically ventilated commercial poultry building, *Biosystems Engineering*, vol.100, no.1, pp. 105-116, San Diego/USA;

[5] Bustamante E., Calvet S., Estelles F., Torres A.G., Hospitaler A., (2017), Measurement and numerical simulation of single-sided mechanical ventilation in broiler houses, *Biosystems Engineering*, vol.160, pp. 55-68, San Diego/USA;

[6] Cheng, Q. Y., Li, H., Rong, L., Feng, X. L., Zhang, G. Q., & Li, B. M. (2018). Using CFD to assess the influence of ceiling deflector design on airflow distribution in hen house with tunnel ventilation. *Computers and Electronics in Agriculture*, 151, pp.165-174. doi:10.1016/j.compag.2018.05.029, Netherlands;

[7] Fidaros D., Baxevanou C., Bartzanas T., Kittas C., (2018), Numerical study of mechanically ventilated broiler house equipped with evaporative pads, *Computers and Electronics in Agriculture*, vol. 149, pp. 101-109, doi:10.1016/j.compag.2017.10.016, Netherlands;

[8] Gorobets V.G., Trokhaniak V.I., Antypov I.O., Bohdan Yu.O., (2018), The numerical simulation of heat and mass transfer processes in tunnelling air ventilation system in poultry houses, *INMATEH-Agricultural Engineering*, vol.55, no.2, pp.87-96, Bucharest/Romania;

[9] Gorobets V., Bohdan Y., Trokhaniak V., Antypov I., (2019), Investigations of heat transfer and hydrodynamics in heat exchangers with compact arrangements of tubes, *Applied Thermal Engineering*, vol.151, pp. 46-54. doi:10.1016/j.applthermaleng.2019.01.059, London/United Kingdom;
[10] Gorobets V.G., Trokhaniak V.I., Rogovskii I.L., Titova L.L., Lendiel T.I., Dudnyk A.O., Masiuk M.Y., (2018), The numerical simulation of hydrodynamics and mass transfer processes for ventilating system effective location, *INMATEH - Agricultural Engineering*, vol. 56, no.3, pp. 185-192, Bucharest/Romania;
[11] Ivanova V. M., (1987), Prediction of heat consumption by livestock buildings (Прогнозирование теплопотребления животноводческими помещениями), *Mechanization and electrification of agriculture (Механизация и электрификация сельск. хоз-ва.)*, vol. 10, pp. 43-46, Moscow/Russia;
[12] Khmelnik S.I., (2018), Navier-Stokes equations. On the existence and the search method for global solutions, *Mathematics in Computers – MiC*, 134 p., Bene-Ayish/Israel;
[13] Mishin V.I., Chuenko R.N., Makarevich S.S., (2013), Conditions for stable joint operation of asynchronous machines of different types in an autonomous electromechanical system. *Russian Electrical Engineering*, vol. 84, no. 9, pp. 518-527, Moscow/Russia;
[14] Mishin V.I., Lut N.T., Makarevich S.S., Chuenko R.N., (2016), Analogs and characteristics of compensated asynchronous machines with different numbers of phases. *Russian Electrical Engineering*, vol. 87, no. 12, pp. 653-660, Moscow/Russia;
[15] Pourvosoghi N., Nikbakht A. M., Sharifian F., Najafi R., (2018), Numerical analyses of air velocity and temperature distribution in poultry house using computational fluid dynamics, *INMATEH-Agricultural Engineering*, vol. 56, no. 3, pp. 109-118, Bucharest/Romania;
[16] Rojano F., Bournet P. E., Hassouna M., Robin P., Kacira M., Choi C. Y., (2019), Modelling the impact of air discharges caused by natural ventilation in a poultry house. *Biosystems Engineering*, vol. 180, pp. 168-181. doi:10.1016/j.biosystemseng.2019.02.001, San Diego/USA;
[17] Shutka O.V., Sukach S.V., (2010), Model of the ventilation complex in the tasks of stabilizing the temperature regime in the room (Модель вентиляційного комплексу в задачах стабілізації температурного режиму в приміщенні), *Transaction of Kremenchuk Mykhailo Ostrohradskyi National University (Вісник КДУ ім. М. Остроградського)*, vol. 3, no. 62, pp. 57–62, Kremenchuk/Ukraine;
[18] Spalart P.R., Rumsey C.L., (2007), Effective inflow conditions for turbulence models in aerodynamic calculations, *Aiaa Journal*, vol. 45, no. 10, pp. 2544-2553 doi:10.2514/1.29373, Reston/USA;
[19] Trokhaniak V., Klendii O., (2018), Numerical simulation of hydrodynamic and heat-mass exchange processes of a microclimate control system in an industrial greenhouse, *Bulletin of the Transilvania University of Brasov, Series II: Forestry, Wood Industry, Agricultural Food Engineering*, vol. 11 (60), no. 2., pp. 171-184, Brasov/ Romania;
[20] Zajicek M., Kic P., (2012), Improvement of the broiler house ventilation using the CFD simulation, *Agronomy Research*, vol. 10, Special Issue 1, pp. 235–242, Tartu/Estonia.

# EFFECT OF TINE GEOMETRY ON PENETRATION RESISTANCE DURING VERTICAL MOVEMENT ON NATURAL GRASSLAND
# /
# 典型刀齿类耕作部件的草地贯入试验研究

**Changbin He [1,2], Yong You *[2], Decheng Wang *[2], Gang He [3], Hongjian Wu [2,4], Bingnan Ye [2]) [1]**

[1] Inner Mongolia Agricultural University, College of Mechanical and Electrical Engineering, Hohhot / China;
[2] China Agricultural University, College of Engineering, Beijing / China;
[3] Hohhot Branch of Chinese Academy of Agricultural Mechanization Sciences CO., LTD., Hohhot / China;
[4] Tsinghua University, Department of Mechanical Engineering, State Key Laboratory of Tribology, Beijing / China;
*Tel: +86 10 010-62737977; +86 10 010-62737208; E-mail: youyong@cau.edu.cn; wdc@cau.edu.cn*
*DOI: 10.35633/INMATEH-59-02*

***Keywords:*** *natural grassland, very narrow tine, penetration resistance, contact area, interaction*

**ABSTRACT**

*Novel tillage tools causing minimizing surface vegetation deterioration are desired in degraded natural grassland mechanical restoration technology development. This paper attempted to study the effect of tine geometry in its vertical movement on penetration resistance. Four very narrow tines were defined (i.e. rectangle, triangle, crescent and mososeries) based on the geometry of the cutting edge, a special test unit was manufactured as well. Field experiments were conducted on natural grassland. The effects of tine geometry and contact surface area on soil penetration resistance were investigated and surface disturbance obtained. Results indicated that the tendencies of penetration resistance varied with the working depth or contact surface area, and showed differences between the four tines affected by different cutting-edge geometries. The crescent tine obtained the highest penetration resistance as compared to the others, and the mososeries tine got the lowest value. Penetration resistances of all the tines increased with the attack surface area with an exponential function ($R^2$≥0.94) or a power function ($R^2$≥0.95) respectively, depending on the penetration angle equalling 90° or being less than 90°, nonlinear tendency with penetration depth. It could be concluded that penetration resistance was influenced a lot by the tine geometry parameters such as contact surface area and penetration angle. The cutting edge of the tine with continuous acute penetration angle that could obtain lower resistance and stable force variation curve was more suitable for operation on natural grassland.*

**摘要**

*为探索适用于退化草地机械化改良作业的关键耕作部件，设计了 4 种不同形状的极窄刀齿，并搭建了试验台，进行草地贯入失效试验，重点对刀齿的贯入阻力进行分析。结果表明：刀齿贯入阻力随深度和接触面积的变化趋势受刀齿形状的影响而存在差异，新月形刀齿的贯入阻力最大，弦月形刀齿的最小，贯入阻力与贯入深度呈非线性正相关规律，与接触面积呈指数函数或幂函数变化规律（R2≥0.94）。刀齿刃口的入土角度和刀齿与土壤的接触面积均对贯入阻力产生影响，且贯入阻力变化程度受刃口的入土角度的影响，入土角度为直角时，贯入阻力存在急剧变化的阶段，入土角度为锐角时，贯入阻力变化相对稳定，宜选择刃口入土角度为连续锐角的刀齿进行作业。*

## INTRODUCTION

Tangled long strong *Leymus chinensis* (Trin.) Tzvel. (referred to as L-C hereafter) roots and soil formed soil-root composite structures underground on natural grassland, weakening the aeration and water permeability of the soil, accelerating the soil compaction and hardness, becoming one of the major reasons of natural grassland degradation in China *(You et al.,2011; He et al., 2016; Hamza et al., 2005)*. Using tillage tools to break the hardened soil-root composite structures on natural grassland that could improve the plant growth environment in the soil by improving the soil physical, chemical and biological properties, was verified to be one effective practice for the degraded natural grassland restoration *(Chen et al., 2017; Alvarez and Steinbach, 2009; Diabate et al., 2018; You et al., 2012)*.

[1] *Changbin He, Lecturer Ph.D. Eng.; Yong You, As. Prof. Ph.D. Eng.; Decheng Wang, Prof. Ph.D. Eng.; Gang He, Eng.; Hongjian Wu, Ph.D. Eng.; Bingnan Ye, Dr. Stud. Eng.*

Common mechanical improvement methods included soil aerating, fertilization, shallow tillage, root cutting, soil loosening and reseeding etc. *(He et al., 2015; Sawtschuk et al., 2012; Bhogal et al., 2011)* have been applied for degraded natural grassland restoration in recent years.

Novel low-disturbance tillage tools (e.g., rectangular tine, triangular tine, rotary blade, and crescent blade) for natural grassland continuously emerged due to problems such as soil nutrient loss and soil erosion brought about by over-turning soil clods, and large surface disturbance area created by conventional tillage tools *(Su et al., 2004; Lal R., 2007; Ramirez et al., 2019; You et al., 2017)*. Such tillage tools belong to narrow tines or very narrow tines because their working width is much smaller than the working depth *(Godwin and O'Dogherty, 2007)*. During operation, these tools will not create large-scale soil surface failures, the soil disturbance being relatively low. The movements can be divided into many combined processes with penetration and rotation. However, their geometry structure parameters affected the working resistances and working performance a lot. Few literatures on the soil-blade interactions, especially the penetration interaction have been found. The interaction relationships between tillage tools and soil layer on natural grassland still need to be investigated.

In order to further explore suitable tools and key components used for mechanized improvement of degraded grassland, this paper mainly investigated the effects of very narrow tine geometry on the penetration resistance and disturbance on natural grassland, providing theoretical reference and technical support for the design and optimization of the special tillage tines for degraded natural grassland restoration.

## MATERIALS AND METHODS

- **Experiment site description**

The experiment site was located in typical natural grassland in Chabei district of Hebei province (41°28'31.649″N, 115°1'28.733″E). L-C was the dominant grass species of this area. A 12 m×12 m block was randomly selected as the experimental field site. Average bulk density, moisture content and porosity of the soil layer within the depth range of 0-20 cm on natural grassland were obtained based on the survey method as He et al. (2016) reported, ranging from 1.04 to 1.37 g/cm$^3$, from 9.19% to 16.68%, and from 48.32% to 60.63%, respectively. The L-C horizontal rhizomes mostly concentrated at the depth range of 5-6 cm underground, and were rarely distributed at the depth of more than 10 cm, as shown in Fig.1 (a). In the depth range of 0-10 cm underground, the tangled roots and soil formed soil-root composite structures underground. The soil cone index was measured using a hand-held cone penetrometer (SC 900, Spectrum Technologies, Inc.) with a small cone as described in ASAE standards S313.3 (2009). The value of soil cone index increased first and then decreased with the depth increasing, the maximum value was obtained at the depth range of about 5 cm. When the depth exceeded 10 cm, there was no big change about the soil cone index values. The soil cone index curves were as shown in Fig.1(b).

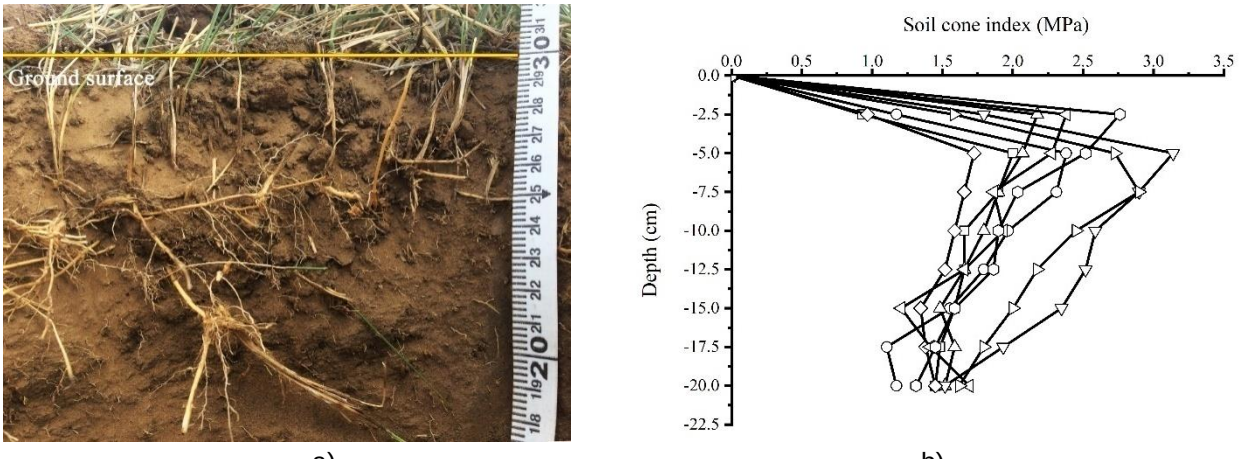


a) b)

**Fig. 1 - The L-C roots distribution underground and soil cone index curves**

- **Experimental tines and test unit**

Four very narrow tines with different geometries were designed and applied in the experiments based on previous research reported by You (2011) and the tools applied on normal soil aeration machine, soil gashing and root cutting machine, and fertilizer injection machine. These tines were defined as rectangle tine (RT), triangle tine (TT), crescent tine (CT), and mososeries tine (MT), respectively, as shown in Fig.2 (a).

The thickness was 7 mm, and maximum value of the height was 207 mm. All tines were designed with a cutting edge with a cutting angle of 30 degrees, but different geometry curves. Three through holes with equal spaces were manufactured for mounting and fixing with the test unit.

A test unit was set up, mainly consisting of frames, a hydraulic cylinder, a reversing valve, a flow valve, a displacement sensor, a force sensor, a data acquisition unit (SQ 2020, Grant Squirrel) and hydraulic pipes etc., as shown in Fig.2 (b). The test unit was mounted with a tractor by a three-point linkage. The hydraulic cylinder, reversing valve and flow valve connected with the tractor hydraulic system through hydraulic pipes. The force sensor and displacement sensor were used for recording the resistance and displacement values of the tines during the penetration operations, respectively, and these values from the sensors were collected by the data acquisition unit.

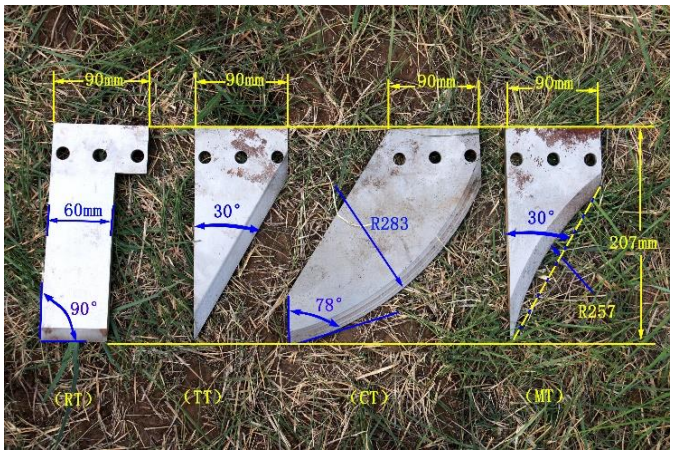


a)

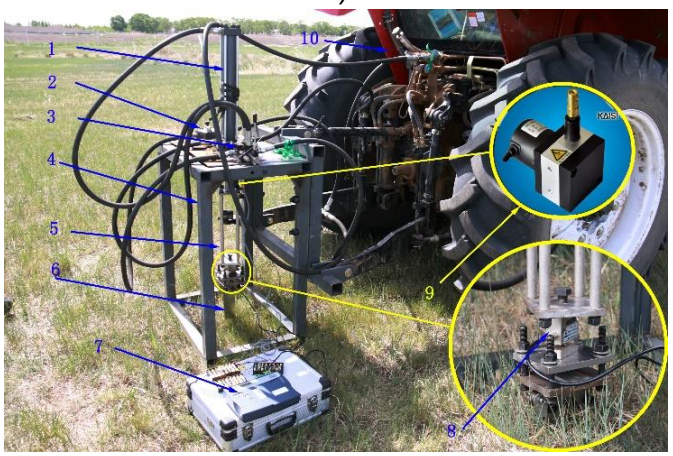


b)

**Fig. 2 – Experimental tines and test unit**

*1- hydraulic cylinder; 2-flow valve; 3- reversing valve; 4-mounted frame; 5-support frame; 6-very narrow tine; 7- data acquisition unit; 8-force sensor; 9-displacement sensor; 10-tractor*

- **Experimental procedure**

For all experiments, the very narrow tine was vertically inserted into the soil on natural grassland by operating the hydraulic system. The reversing valve and flow valve were used to control the movement and speed in the direction of penetration. When the tines reached the maximum effective working depth, then the reversing valve was controlled to change the moving direction of the tine until the tine was pulled back upon the soil surface. Via the hydraulic system and flow valve, the average penetration speed was controlled at 1.06±0.12 cm/s, the average pull-out speed was 1.50±0.04 cm/s. All penetration tests for each very narrow tine were replicated three times at different spots within the experiment field.

The force data from the force sensor was the real resistance of the tine during the penetration experiment; when the sensor was under pressure, the values were negative, and vice versa the values were positive. When the tine was inserted into the soil, the sensor was under pressure, when it was pulled out, the sensor was stretched. The influence of the weight coming from the tines and connecting parts had been eliminated in the experiments.

## RESULTS

- **Effects of cutting edge geometry on working resistances during penetration operations**

The working resistance curves with working depth of the four tines were obtained, as shown in Fig.3.

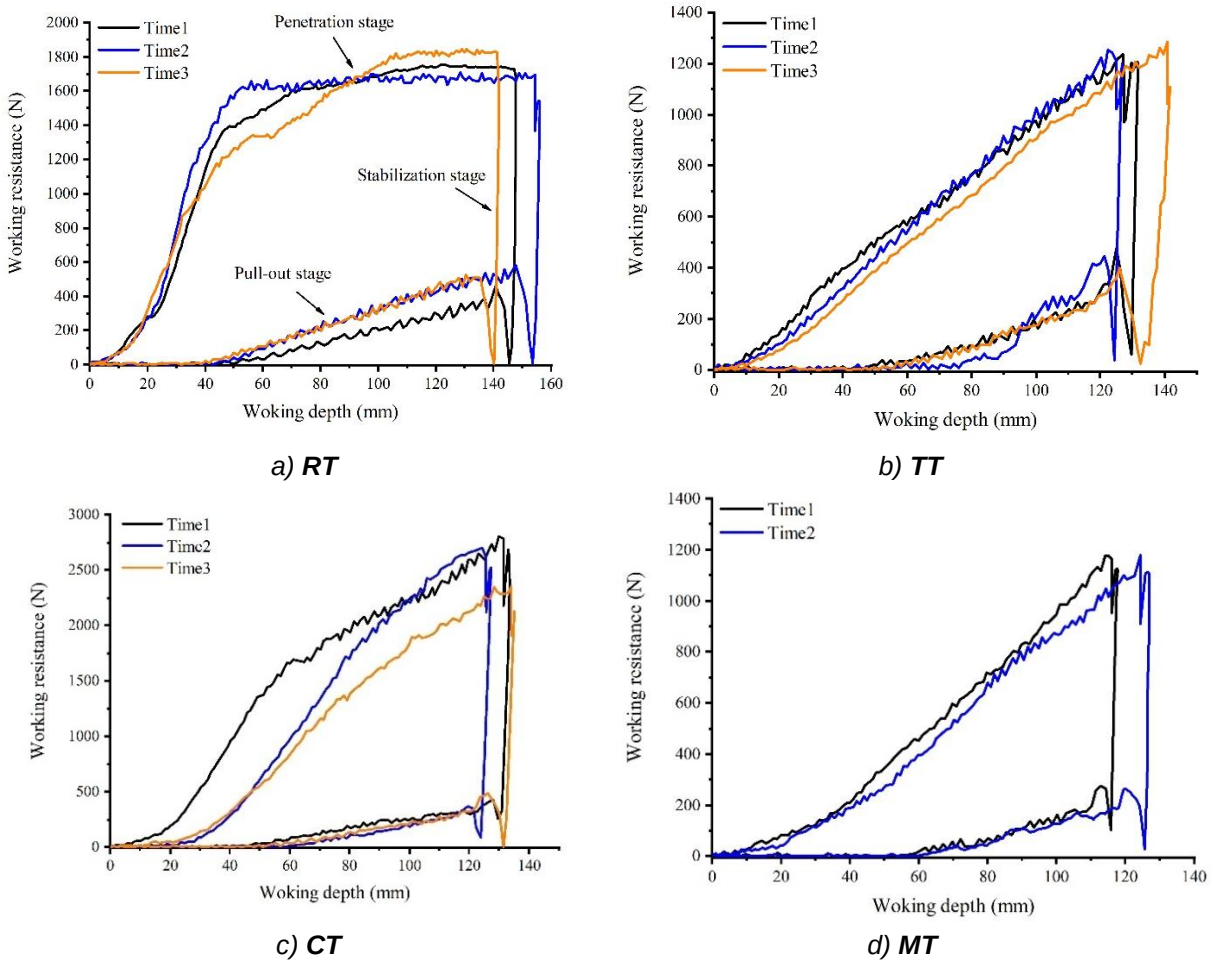


**Fig. 3 – Woking resistance with working depth curves**

*Note: The three parts of the curves, i.e. penetration stage, stabilization stage and pull-out stage, were only marked in fig.3 (a), the other graphs had similar characteristics but not be marked*

These curves of the very narrow tine mainly consisted of three parts, i.e. penetration stage, stabilization stage and pull-out stage. The graphs showed that all tines got larger resistances in penetration stage than pull-out stage. During the penetration process, the resistances increased with the working depth increasing nonlinearly, and the changing tendencies showed different characteristics between RT, TT, CT, and MT. During the pull-out process, the forces decreased with the working depth decreasing. However, at the early stage of the pull-out process, the force showed increased rapidly at first, then decreased gradually after that. This was caused by adhesive resistance of the contact surface between the tine and the soil. When the adhesive interfaces were broken along the pull-out movements of the tine, the friction force became the dominating resistance of the tine during the pull-out process. In addition, it could be observed that the tines with various geometry obtained different penetration resistance changing tendencies as shown in Fig.3.

For all tines, CT had the largest penetration resistance and MT got the lowest value when the tine reached the limit depth. Compared to the penetration resistance of RT, the maximum value of TT and MT had average decrease of 28.83% and 36.56% respectively, but an increase of 47.99% for CT. However, it could be seen in Fig.3 that the rectangle tine (RT) obtained different variation curves of the penetration resistance with the working depth from others during its vertical movement. Turning points of the curves were easily observed in Fig.3 (a). The penetration resistance of RT increased sharply at first, then continued to slowly increase with a lower slope. Though CT obtained larger penetration resistance and the penetration resistance curves also showed two parts with different changing rules, the rapid increasing characteristic was not as obvious as the curves of RT were. For TT and MT, the penetration resistances increased stably with no significant phase differences during the entire curves, the resistance values of TT and MT varying much stably than those of RT and CT.

Combined with Fig.3 (a), it could be found that the cutting edges of RT and TT were straight lines while the others were blending lines. The angle between the cutting edge and the penetration direction was defined as the penetration angle. The penetration angles of CT, TT, and MT were all less than 90° (30° for TT, 13°-51° for MT, 90° for RT, and 27°-78° for CT), except the penetration angle of RT which was 90°. Especially, the angles of CT and MT always changed with the working depth during the entire penetration movements but were all less than 90°. These results indicated that the penetration angle affected the resistances a lot, a bigger penetration angle resulted in larger penetration resistance and variation range of the changing tendency, a smaller angle could obtain stable penetration resistance curves during the penetration process. And a tine owing a cutting edge with continuous acute angles was more suitable for operating on natural grassland because of its lower resistance.

- **Effects of contact surface area on penetration resistance**

During the tine inserting into the soil on natural grassland, the cutting edge cut off and pressed on the soil layer, resulting in the resistance from the soil, the contact surfaces became the main interaction surfaces between the tine and the soil layer. The interaction forces acted on the contact surfaces and impeded the tines vertical movements, so the contact surfaces also affected the penetration resistance. The contact surfaces of the tine included the cutting edge's surfaces and side surfaces. Via the software of CATIA, 3D models of the tines were drawn, and the contact surface area values under different working depth were measured based on these 3D models. The curves between the contact surface area and penetration resistance were obtained, as shown in Fig.4. The figures showed that all penetration resistances of the tines increased with the contact surface areas increasing nonlinearly with the $R^2$ value exceeding 0.94. Except for the rectangle tine (RT), the penetration resistances of other three tines owned power function relationships with the contact surface areas with the $R^2$ value exceeding 0.95. The penetration resistance of RT showed an exponential function relationship with the contact surface area with the $R^2$ value exceeding 0.94.

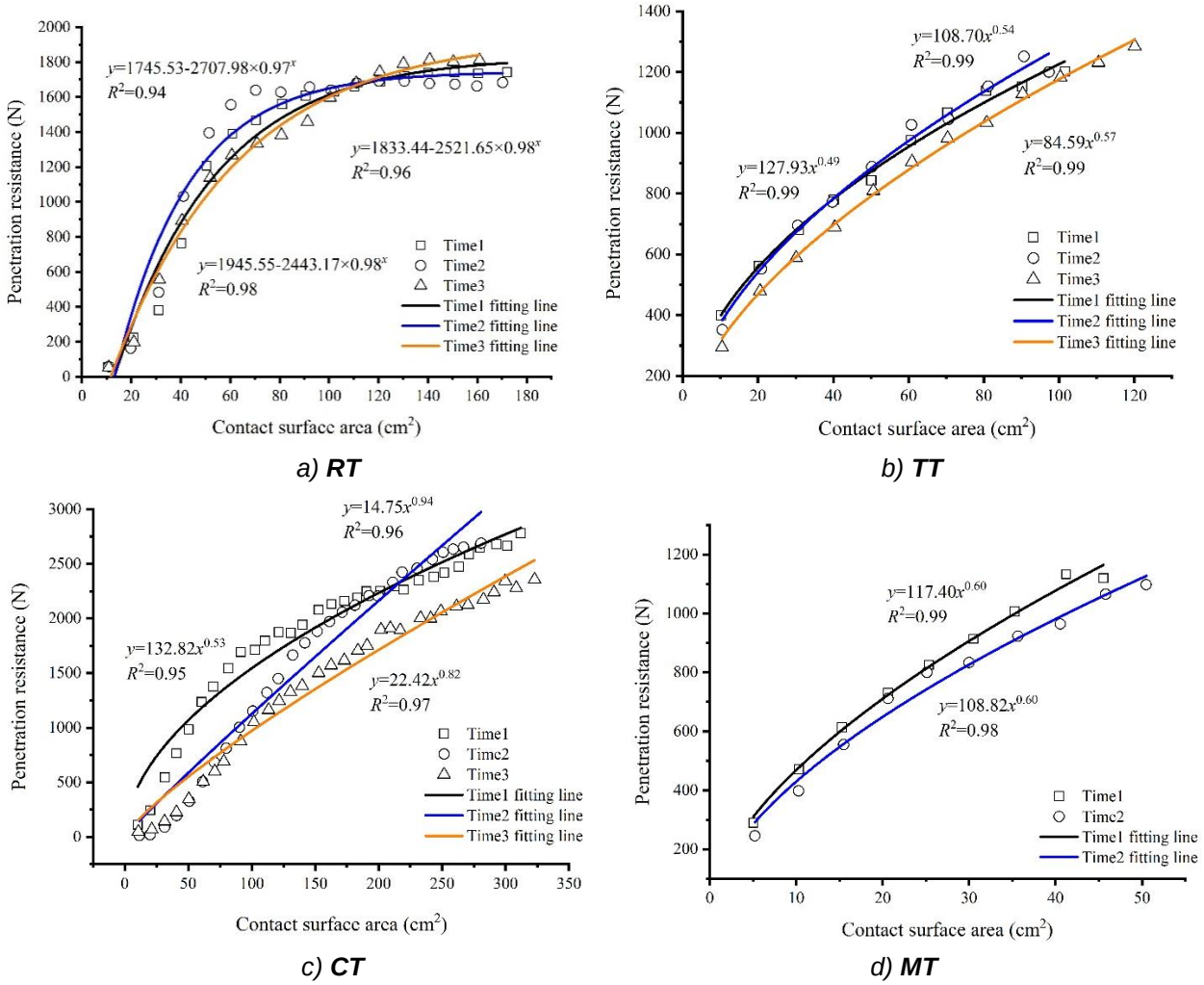


*a) **RT*** *b) **TT***

*c) **CT*** *d) **MT***

**Fig. 4 – Penetration resistance with contact surface area curves**

In addition, as mentioned before, the penetration angle of the rectangle tine was 90° during all the penetration processes, as shown in Fig.5 (a), however, for the other three tines, the penetration angles (θ) were all less than 90° during the vertical movements (Fig.5 (b)).

A function relationship between the penetration resistance and contact surface area could be concluded as follow:

$$P = \begin{cases} a + b \cdot c^{x} & (\theta = 90°) \\ A + B \cdot x^{C} & (\theta < 90°) \end{cases} \quad (1)$$

Where P is penetration resistance (N); $\theta$ is penetration angle (°); a, b, c, A, B, and C are constants.

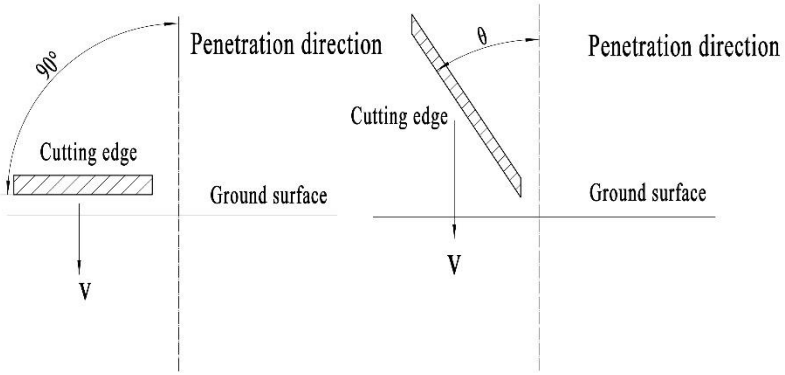


(a) (b)

**Fig. 5 – Diagram of the penetration angles**

- **Surface disturbance on natural grassland after penetration experiments**

When the tine was pulled out from the soil on natural grassland, only a narrow slit was left on the surface. The grass roots and withered grass were cut off, there were no extensive vegetation destruction and overturning soil-roots clods situations found during the penetration experiments, as shown in Fig.6.


**Fig. 6 – Surface disturbance during penetration experiments**

## CONCLUSIONS

(1) The tine geometry affects the penetration resistance substantially. The crescent tine resulted in the highest penetration resistance compared to the rectangle, triangle and mososeries tine, and the mososeries tine got the lowest value during the penetration process. Compared to the rectangle tine, the maximum penetration resistance value of the triangle tine and mososeries tine decreased by 28.83% and 36.56%, respectively, while the value of the crescent tine increased by 47.99%.

(2) The changes of different types, geometries of the tines cause the variation of the contact surface area between the tine and soil which directly affect the penetration resistance during the penetration process. The penetration resistance increases with a power function or an exponential function with the contact surface area with the $R^2$ values exceeding 0.94. The models could well reflect the variation tendency of the penetration resistance with the contact surface area.

(3) The differences of cutting-edge geometries of the tines resulted in varied curves of the penetration resistance with working depth, which affect the resistance values and changing stability. A bigger penetration angle resulted in larger penetration resistance and variation range of the changing tendency, a smaller angle could obtain stable penetration resistance curves during the penetration process. The tine owing a cutting edge with continuous acute penetration angles was more suitable for operating on natural grassland because of its lower resistance and surface disturbance.

**ACKNOWLEDGEMENT**

The authors were funded for this project by High-level Talent Scientific Research Project of Inner Mongolia Agricultural University (No. NDYB2018-7), the Inner Mongolia Natural Science Foundation (No. 2019BS05014), the National Natural Science Foundation of China (NSFC) (No. 51405493), and the earmarked fund for China Agriculture Research System (CARS-34). They also received supports from Zhangjiakou Comprehensive Test Station of China Forage and Grass Research System.

**REFERENCES**

[1] Alvarez R., Steinbach H.S., (2009), A review of the effects of tillage systems on some soil physical properties, water content, nitrate availability and crops yield in the Argentine Pampas. *Soil and tillage research*, vol.104(1), ISSN 0167-1987, pp.1-15, Elsevier B.V., Amsterdam/Netherlands;

[2] Bhogal A., Bentley C., Newell-Price J., Brian C, (2011), The alleviation of grassland compaction by mechanical soil loosening. BD5001: *Characterisation of Soil Structural Degradation Under Grassland and Development of Measures to Ameliorate its Impact on Biodiversity and Other Soil Functions*. Report for Defra, London/UK;

[3] Chen H., Shao L., Zhao M., Zhang X., Zhang D., (2017), Grassland conservation programs, vegetation rehabilitation and spatial dependency in Inner Mongolia, China. *Land Use Policy*, vol.64, ISSN 0264-8377, pp.429-439, Elsevier B.V., England / UK;

[4] Diabate B., Wang X., Gao Y., Yu P., Wu Z., Zhou D., Yang H., (2018), Tillage and haymaking practices speed up belowground net productivity restoration in the degraded Songnen grassland. *Soil and Tillage Research*, vol.175, ISSN 0167-1987, pp.62-70, Elsevier B.V., Amsterdam/Netherlands;

[5] Godwin R. J., O'Dogherty M. J., (2007). Integrated soil tillage force prediction models. Journal of Terramechanics, vol. 44(1), ISSN 0022-4898, pp. 3-14, PERGAMON-ELSEVIER SCIENCE LTD, England/UK;

[6] Hamza M. A., Anderson W. K., (2005), Soil compaction in cropping systems: A review of the nature, causes and possible solutions. *Soil and tillage research*, vol.82(2), ISSN 0167-1987, pp.121-145, Elsevier B.V., Amsterdam/Netherlands;

[7] He Changbin, Wang Decheng, Wang Guanghui, You Yong, Liang Fang, Liu Liangdong, Shao Changyong, (2015), The Development of Grassland Mechanical Restoration Technology Research (天然草地机械化改良技术研究进展). *Journal of Agricultural Mechanization Research*, vol. 37(06), ISSN 1003-188X, pp. 258-263, Heilongjiang Provincial Society for Agricultural machinery, Heilongjiang/China;

[8] He Changbin, You Yong, Wang Decheng., Wang Guanghui, Wu Hongjian, Gong Shuangjie, (2016), Mechanical characteristics of soil-root composite and its influence factors in degenerated grassland (退化草地复合体力学特性与影响因素研究). *Transactions of the Chinese Society for Agricultural Machinery*, vol.47(4), ISSN 1000-1298, pp. 79-89, Chinese Society for Agricultural machinery, Beijing/China;

[9] Lal R., (2007), Evolution of the plow over 10,000 years and the rationale for no-till farming. *Soil and Tillage Research*, vol. 93(1), ISSN 0167-1987, pp.1-12, Elsevier B.V., Amsterdam/Netherlands;

[10] Ramirez P. B., Calderón F. J., Fonte S. J. et al., (2019), Environmental controls and long-term changes on carbon stocks under agricultural lands. *Soil and Tillage Research*, vol.186, ISSN 0167-1987, pp.310-321, Elsevier B.V., Amsterdam/Netherlands.

[11] Sawtschuk J, Gallet S, Bioref F, (2012), Evaluation of the most common engineering methods for maritime cliff-top vegetation restoration. *Ecological Engineering*, vol. 45, ISSN 0925-8574, pp. 45-54.

[12] Su Y. Z., Zhao H. L., Zhang T. H., Zhao X.Y., (2004), Soil properties following cultivation and non-grazing of a semi-arid sandy grassland in northern China. *Soil and Tillage Research*, vol. 75(1), ISSN 0167-1987, pp. 27-36., Elsevier B.V., Amsterdam/Netherlands;

[13] You Y., Wang D., Liu J., (2012), A device for mechanical remediation of degraded grasslands. *Soil and Tillage Research*, vol.118, ISSN 0167-1987, pp.1-10, Elsevier B.V., Amsterdam/Netherlands;

[14] You Yong, (2011), *Mechanical remediation technology of degraded grassland (Leymus-chinensis) by soil-gashing and root-cutting (退化羊草草地机械化破土切根技术优化研究)*, PhD Thesis, China Agricultural University, College of Engineering, Beijing;

[15] You Yong, He Changbin, Wang Decheng, Wang Guanghui, (2017), Interaction Relationship between Soil and Very Narrow Tine during Penetration Process (土壤耕作部件极窄刀齿与土壤作用关系研究). *Transactions of the Chinese Society for Agricultural Machinery*, vol. 48(06), ISSN 1000-1298, pp.50-58, Chinese Society for Agricultural Machinery, Beijing/China;

[16] You Yong, Wang Decheng, Wang Guanghui, (2011), 9QP-830 Soil-gashing and Root-cutting Mechanism (9QP-830 型草地破土切根机). *Transactions of the Chinese Society for Agricultural Machinery*, vol.42(10), ISSN 1000-1298, pp. 61-67, Chinese Society for Agricultural Machinery, Beijing/China;

[17] ***ASAE S313.3, 2009. Soil Cone Penetrometer. ASABE, St. Joseph Mich.

# USING COMBINES FOR CLEANING GRAIN CROPS BY NON-TRADITIONAL TECHNOLOGIES

/

# *ИСПОЛЬЗОВАНИЕ КОМБАЙНОВ НА УБОРКЕ ЗЕРНОВЫХ КУЛЬТУР ПО НЕ ТРАДИЦИОННЫМ ТЕХНОЛОГИЯМ*

**Buryanov Alexey, Chervyakov Ivan** [1]
Federal State Budgetary Scientific Institution «Agricultural Research Centre «Donskoy» / Russia
*Tel: +79515253806; E-mail: bern7771@rambler.ru*
*DOI: 10.35633/INMATEH-59-03*

***Keywords**: combine harvester, stripper header, construction, grain, loss*

**ABSTRACT**

*The application of grain harvesting technology, using the method of stripping plants at the root, allows increasing combines' productivity and efficiency 1.4-2.0 times. As a result of tests which were held both in the fields and in a certain created laboratory setup, it was determined that the share of the heap, entering the straw walkers, will be increased 2.5 times if a gap between the longitudinal ribs of the deck is changed from 11.0 to 9.0 mm while shattering of grain level is preserved as acceptable.*

**РЕЗЮМЕ**

*Применение технологии уборки зерновых культур методом очеса растений на корню позволяет увеличить производительность комбайнов и их эффективность в 1.4-2.0 раза. По результатам исследований, выполненных в полевых условиях и на специально созданной лабораторной установке установлено, что при изменении зазора между продольными ребрами деки с 11.0 до 9.0 mm доля вороха, поступающего на соломотряс, увеличивается в 2.5 раза при сохранении уровня дробления зерна на допустимом уровне.*

## INTRODUCTION

Grain harvesting is one of the energies and resource-intensive work performed in the production of agricultural products. At present, combines are the main tools for harvesting grain and other crops and in the near future they will be the main tools as well. The harvesters' park of the country numbers 150 000 combine harvesters while the required number is 300 000. Due to low availability, the load on one combine is up to 425 hectares *(SHamin A.E. et al, 2018)*. Most of the harvesters which are used in the south of the country are single-drum combines of the "Don" and "Acros" families produced by "Rostselmash". Tending to reduce harvesting time, agricultural enterprises operate with the latest modifications combines with powerful engines in modes which are 1.5-2.0 times higher than recommended; it leads to great increase of grain loses, grain injury and crushing. The correctness of this conclusion is confirmed by the results of the research works given in (*Lizhang X. and Yaoming L., 2011; Patel S.R. and Varshney B.P., 2016*). To solve the problem, science proposes a number of fundamentally new technical and technological solutions based on some new principles of influence on the inflorescence of the harvested crop the implementation of which will considerably improve the quality of the threshing process and the performance of the harvesting machines along with an increasing of the combine park. These are, for example, such new principles as threshing by using compressed air jets or by pneumatic impacts or using ultrasonic vibrations. (*Moskovskij M.N., Kovaleva A.V., Kuren S.G., 2017; Moskovskij M.N. et al, 2015)*.

The ideas listed above are the most interesting among all variety of proposed solutions but it is necessary to conduct basic research works that require relevant research teams and capital investments before applying them in the technical devices, machines.

In prospect, the best way should be considered the use of unconventional technologies for harvesting grain and other crops by stripping plants at the roots, particularly with a stripping combine, and adaptation of stripping devices to zone conditions.

[1] *Alexey Buryanov – d. tech. sc., professor, main research officer; Ivan Chervyakov – junior research officer*

This tendency is developed both in Russia and in the USA, Great Britain and Canada. The feeding of the stripping heap containing the minimum amount of straw mass into the threshing unit of the combine allowed increasing its productivity and efficiency 1.4-2.0 times (*Berenshtein I.B. and Shabanov N.P., 2017; Izmajlov A.YU. and SHogenov YU.H., 2017*). However, this method is a new one and, naturally, needs to be improved. The research investigations carried out for some years at the State Scientific Institution "NSRIMEA", now FSBSI «ARC "Donskoy"», aimed at further developing the process of stripping grain crops with a single-drum header, the mathematical model of the process was worked out, laboratory facilities were created for testing the results obtained on theoretical models (*Buryanov M.A., 2011*), and the production of «Ozone» stripping reapers was started according to the documents developed at our institute (the manufacturer of OJSC "Penzmash" and "Yuzhanka" produced "NSRIMEA" + "AGROTRADE"). This process is studied by a lot of authors in different countries, such as China (*Yuan J., Lan Y., 2007)*, India (*Bhanage G.B., Shahare P.U. et al, 2017*), Iran *(Chegini G.R., 2013; Chegini G.R., Mirnezami S.V., 2012)*, Great Britain (*Shelbourne Reynolds Engineering Ltd)* and others.

Study and tests of combines with stripping headers in field works showed that the stripped heap goes almost entirely to the sieve after passing through the deck, where the gaps between the ribs were rated at a bigger quantity of straw content. In this case, the straw walker is underloaded. The entering stripped mass differs significantly in its fractional composition from the mass in traditional harvesting. The share of grain in the stripping heap varies from 75% to 85%. Therefore, the threshing and separating device of modern combine harvesters, especially single-drum ones, is to work with an unconventional heap, having technological settings for its other fractional composition. It was hypothesized that it was possible to choose such gap between longitudinal ribs of the concave in which a large part of the fractions containing larger particles of the heap would flow to the straw walker, thereby reducing the amount of material entering the sieve.

The probability of the grain crushing growth appears if the gap is decreased below maximal linear dimensions of harvested grain.

In accordance with those mentioned above, the purpose of the research was to determine the influence of the deck gap on the distribution of thrashing mass between cleaning and straw walker, keeping the degree of grain crushing limited with GOST. This research was carried on the threshing of winter wheat stripped heap in a threshing unit with one drum.

## MATERIALS AND METHODS

Experimental studies were carried out in a laboratory setup, the scheme of which is shown in figure 1. The flow of the stripping heap into the device 5 was carried out using the feed conveyor 1 (fig.1).

Stripped heap portion was prepared for the experiments. The stripping harvester "Yuzhanka-6", produced by "NSRIMEA" + "Agrotraid", was used. The harvester coverage was 6.0m. The harvested crop was soft winter wheat "Luchezar" with crop capacity 6.96t/ha and with weak link between grain and ear (*Buryanov A.I., Chervyakov I.V. et al., 2018*); the gluten content in a grain was 20.8%, protein content – 12.2%; the mass of 1000 seeds was 42.6g, grain moisture – 11-12%. There was the following fractional composition: free grain - 65%; un-threshed ears and their parts with grain – 20%; stems, chaff – 15%.

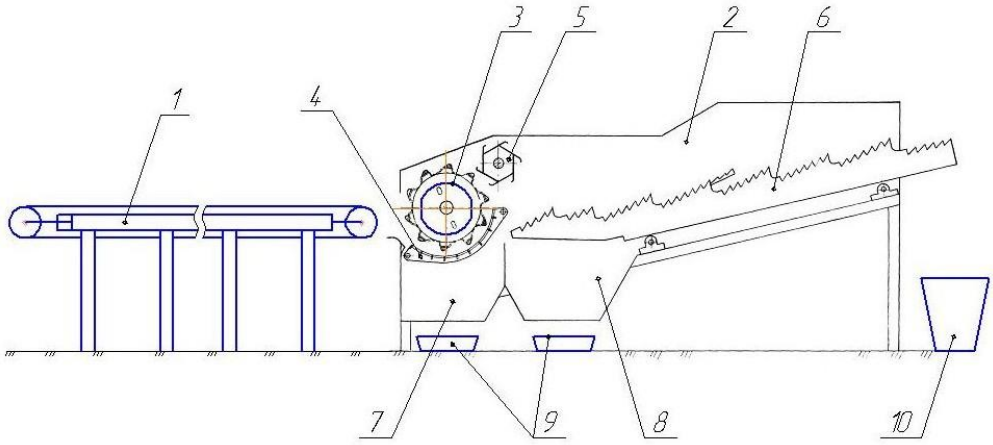


**Fig. 1 – Diagram of the laboratory setup**

*1 – feed conveyor; 2 – replaceable deck; 3 – drum; 4 – beater; 5 – threshing and separating device; 6 – straw walker; 7 – basket; 8, 10 – funnel; 9 – pallet*

The overall dimensions of the laboratory unit and its working parts are taken on the basis of the size of a straw walker key 6 equal 0.3 m (fig. 1).

The working bodies were driven by an electric motor, separately for the threshing-separating device 5 and for the conveyor 1 (fig. 1) by means of chain and V-belt transmissions.

The cylinder-concave gaps 3 and the bars of the deck 2 (fig.1) were pre-installed: at the entrance – 20.0 mm, at the exit – 5.0 mm.

Working out the plan of the experiment, we used the data obtained after the threshing of winter wheat by a combine “Acros”, stripping header “Yuzhanka-6” and header of continuous cutting. It was found that the peripheral speed of the rasp-bar cylinder with a diameter of 0.8 m, which was traditionally recommended for threshing the heap, was exceeded at threshing stripped heap and caused an increase of grain crushing. By reducing peripheral speed to 750 rpm (31.4 m/s) on a combine “Acros”, equipped with stripping header, we achieved the level of grain threshing analogous to the level of grain threshing of combine that was equipped with a direct-flow header of continuous cutting, having peripheral speed of the cylinder 800 rpm (33.5 m/s).

Taking into account the results of field work, we carried on prospecting work by using a part of serial deck that had a gap between ribs of 11.0 mm and changing the peripheral speed of drum (cylinder) in the range 600-800 rpm, which corresponded to a speed of bars of 25.1 – 33.5 m/s.

We observed short threshing to 3% at peripheral speed of a drum of 600 rpm (25.1 m/s), so if a combine is equipped with a finish-threshing device, it leads to circulation of grain for the rethreshing. As there wasn’t a finish-threshing device on the laboratory setup, it was impossible to take into account its contribution to grain crushing process. It was noted more than 2.0% rising of grain crushing at the speed of 800 rpm (33.5 m/s) while the threshing grade wasn’t changed. The following levels of peripheral speed were considered: upper value 31.4 m/s, middle value 29.3 m/s and minimal value 27.2 m/s.

As the gap of standard deck is 11.0 mm, it was taken as upper value; minimal level was 7.0 mm that was less than maximal linear size of “Luchezar” corn seed (which is 8.6 mm); middle value was 9.0 mm. The sequence and conditions of experimentations were made according to the experiment plan (table 1); it was got in the program “Statistica” (13 version). The experiments were carried out triply; then, the mid value was determined.

**Table 1**

**Matrix of experiment planning for the intensification of the stripping heap threshing process and its separation in the laboratory setup**

| Number of experiments | Factors and their magnitudes | |
|---|---|---|
| | Peripheral speed of a threshing drum rotation [m/s] | Gaps between deck bars [mm] |
| 1 | 29.3 | 11.0 |
| 2 | 27.2 | 11.0 |
| 3 | 27.2 | 9.0 |
| 4 | 27.2 | 7.0 |
| 5 | 29.3 | 9.0 |
| 6 | 31.4 | 11.0 |
| 7 | 29.3 | 7.0 |
| 8 | 31.4 | 9.0 |
| 9 | 31.4 | 7.0 |

The rest of parameters were fixed at the next level:

- amount of stripped heap was 1.6 kg/s, which corresponds to the flow of 8.0 kg/s during the operation of the threshing device with a width of 1.5 m installed for commercially available combines;
- moisture content was in the range of 11.0-12.0%;
- fractional composition of the heap supplied to the installation was constant: free grain – 65%, un-threshed ears and their parts with grain – 20%, plant stalks, chaff – 15%.

## RESULTS

A replaceable deck 0.3 m wide was installed just before the test. Figure 2a shows the feed conveyor with a heap on it before the experiment.

During the experiments, a high-speed shooting of the threshing process was carried out with the Sony Mark 4 camera over the planned experiments. One frame of the shooting is shown in figure 2b.

High-speed shooting made it possible to have a good look at the threshing process during the passage of the stripped heap in the threshing device. When the unit worked with a deck having 9.0 mm gap between bars and the peripheral speed of 31.4 m, grain crushing achieved 1.91%, which is almost equal to the damage level with serial deck -1.90%. It was determined that when the gap was decreased to 7.0 mm grain crushing increased to 2.35%.

**a)** **b)**

**Fig. 2 – a) laboratory feed conveyor with stripped heap of winter wheat; b) high-speed shooting frame of the threshing process**

Table 2 shows the planned experimental data, values of heap separation, values of grain crushing obtained at the laboratory setup.

**Table 2**

**The results of the experiments**

| Experiment number | Factors | | Dependent variable | |
|---|---|---|---|---|
| | The gap between the ribs of the deck [mm] | Peripheral speed of drum [m/s] | Heap separation degree [%] | Grain crushing [%] |
| 1 | 11,0 | 29.3 | 15.5 | 1.62 |
| 2 | 11.0 | 27.2 | 17.0 | 1.38 |
| 3 | 9.0 | 27.2 | 30.0 | 1.39 |
| 4 | 7.0 | 27.2 | 35.0 | 1.9 |
| 5 | 9.0 | 29.3 | 33.0 | 1.66 |
| 6 | 11.0 | 31.4 | 13.0 | 1.9 |
| 7 | 7.0 | 29.3 | 35.5 | 2.17 |
| 8 | 9.0 | 31.4 | 26.0 | 1.91 |
| 9 | 7.0 | 31.4 | 28.0 | 2.35 |

Maximal value of heap separation level is 35.5% if a gap is 7.0 mm and peripheral speed is 29.3 m/s, but grain crushing is 2.17%, which is over the value regulated by GOST. If peripheral speed of a drum is increased to 31.4 m/s, heap separation degree is decreased to 28.0% and grain crushing grows to 2.35%. Heap separation decreases while speed grows because of grating increasing of non-grain part of the harvest and because of its passing through the deck.

If the grain crushing level is less 2.0% (according to GOST), heap separation maximal degree is 33.0% when the gap is 9.0 mm and peripheral speed is 29.3 m/s.

When the speed is 27.2 m/s, heap separation degree is practically the same, it equals 30.0% but grain crushing level decreases to 1.39%.

Figure 3 shows the three dimensional surfaces of gap and peripheral speed dependences of the heap separation and crushing level (“Statistica”, ver.13).

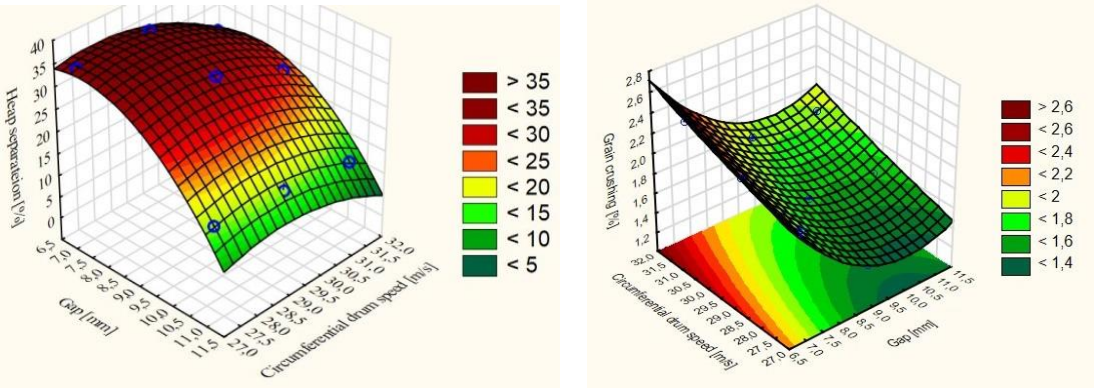


**Fig. 3 – Responses surfaces of heap separation and grain crushing to alternative drum operating speed and gap between the deck's ribs dependencies**

Experimental data were processed by means of program package "Statistica" (ver.13) and the response surface equations were obtained as uncoded ones:

$$Z = -577.7036 + 15.8512 \times X + 39.2810 \times Y - 1.4167 \times X^2 + 0.1786 \times X \times Y - 0.7181 \times Y^2 \quad (1)$$

where:

X – a gap between deck ribs (mm); Y – drum peripheral speed (m/s); Z – heap separation level (%). Coefficient of determination is $R^2 = 0.98$.

As grain crushing degree was determined in the experiment, change rating was defined as the following equation:

$$W = 11.6058 - 1.7111 \times X - 0.2170 \times Y + 0.0650 \times X^2 + 0.0137 \times X \times Y + 0.0034 \times Y^2 \quad (2)$$

where:

X – the gap between deck ribs (mm); Y – drum peripheral speed (m/s); W – grain crushing degree (%). Coefficient of determination is $R^2 = 0.99$.

Both equations show good convergence with real values. High determination coefficients 0.98 and 0.99 show that changing of factors, gap and peripheral speed describe about 99% of dependent variables changes.

It should be noticed that all these data are true for the winter wheat "Luchezar", grown in the south Russia concrete climate conditions; this kind of wheat has weak link between grain and ear. Similar kinds of grain are grown at the half area used for winter wheat in the region. That is why these results may be used for choosing the expendable deck parameters for the combines used for harvesting winter wheat, having similar physical and mechanical features. The researches show that the change of grain kind and conditions of growing *(Khusanov I., Babaev S. at al, 2011)* leads to varying physical and mechanical characteristics such as grain size, its strength even in one field limits. But this technology is used for harvesting winter wheat rigid varieties, barley, rye, cereal sorghum, linen and other crops whose physical and mechanical characteristics are significantly different. That is why the adaptation researches of deck parameters to variety of crops properties and designing of its technological model are high-priority tasks now and for the near future.

## CONCLUSIONS

When threshing winter wheat "Luchezar" stripped heap in a single drum threshing device, furnished with a deck where the gap between ribs is decreased from 11.0 to 9.0 mm, the level of heap separation between cleaning and straw walker increased from 15.5 to 33.0% and it allowed to reduce the air and sieve cleaning load.

It may be suggested that these results are true for all other kinds of wheat with similar physical and mechanical features. The results are very important as winter wheat share is about 50% of the cultivated area of the country. So, one of the ways of winter wheat harvesting by combines with a single drum threshing devices can be the usage of expendable deck with the gap of 9.0 mm between ribs. It is necessary to carry out analogous researches to determine the gap range for other crops threshing.

In perspective, combine threshing devices should have mechanisms for timely changing of the gap between deck's ribs for maintaining optimal regimes with heaps having different fractional composition and for harvesting technology changing.

**REFERENCES**


[1] Berenshtein I.B., Shabanov N.P., (2017), Resource-saving technologies of cereals cleaning (bicycle) cultures (Ресурсосберегающие технологии уборки зерновых (колосовых) культур), *V.I. Vernadsky Crimean Federal University (Федеральное государственное автономное образовательное учреждение высшего образования Крымский федеральный университет им. В.И. Вернадского)*, Issue 10(173), pp. 62-73, Simferopol/Russia;

[2] Buryanov A.I., Chervyakov I.V., Kolinko A.A., Pakhomov V.I., Ionova E.V., Khlystunov V.F., (2018), Methods and results of determining the natural force of the connection of grain with an ear during the period of ripening and full ripeness (Методы и результаты определения естественной силы связи зерна с колосом в период созревания и полной спелости), *Grain economy of Russia (Зерновое хозяйство России),* Issue 6(60), pp. 21-25, Zernograd/Russia (DOI 10.31367/2079-8725-2018-60-6-21-25);

[3] Buryanov A.I., Buryanov M.A., Dmitrenko A.I., Kolesnikov G.E., Chervyakov I.V., (2014), *Laboratory setup for the study of the parameters and modes for grain crops stripping process*, Patent, No.136743, Russia;

[4] Buryanov M.A., (2011), *Parameters and modes of the process of grain crops processing on the harvester header (Параметры и режимы процесса очеса зерновых культур навесной на комбайн жаткой)*, PhD dissertation, Azov-Black Sea State Agro-engineering Academy, Zernograd/Russia;

[5] Bhanage G.B., Shahare P.U., Aware V.V., Dhandeand K.G., Deshmukh P.S., (2017), Development of stripper harvester for paddy, *Journal of Applied and Natural Science*, Issue 9(4), pp. 1943-1948. (DOI: 10.31018/jans.v9i4.1469);

[6] Chegini G.R., Mirnezami S.V., (2012), Analysis and comparison of wheat losses in two harvesting methods, *Agricultural Engineering International: CIGR Journal*, Issue 14, pp. 91-98, Paris/France;

[7] Chegini G.R., **(**2013), Determination of Optimum Operating Conditions of Combine Harvester with Stripper-Header, *World Applied Sciences Journal*, Issue 23(10), pp. 1399-1407, Pakistan (DOI 10.5829/idosi.wasj.2013.23.10.1829);

[8] Izmajlov A.YU., SHogenov YU.H., (2017), Intensive machine technologies and new generation machinery for the production of the main groups of agricultural products (Интенсивные машинные технологии и техника нового поколения для производства основных групп сельскохозяйственной продукции), *Machinery and equipment for the village (Техника и оборудование для села),* Issue 7, pp. 2-6, Moscow/Russia;

[9] Khusanov I., Babaev S., Ravshanov S., Rajabova V., (2011), The effect of humidity on the grain strength of wheat of some varieties (Влияние влажности на предел прочности зерна пшеницы некоторых сортов), *Bread products (Хлебопродукты)*, Issue 2, pp. 54-55, Moscow/Russia;

[10] Lizhang X., Yaoming L., (2011), Modeling and experiment of threshing unit of stripper combine, *African Journal of Biotechnology,* Issue 10(20), pp. 4106-4113, Nigeria (DOI 10.5897/AJB10.2211);

[11] Moskovskij M.N., Kovaleva A.V., Kuren S.G., (2017), Using of the pneumatic blow method at the contactless threshing of grains, *ARPN journal of engineering and applied sciences*, pp. 6414–6418, Islamabad/Pakistan;

[12] Moskovskij M.N., Ignatenko I.V., Pahomov V.I., Lachuga YU.F., (2015), *The device for threshing the ear cultures*, Patent, No.2551163, Russia;

[13] Patel S.R., Varshney B.P., (2016), Modeling of wheat crop harvesting losses, *Agricultural Engineering International: CIGR Journal*, Issue 16(2), pp. 97-102, Paris/France;

[14] Shamin A.E., Zaikin V.P., Igoshin A.N., Lisina A.YU., (2018), Problems of grain harvesting in Russia (Проблемы уборки зерна в России), *Bulletin Nizhniy Novgorod State Engineering-Economic Institute (Вестник Нижегородского государственного инженерно-экономического института)*, Issue 6(85), pp. 130-138, Nizhniy Novgorod/Russia;

[15] Yuan J., Lan Y., (2007), Development of an Improved Cereal Stripping Harvester, *Agricultural Engineering International: CIGR Journal*, Issue 9, pp. 1-12, Paris/France.

# A MATHEMATICAL MODEL OF THE CUTTING PROCESS OF THE SUGAR BEET LEAFY TOPS WITHOUT A TRACER

/

# МАТЕМАТИЧНА МОДЕЛЬ ПРОЦЕСУ БЕЗКОПІРНОГО ЗРІЗУ ГИЧКИ ЦУКРОВОГО БУРЯКУ

**Bulgakov V.[1)], Ivanovs S.[2)], Pascuzzi S.[3)], Boris A.[4)], Ihnatiev Ye[5)] [1]**

[1)] National University of Life and Environmental Sciences of Ukraine;
[2)] Latvia University of Life Sciences and Technologies;
[3)] University of Bari Aldo Moro, Italy;
[4)] National Scientific Centre "Institute for Agricultural Engineering and Electrification" NAAS of Ukraine
[5)] Tavria State Agrotechnological University, Ukraine
*Tel.+37129403708, e-mail: semjons@apollo.lv*
*DOI: 10.35633/INMATEH-59-04*

***Keywords:*** *sugar beet, tops, harvesting, loss of mass*

## ABSTRACT

*A method is proposed for the assessment of the effect of the soil surface irregularities upon the loss of mass and the residues of the leafy tops during the sugar beet harvesting process. A new mathematical model is constructed and dependences of the loss of mass and the top residues are obtained depending on the distribution parameters of the soil surface irregularities. The established dependences of the loss of the root crop mass and the residues of the leafy tops on the root crops depending on the statistical distribution parameters of the soil surface irregularities and the cutting height of the tops without a tracer allowed justification of an agrotechnically acceptable level of mathematical expectation of the soil surface irregularities and the cutting height of the root crops without a tracer.*

## АНОТАЦІЯ

*Запропонована методика оцінювання впливу нерівностей поверхні ґрунту на втрати маси і залишки гички на головках коренеплодів в процесі збирання цукрового буряку. Розроблена нова математична модель та отримані нові формули втрат маси і залишків гички в залежності від параметрів розподілу нерівностей поверхні ґрунту. Встановлені залежності втрат маси коренеплодів і залишків гички на головках коренеплодів в залежності від параметрів статистичного розподілу нерівностей поверхні ґрунту і висоти безкопірного зрізу гички дозволили обґрунтувати агротехнічне допустимий рівень математичного очікування нерівностей поверхні ґрунту і висоти безкопірного зрізу коренеплодів цукрового буряку.*

## INTRODUCTION

The production of sugar beet and sugar is an important branch of agriculture in the leading states of Europe and America (*Marlander B. et al, 2018; Maurus K, et al., 2018, Rajaeirfar M. et al., 2019*). Despite the high technical level of development of the modern beet harvesting machinery, there are problems in the process of sugar beet production that need quick solution (*Lilleboe D., 2014, Merkes R., 2001*). In particular, at the stage of the sugar beet harvesting there are significant losses of the crop (more than 5%), and soiling of the pile of root crops (more than 5%) (*Carenko O., Jacun S., 2000; Hoffmann C., 2018*). These disadvantages are caused by many factors. However, the main ones are the imperfect technical level of the working tools separating the leafy tops of the sugar beet. It has been found out that increased soiling of a root crop pile with the leaves only by 1% above the agrotechnical requirements reduces the sugar output by 0.1%, and, when storing in clamps with a leafy content of about 4%, the average daily sugar losses amount to 0.02% (*Martynenko V.,1996, Zuev N.,1988; Bulgakov V. et al., 2016*). Therefore, an important scientific and technical problem is to reduce the loss of mass and residues of the leaves on the root crops. It has been clarified that the soil surface irregularities have a significant impact upon the accuracy of the cutting height of the sugar beet tops without a tracer; however, there are no studies on how they affect the quality indicators of the separation process of the beet tops (*Pogorelyi L, Tatjanko N., 2004; Ivančan, S. et al., 2002*).

[1] *Bulgakov V., Prof. Ph.D. Eng.; Ivanovs S., Ph.D. Eng.; Pascuzzi S., Prof. Ph.D.; Boris A., Ph.D. Eng.; Ihnatiev Ye, Ph.D. Eng.*

A mathematical model is known for predicting the losses of the sugar-bearing mass and the amount of the top residues (*Martynenko V., 1996, Bulgakov V. & al., 2015*) on the root crops depending on the cutting height without a tracer and the statistical distribution of the protrusion heights of the root crop heads. However, a significant disadvantage of this model is the assumption that the surface of the soil is absolutely flat. Under real conditions, due to imperfect agrotechnics of soil cultivation and many other factors, there are significant soil surface irregularities that have an adverse effect upon the regulation accuracy of the cutting height without a tracer. Therefore, establishment of dependencies between the soil surface irregularities and the loss of mass of the root crops, and the foliage residues on them is an important scientific and practical task. The aim of this work is to develop a mathematical model of cutting the sugar beet tops without a tracer, taking into account the soil surface irregularities. Application of such a model in designing will help reduce the loss of mass of the crop and the residues of the leafy tops in the heap of the root crops.

## MATERIALS AND METHODS

In order to establish a relationship between the soil surface irregularities and the performance quality of the top removing machines, the following assumptions were made: for the base (reference) surface we choose a conditional averaged plane of the soil irregularities (Fig. 1), in relation to which the irregularities of the soil were measured, and their distribution does not contradict the normal law. The heights distribution of the protruding root crop heads relative to the soil surface does not deny the normal law either. The top cutting tools move in parallel to the averaged plane of the soil surface irregularities. Let us consider the cutting process of the sugar beet tops without a tracer, taking into account the soil surface irregularities on which they are located. Since in the well-known model (*Bulgakov et al., 2015*) an absolutely flat surface of the soil is studied, then under real conditions, due to the soil irregularities (depressions and protrusions), an error occurs in setting the height of cutting. To state this error, we consider the following design flow chart (Fig. 1). Let the location of an arbitrary sugar beet root, located in the soil, has deviation from the soil surface *Δh*. It can take positive values (protrusions) and negative values (depressions). We will denote the protrusion height of the root crop head relative to the averaged plane as $h_k$, and the protrusion height of the root crop head relative to the soil surface as *h*. The root crop cutting plane relative to the averaged line of the soil surface irregularities will be at height $h_z$.

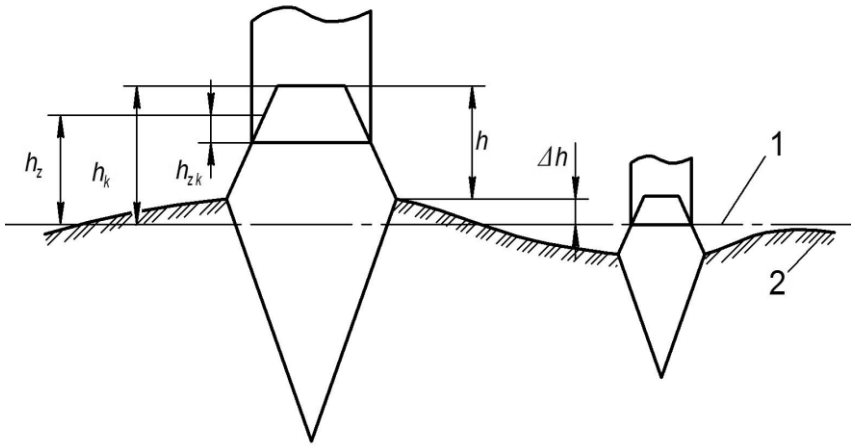


**Fig. 1 – A design flow chart of cutting the sugar beet tops without a tracer, taking into account the soil surface irregularities**
*1 – the averaged plane of the soil surface irregularities; 2 – the surface of the soil irregularities*

To determine the losses of the sugar-bearing mass and the amount of the residues of the tops of an arbitrary sugar beet root, we will determine the thickness of the cut layer of the root crop head $h_{zk}$.
To determine the loss of the sugar-bearing mass and residues of the tops of an arbitrary sugar beet root crop, we will determine the thickness of the cut layer of the root head $h_{zk}$.

$$h_{zk} = h_k - h_z, \quad (1)$$

or

$$h_{zk} = (\Delta h + h) - h_z. \quad (2)$$

Values *Δh* and *h* constitute a distribution system of random values the geometric interpretation of which can be represented using the distribution density (*Kallenberg, 2005*).

The distribution density of a system of two random values according to (*Kallenberg, 2005*) is determined by the expression:

$$f(\Delta h,h)=\frac{\partial^2 F(\Delta h,h)}{\partial \Delta h \partial h}, \quad (3)$$

where $F$ ($\Delta h$, $h$) – the probability function of a combination of random values $\Delta h$ and $h$.

We select an arbitrary region from the range ($A$, $B$; $A_g$, $B_g$) of size $n$. We take the area of the protrusion height from $A$ to $B$, and the area of the soil irregularity distribution from $A_g$ to $B_g$, and divide them into $n$ intervals. Then the probability of occurrence of a region with borders ($h_i$, $h_{i+1}$) ($\Delta h_j$; $\Delta h_{j+1}$) according to (*Bulgakov et al., 2015*) will be equal to:

$$P(\Delta h_j,h_i)=\int_{\Delta h_j}^{\Delta h_{j+1}}\int_{h_i}^{h_{i+1}} f(\Delta h_j,h_i)\,d\Delta h_j\,dh_i\,. \quad (4)$$

Taking into consideration dependence (4), we will write expressions to determine the losses of the sugar-bearing mass $B_{ji}$ and the amount of the residues of the tops $G_{ji}$ for an arbitrary region ($h_i$, $h_{i+1}$; $\Delta h_j$, $\Delta h_{j+1}$). We have for $B_{ji}$:

$$B_{ji}=NP(\Delta h_j,h_i)\rho f\left(\frac{\Delta h_j-h_i}{2}\right), \quad (5)$$

where $N$ – the quantity of the root crops per 1 ha, pcs·ha$^{-1}$;

$P$ – probability of occurrence of root crop head with location parameters $\Delta h_j,h_i$;

$\rho$ – the density of the sugar beet roots, kg·m$^{-3}$;

$f$ – the function of the volume of the cut root crop head, m$^3$.

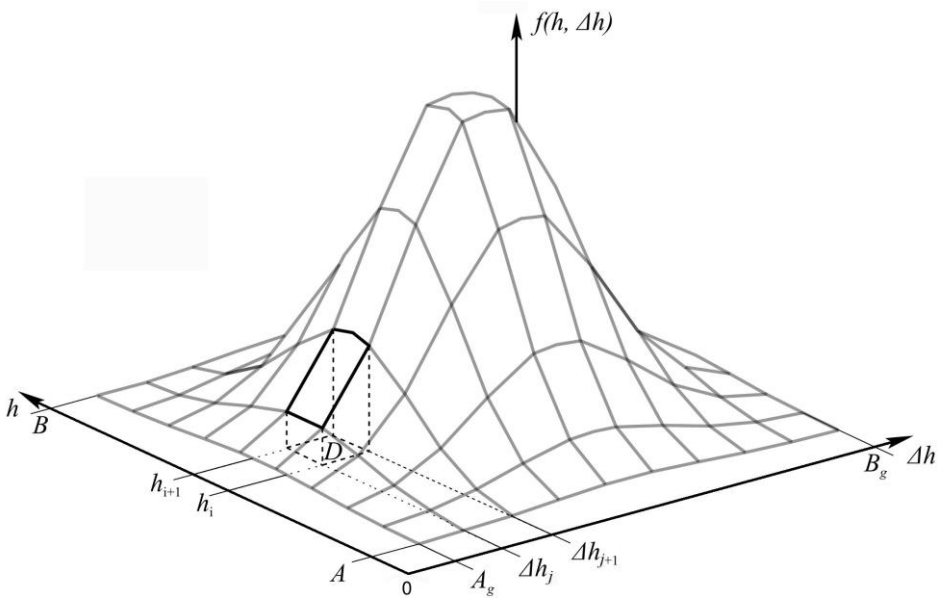


**Fig. 2 – A model of the distribution density of the systems of two random values according to the normal law**

Accordingly, for $G_{ji}$:

$$G_{ji}=NP_g(\Delta h_j,h_i)\rho_g f_g\left(\frac{\Delta h_j-h_i}{2}\right), \quad (6)$$

where $P_g$ – probability of occurrence of root crop head with location parameters $\Delta h_j,h_i$;

$\rho_g$ – the density of the sugar beet tops, kg·m$^{-3}$;

$f_g$ – the function of the volume of tops residues, m$^3$.

In general, for the entire distribution region of the systems of random values $\Delta h_j$ and $h_i$ with the statistical characteristics of the protrusion heights distribution of the root crops $m$ and $\sigma$, and the soil surface irregularities $m_g$ and $\sigma_g$, the losses of the sugar-bearing mass and the amount of the top residues will constitute ($m$, $m_g$ – mathematical expectation, mm; $\sigma$, $\sigma_g$ – mean-square distribution, mm):

$$B = \sum_{j=A_g}^{B_g} \sum_{i=A}^{B} NP(\Delta h_j, h_i) \rho f\left(\frac{\Delta h_j - h_i}{2}\right), \quad (7)$$

$$G = \sum_{j=A_g}^{B_g} \sum_{i=A}^{B} NP_g(\Delta h_j, h_i) \rho_g f_g\left(\frac{\Delta h_j - h_i}{2}\right). \quad (8)$$

Next, we will fix the value of the distribution characteristics of the losses of the sugar-bearing mass and the top residues on the root crops of the mathematical expectation $m$ and the mean-square distribution $\sigma$, and will construct dependencies $B$, $G$ upon the distribution characteristics of the surface irregularities $m_g$ and $\sigma_g$. To this end, we developed a new algorithm for the mathematical model of the cutting process of the sugar beet tops without a tracer, taking into consideration the soil surface irregularities (Fig. 3).

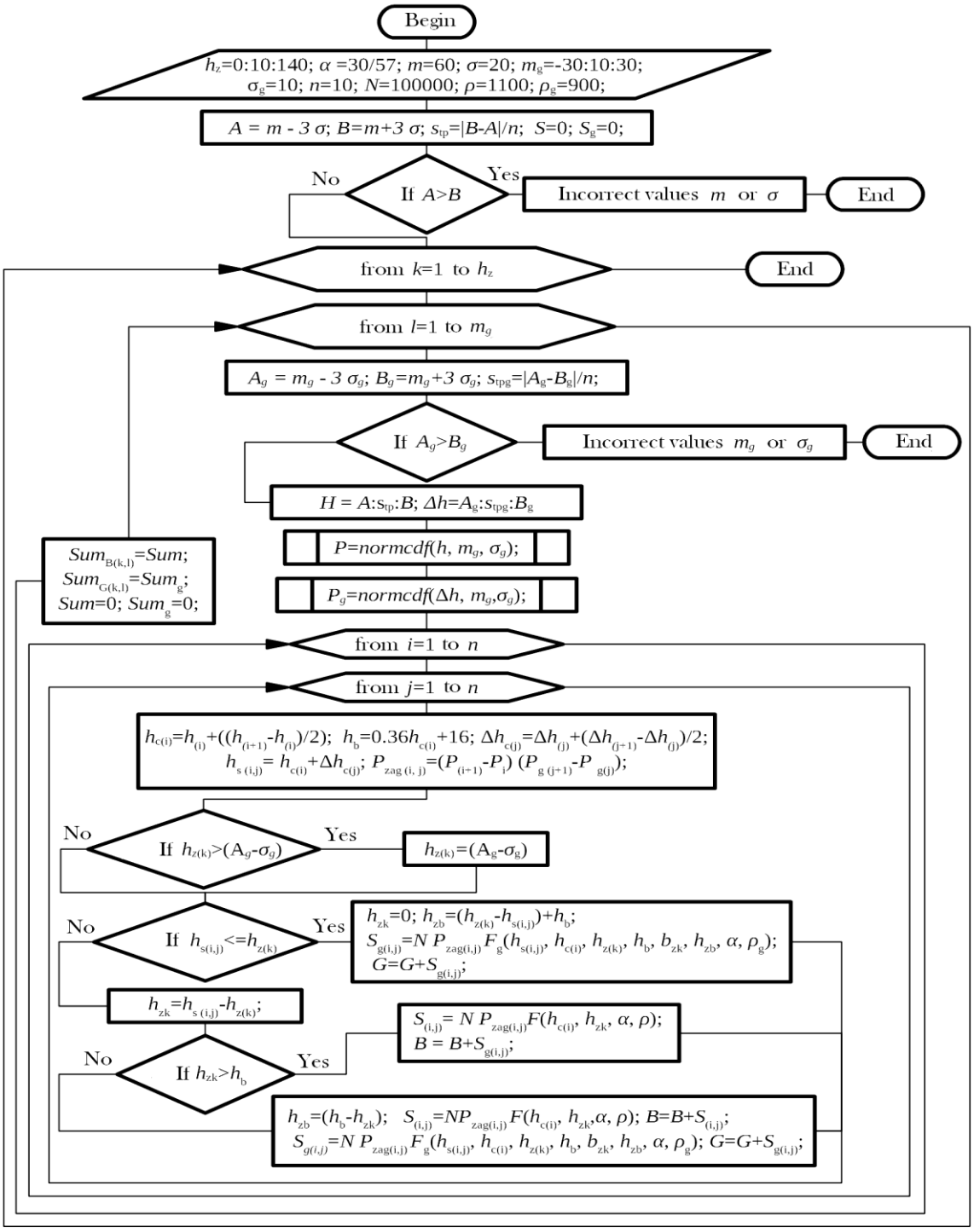


**Fig. 3 – The algorithm of the mathematical model of the cutting process of the sugar beet tops without a tracer, taking into consideration the soil irregularities**

The essence of this algorithm is as follows:

1) Preparation and introduction of the following input data and variable factors of the model*:* $h_z$ = (0: 140) – the variation range of the cutting height without a tracer relative to the averaged row line with a 10 mm step, mm; $\alpha = 30^o$ – the angle of the taper of the root crop, degree; $m$ = 60 is the mathematical expectation of the protrusion height of the root crop heads with respect to the soil irregularities; σ = 20 – the mean-square deviation of the protrusion height of the root crop heads relative to the soil surface irregularities; $m_g$ = (-30: 30) – the variation range of the mathematical expectation of the distribution of the soil surface irregularities relative to the averaged plane, mm (Fig. 2); $\sigma_g = 10$ – the mathematical expectation of the distribution of the soil surface irregularities relative to the averaged plane, mm; $n$ = 10 – the discreteness of the model; $N$ = 100000 – the quantity of the root crops per 1 ha, units; $\rho$ = 1100 – the density of the sugar beet roots, kg·m$^{-3}$; $\rho_g$ = 900 – the density of the sugar beet tops, kg·m$^{-3}$.

2) Calculation of the limits of the protrusion height distribution

$A = m - 3\sigma$; $B = m + 3\sigma$.

3) Division of the range $h = (A; B)$ into intervals with a step $s_{tp}$:

$$s_{tp} = \frac{|B - A|}{n} \tag{9}$$

4) Starting the cycle for each element of the range $h_z$ = (0: 140).

5) Starting the cycle for each element of the range $m_g$ = (-30: 30).

6) Division of the range $\Delta h = (A_g ; B_g)$ into intervals with a step $s_{tg}$:

$$s_{tp} = \frac{|B_g - A_g|}{n} \tag{10}$$

7) Calculation of the value of the integral function for ranges ($A$; $B$) ($A_g$; $B_g$) by integrating, using the Simpson method:

$$P = f(h, m, \sigma) \tag{11}$$

$$P_g = f(\Delta h, m_g, \sigma_g) \tag{12}$$

8) Starting the cycle for each value $h$.

9) Starting the cycle for each value $\Delta h$.

10) Determination of the average value of the interval ($h_i$ ; $h_{i+1}$) $h_{ci}$ :

$$h_{ci} = h_i + \left( \frac{\Delta h_j - h_i}{2} \right) \tag{13}$$

11) Determination of the average value of the interval ($\Delta h_j$: $\Delta h_{j+1}$) $\Delta h_j$:

$$\Delta h_j = h_i + \left( \frac{\Delta h_{j+1} - h_i}{2} \right) \tag{14}$$

12) Determination of the height of the base of the green leaves $h_b$:

$$h_b = 0.36\, h_{ci} + 16 \tag{15}$$

13) Determination of the protrusion height of the root crop heads relative to the averaged plane $h_{s(i,j)}$:

$$h_{s\,(i,j)} = h_{ci} + \Delta h_{cj} \tag{16}$$

14) Determination of the occurrence probability of a combination of intervals ($h_i$ ; $h_{i+1}$) and ($\Delta h_i$ ; $\Delta h_{i+1}$) $P_{zag}$:

$$P_{zag\,(i,\,j)} = (P_{i+1} - P_i) \cdot (P_{g\,j+1} - P_{gj}) \tag{17}$$

15) If the cutting height of the root crop heads relative to the averaged plane $h_{z\,(k)}$ is less than ($A_g$ – $\sigma_g$), then:

$$h_{z(k)} = (A_g - \sigma_g)$$

16) If the protrusion height relative to the averaged plane $h_{s\,(i,\,j)} <= h_{z\,(k)}$ is less than the current cutting height, then the root crop is not cut off $h_{zk}$ = 0. We calculate the height of the base of the green leaves:

$$h_{zb} = (h_{z(k)} - h_{s(i,j)}) + h_b \tag{18}$$

We determine the amount of the top residues for the combination of intervals ($h_i$ ; $h_{i+1}$) and ($\Delta h_i$ ; $\Delta h_{i+1}$):

$$S_{g(i,j)} = N\, P_{zag(i,j)}\, F_g(h_{s(i,j)}, h_{c(i)}, h_{z(k)}, h_b, b_{zk}, h_{zb}, \alpha, \rho_g) \tag{19}$$

We calculate the summary amount of the top residues for the current $h_z$ and $m_g$:

$$G = G + S_{g(i,j)} \tag{20}$$

17) If $h_{s\,(i,\,j)} > h_{z\,(k)}$, then we calculate the cutting height of the root crop:

$$h_{zk} = h_{s\,(i,j)} - h_{z(k)} \quad (21)$$

18) If $h_{zk} > h_b$, then the amount of the top residues is zero, and we calculate only the losses of the sugar-bearing mass:

$$S_{(i,j)} = N\,P_{zag(i,j)}\,F\,(h_{c(i)}, h_{zk}, \alpha, \rho) \quad (22)$$

We calculate the summary loss of the sugar-bearing mass for the current $h_z$ and $m_g$:

$$B = B + S_{g(i,j)} \quad (23)$$

19) If $h_{zk} < h_b$, then the cutting plane passes between the upper part and the base of the green leaves. We calculate the cutting height of the leafy tops:

$$h_{zb} = (h_b - h_{zk}) \quad (24)$$

We calculate the amount of the top residues:

$$S_{g(i,j)} = N \cdot P_{zag(i,j)} \cdot F_g(h_{s(i,j)}, h_{c(i)}, h_{z(k)}, h_b, b_{zk}, h_{zb}, \alpha, \rho_g) \quad (25)$$

We calculate the losses of mass:

$$S_{(i,j)} = N \cdot P_{zag(i,j)} \cdot F\,(h_{c(i)}, h_{zk}, \alpha, \rho) \quad (26)$$

We calculate the summary loss of the sugar-bearing mass for the current $h_z$ and $m_g$:

$$B = B + S_{g(i,j)} \quad (27)$$

We calculate the summary loss of the tops for the current $h_z$ and $m_g$:

$$G = G + S_{g(i,j)} \quad (28)$$

20) Formation of a matrix of values $B_k = B$, $G_k = G$.

## RESULTS AND DISCUSSIONS

As a result of the implementation of the above algorithm on a PC in the Octave 4.2 environment, there were obtained the following dependences of the losses of mass and the leafy top residues on root crops, depending on the height $h_z$ of cutting without a tracer and the mathematical expectation $m_g$ (Fig. 4).

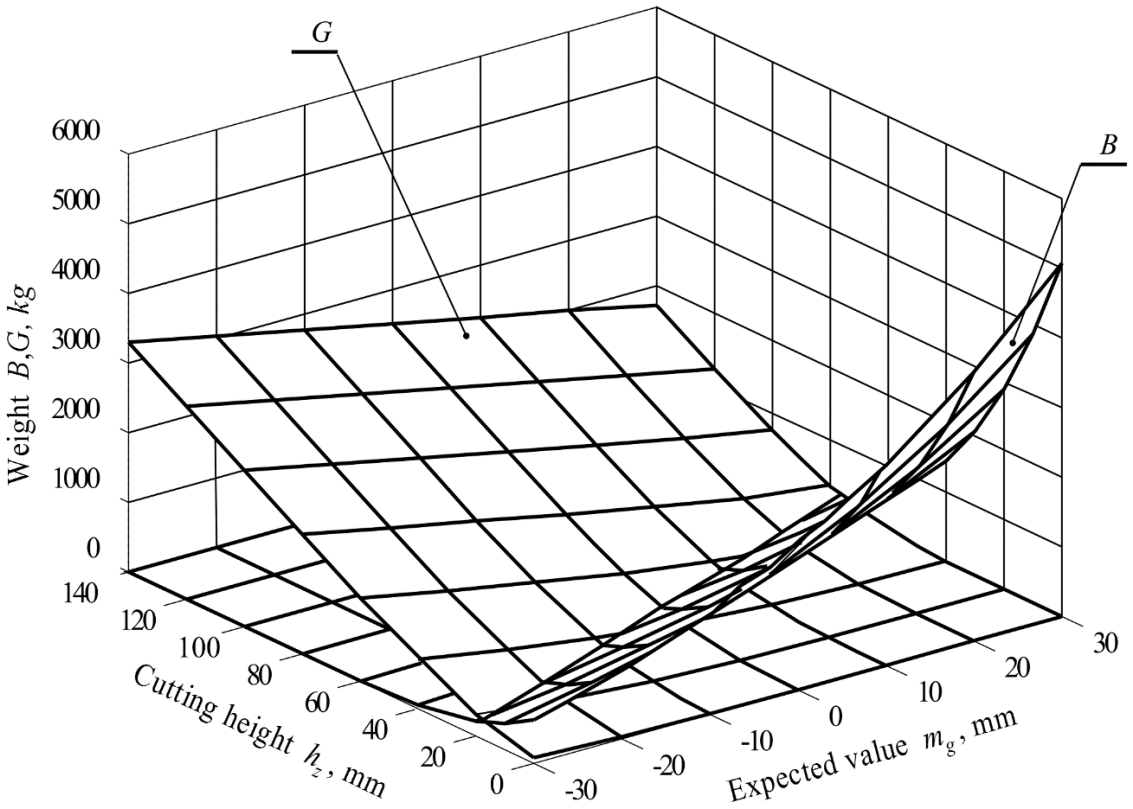


**Fig. 4 – Response surfaces of the losses of the sugar-bearing mass *B* and the residues of the foliage *G* on the root crops, depending on the cutting height $h_z$ of the root crops without a tracer and the mathematical expectation of the distribution of soil irregularities $m_g$**

From the resulting graphical dependences (Fig. 4) we see that under the condition that the cutting height is set at the upper level of the soil irregularities and the mathematical expectation is $m_g$ = 30 mm (which corresponds to increased soil roughness), the losses of mass will be 4 t·ha$^{-1}$ or 8% of the entire root crop yield, which exceeds the agrotechnical requirements for the losses of the root crop mass.

Nevertheless, with the indicator $m_g$ decreasing to -30 mm (30 mm below the averaged plane), the losses of the root crop mass will be 0.6 t·ha$^{-1}$ or less than 2%, which is not a violation of the agrotechnical requirements. But in this case the amount of the top residues exceeds the agrotechnical requirements, constituting more than 3 t·ha$^{-1}$ or 7% of the total root crop mass.

On condition that the cutting height is more than 60 mm, the losses of mass do not exceed the agrotechnical requirements of 2% of the total crop mass. However, the amount of the leafy tops on the root crops, if the cutting height is 60 mm, vary from 2 to 7%, in case $m_g$ = -30 mm and $m_g$ = 30 mm respectively. If the cutting height $h_z$ = 120…140 mm, the residues of the tops will constitute from 5 to 8%.

To confirm the adequacy of the developed new mathematical model for forecasting the losses of the sugar-bearing mass and the residues of the leafy tops during the sugar beet harvesting process without a tracer, preliminary experimental investigations of this process were carried out under real field conditions. The main characteristics of the working area where the experimental studies were conducted are as follows: the yield of the sugar beet root crops - 46.4 t · ha$^{-1}$; the yield of the leafy tops - 44.8 t · ha$^{-1}$; the number of the root crops is 11.2 · 104 pcs · ha$^{-1}$. Determination of the statistical distribution of the soil surface irregularities in the sugar beet inter-row spacing by means of a profilograph showed that they are of a high-frequency character with a period of 0.68 m and with an average amplitude of 0.058 m, which corresponds to the mathematical expectation, equal to $m_g$ = 30 mm.

Fig. 5 shows the results of experimental investigations (graphs) of the losses of the sugar-bearing mass (Curve 2) and tops residues on the sugar beet heads (Curve 4), processed by statistical methods on a PC, the investigations being carried out in five repetitions for the cutting heights without a tracer in a wide range, namely: 0, 20, 40, 60 and 80 mm. Here similar calculation results are shown for the developed mathematical model, carried out using a PC, which are presented by Curves 1 and 3, respectively, and obtained for the above conditions.

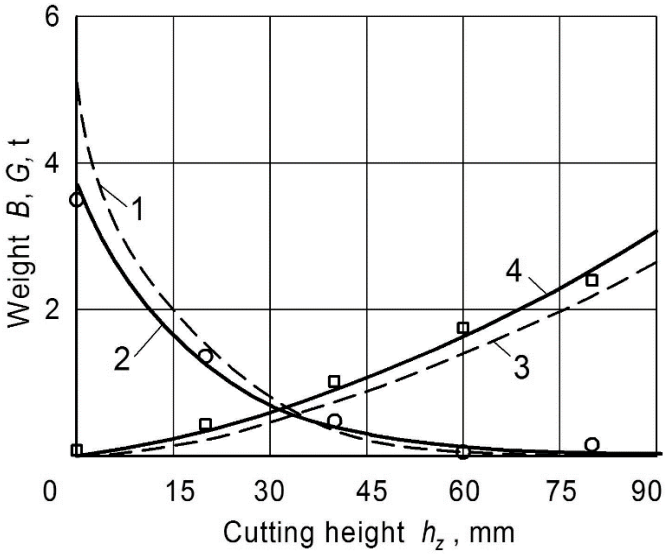


**Fig. 5 - Dependence of the theoretical (1, 3) and the experimental (2, 4) values of the losses of the sugar-bearing mass (1, 2) and the remains of tops on the root crops (3, 4) upon the cutting height without a tracer at $m_g$ = 30 mm**

Analysis of the curves of theoretical and experimental dependences presented in Fig. 5 shows that in all the five variants of setting of the topping aggregate, tested under real field conditions, the difference between the actual and calculated values does not exceed 7.8%. This coincidence of the experimental and the calculated data points to the adequacy of the developed mathematical model, which gives reason to use it for reliable justification of the cutting height without a tracer.

## CONCLUSIONS

A refined mathematical model has been developed for the cutting process of the sugar beet leafy tops without a tracer, taking into account the impact of the soil surface irregularities. Dependences of the loss of the root crop mass and the amount of leafy residues on the root crop tops have been established depending on the parameters of the statistical distribution of the soil irregularities and the cutting height of the tops without a tracer, which make it possible to justify an agrotechnically acceptable level of the mathematical expectation of the soil irregularities $m_g$ = -30...10 mm and the cutting height of the root crops $h_z$ = 60...70 mm. The conducted verification of the adequacy of the developed mathematical model shows a discrepancy between the experimental and the theoretical data not exceeding 8%, which gives reason to use it for the justification of the cutting parameters of the sugar beet tops without a tracer within the working range of the cutting heights $h_z$ = 20 ... 60 mm.

## REFERENCES


[1] Bulgakov V., Ivanovs S**.,** Adamchuk V., Boris A.., (2015), Mathematical model for determination of losses of sugar bearing-mass when sugar beet tops are removed, *Engineering for Rural Development,* Proceedings, Vol.14, pp. 41-45, Jelgava/Latvia;

[2] Bulgakov, V., Ivanovs, S., Ruzhylo, Z., Golovach, I., (2016), Theoretical investigations in cleaning sugar beet heads from remnants of leaves by cleaning blade, *Engineering for Rural Development,* Proceedings, Vol. 15, pp.1090-1097, Jelgava/Latvia;

[3] Carenko O., Jacun S., (2000), Mechanical and technological properties of agricultural materials, 93p, Kiev/Ukraine;

[4] Hoffmann C., (2018), Sugar beet from field clamps – harvest quality and storage loss. *Zuckerindustie*, Vol. 143, Issue 11, pp. 639-647, Berlin/Germany;

[5] Ivančan, S., Sito, S., Fabijanić, G. 2002 Factors of the quality of performance of sugar beet combine harvesters. *Bodenkultur,* 53(3), pp.161-166, Vienna/Austria;

[6] Kallenberg O., (2005), Probabilistic Symmetries and Invariance Principles. 510 p., Springer – Verlag, New York/USA;

[7] Lilleboe D., (2014), Optimizing defoliator & harvester performance, *The sugar beet grower*. July 2014, 53: pp. 6–13, Fargo/USA;

[8] Marlander B., Hoffmann C., Koch H.-J., Ladewig E., Niemann M., Stockfisch N., Varellmann M., Mahlein A.-K., (2018), Sustainable intensification – A quarter century of research towards higher efficiency in sugar beet cultivation [Nachhaltige Produktivitätssteigerung – ein Vierteljahrhundert Forschung für mehr Effizienz beim Anbau von Zückerruben], *Zuckerindustrie,* Vol. 143, Issue 4, April 2018, pp. 200-217, Berlin/Germany;

[9] Martynenko V., (1996), Substantiation of the design parameters of the root crop head cleaners, *Materials of the International Conference "Problems and Perspectives for the Development of the Beet Harvesting Machines"*, pp. 41-44., Vinnica/Ukraine;

[10] Maurus K., Ahmed S., Getz W., Kazda M., (2018), Sugar beet silage as highly flexible feedstock for on demand biogas production, *Zuckerindustrie*, Vol. 143, Issue 12, December 2018, pp. 691-698;

[11] Merkes R., (2001), 50 Jahre Produktionstechnik im Zuckerr. Benbau in Deutchland, *Zucker,* 4, pp. 214-217, Hannover/Germany;

[12] Pogorelyi L., Tatjanko N., (2004), Beet Harvesters, 232 p., Kiev/Ukraine;

[13] Rajaeirfar M., Sadeghzadeh Hemayati, Tabatabaei, M., Aghbashlo, M., Mahmoudi, S., (2019), A review on beet sugar industry with a focus on implementation of waste-to-energy strategy for power supply, *Renewable and Sustainable Energy*, Vol. 103, April 2019, pp. 423-442, Tamil Nadu/India;

[14] Zuev N., (1988), Cutting the Sugar Beet Heads without a Tracer, *Sugar beet*, 6. pp. 42-45, Moscow/Russia.

# IMPACT OF PARAMETERS OF AN AFTER-CLEANING CONVEYOR OF A ROOT CROP HARVESTER ON ITS PERFORMANCE
# /
# *ВПЛИВ ПАРАМЕТРІВ ДООЧИСНОГО ТРАНСПОРТЕРА КОРЕНЕЗБИРАЛЬНОЇ МАШИНИ НА ЯКІСНІ ПОКАЗНИКИ ЇЇ РОБОТИ*

**Hevko R.B.[1)], Tkachenko I.G.[1)], Rogatynskyi R.M.[1)], Synii S.V.[2)], Flonts I.V.[3)], Pohrishchuk B.V.[4)] [1]**

[1)]Ternopil Ivan Puluj National Technical University / Ukraine;
[2)]Lutsk National Technical University / Ukraine; [3)]Separated Subdivision of National University of Life and Environmental Sciences of Ukraine Berezhany Agrotechnical Institute / Ukraine; [4)]Ternopil National Economical University / Ukraine
*E-mail: r_hevko@ukr.net*
*DOI: 10.35633/INMATEH-59-05*

***Keywords:*** *after-cleaning conveyor, design and kinematic parameters, root crop cleaning, root crop harvester*

**ABSTRACT**

*The results of theoretical and experimental study of design and kinematic parameters impact of an after-cleaning rod conveyor with variable path of root crops on their cleaning quality indices are presented in the article. The values of allowable inclination angle of the conveyor intake unit taking into account rod web vibrations have been substantiated in the theoretical part. The impact of inclination angles of the conveyor sections, its linear velocity and the path velocity of loading conveyor scrapers and manufacturing clearances between them on the root crop harvester qualitative characteristics has been determined in the experimental part.*

**РЕЗЮМЕ**

*У статті наведено результати теоретичних і експериментальних досліджень впливу конструктивних і кінематичних параметрів доочисного пруткового транспортера із змінною траєкторією переміщення коренеплодів на показники якості їх очищення. В теоретичній частині обґрунтовано значення допустимого кута нахилу приймальної зони транспортера з урахуванням коливання пруткового полотна. В експериментальній частині встановлено вплив кутів нахилу ланок транспортера, його лінійної швидкості, а також швидкості переміщення скребків завантажувального транспортера і технологічних зазорів між ними на якісні показники роботи коренезбиральної машини.*

## INTRODUCTION

The solution to the problem of root crops quality cleaning and their damage reducing during mechanized harvest is possible due to the complex approach to the development of new root crop harvesters. Their lay-out diagrams will be based on the principle of combination of transport and technological operations to provide the careful attitude to the product under processing and to minimize the negative impact on the environment. Thus, while developing new root crop harvesters the basic ideas are those the introduction of which will provide the maximum separation of soil from the root crops. They will allow leaving the soil on the fields and minimize the degradation of upper humus layer.

Theoretical substantiation and experimental research of the above-mentioned processes and the choice of the most efficient design and kinematic parameters and operation modes of root crop harvesters were done in the papers *(Baranovsky V.M., Potapenko M.V., 2017; Bratucu Gh., Paunescu D.D., 2015; Tsarenko O.M., et al., 2003).*

The results of the study of root crops storage before their processing and agricultural materials transportation were highlighted in the papers *(Liebe S., Varrelmann M., 2014; Lyashuk O.L. et.al., 2015)*.

The procedures of experimental research on this issue are described in the following papers *(Bulgakov V.M. et al., 2000; Hevko, R. et al., 2018)*.

The elastic tools use aimed at reducing the transported material damage and finding the best parameters of the tools was highlighted in the articles *(Hevko R.B. et al., 2015; 2016)*.

[1] *Hevko R.B., Prof. DSc. Eng.; Tkachenko I.G., Assoc. Prof. Ph.D. Eng.; Rogatynskyi R.M., Prof. DSc. Eng.; Synii S.V., Assoc. Ph.D.Eng.; Flonts I.V., Assoc. Ph.D. Eng.; Pohrishchuk B.V., Prof. DSc. Econ.*

This paper follows the previous research described in the articles *(Hevko R.B. et al., 1998; Pavelchak O.B., Tkachenko I.G., Hladyo Y.B. et al., 2000; Tkachenko I.G., Hladyo Y.B., Hevko R.B. et al., 2000; Synii S.V. et al., 2018)*.

To solve the tasks dealing with the improvement of root crops cleaning quality and their minimum damage a design-technological scheme and a design of a root crop harvester after-cleaning conveyor including its parameters and operation modes substantiation are proposed.

## MATERIALS AND METHODS

To increase the root crops cleaning quality at their mechanized harvesting we suggest combining different functions, namely transportation, cleaning from soil and plants remains in one machine. An after-cleaning conveyor can be used in different root crop harvesters which are being developed or modernized.

Let's consider the interaction of an after-cleaning conveyor sections with the root crops thrashed heap. We assume that base coordinate system $Oxy$ refers to the machine where an after-cleaning conveyor is mounted. Centre O of the coordinate system coincides with the axis of a conveyor shaft, axis Ox is directed horizontally, a root crop motion is taking place in vertical plane $Oxy$ (Fig. 1).

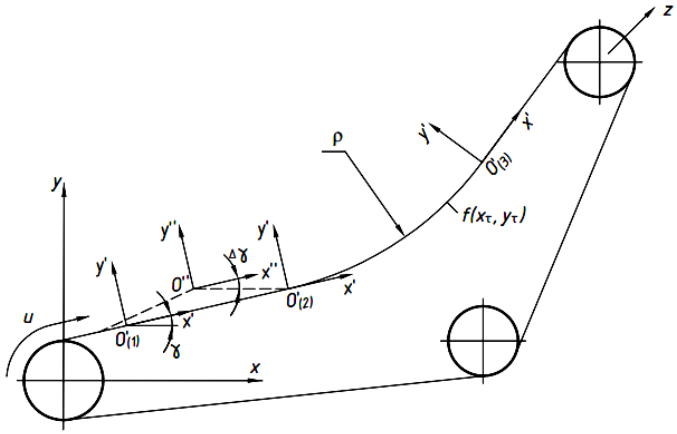


**Fig. 1 – Scheme of determining the parameters of conveyor web path**

On the line of flight path inclined at a running angle $\gamma$ with horizon we place in a certain point $O'(x_0'; y_0')$ the fixed, referred to base system $Oxy$, coordinate system $O'x'y'$ so that the axis $O'x'$ is directed towards the line of flight, and moving coordinate system $O''x''y''$ which is rigidly associated with the moving web where a scraper is fastened, in this case the axis $O''y''$ coincides with the plane of the scraper's location. We assume that at a certain period of time $t = 0$ the coordinate systems coincide. In a general case the coordinate system $O''x''y''$ is travelling referred to the system $O'x'y'$ with velocity $v_c$ which is the same as the conveyor web speed.

Besides, both the web and the system are vibrating along the axis $O'y'$ with a certain amplitude $A_\omega$, cyclic frequency $\omega_A$ and angular oscillations $\Delta\gamma$ of the activator with angle $\gamma$ absolute value change. Centre $O''$ of the system $O''x''y''$ in the system $O'x'y'$, will have running coordinates: $x_0'' = v_m t$; $y_0'' = A_\omega \sin(\omega_A t)\sin\gamma$. (Fig. 2).

Using the known matrix transformations of uniform coordinate systems, we obtain the following connection between the scraper coordinate system and the base coordinate system:

$$\begin{cases} x_c = x_A''\cos(\gamma+\Delta\gamma) - y_A''\sin(\gamma+\Delta\gamma) + x_O' + v_t t\cos\gamma - A_\omega \sin(\omega_A t)\sin\gamma; \\ y_c = y_A''\sin(\gamma+\Delta\gamma) - x_A''\cos(\gamma+\Delta\gamma) + y_O' + v_t t\sin\gamma - A_\omega \sin(\omega_A t)\cos\gamma. \end{cases} \quad (1)$$

The root crop hold on by the scraper is acted by the forces of reaction $N_i$ from the scraper and rods side, which in the scraper coordinate system $O''x''y''$ and, correspondingly in the base system $Oxy$ (Fig. 2) will be as follows:

$$\overline{N_i''} = N_1''(\cos\alpha_i''\cdot\bar{i} + \sin\alpha_i''\cdot\bar{j}); \qquad \overline{N}_i = N_i(\cos\alpha_i\cdot\bar{i} + \sin\alpha_i\cdot\bar{j}) \quad (2)$$

where directing angles $\alpha_i$ with angles $\alpha_i''$ are connected by the relationships $\alpha_i = \alpha_i'' + \gamma + \Delta\gamma$ or, in case of small angular oscillations of the scrapers ($\Delta\gamma = 0$), $\alpha_i = \alpha_i'' + \gamma$.

Now we study the possible root crop location on the conveyor web. We denote the web rod radius $r$, distance between rods – $a$; scraper height – $H$.

We assume the scraper width as $S = 2r$ taking into consideration the design and the radius of the scraper rounding is equal to the rod radius. To make calculations more simple, we take the parameter $h = H - r$ as the scraper height before the centre of rounding.

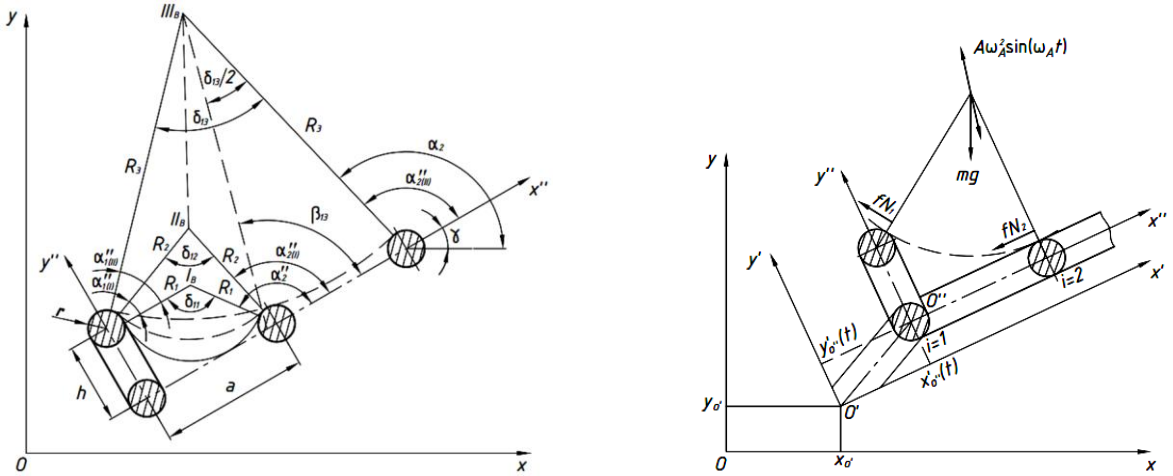


a) b)

**Fig. 2 – Options of a root crop place on the conveyor web (a) and a scheme of forces to find the equations of root crops movement at their transfer and after-cleaning (b)**

According to a root crop size some options of its place on the conveyor web in the coordinate system $O''x''y''$ (Fig. 2) are possible.

1. A root crop of radius $R$ is touching the scraper and the nearest rod surfaces. Such location is taking place when the centre of gravity coordinate $y_C$ of the root crop is less than $h$, $y_C \le h$. In this case the reactions from the scraper and the rod side are found by the dependence (2), where the direction angle of the activator reaction vector $\overline{N_1''}$, is equal to $\alpha_1''$ = 0, and vector $\overline{N_2''}$ is directed from the rod centre to the root crop centre and is found $\cos\alpha_2'' = 1 - a/(R+r)$; $\sin\alpha_2'' = \sqrt{2a(R+r) - a^2}/(R+r)$.

2. A root crop is touching the scraper edge and a rod ($y_C > h$). Then the root crop centre is found from the solution of the system of equations which determines the crossing point of two circles by radiuses $R + r$ in the centre of scraper rounding $O_S''(0; h)$ and in the rod centre $O_R''(a; 0)$. Hence, the equation of bisector of triangle passing through the root crop centre $A(x_A''; y_A'')$ will be $y'' = h/2 + (a/h)(x'' - a/2)$. Accordingly, the direction angles $\alpha_1''$ and $\alpha_2''$ vectors $\overline{N_1''}$ and $\overline{N_2''}$ will be $\alpha_1'' = \beta_{12} - \delta_{12}/2$ and $\alpha_2'' = \beta_{12} + \delta_{12}/2$, where $\beta_{12}$ – bisector angle of inclination, $\beta_{12} = \operatorname{arctg} a/h$; $\delta_{12}$ – angle between vectors $\overline{N_1''}$ and $\overline{N_2''}$. $\delta_{12}/2 = \arcsin[\sqrt{a^2 + h^2}/2(R+r)]$.

3. A root crop is touching simultaneously the scraper and two neighbouring rods. This option is possible only for those root crops the radius of which is equal to $R_3 = \sqrt{(a^2/h + h/2)^2 + a^2/4}$.

In this case the reactions of the conveyor components will be $N_1$, $N_2$ and $N_3$, and the coordinates of the root crop centre: $x_A'' = 3a/2$; $y_A'' = (2a^2 + h^2)/(2h)$. Accordingly, $\cos\alpha_i'' = (x_A'' - x_i)/(R+r)$; $\sin\alpha_i'' = (y_A'' - y_i)/(R+r)$, where $x_i$, $y_i$ – the coordinates of centres of the scraper and the rods rounding.

4. A root crop is touching the scraper edge and the next rod which is possible for big root crops ($R > R_3$). Similar to the second case, the direction angles $\alpha_1'' = \beta_{13} - \delta_{13}/2$; $\alpha_3'' = \beta_{13} + \delta_{13}/2$, where $\beta_{13} = \text{arctg}(2a/h)$; $\delta_{13}/2 = \arcsin[\sqrt{a^2 + (h/2)^2}/(R+r)]$.

When a root crop of circular section ($R = \text{const}$) is falling outside the scraper, its centre will be rotating in the coordinate system $O''x''y''$ against the centre of scraper's rounding with angular velocity $\omega_A = \text{d}(\Delta\alpha_t)/\text{d}t$ and the coordinates of its centre will be the following $x_A'' = (R+r)\cos(\alpha_t'' + \Delta\alpha_t)$, $y_A'' = (R+r)\sin(\alpha_t'' + \Delta\alpha_t)$. Accordingly, linear velocity components of a root crop will be the following: $\dot{x}_A'' = -y_A''\omega_\alpha$; $\dot{y}_A'' = x_A''\omega_\alpha$, and acceleration components: $\ddot{x}_A'' = y_A''\dot{\omega}_\alpha + x_A''(\omega_\alpha)^2$; $\dot{y}_A'' = x_A''\dot{\omega}_\alpha + y_A''(\omega_\alpha)^2$. Angular velocity of a root crop rotation: $\omega_K'' = (1 + r/R)\omega_\alpha$.

In the root crops intake area the motion path is described by a rectilinear function $x_T = x_O' + (u - u_O)\cos\gamma_\alpha$; $y_T = y_O' + (u - u_O)\sin\gamma_\alpha$, where $u$ – path length parameter, $u = u_0 + v_t t$.

In the transition section the conveyor path is considerably curved and has a variable angle $\gamma_t$. We assume that, the path is always curved, i.e. the trajectory is described by a circle of radius $\rho$. The running angle of the path inclination at initial angle $\gamma_{OI}$ is equal to $\gamma_t = \gamma_{OI} + v_t t/\rho$ and equations of the path are written as $x_T = x_O' + \rho[\sin(\gamma_{OI} + v_t t/\rho) - \sin\gamma_{OI}]$, $y_T = y_O' + \rho[\cos(\gamma_{OI} + v_t t/\rho) - \cos\gamma_{OI}]$.

Linear and angular velocities and acceleration of the system $O''x''y''$ will be determined by the dependencies

$$\dot{x}_{O''}'' = v_t\cos(\gamma_{OI} + v_t t/\rho); \quad \dot{y}_{O''}'' = v_t\sin(\gamma_{OI} + v_t t/\rho); \quad \dot{\gamma}_t = v_t/\rho; \tag{3}$$

$$\ddot{x}_{O''}'' = -(v_t^2/\rho)\sin(\gamma_O + v_t t/\rho); \quad \ddot{y}_{O''}'' = -(v_t^2/\rho)\cos(\gamma_O + v_t t/\rho); \quad \ddot{\gamma}_t = 0. \tag{4}$$

In the area, where root crops start rolling down the conveyor web the angle of its inclination is equal to $\gamma_\beta = \beta$ and is determined from the condition of capture of soil and plant remains of the trashed heap and does not include the root crops grab.

In the intake area the necessary requirement of the transporter operation is that all root crops, including the biggest ones, will not lose the contact with their supports (a scraper and a rod). This condition is met when $N_1 > 0$ and $N_2 > 0$. As $\gamma > 0$, it is possible when $N_3 > 0$.

Taking into account that $\alpha_i = \alpha_i'' + \gamma$ and $N_3 > 0$, the condition of the root crop contact with the supports is written as: $\gamma \le \pi/2 - \alpha_1''$.

Taking into account the acceleration force of the conveyor web during its vibration the equilibrium equation is written as:

$$\begin{cases} N_1\cos\alpha_1 + N_3\cos\alpha_3 + mA\omega_A^2\sin(\omega_A t)\sin\gamma = 0; \\ N_1\sin\alpha_1 + N_3\sin\alpha_3 + mA\omega_A^2\sin(\omega_A t)\cos\gamma = mg. \end{cases} \tag{5}$$

For the case $N_3 = 0$ from the solution (5) $(A\omega_A^2/g)\sin(\omega_A t)\cos(\alpha_1 + \gamma) = \cos\alpha_1$. Taking into account that $\alpha_i = \alpha_i'' + \gamma$, the condition of the root crop contact with the supports is written as

$$\cos(\alpha_1'' + \gamma) = (A\omega_A^2/g)\sin(\omega_A t)\cos(\alpha_1'' + 2\gamma). \tag{6}$$

Hence, the condition of the root crop contact with the supports which depends on the inclination angle of the conveyor in the intake area, is found from the equation solution (6) for the case when $\sin(\omega_A t) = -1$.

Limiting value of angle $\gamma_m$, when the root crop losses ties with the supports is found by the approximating dependence $\gamma_m = (0{,}5\pi - \alpha_1'')(1+k)/(1+2k)$, where $k = A\omega_A^2/g$ – coefficient of impact of conveyor web lateral oscillations.

Experimental study on determining the root crops losses, damage and dirtiness was conducted on a combination of an after-cleaning conveyor together with a drag-type loader. The scheme of their parameters control is given in Fig. 3 a.

The conveyor was mounted on a tractor-drawn three-row root crop harvester the design and operation principle of which, as well as the program and methods of experimental research are given in the paper *(Hevko R.B., Tkachenko I.G., Synii S.V., et al., 2016)*.

An after-cleaning conveyor and a loader are mounted on the root crop harvester frame 1. They are running simultaneously carrying and cleaning the root crops. The after-cleaning conveyor has a frame with upper *9* and lower *12* sections which are articulated. The main transporting element is the web with rods *8* which is driven by power shaft *7*, the head pulleys of which are made with grooves for the teethed belt clutching. The bearing supports of the driven shaft are fixed on the frame *1* by shims *6* enabling to estimate the position of the after-cleaning conveyor relative to the frame *1* and separating shaft *18*. Thus, the clearance $l$ adjustment is taking place to study its impact on the quality characteristics of the after-cleaning system operation. Curve *11* and turning *16* sheaves serve for the change of the web motion direction, and supporting rollers *13* provide the proper shape of the web *8* in the section where the root crops are leaving the after-cleaning conveyor for the loader. The axes of supporting rollers *13* are fastened on the side-frames *14* where four holes are made in radial direction relative to the drums axes *4* to change the value of concentric clearance *S*.

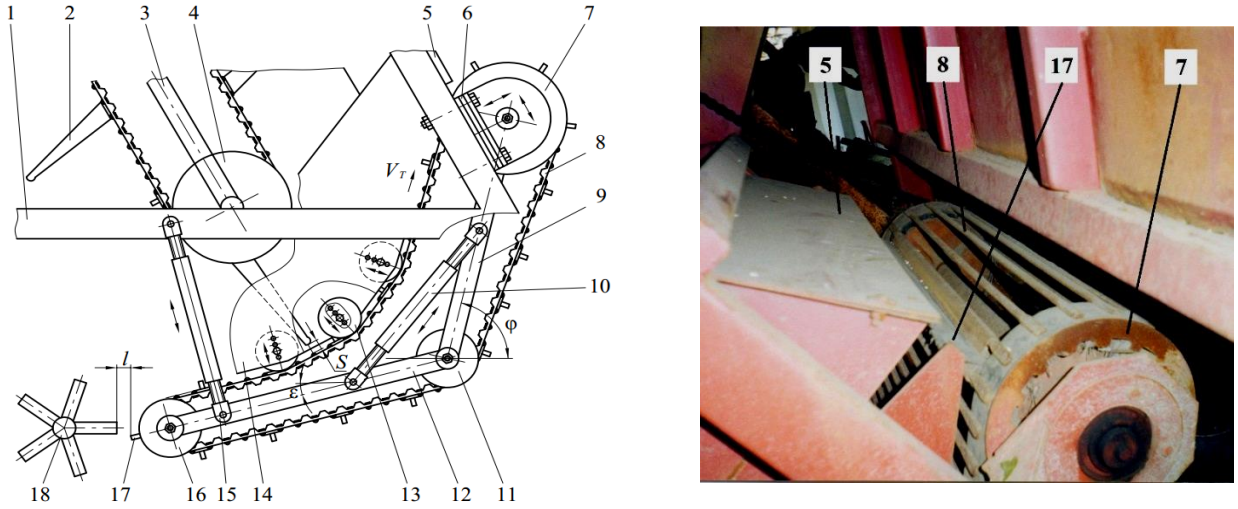


a) b)

**Fig. 3 – Scheme of parameters control of after-cleaning conveyor and loader (a) and general view of after-cleaning conveyor upper section (b)**

The web *8* of the after-cleaning conveyor is equipped with the elastic scrapers *17* for the cut-off soil and plants remains unloading on the harvested part of the field. Screw couplings *10* and *15* are used for the after-cleaning conveyor fixed on the machine frame and for the angles ε and φ change.

The loader consists of a frame *3* and drums *4* including the web with scrapers *2*. The loader is mounted on the frame *1* with possibility of vertical and horizontal shifting. Conveyor casing *5* is used for preventing the root crops to be thrown away from the machine while they are being cleaned on the unloading section of the after-cleaning conveyor.

## RESULTS

### *Results of theoretical investigation*

Moving from theoretical to experimental research we assume that the angle ε is equal to the angle α-α″, and angle $\gamma_m$ = φ, as it is shown in Fig.3. Dependencies of angle ε=α-α″ of reaction $N_1$ of the scraper and limiting angle of inclination $\gamma_m$ = φ of the after-cleaning conveyor intake unit on the root crop radius at the web vibration with different values of the impact coefficient are given in Fig. 4, 5.

According to the data of experimental research, the coefficient of lateral oscillations impact is widely ranging depending on the operation modes, oscillations measuring point and is equal to $k$ = 0.2…0.9.

For guaranteed root crops keeping of all size on the after-cleaning conveyor intake unit in the loading section its inclination angle γ must be within the range of 0…30°.

Taking into account possible elastic angular displacement of the scraper which, according to the experimental data, does not exceed $\Delta\gamma = 5°$ under the equivalent load, the proposed angles of inclination of the intake unit are $\gamma < 25°$. For the unloading section free rolling down the web of all conditioned crops is the condition of the after-cleaning conveyor efficient operation.

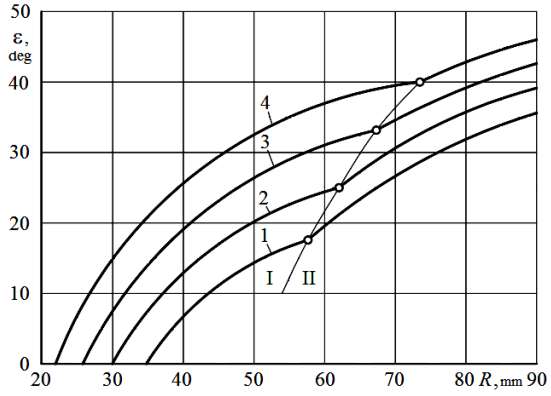


**Fig. 4 – Curves of direction angle ε reaction $N_1$ scraper of different height $H$ and root crop radius $R$:**
*1 – $H$ = 45 mm; 2 – $H$ = 40 mm; 3 – $H$ = 35 mm; 4 – $H$ = 30 mm; I, II – respectively areas of a root crop interaction with a scraper and the following rod*

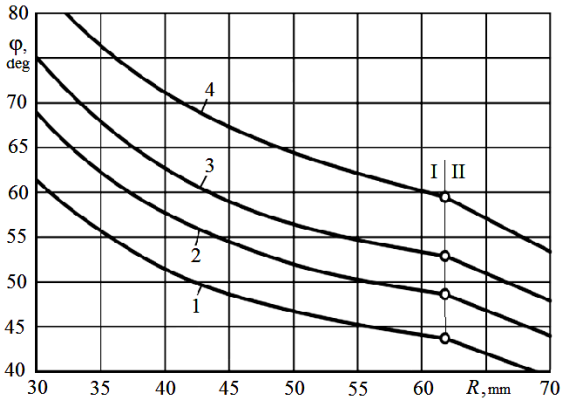


**Fig. 5 – Curves of limit value of inclination angle φ of intake unit at web vibration with coefficient of impact $k$:**
*1 – $k$ = 1; 2 – $k$ = 0,5; 3 – $k$ = 0,3; 4 – $k$ = 0,1; I, II – respectively areas of a root crop interaction with a scraper and the following rod*

Theoretical dependencies can be used for the choice of tools parameters while conducting experimental research.

***Results of experimental research***

According to the results of theoretical research the experiments have been conducted taking into account the recommended angles of inclination of lower section ε (range of value change ε = 10…24 deg.) and upper section of after-cleaning conveyor (range of value change φ = 50…80 deg.).

The experiment-based response surfaces describing dependencies of losses ($L_r$), damage ($D_r$) and dirtiness ($W_r$) of root crops are presented in Fig. 6, 7 and 8.

The obtained regression equations to find $L_r$, $D_r$ and $W_r$ are written as:

$$L_r = 0.074 + 0.007\varepsilon + 0.032\varphi - 0.00024\varphi^2 + 0.00058l^2, \quad (10)$$

$$D_r = 4.15 + 0.05\varepsilon - 0.026\varphi - 0.0009\varepsilon S + 0.00025\varphi^2 - 0.00015\varphi S + 0.00012S^2, \quad (11)$$

$$W_r = 11.515 + 0.113\varphi - 14.36V_T - 0.05\varepsilon V_T - 0.0008\varphi^2 + 6.25\,V_T^2. \quad (12)$$

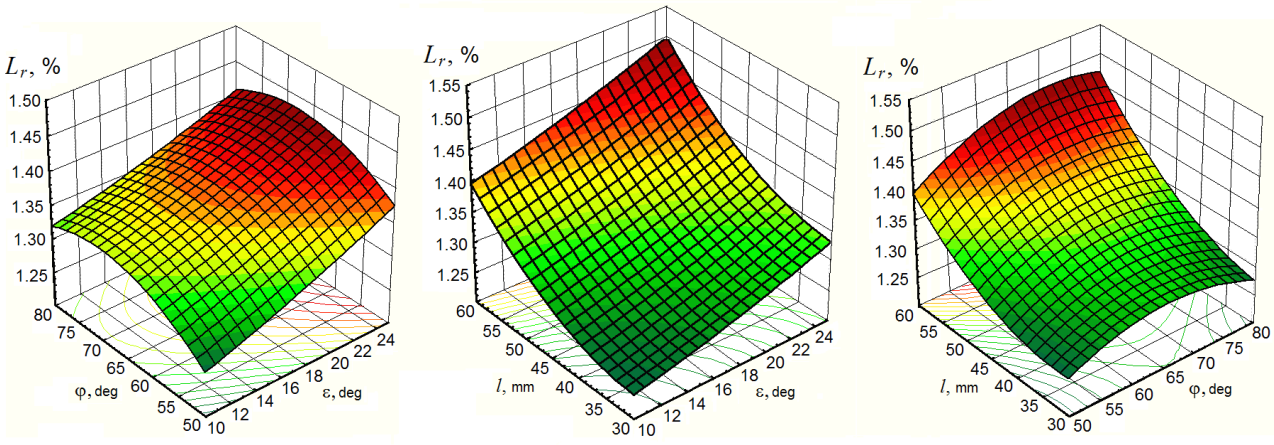


**Fig. 6 – Response surfaces of root crops losses**
*a) $L_r = f(\varphi; \varepsilon)$; b) $L_r = f(l; \varepsilon)$; c) $L_r = f(l; \varphi)$*

Having analyzed the response surfaces of root crops losses $L_r$ it was found that apart from angles ε and φ the clearance size $l$ has the biggest influence on the parameter under discussion, as when the clearance is more than 45 mm the root crops losses are much bigger.

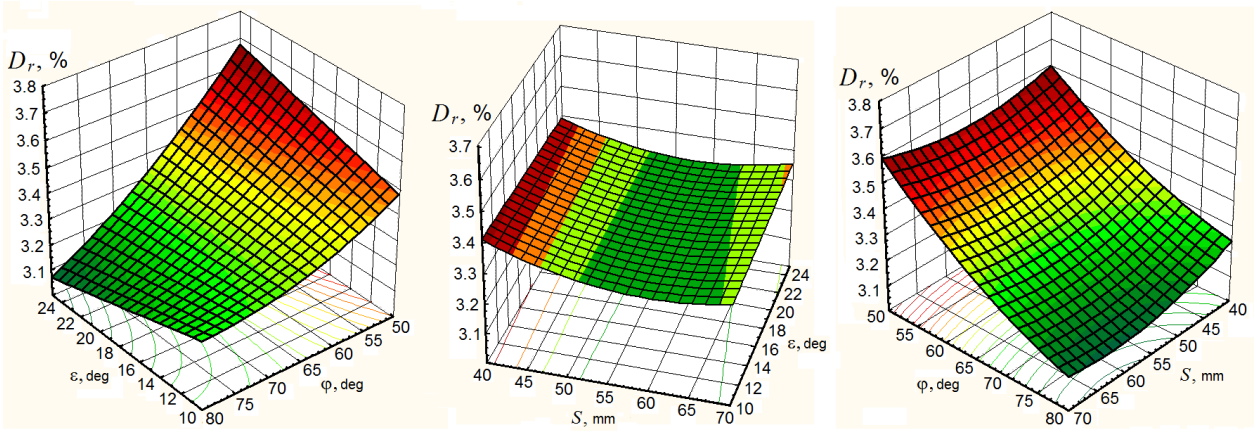


a) b) c)

**Fig. 7 – Response surfaces of root crops damage**

*a)* $D_r = f(\varepsilon; \varphi)$; *b)* $D_r = f(S; \varepsilon)$; *c)* $D_r = f(\varphi; S)$

Having analyzed the response surfaces of root crops damage $D_r$, it was found that apart from angles ε and φ the clearance size $S$ influences the parameter under discussion. Thus, in case when $S$ = 50…60 mm the root crops damage is the minimal one.

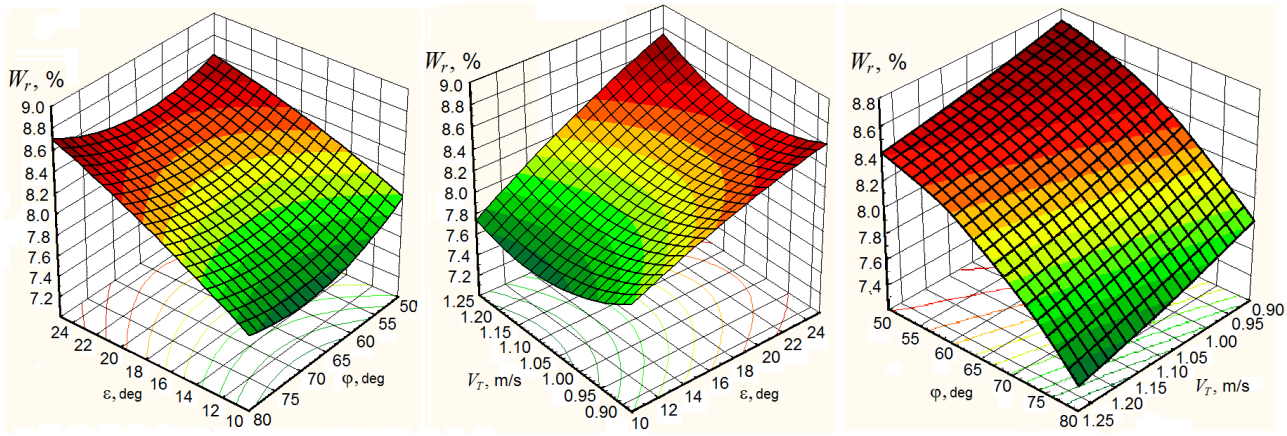


a) b) c)

**Fig. 8 – Response surfaces of root crops dirtiness:**

*a)* $W_r = f(\varepsilon; \varphi)$; *b)* $W_r = f(V_T; \varepsilon)$; *c)* $W_r = f(\varphi; S)$

Having analyzed the response surfaces of root crops dirtiness $W_r$, it was found that apart from angles ε and φ the linear velocity of after-cleaning conveyor belt $V_T$ has the biggest influence on the parameter under discussion. The root crops are the most cleaned at the conveyor velocity $V_T$ = 1.25 m/s, which can be explained by more active running of root crops on the belt surface and soil and plants remains are thrown to the field.

## CONCLUSIONS

The paper under consideration presents a mathematical model of a root crop harvester after-cleaning conveyor operation and conducted experimental research which enabled to make integrated assessment of interaction of root crops and after-cleaning conveyor sections at different operation modes and finds its main design parameters. Within the known range of oscillations of the after-cleaning conveyor web the

mathematical model allows obtaining the complete picture of its operation and can be used in similar systems designing.

Theoretical study on determining the inclination angles of an after-cleaning conveyor parts has allowed narrowing the range of rational values of design parameters of the improved after-cleaning conveyor before its designing and manufacture.

The regression equations to determine losses, damage and dirtiness of root crops have been obtained and correspondent response surfaces have been built on the basis of conducted experiments and statistic processing of the obtained results. It allowed having the most efficient parameters of the after- cleaning conveyor which would meet the agricultural requirements.

The experimental research has proved that the set requirements on root crops losses, damage and dirtiness are satisfied to a greater extent at the following parameters: $\varepsilon$ = 15…20°; $\varphi$ = 60…65°; $V_T$ = 1.1…1.25 m/s; $l$ = 40…50 mm, $S$ = 50…60 mm.

**REFERENCES**


[1] Baranovsky V.M., Potapenko M.V., (2017), Theoretical analysis of the technological feed of lifter root crops, *INMATEH-Agricultural Engineering*, vol. 51, no. 1, pp. 29-38, Bucharest/Romania;

[2] Brătucu Gh., Păunescu D.D., (2015), Establishing the optimum operating mode of sugar beet head cutting equipment using a cylindrical palpator, *Bulletin of the Transilvania University of Braşov*, Series II, vol. 8, pp. 51-56, Braşov/Romania;

[3] Bulgakov V.M., Pavelchak O.B., Hevko R.B. et al., (2000), A method for assessing the damage degree of root crops by the root-carving machine (Методика оцінки ступеня пошкодження коренеплодів коренезбиральною машиною), *Collection of scientific works of the National Agrarian University (Збірник наукових праць Національного аграрного університету)*, vol. 7, pp. 14-19, Kyiv/Ukraine;

[4] Hevko R., Brukhanskyi R., Flonts I. et al., (2018), Advances in methods of cleaning root crops, *Bulletin of the Transilvania University of Braşov*, Series II, vol. 11 (60), no. 1, pp. 127-138, Braşov/Romania;

[5] Hevko R.B., Tkachenko I.G., Synii S.V. et al., (2016), Development of design and investigation of operation processes of small-scale root crop and potato harvesters, *INMATEH-Agricultural Engineering*, vol. 49, no. 2, pp. 53-60, Bucharest/Romania;

[6] Hevko R.B., Tunik I.G., Tkachenko I.G., (1998), Research results on the beet loading system into root harvesting machine tank (Результати дослідження системи завантаження буряків у бункер коренезбиральної машини), *Agricultural machines. Collection of scientific articles (Сільськогосподарські машини. Збірник наукових статей)*, vol. 4, pp. 32–46, Lutsk/Ukraine;

[7] Hevko R.B., Zalutskyi S.Z., Tkachenko I.G. et al., (2015), Development and investigation of reciprocating screw with flexible helical surface, *INMATEH-Agricultural Engineering*, vol. 46, no. 2, pp. 133-138, Bucharest/Romania;

[8] Liebe S., Varrelmann M., (2014), Impact of root rot pathogens on storage of sugar beets and control measures, *Zuckerindustrie. Sugar industry*, vol. 139, no. 7, pp. 443-452, Berlin/Germany;

[9] Lyashuk O.L., Rogatynska O.R., Serilko D.L., (2015), Modelling of the vertical screw conveyor loading, *INMATEH-Agricultural Engineering*, vol.45, no.1, pp.87-94, Bucharest/Romania;

[10] Pavelchak O.B., Tkachenko I.G., Hladyo Y.B. et al., (2000), Definition of rational parameters of the conveyor-separator (Вибір раціональних параметрів транспортера-сепаратора), *Collection of scientific works of the National Agrarian University (Збірник наукових праць національного аграрного університету)*, vol. 8, pp. 41-47, Kyiv/Ukraine;

[11] Synii S.V., Hevko R.B., Flonts I.V. et al., (2018), Improvement of the root crop cleaning efficiency (Підвищення ефективності очищення коренеплодів), *Agricultural machines. Collection of scientific articles (Сільськогосподарські машини. Збірник наукових статей)*, vol. 40, pp. 89–100, Lutsk/Ukraine;

[12] Tsarenko O.M., Voityuk L.M., Shvayko M.V. et al., (2003), Mechanical and technological properties of agricultural materials (Механіко-технологічні властивості сільськогосподарських матеріалів), *Textbook (Підручник)*, 448 p., Kyiv/Ukraine;

[13] Tkachenko I.G., Hladyo Y.B., Hevko R.B. et al., (2000), Substantiation of the conveyor-separator parameters (Обґрунтування параметрів транспортера-сепаратора), *Scientific notes. Intercollegiate collection (Наукові нотатки. Міжвузівський збірник)*, vol. 7, pp. 260-266, Lutsk/Ukraine.

# A NOVEL METHOD FOR THE GROUP CHARACTERISTICS ANALYSIS OF YELLOW FEATHER BROILERS UNDER THE HEAT STRESS BASED ON OBJECT DETECTION AND TRANSFER LEARNING

/

# 基于目标检测和迁移学习的黄羽鸡在热应激下群体特征分析

**Anlan Ding [1)], Xuhui Zhang, Xiuguo Zou *)], Yan Qian, Heyang Yao, Shikai Zhang, Yuning Wei [1]**

[1)] College of Engineering, Nanjing Agricultural University / China;

*Tel: +862558606585; E-mail: xiuguozou@gmail.com*

*DOI: 10.35633/INMATEH-59-06*

***Keywords:*** *broiler, heat stress, deep learning, liveness analysis*

## ABSTRACT

*Temperature is a very important factor in the breeding of yellow feather broilers. Researching the group behaviour of yellow feather broilers under heat stress can help farmers take the corresponding measures to reduce the heat stress of broilers and improve production performance. In this paper, several traditional methods have been employed to detect and locate the broilers. These methods are highly interfered by the background whose colour is similar to broilers, thereby making it difficult to accurately locate the broilers. Meanwhile, although the algorithm YOLOv3 can precisely segment and locate the broilers, it has the disadvantages of incomplete detection and low detection confidence rate. Finally, this paper applies the neural architecture search and transfer learning to train the pre-processed training set, and obtains a detection model with a recognition accuracy of 83%. Then this model is used to process the images under heat stress at every 30 s so as to obtain the distribution of the broilers at each moment. Based on the results, the liveness and distribution characteristics of the broilers are analyzed. The analysis results show that when heat stress occurs, the broilers mainly gather at the vent; that when the temperature further rises above 30°C, the proportion of broilers at the vent increases from 53.3% to 67.3% on average; and that the activity index of the broilers decreases by 22.54% within an average of 3 h after the temperature rises to 30°C.*

## 摘要

*在黄羽鸡生产养殖中，温度是一个非常重要的因素。研究热应激下黄羽鸡的群体行为可以帮助养殖户更深入地了解黄羽鸡在热应激下的反应，从而采取相应的措施减少鸡的热应激现象，提高鸡的生产性能。本文首先研究了几种对黄羽鸡检测的方法，根据检测的结果无法进行下一步的精确分析，而基于 Darknet-53 的 YOLOv3 算法则存在识别不精准的问题。最后本文利用 Neural Architecture Search 和 Transfer Learning 对预处理后的训练集进行训练，获得了识别准确率为 83%的检测模型。基于此模型分析鸡群活跃度和分布特征，结果表明，鸡群在温度上升至 30℃之后平均 3 小时内活跃度指数会降低 22.54%。在分布上，热应激发生时鸡只主要聚集在通风口处，当温度进一步升高至 30℃以上时，通风口处鸡的比例平均由 53.3%上升至 67.3%。*

## INTRODUCTION

Heat stress is one of the most important environmental stressors challenging poultry production worldwide. Nowadays, broiler breeding industry has developed into large-scale and specialized mode. As the number of broilers increases, the heat stress phenomenon of broilers will become more prominent in summer (*Lara L.J., 2013*). The physiological responses of broilers under heat stress divert energy from efficient production and increase the morbidity and mortality (*Shakeri M., 2018*). The negative effects of heat stress on yellow feather broilers include reduced growth and egg production, as well as decreased poultry and egg quality and safety (*Goo D., 2019*). Therefore, breeders must pay attention to the heat stress of broilers and take preventive measures. In most areas of China, especially southern China, the continuous high temperature and humid heat in summer easily bring heat stress to yellow feather broilers, which seriously affect the growth of broilers.

Many researchers have investigated the effects of heat stress on poultry productivity and immune response. However, it is actually scarce on our knowledge of the basic mechanism related to the reported

[1] *Anlan Ding, Mr.; Xuhui Zhang, Mr.; Xiuguo Zou, Assoc. Prof. Ph.D.; Yan Qian, Assoc. Prof. Ph.D.; Heyang Yao, MAE. Stud.; Shikai Zhang, MAE. Stud.; Yuning Wei, MAE. Stud.*

effects and the behaviour of poultry under heat stress. The analysis of the effects of heat stress on broilers mostly focuses on the physiological characteristics of broiler, but seldom on the group behaviour of the whole broiler flock (*Habashy W.S., 2017; Huang S., 2018*). The important information contained in animal behaviour is an intuitive index to evaluate animal welfare, which can enable producers to better manage livestock and poultry production (*Dawkins M.S., 2012*). Therefore, it is of great significance to investigate the behaviour of broilers under heat stress.

In order to research the group behaviour of broilers, it is necessary to separate broilers from the background before further analysis. However, yellow feather broilers are raised in groups and have the same individual appearance, which makes it very difficult to detect and separate them individually. Moreover, the non-rigid bodies of yellow feather broilers make it more difficult to research their behaviour than large animals' behaviour (*Liu L., 2014*). In recent years, some scholars are also trying to automatically identify the individual or group behaviours of laying hens or broilers through image processing technology (*Aydin A., 2010; Leroy T., 2006*). However, due to the unobvious contrast between livestock and poultry, and their backgrounds, background changes and uneven illumination, the extraction of broilers using traditional digital image processing technology would make errors, thus affecting the accuracy of analysis (*Lao F., 2017*).

About the target extraction, a series of traditional algorithms (e.g. background difference method) and deep learning algorithms (e.g. RCNN, Fast RCNN, Faster RCNN and YOLO) have been proposed (*Girshick R., 2014; Ren S., 2015; Redmon J., 2016*). However, most of these algorithms are usually applied to the target extraction of pedestrians, vehicles and ships, etc., and rarely applied to the detection of small targets such as poultry (*Wang D., 2018; Zhang H., 2019*). In this paper, some traditional algorithms and deep learning algorithms are used to extract yellow feather broilers. Through the analysis and comparison of the extraction results, the final detection model is selected.

Based on the accurate extraction of broilers by the detection model, the distribution index and activity of broilers are analyzed. At present, there is little research on calculating broiler distribution index and activity. Lao Tree Peony et al (*Lao F., 2017*) calculated the distribution index and activity of laying hens based on the pixels occupied by laying hens. In terms of distribution index, as the size of broiler is not always the same during the experiment, it is difficult to completely extract the pixels occupied by broilers, and the phenomenon of mutual overlap often occurs, which leads to large errors in calculating distribution index. Therefore, this paper proposes a method of using the number ratio of broiler as an index of distribution index based on the acquired images and the target detection algorithm. In terms of activity analysis, this paper makes some improvements to the original pixel method, where pixel variables are converted into area variables, and the activity is calculated based on the dislocation area of the regions occupied by yellow feather broilers in the previous image and in the next image. The experiment shows satisfactory results, which provides a reference for the prevention of heat stress of yellow feather broilers.

## MATERIALS AND METHODS

### *Data Acquisition*

The broiler house used in this paper has two chambers designed by cotton-coated coloured steel plates. Each broiler chamber has a width of 1.9 m, a length of 2.9 m, a height of 1.88 m on the western side and a height of 1.77 m on the eastern side. The roof is sloped to facilitate rainwater drainage. Inside the broiler chamber, we mounted a temperature and humidity monitoring system, a ventilation system and a video monitoring system. The floor is paved with wood panels and ventilation pipes are laid below (*Zhang S., 2019; Yao H. 2018*). The three-dimensional chamber model was established by SolidWorks and is shown in Figure 1.

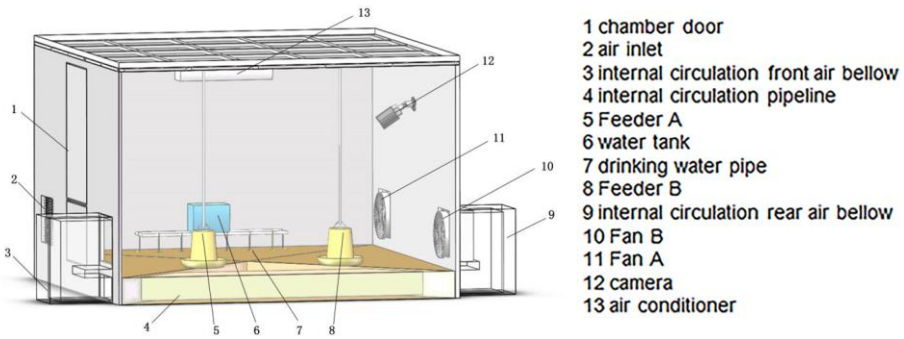


**Fig. 1 - The three-dimensional chamber model was established by SolidWorks**

The data acquisition lasted from July 20th to August 8th, 2018. The cameras worked all day and the data were saved on the hard disk of the host computer.

***Broiler Target Detection Method***

- **Background Subtraction Algorithm**

The background subtraction algorithm is to subtract each current image from the background image stored in advance or acquired in real time, and calculate the area deviating from the background beyond a certain threshold value. Therefore, the target object is extracted. The specific operation flow is shown in Figure 2 (*Zhao K., 2015*).

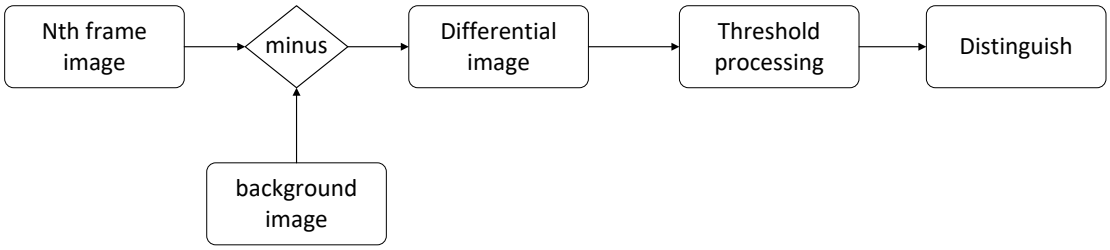


**Fig. 2 - The specific operation flow of background subtraction algorithm**

Let the $n^{th}$ image and the background image be $fn(x, y)$ and $f(x, y)$, respectively, where $x$ and $y$ represent the coordinates of a pixel $(x, y)$. The gray values of the corresponding pixels of the two frames of images are subtracted according to Equation (1), and their absolute values are used to obtain the differential image $Dn$ (*Braham M., 2016; Yang J., 2012*).

$$Dn(x,y)=\left| fn(x,y)- f(x,y) \right| \tag{1}$$

A threshold value $T$ (manual test and selection based on the acquired image, and $T$ = 135 in this experiment) is set to binarize the image according to Equation (2) and a binary image $Rn(x, y)$ is obtained. Among them, the point with a gray level of 255 is the front scenic spot, and the point with a gray level of 0 is the background point. The processing result is shown in Figure 3(c).

$$Rn(x,y)=\begin{cases} 255, Dn(x,y) > T \\ 0, else \end{cases} \tag{2}$$

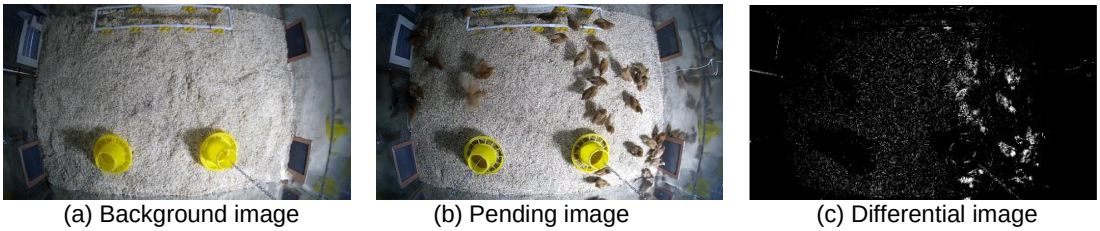

(a) Background image (b) Pending image (c) Differential image

**Fig. 3 - The processing result of background subtraction algorithm**

As shown in Figure 3, the extraction results by background subtraction algorithm are not satisfactory, mainly because the background environment is affected by illumination, camera shaking, and the variations of the background images at different moments. Moreover, the activities of yellow feather broilers change the positions of troughs and other objects in the background image, and their shadows increase the area of foreground, which reduces the extraction effect.

- **Threshold Segmentation based on RGB Space**

RGB colour model is based on the principle of three primary colours of human vision and is the most basic colour model. It uses the three primary colours (red, green and blue) with different proportions to produce a variety of coloured images.

Each *RGB* image can be represented as a three-dimensional matrix of *m***n**3, and the colour of each pixel in the image is obtained from the values of the RGB's three components in the interval [0, 255]. Therefore, *RGB*'s three components can form 256*256*256 colours in total.

Colour extraction uses the difference of RGB's three-component values between each pixel to set a threshold and extract the target object. Before threshold segmentation, a colour histogram is drawn, as shown in Figure 4.


(a) Original image (b) Three-color histograms

**Fig. 4 - The pre-processing of colour component**

The appropriate threshold value $T$ is manually selected according to the colour histogram. In this experiment, we take $T$ =5, and the image is processed according to Equation (3) to obtain the binary image *Rn* (*Dong X., 2009*).

$$Rn(m,n,d)=\begin{cases} Rn(m,n,d), & Rn(m,n,1)\text{-}Rn(m,n,2)>T \\ 255, else \end{cases} \quad (3)$$

The extraction result is shown in Figure 5.

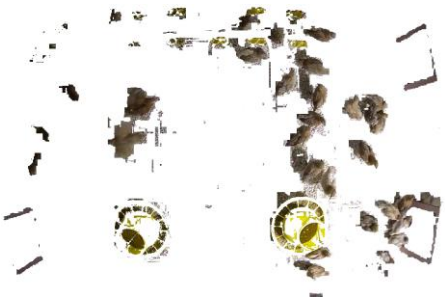

**Fig. 5 - The extraction result obtained using colour components**

As shown in Figure 5, most of the broilers are extracted. However, the colour of the food trough is similar to that of broilers, which leads to poor extraction effect. If the food trough in the image is removed through pre-processing, the broilers foraging around the food trough would also be removed. Besides, some broilers in the image are hidden by shadows. As a result, the corresponding pixels fail to reach the threshold value, resulting in poor extraction. Although the colour extraction method is better than the background difference method, there are still some deficiencies.

- **Colour Clustering based on YCbCr Space**

YCbCr is another common colour model, where $Y$ is the brightness of colour in this colour space, $Cb$ and $Cr$ represent the chromaticity of blue and red, respectively. As YCbCr colour space has good clustering effect on the colour of yellow feather broilers, and RGB colour space is greatly affected by brightness, RGB colour space can be converted into YCbCr colour space, as expressed by (*Patvardhan C., 2017; Shaik K.B., 2015*).

$$\begin{bmatrix} Y \\ Cb \\ Cr \\ 1 \end{bmatrix} = \begin{bmatrix} 0.2990 & 0.5870 & 0.140 & 0 \\ -0.1687 & -0.3313 & 0.5000 & 128 \\ 0.5000 & -0.4187 & -0.0813 & 128 \\ 0 & 0 & 0 & 0 \end{bmatrix} \bullet \begin{bmatrix} R \\ G \\ B \\ 1 \end{bmatrix} \quad (4)$$

Statistical experiments show that the aggregation of feather colour space on YCrCb is mainly concentrated around $Cb$=150. Based on Equation (5), the coloured broiler chamber image is processed, and the binary image of the broiler is obtained through colour clustering (*Das A., 2016; Prasetyo E., 2017*).

$$\begin{cases} (R,G,B) = (255,255,255) & if \quad Cr \in (80,120) \quad and \quad Cb \in (133,165) \\ (R,G,B) = (0,0,0) & if \quad Cr \notin (80,120) \quad or \quad Cb \notin (133,165) \end{cases} \tag{5}$$

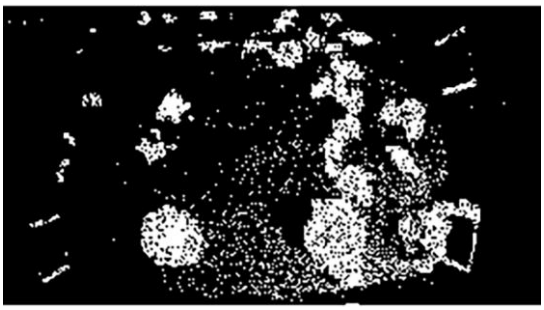

**Fig. 6 - Binary image after colour clustering**

As can be seen from Figure 6, the results of colour clustering are strongly interfered by illumination, causing false detection and missing detection in the lower right corner and the upper left corner. Moreover, some colours similar to the feather colour of yellow feather broilers are also detected and processed, such as troughs and padding, causing interference in the image.

- **YOLOv3 Object Detection Algorithm**

YOLO algorithm uses the whole image as the input of a simple end-to-end network, and adopts the method of regression to detect and classify the coordinate frames, thus greatly accelerating the training process. In addition, YOLOv3 designs a better basic classification network and classifier darknet-53 based on YOLOv2, which greatly improves the prediction accuracy and speed of YOLOv3 compared with other models (*Redmon J., 2017*).

Before using YOLOv3 to train model, the broilers are marked and XML files are created. The main annotation software includes yolo_mark, Sloth, Annotorious, RectLabel and LabelImg, etc. Finally, LabelImg is adopted as the image annotation tool, as it is simple to operate and can directly generate XML files.

LabelImg was used to mark up 100 images and generate XML files. On the NVIDIA GTX 1080ti graphics card with 11GB of memory, the images were trained based on the Keras framework. The batch size was set to 2 and the iteration was performed for 30 times. When the loss of the training set dropped to 109.1595, the loss of the validation set dropped to 156.1932. Then the loss no longer dropped significantly, and the training ended. Some of the detection results are shown in Figure 7.

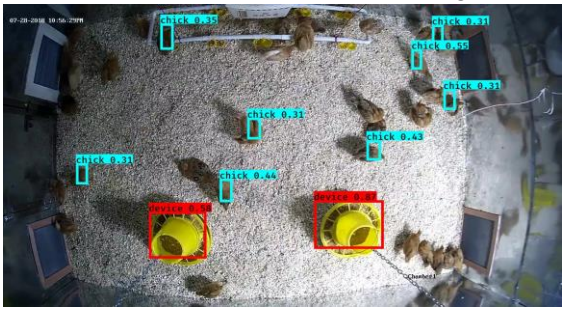


**Fig. 7 - Detection results of YOLOv3 algorithm**

As can be seen from Figure 8, the model only detected two troughs and eight broilers. The frame was generally small and the confidence rate was less than 60%. Due to the use of a single light source, the image brightness was not uniform, and the broiler presented shadows of different sizes, which interfered with the training of the model, resulting in poor performance of YOLOv3 on the dataset.

- **NAS and Transfer Learning**

As the above algorithms have the problems of low detection accuracy and incomplete detection, this paper uses the PaddlePaddle framework, the neural architecture search and transfer learning to train the dataset.

(1) Neural Architecture Search

In order to improve the accuracy of the detection model, this paper uses NAS to search the neural network structure. During the training, multiple model structures and different pieces of training of hyperparameter were initiated, and the corresponding algorithm was used to screen the final model, thus obtaining the optimal model effect (*Zoph B., 2017*).

(2) Transfer Learning

The model was pre-trained on some large-scale datasets, and then the knowledge learned from applying to the yellow feather broiler datasets, which greatly improved the efficiency and accuracy. Since the backbone of transfer learning is a very large network, almost each type of label needs to use more than 20-100 images to complete the training of the later levels of the neural network (*Pan S.J., 2010*).

(3) Training Steps

*Step 1: Make dataset*

Using the labeling tool of the deep learning platform, 10 images of yellow feather broilers with large distribution differences were selected, followed by the labeling of the broilers and troughs in the images.

*Step 2: Training*

The dataset was trained by NAS and transfer learning. The initial training time was 670 s, and the average recognition accuracy for broilers and troughs were 75.17% and 100%, respectively. The results are shown in Figure 8.

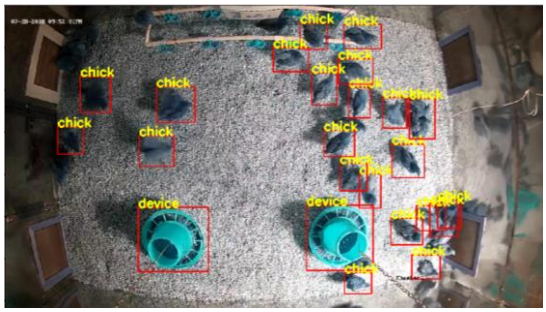


**Fig. 8 - The recognition results of the detection model trained by NAS and transfer learning**

*Step 3: Extended dataset*

Due to the use of transfer learning, the 10-image training model has met the requirement for further analysis. In order to further improve the accuracy of the model, the data set was expanded for retraining.

**Table 1**

**The results of model training**

| Training set size (the number of pictures) | Average precision | |
|---|---|---|
| | Yellow feather broiler | Device |
| 10 | 75% | 100% |
| 20 | 81% | 100% |
| 30 | 76% | 100% |
| 40 | 79% | 100% |
| 50 | 83% | 100% |
| 60 | 81% | 100% |

From the results in Table 1, it can be seen that the model trained with 50 images has the best effect, and the average recognition accuracy of broilers reaches 83%, which can meet the requirement for further analysis. Therefore, this paper selects this model as the final broiler detection model.

## RESULTS

### *Analysis of Distribution Characteristics*

In order to study the distribution of broilers under heat stress, the broiler chamber is divided into four areas, i.e. water trough, trough, vent and other areas. The specific division is shown in Figure 9.


**Fig. 9 - The specific division of the areas in the chamber**

When the cameras worked, the temperature gradually rose from 30°C to 34°C in the broiler chamber. The image was acquired every 30 s, and the distribution index of each area was calculated according to Equation (6) (*Lao F., 2017*).

$$d_i = \frac{n_i}{N} \times 100\% \qquad (i = 1,2,3,4) \tag{6}$$

where: $d_i$ is the distribution index of broilers in sub-region $i$, $n_i$ is the number of broilers captured in sub-region $i$ (more than half of the framed area of extracted broilers is regarded as one broiler in this sub-region), and $N$ is the total number of broilers captured in the current image.

There existed the phenomenon of missing detection in the broiler extraction process. To solve this problem, the images with serious missing detection were manually extracted and the distribution index obtained above was averaged every 10 groups as a new sample value according to Equation (7).

$$D_i = \frac{\sum_{j=1}^{10} d_{i,j}}{10} \qquad (i=1,2,3,4) \tag{7}$$

where: $Di$ is the distribution index averaged for the $i$ sub-region, $d_{i,j}$ is the distribution index in the $j$ image of the $i$ sub-region. The curves of distribution index over 3 days are shown in Figure 10.

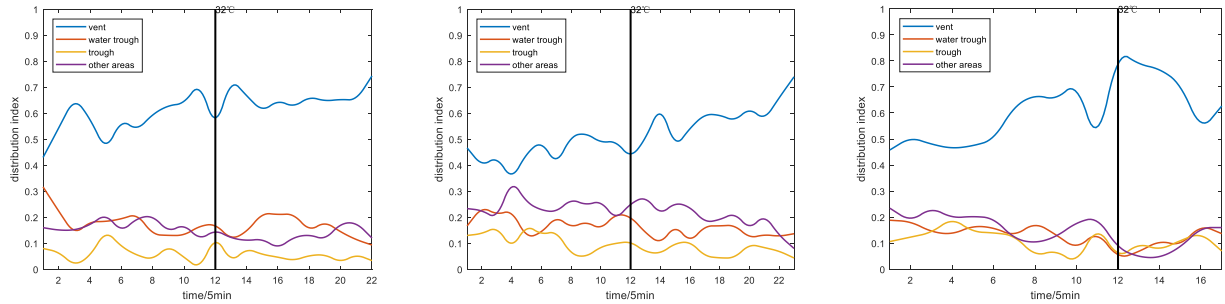


(a) 2:28 pm - 4:22 pm, 26 Jul. 2018 (b) 6:47 am - 8:47 am, 28 Jul. 2018 (c) 7:03 am - 8:32 am, 5 Aug. 2018

**Fig. 10 - The curves of distribution index**

**Table 2**

**The change of distribution index of broilers with the temperature**

| Location | Date | 30~32°C (%) | 32~34 °C (%) | Rate of change |
|---|---|---|---|---|
| Vent | 7.26 | 60 | 69 | +0.15 |
| | 7.28 | 47 | 62 | +0.32 |
| | 8.5 | 59 | 71 | +0.20 |
| Water trough | 7.26 | 18 | 15 | -0.17 |
| | 7.28 | 18 | 13 | -0.28 |
| | 8.5 | 13 | 11 | -0.15 |
| Trough | 7.26 | 6 | 4 | -0.33 |
| | 7.28 | 11 | 6 | -0.45 |
| | 8.5 | 11 | 9 | -0.18 |
| Other areas | 7.26 | 16 | 12 | -0.25 |
| | 7.28 | 24 | 19 | -0.21 |
| | 8.5 | 17 | 9 | -0.47 |

Figure 10 and Table 2 show that under the condition of heat stress, yellow feather broilers tend to be near the vent more and more with the increase of temperature, and it is especially obvious after the temperature in the chamber reaches 32 degrees. When the heat stress is more serious (above 32 degrees), about 68% of the broilers are distributed near the vent, 13% are distributed near the water troughs, 6% are distributed near the troughs, and 13% are distributed in other areas. Therefore, when heat stress occurs, yellow feather broilers tend to gather in cool places.

***Activity Analysis***

The activity of yellow feather broilers is calculated as follows. The activity index (AI) of yellow feather broilers at time $t$ is defined as the area of the staggered part of the yellow feather broilers' coverage area at two times of $-\Delta t$ and $t+\Delta t$ (it is considered that the overlapped part of yellow feather broilers did not move within $2\Delta t$) (*Aydin A., 2010*). Equation (8) calculates the number of pixel points that are opened incorrectly, and Equation (9) obtains the area of the staggered area.

The larger the area, the greater the total activity of yellow feather broilers in $2\Delta t$, the greater the activity index of broilers at time $t$. The activity index is calculated by:

$$\Delta pixel = P_{t+\Delta t} \cap \left(1 - P_{t-\Delta t}\right) \tag{8}$$

$$\Delta S = \Delta pixel \times 1.044 \times 10^{-5} \tag{9}$$

$$AI_t = \Delta S / 2 \tag{10}$$

In the dataset, the relationship between image pixels and the actual area is expressed as:

$$1pixel = 5.51/52780m^2 \approx 1.044 \times 10^{-5} m^2 \tag{11}$$

As shown in Figure 11, Figure 11 (a) and 12 (b) represent the images at time $t$-$\Delta t$, $t$+$\Delta t$, respectively, and Figure 11(c) shows the staggered areas, where the sum of the areas of all white regions is $\Delta S$.

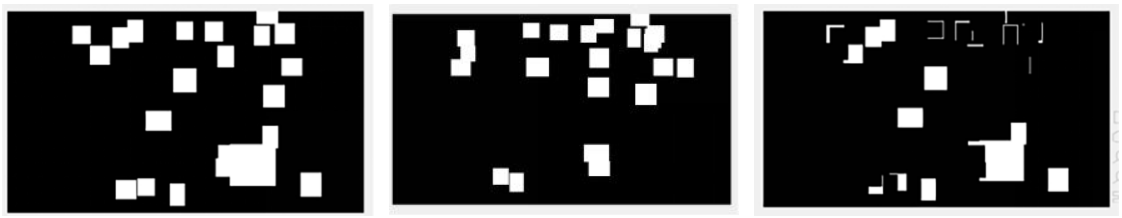

(a) $t$-$\Delta t$ (b) $t$+$\Delta t$ (c) differential region

**Fig. 11 - Schematic diagram of calculating the staggered areas**

In this paper, the images with obvious high temperature in 7.26, 7.28 and 8.5 days were selected to calculate the activity index of broilers before and after the occurrence of 32 °C. The results are shown in Figure 12(a), 12(b) and 12(c). Due to the uncertainty of the activity of a single broiler in the broiler flock, the activity of the broiler flock at a single moment cannot represent the activity of the broiler during the whole period. Therefore, the activity indexes over the period were summed. Figure 12(d) shows the activity indexes after the summing operation every 40 min. The specific results are shown in Table 3.

From Figure 12 and Table 3, it can be seen that within 3 h after the temperature rose to 30°C in three days, the activity index of the broilers decreased from 13.39 m²/40 min to 10.08 m²/40 min, a decrease of 22.54%. This indicates that the activity of the broilers decreased significantly after the heat stress occurred for a period of time.

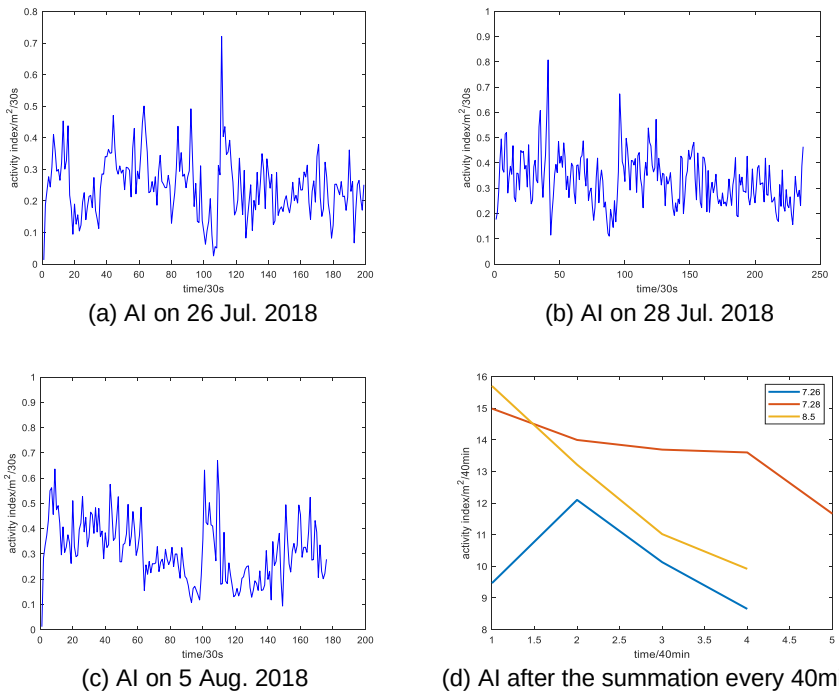


(a) AI on 26 Jul. 2018 (b) AI on 28 Jul. 2018

(c) AI on 5 Aug. 2018 (d) AI after the summation every 40min

**Fig. 12 - The results of AI**

**Table 3**

**The change of activity index with the temperature**

| Date | Activity Index ($m^2$/40min) | | | Decrease (%) |
|---|---|---|---|---|
| | T≤30 °C | T≥32 °C | Decrease of AI | |
| 26.07.2018 | 9.47 | 8.65 | 0.82 | 8.61 |
| 28.07.2018 | 14.99 | 11.67 | 3.33 | 22.18 |
| 05.08.2018 | 15.71 | 9.92 | 5.79 | 36.84 |
| average | 13.39 | 10.08 | 3.31 | 22.54 |

## CONCLUSIONS

The changes of biochemical properties of broilers under heat stress have been extensively investigated, but the group behaviour is rarely seen. In order to accurately locate yellow feather broilers, the algorithm of multi-target detection is discussed, and the detection model of broiler is determined by referring to PaddlePaddle and the algorithms of NAS and transfer learning. The average recognition accuracy reached 83%. Compared with the traditional background difference method, improved performance has been seen in the results by threshold segmentation method based on RGB space, colour clustering method based on YCbCr space and YOLOv3 method.

On the basis of the accurate extraction of broilers, we have investigated the changes of group behaviour indexes of broilers under heat stress. According to the distribution characteristics of broilers, the broiler chamber is divided into four areas, namely vent, water trough, trough and others. A large number of broiler images are processed by the detection model, and the traditional distribution index is also modified, so as to obtain more accurate results. The results show that when heat stress occurs, yellow feather broilers tend to gather at the vent. When the temperature continues to increase, the proportion of broilers at the vent increases from 53.3% to 67.3%.

According to the analysis of broiler's activity, the staggered area of broiler's area detected before and after the time is used as the activity index at the current time. The results show that the activity index is 13.39 $m^2$/40 min when the temperature is less than 30°C, and it decreases to 10.08 $m^2$/40 min, a decrease of 22.54%, within 3 h after the temperature rises to 30°C. The research results obtained by image processing technology and deep learning algorithm help farmers take effective measures to reduce the loss.

## ACKNOWLEDGEMENT

This research was jointly supported by the Fundamental Research Funds for the Central Universities of China (KYTZ201661), China Postdoctoral Science Foundation (2015M571782), Jiangsu Agricultural Machinery Foundation (GXZ14002) and University Student Entrepreneurship Practice Program of Jiangsu Province (NO. 201810307010P).

## REFERENCES

[1] Aydin A., Cangar O., Ozcan S.E. et al., (2010), Application of a fully automatic analysis tool to assess the activity of broiler chickens with different gait scores, *Computers and Electronics in Agriculture*, Vol.73, Issue 2, pp.194-199, Wageningen/Netherlands;

[2] Braham M. and Droogenbroeck M.V., (2016), Deep background subtraction with scene-specific convolutional neural networks, *International Conference on Systems, Signals and Image Processing*, Bratislava/Slovakia;

[3] Das A. and Ghoshal D., (2016), Human skin region segmentation based on chrominance component using modified watershed algorithm, *Procedia Computer Science*, Vol.89, pp.856-863, Bangalore/ India;

[4] Dawkins M.S., Cain R. and Roberts S.J., (2012), Optical flow, flock behaviour and chicken welfare, *Animal Behaviour*, Vol.84, Issue 1, pp.219-223, London/U.K;

[5] Dong X., Wang K. and Jia G., (2009), Moving object and shadow detection based on RGB colour space and edge ratio, *2nd International Congress on Image and Signal Processing,* Tianjin/China;

[6] Girshick R., Donahue J., Darrell T. et al., (2014), Rich feature hierarchies for accurate object detection and semantic segmentation, *CVPR*, pp.580-587, Columbus/Ohio;

[7] Goo D., Kim J.H., Park G.H. et al., (2019), Effect of heat stress and stocking density on growth performance, breast meat quality, and intestinal barrier function in broiler chickens, *Animals*, Vol.9, Issue 3, 107, Basel/ Switzerland;
[8] Habashy W.S., Milfort M.C., Adomako K. et al., (2017), Effect of heat stress on amino acid digestibility and transporters in meat-type chickens, *Poultry Science*, Vol. 96, Issue 7, pp. 2312-2319, Oxford/U.K.;
[9] Huang S., Fu Y., Rehman M.U. et al., (2018), Effect of the acute heat stress on serum endotoxin concentration and the expression of TLR4 mRNA in liver of Arbor Acres broiler chickens, *Animal Production Science,* Vol.58, Issue 12, pp.2200-2206, Clayton South VIC /Australia;
[10] Lao F., Du X. and Teng G., (2017), Automatic recognition method of laying hen behaviours based on depth image processing, *Transactions of the Chinese Society for Agricultural Machinery*, Vol. 48, Issue 1, pp. 155-162, Beijing/China;
[11] Leroy T., Vranken E., Brecht A.V. et al., (2006), A computer vision method for on-line behavioural quantification of individually caged poultry, *Transactions of the ASABE*, Vol.49, Issue 3, pp.795-802, Michigan/USA;
[12] Liu L., Shen M., Bo G. et al., (2014), Sows parturition detection method based on machine vision, *Transactions of the Chinese Society for Agricultural Machinery*, Vol.45, Issue 3, pp.237-242, Beijing / China;
[13] Pan S.J. and Yang Q., (2010), A survey on transfer learning, *IEEE Transactions on Knowledge and Data Engineering*, Vol. 22, Issue 10, pp. 1345-1359, Los Angeles/USA;
[14] Patvardhan C., Kumar P. and Vasantha Lakshmi C., (2017), Effective colour image watermarking scheme using YCbCr colour space and QR code, *Multimedia Tools and Applications*, Vol.77, Issue 10, pp. 12655-12677, Dordrecht/Netherlands;
[15] Prasetyo E., Adityo R.D., Suciati N. et al., (2017), Mango leaf image segmentation on HSV and YCbCr colour spaces using Otsu thresholding, *3rd International Conference on Science and Technology - Computer*, Yogyakarta/Indonesia;
[16] Redmon J. and Farhadi A., (2017), Yolo9000: Better, faster, stronger, *CVPR*, pp.6517-6525, Hawaii/USA;
[17] Redmon J., Divvala S., Girshick R. et al., (2016), You only look once: Unified, real-time object detection, *CVPR*, pp.779-788, Las Vegas/USA;
[18] Ren S., He K., Girshick R. et al., (2015), Faster R-CNN: Towards real-time object detection with region proposal networks, *IEEE Transactions on Pattern Analysis and Machine Intelligence*, Vol.39, pp.1137-1149, Los Angeles/USA;
[19] Shaik K.B., Ganesan P., Kalist V. et al., (2015), Comparative study of skin colour detection and segmentation in HSV and YCbCr colour space, *Procedia Computer Science*, Vol.57, pp.41-48, Ghaziabad India;
[20] Shakeri M., Cottrell J., Wilkinson S. et al., (2018), Betaine and antioxidants improve growth performance, breast muscle development and ameliorate thermoregulatory responses to cyclic heat exposure in broiler chickens, *Animals,* Vol. 8, Issue 10, 162, Basel/ Switzerland;
[21] Wang D., He Y., Li D. et al., (2018), An improved infrared video image pedestrian detection algorithm, *Journal of Xi'an University of Posts and Telecommunications*, Vol.23, Issue 4, pp.48-52+67, Xi'an / China;
[22] Yang J., Shi M. and Yi Q., (2012), A new method for motion target detection by background subtraction and update, *Physics Procedia*, Vol.33, pp.1768-1775, Amsterdam/Netherlands;
[23] Yao H., Sun Q., Zou X. et al., (2018), Research of yellow-feather chicken breeding model based on small chicken chamber, *INMATEH - Agricultural Engineering*, Vol.56, Issue 42, pp.91-100, Bucharest/Romania;
[24] Zhang H., Du Y., Ning S. et al., (2019), Pedestrian detection method based on faster R-CNN, *Transducer and Microsystem Technologies*, Vol. 38, Issue 2, pp. 147-153, Beijing/China;
[25] Zhang S., Ding A., Zou X. et al., (2019), Simulation analysis of a ventilation system in a smart broiler chamber based on computational fluid dynamics, *Atmosphere*, Vol.10, Issue 6, 315, Basel/ Switzerland;
[26] Zhao K. and He D., (2015), Target detection method for moving cows based on background subtraction, *Int J Agric & Biol Eng*, Vol. 8, Issue 1, pp. 42-49, Faisalabad/Pakistan;
[27] Zoph B. and Le Q.V., (2017), Neural architecture search with reinforcement learning, *ICLR*, pp.1-16, Toulon/France.

# DESIGN OF A CROSS-BOUNDARY WARNING SYSTEM FOR SOIL PREPARATION BASED ON BDS

/

# 基于 BDS 的拖拉机整地作业越界预警系统设计

**ChengYang Guo[1)], Xiang Zhao[1)], Shuo Zhang[1)], Adilet S.[1,2)], Jun Chen*[1)], BaoFeng Su[1)]** [1]

[1)] College of Mechanical and Electronic Engineering, Northwest A&F University, Yangling 712100, China;

[2)] Technical faculty, S. Seifullin Kazakh Agro Technical University, Astana 010000, Kazakhstan

*Tel: +86 135721917773; E-mail: chenjun_jdxy@nwsuaf.edu.cn*

*DOI: 10.35633/INMATEH-59-07*

***Keywords:*** *cross-boundary, BeiDou navigation satellite system (BDS), hierarchical, LabVIEW*

## ABSTRACT

*To address issues wherein tractors easily cross boundaries during soil preparation, a cross-boundary model for front, side and any arbitrary boundary was proposed. Based on BeiDou navigation satellite system (BDS), using John Deere Model 1204 tractor as the hardware platform and LabVIEW2018 as the software development platform, a hierarchical cross-boundary warning system of soil preparation was developed, and field tests under different boundary conditions were carried out. The test results show that the cross-boundary warning system for soil preparation proposed in this study had good judging and warning capacities for front, side and any arbitrary boundaries, with the tractor showing no cross-boundary behaviour during operation, suggesting the proposed system is stable and viable for application.*

## 摘要

*针对拖拉机整地作业过程中容易出现越界的问题，本文首先构建了车前、车侧和任意边界的越界预警模型，并基于北斗定位系统，以 LabVIEW2018 为开发平台，设计了一种具有越界预判功能的分级越界预警系统，最后以约翰迪尔 1204 型拖拉机为试验平台，悬挂旋耕机进行实地试验。试验结果表明，本文设计的越界预警系统对于车前、车侧和任意边界都有较好的判别和预警能力，拖拉机均未越界，分级越界预警系统运行整体较为稳定，系统可靠性较高，适用性较强。*

## INTRODUCTION

In agricultural production, soil preparation is important for improving soil quality and increasing crop yield (*Varela et al., 2014*). A soil preparation machine pulled by a tractor can operate more efficiently if the tractor is able to sense and receive an early warning before a boundary of the operation area is crossed. Similarly, when the vehicle is operating repeatedly in the field, retreading a portion of the operation area can easily occur, resulting in a loss of soil preparation efficiency (*Di X et al., 2010*).

Currently, traditional cross-boundary warning systems are mainly based on machine vision (*Mo H and Farid, 2018, Wang Fengyun et al., 2016*) , which obtains the live video of soil by single and binocular CCD cameras, and extracts a frame image for processing to identify the marking line of the farm road (*Chen et al., 2019, Zhao Liming et al., 2018, Meng Qingkuan et al., 2016*) . For example, the AURORA system developed by Carnegie Mellon University in the United States carries out boundary detection through a colour camera mounted on one side of the vehicle (*Ghasemzadeh A. and Ahmed M.M., 2018*). However, cross-boundary warning systems based on machine vision require a complex computation process and exhibit poor stability (*Hu Liping et al., 2019*). To address this, cross-boundary warning systems based on magnetized iron wire have been put forward, which could judge whether the vehicle has crossed the boundary by detecting the change of the magnetic field using Hall element equipped with a bias magnet (*Zhuo Qing et al., 2016*). The method is simple but requires a large amount of wire to be laid before it can function, so it is not suitable for large-area detection (*Li Dawei, 2011*).

Satellite navigation and positioning technology has advantages of high positioning accuracy, strong real-time performance and low cost, and has been widely used in the regulation of agricultural machinery operation (*Xiong Bin et al., 2017, Sui Mingming et al., 2016, Meichen L. et al., 2018*).

[1] *ChengYang Guo, M.S. Stud. Eng.; Xiang Zhao, M.S. Stud. Eng.; Shuo Zhang, Ph.D. Eng.; Adilet S., As. Ph.D. Stud. Eng.; Jun Chen, Prof. Ph.D. Eng.; BaoFeng Su, A/Prof. Ph.D. Eng.*

In this study, a cross-boundary warning system for soil preparation is proposed based on BDS, which could supervise in real-time different cross-boundary conditions and deliver hierarchical cross-boundary warnings by acquiring the cross-boundary distance during soil preparation, enhancing the working efficiency and security of tractor soil preparation.

## MATERIAL AND METHODS

*Cross-boundary warning modeling*

Generally, before the tractor starts soil preparation, the warning boundary is already known and set. According to the demands of actual operation, the boundaries that need to be subject to early warning can be divided into three types, i.e., the front boundary, the side boundary and any arbitrary boundary.

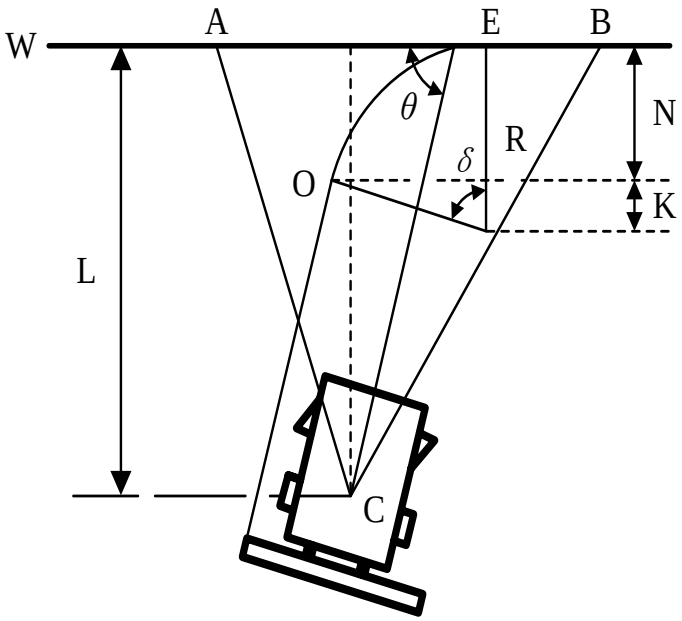


**Fig.1 - Vehicle front boundary model**

In the triangle ABC, the area S could be solved through equation (1):

$$S = \sqrt{P(P - AB)(P - AC)(P - BC)} \quad (1)$$

Where: *AB* - a length of the triangle, mm;

*AC* - a length of the triangle, mm;

*BC* - a length of the triangle, mm;

*P* - the semi-perimeter of triangle *ABC*, mm.

So, the straight-line distance *L* from point *C* to the boundary line *W* and the minimum cross-boundary warning distance *N* could be solved by equation (2) and equation (3):

$$L = \frac{2S}{AB} \quad (2)$$

$$N = R - R\cos\delta \quad (3)$$

Cross-boundary time *T* could be solved by equation (4):

$$T = \frac{2 \times \pi \times R \times \delta}{360 \times v} \quad (4)$$

Where: *v* - the forward speed of the tractor, mm/s.

Since the minimum turning radius of the model has been determined, the warning threshold is unique and is the minimum cross-boundary warning distance *N*. The purpose of introducing the cross-boundary time *T* is to evaluate the rotational velocity of the control system motor. When tractor travels much slower, to make the tractor drive steadily and to guarantee the security when the tractor turns, the rotating speed of the motor should be lower (*Shi Tingna et al., 2017*). When the tractor travels at higher speed, the cross-boundary time *T* is short, so the rotating speed of the motor should be relatively higher.

For two cases where the boundary line is located on the side of the tractor or when the boundary line is the boundary of the preparation range of adjacent soils, it will set a cross-boundary warning for the side boundary. As shown in Fig. 2, *C* is the central point of the tractor, *X* and *Z* are two arbitrary points in the side boundary line *W*, *δ* is the wheel turning angle, and *2D* is the operation width of the rotary cultivator.

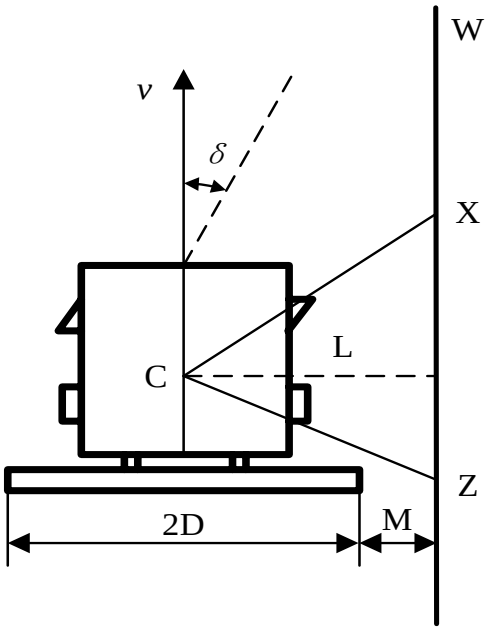


**Fig.2 - Vehicle side boundary model**

In the triangle CXZ, the area S could be solved through equation (5):

$$S = \sqrt{Q(Q-CX)(Q-CZ)(Q-XZ)} \quad (5)$$

Where: *CX* - a length of the triangle, mm;
*CZ* - a length of the triangle, mm;
*XZ* - a length of the triangle, mm;
*Q* - the semi-perimeter of triangle *CXZ*, mm.

So, the straight-line distance *L* from point *C* to the boundary line *W* and the minimum cross-boundary warning distance *M* are respectively solved by equation (6) and equation (7):

$$L = \frac{2S}{XZ} \quad (6)$$

$$M = L - D \quad (7)$$

Cross-boundary time *T* is solved by equation (8):

$$T = \frac{M}{v \times \cos\delta \times \sin\delta} \quad (8)$$

In this model, the current working path is basically parallel with the completed working path. After the cross-boundary warning occurs, in the event the driver does not correct the driving direction immediately, the system will automatically control the steering motor to correct the driving direction of the tractor.

In an instance where the boundary appears in the planned operation area, such as pits, before the warning system is turned on, the two points in the arbitrary boundary are searched and connected to establish a boundary line by marking the coordinate while the safe distance to be reserved is determined. Using the above two models, any boundary warning could be achieved.

***Hardware and software system design***

To create a comprehensively functional cross-boundary warning system for tractor soil preparation, it is necessary to design comprehensively its hardware and software systems.

We used a John Deere Model 1204 wheeled tractor as the platform, making use of the existing BeiDou positioning system and the steering control system, to construct the proposed tractor cross-boundary warning hardware system, as shown in Fig. 3.

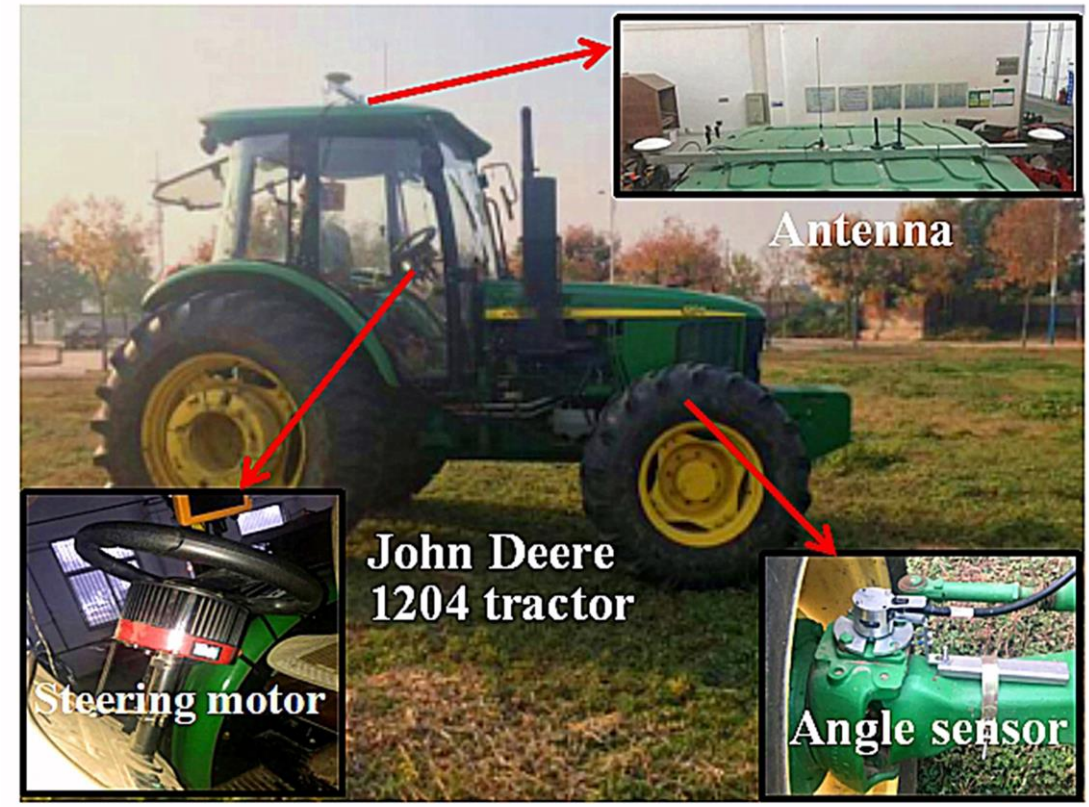


**Fig. 3 - Platform of tractor cross-boundary warning system**

The platform has 9 standard equipped forward gears and 3 backward gears; therefore, different gears may be selected as required by different working conditions.

The main technical parameters of the hardware system are shown in Table 1.

**Table 1**

**Main technical parameters**

| Name | Model | Parameter |
|---|---|---|
| Integrated navigation and positioning system | UM220-INS N | ±2cm |
| Front angle sensor | 424A16A090 | ±40° |
| Permanent magnet brushless DC motor | | 1500 r/min, 19 Nm |

LabVIEW2018 was the development platform. We adopted a modular approach and developed four main subroutines for the BeiDou positioning system, speed measuring system, front wheel angle acquisition system and motor steering control system according to the predetermined functions described above.

Fig. 4 depicts the main cross-boundary warning system for tractor soil preparation, wherein Fig. 4(a) is a user interaction interface, and Fig. 4(b) is a block diagram. The wheel steered angle interface displays mainly the steering information from the tractor, in which the steering direction is indicated by the illumination of two Boolean lights and the steering value is displayed by the data bar. The cross-boundary parameter interface displays three major pieces of information: vehicle speed, cross-boundary time and cross-boundary distance. This interface allows the driver to view the current cross-boundary parameters of the vehicle in real time. The warning light interface uses three Boolean lights to display three-level cross-boundary warning information, with red, orange and yellow warning lights indicating respective cross-boundary distance warning levels.

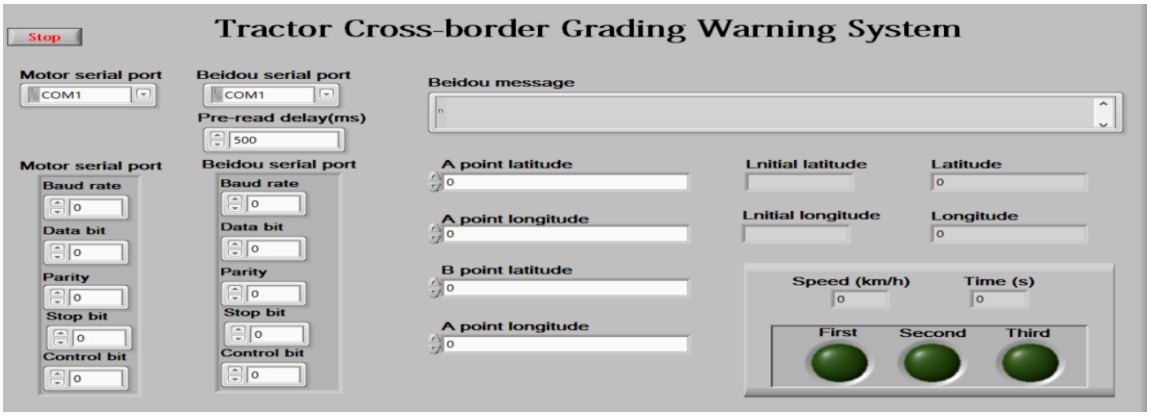


*(a) Version of the cross-boundary warning system*

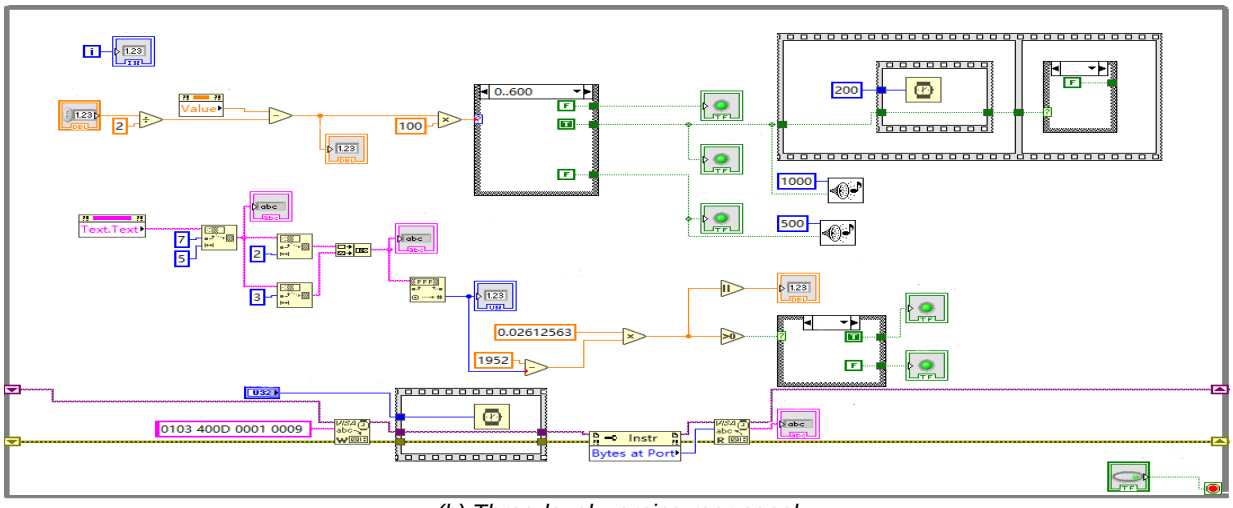


*(b) Three-level warning rear panel*

**Fig. 4 - Tractor cross-boundary warning software main system**

## RESULTS

In order to verify the performance of the cross-border warning system for soil preparation, individual vehicle front boundary, side boundary and arbitrary boundary cross-border warning tests were carried out.

***Cross-boundary warning test for front boundary***

The test site selected was on empty soil at Northwest A&F University. Five red signposts and tape measures were set on the test site as warning distance markers. Standard warning distances of 6m, 12m and 18m were measured and determined by tape measure, and two vertical rods were set at the end to simulate the front boundary of the vehicle, as shown in Fig. 5.

**Fig. 5 - Front boundary test site layout**

The tractor continually approached the front boundary travelling normally. When it arrived at the vertical rod at 18m, the third-level warning light turned on, as shown in Fig. 6 (a), indicating the tractor began to enter its alert state. When it arrived at the vertical rod at 12m, the second-level warning light turned on, as shown in Fig. 6(b), indicating that the rotary cultivator could be damaged in the event the tractor was using wide-angle steering during soil preparation. When the tractor arrived at the vertical rod at 6m, the first-level warning light turned on and the tractor turned with its minimum turning radius and the motor rotated clockwise, driving the front wheel towards the right, as shown in Fig. 6 (c).

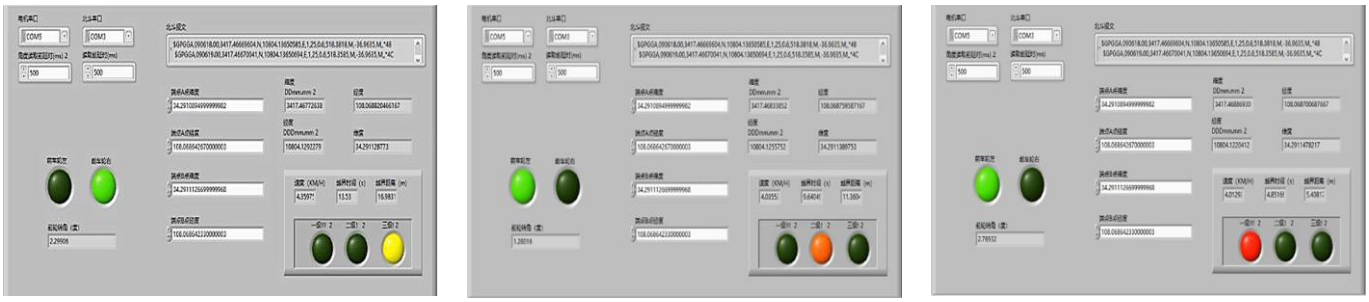

*(a) Three-level warning interface* *(b) Secondary level warning interface* *(c) First level warning interface*

**Fig. 6 - Hierarchical crossing warning interface**

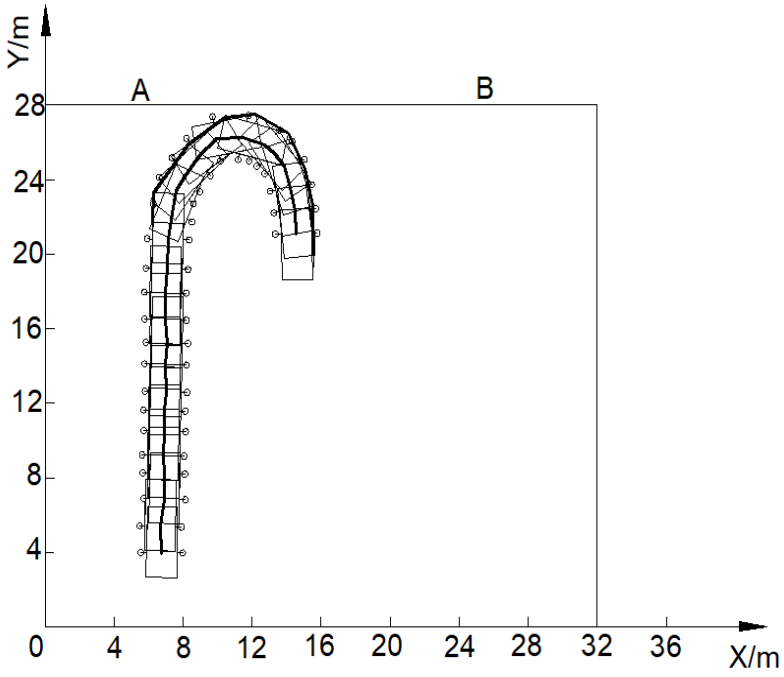


**Fig. 7 - Tractor actual walking route**

The position of the tractor was recorded in real time by the BeiDou satellite locator and the actual travelling route map was recorded, as shown in Fig. 7. The tractor's travel path and its outer wheel path with the minimum turning radius were marked with thick lines.

After 10 iterations of the front cross-boundary warning test, it was determined that the minimum distance between the tractor's turning path to the front boundary was 13cm. The overall operation of the cross-boundary warning system was relatively stable and highly reliable.

***Cross-boundary warning test for side boundary***

The selected test site was mud soil at Northwest A&F University. Six red signposts were used to simulate the side boundary of the vehicle, as shown in Fig. 8. In this test, the operation width of the mounted rotary cultivator was 2.8m and the boundary distance thresholds were set as 0.4m, 0.8m and 1.2m.

**Fig. 8 - Vehicle side test site layout**

As the driver drove the tractor toward the side boundary of the vehicle, the cross-boundary distance gradually decreased. When the cross-boundary distance was less serially detected as less than 1.2m and then 0.8m, the system entered respectively the third-level and second-level warning and the warning lights for third-level and second-level warning turned on in sequence. When the final cross-boundary distance was less than 0.4m, the first-level warning light turned on and the system controlled the motor to steer the tractor.

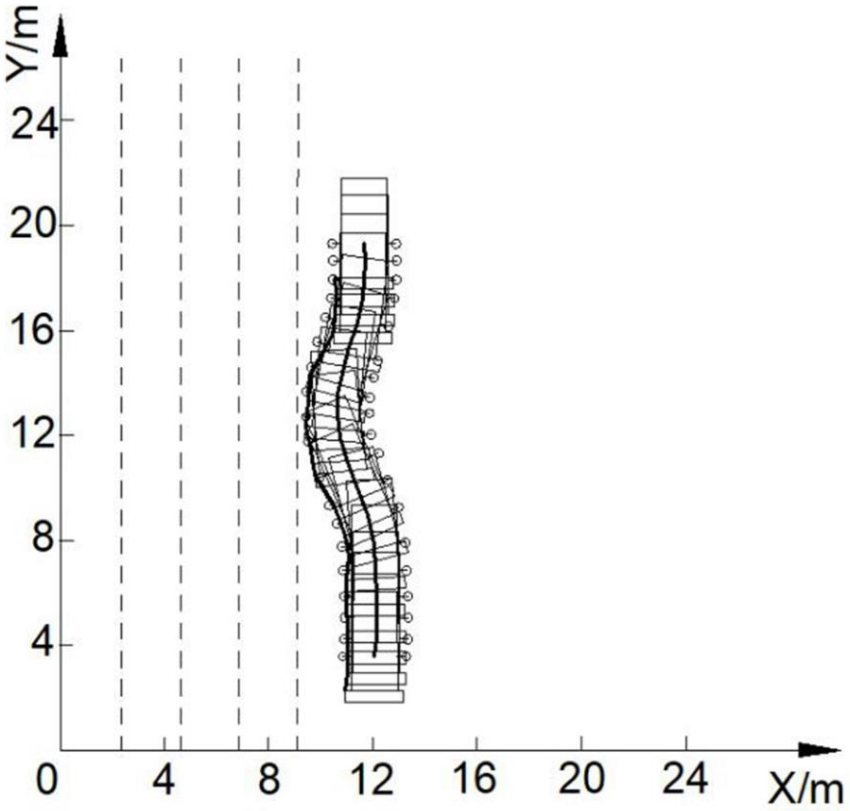


**Fig. 9 - Tractor actual walking route**

Figure 9 shows the recorded actual travelling route of the tractor from the experiment, in which the travel path of the tractor and the working track of the rotary cultivator are marked with thick lines. The figure indicates that when the driver drove the tractor awry of the intended prepared area the system controlled the motor to steer to the opposite direction upon entering the first-grade alert state in order to prevent the tractor from crossing the boundary.

***Cross-boundary warning test for arbitrary boundary***

The selected test site was soil at the Northwest A&F University. A simulated pit was set in advance on the tractor's path. As shown in Figure 10, the vertical rod at the right marked the centre of the simulated pit and the rod at the left marked the boundary of the driving area. The safe radius was set as 0.3m and the three levels warning distance thresholds from most to least alert were 0.3m, 0.6m and 0.9m, respectively.

**Fig. 10 - Arbitrary boundary warning test site layout**

During normal driving of the tractor, the cross-boundary warning system judged the cross-boundary distance between the tractor and the pit in real time. When the tractor drove within 0.9m and 0.6m warning distances, the third-level and second-level lights turned on. When the tractor drove within the scope of 0.3m, the first-level warning light turned on.

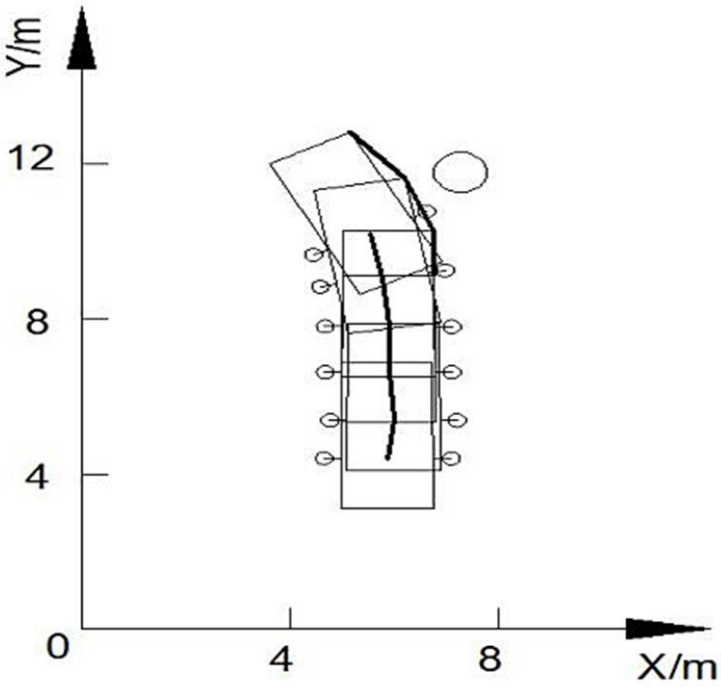


**Fig. 11 - Tractor actual walking route**

Figure 11 shows the recorded actual travelling route of the tractor from the experiment, in which the travel path of the tractor and the outer wheel turning path of the tractor are marked with thick lines. The figure shows that when the tractor approached the pit on the right, the system controlled the motor rotate clockwise upon entering the first-level warning region so that the tractor bypassed the pit smoothly.

The cross-boundary warning test for an arbitrary boundary showed that the cross-boundary warning system effectively operated as intended according to the actual conditions in the operation area.

## CONCLUSIONS

To address potential risks during the process of soil preparation, a hierarchical cross-boundary warning system based on the building of cross-boundary warning model was proposed. It extracted the cross-boundary information of the tractor by acquiring the real-time positioning information of the tractor via BDS, the tractor's soil preparation speed and the steering angle. When the tractor entered the first (highest) warning state, the system automatically controlled the motor to shift so that the tractor bypassed the boundary or hazard. In this study, the relevant field tests were conducted with a John Deere Model 1204 tractor mounted rotary cultivator as the test platform. The test results show that the hierarchical cross-boundary warning system was generally stable and is viable for further application.

## ACKNOWLEDGEMENT

The authors appreciate the financial support provided by the National Key Research and Development Program of China (2017YFD0700402) and the Key Research and Development Program of the Shanxi (2018NY-160). The authors thank the editing team of Editor Bar Editing Company for improving the English language fluency of our paper.

## REFERENCES

[1] Chen W., Zhao L., Tan D. et al., (2019), Human–machine shared control for lane departure assistance based on hybrid system theory. *Control Engineering Practice*, vol.84, pp.399-407;

[2] Di X., Shihong G., Yinong L. et al., (2010), Problem and strategies on development of agricultural water management(农业水管理面临的问题及发展策略), *Transactions of the Chinese Society of Agricultural Engineering*, vol.26, pp.1-7;

[3] Ghasemzadeh A and Ahmed M.M., (2018), Utilizing naturalistic driving data for in-depth analysis of driver lane-keeping behaviour in rain: Non-parametric MARS and parametric logistic regression modeling approaches. *Transportation Research Part C: Emerging Technologies*, vol.90, pp.379-392;

[4] Hu Liping, Liu Jinfan, Wang Hongye, Yan Hua, Yin Hongcheng, (2019), Vehicle SAR Simulation images validation method based on fuzzy comprehensive evaluation(基于模糊综合评判的车辆目标SAR 仿真图像评估方法), *Systems Engineering and Electronics*, vol.41, pp.534-540;

[5] Li Dawei, (2011), *Research of magnetic material detection methods based on machine vision (基于机器视觉的磁性材料检测方法研究)*, Shandong University/China;

[6] Meichen L., Jun C., Xiang Z., Lu W., Yongpeng T., (2018), Dynamic obstacle detection based on multi-sensor information fusion. *IFAC-PapersOnLine*, vol.51, pp.861-865;

[7] Meng Qingkuan, Zhang Man, Yang Yuhuang, Qiu Ruicheng, Xiang Ming, (2016), Guidance Line Recognition of Agricultural Machinery Based on Particle Swarm Optimization under Natural Illumination(自然光照下基于粒子群算法的农业机械导航路径识别), *Transactions of the Chinese Society for Agricultural Machinery*, vol.47, pp.11-20;

[8] Mo H and Farid G., (2018), Nonlinear and Adaptive Intelligent Control Techniques for Quadrotor UAV - A Survey. *Asian Journal of Control*, vol.21, pp.15-20;

[9] Shi Tingna, Zhang Wei, Xiao Meng, Pei Qiang, Xia Changliang, (2017), Predictive current control for permanent magnet synchronous motor based on operating time of vector (基于矢量作用时间的永磁同步电机 预测电流控制), *Transactions of China Electrotechnical Society*, vol.32, pp.1-10;

[10] Sui Mingming, Shen Fei, Xu Aiguo, Ding Shuangwen, (2016), Management System for Mechanized Straw Returning Based on BDS(基于北斗卫星导航的秸秆机械化还田作业管理系统), *Transactions of the Chinese Society for Agricultural Machinery*, vol.47, pp.23-28;

[11] Varela María Florencia, Scianca Carlos María, Taboada M.A, Gerarod Rubio, (2014), Cover crop effects on soybean residue decomposition and P release in no-tillage systems of Argentina. *Soil and Tillage Research*, vol.143, pp.59-66;

[12] Wang Fengyun, Zheng Jiye, Tang Yan, Liu Yanzhong, Li Qiaoyu, Mu Yuanjie, Wang Lei, (2016), Analysis on application and research progress of machine vision in agriculture in China(机器视觉在我国农业中的应用研究进展分析), *Shandong Agricultural Sciences*, vol.48, pp.139-144;

[13] Xiong Bin, Zhang Junxiong, Qu Feng, Fan Zhiqi, Wang Dashuai, Li Wei, (2017), Navigation Control System for Orchard spraying Machine Based on BeiDou Navigation Satellite System(基于 BDS 的果园施药机自动导航控制系统), *Transactions of the Chinese Society for Agricultural Machinery*, vol.48, pp.45-50;

[14] Zhao Liming, Ye Chuan, Zhang Yi, Xu Xiaodong, Chen Jing, (2018), Path recognition method of robot vision navigation in unstructured environment(非结构化环境下机器人视觉导航的路径识别方法), *Acta Optica Sinica*, vol.38, pp.267-276;

[15] Zhuo Qing, Lu Chang, Jin Haozhe, (2016), Based on iron wire magnetizing crossing border detection(基于铁丝磁化的车模越界检测), *Electronic Engineering & Product World*, vol.23, pp.57-59+63.

# CALCULATION OF A TRACK FORMATION PROCESS DURING WHEEL-GROUND INTERACTION
# /
# РОЗРАХУНОК ПРОЦЕСУ УТВОРЕННЯ КОЛІЇ ПРИ ВЗАЄМОДІЇ КОЛЕСА ІЗ ҐРУНТОМ

**Golub G.A.[1)], Chuba V.V.[1)] Kukharets S.M.[2)]. Yarosh Y.D.[2)], Tsyvenkova N.[2)]**
[1)]National University of Life and Environmental Sciences of Ukraine / Ukraine,
[2)] Zhytomyr National Agroecological University / Ukraine,
*Tel: +380676653548*, *E-mail: saveliy_76@ukr.net*
*DOI: 10.35633/INMATEH-59-08*

***Keywords:*** *soil deformation, tire, the contact area of the wheel, support surface.*

**ABSTRACT**

*The article provides the mathematical model of formation of a track depth depending on the size of vertical loading of a machine-tractor unit wheel, the structural parameters of the wheel and the soil properties. Based on the developed mathematical model, the experimental data of wheel-soil interaction and the soil properties, the track formation process in the soil depending on the pressure created by the wheel in a zone of contact with soil is proved. The analysis of the process of forming the track allows us to conclude that the intensity of track formation decreases with the increase in the wheel-ground interaction time.*

**АБСТРАКТ**

*В статті розроблено математичну модель формування глибини колії в залежності від величини вертикального навантаження колеса машинно-тракторного агрегату, конструкційних параметрів колеса та параметрів агротехнологічного середовища. На основі розробленої математичної моделі, отриманих експериментальних даних взаємодії колеса із ґрунтом та параметрів агротехнологічного середовища обґрунтовано процес формування колії в ґрунті в залежності від тиску який створює колесо в зоні контакту з ґрунтом. Аналіз процесу формування колії дозволяє зробити висновок про зменшення інтенсивності формування колії із збільшенням часу взаємодії колеса із ґрунтом.*

## INTRODUCTION

Trends in the development of modern agricultural machinery are to increase the capacity and productivity of technical means, primarily characterized by an increase in the total weight of machine-tractor units (MTU). Increasing the weight of MTU increases the intensity of soil compaction by running systems and accelerates soil degradation processes (*Mueller et al., 2010*). Soil compaction is a worldwide problem that leads to increased soil density, reduced water volume and reduced porosity, impairs soil aeration and water permeability, disrupts plant nutrition metabolism (*Nawaz et al., 2013; De Lima, 2017*), leads to increased greenhouse gas emissions (*Usowicz and Lipiec, 2017*), and decreases soil productivity (*Mueller et al., 2010; Vereecken et al., 2015*). Interaction of a navigation system simultaneously with the soil compaction leads to the formation of a track. Especially intensive process of track formation is observed when performing operations of pre-sowing treatment, sowing, fertilizing, and chemical protection, carried out in the phase when the soil is artificially loosened after plowing and saturated with sufficient moisture. Changes in the relief of the ground surface and the presence of areas with different physical and mechanical characteristics degrade the quality of technological operations and negatively affect the operational performance of MTU. When moving on less compacted soil, the rolling resistance of the movers increases and there is an increase in the power consumption for movement. A number of studies (*Gray et al., 2016; Taghavifar and Mardani, 2016*) are devoted to the development of programs, the algorithm of which allows optimizing the movement of MTU on the field in order to reduce the possible overlaps of the paths of machines wheel movers, and as a consequence, reduce the negative impact on the soil. Understanding the processes of forming a track in the soil will further reduce the negative impact on the soil, improve the efficiency of MTA due to the optimal choice of existing equipment and the design of new technical means and engines.

In some studies (*Kurjenluoma et al., 2009*) the influence of the type of tires on the formation of a track and the formation of rolling resistance was determined using the regression analysis method. It was established that the depth of the track is correlated with the value of the wheel coupling with the soil and soil density indicators, a linear correlation of the depth of the track and rolling resistance was established. It was also noted that the bearing capacity of the soil both vertically and laterally depends largely on the relative strength and moisture content of the soil layers. Having carried out an experimental analysis of the factors influencing the track formation of driven (*Carman, 2002*) and driving (*Taghavifar and Mardani, 2016*) wheels, it was found that the main factor that affects soil compaction is the vertical load. In the studies (*Damanauskas and Janulevičius, 2015; Higa et al., 2015; Taghavifar and Mardani, 2016*) it is noted that in addition to the vertical load, the processes of compaction and deformation of the soil are influenced by the speed and parameters of the wheel movers. The results of the studies provide an understanding of the track formation process flow and compaction of the soil running systems. The obtained regression models are useful for modeling the corresponding parameters of soil interaction, but their wide application is limited by the parameters of similarity of the conditions under which these models are obtained.

A certain number of mathematical models *(Söhne, 1958; Smith, 2000; Défossez, 2002)* for predicting soil compaction and deformation were obtained as a result of improvements in the equations of M.J. Boussinesq (*Naveed et al., 2016*). However, the use of this type of models is only suitable for homogeneous soil and at loads not exceeding the elastic limit of the soil (*Nawaz et al, 2013*). Investigating the influence of the number of passes of wheeled vehicles on the depth of the track formation (*Vennik et al., 2019*), the comparison of experimental data of soil deformation based on the results of calculation using analytical models is performed. The authors noted the high coincidence of the results when using the SoilFlex model to predict the depth of the track formation when moving along the surface of the soil, but also noted the need to refine this model for use on other types of soils and when modeling multiple passes.

The SoilFlex model (*Keller et al, 2007*) implemented an algorithm that combined a wheel-soil contact model, a model for quantifying soil bulk deformation in the longitudinal and lateral directions, and a model for estimating soil deformation depth. In further studies, *Keller et al (2015)*, changes were made regarding the block, taking into account the influence of variable properties of soil structure on the process of deformation and stress propagation and the SoilFlex-LLWR model was obtained. SoilFlex models allow estimating the ultimate conditions of deformation and bearing capacity of the soil (*Lozano et al., 2013; Vennik et al., 2019*). The disadvantage of the SoilFlex and SoilFlex-LLWR models is the lack of a time function during which the soil is subjected to the appropriate loads. These shortcomings prevent the use of these models for the analysis of dynamic processes of interaction between the wheel and the ground.

Models based on the FEM – finite element method (*Hambleton and Drescher, 2009; González Cueto et al., 2016; Silva, 2018*) have been developed to predict soil deformation and track depth. The complexity of the practical use of such models is associated with the need to introduce a sufficiently large number of input experimental parameters. The considered FEM models of soil compaction are aimed at the combination of different soil properties in order to determine the General distribution of stresses and strains. These models do not allow determining the energy costs of soil deformation and require an algorithm to account for the time during which the contact interaction occurs.

For determining the indices of soil deformation and track formation, in some studies (*Mason et al, 2016; Vahedifard et al., 2016*) it was proposed to expand the known analytical model VTI (Vehicle Terrain Interface) by introducing algorithms for the estimation of the pressure of contact interaction of wheels with the soil and strength of soil index (taper index). The application of VTI models to obtain practical results, along with simplicity, requires sufficiently voluminous initial experimental studies of the relevant variables. In Mason's et al study (*Mason et al., 2016*), 2737 experimental measurements were performed to obtain a model capable of predicting the parameters of track formation. A composite database of more than 5,253 studies was used to model the mobility performance of wheeled vehicles when operating on dry sand (*Vahedifard et al., 2016*). Given the number of parameters affecting soil deformation, as well as the possible quantitative variations of these parameters, updating VTI models is a large-scale task in terms of performing the required number of experimental measurements.

The analysis indicates the importance of understanding the phenomena occurring during deformation and the formation of a track during the interaction of wheel travel systems with the soil. Existing models consider the state of the soil, which experiences loads and stress transfer that occur, but do not consider the dynamics of the process of track forming from the load of running systems on the soil. The available models

obtained by means of regression analysis are rather limited by the conditions under which they were obtained. Forming a model that fully takes into account the processes that occur during the formation of the track will allow designing the parameters of the machine, considering the functionality of performing certain operations in accordance with the properties of the working environment in which the engine operates.

## MATERIALS AND METHODS

A mathematical model of the dynamics of track formation under the action of MTU wheels has been developed on the basis of the mechanics laws, based on the power analysis of the MTU work and considering the soil properties and the contact interaction of the wheels with the soil.

When performing experimental studies, the MTU was used as part of a 4WD tractor Kyi-14102 with a total weight of 37.5 kN and a plow PRO-3 with a weight of 8.5 kN (Fig. 1). The weight on the rear axle of this MTU with a raised plow was 36.5 kN. To determine the maximum possible depth of the track, a rectangular section of the floor with a length of 150 m and a width of 100 m was previously plowed. After installing the appropriate pressure in the pneumatic chambers of the wheels, the MTU made some distance on freshly plowed soil while fixing the depth of the rear wheel track (Fig. 1). The average value of 10 measurements made at different points along the length of the experimental section was taken as the track depth. An experimental study of the change in the geometric parameters of the contact zone of the tractor tires with a change in the pressure in the pneumatic chamber of the wheel was performed. To find the contact area of the wheel with the ground, a geometric analysis of the wheel imprint on the ground was performed (*Golub et al., 2019*).

**Fig. 1 - Measurement of the track depth after the MTU passed**

To determine the soil properties, with the help of a manual penetrometer Datafield with a step of 25 mm, a change in the taper index of the fresh-cut soil profile was determined.

When performing theoretical calculations, it was taken the value of the tractor performance indices, soil properties in accordance with those under which experimental studies were carried out.

## RESULTS

Under the weight of a tractor or self-propelled machine, the wheel deforms and sinks into the ground. During the rolling of the wheel, the soil in front of it is compacted by tightening the soil under the wheel. When the wheel compacts the soil, it is compressed from the initial height to the depth of the track, and then can be partially expanded to a certain height (this phenomenon may be slightly manifested only when moving on soils with a high content of organic matter). At the same time, a track is formed in the soil.

With an increase in the depth of the wheel into the ground, the resistance of the soil to the wheel penetration increases. To analyse the change in soil resistance as a function of depth, we make the following assumption: the resistance of the soil *R* as the wheel sinks into the soil is directly proportional to the depth of the wheel $l$ into the soil.

So we can record $dR=kdl$.

Thus, the coefficient of proportionality $k$ can be written as follows:

$$k = \frac{R - R_0}{l}. \quad (1)$$

where

$k$ – the proportionality coefficient, [Pa/m]; $R$ – soil resistance, [Pa]; $R_0$ – initial resistance of the soil, [Pa]; $l$ – depth of immersion of the wheel in the ground, [m].

The penetration of tractor wheels into the ground will be determined by the following equation:

$$m\frac{d^2l}{dt^2} = mg - RS = mg - S\left(R_0 + kl\right) \ldots \quad \ldots\ldots\ldots\ldots\ldots\ldots(2)$$

or

$$\frac{d^2l}{dt^2} = g - \frac{RS}{m} = g - \frac{S}{m}\left(R_0 + kl\right) \quad (3)$$

where $g$ – gravitational acceleration, [m/sec²]; $S$ – the contact area between wheel and soil, [m²]; $m$ – MTU weight per wheel, [kg].

We find the solution of the differential equation (3) in the form:

$$l = \frac{a}{b} + \frac{1}{b}\sqrt{a^2 + 2bC_1^2}\,\sin\left[\sqrt{b}\left(t + C_2\right)\right]. \quad (4)$$

Accept the initial conditions: $t=0$, $l=0$. $\frac{dl}{dt} = 0$, $l=max$.

The constant integrations based on the initial conditions will be:

$$C_1^2 = b\frac{l_{MAX}^2}{2} - al_{MAX}, \quad (5)$$

$$C_2 = \frac{1}{\sqrt{b}}\arcsin\left(-\frac{a}{a - bl_{MAX}}\right). \quad (6)$$

We substitute the obtained integration results into equation (4) and perform the necessary transformations:

$$l = \frac{a}{b}\left\{1 + \left(1 - \frac{b}{a}l_{MAX}\right)\sin\left[t\sqrt{b} + \arcsin\left(-\frac{1}{1 - \frac{b}{a}l_{MAX}}\right)\right]\right\},$$

Substituting the values $\frac{b}{a} = \frac{kS}{m}\frac{m}{mg - SR_0} = \frac{kS}{mg - SR_0}$, we have:

$$l = \frac{mg - SR_0}{kS}\left\{1 + \left(\frac{mg - SR_0 - kSl_{MAX}}{mg - SR_0}\right)\sin\left[t\sqrt{\frac{kS}{m}} + \arcsin\left(-\frac{mg - SR_0}{mg - SR_0 - kSl_{MAX}}\right)\right]\right\} \quad (7)$$

Substituting in the resulting equation (7) the value of the pressure from the wheel $P = \frac{mg}{S}$, we have:

$$l = \frac{P - R_0}{k}\left\{1 - \left(1 - \frac{kl_{MAX}}{P - R_0}\right)\sin\left[\arcsin\left(\frac{1}{1 - \frac{kl_{MAX}}{P - R_0}}\right) - t\sqrt{\frac{kg}{P}}\right]\right\} \quad (8)$$

The obtained solution (8) of the differential equation (3) makes it possible simulating the dynamic processes of soil deformation in the formation of a track depending on the parameters of wheel-soil interaction. When performing the simulation using the dependence (8), it is necessary to take into account that the sine is an odd function the graph of which is symmetric with respect to the origin, so when performing the simulation, we choose the first period in which the sine function is in the positive half-period.

Soil properties and parameters of interaction between the wheel and the support surface were obtained in the field, when performing studies of the MTU at different pressures in the pneumatic chamber of the wheel tire (Table1).

**Table 1**

**The values of the parameters of the interaction of the wheels with the ground**

| Index | Un. | Symbol | The value of the cell pressure, kPa | | |
|---|---|---|---|---|---|
| | | | **0.18** | **0.18** | **0.18** |
| **MTA weight given to the rear wheel (tractor Kyi-14102 + plow PRO)** | kg | $m_T$ | 1825 | 1825 | 1825 |
| **The initial soil resistance** | Pa | $R_0$ | 11000 | | |
| **The coefficient of proportionality of soil resistance** | Pa/m | $k$ | 2742831 | 2524858 | 2234227 |
| **The pressure on the ground in the contact patch** | Pa/m$^2$ | $P$ | 92523 | 114764 | 127880 |
| **The length of the contact patch** | m | | 0.45 | 0.39 | 0.35 |
| **The maximum track depth** | m | $l_{MAX}$ | 0.123 | 0.139 | 0.151 |
| **The MTU speed** | km/h | | 8.2 | 5.4 | 3.6 |
| **The time of interaction of the wheels with the ground at a given speed** | sec | $t$ | 0.3 | 0.195 | 0.35 |

Experimental dependences of the influence of pressure in the pneumatic chamber of the wheel tire on the change of the contact area of the wheel with the support surface and on the track depth are obtained (Fig. 2).

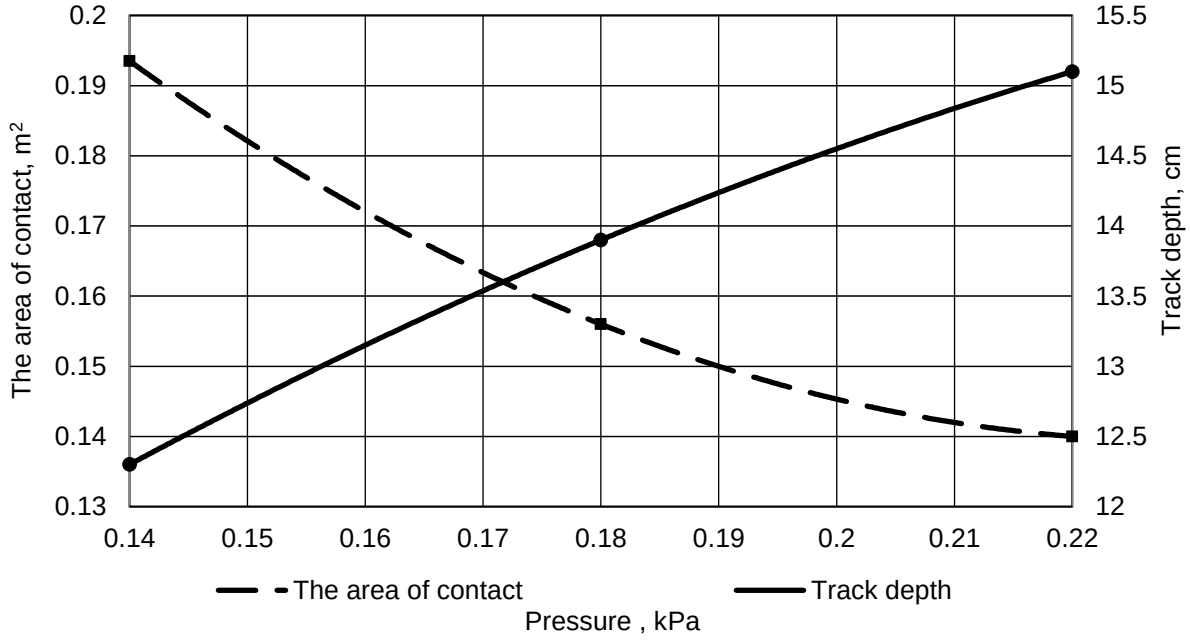


**Fig. 2 - The effect of pressure in the pneumatic chamber of the wheel on the contact area of the wheel with the soil and the track depth**

On the basis of the obtained mathematical model (8) and the data of Table 1, the simulation of soil deformation in the formation of a track depending on the pressure in the pneumatic chamber of the wheel is shown in (Fig. 3).

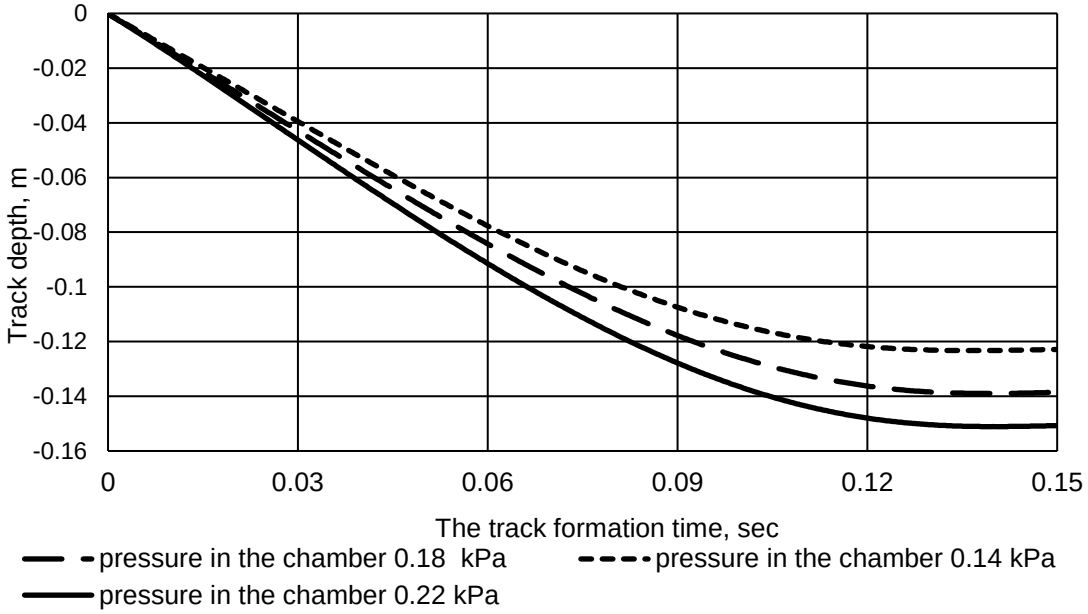


**Fig. 3 - Dynamics of the soil deformation process in the formation of the track in interaction with the wheel at different pressures in the pneumatic chamber of the tire**

The contact interaction of the wheel with the ground during the formation of the track occurs in the contact plane, which in the longitudinal section has a sinusoidal shape. The sinusoidal shape in the longitudinal section plane is affected by the contact pressure in the wheel - soil contact zone, the maximum track depth and properties of soil environment, as well as the time of contact interaction.

The analysis of the obtained dependences showed that at different wheel pressures on the soil, the time to reach the maximum depth of the track formation is almost unchanged and is about 0.13 s. The nature of the obtained dependences of the track formation dynamics allows concluding that the intensity of the track formation decreases with increasing the interaction time. At a tire pressure of 0.14 kPa, at an interval of 0.03 seconds from the beginning of contact, the depth of deformation of the track is 3.95 cm; in the interval 0.03 - 0.06 seconds, the soil deformation was 3.82 cm, which is 3.29% less than in the previous interval; in the interval 0.06 - 0.09 sec, the soil deformation is 2.95 cm, which is 22.8% less than the deformation in the previous interval; in the interval 0.09 - 0.13 sec, the soil deformation was 1.57 cm. At a pressure of 0.18 kPa deformation for the first 0.03 sec is 4.27 cm; in the range 0.03 - 0.06 sec, the deformation was 4.16 cm, which is 2.58% less than in the previous interval; in the interval 0.06 - 0.09 sec, the deformation of the soil was 3.33 cm, namely 19.95% less than in the previous interval; in the range 0.09 - 0.13 sec, the deformation of the soil was 2.1 cm. At a pressure of 0.22 kPa, the deformation over the first 0.03 sec was 4.62 cm; in the range 0.03 - 0.06 sec – 4.53 cm, which is 1.94% less than in the previous interval; in the range 0.06 - 0.09 sec, the soil deformation was 3.62 cm, which is 20.08% less than in the previous interval; in the range 0.09 - 0.13 sec, the soil deformation was 2.27 cm. With greater pressure in the wheel-soil contact zone, an increase in the intensity of the track depth formation is observed. In the interval from the beginning of the wheel contact with the soil to 0.03 sec at a pressure in the tire chamber of 0.22 kPa, the soil deformation is 4.62 cm, which is 8.19% more than the deformation at a pressure in the chamber of 0,18 kPa and 16.96% more than at a pressure of 0.14 kPa.

It should also be noted that the time of track formation (Fig. 3) is considerably shorter than the time of wheel - ground contact interaction (table 1). The obtained results allow us to assert that for these conditions of soil interaction at a pressure in the wheel chamber of 0.22 kPa and a contact zone length of 0.35 m, the movement speed up to 9.69 km/h does not affect the formation of the track depth, for a pressure of 0.18 kPa, this speed is 10.8 km/h, for a pressure of 0.14 kPa, the speed is 12.46 km/h.

As a result of the conducted researches the mathematical model of dynamics of a track depth formation at the interaction of a MTU wheel with soil is developed. A mathematical model establishes a

relationship between the parameters of the MTU, soil properties, the geometric engagement of the wheel with the ground. The obtained model of the track formation dynamics is suitable for modelling the effects on track depth the parameters of soil, parameters of the pneumatic tire wheel of the MTU, the vertical load on the wheel.

The obtained results allow checking the design solutions in the development of new machines, assembling the MTU depending on the soil properties, optimizing the modes of the MTU operation.

In carrying out further research, it is advisable to improve the obtained mathematical model of the formation of the MTU track depth by clarifying the influence of the pneumatic tire properties on the parameters of interaction with the soil. This will make it possible to more fully characterize the processes of interaction between the wheel movers and the soil and will allow obtaining dependencies that will increase the accuracy of mathematical modeling of the movers' impact on the soil during the operation of the MTU.

## CONCLUSIONS

The studies established the relationship between the operational and structural parameters of MTU engines and the soil properties. On the basis of the mass per MTU wheel, geometric parameters of the contact zone of the wheel with the support surface, the coefficient of resistance of the soil, deformation and the track depth, a differential equation is obtained to determine the depth of the track formation. The solution of the obtained equation allows determining the dynamics of the formation of soil paths depending on the resistance of the soil, the area of contact interaction of the wheel with the support surface and the vertical load.

The simulation of the influence of pressure in the wheel pneumatic chamber, for certain agrotechnological conditions, showed that the formation of the track occurs within 0.13 seconds of the wheel - ground contact interaction and does not depend on the pressure in the wheel. It should be noted that with increasing pressure in the contact zone with the soil, there is an increase in the intensity of the depth of the track formation. It should also be noted that the intensity of the track formation decreases with increasing time, so at a tire pressure of 0.14 kPa, from the beginning of contact and for the first 0.03 seconds, the depth of track deformation is 3.95 cm, for the next 0.03 seconds, the deformation is 3.82 cm, which is 3.29% less than the previous one, for the next 0.03 seconds, the deformation of the soil is 2.95 cm, which is 22.8% less than the previous one, for the last 0.03 seconds, the deformation of the soil is 1.57 cm; speed up to 9.69 km does not affect the formation of the track depth. The obtained results allow us to determine the dynamics of a track formation in the soil during the movement of the MTU.

## REFERENCES

[1] Carman K., (2002), Compaction characteristics of towed wheels on clay loam in a soil bin. *Soil and Tillage Research*, Vol.65, pp.37–43, Netherlands;

[2] Damanauskas V., Janulevičius A., (2015), Differences in tractor performance parameters between single-wheel 4WD and dual-wheel 2WD driving systems. *Journal of Terramechanics*, Vol.60, pp.63-73, United Kingdom;

[3] De Lima R. P., da Silva A. P., Giarola N.F. B. et al., (2017), Changes in soil compaction indicators in response to agricultural field traffic. *Biosystems Engineering*, Vol.162, pp.1–10, United States;

[4] Défossez P., Richard, G., (2002), Models of soil compaction due to traffic and their evaluation. *Soil Tillage Research*, Vol.67, pp.41–64, Netherlands;

[5] Golub G.A., Chuba V.V., Marus O.A., (2019), Determination of rolling radius of self-propelled machines' wheels. *INMATEH - Agricultural Engineering*, Vol.57, pp.81-90, Bucharest/Romania;

[6] González Cueto O., Iglesias Coronel C.E., López Bravo E., et al., (2016), Modelling in FEM the soil pressures distribution caused by a tire on a Rhodic Ferralsol soil, *Journal of Terramechanics*, Vol. 63, pp, 61–67, United Kingdom;

[7] Gray J.P., Vantsevich V.V., Paldan J., (2016), Agile tire slippage dynamics for radical enhancement of vehicle mobility. *Journal of Terramechanics*, Vol.65, pp.14-37, United Kingdom;

[8] Hambleton J.P., Drescher A., (2009), Modeling wheel-induced rutting in soils: Rolling. *Journal of Terramechanics*, Vol.46, pp.35–47, United Kingdom;

[9] Higa S., Nagaoka K., Nagatani K., Yoshida K., (2015), Measurement and modeling for two-dimensional normal stress distribution of wheel on loose soil. *Journal of Terramechanics*, Vol.62, pp.63-73, United Kingdom;

[10] Keller T., da Silva A.P., Tormena C.A. et al., (2015), SoilFlex-LLWR: Linking a soil compaction model with the least limiting water range concept. *Soil Use and Management*, Vol.31 Issue 2, pp.321-329, United States;
[11] Keller T., Défossez P., Weisskopf P. et al., (2007), Soil Flex: A model for prediction of soil stresses and soil compaction due to agricultural field traffic including a synthesis of analytical approaches. *Soil and Tillage Research*, Vol.93, Issue 2, pp.391-411, Netherlands;
[12] Kurjenluoma J., Alakukku L., Ahokas J., (2009), Rolling resistance and rut formation by implement tires on tilled clay soil. *Journal of Terramechanics*, Vol.46, Issue 6, pp.267–275, United Kingdom;
[13] Lozano N., Rolim M.M., Oliveira V.S., (2013), Evaluation of soil compaction by modeling field vehicle traffic with SoilFlex during sugarcane harvest. *Soil and Tillage Research*, Vol.129, pp.61–68, Netherlands;
[14] Mason G. L., Vahedifard F., Robinson J. D. et al., (2016), Improved Sinkage Algorithms for Powered and Unpowered Wheeled Vehicles Operating on Sand. *Journal of Terramechanics*, Vol.67, pp.25-36, United Kingdom;
[15] Mueller L., Schindler U., Mirschel W. et al, (2010), Assessing the productivity function of soils: a review. *Agronomy for sustainable development*, Vol.30, Issue 3, pp.601-614, France;
[16] Nawaz M.F., Bourrie G., Trolard F., (2013), Soil compaction impact and modelling. A review. *Agronomy for Sustainable Development*, Vol.33, Issue 2, pp.291–309, France;
[17] Naveed M., Schjonning P., Keller T. et al., (2016), Quantifying vertical stress transmission and compaction-induced soil structure using sensor mat and X-ray computed tomography. Soil and Tillage Research, Vol.158, pp.110–122, Netherlands
[18] Silva R.P., Rolima M.M., Gomes I.F. et al, (2018), Numerical modeling of soil compaction in a sugarcane crop using the finite element method. Soil and Tillage Research, Vol.181, pp.1–10, Netherlands;
[19] Smith R., Ellies A., Horn R., (2000), Modified Boussinesq's equations for non-uniform tire loading. *Journal of Terramechanics*, Vol.37, pp.207–222, United Kingdom;
[20] Söhne W., (1958), Fundamentals of pressure distribution and soil compaction under tractor tires. Agricultural Engineering, Vol.39, pp.276–281.
[21] Taghavifar H., Mardani A., (2015), Net traction of a driven wheel affected by slippage, velocity and wheel load. Journal of the Saudi *Society of Agricultural Sciences*, Vol. 14, pp.167–171, Saudi Arabia;
[22] Usowicz B., Lipiec J., (2017), Spatial variability of soil properties and cereal yield in a cultivated field on sandy soil, *Soil and Tillage Research*, vol.174, pp.241-250, Netherlands;
[23] Vahedifard F., Robinson J.D., Mason G.L. et al., (2016)., Mobility algorithm evaluation using a consolidated database developed for wheeled vehicles operating on dry sands. *Journal of Terramechanics*, Vol.63, pp.13-22, United Kingdom;
[24] Vennik K., Kukk P., Krebstein K. et al., (2019), Measurements and simulations of rut depth due to single and multiple passes of a military vehicle on different soil types. *Soil and Tillage Research*, Vol.186, pp.120-127, Netherlands;
[25] Vereecken H., Schnepf A., Hopmans J.W. et al., (2015), Modeling Soil Processes: Review, Key Challenges, and New Perspectives. *Vadose Zone Journal*, Vol.15, Issue 5, pp.1-57, United States.

# HYBRID RENEWABLE ENERGY SYSTEMS FOR ISOLATED FARMS. A REVIEW
# /
# SISTEME HIBRIDE DE ENERGIE REGENERABILĂ PENTRU FERMELE INSULARIZATE. O TRECERE IN REVISTĂ

**Maican E.*[1)], Vlădut V.[2)], Vîlcu C.[2)], Sorică C.[2)], Dorian M.[3)], Mirea D.P.[4)], Bogăţeanu R.[5)] [1]**
[1)] "Politehnica"University of Bucharest, Faculty of Biotechnical Systems Engineering / Romania;
[2)]INMA Bucharest / Romania; [3)]ICPE-CA Bucharest / Romania; [4)]University of Bristol / UK; [5)]INCAS Bucharest / Romania
*Tel: +40721090813; E-mail: constantin.vilcu@inma.ro*
*DOI: 10.35633/INMATEH-59-09*

***Keywords:*** *hybrid renewable energy systems, renewable power generation, environment protection, sustainable agriculture*

***Abbreviations:***

*AC – Alternating Current;*
*CAE – Computer-Aided Engineering;*
*CAD – Computer-Aided Design;*
*CFD – Computational Fluid Dynamics;*
*DC – Direct Current;*
*HAWT – Horizontal-axis Wind Turbines;*
*HVAC – High Voltage Alternating Current;*
*HVDC – High Voltage Direct Current;*
*HK – Hydrokinetic;*
*HKS – Hydrokinetic System;*
*HRES – Hybrid Renewable Energy Systems;*
*MN – Micro-networks;*
*NPS – National Power System;*
*PLC – Programmable Logic Controller;*
*PV – Photovoltaic Panel;*
*RES – Renewable Energy Sources;*
*SPV – Solar Photovoltaic System;*
*VAWT – Vertical-axis Wind Turbines;*
*VRFB – Vanadium Flow Redox Battery;*
*WT – Wind Turbine;*
*WPS – Wind Power System;*
*WTS – Wind Turbine System.*

**ABSTRACT**

*In this paper a preliminary analysis of hybrid renewable energy systems (HRES) able to generate at least 100 kW electric power is carried out. Restrictions on the installed power of small farms that are in isolated locations and cannot connect to NPS generally diminish productive activities and, implicitly, profit. Depending on the renewable energy resources (sun, wind, hydro) the characteristics of the isolated location of the work point, the optimal HRES system required for an efficient operation of the agricultural farm even under isolated conditions can be determined by the synthesis elaborated in this paper.*

*Renewable energies that are characteristic to abiotic environment have been approached, describing the current technological methods of transforming them into electricity. Critical issues related to energy storage variants were also considered for periods of time when renewable sources are not sufficient to ensure the electricity consumption needs. The mathematical model of the process of generating electricity from renewable sources has been elaborated in order to perform the global energy calculation of the optimum hybrid system required for the isolated farm.*

*These elements lead to the determination of the technical-economic indicator ζ €/kW of the HRES system in the management of the agricultural farm from the perspective of a sustainable agriculture that produces more with lower costs and in environmentally friendly conditions.*

**REZUMAT**

*În prezenta lucrare se face o analiză preliminară a sistemelor hibride de energie regenerabilă (HRES) a căror putere electrică generată poate să acopere un necesar de min. 100 kW. Restricţiile privind puterea electrică instalată a fermelor agricole de mică anvergură care sunt amplasate în locaţii insularizate şi fără posibilitate de racordare la SEN diminuează în general activităţile productive şi implicit profitul. În funcţie de resursele de energie regenerabile (soare, vânt, hidro) caracteristice locaţiei terestre insularizate a punctului de lucru se poate determina prin sinteza elaborată în această lucrare sistemul optim HRES necesar unei funcţionări eficiente a fermei agricole chiar şi în condiţii izolate.*

[1] *Maican E., Prof. Ph.D. Eng.; Vlăduţ V., Ph.D. Eng.; Vîlcu C., Ph.D. Stud.Eng.; Sorică C., Ph.D. Eng.; Dorian M., Ph.D. Eng.; Mirea D.P., Stud.; Bogăţeanu R., Ph.D. Eng.*

*S-au abordat tipurile de energii regenerabile caracteristice mediului abiotic prin descrierea metodelor tehnologice actuale de transformare a formei lor in energie electrică. S-a avut în vedere şi problematica critică referitoare la variantele de stocare a energiei pentru perioadele de timp în care sursele regenerabile nu sunt suficiente pentru asigurarea necesarului de consum de energie electrică. Modelarea matematică a procesului de generare a energiei electrice din surse regenerabile s-a elaborat în vederea realizării unui calcul global energetic al sistemului hibrid optim necesar fermei insularizate.*

*Aceste elemente conduc la determinarea indicatorului tehnico-economic ζ €/kW al sistemului HRES în managementul fermei agricole din perspectiva unei agriculturi durabile care produce mai mult cu cheltuieli mai mici şi în condiţii prietenoase cu mediul înconjurător.*

## INTRODUCTION

Energy is conceptually defined as a state function of a physical or chemical process. It can be obtained from exhaustible resources (non-renewable energy) or from the Sun and other inexhaustible resources (renewable energy) through conversion technologies in various forms of energy transfer. Table 1 shows the renewable energy sources (RES), the current conversion technologies used and the energy transfer form of the application, (*ECA, 2018*).

**Table 1**

**Renewable energy sources, technologies and applications** (*ECA, 2018*)

| **Source** | Solar | Wind | Water | Waves, tides | Geothermal | Biomass, waste |
|---|---|---|---|---|---|---|
| **Technologies** | Photovoltaics, Solar thermal | Wind turbines | Hydropower plant | Dams, tidal barrages | Geothermal, heat pumps | Biomass comb biogas plants, biofuels |
| **Applications** | Electricity, Heating and Cooling | Electricity | Electricity | Electricity | Electricity, Heating and Cooling | Electricity, Heating and Cooling, Transport |
| **% actually used in UE** | 6.4 % | 12.7 % | 14.4 % | - - - | 3.2 % | 63.3 % = (4.7 + 6.7 + 7.7 + 44.2) |

Global use of non-renewable energy (coal, oil, natural gas) also has unwanted effects such as greenhouse gas emissions that have fuelled global warming, acid rain, ecological disasters or environmental pollution. Through current clean energy conversion technologies, renewable energy resources are becoming increasingly valued. In this context, renewable energy is a cross-cutting priority relevant to many EU policy areas. The EU provides support for renewable energy under several funding programmes, like the European Regional Development Fund (ERDF), the European Agricultural Fund for Rural Development (EAFRD) as well as the Horizon 2020 and LIFE programmes.

In Romania, in the agricultural sector, farmers become more and more interested in renewable energy sources (*Brunswick, 2019*). Fortunately, there are several renewable or alternative energy options available. However, it is often hard to identify which of the technologies are best suited to a specific farm operation. Fig.1 illustrates the country's energy potential for the following renewable resources: a) sun; b) wind and c) rivers.

Currently, converting solar energy into electricity directly through photovoltaic panels is the easiest method used globally to obtain electricity in the form of direct current from solar radiation reaching the surface of the Earth. At the upper limit of the atmosphere, the radiated sunshine energy is 1367 W/m$^2$ and measured at ground level on a surface perpendicular to the direction of the rays, can generally reach 1000 W/m$^2$. Analyzing the map of solar radiation at ground level in Romania (Fig.1a), (*SolarGis, 2019)* agricultural farms located in the south part of the country, such as Oltenia, Baragan and Dobrogea, are benefiting the use of solar energy.

For the exploitation of the wind resource at the location of the isolated farm, it is of interest to know the variation of the wind speed up to a height of 50…150 m in relation to the land surface and statistically in time, throughout the entire calendar year. Because wind power is proportional to its cube velocity (*Ehrlich R., 2013*), for designing and manufacturing wind power conversion systems, it is recommended that farmers first consult their farm positioning on the map from a wind resource point of view. From the analysis of the wind map of Romania presented in Fig. 1b), (*AddEnergy, 2019*) three wind potential areas are distinguished for the following average wind speeds: ~ 8 m/s - mountain area; ~ 6 m/s - the second area with wind potential that can be used cost-effectively (Black Sea coast, Danube Delta and northern Dobrogea, areas where wind

energy exploitation is favoured by lower wind turbulence); 4…5 m/s - the third area with considerable potential, which is the Barlad Plateau. Also, favourable wind speeds are reported in other more restricted areas in the western part of the country.

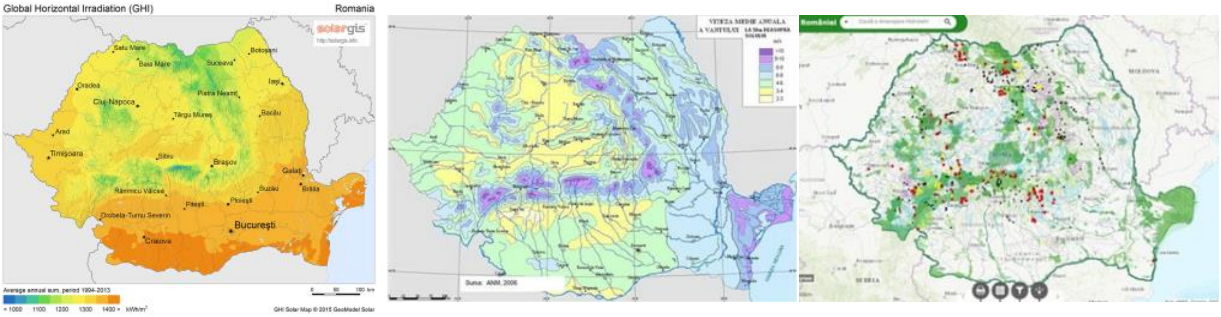


*a) sun* *b) wind* *c) rivers*

**Fig. 1 – The country's energy potential for the renewable resources (RO)**

The map of Romania's hydrographic network is presented in Fig.1c). Except rivers in the Dobrogea area, most of the running waters spring from the Carpathians and belong to the Danube river basin. Due to the varied configuration of Romania's terrain, the flowing water network is radially disposed. The main flowing waters have a longitudinal profile characterized by large slopes in the mountainous region where the water velocity is $v > 1$ m/s, while in the plain regions the water flow is more uniform, with lower velocities $v < 1$ m/s.

The most important RES in Romania is hydro energy (*WWF, 2019*). Agricultural farms located in the river meadows in the country's large river basins can benefit from the hydro-energetic micro-potential of fast rivers through simple facilities made to exploit the kinetic energy of flowing waters.

According to the RES maps in Fig.1, wherever it is located within the country, an isolated farm (without the possibility of connecting to the NPS) benefits from a dominant source of renewable energy. The other renewable resources are complementary so that a properly sized HRES system can continuously provide, through the integrated energy storage system, the power needed to operate in off-grid mode.

HRES is actually a combination of two or more renewable energy sources, or at least one renewable and one conventional source. HRES can be connected or not to the grid. For the presented case, the HRES system operates in stand-alone mode (off-grid mode). The hybrid energy system is defined as a combination of energy sources with different characteristics and an energy storage environment. With regard to stand-alone applications, choosing the optimal hybrid energy system is a challenging process due to many reasons, such as: determining the best combination of sources; reduce initial capital investment; reliability of power supply; system components, etc. Fig. 2 (*Zohuri B., 2018*) shows the block diagram of an autonomous hybrid system for small farms located in isolated locations. HRES hardware and software components are included in the Control System block and they perform process control and HRES efficiency improvement.

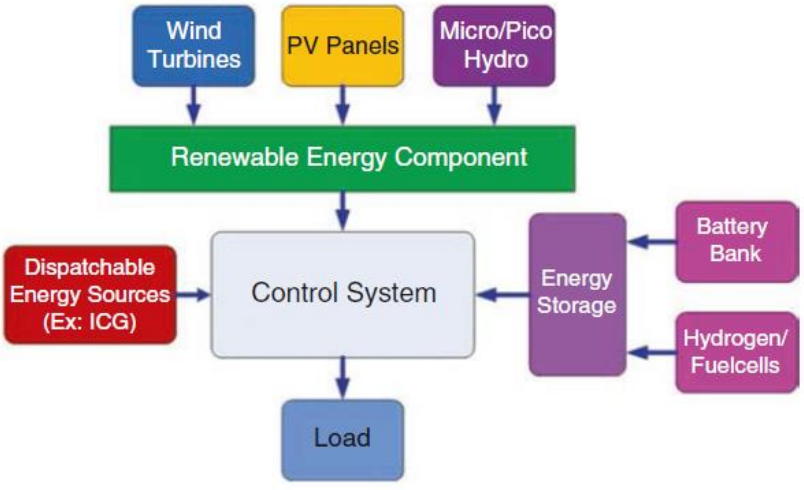


**Fig. 2 – Diagram bloc of a stand-alone hybrid energy system**
(*Zohuri B., 2018*)

The use in situ of HRES systems for isolated locations is a new step towards decentralized electrification. The systems can be grouped into single-phase or three-phase MNs, which feed local consumers and/or small farms. The interconnection of these sources of electricity in parallel on a common network raises many problems, caused mainly by their different functioning mode, by the different installed electric power, as well as by other particular aspects of each system. Often, in a HRES type system, in addition to renewable energy sources, conventional fossil fuel generators, generally Diesel engine generators, are used intermittently. They are introduced into the system when the demand for electricity of the consumers exceeds the capacity of the renewable sources. Combinations of more than two renewable sources become complex hybrid systems requiring higher-order investments. Reducing the techno-economic *ζ [€/kW]* indicator of such a hybrid energy system involves complex studies and detailed analyses before manufacturing. Fig. 4 shows the main systems of a hybrid HRES network: solar, wind, hydrokinetic, energy storage.

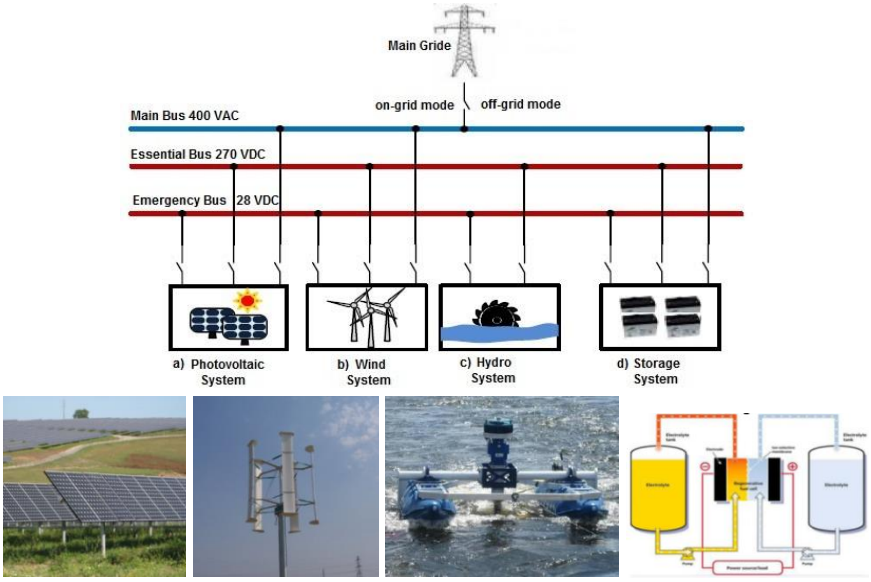


*a) SPV b) WT c) HK d) VRB storage*

**Fig. 4 – Micro-grid topology of hybrid renewable energy systems**

*Source (MICROREN, 2015)*

## METHODOLOGICAL APPROACH TO THE HRES SYSTEM FOR SMALL FARMS

### 1. ESTABLISHED SYSTEMS FOR RENEWABLE ENERGY CONVERSION INTO ELECTRICAL ENERGY

#### 1.1. Solar energy conversion system into electricity. PV technology and computational elements

Made out of semiconductor materials, the photovoltaic panels (PV) make direct conversion of solar energy into continuous current due to the photoelectric effect. Being the easiest method to convert solar radiation into electricity, PV technology is used today at any scale (Fig.5a). Typically, solar panels are modular, being made from sets of 36, 60 or 72 photovoltaic cells depending on the destination of the application in which they can be used. Voltage and PV power is directly proportional to the number of cells per module.

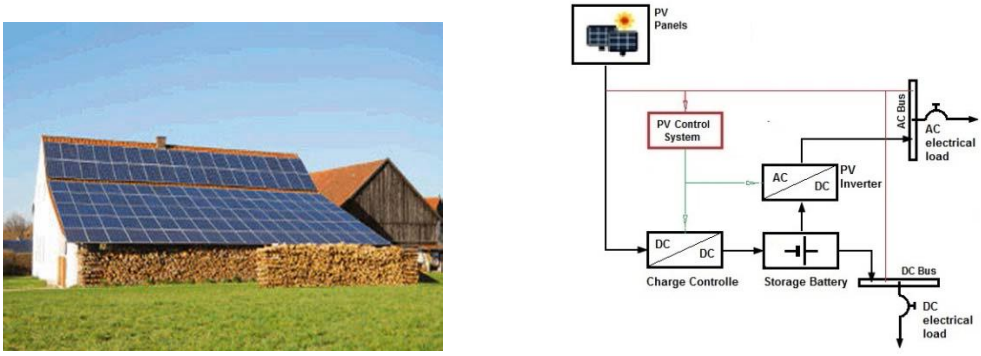


*a) The isolated farm location (Zohuri B., 2018)* *b) Block diagram of a SPV system*

**Fig. 5 – Basic structure of a photovoltaic system (SPV)**

Depending on the type of material from which the photovoltaic cells are made of (Si - silicon, GaAs - gallium arsenide, CdTe - cadmium telluride or based on polymers), their conversion efficiencies range between 8 % and 25 % in standard operating conditions (cell temperature: 25° C, irradiance of incident light perpendicular to the cell: 1000 W/m$^2$, air mass index: AM = 1.5), and can reach up to 44% for PVs with satellite-space destination. The efficiency of photovoltaic conversion decreases with the decrease of solar radiation. Photovoltaic cells are characterized by the current-voltage (IU) characteristic and by the power curve that leads to the determination of the nominal cell power, (*Maican E., 2015*). The basic block diagram of the SPV photovoltaic system corresponding to a small farm is shown in Fig.5b). A preliminary global calculation of electric power generated by the SPV system is based on the formula (*Bhandari et al., 2014*):

$$P_{SPV} = \eta_{PV} * G * A_t \quad [W] \tag{1}$$

where: $G$ – represents the solar irradiation at the location of the farm: (0…1367) [W/m$^2$];

$A_t$ – total area for $n$ panels installed in the system with active surface $A_{PV}$ given by the following relationship:

$$A_t = n * A_{PV} \quad [m^2] \tag{2}$$

$\eta_{PV}$ – the conversion efficiency of solar energy into alternating current (AC) is given by:

$$\eta_{PV} = \eta_{DC} * \eta_{AC} * \eta_{GC} \tag{3}$$

where:

$\eta_{DC} \cong 0.25$ – efficiency of photovoltaic cells under standard operating conditions; (4)

$\eta_{AC} \cong 0.77$ – DC - AC conversion efficiency of the SPV system; (5)

$\eta_{GC} \cong 0.90$ – PV efficiency correlated with other global operating coefficients: dust and impurities, trajectory and PV position orientation, old panels, etc. (6)

For an average conversion efficiency ($\eta_{PV} \cong 17.325$ %) corresponding to the photovoltaic panels and the industrial electrical equipments integrated into the SPV system, from equation (1.1) one can obtain in 3D coordinates the variation of the electric power generated as a function of two variables:

$$P_{SPV} = f_1(G, A_t) = 0.17325 * G * A_t \quad [W] \tag{7}$$

For $G \in (0, 1400)$ W/m$^2$ and $A_t \in (100, 1000)$ m$^2$, the 3D-chart from Fig.6a) is plotted. As an example, for an average solar radiation of $G \cong 1230$ [W/m$^2$] from the farm location, the chart in the Cartesian coordinates from Fig.6b) is given by: $P_{SPV} = f_1(1230, A_t)$. From the preliminary analysis, depending on the load installed on the farm, the number of photovoltaic panels of the SPV system is calculated so that the necessary power is provided for a safe operation of the local consumers.

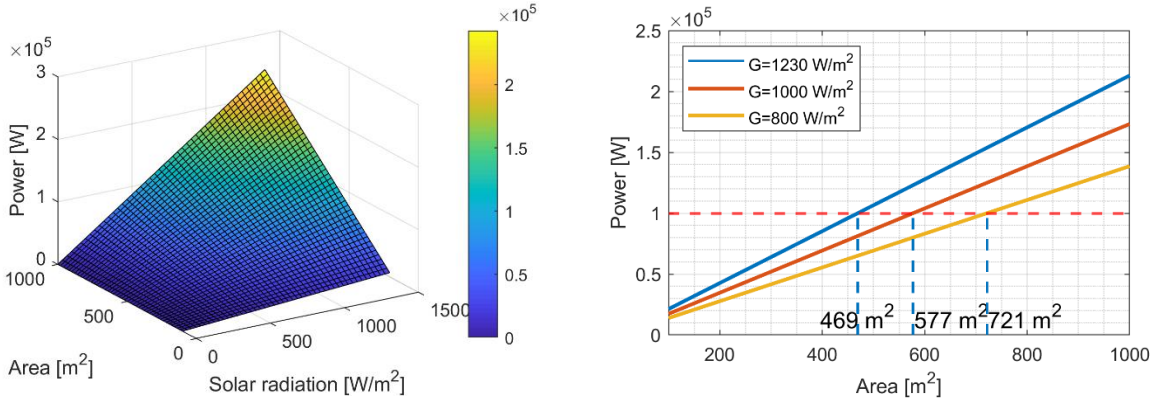


a) $P_{SPV} = f_1(G, A_t)$ b) $P_{SPV} = f_1(1230, A_t)$

**Fig. 6 – The power variation chart generated by an SPV system depending on PV area and solar radiation**

The single-wire electrical diagram in Fig.7 shows the configuration of the SPV solar system for stand-alone operation. The integrated hardware of the SPV system consists in the following devices: Battery Charge Controller, PV Inverter, PLC - DC power supply and SPV Control System. The command and control system of the SPV monitors the power generation process and, by means of the S1 ÷ S6 switches, controls the interconnection of the power distribution bars through the integrated devices. The software implemented in the SPV Control System increases the reliability of the solar power generation system and ensures the amount and quality of energy for both DC and AC consumers.

The connection diagram anticipates the possibility of further developing a hybrid system by setting up the electric circuits on an HVDC Essential Bus 270 VDC.

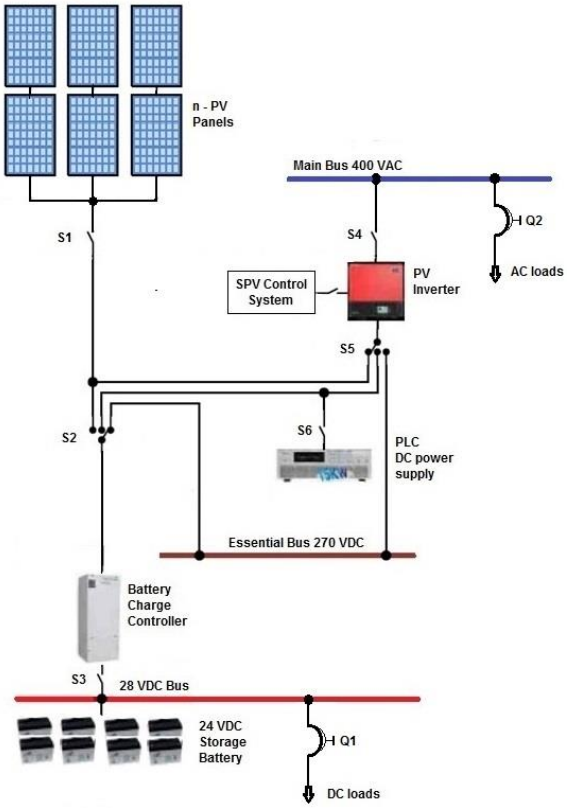


**Fig. 7 – Schematic diagram on the SPV in off-grid mode (stand-alone)**

### 1.2. *Wind power conversion system; Giromill technology and computational elements*

Wind energy is converted into electricity by wind turbines (WT). Currently, there are two basic categories of wind turbines: horizontal axis (HAWT) and vertical axis wind turbines (VAWT), depending on the orientation of the rotor axis. A wind turbine consists of three basic components: the rotor, gearbox or multipurpose drive and power generator. The rotor is a fluid-dynamic machine that converts the kinetic energy of an airflow into mechanical energy. The multiplier connects the turbine rotor to the electric generator with the transmission ratio required for the gearbox. The electric generator (asynchronous or synchronous) converts mechanical energy into electricity and delivers it to an electrical network, directly or via a transformer to the installed load.

Regardless of the WT type, depending on the rated electric power of the generator in the grid, wind turbine systems (WTS) are divided into three categories: small, for $P_{WTS} \leq 100\ \mathrm{kW}$; average, for $100\ [\mathrm{kW}] < P_{WTS} < 1\ \mathrm{MW}$; large, for $P_{WTS} \geq 1\ \mathrm{MW}$. The Danish HAWT turbines, also considered classic WT, dominate the global energy market for large category WTS.

Giromill type VAWT turbines (Fig.8b) are H-Darrieus turbines frequently used in agricultural applications for which the installed power load is lower than 100 kW. Figure 8a shows the efficiency of WT rotors for various types of wind turbine models. The theoretical wind turbine power coefficient $C_p$ cannot exceed the limit of $\frac{16}{27}$, as calculated by Albert Betz based on the principles of energy conservation (*Patel M.R., 2006*). Various approaches, with a variety of weightings of the involved parameters, have been published. In the case of H-Darrieus wind turbines, most authors specify values of 0.32 to 0.42 for the maximum $C_p$ (*D'Ambrosio M., 2010*). Wind power is described by the following equation:

$$P_w = \frac{1}{2} \cdot \dot{m} \cdot v^2 = \rho \cdot R \cdot h \cdot U^3 \quad [\mathrm{W}] \tag{8}$$

where:

$\dot{m}$ – air mass flow, given by: $\dot{m} = \rho \cdot A \cdot v$ [kg/s];

$\rho$ – air density [kg/m$^3$];

$A$ – area of the rotor surface [m$^2$]; for Giromill: $A = 2R \cdot h$;

$R$ – rotor radius [m];

$h$ – height of the rotor blades [m];

$v$ – wind speed (U) [m/s].

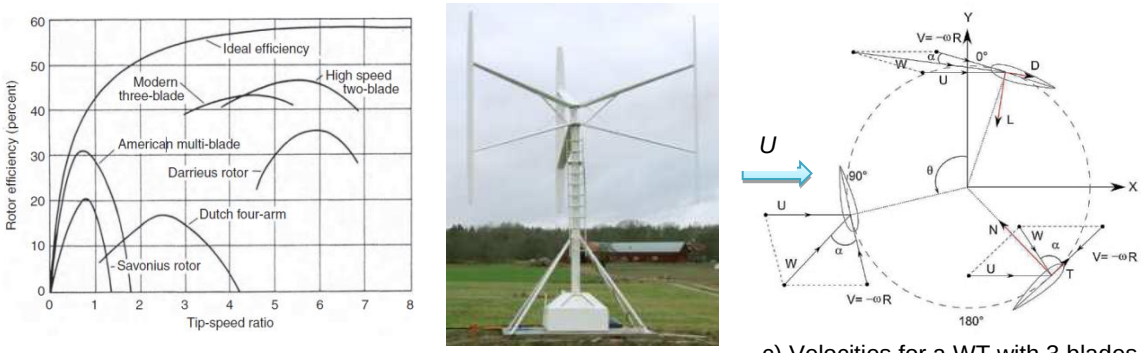


a) $C_p$=f(λ) b) Giromill WT (20 [kW]) c) Velocities for a WT with 3 blades

**Fig. 8 – Basic data on the wind turbines system (WTS)**

*a) Rotor efficiency vs. TSR (tip-speed ratio) for different types of WT; b) Giromill WTS; c) The fluid-dynamic kinematics of a Giromill wind turbine*

As an example, Fig. 8b shows the size of a 3-bladed Giromill WT with a nominal power of 20 kW, (*D'Ambrosio M., 2010*). Using Eq.8 for a turbine in this category and taking into account the rotor efficiency, the mechanical power obtained at the WT axis is given by (*Malael I., 2019*):

$$P_m = C_p \cdot \left(\frac{1}{2} \cdot \rho \cdot A \cdot v^3\right) = C_p \cdot \rho \cdot R \cdot h \cdot U^3 \quad [\text{W}] \tag{9}$$

$Cp$ depends on wind speed, turbine speed, aerodynamic solution of WT and aerodynamic profile chosen for the blade. The TSR (tip-speed ratio) is defined as:

$$\lambda = \frac{\omega \cdot R}{U} \tag{10}$$

where the meanings of $U, R, \omega$ are shown in Fig. 8c).

Wind power *($P_w$)* acts on the wind turbine blades and is converted into mechanical power to the turbine shaft *($P_m$).* By means of a mechanical transmission with efficiency $\eta_t$, the power to operate the electric generator is $P_t = \eta_t \cdot P_m$. The electric power produced by the generator is $P_g = \eta_g \cdot P_t$, where $\eta_g$ is the generator efficiency. If $P_{WTS}$ is the electric power *($P_g$)* produced by the wind system, one can calculate that:

$$P_{WTS} = C_p \cdot \eta_t \cdot \eta_g \cdot \left(\frac{1}{2} \cdot \rho \cdot A \cdot v^3\right) = \eta_{WTS} \cdot \frac{\rho A U^3}{2} \quad [\text{W}] \tag{11}$$

where: $\eta_{WTS}$ – wind turbine system efficiency, whose value is maximized by increasing the performance coefficient of the turbine $Cp$. Equation 11 is based on the diagram of the WPS system presented in Fig. 9.

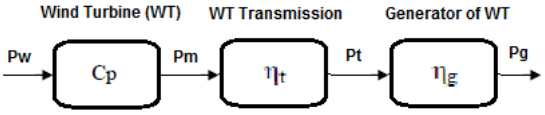


a) $P_g$ – Power generated by the wind turbine

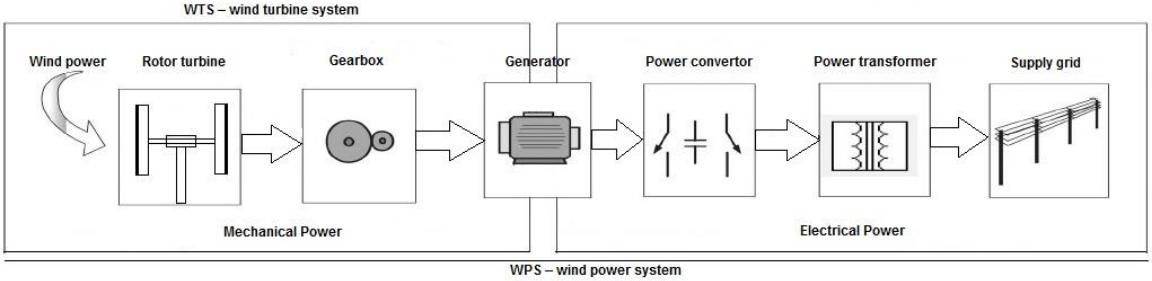


b) $P_{WTS}$ – The electric power for the wind system injected in the grid (*Chen Z., Guerrero J.M, Blaabjerg F., 2009*)

**Fig. 9 – Basic data on the power generated by the WPS**, source (*MICROREN, 2015*)

Often, the preliminary calculation of the $C_p$ performance coefficient is made by semi-empirical methods. The calculation method allows determining the power and torque of the vertical axis wind turbine

based on the load factor and forward resistance coefficients determined experimentally for the selected aerodynamic profile of the turbine blade.

According to Fig. 8c), the following parameters are defined:

$U$ - upstream undisturbed wind speed; $R$ - rotor radius WT;

$V$ - the tangential speed of the turbine rotor blade; $\theta$ - the variation angle of the blades;

$W$ - the resulting wind speed on the turbine blade; $\omega$ - angular velocity of the blade.

A discretization of the variation angle of the blades $\theta_i$ is chosen in the range of 0° to 360°. For each angle of variation $\theta_i \in$ (0°, 30°, 60°, 90°) the following algorithm is executed:

*Step i).* It is assumed, as a first approximation, that the velocity of the blade in position *i*, $V_i$, is equal to the upstream undisturbed wind speed, $U$:

$$a_i = \frac{V_i}{U} = 1 \tag{12}$$

where $a$ is the speed loss coefficient.

*Step ii).* The incidence angle is calculated:

$$\alpha_i = arctan\left(\frac{V_i cos\theta_i}{\lambda U - V_i sin\theta_i}\right) + \alpha_0 \tag{13}$$

where $\alpha_0$ is the angle of attack, and $\lambda$ is the ratio of the peripheral velocity of the blade to the undisturbed airflow speed (2.3).

*Step iii)*. Calculate the resulting speed:

$$W_i = \sqrt{(V_i cos\theta_i)^2 + (\lambda U - V_i sin\theta_i)^2} \tag{14}$$

*Step iv).* Calculate the Reynolds number:

$$Re_i = \frac{W_i b}{\nu} \tag{15}$$

where $b$ is the length of the chord line, and $\nu$ is the kinematic viscosity of the air.

*Step v).* Calculate the coefficient of the normal force:

$$C_{n,i} = C_z(\alpha_i) cos\alpha_i + C_x(\alpha_i) sin\alpha_i \tag{16}$$

where $C_x$ and $C_z$ are the drag and load strength coefficients, respectively, determined experimentally in accordance to blade profile and angle of incidence.

*Step vi).* Calculate the function of the speed loss coefficient:

$$G(a) = \frac{Nb}{8\pi R|cos\theta_i|}\left(C_{n,i} cos\theta_i + C_{t,i} sin\theta_i\right)\frac{W_i^2}{V_i^2} \tag{17}$$

where $N$ is the number of rotor blades and $G_a = G(a_i)$ for $i$-th iteration.

*Step vii).* The speed loss ratio is recalculated:

$$a = \frac{1}{1 + G_a} \tag{18}$$

The above steps are repeated until the desired precision is reached; the torque is determined for each $\theta_i$:

$$T_i = \frac{\rho R W_i^2 b C_t h}{2} \tag{19}$$

where $h$ is the height of the turbine.

*Step viii).* The torques generated by each blade are added for each angle of variation, and the turbine total torque is determined according to $\theta_i$. The average torque $(T_{med})$ of the wind turbine is the average of these values, and the resulting average power is given by:

$$P_{med} = \omega \cdot T_{med} \tag{20}$$

*Step ix).* Finally, if the wind power is given by the Equation 8, then the wind turbine coefficient of performance is calculated as:

$$C_p = \frac{P_{med}}{P_w} = \frac{\omega \cdot T_{med}}{\rho R h U^3} \tag{21}$$

Although laborious, the calculation methodology presented can be simplified by means of CAE techniques. Figure 10 shows the CFD analysis of the hydrodynamic flow for a Giromill three-bladed rotor, using the ANSYS Fluent software package.

From the CFD numerical simulations performed on the rotor of a three-blade Giromill wind turbine, the performance coefficient $Cp \cong 0.37$ was determined to be optimal for the given application.

Taking into account that the efficiency of the mechanical transmission is $\eta_t \cong 0.98$ and for the integrated electric generator working in this power category is $\eta_g \cong 0.92$, the efficiency of the WTS system is:

$$\eta_{WTS} = C_p \cdot \eta_t \cdot \eta_g = 0.37 \cdot 0.98 \cdot 0.92 \cong 0.334 \quad (22)$$

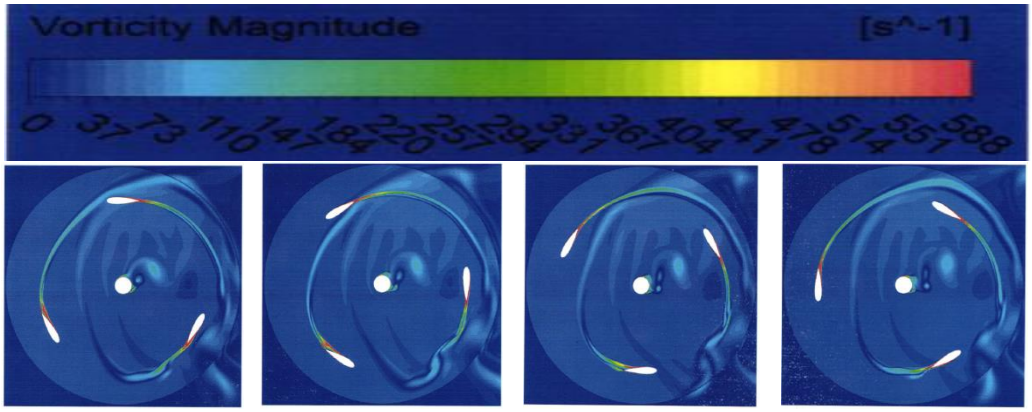


$\theta$ = 0° $\theta$ = 30° $\theta$ = 60° $\theta$ = 90°

Vorticity Magnitude V = 11 [m/s] for TSR = 2

**Fig. 10 – CFD analysis for a three-blade Giromill rotor**

Substituting the determined value for $\eta_{WTS}$ in Equation 11, the variation of the generated electric power as a function of two variables $(A, U)$ is obtained:

$$P_{WTS} = f_2(A, U) = \frac{0.344}{2} \cdot \rho \cdot A \cdot U^3 \quad [\text{W}] \quad (23)$$

where: $\rho = 1.225$ kg/m³ is the air density for the location of the WT.

With the following predefined domains: $A \in (10, 100)$ m² and $U \in (0, 15)$ m/s, one can get the 3D chart in Fig. 11a). As an example, for a wind speed $U \cong 8$ [m/s] at farm location, and in order to generate an electric power of 30 kW, the required area of the H-type rotor of a Giromill wind turbine is determined from the plot in Fig. 11b). Similarly, the WTS analysis is performed for other wind speeds.

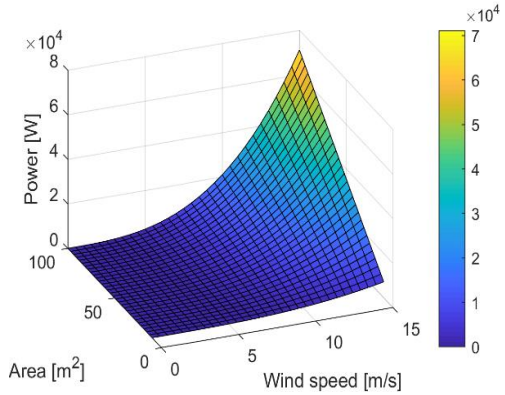


a) $P_{WTS} = f_2(A, U)$

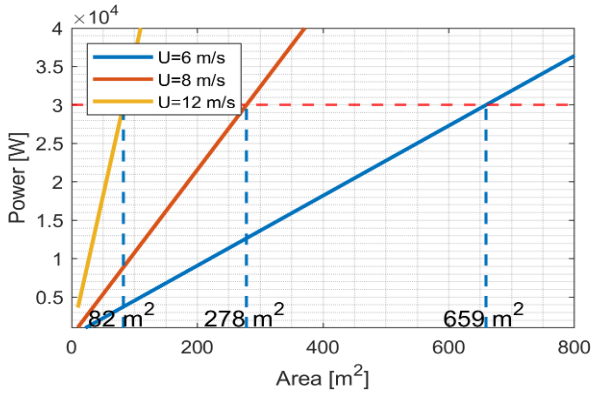


b) $P_{WTS} = f_2(A, 6)$; $P_{WTS} = f_2(A, 8)$ ; $P_{WTS} = f_2(A, 12)$

**Fig. 11 – Plots of the power variation generated by a WTS, depending on rotor area and wind speed**

VAWT wind turbines have the advantages of no guidance systems and heavy equipment (gearbox, electric generator, etc.) located close to the ground. The main disadvantage of the classic solution is the vertical shaft provided with a top bearing that requires ground anchorage. This disadvantage is overcome by the Girromill solution (H-Darrieus) and makes VAWTs feasible especially for relatively small powers. The connections diagram from Fig. 12b) shows the configuration of the WTS for the autonomous mode (off-grid).

The hardware integrated into the WTS system consists of Wind Inverter, Wind Interface, WTS Control System, Hybrid Inverter and Battery Charge Controller. The WTS control system supervises the process of electricity generation and, by means of switches S2, S3, S7, … S9, controls the interconnection of the electricity distribution bars through integrated devices. The WTS Control System software increases the reliability of the wind power generation system and ensures the quantity and quality of energy for both DC

and AC consumers. The connection diagram also anticipates the possibility of developing a hybrid system of renewable energy by developing electrical circuits on a HVDC essential bus at 270V.

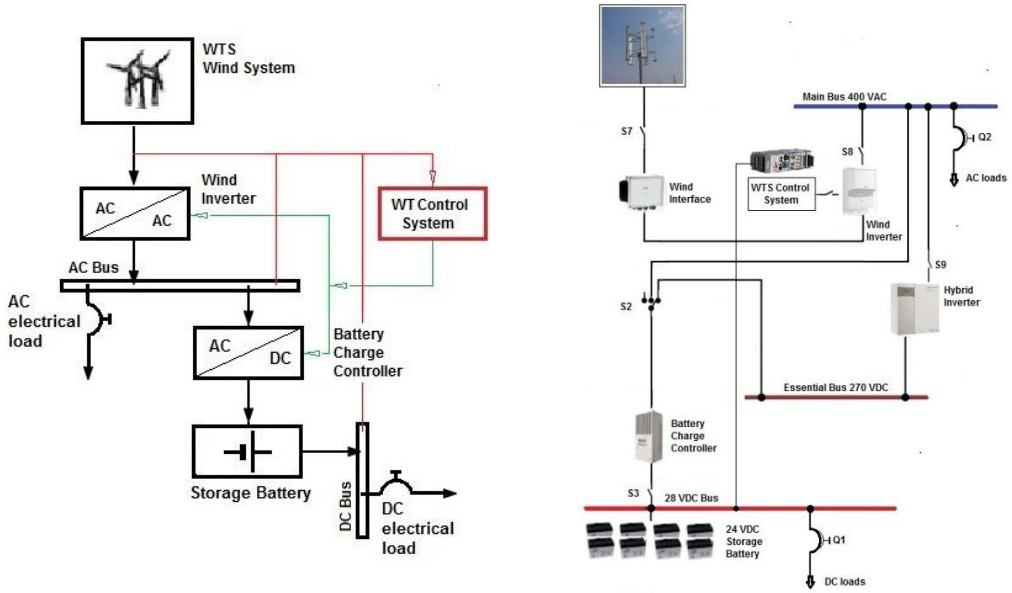


*a) Block diagram of WTS* *b) Sigle wire electrical connection scheme of WTS*

**Fig. 12 –Schematic diagram of the WTS system for off-grid mode**

### 1.3. Systems for hydropower energy conversion into electric power. Kaplan technology and computational elements

All systems converting the hydro energy into another form of useful energy exploit the potential energy of water (Fig. 13. *a*, *b*). The objective of a hydroelectric system is to convert the potential energy of the water flow (*Q*) flowing from a certain height (*H*) into electrical energy. The key element of the hydro energy conversion system is the hydraulic turbine (Fig. 13 *c*) which can be an impulse or a jet turbine. The mechanical torque is transmitted through a multiplier gear to an electric current generator, (*ENER-SUPPLY, 2012*).

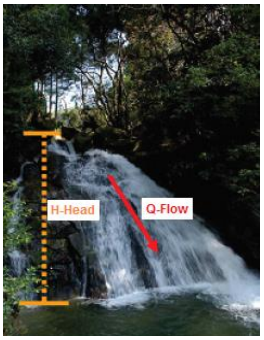


*a) On-site hydro potential*

*b) In situ HKS installation*

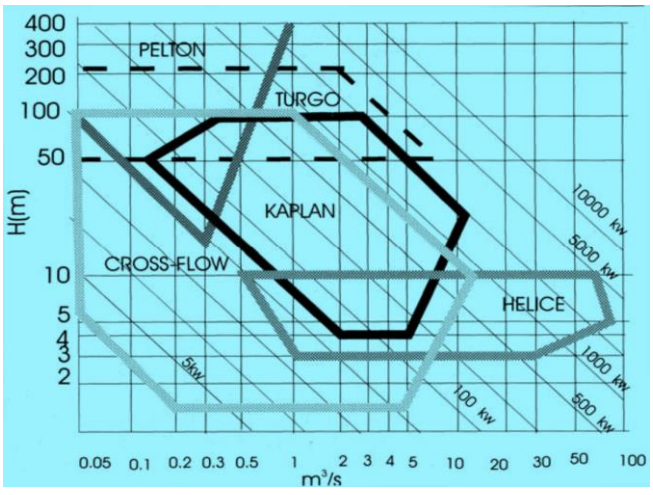


*c) diagram of the applicability domains for hydro turbines*

**Fig. 13 – Basic data of the HKS system**

The available power produced by the hydroelectric system is given by:

$$P_{HKS} = \eta_{HKS} \cdot \rho \cdot g \cdot Q \cdot H \quad [W] \tag{24}$$

where:

$\rho$ – water density (1000 kg/m³); $Q$ – water flow through the turbine [m³/s];
$g$ – gravitational acceleration (9.81 m/s²); $H$ – effective water drop at turbine level [m];
$\eta_{HKS}$ – the efficiency of the hydroelectric system corresponding to the efficiencies of system components: hydraulic turbine, $\eta_{HT} \in (0.60 \div 0.80)\%$; mechanical transmission from the turbine to the generator, $\eta_t \cong 0.98$ ; integrated electric generator, $\eta_g \cong 0.92$; by substituting, the approximate value is:

$$\eta_{HKS} = \eta_{HT} \cdot \eta_t \cdot \eta_g = 0.80 \cdot 0.98 \cdot 0.92 \cong 0.727 \quad (25)$$

For a preliminary calculation, entering the value from (Eq.25) in (Eq.24), the power $P_{HKS}$ can be written as:

$$P_{HKS} = f_3(Q,H) = 7.13 \cdot Q \cdot H \quad [\text{kW}] \quad (26)$$

Figure 14 shows the variation of $P_{HKS} = f_3(Q,H)$ in both 3D and Cartesian coordinates for preset values of *H*. For guidance, for unit values of $Q = 1$ m³/s and $H = 1$ m an electric power of $P_{SH} = 7.13$ kW is obtained. Multiplying this value with concrete values from the specific site gives the field of hydropower potential from the location of the isolated farm regarding the coverage of the required electric power. For the $Q \in (0, 10)$ m³/s and $H \in (0, 10)$ m, the 3D plot is shown in Fig. 14 *a*). For various water drops at turbine level ($H \cong 2;\ 4;\ 8$ m) from the farm location, the required water flow *Q* [m³/s] passing through the turbine to generate an electric power of 70 kW is automatically determined from the chart in Fig. 14 *b*).

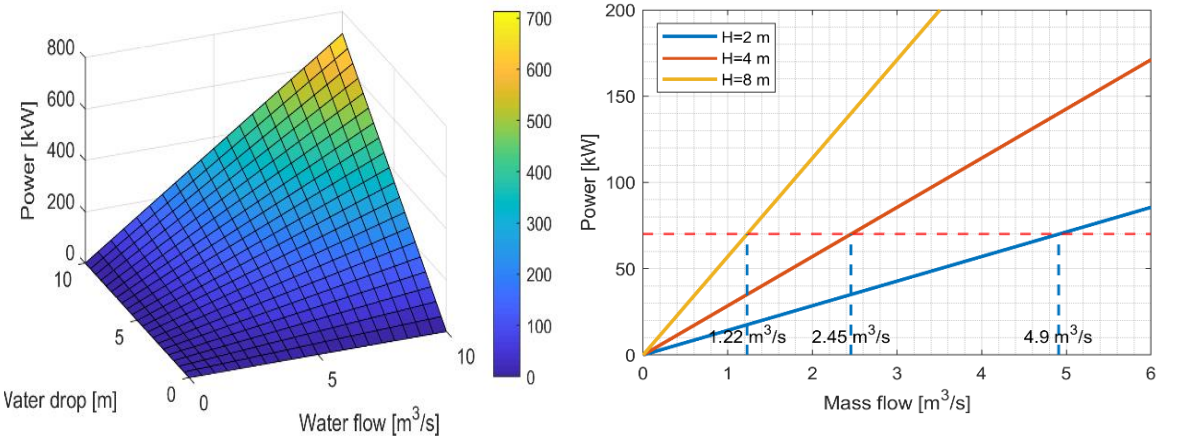


a) $P_{HKS} = f_3(Q,H)$ [kW]

b) $P_{HKS} = f_3(Q,2)$ ; $P_{HKS} = f_3(Q,4)$ ; $P_{HKS} = f_3(Q,8)$

**Fig. 14 – The power variation graph generated by an HKS depending on Q and H**

Low power hydroelectric stations include micro-hydroelectric power stations and hydro-kinetic systems (HKS) that can generate less than 100 kW electric power. HKS systems are anchored floating structures with the reactive turbine immersed, are installed on fast running surface water (see Fig. 13*b*), and does not require additional construction work. The water flow kinetic energy is converted directly into electrical energy through the system consisting of hydraulic turbine, multiplier gear, and synchronous generator.

For a floating hydro-kinetic system installed on the water surface, from Eq. 24, the produced power is determined by successive replacements, depending on the speed of the running water $v_a$ and the active surface of the hydro turbine $A_T$:

$$P_{HKS} = f_4(A_T, v_a) = 363.6 \cdot A_T \cdot v_a^3 \quad [\text{W}] \quad (27)$$

where: $\rho$ – water density (1000 kg/m³);
$g$ – gravitational acceleration (9.81 m/s²);
$R_e$ < 2000 – Reynolds number.

The 3D plot in Fig. 15 *a*) is obtained based on the following predefined values: $v_a \in (0, 5)$ m/s and $A_T \in (0, 5)$ m². For different water speeds at turbine level $v_a \cong 1;\ 2;\ 3$ [m/s] measured at farm location, the area of the turbine rotor surface $A_T$ [m²] required to generate 10 kW is determined from Fig. 15 *b*). In Fig. 16

the block diagram of an autonomous hydro-kinetic system for isolated farm locations with the schematic representation of the local network is presented.

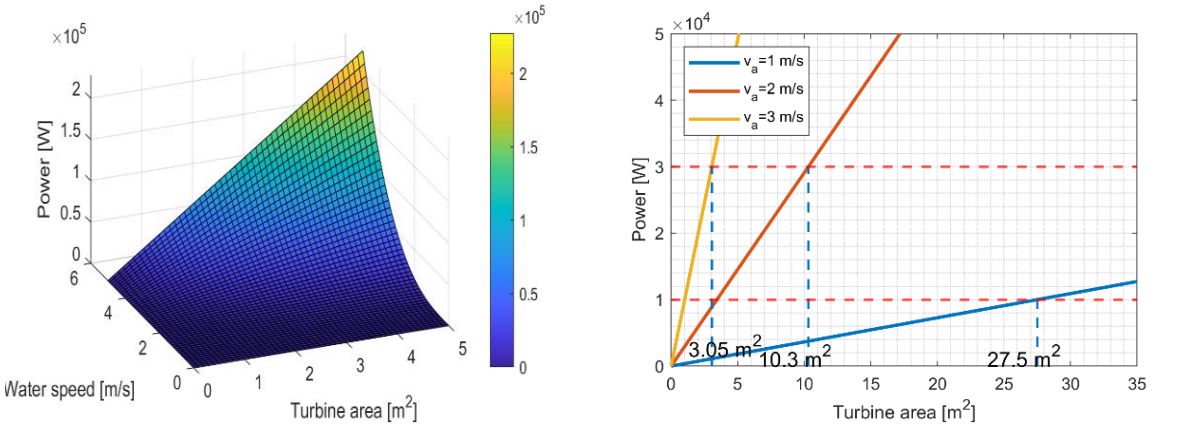


a) $P_{HKS} = f_4(A_T, v_a)$ b) $P_{HKS} = f_4(A_T, 1)$ ; $P_{HKS} = f_4(A_T, 2)$ ; $P_{HKS} = f_4(A_T, 3)$

**Fig. 15 – Power variation graph generated by an HKS depending on turbine area and water speed**

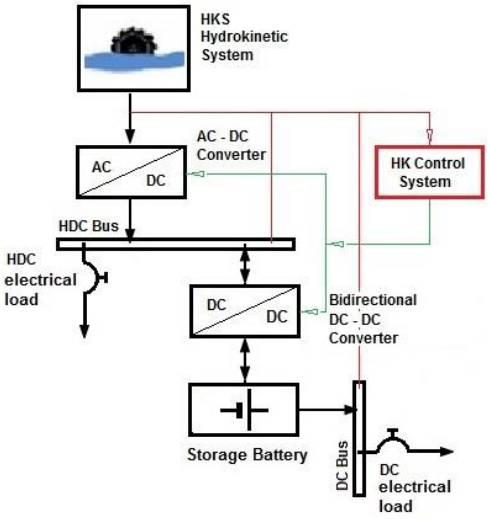


**Fig. 16 – Schematic diagram of the HKS system in off-grid mode (stand-alone)**

## 2. HYBRID CONVERSION SYSTEMS OF RENEWABLE ENERGY IN ELECTRIC POWER

### 2.1. Dual systems for converting renewable energy into electricity

Crucial for off-grid systems is the climate because it can make one type of hybrid system more profitable than another. Currently, the dual systems are most widespread in HRES applicability, being ideal no matter the location and climate of the area. The most frequently used are photovoltaic-wind systems. Fig. 17 presents the simplified connection diagram of a low-power HRES structure (the 230VAC / 50Hz single-phase hybrid micro-network at the University of Aalborg in Denmark, Institute of Energy Technology), (*E-FARM, 2008*). It consists of a Windy Boy 1.7 kW wind farm, a Sunny Boy 1.7 kW photovoltaic panels system, and a VRB energy storage system with redox-flow vanadium battery, interfaced with the microgrid through a Sunny Island 5048 inverter of 5 kW. The main micro-core component is the Sunny Island inverter that controls the microgrid (voltage and frequency) to provide optimal VRB battery usage. Depending on the required load and the power produced by the wind and photovoltaic systems, the Sunny Island inverter provides power balance, controlling the micro-grid frequency. The inverter can also provide the interconnection of the HRES micro-grid with the local public grid when the location allows it, (*E-FARM, 2008*). Thus, it becomes an Emergency system that automatically switches to off-grid mode when the University's main grid is faulty.

Other dual configurations are photovoltaic-hydro, wind-hydro, photovoltaic-geothermal, etc. All of them require the inclusion of an electrical energy storage system that can operate in a buffer with the generators connected in parallel through the interfacing equipment. In the case of dual stand-alone hybrid systems for increasing safety in operation, there is a third system, for emergency (fossil fuel powered generator set), which normally is in stand-by mode.

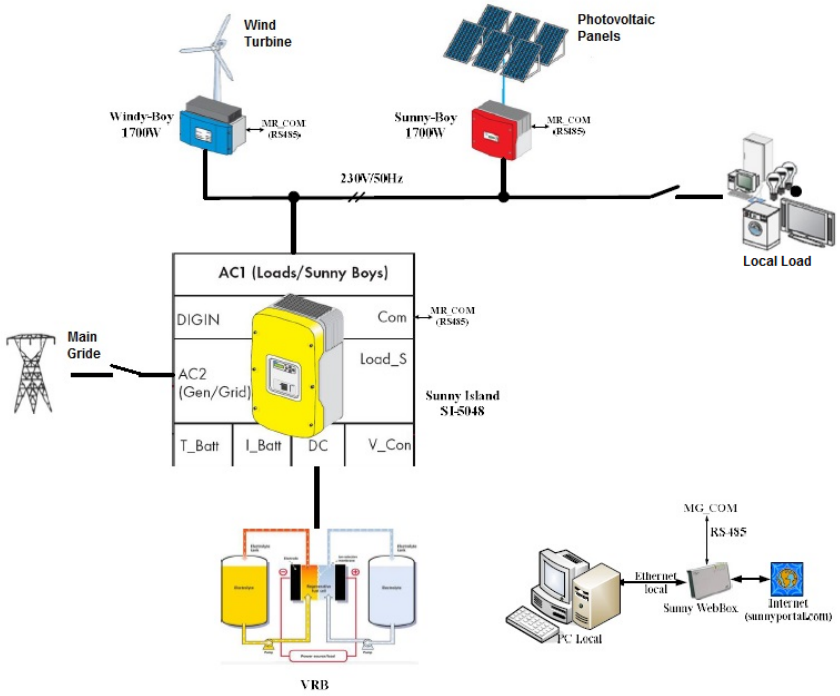


**Fig. 17 – Micro-grid topology of HRES dual system** (*E-FARM, 2008*)

### 2.2. A complex system to convert renewable energy into electricity for isolated areas

HRES are an adequate and competitive solution for rural electrification and/or for isolated agricultural farms. Reliability and cost are the two most important aspects that must be considered while designing the hybrid energy system. The most important advantage is that HRES makes best use of the renewable power generation technologies operating characteristics, and efficiency is higher than the one that could be obtained if a single power source is used (*Bajpai O., Dash V., 2012*). It can also address limitations in terms of fuel flexibility, efficiency, reliability, emissions and economics. A HRES network (Fig. 18) is composed of solar, wind, hydrokinetic and energy storage systems. In this research, the hybrid system is conceived as a complex HRES off-grid system for a payload of 100 kW, designed for isolated farms that cannot connect to NPS.

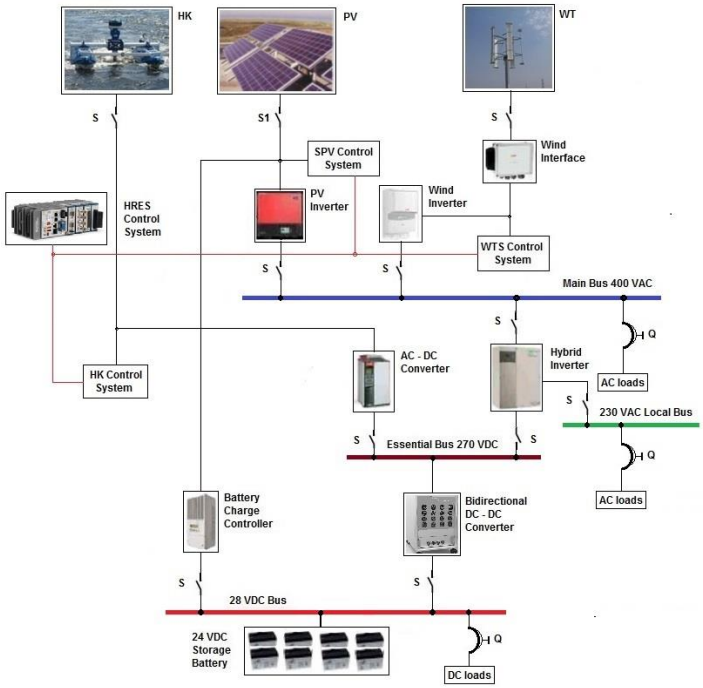


**Fig. 18 – Block diagram of HRES stand-alone system for off-grid mode**

The basic PV, WT and HK systems convert solar, wind and water hydro-kinetic energy into electrical energy respectively. This is injected into the bars of the energy node for electricity distribution, through the interfacing equipment of the micro-network. All electronic devices in Fig. 18 are installed in two separate cabinets, depending on the performed service. One cabinet includes electric elements and power circuits for conversion, switching and distribution of electricity through the protection elements. The second cabinet is for automation and includes elements and signal circuits with special purpose regarding the command and control of power generation, providing real time protection for the HRES micro-network. Due to the off-grid mode, the micro-network is designed on three levels that allow autonomous operation regardless of the external disturbances. The bars of the energy node have different voltages and are interconnected by the conversion elements, in order to operate in buffer with the energy storage system. Analogous to the energy systems on board the airplanes, the following configuration of the HRES micro-network is designed:

- Main Bus 400VAC, 50 Hz;
- Local Bus 230VAC, 50 Hz;
- Emergency Bus 28 VDC.
- Essential Bus 270 VDC

The reliability of the HRES system increases not only through the possibilities of interconnecting the voltage bars but also by integrating the System Controller, for real time process monitoring and for an optimum operation of the HRES hybrid system.

**RESULTS AND DISCUSSIONS**

For the small agricultural farm located in an isolated location (45°13'13.24" N; 28°45'24.75" E; elevation 7ft; Fig. 19 *a*), a total installed electric load of 100 kW was provided in order to carry out the farm activities under optimum working conditions. Local environmental data can be extracted from Fig. 19.

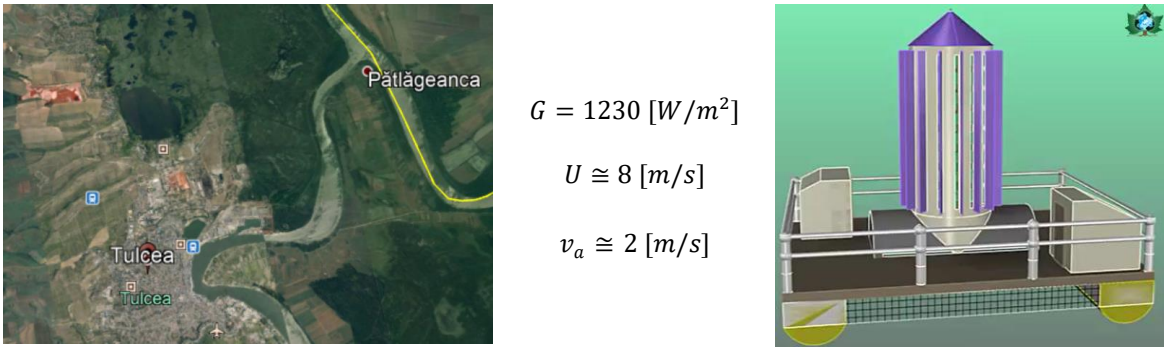


*a) The farm location* *b) Local environmental data* *c) TEACHERS HRES*

**Fig. 19 – Location and primary environmental data for HRES**

The hybrid HRES system is configured in the following order: photovoltaic, wind, hydrokinetic. HRES necessarily includes the electrical energy storage system consisting of battery packs and optionally an electro-generator group on fossil fuel, to be used as an emergency system. By means of the energy balance of the small farm simulated during one year of agricultural process, for an installed electric load of 100 kW an average power $P_m = 78.9$ kW is obtained. The HRES power generators are calculated to have the capacity to simultaneously inject into the energy distribution node an electric power of:

$$P^*_{HRES} = 1.10 * P_m = 86.79 \cong 87 \text{ kW} \quad (28)$$

Loads demands that give the short or long term peaks of electricity can be covered by the electricity storage system and/or by the emergency system.

The main component of HRES is the photovoltaic system (SPV). From Fig. 6 *b*), a total active panels' surface $A_t = 469$ m² corresponding to a maximum generated power $P_{SPV} = 100$ kW is chosen. Because the SPV system is characterized by the day-time power generation, a constraint was imposed: $P_{SPV} \geq P^*_{HRES}$ The second component of HRES is the WTS wind system. From Fig. 11 *b*), an active HAWT surface $A = 278$ m² corresponding to a maximum generated power $P_{WTS} = 30$ kW is selected. Because the WTS wind energy conversion system has a random characteristic of power generation, the following constraint was imposed: $P_{WTS} \leq \frac{1}{2} \cdot P^*_{HRES}$.

The tertiary component system of HRES is the HKS hydro-kinetic system. Considering Fig. 15 *b*), the chosen active surface of immersed turbines is $A = 10.3$ m², corresponding to a generated power of $P_{HKS} = 30$ kW. Because the HKS hydro power conversion system has size restrictions due to water depth, and because the running water speed is low, the following constraint is imposed: $P_{HKS} \leq \frac{1}{3} \cdot P^*_{HRES}$. HKS is the only HRES component system with continuous conversion of hydro-kinetic energy into electricity.

The electric power generated by the HRES hybrid system is the sum of the electric powers generated by each component:

$$P_{HRES} = \sum_{i=1}^{3} P_i = P_{SPV} + P_{WTS} + P_{HKS} \quad [\text{kW}] \tag{29}$$

Replacing the previously determined power values, the maximum power of the HRES system in the local micro-network of the farm is $P_{HRES} = 160$ kW. These peak operating moments are random, the surplus of electricity being taken over by the storage system.

The ratio between the maximum generated power and the calculated average one is:

$$\varsigma = \frac{P_{HRES}}{P^*_{HRES}} = 1.839 \tag{30}$$

This ratio represents the degree of over-dimensioning of HRES and it is necessary to provide the operational safety of the hybrid system. Fig. 19c presents a new concept of HRES system whose no. $\varsigma \rightarrow 1.0$

## CONCLUSIONS

The aim of this article was to develop a calculation methodology for defining the component of a hybrid HRES system for converting renewable energy into electricity for a small farm in an isolated location. A preliminary global calculation was performed for a small farm in the Patlageanca cross-border area. The configuration of the hybrid HRES system is summarized in Table no. 2.

**Table 2**

| **160 k] HRES – Hybrid Renewable Energy Systems (sun, wind, water)** | | | | |
|---|---|---|---|---|
| # P.N. | System component | Basic data | | |
| 1. | The **SPV** photovoltaic system | $G = 1230$ W/m² | $A_t = 469\ m^2$ | $\boldsymbol{P_{SPV} = 100}$ **kW** |
| 2. | The **WTS** wind system | $U \cong 8$ m/s | $A = 278\ m^2$ | $\boldsymbol{P_{WTS} = 30}$ **kW** |
| 3. | The **HKS** hydro-kinetic system | $v_a \cong 2$ m/s | $A = 10.3\ m^2$ | $\boldsymbol{P_{HKS} = 30}$ **kW** |
| 4. | Electrical energy storage system | battery bank of 24V DC∗4000 Ah | | |
| 5. | Emergency system | It is optionally an electric-generator group on fossil fuel | | |
| 6. | The technical-economic execution indicator of the HRES system | | | $\boldsymbol{\zeta = 1.00}$ €/W |
| 7. | The degree of over-dimensioning for operational safety of the HRES | | | $\boldsymbol{\varsigma = 1.839}$ |

## ACKNOWLEDGEMENT

Within the project *"Innovative Technologies for Renewable Energy Production from Integrated Natural Sources in Complex Installations"*, which is carried out in contract 81PCCDI / 27.03.2018, through component no. 1 of the project *"Significant optimization of complex systems for the production of renewable energy in coastal and running waters"*, the documentation study on the stand-alone HRES hybrid systems was initially performed. This paper reviews the main RES systems and how they can be combined into a hybrid system. The optimal development of a complex hybrid system with applicability in the micro-networks of the isolated agricultural farms without possibility of connection to the NPS was followed.

## REFERENCES

[1] Bajpai O., Dash V., (2012), Hybrid renewable energy systems for power generation in standalone applications: a review*, Renewable and Sustainable Energy Reviews*, vol. 16(5), pp. 2926-2939;

[2] Bhandari B., Poudel S.R., Lee K.T., Ahn S.H., (2014), Mathematical Modeling of Hybrid Renewable Energy System: A Review on Small Hydro-Solar-Wind Power Generation, *International Journal of Precision Engineering and Manufacturing-Green Technology*, vol. 1(2), pp. 157-173, Springer;

[3] Chen Z., Guerrero J.M., Blaabjerg F., (2009), A Review of the State of the Art of Power Electronics for Wind Turbines, *IEEE Transactions on Power Electronics,* vol. 24(8), pp. 1859-1875;

[4] D'Ambrosio M., Medaglia M., (2010), Vertical Axis Wind Turbines: History, Technology and Applications, Master Thesis in Energy Engineering, Halmstad University, Sweden;

[5] Ehrlich R., (2013), *Renewable energy, A First Course*, CRC Press Taylor & Francis Group, ISBN 978-1-4665-9944-4;
[6] Maican E., (2015), *Renewable energy systems*, (*Sisteme de energii regenerabile*), Printech Publishing House, Bucharest / Romania;
[7] Malael I., (2019), *TECC Project*; Retrieved from "COMOTI - Romanian Research & Development Institute for Gas Turbines": http://www.comoti.ro/ro/Proiect_TECC.htm?pag=3;
[8] Patel Mukund R., (2006), *Wind and Solar Power Systems: Design, Analysis, and Operation,* CRC Press Taylor & Francis Group, ISBN 9780849315701;
[9] SolarGis, (2019), *Solar resource maps of Romania*. Retrieved from "Weather data and software for solar power investments": https://solargis.com/maps-and-gis-data/download/omania;
[10] Zohuri B., (2018), Hybrid Renewable Energy Systems, Springer International Publishing AG 2018, https://doi.org/10.1007/978-3-319-70721-1_1, University of New Mexico, USA.
[11] ***AddEnergy, (2019), *Romania's Wind Energy Potential (RO: Potentialul eolian al Romaniei),* Retrieved from Add Energy Renewable: http://add-energy.ro/potentialul-eolian-al-Romaniei;
[12] ***Brunswick, (2019), An Introduction to Renewable Energy - Options for Farmers, https://www2.gnb.ca/content/dam/gnb/Departments/10/pdf/Agriculture/RenewableEnergy.pdf, Canada;
[13] ***ECA, (2018), Special Report no. 5, *Renewable energy for sustainable rural development: significant potential synergies, but mostly unrealised*, ECA – European Court of Auditors, 12, rue Alcide De Gasperi, 1615 Luxembourg;
[14] ***Ener-Supply, (2012), *Manual-Renewable Energy Sources*, (*Manual - Surse regenerabile de energie*), SEE Project, Energy Efficiency and Renewable Energies - Local Energy Support Policies;
[15] ***MICROREN, (2015), *Hybrid renewable energy conversion systems of small power integrated into a micro-network – MICROREN*, (Sisteme hibride de conversie a energiei regenerabile de mică putere integrate într-o microreţea – MICROREN), Scientific and technical report, PCCA project no. 36/2012 - stage 4 – 2015, Polytechnic University of Timisoara / Romania;
[16] ***WWF, (2019). *Romanian Rivers and the Impact of Hydro Energy Adjustments*. Retrieved from "Rivers of Romania": https://raurileromaniei.ro/harta/.

# KINEMATIC ANALYSIS OF A MECHANISM, WITH ARTICULATED PRECOMPACTION BARS, OF MUNICIPAL SOLID WASTE COLLECTING MACHINES

# /

# *ANALIZA CINEMATICĂ A UNUI MECANISM, CU BARE ARTICULATE DE PRECOMPACTARE, AL MAȘINILOR DE COLECTAT DEȘEURI MENAJERE*

**Voicu Gh.[1)], Moise V.[1)], Popa L.[2)], Lazea M.[3*)], Tudor P.[1)], Niculae L.[1)], Polena A. [1]**

[1)] University Politehnica of Bucharest / Romania; [2)] National Institute of Research – Development for Machines and Installations Designed to Agriculture and Food Industry –INMA Bucharest / Romania; [3)] CCR Romania

**) Corresponding author: Tel: 0753044289; E-mail: mircealazea2005@yahoo.com*

*DOI: 10.35633/INMATEH-59-10*

***Keywords:*** *municipal waste, garbage truck, precompacting mechanism, kinematic analysis*

**ABSTRACT**

*In this paper, the structural and kinematic analysis of the mechanism of a municipal waste pressing system is made. The mechanism works in four phases. Two of the phases represent the operation itself, and two phases are for bringing the mechanism into pressing position. For the modules of which the actuation mechanism is constituted, kinematic calculation procedures have been drawn up, procedures that have been accessed by a main computing program. The results obtained were transposed graphically in the form of diagrams to give a clearer picture of the kinematic parameters of the mechanism elements.*

**REZUMAT**

*În lucrarea de față se face analiza structurală și cinematică a mecanismului unui sistem de presare a materialului menajer. Mecanismul lucrează în patru faze. Două dintre faze sunt de lucru propriu-zis, iar două faze sunt de aducere a mecanismului în poziție de presare. Pentru modulele din care este constituit mecanismul de acționare s-au întocmit proceduri de calcul cinematic, proceduri ce au fost apelate într-un program principal de calcul. Rezultatele obținute au fost transpuse grafic sub formă de diagrame, pentru a da o imagine mai clară asupra parametrilor cinematici ai elementelor mecanismului.*

## INTRODUCTION

The transport of residues is the second operation of the organized evacuation process, linked to the collection operation, as an inseparable part of it, after pre-collection at the level of economic agents and housing assemblies. There are very varied types of machines which, in addition to transport, allow easier loading of residues in the collector's bins *(Voicu Gh., 2007).* The basic condition of the transport economy is the compaction degree of municipal solid waste in the garbage trucks, correlated with the loading to its useful capacity *(Voicu Gh., 2007).*

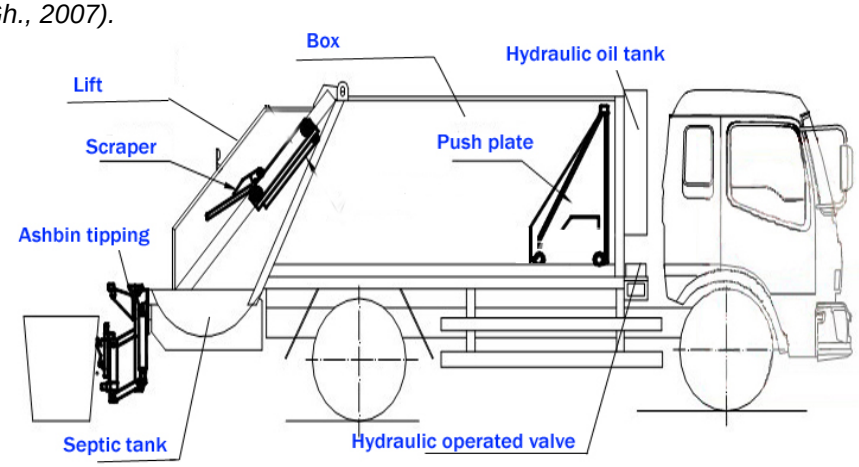


**Fig. 1 - Garbage truck for collecting and transporting municipal solid waste with hydraulic compaction** *(Voicu Gh., 2007)*

[1] *Voicu Gh., Prof. Ph.D. Eng.; Moise V., Prof. Ph.D. Eng.; Popa L., Ph.D. Eng.; Lazea M., Ph.D. Stud.; Tudor P., Lect. Ph.D. Eng.; Niculae L., Asist. Ph.D. Eng.; Polena A., Asist. Ph.D. Eng.*

The fast displacement of the material from the loading area to the front side of the collector container and its uniform filling is a requirement that has been solved differently for different types of municipal waste trucks. Most municipal waste collection and transport machines are today with transshipment compaction. In these, the collection container has parallelipipedic shape, inside which a compaction and unloading plate moves from one end to the other. At the back of the machine is located the system of pickup and lifting of waste in the collection container, which effectively closes the collection container. The supply of the container is made through the scraping system mechanism, which has different constructions. Compaction is progressively achieved between the compaction plate in the container and the inclined plate of the scraping and lifting system as the waste is raised in the container *(Voicu Gh., 2007; Voicu Gh., Lazea M., Zabava B.S. et al., 2019; Voicu Gh., Lazea M., Tudor P.et al., 2019)*

Most of the pick-up and precompacting mechanisms are plane mechanisms with articulated bars, the elements of which are operated by one or two pairs of hydraulic cylinders *(Voicu Gh., 2007; Voicu Gh., Lazea M., Zabava B.S. et al., 2019; Voicu Gh., Lazea M., Tudor P.et al., 2019).*

## MATERIALS AND METHODS

In figure 2 is presented, the kinematic scheme of a mechanism for the scraping and precompaction of the residual material from the collecting and transporting truck for municipal solid waste.

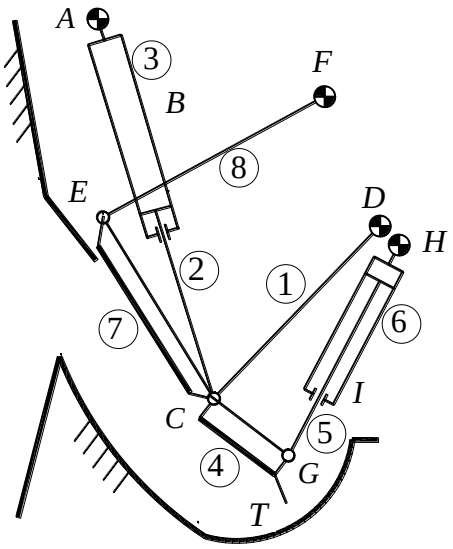


**Fig. 2 – Kinematic scheme of the scraping and precompaction mechanism**
*(Voicu Gh., Lazea M., Zabava B.S. et al, 2019; Voicu Gh., Lazea M., Tudor P.et al, 2019)*

*A,F,D,H – fixed cylindrical joints ; C,E,G – mobile cylindrical joints; B,I – hydraulic cylinders; 1,4,7,8 – fixed length bars; 2-3 and 5-6 – hydraulic cylinders*

The displacement trajectory of the tracer *T* point is shown in figure 3. It should be noted that the tracer *T* point is the tip of the collection and lifting plate of the machine, pos. *4*, while the bare, pos.*7*, represents the precompaction plate of the pickup and precompaction mechanism.

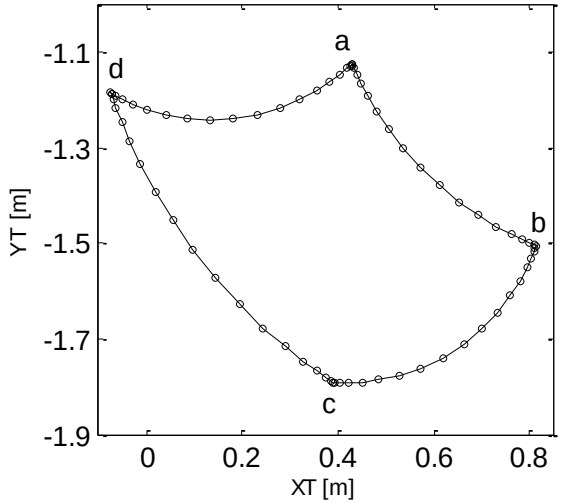


**Fig. 3 – Tracer *T* point displacement diagram**

Phase 1, trajectory *ab*:
s23(1) ∈ [s230,s230+course23];
s56(1) = s560;
Phase 2, trajectory *bc*:
s23(1) =s230+course23;
s56(1) ∈ [s560,s560+course56];
Phase 3, trajectory *cd*:
s23(1) ∈ [s230+course23,s230];
s56(1) = s560+course56;
Phase 4, trajectory *da*:
s23(1) = s230;
s56(1) ∈ [s560+course56, s560];

To determine the kinematic parameters of the mechanism elements, theoretical research regarding the structural analysis must first be carried out *(Artobolevski I.I., 1977; Demidovitch B., Maron I., 1987; Duca C., Buium Fl., Părăoanu G., 2003; Moise V., Maican E., Moise Şt. I., 2003).*

To determine the kinematic parameters of the mechanism elements, the procedures used were **A2APVA** and **D1PVA**, drawn up by the authors *(Moise V., Simionescu I., Ene M., et al, 2008; Moise V., Simionescu I., Ene M., Rotaru Al., 2015; Moise V., Simionescu I., Ene M., 2018; Simionescu I., Moise V., 1999).*

**1. Structural analysis of the mechanism**

If the relative movements between the elements are taken into account, it is noted that the mechanism has following kinematic joints: $A(3R0)$, $B(2T3)$, $C12(1R2)$, $C14(1R4)$, $C17(1R7)$, $E(7R8)$, $F(8R0)$, $G(4R5)$, $E(3R8)$, $F(4R7)$, $I(7T8)$ (.

The number of upper couplings is zero.

The mobile elements of the mechanism are: $1(A,B,C_{14},C_{17})$, $2(B,C_{12})$, $3(C_{12},D)$, $4(C_{14},G)$, $5(G,I)$, $6(H,I)$, $7(C_{17},E)$, $8(E,F)$;

Considering the number of mobile elements and the number of kinematic joints, the mobility of the mechanism is: *M=2*.

The structural scheme of the mechanism is shown in the figure 4 *a.* The multipolar scheme and structural relationship of the mechanism are presented in the figure 4 b and figure 4 c.

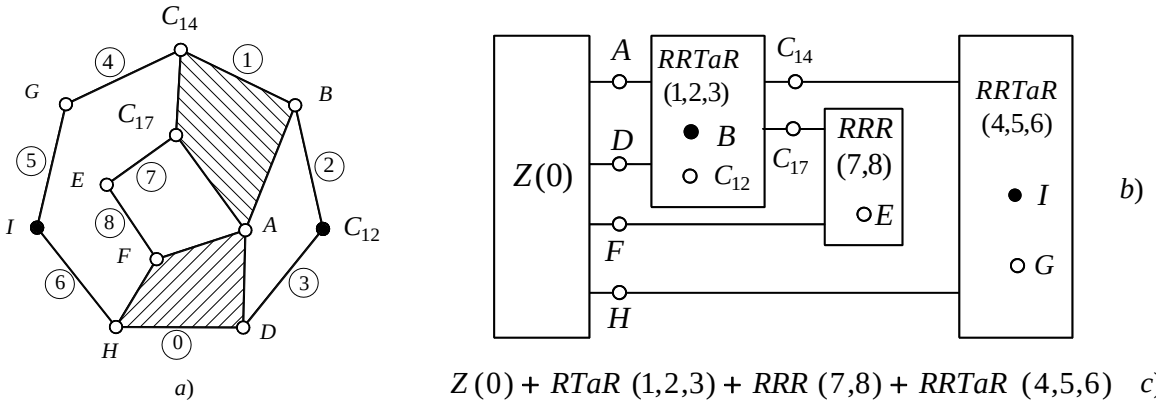


**Fig. 4 – Structural and multipolar schemes of the mechanism as the structural relationship**

From the structural scheme, it is noted that the mechanism consists of the base *Z(0)*, the motor groups *RRTaR*(1,2,3), *RRTaR*(4,5,6) and dyad of appearance 1, *RRR*(7,8).

During the technological process, the mechanism in figure 2 has a variable structure, due to the fact that hydraulic cylinders *2-3* and *5-6* do not work simultaneously.

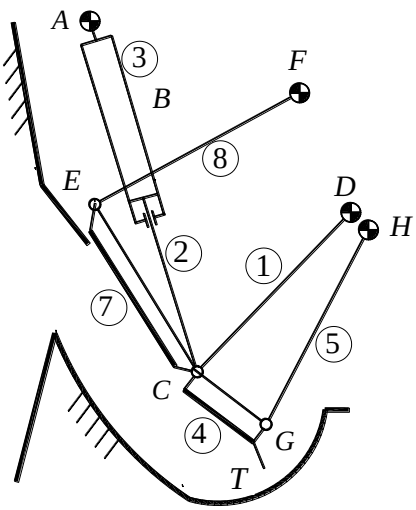


Therefore, if the hydraulic cylinder *5-6* (fig.2) is blocked, which means that the motor coupling *I* is canceled, elements *5* and *6* form a rigid, denoted by *5*. In this case, the kinematic scheme of the mechanism is shown in figure 5.

Structural and multipolar schemes, as well as the structural relationship, are shown in figure 6.

From figures 5 and 6, it is noted that the mechanism consists of *Z* base (0), *RRTaR(1,2,3),* motor groups and dyads *RRR(7,8)* and *RRR(4,5)*

**Fig. 5 - The kinematic scheme of the mechanism for the *ab* and *cd* trajectory of the diagram in figure 3**

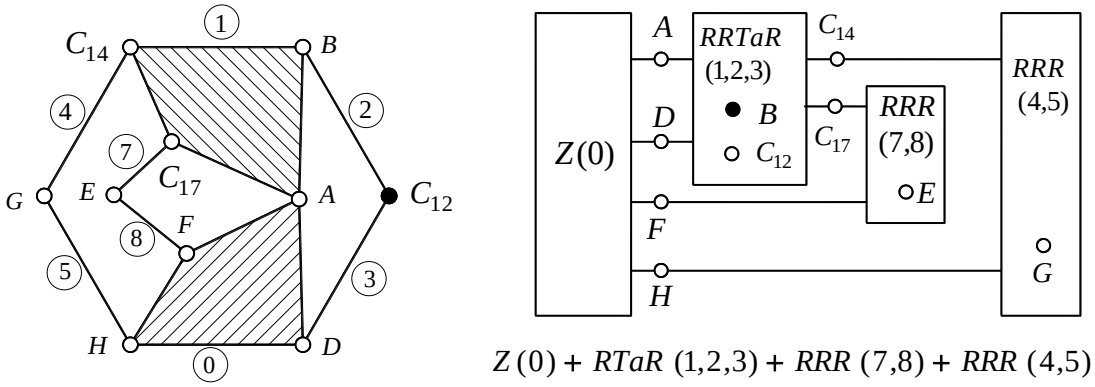


*a)* *b)*

**Fig. 6 - Structural scheme**

*a) Multipolar scheme; b) Structural relationship of the mechanism, for the AB and CD branches of the diagram in figure 3*

*Observation*. On the *ab* and *cd* branches of the diagram in figure 3, the mechanism can be studied from kinematic and kinetostatic standpoint even if it considered the constant length of the hydraulic cylinder consisting of elements *5* and *6* so, the relative velocity between these elements equals zero.

When the tracer *T* is moving on the branches of *bc* and *da* of the diagram in figure 3, it cancels the motor coupling B, and elements 2 and 3 form a rigid, denoted by *2*. As a result of the triangle formed by points *A*, *C* and *D*, elements *1,2,7* and *8* form a rigid, fixed at the base. The kinematic, structural and multipolar schemes as well as the structural relationship are presented in figure 7.

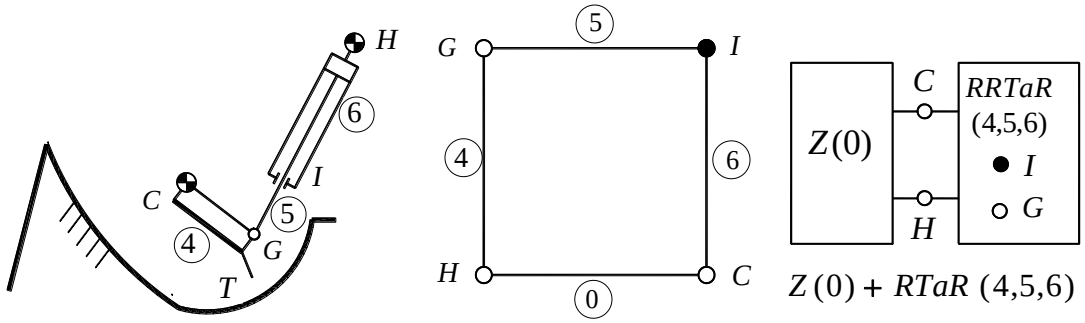


*a*) *b*) c)

**Fig. 7 - The kinematic scheme**

*a) structural scheme; b) multipolar scheme and structural relationship of the mechanism, for BC and DA branches of the diagram in figure 3*

From figure 7, it is noted that the mechanism is composed of the base *Z*(0) and the motor group *RRTaR(4,5,6)*

**2. Kinematic analysis of the mechanism**

The kinematic analysis of the mechanism consists in determining the parameters of positions, speeds and accelerations, corresponding to all its elements.

Figure 8 presents the kinematic scheme of the mechanism, with the position parameters.

For the kinematic analysis of the mechanism there are several stages, namely:

a) elaboration of the calculation program for the determination of the kinematic parameters of the mechanism elements, considering the four phases of a kinematic and dynamic cycle.

b) tabular presentation of the angles values made by vectors $\overline{AC}$, $\overline{DC}$, $\overline{CG}$, $\overline{HG}$, $\overline{CE}$ and $\overline{FE}$ corresponding to the elements of the mechanism, with the positive meaning of the axis *AX*

c) drawing the diagrams of variation of angles, velocities and angular accelerations of the mechanism elements, depending on the position of the mechanism.

d) drawing of velocities and accelerations hodographs corresponding to the tracer T point.

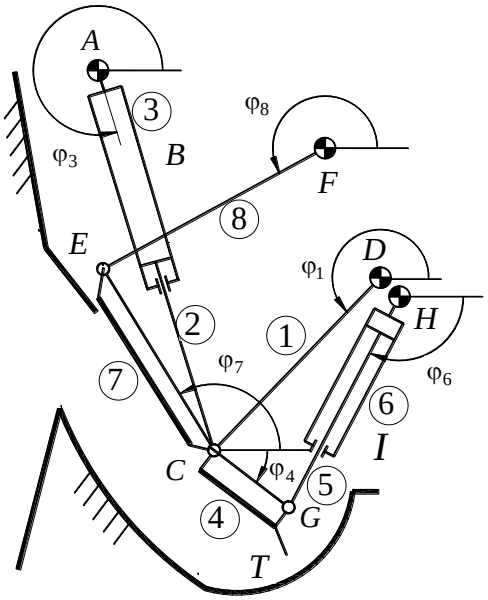


**Fig. 8 - The kinematic scheme of the mechanism, with the parameters of positions**

Figure 9 shows the kinematic diagrams of the structural groups, based on which the formal parameters of the calculation procedures are selected.

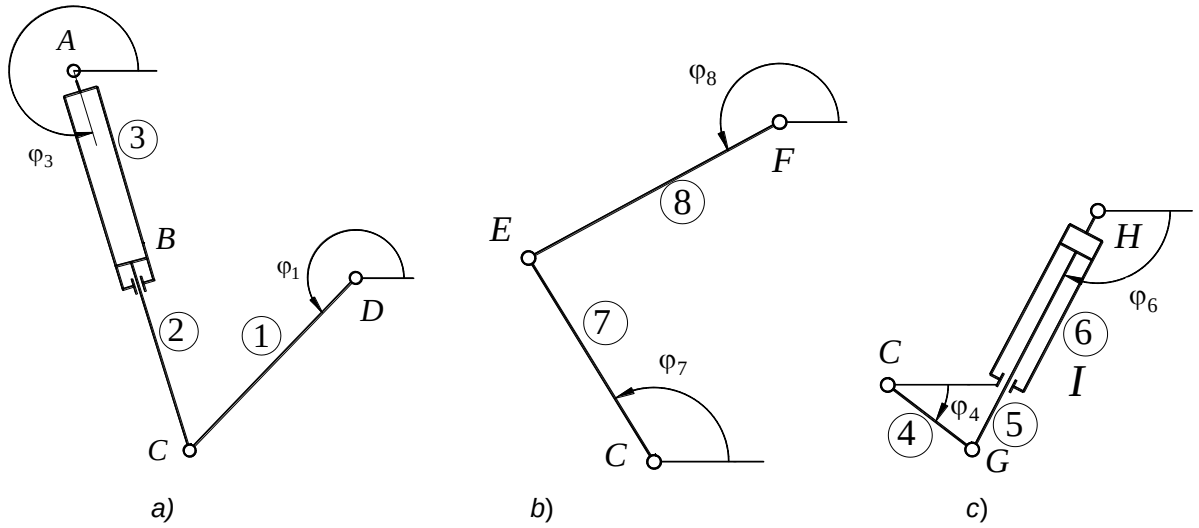


**Fig. 9 – a) The kinematic diagrams of structural groups in the composition of the mechanism motor group *RRTaR*(1,2,3); b) dyad *RRR*(7,8); c) motor group *RRTaR*(4,5,6)**

**RESULTS**

The theoretical investigations presented in the previous chapter were used, taking into account the constructive elements of the mechanism that equipped the machine, to obtain concrete results regarding the kinematics of the mechanism.

For the analysis of the mechanism, they are known:

a) The kinematic scheme of the mechanism (Fig.3);

b) The position of the coupling adjacent to the base and dimension of the elements as follows: *XA* = 0 m, *YA* = 0 m, *XD* = 1.000 m, *YD* = –0.733 m, *XF* = 0.800 m, *YF* = –0.270 m, *XH* = 1.100 m, *YH* = –0.800 m, *CE* = 0.770 m, *CD* = 0.870 m, *EF* = 0.900 m; *CG* = 0.330 m;

c) Phase working times: $t_1$ = 5 sec, $t_2$ = 5 sec, $t_3$ = 5 sec, $t_4$ = 5 sec,

d) Initial positions of the mechanism: S230 = 0.833 m, $S_{560}$ = 0.667 m;

e) Hydraulic cylinder piston work strokes: $Stroke_{23}$ = 0.600 m, $Stroke_{56}$ = 0.400 m;

f) Transmission function used for hydraulic cylinder actuation: sinusoidal function (reduced acceleration is of sinusoidal type)

Figure 10 shows the variation diagram of the angles $\varphi_1$, $\varphi_1$, $\varphi_3$, $\varphi_4$, $\varphi_6$, $\varphi_7$ and $\varphi_8$.

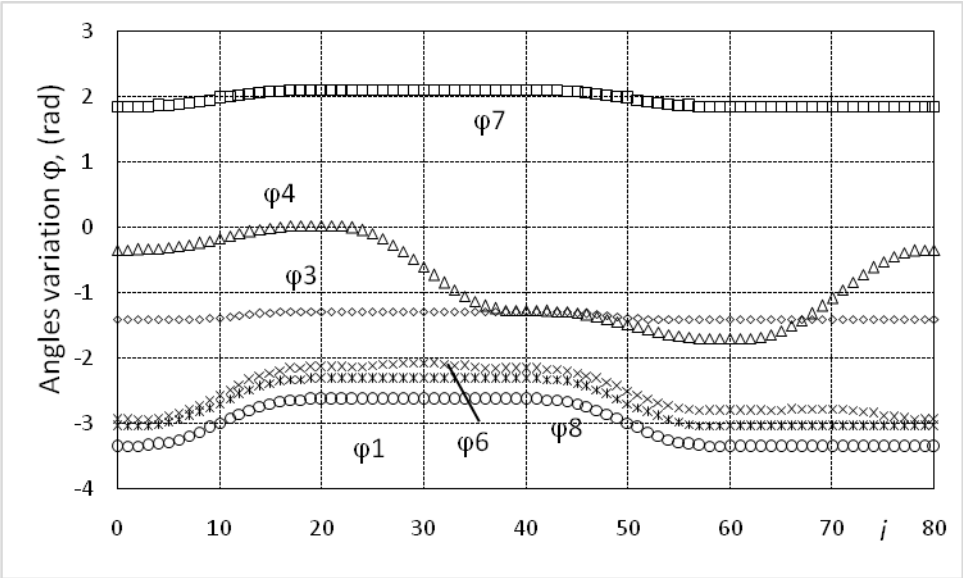


**Fig. 10 – The diagram of variation of angles** $\varphi_1$, $\varphi_2$, $\varphi_3$, $\varphi_4$, $\varphi_6$, $\varphi_7$ and $\varphi_8$

Figure 11 shows the diagrams of the angular velocities of the mechanism elements and in figure 12, the diagrams of the corresponding angle accelerations.

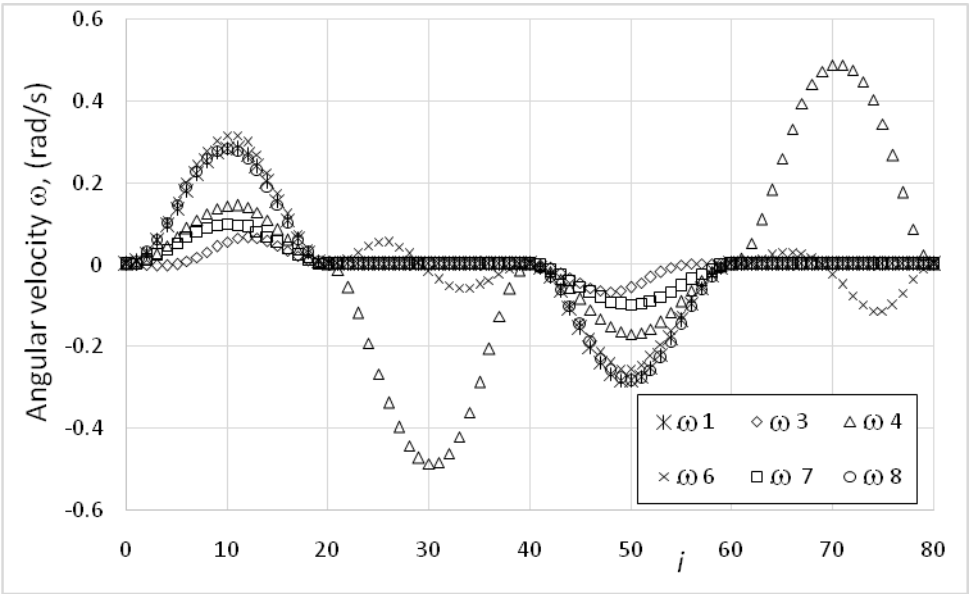


**Fig. 11 - The diagram of the angular velocities of the mechanism elements**

From the analysis of the angular velocities hodographs (fig.11) of the working element 4 (fig.8) it is observed that this follows a cyclical variation with maximum values (about 0.5 rad / s) for positions 30 and 70 respectively of the driving element ( ie the hydraulic drive cylinder), on the pushing stroke, respectively on the retraction stroke.

The same cyclical variation is also observed for the angular acceleration of the working element 4 (see fig. 12), maximum values for this being noted for four positions of the mechanism (respectively of the hydraulic actuating cylinder).

The maximum values of the angular acceleration, for the working element of the mechanism, are around 0.35 rad / s2, for positions 23-24, respectively 63-64, slightly higher for positions 37-38 and 77-78 respectively.

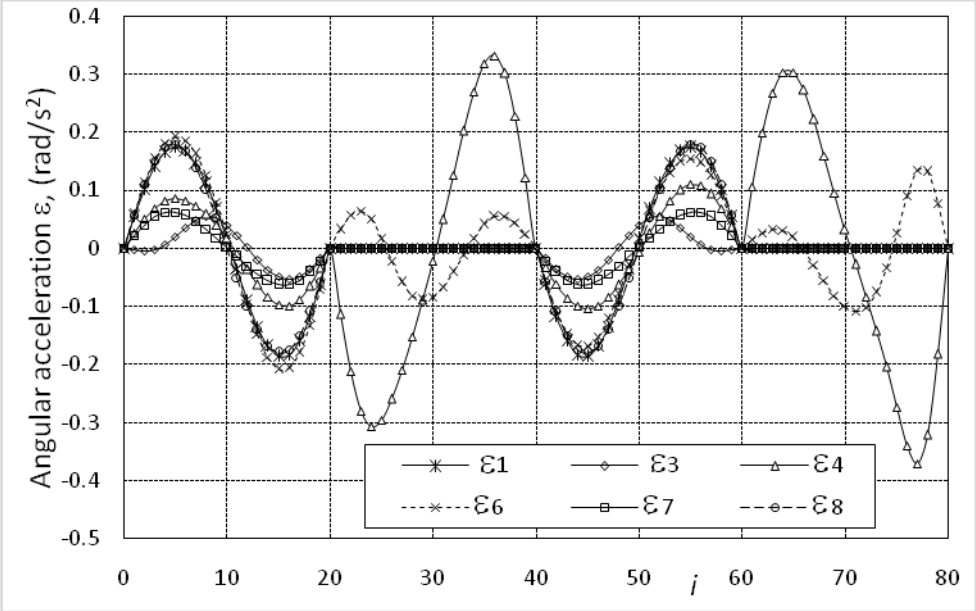


**Fig. 12 - The diagram of the angular accelerations of the mechanism elements**

Table 1 shows the numerical values of the kinematic parameters of positions for the mechanism elements

**Table 1**

| Pos. | φ1 | φ3 | φ4 | φ6 | φ7 | φ8 |
|---|---|---|---|---|---|---|
| 0 | -3.0390 | -1.4085 | -0.3369 | -2.9437 | 1.8536 | -3.3513 |
| 1 | -3.0385 | -1.4086 | -0.3366 | -2.9431 | 1.8538 | -3.3507 |
| 2 | -3.0346 | -1.4088 | -0.3347 | -2.9388 | 1.8553 | -3.3465 |
| 3 | -3.0244 | -1.4093 | -0.3297 | -2.9277 | 1.8593 | -3.3355 |
| 4 | -3.0055 | -1.4100 | -0.3204 | -2.9071 | 1.8667 | -3.3152 |
| 5 | -2.9764 | -1.4103 | -0.3061 | -2.8753 | 1.8778 | -3.2842 |
| | | | ..... | | | |
| 24 | -2.3151 | -1.2802 | -0.0358 | -2.1222 | 2.1090 | -2.6285 |
| 25 | -2.3151 | -1.2802 | -0.0935 | -2.1095 | 2.1090 | -2.6285 |
| 26 | -2.3151 | -1.2802 | -0.1695 | -2.0958 | 2.1090 | -2.6285 |
| 27 | -2.3151 | -1.2802 | -0.2618 | -2.0836 | 2.1090 | -2.6285 |
| 28 | -2.3151 | -1.2802 | -0.3671 | -2.0749 | 2.1090 | -2.6285 |
| 29 | -2.3151 | -1.2802 | -0.4819 | -2.0713 | 2.1090 | -2.6285 |
| 30 | -2.3151 | -1.2802 | -0.6023 | -2.0732 | 2.1090 | -2.6285 |
| 31 | -2.3151 | -1.2802 | -0.7241 | -2.0803 | 2.1090 | -2.6285 |
| | | | ..... | | | |
| 70 | -3.0390 | -1.4085 | -1.0760 | -2.7729 | 1.8536 | -3.3513 |
| 71 | -3.0390 | -1.4085 | -0.9535 | -2.7820 | 1.8536 | -3.3513 |
| 72 | -3.0390 | -1.4085 | -0.8326 | -2.7978 | 1.8536 | -3.3513 |
| 73 | -3.0390 | -1.4085 | -0.7171 | -2.8198 | 1.8536 | -3.3513 |
| 74 | -3.0390 | -1.4085 | -0.6106 | -2.8465 | 1.8536 | -3.3513 |
| 75 | -3.0390 | -1.4085 | -0.5169 | -2.8752 | 1.8536 | -3.3513 |
| 76 | -3.0390 | -1.4085 | -0.4402 | -2.9023 | 1.8536 | -3.3513 |
| 77 | -3.0390 | -1.4085 | -0.3847 | -2.9239 | 1.8536 | -3.3513 |
| 78 | -3.0390 | -1.4085 | -0.3520 | -2.9373 | 1.8536 | -3.3513 |
| 79 | -3.0390 | -1.4085 | -0.3388 | -2.9429 | 1.8536 | -3.3513 |
| 80 | -3.0390 | -1.4085 | -0.3369 | -2.9437 | 1.8536 | -3.3513 |

## CONCLUSIONS

From the analysis of numerical data, as well as the distribution diagrams of angles, speeds and accelerations, conclusions can be drawn on the driveline operation of the mechanism. Based on this data, it can be interfered with improving the performance of the mechanism. To improve the performance of the mechanism, different transmission functions may be used to actuate hydraulic cylinders *2-3* and *5-6*.

After the cinematic analysis of the mechanism, we passed to its kinetostatic analysis (determination of the forces and moments acting on the elements of the mechanism).

**ACKNOWLEDGEMENT**

Part of this paper has been funded by the European Social Fund from the Sectoral Operational Programme Human Capital 2014-2020, through the Financial Agreement with the title "Scholarships for entrepreneurial education among doctoral students and postdoctoral researchers (Be Antreprenor !)", Contract no. 51680/09.07.2019 - SMIS code: 124539.

**REFERENCES**

[1] Artobolevski I.I., (1977), *Theory of mechanisms and machines (Theorie des mecanismes et des machines)*, 453 p., Mir Publishing House, Moscow / Russia;

[2] Demidovitch B., Maron I., (1987), *Elements of numerical calculation (Elements de calcul numerique)*. 717 p., Mir Publishing House, Moscow / Russia;

[3] Duca C., Buium Fl., Părăoanu G., (2003), *Mechanisms*, 481 p., Gh. Asachi Publ. House, Iasi/ Romania;

[4] Moise V., Maican E., Moise Şt. I., (2003), *Numerical method in engineering*, 305 p., Bren Publishing House, Bucharest / Romania;

[5] Moise V., Simionescu I., Ene M., Neacşa M., Tabără I.A., (2008), *Analysis of applied mechanisms*, 282 p., Printech Publishing House, Bucharest / Romania;

[6] Moise V., Simionescu I., Ene M., Rotaru Al., (2015), *Analysis of plane mechanisms with articulated bars. Applications in MATLAB*, Printech Publishing House, Bucharest / Romania;

[7] Moise V., Maican E., Moise Şt.I., (2016), *Numerical methods. Applications in MATLAB*, Printech Publishing House, Bucharest / Romania;

[8] Moise V., Simionescu I., Ene M., (2018), *Optimal synthesis of flat cam mechanisms*, Printech Publishing House, Bucharest / Romania;

[9] Pelecudi Chr., (1975), *Precision of the mechanism*, 398 p., Publishing House of the Academy of the Socialist Republic of Romania, Bucharest / Romania;

[10] Pelecudi Chr., Maroş D., Merticaru V., Pandrea N., Simionescu I., (1985), *Mechanisms*, 394 p., Didactic and Pedagogical Publishing House Bucharest / Romania;

[11] Simionescu I., Moise V., (1999), *Mechanisms*, 238 p., Technical Publishing House, Bucharest / Romania;

[12] Voicu Gh., (2007), *Equipment for municipal management and greening of localities*, 255 p., MatrixRom Publishing House, Bucharest / Romania;

[13] Voicu Gh., Lazea M., Zabava B.S., Tudor P., Moise V., (2019), Kinematic analysis of the pre-taking and pre-compacting mechanisms of some garbage trucks, *Journal of Engineering Studies and Research*, Vol. 25, No. 2, pp.56-62, Bacau / Romania;

[14] Voicu Gh., Lazea M., Tudor P., Zabava B.St., Moise V., (2019), Comparative analysis of the municipal waste collection and pre-compacting systems, *Sixth International Conference Research people and actual tasks on multidisciplinary sciences*, pp.354-359, Lozenec / Bulgaria.

# RESEARCH OF CONSTRUCTIVE AND REGULATORY PARAMETERS OF THE ASSEMBLY WORKING PARTS FOR POTATO HARVESTING MACHINES
/
# *ДОСЛІДЖЕННЯ КОНСТРУКТИВНИХ ТА РЕЖИМНИХ ПАРАМЕТРІВ ПІДКОПУВАЛЬНИХ РОБОЧИХ ОРГАНІВ ДЛЯ КАРТОПЛЕЗБИРАЛЬНИХ МАШИН*

**Hrushetsky S.M.[1)], Yaropud V.M.[2)], Duganets V.I.[1)], Duganets V.I.[1)], Pryshliak V.M. [2)], Kurylo V.L.[2)] [1]**
[1)] State Agrarian and Engineering University in Podilia / Ukraine,
[2)] Vinnitsa National Agrarian University / Ukraine
*Tel: +380978399834; E-mail: yaropud77@gmail.com*
*DOI: 10.35633/INMATEH-59-11*

**Keywords:** *potato masses with soil, potato tuber, digging working part, model, separation, potato harvesting machines*

**ABSTRACT**
*The problem of improving the quality of potato tuber separation by improving the digging working parts from the construction of potato harvesters is investigated. Based on the analysis of the theoretical and experimental studies on the existing working parts, the design scheme was established and the optimum values of the parameters and operation modes of the digging working parts were established, for potato harvesting machines, which would allow improving the quality performances of the potato harvester as a whole. According to the research results, an experimental sample of digging working parts for potato harvesting machines was developed and manufactured, whose verification in operation confirmed their workability and efficiency.*

**РЕЗЮМЕ**
*Досліджується проблема підвищення якості сепарації картопляного вороху за рахунок удосконалення підкопувальних робочих органів для картоплезбиральних машин. На основі аналізу існуючих робочих органів, теоретичних і експериментальних досліджень визначено конструктивну схему та встановлено оптимальні значення параметрів та режимів роботи елементів підкопувальних робочих органів для картоплезбиральних машин, які дозволять підвищити якісні показники роботи картоплезбиральної машини в цілому.*
*За результатами досліджень розроблено та виготовлено експериментальний зразок елементів підкопувальних робочих органів для картоплезбиральних машин, виробнича перевірка яких при роботі на картоплезбиральній машині підтвердила його працездатність та ефективність.*

## INTRODUCTION

Ukraine has a unique natural potential, which allows it to become a leader in the production of agricultural products in Europe. However, in order successfully enter the western markets it is necessary to ensure, first of all, the competitiveness of its own products, which is achieved by the complex mechanization of technological processes, reducing labour costs, increasing the yield and quality of the products (*Hrushetsky S.M., 2016*). Potato cultivation in our country is carried out according to the technology of the last century, and if earlier potato cultivation was mechanized, now it is performed in most farms manually. With the reforms in the village, potato growing scattered over small peasant, farmer and garden lands, where about 95% of this crop is located.

Machines for growing potatoes in Ukraine were imported mainly from the Russian Federation, Belarus and Germany. Potatoes producers on all scales often take the example of neighbouring Belarus, where the technological cycle is fully provided by the state, the corresponding factories operate.

There is a problem of improving the existing and inventing new promising technologies and working parts of potato harvesting equipment, justifying the optimal modes of their work and, ultimately, providing this crop sector with modern, high-performance and reliable harvesting equipment.

[1] *Hrushetsky S.M., Assoc. Prof. Ph.D. Eng.; Yaropud V.M., Assoc. Duganets V.I., Prof. Ph.D. Eng.; Prof. Dr. in Pedagogy; Duganets V.I., Assoc. Prof. Ph.D. Eng.; Pryshliak V.M., Assoc. Prof. Ph.D. Eng.; Kurylo V.L., Prof. Dr. in Agriculture*

## MATERIALS AND METHODS

The problem of growing and collecting potatoes is tackled in a lot of published works. Increasing the technological level of modern potato harvesting machines, the criteria for assessing loss ratio, contamination and damage of the products to their mass, remain a scientific and actual problem for the further development of domestic machinery for tubers harvesting.

An analysis of the evolution of the design and layout and technological schemes of potato harvesting equipment shows that, at present, powerful self-propelled bunker combines are increasingly used for harvesting, which annually collect crop on up to 70% of world's land (*Pogorel'y L.V. & Tatianko M.V., 2004*).

Further deepening and development of the general concept of modern machines rational outlines are possible based on world experience analysis of phased improvement of harvesting root crops process, or based on a more detailed analysis of the working parts functioning of the main transport and technological systems for digging and cleaning root crops.

The efficiency of root crops harvesting depends to a large extent on the construction and layout scheme and the work quality of the heap purifier, which must separate at least 92% of impurities according to the initial requirements for potato harvesting machines, while adhering to the allowable values of losses and damage to the root crops (*Dubrovin V., Golub G., Baranovsky V. & Teslyuk V., 2013*).

A significant variation in the working conditions of potato harvesting machines and the lack of adaptation of existing constructions of digging and especially cleaning working parts to these changes in the working conditions do not allow obtaining stable agrotechnical parameters, especially for dry and wet soil, field's weeds, etc. With an increase in soil moisture to 22-28%, the quality of machines deteriorates by 2-6 times, and on solid soils there is observed a significant (up to 20-40%) amount of root heap with lumps of soil (*Ramsh V.Y., Baranovsky V.M. & Pankiv M.R., 2011*).

Despite the rather complex transport and technological systems of the working parts for cleaning the remaining root heap, after clearing by the energy-intensive multi-stage systems for cleaning the excavated amount of ground of soil impurities from the fields, the amount of fertile soil which is extracted, is the equivalent of 10...15 cm of the arable layer on the harvesting area equal to 100 ha, in spite of the fact that the total length of the treatment surfaces reaches 8...10 m (*Baranovsky V.M., Onishchenko V.B. & Solomka V.O., 2002*).

The aim of the work is to systematize and synthesize the research of modern technologies of cultivating and harvesting potatoes and create a new design of a sub-cultivating working body that would collect the minimum amount of soil together with the tubers and provide the possibility of better fragmentation of the formation to facilitate separation with increased operational efficiency, technological reliability of the sub-cavern body and reduction of its traction support.

To achieve this goal, you need:

1. To analyse the existing designs of the sub-cultivating working parts of potato harvesting machines, the results of experimental and theoretical studies of the digging working parts and to improve the design on their basis;

2. Theoretically explain the improvement of the parameters and modes of operation of the digging machines for potato harvesting;

3. Based on the results of laboratory-field experimental studies specify the optimal parameters and work modes of the investigated working body and determine the agronomic indicators according to the performance of the potato harvesting machine;

4. To determine the effectiveness of the use of combined digging working parts.

Well known digging working parts according to the type of needed work are divided into the passive ones, active ones and mixed ones (*Hrushetsky S.M., Zbaravskaya L.Y. & Semenishena I.V., 2017*). Depending on the shape, they are flat, sectional and cylindrical, where the shape of the curved front is similar to the shape of the nest of the root tubers, the cylindrical surface is flat, and the back side - is convex (*Hrushetsky S.M., Bendera I.M. & Belous S.V., 2008*).

The technical result depends on reducing the time spent on stopping the harvesting unit and cleaning the digging working body from the plant residues, as well as in reducing the energy costs of digging the potato tuber. Fig. 1 shows tubers zone of placement: $B_r$ - row width, $B$ - the capture width of the border front undercut part is equal to the width of the nest bug placement of tubers, taking into account the transverse deviations of the line from the axial line $2\delta$; $h_d$ - digging depth; $h$ - depth of occurrence of extreme tubers. The width of the final part of the potato cutter's digging is equal to the width of the separating part.

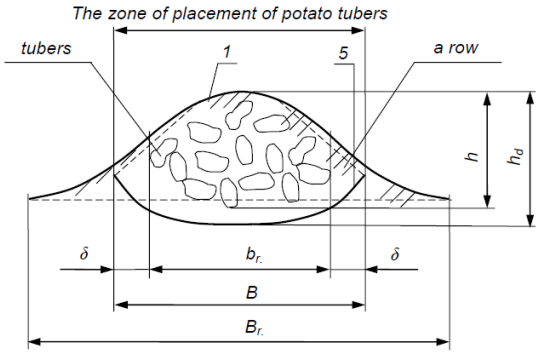


**Fig. 1** – **Zone of tuber placement**

The proposed digging working body for potato harvesting machines is shown in Fig. 2 (*Hrushetsky S.M., Horodinsky V.O., Stavruk D.V., Gromik B.I. & Dudar M.O., 2015; Hrushetsky S.M., Zbaravskaya L.Y. & Semenishena I.V., 2018*) – side view of potato harvesting: $V_м$ – speed of the machine; $Q_o$ – filing of the general amount of potato's soil mass which has $r(t_i)$ – the amount of small particles of soil at the time $t$, $k(t_i)$ – the number of tubers at the time $t$, $m(t_i)$ – amount of plant residues at the time $t$, $q(t_i)$ – the number of large lumps at the time $t$; $\alpha_p$ – angle of inclination of a cylindrical catcher to the horizon; fig. 3 – top view of a cylindrical catcher: $\gamma$ – the sloping angle of the slice with the excavated bunch of tubers down the blade; fig. 4 – a view of the catcher in the cut position *A-A*, *B-B*, *C-C* and *D-D* – fig. 3; fig. 4 – view *E* above the flat triangle – fig. 2.

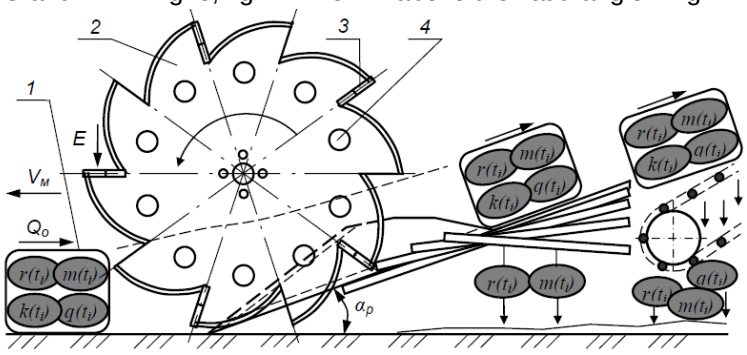


**Fig. 2 − Working body for potato harvesting machines (side view)**

The technological scheme of the digging process consists of a potato's soil mass *1,* on both sides of which there are two vertical toothed gears *2,* with soil compactors *3*. The disc has a series of openings *4* with centres which are located concentrically on the axis of rotation of the toothed disc, while the distance between the outer edge of the disc tooth to the axis of the opening is permissible to 140...250 mm. The diameter of the hole in the toothed disc can be made within the limits of 30...37 mm. A root heap harvesting part which has a cylinder surface shape *5* (fig. 3), of the potato harvesting machine, on which the potato's soil mass *1* moves, which after a certain change in shape and deformation on the separation rods *6,* in the longitudinal vertical surface, enters the separator *7*, followed by the subsequent technological process - separation.

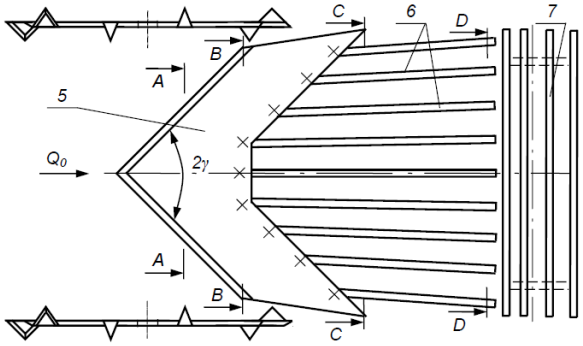


**Fig. 3 − Working part for potato harvesting machines (top view)**

The digging working part of the potato harvesting machine works in the following way. When moving the machine along the rows of potato fields due of the tractor traction, the working part gets deeper into the potato tuber, while there is a trimming of the reservoir from the bottom of the heap harvesting part which has a

cylinder surface shape *5*. Due to the gradual movement of the potato digger and the grip of the toothed wheels *2* with soil, which are provided by the friction forces on the lateral surfaces, directly by soil harvester *3* turn discs on their axis. In this case happens the cutting of plant residues by the working edge of the toothed disc *2* and by the cutting edges of the soil tillers *3*, as well as cutting the potato layer on the sides occurs. Due to jamming between the discs *2* and the cylindrical surface of the potato harvesting machine, the reduced layer of the potato's total left mass *1* is applied along the curved forward part, further along the median flat bar *6* of the longitudinal and vertical surface and, upon approaching it, by the convex rod-separating surface in the transverse vertical surface, gets to the separation working part *7* partially crushed, separated and evenly distributed for further separation.

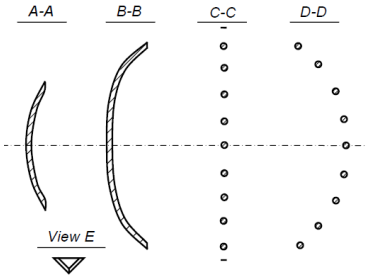


**Fig. 4 – The heap harvesting part which has a cylinder surface shape**

The best separation of tubers from the soil will occur due to:

a) cutting off the potato layer on the sides of the teeth gears and the cutting edges of the soil cultivators with partial destruction of it;

b) reduction of the amount of potato's soil mass of the reservoir during the movement on the cylindrical surface of the potato harvesting machine;

c) the transverse deformation of the soil layer and partial separation during its movement on the middle flat net bars surface of the potato harvesting machine;

d) the transverse deformation of the soil layer and partial separation during its movement on a convex rod net surface at the output of the potato harvesting machine;

e) the equal distribution of the potato's soil mass at the output from the rod net surface of the potato harvesting machine on the separating surface.

To determine the area of the soil tiller it is necessary to know its height and width. The soil tiller's height, considering the technological feature of the disc, cannot exceed the height of the gear tooth, therefore we accept the following parameters $h_r = h_a$.

The width and shape of the soil tiller should ensure rational working conditions of the toothed disc.

To find out the optimal shape and width of the toothed discs of the gear disc, we will carry out studies of soil-blades having the shape: *1* – rectangle*; 2* – rectangular trapezoid*; 3* – a rectangular triangle.

To verify the rational form and geometrical parameters of the cutting edge, several forms of soil tillers were considered and their comparison was made on the following indicators: metal capacity of constructions of a disc with soil tillers; traction resistance of a disc with soil tillers; cutting elements of weed plants and buds.

The main element of the proposed disc is a gear tooth with a cutting edge, executed on a logarithmic curve. In our case, the logarithmic curve equation has the form (fig. 5) (*Stavruk D.V. & Hrushetsky S.M., 2015*):

$$r = \frac{1}{2} r_0 (1 + e^{\psi ctg\tau}), \quad (1)$$

where $r$ – value of the radius vector, *m*; $r_0$ – initial value of the radius vector, *m*; $r = r_v$ – the final value of the radius vector, *m*; $\psi$ – the angle of the blade's edge, *rad*.; $\tau$ - sliding angle, *rad*. In this case, $\tau$ = *const.*

From the scheme (fig. 5):

$$r_v - r_0 = h_a = \frac{1}{2} r_0 (e^{\psi ctg\tau} - 1). \quad (2)$$

Then the formula to determine the length of the cutting edge is the following (*Horodinsky V.O., Hrushetsky S.M., 2016*):

$$c = \frac{r_0}{2 \sin\tau} \int_0^{\psi} \sqrt{\sin^2\tau + 2 \cdot \sin\tau \cdot e^{\psi ctg\psi} + e^{2\psi ctg\tau}} \cdot d\psi = \frac{1}{2} r_0 \left( \psi + \frac{e^{\psi ctg\tau}}{\cos\tau} \right). \quad (3)$$

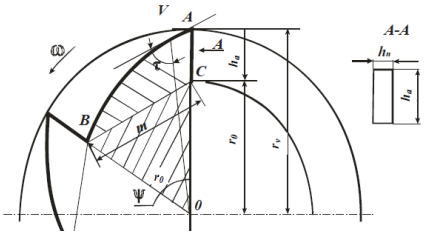


**Fig. 5 − Scheme for determination of metal capacity of a toothed disc with soil tillers, the gear teeth of which have a cutting edge in the form of a logarithmic curve**

Then the formula to determine the length of the cutting edge is the following:

$$S_a = (S_t + S_n) \cdot Z \,, \tag{4}$$

where: $S_n$ – area of the soil tiller, $m^2$; $S_t$ – area of the gear tooth, limited by the radii $r_0$ in the low curves, $m^2$;

$Z$ – number of gear teeth, *pcs*.

Determine the area of the gear tooth:

$$S_t = S_{OAB} \,, \tag{5}$$

$$S_{OAB} = \frac{S_a}{Z} \,. \tag{6}$$

In general view, we can write:

$$S_{OAB} = \frac{1}{2}\int_{\psi^1}^{\psi^2} r_0^2 d\psi \quad , \tag{7}$$

$$S_{OAB} = \frac{1}{2}\int_0^{\psi}\left(\frac{1}{2}r_0 + \frac{1}{2}r_0 \cdot e^{\psi ctg\tau}\right)^2 d\psi = \frac{1}{2}\int_0^{\psi}\frac{1}{4}r_0^2\left(1+e^{\psi ctg\tau}\right)^2 d\psi = \frac{r_0^2}{4}\left(\psi + \frac{e^{2\psi ctg\tau}}{ctg\tau} + \frac{e^{2\psi ctg\tau}}{2ctg\tau} + \frac{5}{2ctg\tau}\right). \tag{8}$$

The area of the soil tiller will be determined as the area of the rectangle:

$$S_n = h_a \cdot k_n \,, \tag{9}$$

where $k_n$ – width of the heap harvesting part which has a cylinder surface shape, *m*.

Ultimately, we obtain a formula for determining the area of the gear toothed disc with the rectangular shape of the soil tillers:

$$S_a = 10\left(\frac{r_0^2}{8}\left(\psi + \frac{e^{2\psi ctg\tau}}{ctg\tau} + \frac{e^{2\psi ctg\tau}}{2ctg\tau} + \frac{5}{2ctg\tau}\right) + h_a \cdot k_n\right), \tag{10}$$

$$\begin{aligned} S_{заг.} &= \frac{5}{4}r_0^2\left(\psi + 2\cdot e^{\psi ctg\tau}\cdot tg\tau + \frac{1}{2}e^{\psi ctg\tau}\cdot tg\tau + \frac{5}{2}tg\tau\right) + 5r_0\left(e^{\psi ctg\tau} - l\right)\cdot k_n = \\ &= \frac{5}{4}r_0^2\left(\psi + 2\cdot tg\tau\cdot e^{\psi ctg\tau} + \frac{1}{2}\cdot tg\tau\cdot e^{2\psi ctg\tau} + \frac{5}{2}tg\tau\right) + 5r_0\left(e^{\psi ctg\tau} - l\right)\cdot k_n \end{aligned} \,. \tag{11}$$

The area of the soil cultivator having the shape of a rectangular trapezoid is determined:

$$S_n = h_a \cdot k_n - \frac{1}{2}k^2 \cdot tg\alpha_n \,, \tag{12}$$

where $\alpha_n$ – angle of inclination of the working edge of the soil tiller to the trapezium height, *degrees*.

The area of a gear toothed disc with soil tillers, executed in the form of a rectangular trapezoid is equal to:

$$S_a = \frac{5}{4}r_0^2\left(\psi + 2\cdot ctg\cdot e^{\psi ctg\tau} + \frac{1}{2}\cdot tg\tau\cdot e^{2\psi ctg\tau}\right) + 5r_0\left(e^{2\psi ctg\tau} - l\right)\cdot k_n - 5r_n^2 tg\alpha_n \,. \tag{13}$$

The area of the ground tiller, which has the shape of a rectangular triangle, will be determined:

$$S_n = \frac{1}{2}h_a \cdot kj_n. \tag{14}$$

The area of a toothed disc with soil compactors, executed in the form of a rectangular triangle is:

$$S_a = \frac{5}{4}r_0^2\left(\psi + 2\cdot tg\tau\cdot e^{\psi ctg\tau} + \frac{1}{2}\cdot tg\tau\cdot e^{2\psi ctg\tau}\frac{5}{2}tg\tau\right) + \frac{5}{2}r_0\left(e^{\psi ctg\tau} - l\right)\cdot k_n \,, \tag{15}$$

With the help of formulae (11), (13), (15) you can find the hard disc volume:

$$Q_a = p_{cm} \cdot S_a \cdot b_\partial \,, \tag{16}$$

where $p_{cm}$ – specific gravity of steel, kg/m$^3$; $b_\partial$ – disc thickness, m; $S_a$ – area of the toothed disc, m$^2$.

As a result of the calculation, we came to the conclusion that the metal capacity of the disc with steel blades in comparison with the disc without steel blades has increased by a magnitude from 1.7% to 3.4%.

Depending on the shape of the soil harvester, its area is:

- rectangle $$S_n = h_a \cdot k_n ,$$ (17)

- rectangular trapezoid $$S_n = h_a \cdot k_n - \frac{1}{2} k_n^2 \cdot ctg_n ,$$ (18)

- triangle $$S_n = \frac{1}{2} h_з \cdot k_n .$$ (19)

The length of the working edge of the tooth is determined by the height of the tooth, the length of its cutting surface, the width of the soil cultivator, the number of teeth per segment of the blade which are immersed in the soil, namely (*Stavruk D.V. & Hrushetsky S.M., 2015*):

$$l_{kp} = Z'\left(h_a + c_a + k_n\right), \quad (20)$$

where:

$h_a$ – height of the tooth, m; $c_a$ – length of the curvilinear side of the tooth, m; $k_n$ – width of soil harvester, m; $Z'$ – the number of teeth that are on the segment of the blade which is immersed in the ground, pcs.

It is necessary to determine the number of teeth on the segment of the blade which is immersed in the soil. To do this, use the scheme presented in fig. 6.

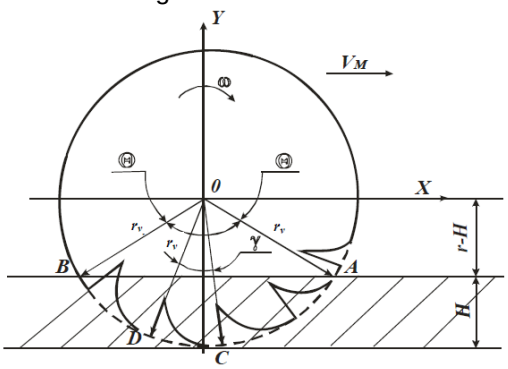


**Fig. 6 − Scheme to determine the number of a disc teeth which are immersed in the soil**

The length of the arc $l_{AB}$ is determined by the formula (*Stavruk D.V. & Hrushetsky S.M., 2015*):

$$l_{AB} = r_v \left( \pi - 2\,arcsin \frac{r_v - H}{r_v} \right). \quad (21)$$

The length of the arc $l_{DC}$ which corresponds to the placement of one of the gear teeth on the arc AB is determined as follows:

$$l_{DC} = r_v \cdot y , \quad (22)$$

where $r_v$ – radius of the disc at the tops of the teeth, m; $y$ – central angle for one tooth, degrees.

With a known number of teeth Z we define:

$$\gamma \frac{2\pi}{Z} . \quad (23)$$

The number of teeth which are immersed in the soil is equal to (*Stavruk D.V. & Hrushetsky S.M., 2015*):

$$Z' \approx \frac{l_{AB}}{l_{DC}} = \frac{Z \cdot \left( \pi - 2\,arcsin \frac{r_v - H}{r_v} \right)}{2\pi} . \quad (24)$$

We obtain the length of the cutting edge immersed in the soil:

$$l = \frac{\left(h_a + c_a + k_n\right) \cdot \left( \pi - 2\,arcsin \frac{r_v - H}{r_v} \right)}{2\pi} . \quad (25)$$

Let us consider the effect of the forces of resistance of soil on a toothed disc with soil compactors, for which we will use the scheme represented in fig. 7.

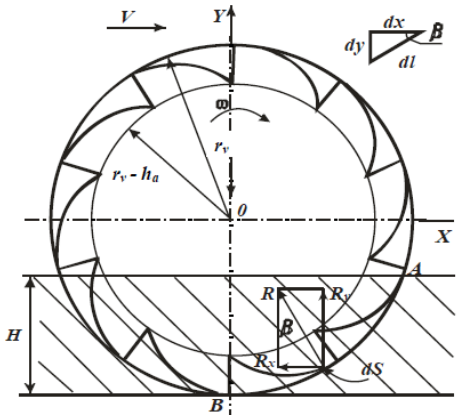


**Fig. 7 − Scheme for determining the traction resistance of a disc with soil compactors, the teeth of which have a cutting surface in the form of a logarithmic curve**

After transformation, the formula for determining the traction resistance of a disc with a logarithmic gear cutting edge and soil tillers without taking into account the friction forces will look as follows (*Stavruk D.V. & Hrushetsky S.M., 2015*):

$$R_x = \frac{Q_{z.u.}\left(b_0 \cdot H + \sum_{i=Z'} S_n \cdot \cos\beta_i\right)}{\frac{2 \cdot Z \cdot b_0 \cdot r_0}{2 \cdot 2\pi}\left(\psi + \frac{2k_n}{r_0} - 1 + e^{\psi ctg\tau}\left[1 + \frac{1}{\cos\tau}\right]\right) \cdot \left(\pi - 2\arcsin\frac{r_v - H}{r_v}\right) + \sum_{i=Z'} S_n \cdot \sin\beta_i} = \quad (26)$$

$$= \frac{Q_{z.u.}\left(b_0 \cdot H + \sum_{i=Z'} S_n \cdot \cos\beta_i\right)}{Z \cdot b_0 \cdot r_0\left(\psi + \frac{2k_n}{r_0} - 1 + e^{\psi ctg\tau}\left[1 + \frac{1}{\cos\tau}\right]\right) \cdot \left(\pi - 2\arcsin\left[1 - \frac{2PH}{r_0\left(1 + e^{\psi ctg\tau}\right)}\right]\right) + \sum_{i=Z'} S_n \cdot \sin\beta_i}.$$

According to the performed calculations results was done a comparative analysis of the digging working part disc elements of the following types: a disc with teeth, made on a logarithmic curve, a disc with soil-cutters having the shape of a rectangle, a disc with soil-cutters having the shape of a rectangular trapezoid, and a disc with soil compactors that have the form of a rectangular triangle (Table 1).

**Table 1**

**Comparative characteristics of discs with soil compactors of different shapes**

| Benchmarks | Disc without steel blades | Tiller disc with soil compactors | | |
|---|---|---|---|---|
| | | Rectangular shape | Rectangular shape | Rectangle triangle |
| 1. Increase in metal content, % | 0,0 | 3.4 | 3.3 | 1.7 |
| 2. Increase of traction resistance, % | 0,0 | 14.5 | 11.2 | 8.7 |

Let's consider the effect of the soil tiller working edge on the plant remains and the weed. First, let's assume that the soil tiller has the shape of a rectangular trapezoid. We use the scheme presented in fig. 8.

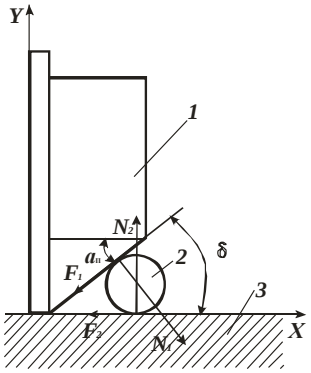


**Fig. 8 – Scheme of the working edge of the soil tiller on the element of the plant**

*1 – disc tiller; 2 – an element of the plant; 3 – the surface of the field*

Let the element of the plant act with forces $N_1$ and $N_2$, normal to the working edge and the surface of the soil. If it is pushed out from the solution of the working edge and the surface of the soil, then the strength of friction forces will affect $F_1$ and $F_2$ on it, the values of which we can find from the formulae (*Stavruk D.V. & Hrushetsky S.M., 2015*):

$$F_1 = N_1 \cdot tg\phi_1 \quad (27)$$

$$F_2 = N_2 \cdot tg\phi_2 \quad (28)$$

where: $tg\varphi_1$ and $tg\varphi_2$ – coefficients of friction of the element of the plant, respectively, to the steel and to the soil adjustment.

To prevent plant residues from being pushed away from the aforementioned substance, the force $F_2$ must be greater or equal to the sum of projections of all forces acting on the stalk along the *OY* axis, i.e., the condition must be met:

$$F_2 \geq N_1 \cdot \sin\delta - F_1 \cdot \cos\delta, H \quad (29)$$

Then the condition of plant elements jamming by the working edge of the soil tiller will have the following form (*Stavruk D.V. & Hrushetsky S.M., 2015*):

$$a_n \leq \phi_1 + \phi_2 \quad (30)$$

The angles $\varphi_1$ and $\varphi_2$ are known and, therefore, the angle of inclination of the soil cultivator working edge, which determines the cutting of the elements of plants and weeds, must be less or equal to 63° (*Stavruk D.V. & Hrushetsky S.M., 2015*):

$$a_n \leq 27° + 36° = 63° \quad (31)$$

Analysing the formula (31), we can conclude that the ground-tiller which is made in the form of a rectangular trapezoid is the most rational solution for the cutting of plant residues. So, when cutting blades have a rectangular triangle shape, for preserving the condition of the blades for fixing state, they must have width of at least 50 mm to ensure the condition of jamming, which negatively affects the metal capacity and traction resistance. The rectangular form of the soil tillage is the cutting of vegetable residues by cutting without slipping (that is, $\delta$ = 0), which is more energy-efficient than cutting with slipping (*Stavruk D.V. & Hrushetsky S.M., 2015*).

**RESULTS**

The tests were carried out on loamy soils at a yield of potatoes of 13.2 tons/ha. Experimental potato diggers which are based on KST-1,4A participated in the harvesting of potatoes along with serial potato diggers KST-1,4A. Experimental potato diggers had a changed undercut part consisting of a sectional passive bench steel blades and vertical discs mounted on the outside of the working body.

The disc element has steel blades, made in the form of a rectangular trapezoid. The tread depth was set with the help of a support wheel, which goes along the inter-row.

In fig. 9 and 10 are shown the results of field experiments of the experimental potato digger compared to the serial loss and damage of potato tubers depending on the machine working speed.

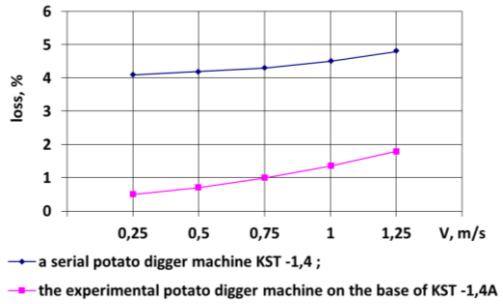


**Fig. 9 − Loss of potato tubers depending on working speed and constructions of potato digger working parts**

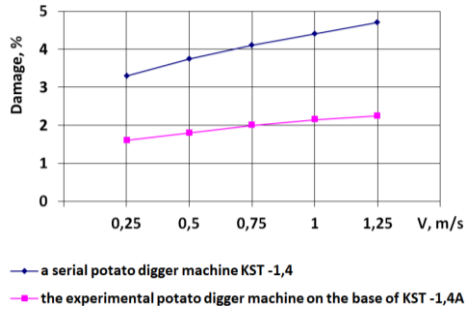


**Fig. 10 − Damage of potato tubers is depending on working speed and constructions of potato digger working parts**

The conducted studies showed the following:

1. The digging working part of the experimental potato digger, with a reduction of traction resistance by 18%, has an improved buckling rate of the potato soil level to 19%.

2. The completeness of digging with an experimental potato digger machine based on KST-1,4A amounted to 99.1%, compared to 97.6% with the serial digger KST-1,4. The obtained data can be explained by the more advanced design of the digging working parts.

3. Increasing the purity of residues amount of the experimental potato digger by 30.8% compared to the serial KST-1,4A is due to a decrease in the taken amount of "free" soil from the inter-row, as well as better soil cracking by the digging working parts.

4. As a result of the application of the disc sidewalls with the steel blades in the digging working part, the technological reliability of the experimental potato digger has increased and the downtime decreased by 33%.

5. The use of a potato digger machine with an experimental digging working part has allowed increasing productivity by 22%.

A potato digger machine allows harvesting potatoes with the determined quality level of working speed from 2.2 to 4.7 km/hour.

Research was performed to find out the capacity level of metal vertical cutting discs which have steel blades on potato harvesting machines for advanced digging performance.

The study of the capacity of metal vertical cutting discs with steel blades was conducted during the field trials. The deterioration value was determined by decreasing the sample weight by weighing on the analytical scales before and after the tests. The results of the tests were expressed as a measure of specific capacity level of *J* (g/ha), which is equal to the ratio of the difference in mass of the toothed disc before and after the test *m* (g) to the area of the field treated area $S_n$ (ha).

$$J_n = \frac{m_n}{S_{Пn}}. \tag{32}$$

$$m_n = m_{2n} - m_{1n}. \tag{33}$$

Weighing was subjected to all toothed discs, after which the average specific capacity level is calculated:

$$J = \frac{J_1 + ... + J_n}{n}. \tag{34}$$

Also, during the study, the control of the intensity level of the steel blades in width and thickness was carried out. Thickness measurement was carried out using an indicator head with an accuracy of 0.01 mm; width measurement was made using a calliper with an accuracy of 0.05 mm.

The results of the capacity level study of the toothed discs with steel blades and the soil tillers by weight and according to the linear indicators are presented in Table 2.

It should be noted that studies on sandy soils were carried out on an area of 17 hectares and on loamy soils - 10 hectares.

Based on the study results, it can be concluded that for the entire term of the improved potato harvesting machine work it is not necessary to replace the vertical cut-off toothed discs with soil compactors due to their excessive capacity level.

**Table 2**

**Research results of capacity level of toothed discs with soil compactors by weight and soil compactors according to the linear indices**

| Indicator | Units of measurements | Type of soil | |
|---|---|---|---|
| | | Sandy | Loamy |
| Number of discs | unit | 2 | 2 |
| Average specific capacity level | g/ha | 1.34 | 0.61 |
| Changing linear indicators soil compactors during the study: | | | |
| – average in length | mm | 1.36 | 0.71 |
| – average in width | mm | 0.25 | 0.61 |
| – average in thickness | mm | 0.19 | 0.11 |

## CONCLUSIONS

A combined digging working part, which contains a passive blade and cutting discs with soil compactors, provides work at speeds up to 4.7 km/h. The use of new digging working parts has allowed increasing the purity of the residues amount by 30.8% compared to the base version.

Installation in the undercut part of the discs with the steel blades compactors on the lateral surface allows, compared with the basic variant to improve the fracture of the layer formation by 19%.

Comparative tests of experimental potato-diggers equipped with a developed digging part with a serial potato-digger KST-1,4A showed that its application yields positive results: the completeness of the harvesting is 99.1% versus 97.6%, no tubers that are not dug out.

The use of cutting discs in the underside reduces the traction resistance of the experimental digging working part by 15% compared to the basic version of their operation, improves the crumbling of the potato soil layer by 11%, increases the purity of the residues amount by 16%.

The study of the capacity level of developed gear discs during the research period showed that in the absence of production shortage, the capacity term of the discs will be equal to the term of the potato harvesting machine for 8 years.

The direction of further research in this area may be a wide range of issues of theoretical justification of the parameters of digging and separation working parts of potato harvesting machines, and also the calculation and explanation of the joining parts and body parts of the developed construction to its capacity level (*Kutsenko A., Bondar M. & Pryshliak V., 2018*).

**REFERENCES**


[1] Baranovsky V.M., Onishchenko V.B. & Solomka V.O., (2002), Improvement directions of separating working parts of the root tubers machines, *Scientific journal: The works of the NAU "Mechanization of agricultural production"*, Vol. XII, pp. 31-42, Kyiv / Ukraine;

[2] Dubrovin V., Golub G., Baranovsky V. & Teslyuk V., (2013), Identification of the development process of an adapted root cropping machine, *MOTROL. Commission of Motorization and Energetics in Agriculture*, Vol. 15, No 3, pp. 243-255, Lublin / Poland;

[3] Firman Yu. & Hrushetsky S., (2015), Investigation and substantiation of the parameters of the potato digger with a drum separator of potato tubers and residues, *MOTROL. Commission of Motorization and Energetics in Agriculture*, Vol. 17, No 1, pp. 17-26, Lublin / Poland;

[4] Firman Yu. & Hrushetsky S., (2015), Kinematic analysis of the dynamic belt separator, *MOTROL. Commission of Motorization and Energetics in Agriculture*, Vol. 17, No 1, pp. 11-16, Lublin / Poland;

[5] Horodinsky V.O., Hrushetsky S.M., (2016), Substantiation of design and parameters of digging working parts for potato harvesting machines, *Scientific. Work*, 87 p., Kharkiv / Ukraine;

[6] Hrushetsky S.M., (2016), Analysis of modern potato cultivating and growing technologies, *Journal of scientific works of PDATU*, Issue 24, Part 2, pp. 55-64, Kamianets-Podilsky / Ukraine;

[7] Hrushetsky S.M., (2008), Justification of the design and parameters of the floating potato digger with a drum separator of potato tubers and residues, *Dissertation Candidate of tech Sciences*, 285 p., Vinnytsia / Ukraine;

[8] Hrushetsky S.M., Bendera I.M. & Belous S.V., (2008), Potato harvesting machine, Pat. No. 31779, Bull. No. 8, 6 p., Kyiv / Ukraine;

[9] Hrushetsky S.M., Horodinsky V.O., Stavruk D.V., Gromik B.I. & Dudar M.O., (2015), Digging working part for potato harvesting machines, Pat. No. 99259, Bull. No. 10, 4 p., Kyiv / Ukraine;

[10] Hrushetsky S.M., Zbaravskaya L.Y. & Semenishena I.V., (2017), Analysis of the structural and technological schemes of the digging working parts of potato harvesting machines, *Modern Problems of Agricultural Mechanics: A Journal of Scientific Papers XVIII International. scientific conf.*, Krok, pp. 63-65, Ternopil / Ukraine;

[11] Hrushetsky S.M., Zbaravskaya L.Y. & Semenishena I.V., (2018), New digging working part for potato harvesting machines, *Journal of scientific works of PDATU*, Issue 26, Part 2, pp. 72-75, Kamianets-Podilsky / Ukraine;

[12] Kutsenko A., Bondar M. & Pryshliak V., (2018), Mechanics of materials: Theory and Problems, *Textbook, LTd "A Centre of the educational literature"*, 598 p., Kyiv / Ukraine;

[13] Pogorel'y L.V. & Tatianko M.V., (2004), Beet harvesting machines: history, construction, theory, forecast, *Phoenix*. 232 p., Kyiv / Ukraine;

[14] Ramsh V.Y., Baranovsky V.M. & Pankiv M.R., (2011), Analysis of trends in the development of working parts for the separation of root crops amounts, *Scientific Notes*, Issue. 31, pp. 298-305, Lutsk / Ukraine;

[15] Stavruk D.V. & Hrushetsky S.M., (2015), Improvement of digging working parts for potato harvesting machines, *Scientific. Work*, 98 p., Kharkiv / Ukraine.

# DESIGN AND TEST OF KEY COMPONENTS OF 3ZFS-520 INTERTILLAGE DEEP FERTILIZER APPLICATOR

# /

# *3ZFS-520 型中耕深施肥机施肥铲仿真分析与试验*

**Yan Yang[1)], Zhongyu Chen[1*)], Fang Ma[1*)], Yuansheng Wang[1)], Yongzhe Shen[2)]** [1]

[1)] Yancheng Vocational Institute of Industry Technology, Yancheng 224005, China;

[2)] Liaoning Agricultural Mechanization Development Center, Shenyang 110000, China

*Tel: 15851045245; E-mail: chenzhongyu_1981@126.com, mafang_bslw@126.com*

*DOI: 10.35633/INMATEH-59-12*

***Keywords:*** *Cultivator, Fertilizing, Design, Test*

**ABSTRACT**

*Considering the problems of current intertillage deep fertilizer applicators such as insufficient topdressing depth and poor adaptability in ridge forming, this paper designs a 3ZFS-520 intertillage deep fertilizer applicator by making some improvements to the deep application shovel and hiller. With a lengthened and narrowed deep application shovel and optimized penetration angle, clearance angle and curvature radius, this applicator experiences reduced working resistance and soil disturbance while increasing the fertilizing depth, and has enhanced adaptability in ridge forming and achieves better ridge forming effects through the integration of the hilling shovel and the hiller with adjustable extent. Test results show that, the 3ZFS-520 intertillage fertilizer applicator can reach a fertilization depth of 20cm with good ridge forming effects, strong applicability and adaptability, and stable working performance, and thus can meet the requirements set by the national standard.*

**摘要**

*针对现有中耕施肥机追肥深度不足和起垄适应性差的问题，研制了 3ZFS-520 型中耕深施肥机，并就深施铲和培土器进行了改进设计。采用增加深施铲长度、减小深施铲宽度，优化入土角、入土隙角和曲率半径的方法解决了在增加施肥深度的同时降低工作阻力和土壤扰动量的问题；采用培土铲和张度可调的培土器相结合的方式增加起垄适应性并提高起垄效果。经试验测试，3ZFS-520 型中耕深施肥机各项作业性能指标满足国家标准要求，通用性及适应性强，施肥深度可达 20cm，起垄效果好，作业性能稳定。*

## INTRODUCTION

Intertillage and fertilizing are important steps in crop planting. Intertillage is to loosen soil, increase soil temperature, speed up decomposition of organic matters, weed and preserve moisture; and fertilizing is to supplement nutrition in soil to meet the demand of crop growth *(Baimba et al., 2014; Hamdi et al., 2018; Pedrazzi et al., 2018; Wu et al., 2011).*

At present, although mechanization has been widely applied in intertillage and fertilizing, there are still some deficiencies in current machines, especially the following two problems that require prompt solution.

The first is insufficient depth of topdressing. Compared with the working performance of other fertilizing methods, deep fertilization can apply a given amount of fertilizers uniformly to areas with concentrated roots to ensure full absorption of fertilizers by roots, so as to enhance their development and increase their abilities to absorb nutrients and water and their drought resistance. In this way, the utilization rate of fertilizers can be improved, and the volatilization and loss of active ingredients in fertilizers can be reduced, which will promote production *(Engel et al., 2003; Morrison et al., 1988; Fujii et al., 2015).*

The second problem is the poor adaptability of the integrated ridging plough in ridge forming. The ridging plough of a common intertillage fertilizer applicator is made up of a shovel head, a soil separating board, a soil covering board and a plowtail through rigid coupling and fixation. The plowtail spacing can be adjusted, depending on different crops and different agronomic requirements, but such working method is complicated and cannot meet all spacing requirements, and its ridge forming effects are poor.

[1] *Yan Yang, Prof.; Zhongyu Chen, Ph.D. Eng.; Fang Ma, Ph.D.Eng.; Yuansheng Wang, Prof.; Yongzhe Shen, MA. Eng.*

By referring to the working principles of intertillage deep fertilizer applicators in China and abroad and by adopting virtual prototype technology and performing field performance tests, this study designed and tested the key components of an intertillage fertilizer applicator. This shortened the development cycle of intertillage deep fertilizer applicator supported by high-horsepower, and achieved the integration of technology advancement and practicability.

## MATERIALS AND METHODS

### • *OVERALL STRUCTURE AND WORKING PRINCIPLE*

#### *Basic structure*

As shown in Fig.1, the 3ZFS-520 intertillage deep fertilizer applicator is made up of a ground wheel assembly, a transmission system, a fertilization system, a hilling and ridge forming mechanism, a traction frame and a depth wheel. The transmission system is composed of transmission chain I, intermediate support, transmission chain II and a drive shaft of the fertilizer distributor; the fertilization system is composed of a fertilizer tank, a fluted wheel fertilizer distributor, a deep application shovel and a fertilizer pipe; the hilling and ridge forming mechanism is mainly composed of a hilling shovel and a hiller with adjustable extent and spacing.

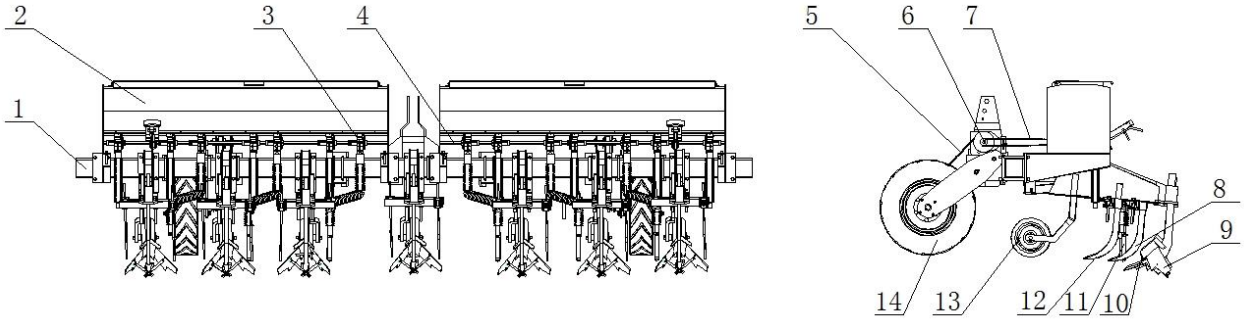


**Fig. 1 - Overall structure of the 3ZFS-520 intertillage deep fertilizer applicator**

*1-Main beam; 2-Fertilizer tank; 3-Fertilizer distributor; 4-Drive shaft of the fertilizer distributor; 5-Transmission chain I; 6-Intermediate support; 7-Transmission chain II; 8-Soil loosening and weeding shovel; 9-Hiller; 10-Hilling shovel; 11-Fertilizing pipe; 12-Deep application shovel; 13-Depth wheel; 14-Ground wheel*

#### *Working principle*

The 3ZFS-520 intertillage deep fertilizer applicator is compatible with large tractors. It can complete the operations of sub-soiling, sounding and topdressing, and ridge repairing at one time. It works in 6-8 rows in suspension connection with a tractor. The accompanying guide depth-controlled technology is adopted in intertillage and fertilization. Thanks to the great tilling depth of the deep application shovel, it can meet perform sub-soiling and side deep fertilization at the same time, and also achieve drag reduction. During operation, the two ground wheels, as the driver, convey the power symmetrically via transmission chain I to the intermediate support, and to the drive shaft of the fertilizer distributor through transmission chain II. The depth wheel limits the depth of sounding and fertilization. After hilling by the ridge forming mechanism, the entire intertillage fertilization is completed. Table 1 shows the main parameters of the 3ZFS-520 intertillage deep fertilizer applicator.

**Table 1**

**Main parameters of the 3ZFS-520 deep intertillage fertilizer applicator**

| Items | Parameters |
|---|---|
| Size (Length * width * height)/(mm × mm × mm) | 5380×2390×1370 |
| Total weight/kg | 1274 |
| Matched power/kw | 75~90 |
| Number of rows | 7 |
| Ridge spacing/cm | 35~75 |
| Working speed, km·h$^{-1}$ | 6.2~7.5 |
| Fertilization depth/cm | 15~20 |
| Fertilizer amount/(kg·hm$^{-2}$) | 65~110 |

## • DESIGN OF KEY COMPONENTS

### Design of the deep application shovel

The deep application shovel is of an integrated structure, as shown in Fig. 2. Its main parameters are penetration angle α, clearance angle β and radius of curvature R. In order to ensure the fertilization depth, the shovel length is 600 mm; the acute angle of the ditching part can ensure the penetration ability of the fertilizing shovel, and the shovel has a thickness of 15 mm; the curving part of the shovel can reduce the working resistance from soil *(Alagusundaram et al., 1990)*.

(1) Penetration angle of the deep application shovel α. IF the shovel is penetrating into the soil, the angle between the working surface of the fertilizing shovel and the ditch underneath is the penetration angle α. When α is large, there will be more soil disturbance, causing more mixture of dry and wet soil, which is not good for dissolution of fertilizers. Experts both in China and abroad made a great deal of in-depth studies on the penetration angle, and it is found that when the penetration angle α is between 0°~20°, the working resistance from soil to the deep application shovel is low; when α>20°, the working resistance increases with the increase of α. During intertillage, the soil disturbance should be controlled; therefore, the penetration angle α should not be excessively large; otherwise, dry and wet soil will be severely mixed. Considering the strength of the shovel tip and the narrowness of the shovel, the penetration angle α is set at 20°. With a smaller width, the shovel will have a stronger soil penetration power. The shape of the shovel tip also affects the working quality of the fertilizing shovel. In this study, the shovel tip is arc-shaped, so that after the shovel penetrates into the soil, the soil may be elevated a little and becomes flat. This design can reduce soil disturbance as much as possible *(Li et al., 2016)*. Then the shaft of the deep application shovel squeezes away the soil to form a fertilizer ditch. Loose soil is left in the ditch by the deep application shovel, allowing the hilling and ridge forming mechanism to cover fertilizer and soil on the ridge.

(2) Clearance angle β. The angle between the deep application shovel and the soil surface is the clearance angle β. This angle can increase the soil penetration ability of the fertilizing shovel. If β is too small, the fertilizing shovel will have a poor soil penetration ability, which will speed up the wearing of the shovel tip; if it is too big, the penetration angle should also be increased, and in this way, the disturbed soil will quickly drop to the ditch bottom, affecting the ditching depth and thus leading to insufficient fertilizing depth. According to some in-depth studies by agricultural technicians, the clearance angle β should be within the range of 5°~10°. Based on the requirements of topdressing in intertillage, the clearance angle is finally set as β=7°*(Shi et al., 2015)*.

(3) Radius of curvature R. The tip of the deep application shovel is arc-shaped, and there is a certain linear relationship between its radius of curvature R and penetration angle α. If the radius of curvature R is too big, the total structure of the shovel tip will be too large; if it is too small, the penetration angle α will be too small to have enough strength in penetration. After comprehensive consideration, the radius of curvature is finally set as R=120 mm.

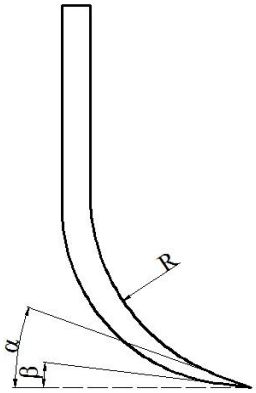


**Fig. 2 - Structure of the deep application shovel**

*R- Radius of curvature; α-Penetration angle; β-Clearance angle*

### Design of the hilling and ridge forming mechanism

The hilling and ridge forming mechanism has two parts – the hilling shovel and the hiller. The former mainly performs ditching, and the latter mainly performs ridge forming. The hilling shovel is fixed by bolting the L-shaped shovel shaft and the shovel tip. The hiller is composed of the hilling wall and the adjusting

plate, with its extent adjustable. With a certain curvature, the hilling wall has a very strong soil turning ability. With a narrow shovel tip, the hilling shovel opens a narrow ditch. It is also good at weeding on both sides of the ridge. Therefore, the hilling shovel can be designed based on the row spacing of crops and size of ridge *(Shi et al., 2017; Wohab et al., 2017)*.

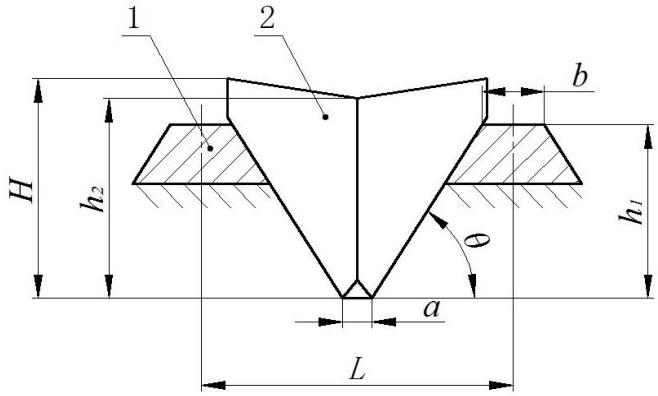


**Fig. 3 - Working process of the hiller**

*1-Ridge; 2-Hiller wall; H-Total height of the hiller; $h_1$-Total height of the ridge; $h_2$-The height of hilling wall; α-Ditch width; b-Width of ridge top; θ-Natural angle of repose of soil*

Take the intertillage and fertilization of potato for example. The row spacing L=700 mm, ditch width α=100 mm, ridge top width b=400 mm, and the total height of the ridge $h_1$=1/2 (L-a-b)tan θ=100 mm, where θ is the soil natural angle of repose of the ridge wall, and θ=45°. Based on the requirements for actual operation, the height of the hilling wall $h_2$ is designed as $h_2$=(1.1~1.2)$h_1$. In order to ensure the soil amount of the ridge, and $h_2$=1.2$h_1$=120 mm, the total height of the hiller H=1.1$h_2$=132 mm. The extent of the hiller can be adjusted and controlled by the adjusting plate, with an adjustment range of 325-480 mm, which can meet the requirements of ridging of normal row spacing and ditching *(Shimonasako, 2010).*

## • *FIELD TEST*

### *Test conditions*

The test instruments including the *SM150 High-Precision Soil Moisture Meter* with measuring range of 0~100%, volume content precision of 0.5% under 5~40°C; the *SC900 Soil Compaction Meter, and* the measuring range of which is 0~700kPa, measuring precision is ±103 kPa; the *KTC1-200mm Linear Displacement Sensor* which can be used to measure soil work components operation depth variation, its effective range is 200mm, maximum permissible DC voltage is 42V; the *National Instruments USB-6008 Data Acquisition Board(DAQ)* which has basic data acquisition function, wide application, easy to use and portable data measurement with high mobility, in addition the lead-acid battery, tape, locking tape measure, straight edge and balance etc. are needed.

The field performance test was carried out in the experimental base in Dafeng District of Yancheng, Jiangsu Province, China. The test field was a corn ridge plotted field with average row spacing of 650 mm and a soil moisture content of 17.36% (0-100 mm). The soil compactness of the ridge platform was 0.92 MPa (0~150), the compactness of the ditch soil 1.32 MPa (0~150 mm), the working area 3hm$^2$, the working depth of the deep application shovel 200 mm, and the ridging height of the hilling shovel 230 mm. There was no case of seedling pressing by soil during the test, and the machine exhibited a good passability.

### *Test methodology*

According to the machinery industry standard of the People's Republic of China *JB/T7864-2013 Cultivator-Fertilizer Machinery Industry Standard* and relevant agricultural machinery test methods, this study tested and analyzed pulverization rate, seeding damage rate, variable coefficient of tilling depth in each row and variable coefficient of consistency in ridge forming spacing (JB/T7864-2013, 2013).

### *Pulverization rate*

After intertillage fertilization operation, a 0.25 m$^2$ field was selected in any row, and the soil block can be divided into two parts with diameter or length more or less than 25 mm and the ratio of the mass of soil blocks less than 25 mm to the total mass of crushed soil in the survey area was calculated as the pulverization rate. Six plots of land were randomly measured and averaged values were obtained.

***Seeding damage rate***

The seeding damage rate is the ratio of damaged seedings to the total plants in the tillage area of 1 m in length, which can be calculated by the following formula (1):

$$Y = \frac{X}{N} \times 100\% \quad (1)$$

Where:

*X* is the number of damaged seedings, plant;

*N* is the total number of corn seedings after machine operation, plant;

*Y* is the seeding damage rate, %.

***Variable coefficient of tilling depth in each row***

The tilling depth data was obtained from the *KTC1-200mm Linear Displacement Sensor* and the *National Instruments USB-6008 Data Acquisition Board (DAQ)*, the variable coefficient was calculated using the following formula (2), (3), (4).

$$\overline{D} = \frac{\sum D}{n} \quad (2)$$

$$S_D = \sqrt{\frac{\sum (D - \overline{D})^2}{n-1}} \quad (3)$$

$$V_D = \frac{S_D}{\overline{D}} \times 100 \quad (4)$$

Where:

*D* is single tilling depth, mm;

$\overline{D}$ is average tilling depth, mm;

$S_D$ is tilling depth standard deviation, mm;

$V_D$ is tilling depth variable coefficient, %.

***Variable coefficient of consistency in ridge forming spacing***

In the test area, a test point was selected every 1m along the direction of the machine, and each row distance was measured with 6 test points, the variable coefficient being calculated using the following formula (5), (6), (7):

$$\overline{B} = \frac{\sum B}{n} \quad (5)$$

$$S_B = \sqrt{\frac{\sum (B - \overline{B})^2}{n-1}} \quad (6)$$

$$V_B = \frac{S_B}{\overline{B}} \times 100 \quad (7)$$

Where:

*B* is row between each test point, mm;

n is row test times;

$\overline{B}$ is average row, mm;

$S_B$ is row standard deviation, mm;

$V_B$ is row variable coefficient, %.

**RESULTS**

In order to find the proper speed of fertilization, ensure the low seeding damage rate and improve the pulverization rate, maintain the stability tilling depth and ridge forming spacing. In this study, the experiment was carried out in the designated field at different operation speed, and the operation speed of the prototype of 3zfs-520 deep plough fertilizer applicator was set to 6 levels from 1.8m•s$^{-1}$ to 2.8m•s$^{-1}$, after measuring the test data, using the test methodology to calculate the seeding damage rate, the pulverization rate, the variable coefficient of tilling depth in each row and the variable coefficient of consistency in ridge forming spacing.The test results are shown in Table 2.

**Table 2**

**Field test results of the 3ZFS-520 intertillage deep fertilizer applicator**

| Working speed ($m \cdot s^{-1}$) | Seeding damage rate [%] | Pulverization rate [%] | The variable coefficient of tilling depth in each row [%] | The variable coefficient of consistency in ridge forming spacing [%] |
|---|---|---|---|---|
| 1.8 | 1.31 | 87.17 | 10.73 | 8.94 |
| 2.0 | 1.63 | 87.43 | 10.92 | 9.26 |
| 2.2 | 2.38 | 87.84 | 11.21 | 10.07 |
| 2.4 | 4.09 | 88.08 | 12.11 | 11.15 |
| 2.6 | 4.83 | 88.21 | 14.06 | 13.03 |
| 2.8 | 5.06 | 88.36 | 16.92 | 15.58 |

The seeding damage rate, the pulverization rate, the variable coefficient of tilling depth in each row and the variable coefficient of consistency in ridge forming spacing with the change of working speed were generated in scatter gram, shown in Fig. 4.

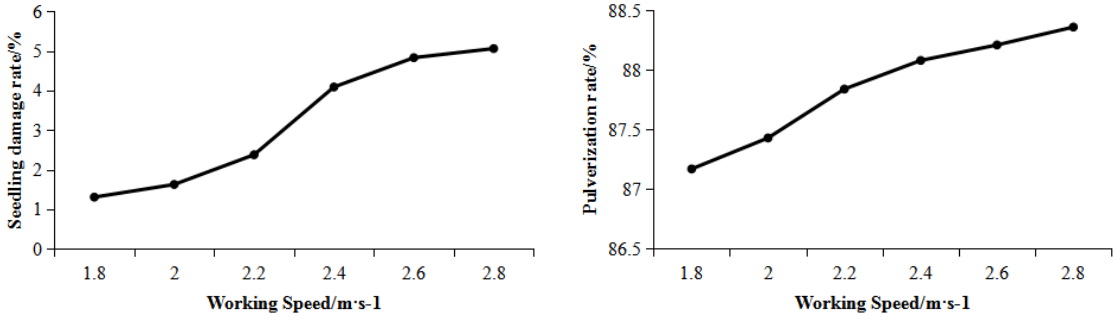


*(a) Seeding damage rate [%]* *(b) Pulverization rate [%]*

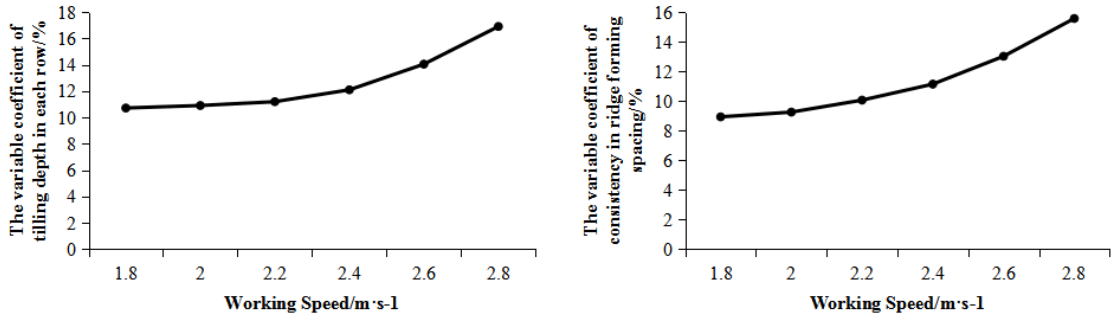


*(c) The variable coefficient of tilling depth in each row [%]* *(d) The variable coefficient of consistency in ridge forming spacing [%]*

**Fig. 4 - The test result scatter gram**

After analyzing the test results and observing the scatter gram, we noticed that:

(1) The seeding damage rate, the pulverization rate, the variable coefficient of tilling depth in each row and the variable coefficient of consistency in ridge forming spacing were significantly affected by the working speed, and increased with the working speed, and the change tended to be gentle after the working speed was greater than 2.4 $m \cdot s^{-1}$, the percentage of pulverization rate increased with the increase of working speed, and the variation tended to be gentle after the working speed was more than 2.2 $m \cdot s^{-1}$; the variable coefficient of tilling depth in each row and the variable coefficient of consistency in ridge forming spacing increased significantly with the increase of the working speed. In order to ensure that the seeding damage rate meets the standard (less than 5%), and the stability of the ploughing depth and the row spacing between ridges (JB/T7864-2013) are maintained, considering the operation efficiency, the appropriate working speed range is selected as: 2.0~2.4$m \cdot s^{-1}$.

(2) The pulverization rate could reach 87% at a low seeding damage rate. There were mostly small clods and only few big ones, it was proved that the deep application shovel and the hiller combined together had good soil breaking rate; the rate satisfied the agronomic requirement of intertillage operation and there was no damage of the plants *(Kumar et al., 2013)*.

(3) Table 2 shows that, within the range of appropriate operation speed, the variable coefficient of tilling depth in each row and the variable coefficient of consistency in ridge forming spacing could meet the national standards; it was proved that during the operation, both the deep application shovel and the hiller did not have large amount of vibration and deformation under soil resistance, demonstrating good stability in tilling depth and ridge forming. In fertilization, the fertilizing depth had no obvious variation, and thus it could meet the agronomic requirements.

## CONCLUSIONS

In this paper, the author designed an intertillage deep fertilizer applicator that could accomplish intertillage, fertilization, soil cultivation and ridging in one-time operation. Considering the current problems of intertillage deep fertilizer applicators, the length of the deep application shovel was increased to 600 mm, so as to ensure that the fertilizer could be applied evenly and quantitatively to the dense part of the crop root system, and the fertilizer could be fully absorbed by the root of the crop, so as to improve the utilization rate of the fertilizer, reduce the volatilization and loss of the effective ingredients of the fertilizer, and achieve the purpose of making full use of the fertilizer efficiency, saving fertilizer and increasing production. In order to prevent the working resistance from increasing with the increase of fertilization depth and soil disturbance, the width of the deep application shovel was decreased to 15 mm, and the penetration angle, clearance angle and radius of curvature were optimized. In light of the poor adaptability of the current intertillage deep fertilizer applicators in ridge forming at present, the hilling and ridge forming mechanism is applied, which consists of a hilling shovel and a hiller. The hilling shovel mainly performs ditching, and the hiller mainly completes ridge forming. The extent of the hiller can be adjusted and controlled by the adjusting plate, with an adjustment range of 275~430 mm, which meets the requirements of ridging and ditching at normal row spacing. In order to find a suitable speed for the application of fertilizer, the experiment was carried out at different speeds in the designated experimental field. After measuring the statistics of the experimental data, the seeding damage rate, the pulverization rate, the variable coefficient of tilling depth in each row and the variable coefficient of consistency in ridge forming spacing were calculated, and the results of the experiment were generated in a scatter gram. Through the analysis of the experimental results and observation of the scatter gram, the suitable operating speed range of low seedlng damage rate and stability of ploughing depth and ridge spacing is 2.0~2.4 m•s-1.

## ACKNOWLEDGEMENT

The authors thank the help of two corresponding authors Ph.D. Eng Zhongyu Chen and Ph.D. Eng Fang Ma. The study was supported by the National Key Research and Development Program of China (2016YFD0700905) and The Agricultural Technology Innovation Specific Guiding Fundation of Yancheng City of China (YK2016006), The scientific research fund of Yancheng Polytechnic College of China(GYYJRC2018-1).

## REFERENCES

[1] Alagusundaram K.R., Clough D.G., Jayas D.S., (1990), Drag force analysis of deep placement fertilizer applicator for rice, *Agricultural Mechanization in Asia Africa & Latin America*, pp.21-26, Tokyo/Japan;

[2] Baimba K.M., Shenggang P., Zhaowen M., Zaiman W., Xiwen L., Hua T., Farouque H, Ru T.X., (2014), Effect of Deep Fertilizer Application with Precision Hill-Drilling Machine on Yield Formation and Fertilizer Use Efficiency in Rice (Oryza sativa), *International Journal of Agriculture & Biology*, vol. 16, issue 6, pp.1091-1097, Faisalabad/Pakistan;

[3] Chen C., He P., Zhang J., Li X., Ren Z., Zhao J., He J.C., Wang Y., Liu H.B., Kang J., (2018), A fixed-amount and variable-rate fertilizer applicator based on pulse width modulation, *Computers and Electronics in Agriculture*, vol. 148, pp.330-336, Oxford/England;

[4] Engel R.E., Fischer T., Miller J., Jackson G., (2003), A Small-plot Seeder and Fertilizer Applicator, *Agronomy Journal*, vol. 95, issue 5, pp.1337-1341, Madison/US;

[5] Fujii T., Hasegawa H., Ohyama T., Sinegovskaya V.T., (2015), Evaluation of tillage efficiency and power requirements for a deep-placement fertilizer applicator with reverse rotational rotary, *Russian Agricultural Sciences*, vol. 41, issue 6, pp.498-503, Moscow/Russian;

[6] Hamdi O., Brima A., Moummi N., Nebbar H., (2018), Experimental study of the performance of an earth to air heat exchanger located in arid zone during the summer period, *International Journal of Heat and Technology*, vol. 36, issue 4, pp.1323-1329, Berlin/Germany;
[7] JB/T7864-2013, (2013), *Cultivator-fertilizer machinery industry standard*, Standards Press of China, Beijing/China;
[8] Kumar M., Thakur T.C., (2013), Design, Development and Evaluation of Deep Soil Volume Loosener-cum-Fertilizer Applicator, *Journal of Agricultural Engineering*, vol. 50, issue 2, pp.1-9, Pavia/Italy;
[9] Lang C., Wang J., Shi Y., Xi X., (2011), Design and Development Control System for Deep-Fertilization Variable Liquid Fertilizer Applicator, *2011 Second International Conference on Digital Manufacturing & Automation.* IEEE Computer Society, Zhangjiajie/China;
[10] Li M., Zhang T., Dong X., Wang C., Niu Z., Ge C., Wei L., (2016), Parameter optimization on scraper fertilizer feed unit of 3ZSP-2 type sugarcane intertillage fertilizer applicator-cum-hiller, *Transactions of the Chinese Society of Agricultural Engineering*, vol. 32, issue 23, pp.36-42, Beijing/China;
[11] Li Y., Liu C., Miao Y., (2007), Study on Smartly Prescription Generating and Control for a Variable-rate Fertilizer Applicator, *Progress of Information Technology in Agriculture-International Symposium on Intelligent Information Technology in Agriculture*, pp.23-31, Beijing/China;
[12] Morrison J.E., Chichester F.W., (1988), Subsurface Fertilizer Applicator for Conservation-Tillage Research, *Applied Engineering in Agriculture*, vol. 4, issue 2, pp.130-135, St Joseph/US;
[13] Pedrazzi S., Allesina G., Tartarini P., (2018), By-products of wheat milling process as fuel for biomass boilers and stoves, *TECNICA ITALIANA-Italian Journal of Engineering Science*, vol. 61+1, issue 1, pp.22-26, Rome/Italy.
[14] Shi Y.Y., Chen M., Wang X.C., Odhiambo M.R.O., Ding, W.M., (2018), Numerical simulation of spreading performance and distribution pattern of centrifugal variable-rate fertilizer applicator based on DEM software, *Computers and Electronics in Agriculture*, vol. 144, pp.249-259, Oxford/England;
[15] Shi Y.Y., Chen M., Wang X.C., Sun G.X., Di J., Yu H.M., (2015), Design and experiment of precision fertilizer applicator actuator of rice and wheat, *Journal of South China Agricultural University,* 36(6):119-124, Guangzhou/China;
[16] Shi Y.Y., Chen M., Wang X.C., Odhiambo M.R.O., Zhang Y.N., Ding W.M., (2017), Analysis and Experiment of Fertilizing Performance for Precision Fertilizer Applicator in Rice and Wheat Fields, *Transactions of the Chinese Society of Agricultural Machinery,* 2017, 48(7):97-103, Beijing/China;
[17] Shimonasako H., (2010), Adjusting method of discharging rate for roll type fertilizer applicator with groove, *Journal of the Japanese Society of Agricultural Machinery*, vol. 52, pp.45-52, Saitama/Japan;
[18] Wohab M.A., Gaihre Y.K., Ziauddin A.T.M., Hoque M.A., (2017), Design, Development and Field Evaluation of Manual-Operated Applicators for Deep Placement of Fertilizer in Puddled Rice Fields, *Agricultural Research*, vol. 6, issue 3, pp.259-266, New Delhi/India;
[19] Wu X.B., Peng F.T., Cui X.M., Xu Y.R., Sun Y.Y., Zhang X.D., Guo L.F., (2011), Effects of fertilization with a fertilizer applicator on nitrogen absorption and distribution, and fruit yield and quality of peach, *Plant Nutrition & Fertilizer Science*, vol. 17, issue 3, pp.680-687, Beijing/China;
[20] Yu H.F., Ding Y.Q., Tan X., Bi W.P., Wang B., Ding W.M., (2016), Design and experiments on equipment for detecting performance of fertilizer applicator, *Journal of Nanjing Agricultural University*, vol. 39, issue 3, pp.511-517, Nanjing/China;
[21] Yuan J., Liu C.L., Li Y.M., Zeng Q.B., Zha X.F., (2010), Gaussian processes based bivariate control parameters optimization of variable-rate granular fertilizer applicator, *Computers and Electronics in Agriculture*, vol. 70, issue 1, pp.33-41, Oxford/England.

# RESEARCHES ON THE STATISTICAL MODELLING OF THE PROCESSES OF PELLETING BIOMASS, TESTING CLASSIC POWDER COMPACTION MODELS

/

# *CERCETĂRI PRIVIND MODELAREA STATISTICA A PROCESELOR DE PELETIZARE A BIOMASEI, TESTAREA MODELELOR CLASICE ALE COMPACTARII PULBERILOR*

**Găgeanu I.*[1)], Cârdei P.[1)], Matache M.[1)], Voicu Gh.[2)] [1]**

[1)] National Institute of Research – Development for Machines and Installations Designed to Agriculture and Food Industry- INMA Bucharest / Romania; [2)] University Politehnica of Bucharest / Romania

*E-mail: iulia.gageanu@gmail.com*

*DOI: 10.35633/INMATEH-59-13*

***Keywords:*** *biomass, pelleting, mathematical modelling, pressure*

**ABSTRACT**

*The paper presents the main performances of formulas used in the literature in the field of compacting metallic, ceramic and pharmaceutical powders, in the case of applying them to biomass powders (fir tree sawdust). Because the authors have modified classic formulas in this field, the research of statistic modelling of the powder compaction process, it was normal to begin with functions of the same type as those presented in this paper. The performance of these formulas will constitute a comparison basis for any possible new formulas proposed. Through the modifications brought to formulas in the classic literature, formulas used in this material have an originality character and are subjected to validation for biomass powders in this paper.*

**REZUMAT**

*Articolul prezintă principalele performanțe ale formulelor folosite în literatura de specialitate în domeniul compactării pulberilor metalice, ceramice şi farmaceutice, în cazul aplicării puberilor din biomasă (rumeguş de brad). Deoarece autorii au modificat formulele clasice din acest domeniu, cercetarea modelării statistice a procesului de compactare a pulberilor, era normal să fie început cu funcții de tipul celor expuse în acest articol. Performanțele acestor formule vor constitui o bază de comparație pentru eventualele formule noi propuse. Prin modificările efectuate formulelor din literatura clasică, formulele folosite în acest material au un caracter de originalitate şi sunt supuse în acest articol validării pentru pulberi de biomasă.*

## INTRODUCTION

Powder compaction processes, thus obtaining tablets, have been already used for a considerable and even very long period of time compared to human lifetime. It is estimated, that the sintering of ceramic powders can be considered as being 26000 years old (*German R.M., 2013*). Also, it is considered that the science of sintering emerged in 1940 and matured beginning with the 80's. (*German R.M., 2016)*. Among the first powders processed through compaction we find ceramic and metallic powders. The first papers on obtaining medical tablets through compaction have begun to appear after 1940, (*Celik M., 2016*). Plastic powders are also processed through cold or thermally controlled compaction processes. Composite materials are in some cases obtained by mixing and compacting metallic, ceramic, plastic or other types of powders.

Coal was also subjected to this type of manufacturing process, (*Nadon G.C., 1998*), thus obtaining briquettes, blocks, etc. Biomass also started to be compressed and prepared in compact units, easier to be handled and used for feeding animals, obtaining biofuels, useful chemical compounds, etc. In India, manure cakes are also used from time immemorial. The first commercial production factory opened in 1982, producing almost 900 metric tons of biomass. In 1984, improvements were brought, building factories that improved the efficiency and quality of briquettes (using among others rice husk and molasses) (*https://en.wikipedia.org/wiki/Biomass_briquettes*).

[1] *Găgeanu I., Ph.D. Stud. Eng.; Cârdei P., Math.; Matache M., Ph.D. Eng.; Voicu Gh., Prof. Ph.D. Eng.*

Densification or compaction of biomass thus forming pellets or briquettes is an essential process for the production of biofuels. The particles of grinded biomass behave differently under the action of the different applied forces. Thus, it is important to investigate changes in the density and volume of the compacted material with the application of pressures. (*Adapa et al., 2009; Comoglu, 2007; Tabil et al., 2011*).

Taking into consideration the development of this processing procedure in the field of biomass, it was natural to have a large quantity of papers dedicated to the mathematical modelling of this process.

The literature provides a series of simple mathematical models, listed and reconsidered in (*Cardei and Gageanu, 2017*), which can be tested in the purpose of mathematically modelling the studied process. Generally, the models in (*Cardei and Gageanu, 2017*) limit themselves to considering initial and final density and volume parameters and the pressure (force) control parameter. If these models are satisfactory from the point of view of precision, they can be further extended with additional parameters considered for the process of compacting powders in our experiments [8]. Such models are not new. After 1950, more and more complex models began to appear in the literature, containing more parameters for the process of compacting powders or grinded materials.

A series of models for biomass, which were not examined in (*Cardei and Gageanu, 2017*), are given in (*Mani et al, 2003*). There, researches beginning from the 60's on the influence of temperature, moisture, additives, granulation, etc. are highlighted. A comprehensive list of parameters for the process of compressing biomass, and of the main laws of the compression process, are given in (*Shaw M, 2008*). (*Voicea et al, 2016*) propose a formula for the phenomenon of compacting biomass, also covered in this paper, where compression force appears instead of pressure, as well as other parameters, the formula having dimensional substantiation.

## MATERIALS AND METHODS

The first attempts for mathematical modelling that we tested are based on calculation formulas describing the process of compacting powders found in the literature synthetized in paper (*Cardei and Gageanu, 2017*). Due to the fact that among the parameters taken into account for the processes of compacting metallic, ceramic or pharmaceutical powders, only the relative density and pressure are found in (*Cardei and Gageanu, 2017*) and also in the experiments conducted in (*Mani et al, 2003*), this paper will only evaluate the assessment precision of formulas including these parameters.

In the purpose of evaluating the modelling capacity of formulas in (*Cardei and Gageanu, 2017*), for the process of pelleting fir tree sawdust, original versions proposed by the authors were used for these formulas, by dimensionally correcting the initial versions of formulas considered in (*Cardei and Gageanu, 2017*).

For each formula with potential of modelling the experimental process of pelleting fir tree sawdust, the model parameters are determined using the least squares method applied on the set of 243 data groups recorded for the 10 mm diameter die. The same thing can be done for the 8 mm diameter die. Two versions are considered for the approximation precision estimators and the models are compared through the means of their values.

In table 1, we present the parameters involved in the experimental process. The same table presents the measurement units and the physical dimension.

**Table 1**

**Parameters of the pelleting process and of the pellets obtained**

| Parameter | Name | Notation | Unit | Physical dimension |
|---|---|---|---|---|
| 1 | Sawdust moisture | $U_i$ | % | - |
| 2 | Die diameter | $Ø_m$ | m | L |
| 3 | Die temperature | $\theta$ | °C | |
| 4 | Maximum applied force | $F_{max}$ | kN | $MLT^{-2}$ |
| 5 | Piston movement speed | $v$ | m/s | $LT^{-1}$ |
| 6 | Consumed energy | $E_c$ | Wh | $ML^2T^{-2}$ |
| 7 | Pellet length | $L$ | M | L |
| 8 | Pellet moisture | $U_p$ | % | - |
| 9 | Pellet density | $\rho_p$ | $kg/m^3$ | $ML^{-3}$ |
| 10 | Pellet volume | $V_p$ | $m^3$ | $L^3$ |
| 11 | Raw material density | $\rho_0$ | $kg/m^3$ | $ML^{-3}$ |
| 12 | Raw material initial value | $V_0$ | $m^3$ | $L^3$ |
| 13 | Raw material granulation | $g$ | m | L |

*Jones formula*

The first formula investigated is Jones formula:

$$\rho_p(\rho_0, P) = \rho_0 e^b \left(\frac{P}{P_0}\right)^m \quad (1)$$

where $b$ and $m$ dimensionless model parameters, $e$ is defined by the limit:

$$e = \lim_{n\to\infty}\left(1+\frac{1}{n}\right)^n \quad (2)$$

$P_0$ is the atmospheric pressure:

$$P = \frac{4F_{max}}{\pi\emptyset^2} \quad (3)$$

By applying the least squares method for all 243 experiments, relative to the parameters involved in formula (1), the values of model parameters are obtained:

$$b = 1.321, m = 0.081 \quad (4)$$

A graphical comparison between the experimental and the calculated data is shown in figure 1.

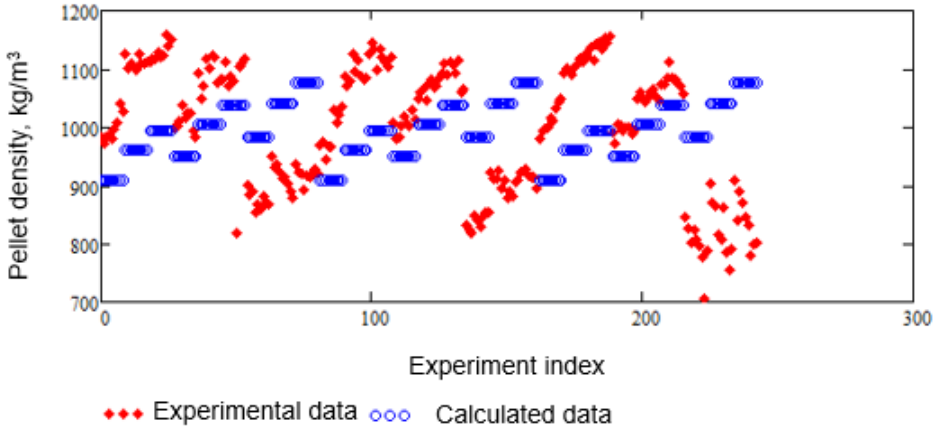


**Fig. 1 - Comparative graphical representation of the experimental data and the data calculated using formula (1), with values (4) of model parameters**

To measure the error of the data calculated compared to the experimental data, two norms were used:

$$\varepsilon_g = \frac{\sqrt{\sum_{i=1}^{n}\left(\rho_{p\ exp\ i} - \rho_p(\rho_{0\ \exp\ i}, P_i)\right)^2}}{n\cdot\overline{\rho_{p\ exp}}} \quad (5)$$

and

$$\varepsilon_{max} = \frac{\max\limits_{i=1,\ldots,n}\left|\rho_{p\ exp\ i} - \rho_p(\rho_{0\ \exp\ i}, P_i)\right|}{\overline{\rho_{p\ exp}}} \quad (6)$$

where $\varepsilon_g$ is the global error, $\varepsilon_{max}$ is the maximum error, $\rho_{p\ exp\ i}$ is the value of the pellet obtained during the experiment with the order index $i$, $\rho_p(\rho_{0\ \exp\ i}, P_i)$ is the theoretical value of the density of the pellet resulted in the experiment with the order index $i$, $\overline{\rho_{p\ exp}}$, is the average value of the string of experimental pellet densities, and $n$ is the number of experiments.

As seen in Eq.1, Jones formula seeks a relation connecting the relative density to the relative pressure, both maximums of the compression process. In order to estimate the expectations on the interpolation precision, it is useful to estimate the correlation between the two quantities. For the experimental data obtained for the 10 mm diameter die, Pearson correlation between the relative density and the relative pressure has the value of 0.271.

The graphical representation of the dependency of pellet density to the sawdust density and maximum pressure applied by the pelleting installation is given in figure 2 and 3. Figure 2 gives the graphical representation of pellet density as partial functions of raw material density for two values of the maximum pressure applied. Figure 4 represents, in the form of surface and isocline, the dependency of pellet density on two variables (according to formula (1)), the initial pellet density and the maximum applied pressure in the pelleting installation.

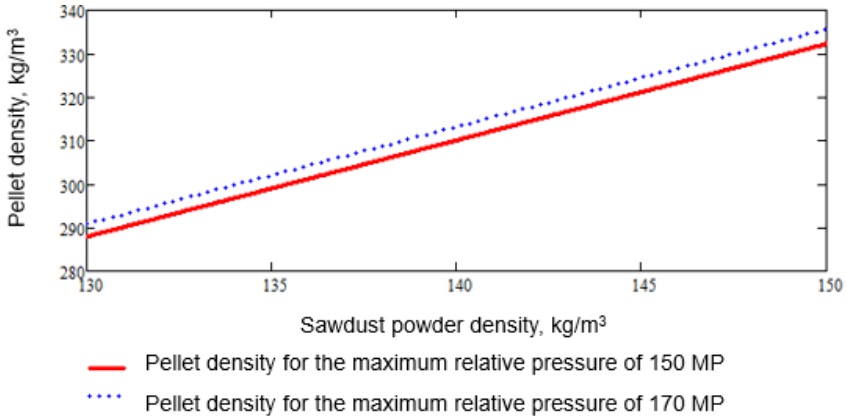


**Fig. 2 - The dependency of pellet density on the density of sawdust used as raw material**

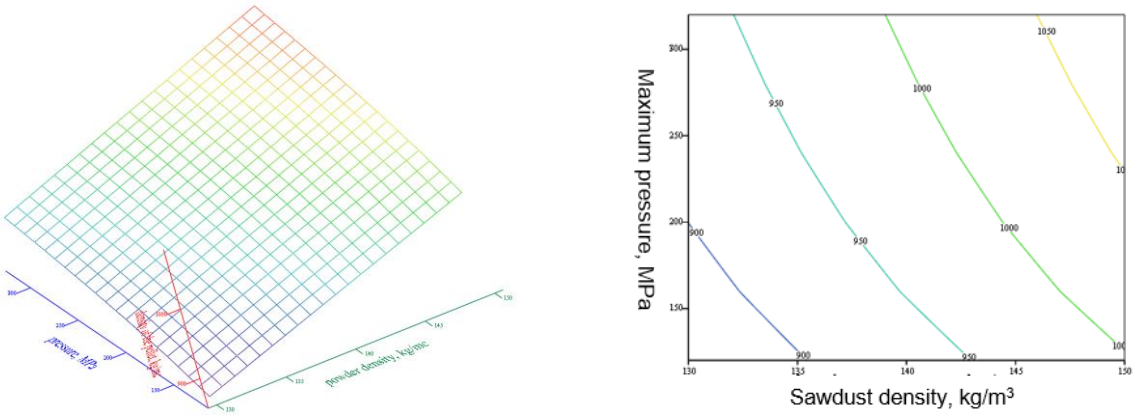


**Fig. 3 - The dependency of pellet density on the sawdust density and on the maximum pressure applied**

## RESULTS

According to the method given in the previous chapter, other laws were tested, describing the dependency between the relative density (the ratio between pellet density at the finish of the pelleting process and the density of the powder introduced in the process) and relative pressure (the ratio between the maximum pressure of the piston and the atmosphere pressure) or between the relative volume (the ratio between pellet volume after compression and the initial volume of the powder raw material) and the relative pressure.

*Heckle* model has the form:

$$\rho_p(\rho_0, P) = \frac{\rho_0}{1-e^{0.00000552\frac{P}{P_0}-0.17}} \tag{7}$$

*Panelli-Filho* model:

$$\rho_p(\rho_0, P) = \rho_0 \cdot \left(1 + e^{0.003913\sqrt{\frac{P-P_0}{P_0}}+1.598}\right) \tag{8}$$

*Ge* model:

$$\rho_p(\rho_0, P) = \frac{\rho_0}{1-e^{-10^{-0.518}\left(\frac{P}{P_0}\right)^{-0.087}}} \tag{9}$$

*Shapiro Kopopicki* model:

$$\rho_p(\rho_0, P) = \rho_0 \cdot e^{1.958-0.0001453\sqrt{\frac{P-P_0}{P_0}}-0.000001531\frac{P-P_0}{P_0}} \tag{10}$$

*Gurnham* model:

$$\rho_p(\rho_0, P) = \rho_0 \cdot \left(0.583 \cdot \ln\left(\frac{P}{P_0}\right) + 2.553\right) \quad (11)$$

*Walker* model:

$$V_p(V_0, P) = V_0 \cdot e^{-1.321} \cdot \left(\frac{P}{P_0}\right)^{-0.081} \quad (12)$$

*Kawakita-Lude* model:

$$V_p(V_0, P) = V_0 \cdot \left(1 - \frac{0.039(P-P_0)}{P_0 + 0.045 \cdot (P-P_0)}\right) \quad (13)$$

*Smith* model:

$$V_p(V_0, P) = \frac{V_0}{1 + 0.119 \cdot \left(\frac{P}{P_0}\right)^{\frac{1}{2}}} \quad (14)$$

*Mewes* model (for straw compaction): the model is the first of the three given by (*German, 2013*) and after processing and taking into account the dimensionless requirement of the arguments of transcendent functions, we obtain:

$$\rho_p(\rho_0, P) = \rho_0 \left(290.133 \cdot \frac{P}{P_0}\right)^{1.13} \quad (15)$$

*Faborode – O'Callaghan* formula, elaborated for straw compaction, is explicit in compaction pressure and, for the experiments to which this paper refers, the following concrete formula is obtained:

$$P(\rho_0, \rho) = 8712.225871 \cdot P_0 \cdot \frac{\rho_0}{\rho} \cdot \exp\left(0.281488 \cdot \left(\frac{\rho}{\rho_0} - 1\right) - 1\right) \quad (16)$$

*Ferrero* model, takes, using the experimental results from this paper, the concrete form in formula (17):

$$\rho_p(\rho_0, P) = \rho_0 \cdot \left[1 + \left(5.996517 + 0.000087 \frac{P}{P_0}\right) \cdot \left(1 - \exp\left(-0.002117 \frac{P}{P_0}\right)\right)\right] \quad (17)$$

*Viswanathan-Gothandapani* model, leads, for the experimental data used in this paper, to relation (18):

$$P(\rho_0, \rho) = P_0 \cdot \left[18286.179625 - 4981.649819 \cdot \left(\frac{\rho}{\rho_0}\right) + 383.046581 \cdot \left(\frac{\rho}{\rho_0}\right)^2\right] \quad (18)$$

*Cardei-Voicea* model, is a simplified version of the model in paper (*Voicea et al., 2016*) and leads, for the experimental data used in this paper, to relation (19):

$$\rho_p(\rho_0, F_{max}, v, U_i) = \rho_0 \left(\frac{F_{max} + F_0}{F_0}\right)^{0.225} \cdot \left(\frac{v + v_0}{v_0}\right)^{-0.0008844} \cdot U_i^{-0.449} \quad (19)$$

where $F_0$ =0.02 N (the product of raw material mass per pellet and the gravitational acceleration), $v_0$ = 0.0013 m/s (the minimal value of the piston's forwarding speed).

Table 2 presents the precision estimators for the dependency laws determined through the method described in the previous chapter. It is noted that the values of precision estimators are similar for many of the formulas proposed and objectified for the experimental data obtained for compacting fir tree sawdust.

**Table 2**

**Precision estimators of dependence laws taken from the literature dedicated to the compaction of metallic, pharmaceutical and ceramic powders**

| Law | $\varepsilon_g$ | $\varepsilon_{max}$ |
|---|---|---|
| Jones | 0.008229 | 0.29711636 |
| Heckel | 0.008295 | 0.28733083 |
| Panelli-Filho | 0.008244 | 0.29698397 |
| Ge | 0.008230 | 0.29625440 |
| Shapiro-Kopopicki | 0.008613 | 0.33068074 |
| Gurnham | 0.008241 | 0.30700960 |
| Walker | 0.008715 | 0.39496253 |
| Kawakita-Ludde | 0.008767 | 0.38793788 |
| Smith | 0.014000 | 0.46457425 |
| Mewes-1 | 0.010000 | 0.43145241 |
| Faborode-O'Callaghan | 0.025000 | 0.70467121 |
| Ferrero | 0.008227 | 0.30515891 |
| Viswanathan-Gothandapani | 0.024000 | 0.76075107 |
| Cardei-Voicea | 0.005742 | 0.28148792 |

In a similar manner, each of the models (7) – (19) can be completed with graphical representations made for model (1) in figures 1-3.

## CONCLUSIONS

All the dependency laws taken into consideration, calibrated on the experimental data obtained are linear in the density of the raw material and in its volume. Therefore, the density and volume of pellets depend linearly on the density and volume of the raw material introduced in the process. The dependency of pellet density and volume is nonlinear in relation to the relative pressure and, therefore with the maximum force of pressing the material in the die.

Pellets density function increases monotonously with the density of the raw material and with the maximum pressing force and does not show interesting critical points. The only extremal points are found on the frontiers of the definition domain considered experimentally.

Out of the formulas tested, the best global precision as well as the one given by the maximum error is obtained for Cardei-Voicea formula. This formula can still be improved, taking into account the granulation and temperature. In this paper, only formula (20) considers the very important factor represented by raw material moisture. It is possible for formulas (1) – (19) to obtain precision performances even better than (20) if, in each of them, the factor dependent on moisture is considered. We remind that the powder compression models (1)-(19), presented in this paper, are not those initially proposed by their original authors, but are modified to meet the dimensionless criterion of transcendent function arguments.

## ACKNOWLEDGEMENT

This work was supported by a grant of the Romanian Research and Innovation Ministry, through Programme 1 – Development of the national research-development system, subprogram 1.2 – Institutional performance – Projects for financing excellence in RDI, contract no. 16PFE.

## REFERENCES

[1] Adapa P. K., L. G. Tabil, and G. Schoenau, (2009), Compression Characteristics of Selected Ground Agricultural Biomass Agricultural Engineering International: *CIGR E-journal*, Manuscript 1347, Vol. 11;

[2] Cardei P., Gageanu I., (2017), A Critical Analysis of Empirical Formulas Describing the Phenomenon of Compaction of The Powders, *J. Modern Technology & Engineering*, vol. 2, No. 1, pp. 1-20;

[3] Celik M., (2016), Pharmaceutical Powder Compaction Technology, Drugs and Pharmaceutical Sciences, vol. 197, ISBN-13: 978-1420089172;

[4] Çomoğlu T., (2007), An Overview of Compaction Equations, *Journal of the Faculty of Pharmacy*. 36(2), pp.123-133, Ankara / Turquie;

[5] Gageanu I., Cardei P., Matache M., Voicu Gh., (2019), Description of the experimental data of the pelleting process using elementary statistics, *Proceedings of the Sixth International Conference "Research People and Actual Tasks on Multidisciplinary Sciences*", C, pp. 436-444, Lozenec / Bulgaria;

[6] German R.M., (2013), History of sintering: empirical phase, Powder Metallurgy, vol. 56, issue 2, pp. 117-123, https://www.tandfonline.com/doi/abs/10.1179/1743290112Y.0000000025;

[7] Mani S., Tabil L.G., Sokhansanj S., (2003), An Overview of Compaction of Biomass Grinds, *Powder handling & processing*, vol. 15, no.2, pp. 1-9;

[8] Nadon G.C., (1998), Magnitude and timing of peat-to-coal compaction, *Geology*, vol.26(8): pp.727-730;

[9] Shaw M., (2008), *Feedstock and process variables influencing biomass densification*, Thesis for Degree of Master in Science, Department of Agricultural and Bioresource Engineering University of Saskatchewan Saskatoon, Saskatchewan;

[10] Tabil L.G.,Adapa P, Kashaninejad M., (2011), Biomass Feedstock Pre-Processing. Part 2: Densification, *Biofuels Engineering Process Technology*, pp. 440-464;

[11] Voicea I., Voicu Gh., Cardei P., Vladut V., Gageanu I., Daraban A., (2016), Theoretical and experimental research on the process of biomass briquetting, *U.P.B. Scientific Bulletin*., Series D, Vol. 78, Issue 3; pp. 203-214;

[12] *https://en.wikipedia.org/wiki/Biomass_briquettes.*

# ESTIMATION OF LOSS RATE OF OATS CLEANING BASED ON WATERSHED SEGMENTATION

# /

# 基于分水岭分割的燕麦清选损失率估计研究

**Hongwen Yan, Qingliang Cui*), Xuefeng Deng** [1]
College of Information Science and Engineering, Shanxi Agricultural University, Taigu/China
*Tel: +86-0354-6289253; E-mail: qlcui@126.com*
*DOI: 10.35633/INMATEH-59-14*

***Keywords:*** *oats, cleaning, watershed segmentation, loss rate*

**ABSTRACT**

*This paper studied the loss rate of oats in the process of cleaning from the perspective of image processing. The sample was divided into group a that contained no impurities and group b that contained impurities. Otsu method was used to segment the oat kernels, with the recognition rate reaching 94.20%, and morphological opening was used for the openings appearing during the segmentation process for filling, while watershed segmentation algorithm was used for segmentation of adhesion area, with the recognition rate reaching 98.50%. For group b, the area method was used to identify and separate the impurities. Through statistical analysis, the area threshold was 600 pixels, and impurities could be removed without excessive segmentation. The estimated 5 g-sample loss rate in group a was 2.08%, which met requirements, so 5 g-sample was selected in group b, and it was calculated that the estimated loss rate of group b was 2.60%, The study showed that having good effect on image processing with less adhesion after cleaning, the algorithm could provide theoretical and methodological support for on-line monitoring of loss rate during oats cleaning.*

**摘要**

*本文从图像处理角度研究燕麦在清选过程中的损失率。将样品分为不含杂质的 a 组和含杂质的 b 组，使用 Otsu 方法分割燕麦籽粒，识别率达 94.20%。并对分割过程中的孔洞使用形态学开运算填充，对粘连区域采用分水岭分割算法进行分割，识别率达 98.50%。对 b 组采用面积法对杂质识别并分离，经统计分析，面积阈值为 600 个像素，可去除杂质且不会出现过度分割。a 组中 5g 样品损失率估计值为 2.08%，满足要求，故在 b 组选取 5g 的样品，计算 b 组损失率估计值为 2.6%。研究表明，该算法对于清选后粘连较少的图像处理效果好，可对燕麦清选损失率的在线监测提供理论和方法支持。*

## INTRODUCTION

Oats are traditional health food that has an irreplaceable role in stabilizing food production and maintaining dietary diversity in drylands. The loss of grain is unavoidable in the process of cleaning during oat harvesting *(Tang et al., 2013; Wei et al., 2016)*. The loss rate is an important technical indicator for measuring the performance of the cleaning machine and an important basis for the adjustment of the working parameters of the cleaning machine *(Liang et al., 2015; Zhang et al., 2012)*. Most of the calculation of the loss rate was manually calculated *(Zhou et al., 2010)*, which was low in accuracy and inefficient. It is a prerequisite to study the algorithm for automatic calculation of the loss rate during the cleaning process for the development of intelligent cleaning equipment.

The use of machine vision on the quality of kernel of bulk grain had been studied in depth at home and abroad *(Diego and Rafael, 2018; Uryi et al., 2018; Vithu and Moses, 2016)*, but the researches on loss rate were few and most of the previous researches focused on the use of sensors *(Eric, 2018; Gao et al., 2011; Mao et al., 2012)*. Some studies have focused on monitoring grain harvest losses through temperature differences captured by thermal sensor arrays, and optimizing sensor size and layout to improve signal recognition accuracy for rice loss monitoring *(Liang et al., 2017)*, and designing a real-time monitoring system for losses during the cleaning process *(Zhou et al., 2010)*, which could effectively differentiate the signals of

[1] *Hongwen Yan, As. Ph.D. Eng.; Qingliang Cui, Prof. Ph.D. Eng.; Xuefeng Deng, Ph.D. Eng.*

clods, stalks and stones in wheat, however, there were few reports on the calculation of the loss rate by directly obtaining the amount of oat kernels through images.

To explore the loss rate during the oat cleaning process, in this study, the cleaning machine developed by Shanxi Agricultural University was used as the test bench, oats of different weights were used as experimental samples, and oats going through the cleaning process of the test bench were collected. Watershed segmentation algorithm was adopted to count the number of oats after cleaning, via which their weight could be estimated to offer support for online monitoring of loss rate of oats during cleaning.

## MATERIALS AND METHODS

### Sample collection

The experimental materials of this study were collected in Youyu County, Shanxi Province, China (112º27′ E, 39º59′ N), and the sampling date was July 10, 2018. Since the cleaning machine would inevitably have some impurities after the cleaning operation was completed, in order to facilitate the comparison of effects of the algorithm, the sample was divided into group a that contained no impurities and group b that contained impurities. Impurities referred to oat stalks, twigs, hulls, and oat leaves in the sample, as shown in Fig.1.

*a. stalk* *b. twig* *c. hull* *d. leaves*

**Fig. 1 - Images for Impurities in oat**

### Equipment

In the study, the cleaning machine developed by Shanxi Agricultural University was used as the test bench, and the oat samples taken were collected via this test bench. The speed used in the test was 68 rpm.

The image acquisition system used M0814-MP type lens (Computar, f = 8mm, F1.4), F201C type CCD (Allied vision technologies Gmb H, 1/2.3 inch CCD), RL500W type circular diffuse reflection LED light source (by Victor Digital Image Technology Co., Ltd. with polarizer, 9W), CP502 electronic balance (by Ohaus, with sense quality of 0.01 g) and R2004 tripod (by Si Rui Group, with a working height of 48.5~1 740 mm) as equipment.

### Image acquisition

The oat sample fell from the screen box of the cleaning machine to the buffer receiving board on the floor. In order to reduce the shadow of the cleaning machine when the image was acquired, the buffer board was carefully removed from the lower end of the cleaning machine in this test during preparation for image acquisition.

(1) Mount the light source and CCD camera on a tripod and fix them;

(2) Adjust the electronic balance to zero in advance and clean the weighing environment;

(3) Make calibration when recording image data to ensure that the image data acquired are uniform.

### Data analysis software

The data processing and analysis in this study was based on the software Matlab 7.5 (The MathWorks, Natick, USA).

## STATISTICAL ANALYSIS OF THE NUMBER OF OAT KERNELS

The sample collected in this study was divided into oat kernel sample that contained no impurities and oat kernel sample that contained impurities. The basic process of the study is as shown in Fig.2. The acquired image was preprocessed; the median filtering was used to reduce noise; the image was pre-segmented by Otsu method; the holes in the binarized image were filled; the watershed segmentation algorithm was used to segment the adhered oats, and oat image containing impurities was identified and separated by area method.

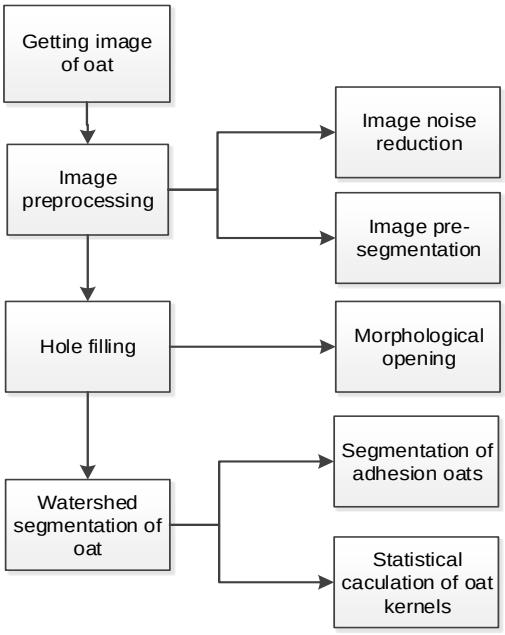


**Fig. 2 - Flow chart for oat image processing**

## Image preprocessing

Oat images are affected by noise such as light source distribution, background selection, image acquisition speed, and external features of the target during acquisition, transmission and storage. In order to remove image noise, this study used median filtering, mean filtering, Wiener filtering, sharpening filtering and other methods to reduce noise for the images. Fig.3a is a grayscale diagram of the oat kernel after the adaptive median filtering process using the median filtering of 7×7 pixel. The experimental results showed that the median filtering could effectively preserve the edge information of the images on basis of eliminating image noise, and the preprocessing effect was good. Therefore, this study used the median filtering results for subsequent experiments.

In order to achieve statistical calculation of oat kernels, the image needed to be segmented to separate the oat kernels from the complex background. The Otsu method was an adaptive threshold segmentation method commonly used in threshold segmentation, and its criterion for determining the optimal threshold is to minimize the variance within each pixel class and maximize the variance between classes. In this study, Otsu method was used to segment the oat kernels, with the segmentation results as shown in Fig.3b. The segmentation threshold was 94 pixels and the separability measure was 0.7673.

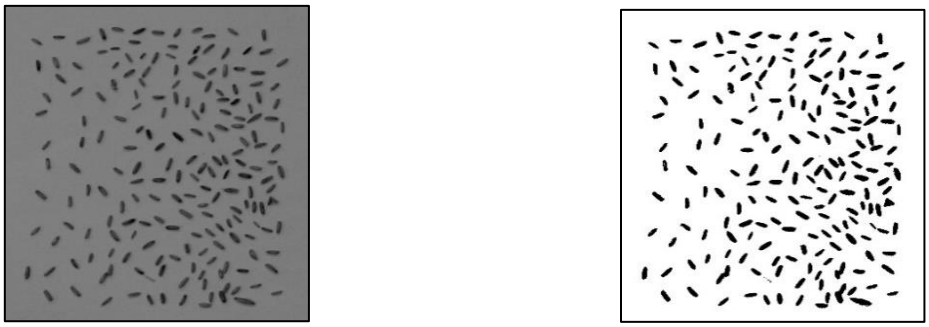

*a. Grayscale image* *b. Otsu segmentation result*

**Fig.3 - Image segmentation results for oat containing no impurities**

As could be seen from Fig.3b, the method was able to separate oat kernels from complex backgrounds.

$$\sigma_B^2(k) = \frac{[m_G p_1(k) - m(k)]^2}{p_1(k)[1 - p_1(k)]} \quad (1)$$

where: $m_G$ represents the average grayscale of the image;
$m(k)$ represents the cumulative mean;
$p_1(k)$ represents the probability of occurrence of set *C1*;

$\sigma_B^2(k)$ represents the variance between classes.

$$\eta_k = \frac{\sigma_B^2(k)}{\sigma_G^2} \quad (2)$$

where: $\eta_k$ represents a normalized dimensionless matrix
$\sigma_B^2(k)$ represents the variance between classes;
$\sigma_G^2(k)$ represents the total gray scale variance of the image.

**Hole filling**

In the image processing process, due to the complexity of the environment or the defects of the detection algorithm, the binary images obtained by "binarization" usually had holes, which not only affected the detection effect of the oat kernel, but also destroyed the integrity of the oat kernel profile, which had an adverse effect on the statistical analysis of oat kernels. However, the morphological method could convolve the original image through structural elements to achieve the purpose of removing image noise and eliminating object boundary points *(Zhang et al., 2015)*. Therefore, in this study, the morphological method was used to fill the images with holes, i.e., the images were first etched and then expanded to remove fine debris and separate the slightly adhered oats. After many experiments, it was found that when the structural element of the corrosion operation was set to 5×5 pixel, the short stems could not be eliminated due to the presence of fine impurities in the original image, and the short stems could be removed when the structural element was set to 9×9 pixel. Thus, the effect of fine impurities on the processing results could be eliminated. Fig.4 shows the results of the etching operation and the expansion operation. The filling of the holes was implemented by Equation 3.

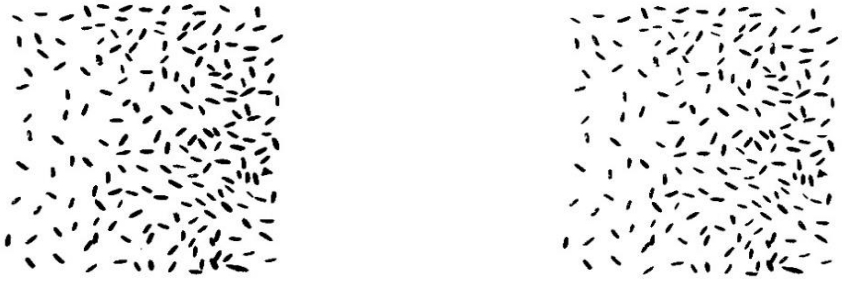

*a. Corrosion operation* *b. Expansion operation*

**Fig. 4 - Morphological processing results**

$$X_k = (X_{k-1} \oplus B) \cap A^C \quad (3)$$

where: $X_k$ represents the $k_{th}$ iteration boundary of set *A*;
$X_{k-1}$ represents the $(k-1)_{th}$ iteration boundary of set *A*;
*B* represents the structural element;
*A* represents collection, with the element of an 8-connected boundary;
$A^C$ represents a complement of *A*.

## STATISTICAL CALCULATION OF THE NUMBER OF OATS BASED ON WATERSHED SEGMENTATION

**Segmentation of adhered oats**

In grain kernel image processing, due to object adhesion, overlap, etc., often it is impossible to achieve complete and effective segmentation. Through the images of the oat kernel after the threshold segmentation, some of the kernel contacts were dense, there was adhesion and the accuracy of the kernel count was affected. In view of the above situation, the watershed segmentation algorithm introduced the concepts of topography and hydrology into region-based image segmentation, which was suitable for segmentation of adhesion regions. The method regarded the image as a topographic map, the pixel value represented the altitude, the topographical watershed was introduced into the image, and the watershed was used as the image dividing line *(Shen et al., 2015)*. When the rain fell to the side of the watershed, it would flow down the hillside and gather at the lowest point of the valley. Therefore, the valley line was also called the catchment line, and the lowest point at the exit of the valley was called the valley mouth. Since the oat kernel was elliptical, the contour of the cohesive grain had a convex boundary, the binary image of the cohesive grain would form a distinct valley line after the Euclidean distance transformation, and the continuous valley line in

the binary image could be used as the adhesion image segmentation line. In general, there was a problem of over-segmentation by using the watershed segmentation algorithm *(Cai et al., 2017)*. In this study, the marker-based watershed segmentation algorithm was used to segment the oat images, and internal mark and external mark were used to mark them. The internal mark represented the oat kernel and the external mark represented the background. In the segmentation the internal mark was used as low-lying, and the watershed of segmentation result was used as the external mark. The specific implementation process of the algorithm was divided into the following steps.

(1) Performing Euclidean distance transformation on the binary image to obtain a distance map;

(2) Calculating the position of a large number of "local minimum regions" in the image, wherein the "local minimum region" had the same brightness value and the brightness values around it were larger than it;

(3) Calculating the "extended minimum transform" of the image, i.e., expanding the "local minimum region" by a certain threshold, and merging more pixels with similar minimum regions into the minimum region, and taking the "extended local minimum region" as internal tag set;

(4) Segmenting the image by the general watershed segmentation algorithm, and the watershed of the segmentation result was used as an external mark to obtain the marking result.

Fig.5 shows the segmentation results based on the mark-based watershed segmentation algorithm, where in Fig. 5a was a binary image, and Fig. 5b showed the watershed segmentation result. As can be seen from Fig. 5b, the method could effectively separate the adhered oat kernels.

*a. Binary image* *b. Watershed segmentation results*

**Fig. 5 - Segmentation results based on mark-based watershed segmentation algorithm**

**Oat kernel count**

The image obtained by the watershed segmentation algorithm was a binary one. In the counting statistics of oat kernel, for the image pixels of the oat kernel were continuous, the connectivity was expressed in the binary image. Therefore, this study achieved oat kernel count by finding the number of connected regions in the image. The connected region referred to the region whose value was 0 or 1 in the binary image. After detection, the regions of corresponding pixel shall be determined, and the points with the same pixel value were integrated to form a region, that is, a set of adjacent pixels in the image was detected. After dividing the area in the image, the area, shape and other parameters of the region could be calculated to provide a basis for analyzing the classification and measurement of oat kernels.

The connected area of the image was obtained by scanning the image. According to different neighbouring relationship of the pixels, the connected regions were generally divided into 4-neighbor regions and 8-neighbor regions. The 4- neighbour regions were scanned in four directions of up, down, left, and right of the detection points, and the 8-neighbour areas were scanned in eight directions of up, down, left, and right as well as four diagonal directions of the detection points. Generally, the number of neighbour regions was no less than that of 8-neighbor regions. In this study, the 8-neighbor region analysis was used to mark oat kernels and calculate the area and number of regions in each region. Fig.6 was a statistical result of the image connectivity area of 5g oat kernel image, in which the actual number of oat kernels was 207. In Fig.6a is showed the statistical result of Otsu segmentation, in which the number of oats was 195, while in Fig.6b is showed the statistical result of the division of the adhered oat kernels by watershed, and the number of oats was 204. As can be seen from the figure, the method was able to mark the oat kernels in the image well, and the oat kernels after the watershed segmentation could also be well marked, indicating that the number of oat kernels could be obtained by the image analysis method. Through statistical analysis, the average area of oat kernels was 295 pixels.

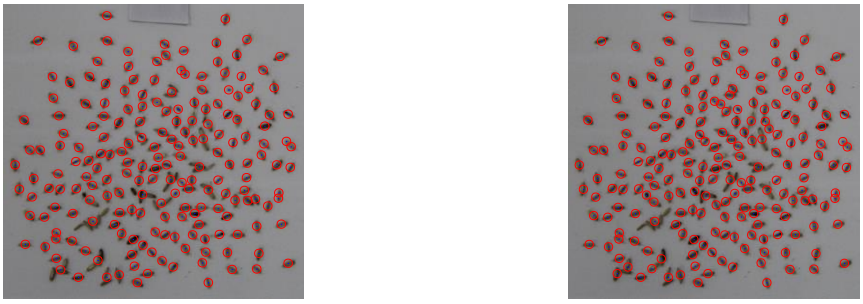

*a) Otsu segmentation statistics* *b) Watershed segmentation statistics*

**Fig. 6 – Results of analysis of connected regions**

**Separation of impurities by area method**

According to the above statistical results, the area parameters of the oat kernels were obtained. As the actual oats were obtained, they contained impurities such as stalks, twigs, hulls, leaves, etc., and the colour of the impurities was close to the colour of the oats, they were different mainly in shape and size, therefore, the area method was adopted to identify and separate the impurities, and the area threshold T was selected. When T>T_mean, the pixel value of the point was marked as the background, that is, the impurities were removed. In this study, after several experiments, the area threshold was selected to be 300 pixels and 600 pixels to remove impurities. The selection of the threshold affects the recognition rate of impurities. Fig.7 showed the result of removal of impurities by the area method. When T was 600 pixels, the experimental result showed that impurities was better removed and while the basic information of oats was retained. When T was 300 pixels, as shown in Fig.7c, while removing impurities, some oats were also removed, and there was over-segmentation. Therefore, in this paper, it was finally determined the threshold value would be 600 pixels, and the oat image after removing impurities was obtained.

*a. Original image with impurities contained* *b. Area threshold 600* *c. Area threshold 300*

**Fig. 7 – Results of impurity removal by area method**

## RESULTS AND DISCUSSION

**Analysis of loss rate of cleaning of oats without impurities**

The loss rate of oat cleaning was expressed by the ratio of mass loss after the sample going through the cleaning machine and the mass before operation, as stated in Formula 4.

$$L = \frac{\Delta w}{w_1} \times 100\% \quad (4)$$

where: $w_1$ represents the sieve mixture, [g];
$\Delta w$ represents change in weight, [g];
$L$ represents the loss rate, [%].

$w_1$ was obtained by using an electronic balance, while $w_2$ was calculated by referring to the thousand-grain weight of oats. The number of oat kernels shall be obtained by the algorithm, and the calculation of $w_2$ could be based on the following Formula 5.

$$W_2 = \frac{ax}{1000} \quad (5)$$

where: $w_2$ represents the grain under the sieve, [g];
$a$ represents thousand-grain weight of oats, [g];
$x$ represents the number of oat kernels obtained by the algorithm, [grain].

In this study, the reference value of sample $a$ was 25.5g, and the test data obtained in group a were substituted into Formula 4 and Formula 5, respectively, and the results were shown in Table 1.

**Algorithm statistical number value and loss rate of cleaning** **Table 1**

| $W_1$ [g] | Average number [grain] | Algorithm result [grain] | Recognition rate [%] | $W_2$ [g] | Δw [g] | L [%] |
|---|---|---|---|---|---|---|
| 5 | 194 | 192 | 98.97 | 4.90 | 0.10 | 2.08 |
| 8 | 308 | 231 | 75.00 | 5.89 | 2.11 | 26.37 |
| 10 | 382 | 239 | 62.57 | 6.09 | 3.91 | 39.06 |
| 12 | 459 | 264 | 79.30 | 6.73 | 5.27 | 43.90 |
| 15 | 582 | 261 | 44.84 | 6.66 | 8.34 | 55.63 |
| 18 | 708 | 225 | 32.34 | 5.74 | 12.26 | 68.13 |
| 20 | 775 | 313 | 40.38 | 7.98 | 12.02 | 60.09 |

With the data in Table 1, it could be seen that the 5 g-sample recognition rate of the algorithm reached 98.97%, and the calculated loss rate of cleaning was 2.08%, which was in line with national standards, while the recognition rate of other groups was generally lower. The 18 g-sample was with the lowest recognition rate of only 32.34%, with a corresponding cleaning loss rate of 68.13%. Analysis of the image processing process showed that the oat image obtained from the 5 g-sample had less adhesion of oat kernels, and no overlap or cover was there, also the algorithm statistics were accurate, and the statistical results of the algorithm were accurate. The recognition rate of samples from 8g to 20g was generally low, with the recognition rate basically negatively correlated with the weight of oats, and calculation result of loss rate far exceeded the national standard, for which the reason was that as the sample quality increased, more large-area adhesion and overlap occurred, but the recognition ability of the algorithm was limited in face of these conditions, so the statistically calculated loss rate of cleaning could not reflect the actual loss.

**Analysis of loss rate of oats containing impurities**

It can be seen in Table 1 that the identification rate of other oat samples other than the 5 g-sample was generally low, and the calculation of the loss rate could not reflect the actual cleaning loss. Therefore, in the experiment with impurities, other groups were discarded, leaving only the 5g group, where the adhesion region well handled by the watershed segmentation algorithm. Short stalks and some fine impurities were separated by area method. After many experiments, it was determined that when the threshold value was 600 pixels, the short stalks and fine impurities could be well removed, while the basic information of oats could be well preserved. In the 5g group test, the $w_2$ was calculated to be 4.87g, and the $L$ was 2.60%, which was slightly higher than the no-hybrid statistics and basically met the standard. The results were shown in Table 2.

**Table 2**

**Statistical calculation of the number of oats containing impurities and the loss rate of cleaning**

| $W_1$ [g] | Average number [grain] | Algorithm result [grain] | Recognition rate [%] | $W_2$ [g] | Δw [g] | L [%] |
|---|---|---|---|---|---|---|
| 5 | 194 | 191 | 98.97 | 4.87 | 0.13 | 2.60 |

## CONCLUSIONS

(1) Based on the content of this experiment, the watershed segmentation algorithm was effective in calculating the loss rate of oat in its cleaning process, also the loss rate could be calculated by directly acquiring images in the cleaning process. Currently this method was limited to small masses.

(2) To obtain the impurity-free image, the Otsu algorithm shall be adopted to pre-segment the grain and the background image, to get a binary image in which "holes" might appear. Then the morphological opening algorithm could be used to fill the image with holes, so as to remove fine debris and separate the slightly adhered oats.

(3) In this study, the condition of the oat kernels containing impurities was relatively simple, and the impurities were stalks having a large difference in shape from oat. In actual situations, a mixture of various impurities might be there. For example, the impurities might also contained hulls or dust residue similar to oats in shape. If the fixed threshold of this paper could not achieve the expected effect, in the future, it is desirable to find a self-adapting threshold to remove different impurities.

(4) The calculation of the cleaning loss rate was closely related to the quality of image obtained. Designing a suitable buffering facility at the receiving position of the cleaning machine could minimize the adhesion and overlap regions to the maximum, so that the calculation of the loss rate could be more accurate.

(5) In the case of increased sample quality, large adhesion-and-overlapping regions might occur. For these regions, the number count and the estimation of loss rate of cleaning might be distorted, and the seriousness of distortion is negatively correlated with quality. It is the content of following research of this research group as to how to solve the problem of identifying the number of grains in large adhesion-and-overlapping regions and estimating their weight.

**ACKNOWLEDGEMENTS**

This research, titled 'Estimation of Loss Rate of Oats Cleaning Based on Watershed Segmentation', was funded by the National Key Research and Development Plan of China (2016YFD0701801). The authors are grateful and honoured to have obtained support from the Key Laboratory of Biomechanics.

**REFERENCES**

[1] Cai Q., Liu Y.Q., Cao J., Li H.S., Du J.P., (2017), A Watershed Image Segmentation Algorithm Based on Self-adaptive Marking and Interregional Affinity Propagation Clustering. *Acta Electronica Sinica*, Vol.45, Issue 8, pp.1911-1918, Beijing/P.R.C.;

[2] Diego I.P., Rafael R., (2018), Computer vision and artificial intelligence in precision agriculture for grain crops: A systematic review. *Computers and Electronics in Agriculture*, Vol.153, pp.69-81, Oxford/England;

[3] Eric l.W., (2018), *Grain loss sensor array for crop harvesting machine*. Patent No. 20180053067A1, USA;

[4] Gao J.M., Zhang G., Yu L., Li Y.B., (2011), Chaos detection of grain impact at combine cleaning loss sensor. *Transactions of the Chinese Society of Agricultural Engineering*, Vol.27, Issue 9, pp. 22-27, Beijing/P.R.C.;

[5] Liang Z.W., Li Y.M., Xu L.Z., Tang Z., (2015), Monitoring Mathematical Model of Grain Cleaning Losses on Longitudinal-axial Flow Combine Harvester. *Transactions of the Chinese Society for Agricultural Machinery*, Vol.46, Issue 1, pp.106-111, Beijing/P.R.C.

[6] Liang Z.W., Li Y.M., Xu L.Z., Zhao Z., Tang Z., (2017), Optimum design of an array structure for the grain loss sensor to upgrade its resolution for harvesting rice in a combine harvester. *Biosystems Engineering*, Vol.157, pp. 24-34, San Diego/USA;

[7] Mao H.P., Liu W., Han L.H., Zhang X.D., (2012), Design of intelligent grain cleaning losses monitor based on symmetry sensors. *Transactions of the Chinese Society of Agricultural Engineering*, Vol.28, Issue 7, pp. 34－39, Beijing/P.R.C.;

[8] Shen X.J., Wu X.Y., Han D.J., (2015), Survey of Research on Watershed Segmentation Algorithms. *Computer Engineering*, Vol.41, Issue 10, pp.26-30, Shanghai/P.R.C.;

[9] Tang Q., Wu C.Y., Wang S.Z., Zhang C.W., Sun Y.F., (2013), Research Advances and Prospects in Cleaning Device of Grain. *Journal of Agricultural Mechanization Research*, Vol.12, pp.225-228, Harbin/P.R.C.;

[10] Uryi I.M., Aleksei V. P., Aleksandr Y. S., Ivan A. K., Dmitry N. P., Rinat N. S., (2018), Computer vision system: a tool for evaluating the quality of wheat in a grain tank, *Proceeding of the 10th International Conference on Machine Vision*, Vol.10696, pp.451-457, Vienna/ Austria;

[11] Vithu P., Moses J.A., (2016), Machine vision system for food grain quality evaluation: A review. *Trends in Food Science & Technology*, Vol.56, pp.13-20, London/England;

[12] Wei C., Li M., Yu L.J., Zhu L., (2016), Research on Loss Monitoring of Grain Cleaning in Combine Harvester Based on Kalman Filter. *Journal of Agricultural Mechanization Research*, Vol.3, pp.23-27, Harbin/P.R.C.;

[13] Zhang G., Gao J.M., Yu L., (2012), Chaos Detect System of Cleaning Loss Based on ARM9. *Journal of Agricultural Mechanization Research*, Vol.3, pp.159-161+216, Harbin/P.R.C.;

[14] Zhang Y.H., Li Y., Wang F.Q., Zhang Z.X., (2015), A Watershed Segmentation Algorithm Based On Morphological Reconstruction and Maxima Mark. *Computing Technology and Automation*, Vol.2, pp.78-81, Changsha/P.R.C.;

[15] Zhou X.L., Zhu R.X., Zhou X.J., Tang Y., (2010), The Monitoring System for Cleaning Loss of the Grain Combine Harvester Based on Sensor Technology. *Journal of Agricultural Mechanization Research*, Vol.12, pp.85-87, Harbin/P.R.C.

# EXPERIMENTS ON PADDY DRYING MECHANISM OF FAR-INFRARED CONVECTION COMBINATION IN COMBINE HARVESTER

/

# 联合收割机中对流远红外联合稻谷在机干燥机理试验研究

**Chen P.L.[1,2], Xu J.[*1,2], Tang Y.[1], Liu M.H.[1,2]**

[1] College of Engineering, Jiangxi Agricultural University, Nanchang/China; [2] Key Laboratory of Modern Agricultural Equipment, Jiangxi Province, Nanchang/China;

*Tel: +8613979166680; E-mail: xujing0085@163.com*

*DOI: 10.35633/INMATEH-59-15*

***Keywords**: grain dying; infrared; hot air; combine harvester*

***ABSTRACT***

*In order to acquire the coupling mechanism of the paddy flow, hot air and far-infrared radiation, an experiment bench based on the screw conveyor and grain collecting tank of combine harvester was set up, and then the orthogonal experiment with six factors and five levels was conducted using the dehydration rate (DR), increased crack percentage (ICP) and specific energy consumption (SEC) as indexes. The optimal combination of factors for each index was acquired and the experiment results show: the drying combination could achieve rapid drying with good drying quality and low energy consumption; the initial water content of paddies is the dominant factor for the DR, ICP and SEC; the hot air has more effect on the drying performances compared with the IR radiation.*

***摘要**:*

*为了获取谷物流、热风和远红外场的耦合机理，以联合收割机的搅龙和收粮箱为基础，搭建了远红外热风联合干燥实验平台，以干燥速率、爆腰增率以及单位能耗为目标，进行了六因素五水平正交实验，获取了各实验目标最优的因素组合，实验结果表明：该嵌入联合收割机中的组合干燥系统能够实现快速、高质以及低能耗干燥；水稻的初始含水率是影响干燥速率、爆腰增率以及单位能耗的主要因素；相比于红外辐射，热风对干燥性能具有更大的影响。*

## INTRODUCTION

The widely using paddy combine harvester significantly reduces the harvest time of paddy; moreover, the paddy should have high moisture when it is harvested in order to decrease the loss of it. Harvesting the high moisture paddy rapidly makes the grain-sunning ground not big enough for farmers to dry paddy efficiently, and thus many farmers lay out the paddy on the road or highway which may seriously affect traffic in China. Meanwhile, farmers' use of sun drying totally depends on the weather; they have to stack the wet paddy at home and if there is continuous rainy weather, mildew appears. Although the stationary drying machine has been used since 2004 in China, it is inconvenient for the hilly area because of the excess carriage expense and energy consumption.

One solution to solve the problems above is to design a combine harvester with the function of grain drying simultaneously, and the drying system should be energy-saving and quick-drying to synchronize the harvest speed of combine harvester. Many works have been done to reduce the energy consumption of the drying system such as optimizing the drying process, taking the new heating device, recycling the exhaust heat and so on (*Niu X.H., Cao C.W., 1999; Chen K.J., Chen Q.C., Zhang Y., 2005*). Since the cooling water and exhaust gas takes away more than 60% of fuel energy of diesel engine equipped on the tractor and combine harvester, recovering the waste heat of diesel engine to dry grain has been the concern of many researchers. Bai et al. *(Bai J.W., Luo S.Q. et al., 2008)* equipped a semi-drying system on a tractor powered by the waste heat, and their drying system could decrease the grain water content by 3 to 6 percent. Fei et al. *(Xiang F., Wang L., Yue X.F.,2011)* developed a vehicle-mounted heat pump–assisted fluidization drying system driven by the waste heat recovered from the jacket water of diesel engine and flue gas of the drying system; their analysis results showed that the actual specific diesel consumption can reach 0.081 [(kg

diesel)/(kg water)].

The hot air drying is often used for the method of recycling the heat waste of agricultural machinery to dry grain, and it usually requires a long period of drying time and a large amount of thermal energy *(Celma R.A., Rojas S., Lopez-Rodriguez F., 2008*); hence, it is not suitable for drying grain directly on the combine harvester because of the high harvest speed. To overcome the drawbacks of the hot air drying, infrared radiation has been integrated with it. Far-infrared convection combination drying is widely used for foodstuffs such as corn *(Rahmanian- Koushkaki H., Nourmohamadi-Moghadami A., Zare D. et al., 2017)*, rice (*Sarobol M., Teeta S., Pharanat W. et al., 2018)*, potato (*Onwude D.I., Hashim N., Abdan K. et al., 2019*) and so on. In contrast to pure hot air drying, the combined technique was found to accelerate heat and mass transfer, leading to a shorter drying time and better drying quality *(Liu C.S., Shang T., Yang S.Q., 2017; Zare D., Naderi H., Ranjbaran M., 2015).*

Noting far-infrared convection combination can not only use the waste heat of combine harvester but also dry grain quickly with less damage to its quality, the new drying system equipped with far-infrared and supplementary hot air could dry paddy directly in the drying chamber embedded on the screw conveyor and grain collecting tank of combine harvester was proposed. Then a test bench was setup to acquire the coupling mechanism of paddy flow, hot air and far-infrared using the orthogonal test.

## MATERIALS AND METHODS

### EXPERIMENT BENCH

The experiment bench designed is shown in Fig.1. A hot air blower pushes the hot air into the screw conveyor and grain collecting tank of combine harvester, and the hot air from the hot air blower simulates the hot air heated by the waste heat of combine harvester. The air temperature and velocity can be regulated by the voltage regulator 1 and the throttle, the actual air temperature and velocity can be detected by the air temperature and velocity sensors. Infrared (IR) radiator *1* and IR radiator *2* are embedded in the walls of screw convey and grain collecting tank and their powers can be regulated by the voltage regulator *2* and *3*. The paddy is put into the hopper, and the screw conveyor driven by the motor promotes the paddy into the grain collecting tank. The paddy is dried by the hot air and far IR radiators.

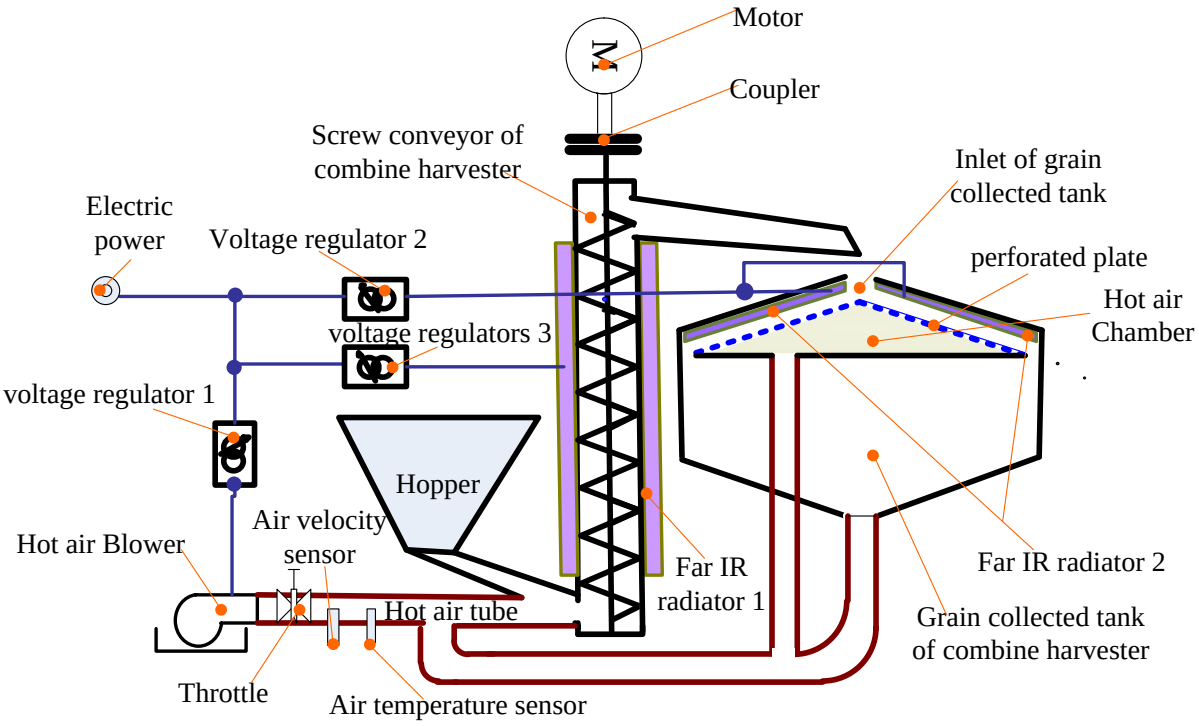


**Fig. 1 - Layout of the experiment bench**

In order to simulate the actual working process, the hot air blower is started and the air pushed by it is conditioned to a suitable velocity and temperature to preheat the bench for about 3 to 5 min before the experiment, and then the paddy to be dried is added to the hopper and is stuffed up by a strikerplate to prevent it from rushing into the screw conveyor of the combine harvester. Only when the parameters of far IR radiator *1*, far *IR* radiator *2* and the hot air blower are adjusted to the pre-set values according to the test arrangement, can the strikerplate be opened. Then, the paddy flows to the screw conveyor and is dried by the far IR radiator *1* combined hot air while the paddy is promoted by the screw convey. A pipe connects the outlet of screw conveyor and inlet of the grain collecting tank of combine harvester and it forms a tempering period of dried paddy. After tempered, the paddy is homogeneously dispersed on a perforated plate, and the thin-layer paddy is dried by the far IR radiator2 and the hot air penetrated from the holes in the perforated plate.

The parameters of hot air blower are listed in Tab.1.

**Table1**

**Hot air blower technical parameters**

| Parameter | value | Parameter | value |
|---|---|---|---|
| Supply voltage [V] | 380 | Blower power[kW] | 0.75 |
| Outlet air pressure [Pa] | 1500 | Blower speed [r.min-1] | 2800 |
| Max air flux [m3.h$^{-1}$] | 1320 | Max air temperature[K] | 623K |
| Heating Power [kW] | 6 | | |

*The voltage regulators are made by Shanghai Nenggong Electronic CO., LTD, P.R. China, and their model number is NG3A-30A*.

## EXPERIMENT MATERIALS

The paddy for the experiment is the late paddy of 2018 and it comes from the experimental field of Jiangxi Agricultural University. In Fig.2 is the paddy to be dried. Impurities had been removed from the paddy and it was grouped; then, each group underwent the conditioning treatment according to the reference (*Li C.L., 2004*) to attain different water contents.

**Fig. 2 - Paddy to be dried**

## EXPERIMENT METHOD

The purpose of the experiment is to acquire the influence laws of energy distributions on the drying performances and energy consumption under different harvest conditions. The orthogonal method is adopted to solve this multi-factor and multi-object problem because of its effectiveness, scientificity, convenience and economy. The orthogonal method can reduce workload and experiment cost compared to the comprehensive test method, especially for the multiple-factor and multiple-level experiment.

**Factors and levels.** The factors and levels are listed in Tab.2. Since the higher the hot air temperature is, the more the paddy rice cracks, the hot air temperature range is set as 40°C-60°C (*Wang J.H., 2000*). The ranges of hot air velocity (HAV), the speed of screw conveyor(SSC), the power of IR radiator 1(PIR1) and the power of IR radiator 2(PIR2) are set as 4 m/s-5.3 m/s, 264r/min-288r/min, 1kW-3kW and 3kW-5kW respectively according to the reference (*Kuang P., 2016*). The initial water content (IWC) of paddy could vary from 18% to 28%.

**Table 2**

**Factors and levels**

| Factors / Levels | HAT [°C] | HAV [m/s] | SSC [r/min] | PIR1 [kW] | PIR2 [kW] | IWC [%] |
|---|---|---|---|---|---|---|
| **1** | 40 | 4.00 | 276 | 1 | 3 | 20 |
| **2** | 45 | 4.10 | 270 | 1.5 | 3.5 | 18 |
| **3** | 50 | 4.95 | 282 | 2 | 4 | 22 |
| **4** | 55 | 4.66 | 264 | 2.5 | 4.5 | 24 |
| **5** | 60 | 5.30 | 288 | 3 | 5 | 28 |

**Orthogonal table**. According to the number of factors and levels, the orthogonal table$L_{25}5^6$ is adopted without concerning the interactions of factors.

**Experiment indexes.** There are three indexes including dehydration rate (DR), increased crack percentage (ICP) and specific energy consumption (SEC). The DR is the index of the drying speed and it can be expressed as:

$$v_t=\Delta w/\Delta t \quad (1)$$

where $v_t$ is the average dehydration speed [%/min]; $\Delta w$ is the changes in water content before and after drying [%]; $\Delta t$ is the drying time [min].

The ICP is the index of drying quality and it could be acquired abiding by the following steps:

(1) The paddy is sampled and packaged after drying and returning to the indoor temperature;

(2) After packaged for 48 hours, 150 g paddy is taken out by random sampling and divided into three groups as shown in Fig.3;

(3) The paddy of each group is carefully hulled by hand as shown in Fig.4, and then the hulled paddy is checked with a magnifying glass to obtain the crack ratio;

(4) The mean value of three groups' crack ratio is the final crack ration, and increased crack percentage of the final crack ration after and before drying is the ICP (*Dhib R., Broadbent A.D., Thérien N., 1994*).

**Fig. 3 - Dried paddy sample**

**Fig. 4 - Hulled paddy**

The SEC is the heat consumption per water dehydrated, and it can be calculated as:

$$q=Q/W \quad (2)$$

Where, $q$ is the SEC [kJ/kg.$H_2O$]; $Q$ is the total heat consumption [kJ]; $W$ is the water dehydrated [kg], and it can be expressed as:

$$W=G-G_0 \quad (3)$$

Where, $G$ and $G_0$ are the paddy weight [kg] into and outside the drying system respectively;
According to the law of conservation of mass, we can acquire:

$$G\ (1\text{-}w_1)\ = G_0\ (1\text{-}w_0) \tag{4}$$

Where, $w_1$ and $w_0$ are the water content of paddy [%] after and before drying respectively; combining Eq.3 with Eq.4, $W$ can be expressed as:

$$W = \frac{G\left(w_1 - w_0\right)}{1 - w_1} \tag{5}$$

## RESULTS

The arrangement and results are listed in Tab.3.

**Table 3**

**Arrangement and results of experiment**

| No. | Factors | | | | | | Indexes | | |
|---|---|---|---|---|---|---|---|---|---|
| | HAT [°C] | HAV [m.s$^{-1}$] | SSC [r.min$^{-1}$] | PIR1 [kW] | PIR2 [kW] | IWC [%] | DR [%/min] | ICP[%] | SEC [kJ/kg.$H_2O$] |
| 1 | 1(40) | 1(4.00) | 1(276) | 1(1.0) | 1(3.0) | 1(20) | 0.48 | 4.48 | 3406.59 |
| 2 | 1 | 2(4.10) | 2(270) | 2(1.5) | 2(3.5) | 2(18) | 0.25 | 7.32 | 4473.10 |
| 3 | 1 | 3(4.95) | 3(282) | 3(2.0) | 3(4.0) | 3(22) | 0.27 | 2.51 | 2938.00 |
| 4 | 1 | 4(4.66) | 4(264) | 4(2.5) | 4(4.5) | 4(24) | 1.37 | 3.45 | 1793.23 |
| 5 | 1 | 5(5.30) | 5(288) | 5(3.0) | 5(5.0) | 5(28) | 1.85 | 0.93 | 1365.58 |
| 6 | 2(45) | 1 | 2 | 3 | 4 | 5 | 2.00 | 0.63 | 917.66 |
| 7 | 2 | 2 | 3 | 4 | 5 | 1 | 0.73 | 3.89 | 4021.30 |
| 8 | 2 | 3 | 4 | 5 | 1 | 2 | 0.68 | 11.23 | 2694.51 |
| 9 | 2 | 4 | 5 | 1 | 2 | 3 | 0.74 | 0.41 | 1738.58 |
| 10 | 2 | 5 | 1 | 2 | 3 | 4 | 2.03 | 5.19 | 894.32 |
| 11 | 3(50) | 1 | 3 | 5 | 2 | 4 | 2.15 | 4.27 | 984.64 |
| 12 | 3 | 2 | 4 | 1 | 3 | 5 | 2.38 | 1.45 | 636.90 |
| 13 | 3 | 3 | 5 | 2 | 4 | 1 | 0.45 | 6.59 | 5009.85 |
| 14 | 3 | 4 | 1 | 3 | 5 | 2 | 1.95 | 16.07 | 1500.78 |
| 15 | 3 | 5 | 2 | 4 | 1 | 3 | 1.32 | 3.27 | 1331.92 |
| 16 | 4(55) | 1 | 4 | 2 | 5 | 3 | 1.42 | 2.86 | 1515.64 |
| 17 | 4 | 2 | 5 | 3 | 1 | 4 | 1.19 | 4.39 | 1301.37 |
| 18 | 4 | 3 | 1 | 4 | 2 | 5 | 2.85 | 1.99 | 650.17 |
| 19 | 4 | 4 | 2 | 5 | 3 | 1 | 0.57 | 5.53 | 4327.77 |
| 20 | 4 | 5 | 3 | 1 | 4 | 2 | 2.43 | 7.87 | 1029.87 |
| 21 | 5(60) | 1 | 5 | 4 | 3 | 2 | 1.05 | 8.90 | 2122.63 |
| 22 | 5 | 2 | 1 | 5 | 4 | 3 | 1.62 | 3.91 | 1620.35 |
| 23 | 5 | 3 | 2 | 1 | 5 | 4 | 1.46 | 5.51 | 1502.18 |
| 24 | 5 | 4 | 3 | 2 | 1 | 5 | 1.96 | 1.70 | 647.10 |
| 25 | 5 | 5 | 4 | 3 | 2 | 1 | 0.81 | 4.81 | 2406.99 |

Fig.5 shows the influence of the HAT, HAV, SSC, PIR1, PIR2 and IWC on the DR. The extreme difference analysis shows $R_{IWC}>R_{HAT}>R_{SSC}>R_{HAV}>R_{PIR2}>R_{PIR1}$, where $R$ with the corresponding subscribing represents the extreme different value of each factor. Since the higher the water content of paddy is, the higher the rate of dehydration is and the more the hot air is needed to bring the water out of the drying system, the IWC and HAT become the key factors to the DR. To achieve the maximum DR, HAT=55°C, HAV=5.3m/s, SSC=276 r/min, PIR1=1.0kW, PIR2=4.5kW and IWC=28%.Because the duration of the IR radiation drying process is very short and there is less bound water in the experiment paddy using the conditioning treatment than the actual field paddy, the hot air has more effect in contrast to the infrared radiator.

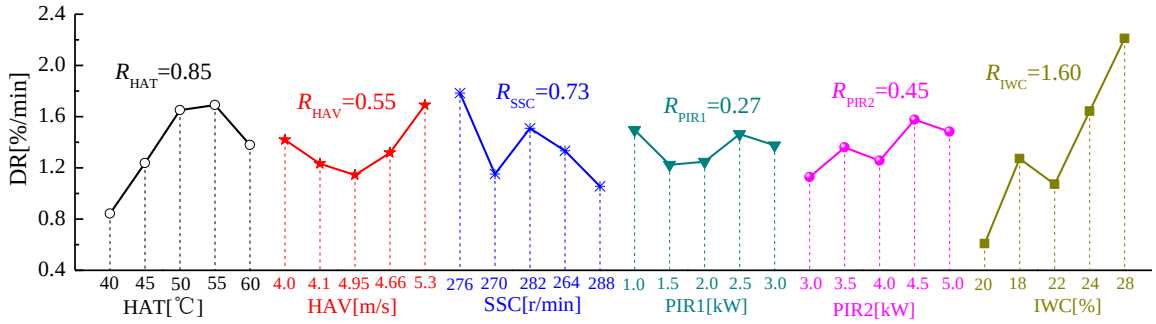


**Fig. 5 - Influence of the drying factors on the dehydration rate (DR)**

The six factors affecting the ICP in a descending order are: IWC, HAT, SSC, PIR2, PIR1 and HAV according to their extreme difference values. The ICP increases with the rising of DR; hence, the IWC and HAT are also the dominant factors to ICP. The optimal combination of factors can be also obtained as: HAT=40°C, HAV=4.1 m/s, SSC=282 r/min, PIR1=1.0kW, PIR2=3.5kW and IWC=28%.

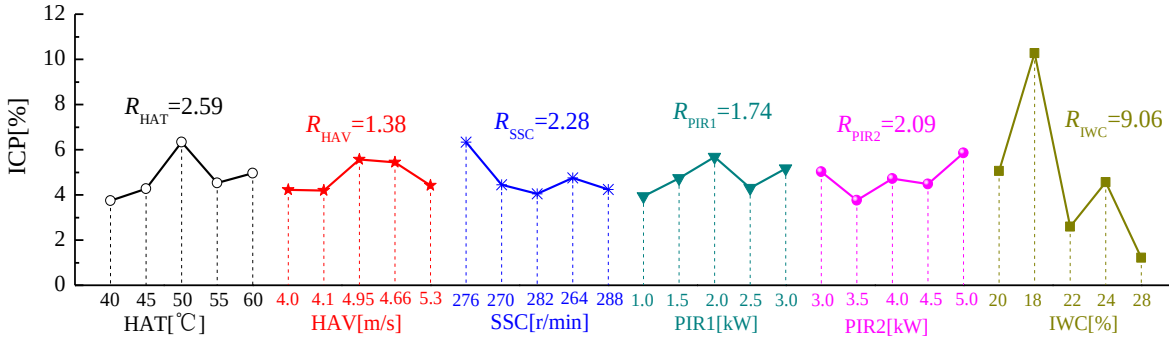


**Fig. 6 - Influence of the drying factors on the increased crack percentage**

As shown in Fig.7, the influence of the conditions on SEC follows the sequence: IWC, HAV, HAT, SSC, PIR1 and PIR2, and the optimal combination is: HAT=60°C, HAV=5.3 m/s, SSC=276 r/min, PIR1=1.0kW, PIR2=3.0kW and IWC=28%. That is to say, in order to reduce the drying energy consumption, the convection drying should be enhanced while the IR radiator drying should be weakened; meanwhile, the paddy flow should be reduced.

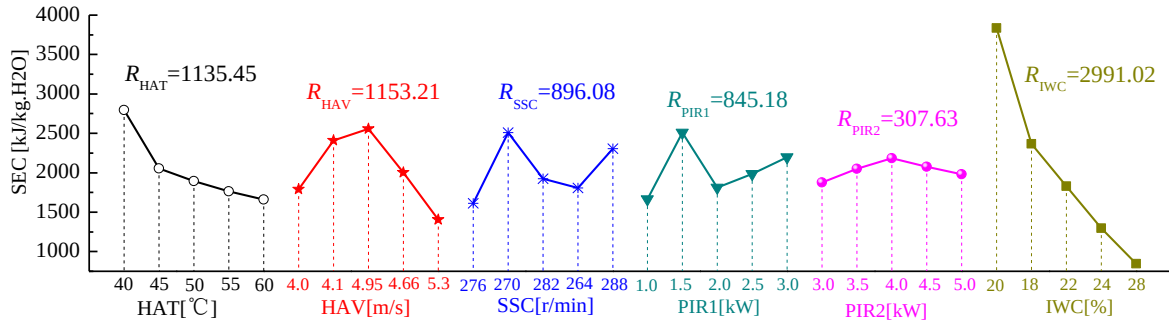


**Fig. 7 - Influence of the drying factors on the specific energy consumption**

Since the IWC varies with the climate and harvest time and cannot be controlled, the other five factors should be selected according to the DR, ICP and SEC during the actual harvesting process.

## CONCLUSIONS

A kind of new paddy drying system was proposed in order to decrease the grain loss due to no timely drying for the high moisture content paddy in the rice main production region of southern China (especially in the double cropping rice region), reduce the handling cost for paddy drying and solve the problem of drying paddy on roadway in our country. Using the electric current generated by the integrated starter/generator(ISG) driven by diesel engine and the exhaust heat of diesel engine as the source of energy, the new drying system equipped with far-infrared and hot air could dry paddy directly in the drying chamber integrated with the screw conveyor and grain collecting tank of the combine harvester. The key problem of multi-field coupling mechanism of paddy flow, hot air and far-infrared was solved through the experimental researches on the effect of paddy flow, hot air and far-infrared radiation on the paddy drying process, and the test results show:

(1)The drying combination of infrared convection embedded in the combine harvester could achieve rapid drying with good drying quality, and the SEC can meet the specification of JB/T10268-2001.

(2)When HAT=55°C, HAV=5.3m/s, SSC=276r/min, PIR1=1.0kW, PIR2=4.5kW and IWC=28%, the highest DR can be achieved; under the case of HAT=40°C, HAV=4.1m/s, SSC=282 r/min, PIR1=1.0kW, PIR2=3.5kW and IWC=28%, the drying quality is the best; in order to acquire the minimum energy consumption, the conditions are: HAT=60°C, HAV=5.3 m/s, SSC=276 r/min, PIR1=1.0kW, PIR2=3.0kW and IWC=28%.

(3)The IWC is the dominant factor to the DR, ICP and SEC, but it cannot be controlled in the actual producing process. The convection drying has more effect on the drying performances compared with the IR radiation drying because of its longer drying duration.

The future work will focus on embedding the whole drying system on the combine harvester and experiment in the actual harvest process.

## ACKNOWLEDGEMENT

This work was supported by the National Natural Science Foundation of China (grant number31560344) and Science and Technology Project of Jiangxi Province (grant number 20181BBF68016).

## REFERENCES

[1] Bai J.W., Luo S.Q., Ye J. et al., (2008), Design of the waste heat utilizing system on multifunctional tractor, *Journal of Agricultural Mechanization Research*, vol. 12, pp. 95-197;

[2] Celma R.A., Rojas S., Lopez-Rodriguez F., (2008), Mathematical modeling of thin-layer infrared drying of wet olive husk, *Chemical Engineering and Processing,* vol. 47, pp.1810-1818;

[3] Chen K.J., Chen Q.C., Zhang Y., (2005), Energy consumption for grain drying in China (中国谷物干燥加工中的能源消耗状况), *Transactions of the CSAE*, vol. 21, pp.173-177;

[4] Dhib R., Broadbent A.D., Thérien N., (1994), Modeling and simulation of the drying of thin sheets in a continuous infrared dryer, *Canadian Journal of Chemical Engineering*, vol. 72, pp. 894-905;

[5] Kuang P., (2016), *Research and development of exhaust heat assisted far IR Rice drying equipment in combine harvester*. (联合收割机中排气余热联合远红外稻谷干燥装置的研发), Dissertation of Jiangxi Agricultural University, pp. 39-46;

[6] Li C.L., (2004), The brief introduction of moisture condition. (米厂谷物加工中水分的调质), *Grain processing*, vol.5, pp.18-19+29;

[7] Liu C.S., Shang T., Yang S.Q., (2017), Analysis on the Influence of the Exchange Area on the Heat Exchange Efficiency during Far-Infrared Convection Combination Grain Drying Process, *ICSGEA: IEEE Computer Society*, pp.117;

[8] Niu X.H., Cao C.W., (1999), Energy saving techniques in grain drying (谷物干燥节能技术), *Transactions of CSAE*, Vol. 6, pp.87-94;

[9] Onwude D.I., Hashim N., Abdan K. et al., (2019), The effectiveness of combined infrared and hot-air drying strategies for sweet potato, *Journal of Food Engineering,* vol. 241, pp.75-87;

[10] Rahmanian- Koushkaki H., Nourmohamadi-Moghadami A., Zare D. et al., (2017), Experimental and theoretical investigation of hot air- infrared thin layer drying of corn in a fixed and vibratory bed dryer, Engineering in Agriculture, *Environment and Food*, vol. 10, pp.191-197;

[11] Sarobol M., Teeta S., Pharanat W. et al., (2018), Numerically simulations of the germinated parboiled thunya-siringlutinous rice under a combined far infrared radiation and air convection drying, *Journal of Physics: Conference Series,* 1144, 012178;

[12] Wang J.H., (2000), Analysis of effecting factors for rice crackle ratio during drying (稻谷干燥爆腰率因素分析), *Cereal & Feed Industry*, vol. 8, pp. 20-21;

[13] Xiang F., Wang L., Yue X.F., (2011), Exergy analysis and experimental study of a vehicle-mounted heat pump–assisted fluidization drying system driven by a diesel generator, *Drying Technology*, vol. 29, pp.1313–1324;

[14] Zare D., Naderi H., Ranjbaran M., (2015), Energy and quality attributes of combined hot-air/infrared drying of paddy*, Drying Technology*, vol. 33, pp. 570-582.

# DESIGN OF SIEVE-ROLL COMBINED PEANUT PODS CLEANING DEVICE
/
# 筛-辊组合式花生荚果清选装置设计

**Wang Shengsheng[1,2], Ji Jiangtao[1,2], Geng Lingxin[1] [1]**
[1] Henan University of Science and Technology, College of Agricultural Equipment Engineering/ China;
[2] Collaborative Innovation Centre of Machinery Equipment Advanced Manufacturing of Henan Province/ China
*Tel: +86-379-64877837; Email: wangsheng5288@126.com*
*DOI: 10.35633/INMATEH-59-16*

***Keywords:*** *Peanut pods, Cross flow fan, Vibrating screen, Separation of roller, Motion analysis*

## ABSTRACT

*In order to meet the requirements of peanut pods cleaning by the pick-up peanut combine harvester, and enhance the processing ability of branches, leaves, broken stalks and hard fruit stalks of the cleaning system, a kind of sieve-roll combined peanut pods cleaning device was designed based on the analysis of material cleaning characteristics. It mainly includes key components, such as cross flow fan, vibrating screen and separation roller. The force and movement state of the picking peanut extraction on the sieve surface and the separation roller were analysed. Through field loading test and verification, when the vibration screen width is 1200 mm, the crank speed is 650 rpm, the cross flow fan speed is 920 rpm, the separation roll speed is 410 rpm, the separation roll gap is 3 mm, then the peanut pod containing impurities rate is 1.52% and the loss rate is 0.64%, which meets the national industry standards.*

## 摘要

*为了满足捡拾式花生联合收获机对花生荚果的清选要求，增强清选系统对枝叶、断杆和硬果梗的处理能力，在物料清选特性分析的基础上，设计了一种筛-辊组合式花生荚果清选装置，主要包括横流风机、振动筛、分离辊等关键部件。对花生摘果脱出物在筛面和分离辊上的受力及运动状态进行了分析.通过田间装机试验验证，当振动筛宽度为 1200mm，曲柄转速为 650r/min、横流风机转速为 920r/min、分离辊转速为 410r/min、分离辊间隙为 3mm 时，花生荚果的含杂率为 1.52%，损失率为 0.64%，满足国家行业标准要求。*

## INTRODUCTION

Peanut is an important oil crop in China, with a total output of 17 million tons, which is accounting for about 40% of the global total output, ranking first in the world *(Liao, 2003; Liu, 2011)*. According to the statistics of mechanization department of agriculture ministry, the mechanization rate of peanut harvest in China is about 33%, which has become the main bottleneck restricting the development and benefit growth of peanut industry in China *(Zheng and Li, 2005)*. The pick-up peanut combine harvester is an important model in the two-stage harvesting of domestic peanuts due to its large feeding capacity and high harvesting efficiency *(Lv Xiaolian et al., 2012)*.

As an important part of the peanut harvester, the operating performance of the cleaning device directly affects the operating quality and production efficiency of the whole machine *(Tang et al., 2016; Mekonnen Gebreslasie Gebrehiwot et al., 2010; K. Maertens et al., 2000)*. During the operation of the harvester, the excavated peanut plants are sent into the picking mechanism by the harvester, and the peanut vine is discharged from the grass outlet of the picking mechanism. The peanut pods, stems, light sundries, hard fruit stalks and lumps fall into the cleaning device through the separation concave plate of the picking mechanism.

At present, the foreign peanut combine harvester has structural innovations in the cleaning system, for example, a gas stream that can be adjusted at any time is attached to the cleaning sieve; using a higher volume vacuum fan, the debris is gradually raised as the peanuts fall to the back of the shaker plate. The existing fan-vibrating screen cleaning system is widely used in the existing peanut harvesting machines in China (*Liu, 2018*).

[1] *Wang Shengsheng, Ph.D. Eng.; Ji Jiangtao, Prof. Ph.D. Eng.; Geng Lingxin, Prof. Ph.D. Eng.*

Because the basic physical parameters such as the shape, size and density of the peanut pod extract are different *(Chakraborty et al., 2018; Zdzisław Kaliniewicz, Zbigniew Żuk, 2018)*, this sorting system cannot effectively remove the broken stem and hard fruit stem in the material.

Due to the differences in the shape, size, density and other basic physical parameters of the components of peanut extraction *(Chakraborty et al., 2018; Zdzisław Kaliniewicz, Zbigniew Żuk, 2018)*, the existing peanut harvesters generally use the traditional fan-vibrating screen cleaning system, which cannot effectively remove the broken stalks and hard stalks in the material, meanwhile there are some problems, such as high content of stem breakage, large loss of pod and poor adaptability (*Liu, 2018*). Therefore, it is of great theoretical significance and practical value to develop a new type of cleaning and removing system suitable for the pick-up peanut combine harvester.

In order to effectively solve the problem of cleaning and removing impurities in the pick-up peanut combine harvester, this paper designs a kind of sieve-roller combined peanut pod cleaning device, which is able to reduce the overall size and increase the adaptability of peanut harvester on the premise of ensuring the cleaning and sorting performance. On the basis of theoretical calculation, from the kinematics point of view, the force and motion state of the picking peanut extraction on the sieve surface and the separation roller are analyzed; the conditions for the normal work of the separation roller are given; and the velocity formula of the exudates in the cleaning device is deduced. Moreover, through the field verification test, impurity content and the loss rate of the cleaning device during operation are obtained.

## MATERIALS AND METHODS

### Study on the cleaning characteristics of picking peanut extraction

### Proportion of extraction

Picking peanut extraction refers to all the materials separated by the concave plate after the picking roller picks the fruits, mainly including peanut pods, broken culms, roots, light sundries, soil, etc. and all components are mixed in a certain proportion. The peanut used in this experiment is Yuhua No.15, and the picking mechanism adopts the full-feed picking roller. The moisture content of peanut pod and stem measured at the time of fruit picking was 18% and 15% respectively. The picking peanut extraction was classified, weighed as well as calculated, and the results were as shown in Tab.1.

**Table 1**

**Components and proportion of the picking peanut extraction**

| Components | Peanut pods | Break culms and stalks | Impurities | The soil |
|---|---|---|---|---|
| The proportion [%] | 65.82 | 13.52 | 11.01 | 9.65 |

### Measurement and statistical analysis of the shape and size of peanut pods

At harvest time, each peanut plant will have about 15 to 40 pods, most of which are mature and full, but there are also a few immature pods. Each pod usually contains one or two peanuts, and the morphology of these pods varies greatly. Due to the irregular appearance of peanut pod, the pod was approximately regarded as a cuboid for easy measurement, and its shape characteristics were described by measuring its length, width and thickness. 100 samples were randomly selected from peanut pods used in the experiment; the length, width and thickness of each sample were measured by digital vernier caliper; and the measurement results were recorded. Statistical analyses were carried out on the measurement results, which were as shown in Tab. 2.

**Table 2**

**Statistical analysis of peanut pods physical dimension**

| Statistical parameter | Pod length [mm] | Pod width [mm] | Pod thickness [mm] |
|---|---|---|---|
| The minimum | 17.09 | 11.66 | 8.7 |
| The maximum | 42.22 | 19.12 | 16.88 |
| The average | 31.678 | 15.304 | 13.998 |
| The standard deviation | 7.217 | 2.248 | 2.280 |
| Coefficient of variation [%] | 22.8 | 14.7 | 16.2 |

**Determination of length and diameter of broken stalks**

Broken stalks are the impurities with the largest proportion in the picking peanut extraction. When peanuts are fully fed and picked, a large number of broken stalks will be produced in the extraction components, especially when the moisture content of peanut plant is low. In order to remove the broken stalks in the extraction better, the broken stalks should be graded according to different lengths. In this paper, the broken stalks were divided into three grades according to the length less than 50 mm, between 50 and 130 mm and greater than 130 mm, and their proportions were counted. The statistical results show that the stalk with the length between 50 and 130 mm takes the largest proportion, accounting for 56%, followed by the stalk with the length greater than 130 mm, accounting for 34%, and the short stalk with the length less than 50 mm takes the smaller proportion, accounting for 10%. A large number of broken culms were randomly selected as samples from the picking peanut extraction. Through measurement and statistical analysis, it was found that the diameter of the broken culms was 1.3-5.2 mm.

**Suspension velocity of picking peanuts extraction**

Suspension speed refers to the velocity of the airflow when the material acts under the vertical airflow, and the force of the airflow on the object is equal to the weight of the object itself to keep the object in suspension *(Ghafori and Ebrahimi, 2018)*. It is one of the important factors affecting the movement of materials in the airflow field *(Ma Zheng et al., 2011)*. In this paper, DFPF-25 suspension velocity test device was selected to measure the suspension velocity of each component of the extraction. Its structure is as shown in Fig.1. The small end diameter of the conical tube is 81mm and the angle of the conical top is 5.5°. The device adopts a variable speed motor as the supporting power. The power of the motor is 5.5 kW, the speed adjustment range is 300~1000 rpm, and the maximum suspension speed can be measured to be 25 m/s. The measurement results are as shown in Table 3.

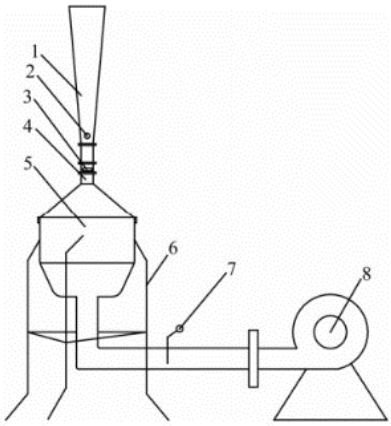


**Fig. 1 - Schematic diagram of floating velocity instrument for peanut mixture**
*1-Tapered tube; 2-Pitot tube speed gauge; 3-Material release port; 4-Convergence tube; 5-Voltage regulator tube; 6- Stents; 7-Damper; 8-Fan*

**Table 3**

**Floating velocity of peanut mixture**

| Determined material | Minimum suspension Velocity [m/s] | Maximum suspension Velocity [m/s] |
|---|---|---|
| Plump pod | 7.5 | 9.7 |
| Incomplete pod | 4.5 | 6.3 |
| Long stem | 4.2 | 5.9 |
| Short stalk | 3.6 | 4.0 |
| Impurities | 2.1 | 3.2 |

It can be found from the results in Table 3 that the suspension speed of full peanut pod is the highest, followed by that of incomplete peanut pod and long stalk, and that of light sundries is the lowest. Among them, the suspension speed of peanut pod is much higher than that of light sundries and short stalk, while the range of suspension speed of long and short stalks overlaps to some extent.

**The whole design and working principle of cleaning mechanism**

According to the research on the cleaning characteristics of picking peanut extraction components, it can be known that it is necessary to use the air-and-screen cleaning mechanism to clean peanut pods. Therefore, a kind of sieve-roll combined peanut pods cleaning device is designed in this paper. Its structure is as shown in Fig.2. During work, the picking peanut mixture is discharged onto the vibrating screen of the cleaning device through the separating concave plate of the picking mechanism, and moves toward the tail of the vibrating screen. Under the stratification of the vibrating screen, the clods with small volume and large weight in the materials are located at the bottom layer of the material and then fall below the screen surface through the sieve hole of the vibrating screen. The light sundries with large volume and light weight and the short stalk are located on the top layer of the material. When moving to the tail of the vibrating screen, it is sucked away by the cross-flow fan and discharged from the air outlet. The remaining material is peanut pods and some large stalks as well as rhizomes with large volume and large mass. When they fall onto the stalk removal device and move along the axial direction of the separation roller, several pairs of oppositely rotating separation rollers will pick up the long stalks and rhizomes of smaller diameter, which will be sent to the lower side of the separation roller. Until only the clean peanut pods remain on the stalk removal device and then fall through the fruit outlet into the fruiting device, the peanuts are cleaned and sorted.

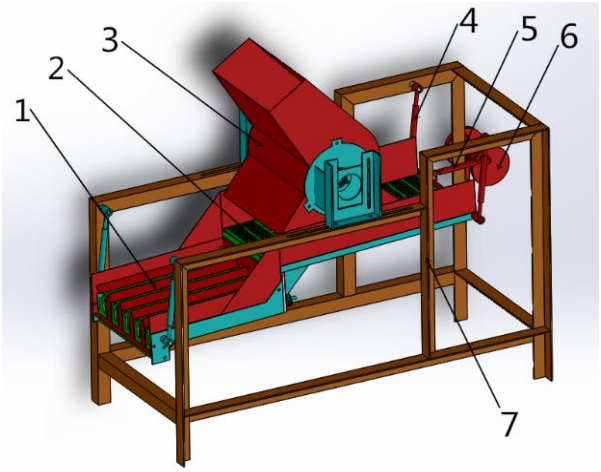


**Fig. 2 - Structural schematic diagram of screen-roller combined peanut pod cleaning device**

*1-Separation roller; 2-Vibrating screen; 3-Cross flow fan; 4-Derrick; 5-Connecting rod;6-The crank; 7-Stents*

**Design of key component**

***Cross flow fan***

The cross-flow fan designed in this paper is as shown in Fig.3, which is mainly composed of impeller and fan casing. The impeller is multi-bladed and mainly composed of forward-curved blades, flanges, blade-wheel axles, bearings, and belt wheels, etc. The fan casing is mainly composed of a side plate sealed on both sides, a volute and a volute tongue, which is welded by a steel plate with a thickness of 1.5 mm. Volute inner wall profile is an Archimedes spiral.

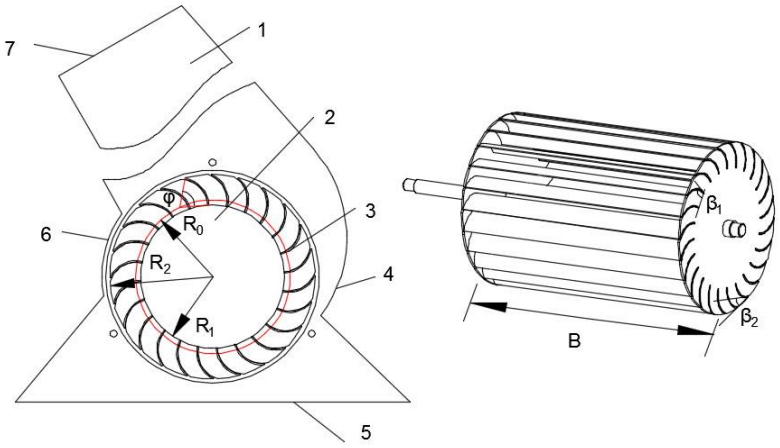


**Fig. 3 - Structure diagram of cross-flow fan**

*1-Shell; 2-The impeller; 3-Leaf blade; 4-Pan; 5-Air inlet; 6- Tongue; 7-The outlet;*

Where $R_1$ is inner radius of impeller, $R_1$ =91mm; $R_2$ is outer radius of impeller, $R_2$ =91mm; $Z$ is the number of blade, $Z$=24; $\beta_1$ is the blade inlet mounting angle, $\beta_1$=90°; $\beta_2$ is the blade outlet mounting angle, $\beta_2$=25°; $B$ is the impeller width, $B$=580 mm.

The calculation formula of the radius of curvature $R$ of the blade, the positioning radius $R_0$ of the centre of the blade and the central angle $\varphi$ corresponding to the arc length of the blade is:

$$R = \frac{R_2^2 - R_1^2}{2(R_2 \cos\beta_2 - R_1 \cos\beta_1)} \quad (1)$$

$$R_0 = 2R_2\sqrt{\frac{R}{2R_2}\left(\frac{R}{2R_2} - \cos\beta_2 + 0.25\right)} \quad (2)$$

$$\varphi_1 = \cos^{-1}\frac{R^2 + R_0^2 - R_1^2}{2RR_0} \quad (3)$$

$$\varphi_2 = \cos^{-1}\frac{R^2 + R_0^2 - R_2^2}{2RR_0} \quad (4)$$

$$\varphi = \varphi_2 - \varphi_1 \quad (5)$$

$R$, $R_0$ and $\varphi$ are calculated by substituting the above parameters data into the formula (1) to (5). The calculated radius of blade curvature $R$ is 36.58 mm, the positioning radius of the blade centre $R_0$= 98.07 mm and the central angle corresponding to the blade arc length $\varphi$ = 77.83 °.

**Vibrating screen and Separation rollers**

Vibrating screen is generally composed of vibrator, screen surface, supporting or suspension device, transmission device and other parts *(Li, 2003)*. The screen surface of the vibrating screen designed in this paper is as shown in Fig.4. The screen hole is a strip hole. According to the design principle, the narrow side width of the strip hole $a=(0.7\sim0.8)d_{max}$, and the long side width $b=(1.1\sim1.15)d_{max}$. In order to ensure that dirt and other debris pass through the sieve hole, while the peanut pod does not pass through the sieve hole, $d_{max}$ is taken as the average value of the thickness of the peanut pod, which is 13.998 mm; and both a and b take the minimum value; the narrow width of the sieve hole is 9.8 mm and the long side width is 15.4 mm.

As shown in Fig.5, the action of the separating roller is to grab the long stalk and root in the extraction components. The separating roller is made of nylon rod. The two ends are inlaid with steel shaft head, which is installed on the special bearing support by bearing. External mesh gears are used to transfer power between the separation rollers, besides that the modulus and number of teeth of the adopted gears are the same. The rotation speed of each two adjacent spur gears is the same and the direction is opposite. The active roller is connected with the speed regulating motor through the V-belt, and controlling the digital frequency converter can achieve the purpose of adjusting the speed of the separation roller.

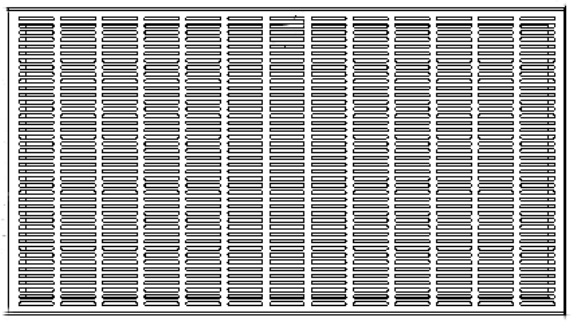

**Fig. 4 - Vibrating screen surface**

**Fig. 5 - Physical drawing of separating rollers**

**RESULTS**

**Force and motion analysis of extraction**

**Force and motion analysis of the extraction on the screen surface**

When the extraction slides down the vibrating screen, it will be affected by the three forces of its own gravity $G$, the supporting force $F_N$ of the screen facing the material and the frictional force $F_f$ of the screen facing the material, as shown in Fig.6.

However, when the material slides down to the inlet of the cross-flow fan, under the action of the high-speed airflow, the light debris and short stalks with smaller suspension speed will leave the screen surface and move upwards obliquely with the airflow. At this point, they are only affected by two forces, namely their own gravity $G$ and the airflow force $F_p$.

The direction of the force $F_P$ of the air flow on the material is opposite to the direction of the relative velocity *v* of the material on the air flow.

Since each component moves independently of each other in the form of a single individual after the extraction enters the airflow field, and in order to facilitate analysis and calculation, each component of the picking peanut extraction is regarded as a spherical particle with mass *m*.

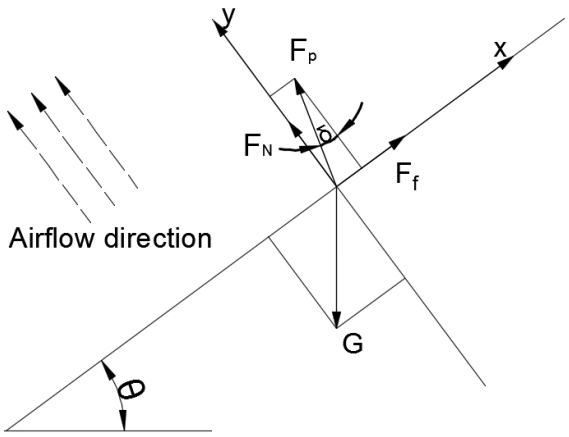


**Fig. 6 - Force Analysis Diagram of Material on Screen Surface**

According to Newton's formula, force $F_P$ of airflow on material can be expressed by equation (6):

$$F_P = mK_P v^2 = m\frac{g}{v_P^2}v^2 \tag{6}$$

Where $F_P$ is airflow force, [N]; $K_P$ is floating coefficient; *m* is mass of material [kg]; $v_P$ is floating speed [m/s]; *v* is relative velocity of material to airflow [m/s].

For the peanut pods and long stalks in the extraction, due to their large suspension speed, they will not leave the screen surface after being subjected to the airflow force, but will continue to slide along the screen surface. At this time, in addition to being subjected to the airflow force $F_p$, they are also subjected to the self-gravity $G$, the supporting force $F_s$ of the screen facing the material, and the frictional force $F_f$ of the screen facing the material. Since the material continues to slide down the screen surface, it can be seen that the direction in which the material is subjected to the resultant force is in the negative direction along the X-axis.

The resultant force is obtained by decomposing and synthesizing the above four forces:

$$F_x = G\sin\theta - F_f - F_P\sin\delta \tag{7}$$

Also, because the resultant force of the material on the y-axis is 0, so:

$$\begin{gathered} F_p\cos\delta + N - G\cos\theta = 0 \\ N = G\cos\theta - F_P\cos\delta \end{gathered} \tag{8}$$

Because of $F_t = \mu N$, if we substitute in the above equation, we can simplify it:

$$F_x = mg[(\sin\theta - \mu\cos\theta) - \frac{v^2}{v_P^2}(\sin\delta - \mu\cos\delta)] \tag{9}$$

Therefore, it can be calculated that the material sliding acceleration a is:

$$a = \frac{F_x}{m} = g[(\sin\theta - \mu\cos\theta) - \frac{v^2}{v_P^2}(\sin\delta - \mu\cos\delta)] \tag{10}$$

Where $\delta$ is the angle between the direction of the relative velocity of material to the flow *v* and the direction of the flow velocity, [°]; $\varnothing$ is angle of slide, [°].

**Analysis of force and motion of the extraction on the separating roller**

After being cleaned and sorted by air, the main materials that fall from the vibrating screen surface to the separation roller are peanut pods and long stalks. Under the action of their own gravity *G*, they will slide axially along the inclined separation roller, and at the same time, they will be guided by the guide plate into the material channel composed of the separation roller, meanwhile the long stem among them will be separated by a number of separation rollers rotating in opposite directions, as shown in Fig.7.

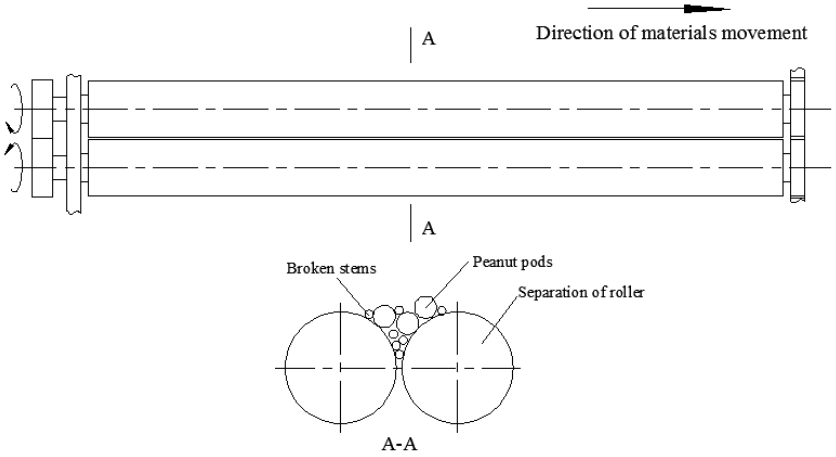


**Fig. 7 - Position diagram of double separation rollers in relationship to each other**

**Analysis of force of extraction on separating roller**

A properly functioning separation roll should be able to grab the long stem without damaging the peanut pod. In order to facilitate analysis, it is assumed that both the broken stem and peanut pod are regular cylindrical. When the long stem and peanut pod are grabbed by the separation roller, they are respectively subjected to the reaction forces *N*, $N_g$ and the gripping forces *T* as well as $T_g$ of the separating roller acting on the gripping portion, and the force analysis is as shown in Fig.8.

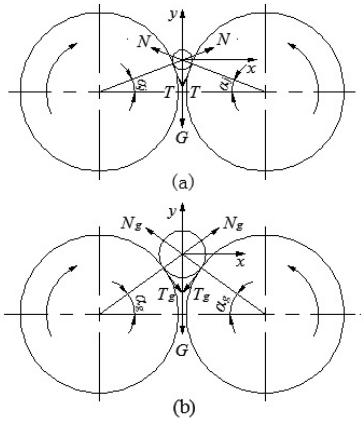


**Fig. 8 - Diagram of force analysis**

*(a) Stress analysis diagram of broken stem (b) Stress analysis diagram of pod*

For the separation roller to be able to grab the long stem without the influence of gravity, the resultant force on the *Y* axis of the long stem should be in the negative direction, it needs to be satisfied:

$$N\sin\alpha_j - T\cos\alpha_j < 0 \tag{11}$$

$$T = N\mu_j$$

$$\tan\alpha_j < \mu_j \tag{12}$$

Where, $\mu_j$ is the friction coefficient between the separating roller and the long stalk; $\alpha_j$ is initial grasping angle of separating roller on long stem, [°].

When the separation roller grabs the long stem, in order to prevent the peanut pod from being squeezed and broken by the separation roller, the following conditions must be satisfied:

$$N_g \sin\alpha_g - T_g \cos\alpha_g > 0 \tag{13}$$

$$\tan\alpha_g > \mu_g \tag{14}$$

Where, $\mu_g$ is friction coefficient between separating roller and peanut pod; $\alpha_g$ is initial grab angle of separating roller to peanut pod, [°].

Set the friction angle between the separation roller and the long stem and peanut pod as $\varnothing_j$, $\varnothing_g$ respectively, then:

$$\mu_j = \tan\phi_j, \quad \mu_g = \tan\phi_g$$

The normal working conditions of the separation roller are: $\alpha_j < \varnothing_j$, and $\alpha_g < \varnothing_g$.

In conclusion, in order to work properly, the separation roller must satisfy the following conditions: the initial grasping angle $\alpha_j$ of the separation roller on the broken stem should be smaller than the friction angle $\varnothing_j$ between the separation roller and the broken stem, meanwhile the initial grasping angle $\alpha_g$ of the separation roller on the peanut pod should be larger than the friction angle $\varnothing_g$ between the separation roller and the peanut pod.

**Motion analysis of the extraction on the separating roller**

When the separation roller works normally, the material will slide down uniformly and accelerate in the direction parallel to the axis line of the separation roller, besides that the broken culms will be constantly grabbed and separated by the separation roller until only clean peanut pods are left. According to observation of experimental phenomena, peanut pod will rotate around its own axis while sliding down uniformly and accelerating on the separation roller. Its motion rule is analyzed by setting three-dimensional coordinate system, as shown in Fig.9.

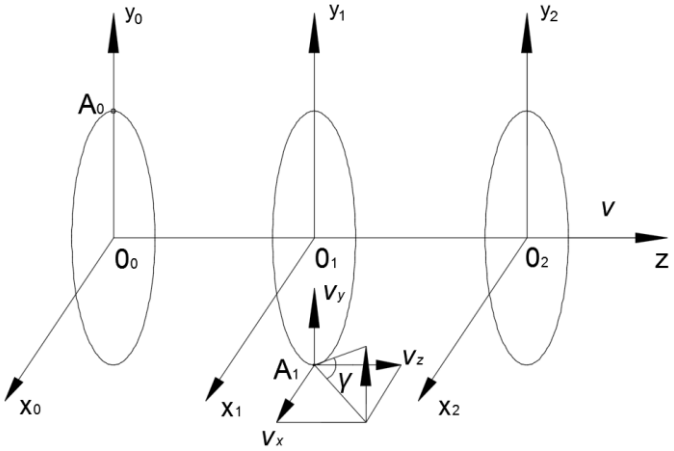


**Fig. 9 - Kinematic analysis diagram of peanut pods**

In this coordinate system, the origin point is the rotation centre of peanut pod; the z-axis coincides with the axis of pod centre; and the direction is the same as the axial movement direction of peanut pod. $A_0$ is the initial point of motion on the peanut pod; the $x_0O_0y_0$ plane, $x_1O_1y_1$ plane and $x_2O_2y_2$ plane are perpendicular to the z-axis, respectively; the $x_0O_0y_0$ plane is the plane; the pod motion initial point $A_0$ is located and the $x_1O_1y_1$ plane is the plane after the $A_0$ moves t seconds.

The coordinates of position $A_1$ after the initial point $A_0$ moves t seconds are:

$$\begin{cases} x = r\sin\omega t \\ y = r\cos\omega t \\ z = v_0 t + \frac{1}{2}at^2 \end{cases} \quad (15)$$

Where, $r$ is the turning radius of peanut pod (mm); $w$ is peanut pod rotation [rad/s]; $v_0$ is initial axial velocity of peanut pod movement [m/s]; $a$ is acceleration of peanut pod axial movement [m/s$^2$]; $a=g(\sin\beta-\mu_g\cos\beta)$; $\beta$ is the included angle between separating roller axis and horizontal plane.

By differentiating equation (15), the velocity $v_1$ and the speed direction angle at point $A_1$, can be obtained:

$$\begin{cases} v_x = \dfrac{dx}{dt} = r\omega\cos\omega t \\ v_y = \dfrac{dy}{dt} = r\omega\sin\omega t \\ v_z = \dfrac{dz}{dt} = v_0 + at \end{cases} \quad (16)$$

$$\left|\overrightarrow{v_1}\right| = \sqrt{v_x^2 + v_y^2 + v_z^2} = \sqrt{r^2\omega^2 + (v_0 + at)^2} \tag{17}$$

$$\gamma = \arctan\frac{v_y}{\sqrt{v_x^2 + v_z^2}} = \arctan\frac{r\omega\sin\omega t}{\sqrt{r^2\omega^2\cos^2\omega t + (v_0 + at)^2}} \tag{18}$$

The second differential of equation (16) is used to calculate the acceleration of point $A_1$ and the direction angle of acceleration $\varphi$ is:

$$\begin{cases} a_x = \dfrac{dv_x}{dt} = -r\omega^2\cos\omega t \\ a_y = \dfrac{dv_y}{dt} = r\omega^2\sin\omega t \\ a_z = \dfrac{dv_z}{dt} = a \end{cases} \tag{19}$$

$$\left|\vec{a}\right| = \sqrt{a_x^2 + a_y^2 + a_z^2} = \sqrt{r^2\omega^4 + a^2} \tag{20}$$

$$\varphi = \arctan\frac{a_y}{\sqrt{a_x^2 + a_z^2}} = \arctan\frac{r\omega^2\sin\omega t}{\sqrt{r^2\omega^4\cos^2\omega t + a^2}} \tag{21}$$

**Performance test**

To test the cleaning effect of the screen-roller combined peanut pods cleaning device, the cleaning device was placed on the pick-up peanut combine harvester designed and produced by Henan Ruifeng Machinery Co., Ltd. In the late September of 2018, a field trial was conducted in a peanut test field on the outskirts of Jiaxian County in Xinxiang City, Henan Province. Peanut plants are first excavated from the soil by peanut excavators and laid into ridges. After drying for 3 to 5 days, they are picked up by the pick-up peanut combine harvester. The field harvesting test process is as shown in Fig. 10 (left). The quality of peanut pod harvesting and cleaning is as shown in Fig.10 (right).

According to field test, when the vibrating screen width is 1200 mm, the crank speed is 650 rpm, the cross-flow fan speed is 920 rpm, the separation roller speed is 410 rpm and the separation roller gap is 3 mm, the peanut pod has an impurity ratio of 1.52 %, the loss rate is 0.64%, the peanut pod cleaning device is applied to the pick-up peanut combine harvester with good effect. And it is found that the impurity content ≤2.0% and the cleaning loss rate ≤1.5%, which are meeting expected design requirements and satisfying the national industry standard requirements of NY/ T502-2016 "Peanut Harvester Operation Quality".

**Fig. 10 - Field test process and cleaning effect of combine harvester for peanut picking-up**

**CONCLUSIONS**

The theoretical basis for the design of the cleaning and separation devices is provided by studying the composition ratio of peanut extraction, 100-grain weight of pod, the size and difference of pod and broken straw, the friction coefficient of each component and the floating speed, etc.

The sieve-roll combined peanut pod cleaning and sorting device designed consists of cross-flow fan, vibrating screen, separation roller etc.

The vibrating screen sorts the clods with small volume and large mass; the cross-flow fan sucks away the light debris; the separation roller grabs and separates the long stems; and the trinity completes the clearing of the picking peanut extraction.

By analyzing the force and motion of the extraction components on the screen, the force of air flow on the material and the horizontal acceleration of material slide are obtained. By analyzing the force and motion of the extraction components on the separating roller, the normal working condition of the separating roller and the moving velocity formula of peanut pod on the separating roller are obtained.

Through field test, the sieve-roll combined peanut pod cleaning device is applied to the pick-up peanut combine harvester with good effects of impurity rate ≤2.0% and cleaning loss rate ≤1.5%, which meets the expected design requirements and meets the national industrial standards.

**ACKNOWLEDGEMENTS**

The work was sponsored by the University-Industry Cooperation Project of Henan Province (No.182107000015) and the Key Scientific Research projects of Henan colleges and universities (No.19B416003).

**REFERENCES**

[1] Chakraborty S K, Chandel N S, Kotwaliwale N. et al, (2018), Characterisation of properties for Karanj, *(Pongamia pinnata*) seeds and kernels in relation to bulk handling and processing applications, *Agricultural Research*, Vol.7, Issue 3, pp.280-289, Bhopal/India;

[2] Ghafori H., Ebrahimi H.R., (2018), Numerical and experimental study of an innovative pipeline design in a granular pneumatic-conveying system, *Journal of Particles*, Vol.38, Issue 3, pp.196-203, Isfahan/Iran;

[3] Li Baofa, (2003), Agricultural Machinery, *China Agricultural Publishing House*, Zhenjiang/China;

[4] Liao Boshou, (2003), Analysis on the competitiveness of China's peanut oil industry, *Journal of Peanut Science*, Vol.32, Issue z1, pp.11-15, Wuhan/China;

[5] Liu Ming-jin, (2011), Present status analysis of peanut processing in China, *Guangdong Agricultural Sciences*, Vol.38, Issue 17, pp.161-164, Guangzhou/China;

[6] Lv Xiaolian, Wang Haiou, Zhang Huijuan et al, (2012), Research and situation on peanut machinery harvesting in China, *Journal of Agricultural Mechanization Research,* Vol.34, Issue 6, pp.245-248, Chuzhou/China;

[7] Liu Chunya, (2018), *Experimental Research of Cleaning Device for Peanut Harvester* (花生收获机清选装置的试验研究), Henan University of Science and Technology/China;

[8] Maertens K., De Baerdemaeker J., Ramon H. et al, (2000), An analytical grain flow model for a combine harvester, Part I: Design of the Model, *Journal of agricultural engineering research*, Vol.79, Issue 1, pp.55-63, Leuven/Belgium;

[9] Ma Zheng, Li Yaoming, Xu Lizhang, (2011), Testing and analysis on rape excursion components characteristics in floating, friction and wettability, *Transactions of the Chinese Society of Agricultural Engineering*, Vol.27, Issue 9, pp.13-17, Zhenjiang/China;

[10] Mekonnen Gebreslasie Gebrehiwot, Josse De Baerde-maeker, Martine Baelmans, (2010), Numerical and experimental study of a cross-flow fan for combine cleaning shoes, *Biosystems Engineering*, Vol.106, Issue 4, pp.448-457, Heverlee/Belgium;

[11] Shang Shuqi, Liu Shuguang, Wang Fangyan et al, (2005), Current Situation and Development of Peanut Production Machinery, *Transactions of the Chinese Society for Agricultural Machinery*, Vol.36, Issue 3, pp.143-147, Qingdao/China;

[12] Tang Bei, Lu Zemin, Guo Jun et al, (2016), Experimental Investigation on Cleaning Device of Peanut Combine Harvester, *Journal of Agricultural Mechanization Research*, Issue3, pp.191-195, Zhenjiang/ China;

[13] Zheng Shengyong, Li Chongguang, (2005), The Comparative Advantage Analysis on the Peanut Production of China, Journal of South China Agricultural University (Social Science Edition), Vol.4, Issue1, pp.11-15, Wuhan/China;

[14] Zdzisław Kaliniewicz, Zbigniew Żuk, (2018), A relationship between friction plate roughness and the external friction angle of wheat kernels*, International Journal of Food Properties*, Vol. 20, Issue 3, pp.1-9, Olsztyn/Poland.

# SPRAY DROPLET CHARACTERIZATION USING A PIEZOELECTRIC SENSOR THROUGH CLASSIFICATION BASED ON MACHINE LEARNING

/

# تعیین ویژگی‌های پاشش نازل با بکارگیری سنسور پیزوالکتریک از طریق طبقه‌بندی مبتنی بریادگیری ماشین

**Hassan Poorvousooghi Gargari[1)], Rahman Farrokhi Teimourlou*[1)], Morteza Valizadeh[2)]** [1]
[1)] Urmia University, Department of Mechanical Engineering of Biosystems, Iran
[2)] Urmia University, Department of Electronics and Computer Engineering, Iran
*Tel: 00989141398929; E-mail: r.farrokhi@urmia.ac.ir*
*DOI: 10.35633/INMATEH-59-17*

***Keywords:*** *Classification, Deposit, Machine Learning, Piezoelectric, Spray Droplet*

## ABSTRACT

*Nowadays, the indiscriminate use of pesticides for plant protection, has led to severe environmental pollution. This input accounts for a portion of the agricultural economy and should be sprayed in a way that has the highest biological efficacy and the least run-off. Therefore, real-time evaluation of spray characteristics and its classification is necessary. In the current research, a piezoelectric sensor was employed for detection of vibration signals from impaction of droplets to the active surface of the sensor. To supervised classification, the Support Vector Machine classifier as a Machine Learning model was implemented by means of extracted features from conditioned signals. By using a feature selection algorithm, six features were selected comprising mean, median, mode of signal peaks, root mean square, mean deviation and impulse factor of the signals. These features used as Support Vector Machine inputs. Model targets were spray droplet characteristics that were determined using image processing techniques on water sensitive papers. The results showed that the Linear and medium Gaussian models have the highest overall accuracy. Linear Support Vector Machine has higher accuracy and precision for training data (94.60% and 94.63%) and its model was able to predict with 92.59% accuracy. Precision of classifier model was higher than 92% for all classes. The highest miss rate of the model was approximately 15% in the separation of class C. Accurate and precise performance of linear classifier was confirmed by determining the Kappa coefficient of 0.77.*

## چکیده

*امروزه مصرف بی رویه آفت کش ها در عملیات حفظ نباتات، موجبات آلودگی شدید محیط زیست را فراهم می آورد. این نهاده که بخشی از اقتصاد کشاورزی را به خود اختصاص می دهد باید طوری استفاده شود که درعین بیشترین اثرگذاری بیولوژیک، کمترین هدررفت را داشته باشد. بنابراین ارزیابی بلادرنگ ویژگی های قطرات افشانه و طبقه بندی وضعیت های پاشش در سمپاشی امری ضروری است. در این پژوهش با بکارگیری سنسور فیلم پیزوالکتریک برخورد قطرات به سطح موثر سنسوری آشکارسازی شده و سیگنال های ارتعاشی ناشی از برخوردها جمع آوری شدند. با پیاده سازی ماشین بردار پشتیبان و استفاده از ویژگی های استخراج شده از سیگنال های آماده شده به عنوان ورودی های مدل، طبقه بندی نظارت شده انجام شد. برای نمونه گیری از قطرات از کاغذهای حساس به آب استفاده شد وبا بکارگیری تکنیک های پردازش تصویر، ویژگی های قطرات افشانه تعیین شدند و به عنوان اهداف مدل بکار رفتند. نتایج نشان داد که مدل ماشین بردار پشتیبان خطی و گوسین متوسط بالاترین صحت طبقه بندی کل را دارند. با کاهش ابعاد ویژگی ها، شش ویژگی شامل میانگین، میانه و مد پیک ها و نیز جذر میانگین مربعات، انحراف ازمیانگین و فاکتور ضربه سیگنالها انتخاب شده و مورد استفاده قرار گرفتند. طبقه بند خطی بالاترین صحت و دقت عملکرد را در داده های آموزشی داشت (94.60 درصد و 94.63 درصد) و مدل آن قادر به پیش بینی با صحت 92.5 درصد بود. دقت مدل در تفکیک تمامی طبقات ازهم بالاتر از 92 درصد بود و بالاترین نرخ خطای مدل تقریبا 15 درصد و مربوط به تفکیک طبقه C بود. صحت و دقت عملکرد مدل خطی با تعیین ضریب کاپای 0.77 مورد تایید قرار گرفت.*

## INTRODUCTION

Despite the disadvantages of using pesticides, while development and research on various methods of plant protection is ongoing, spraying is still the most effective and fastest method. Unfortunately, pesticide application techniques are such that even in the most optimistic way, too much of the pesticides enter the environment, disrupts natural balance and causes pests and diseases to emerge.

[1] *Hassan Poorvousooghi Gargari, Ph.D. Stud.; Rahman Farrokhi Teimourlou, As Prof.; Morteza Valizadeh, As Prof.*

In addition, it is not getting the desired result, its environmental and health destructive effects appear over time. About 30 to 50 percent of the sprayed solution is dissipated by drift and pouring on the soil *(Fallahjeddi, 2005)*. Also, it is difficult to determine how droplets deposits on the plant surfaces have the least run off and the highest biological efficacy. Limiting the use of chemical pesticides to the extent possible in the context of Integrated Pest Management programs and their impact on the actual goals is the basis of optimal pest management *(Mathews, 2008)*. Indiscriminate use of pesticides and their detrimental environmental impacts of spraying on various targets (e.g. pests, diseases or weeds) and the excessive waste of pesticides as an economically expensive input doubles the importance of spraying monitoring.

Methods to determine spray characteristics are typically low-precise, time-consuming and sometimes costly. The use of water sensitive papers (WSPs) is a common and practical method for estimating spray characteristics with relatively acceptable results with the advent of digital imaging and processing techniques. Expensive laser instruments and high-speed imaging in spray studies is a relatively new and precise method. The subject of atomization, spraying, and impaction of droplets to the surface have complex natures and is influenced by many parameters. Therefore, by conducting theoretical studies and using computational fluid dynamics (CFD) and experimental tests, some mathematical and numerical models are presented as well.

The time-consuming and cost-effective tests have led many researchers to find suitable alternatives such as the development of computer simulations as their main advantage is their repeatability. Spray quality is a term used to describe the properties of sprayed droplets, which can be assessed by estimation of parameters such as droplet size, spray density and deposition rate. So, the fine droplets tend to be most prone to drift and the coarse droplets, due to their high kinetic energy, penetrate better through the foliage, but are more likely to run off from the plant surfaces *(Minov et. al., 2016)*. *Koch and Knewitz (2008)* studied methods for determining the spray deposition and distribution in the vineyards. They concluded that although artificial samplers such as WSPs don't provide a detailed image of the droplet deposition, are more common due to the ease of handling and use. *Zhu et al (2011)* launched a portable scanning system for evaluating of spray deposit distribution which includes an image processing software, laptop computer and handheld card scanner. The scanning resolution can be increased up to 2400 dpi, which enables it to detect minimum 17 micron droplets. Canopy-spray interaction models were formed for predicting impaction behaviour at the leaf surface by scanning plant leaves and creating virtual leaf surface models and virtual spray models. The results revealed that the droplet retention increased with decreasing surface tension, static contact angle, droplet size and its velocity *(Dorr et. al., 2014)*. *Delele et. al. (2016)* investigated the dynamic impact behaviour of spray droplets on plant surfaces by using a high-speed camera imaging technique with multi-phase computational fluid dynamics model and volume of fluid (VOF) approach. It was reported that the process is highly influenced by the surface and droplet characteristics during impact. The various combinations of Weber, Reynolds and Ohnesorge numbers determine the droplet maximum spread factor and the number of secondary droplets produced in the impaction. These criteria can be used on a farm scale to determine droplet deposition and drift models to better understand agricultural spraying operations. A sensor was developed for measuring low volume spray deposit. The sensor surfaces had parallel conductive lines that varied the voltage of the sensor according to the droplet deposition on the surface. Two types of sensor surface with constant and variable line spacing were tested. Results showed that R-squared for the constant width line sensor and variable width sensor was 0.901 and 0.934 respectively *(Maze and Parekh, 1993)*. *Crow et. al. (2008)* developed a digital device for sensing distribution of spray deposition. The system used sensor surfaces with 15 lead conductive elements. The presence of droplets on the sensor surface caused electrical connection and their size and position were detected by the comparator circuit. They concluded by testing that the system was able to detect coarse droplets by using a low reference voltage and stated that the technique needed further investigation. A spray deposition sensing system was developed and evaluated preliminary. The sensor surface consisted of several parallel tin-plated copper traces of variable gap widths. The investigations showed that there was a significant difference in the output voltage of the sensor with different deposits and droplets size. Multiple sensing configurations and further experiments were needed to separate out the effects of application rate versus droplet sizes *(Kesterson et. al., 2015)*. A system based on solution conductivity theory was developed to quickly measure the accumulating droplet mass of sprays. The relationship between accumulating droplet mass and solution conductivity was found as a linear regression relationship with high correlation and coefficient of determination of 0.99. The relative error of this system compared with WSPs was 7.75% and droplet collection and recovery rates were 84%

and 91%, respectively *(Su et. al., 2017)*. *Wang et. al. (2019)* monitored pesticide droplet deposition with a novel capacitance sensor. The results indicated that there was a linear relationship between the deposition mass due to the impact of droplets on the sensor surface and the output voltage of the sensor. *R*-squared values for the ionized and non-ionized solutions were 0.835 and 0.882, respectively.

Piezoelectric sensors have piezoelectric materials as a sensor element. They can create electricity when subjected to a mechanical stress. They will also work in reverse, generating a strain by the application of an electric field. The piezoelectric effect can be defined by the Eq.1.

$$D = d * T + \varepsilon * E_c \quad (1)$$

Where:

*D* is the electric charge displacement, *d* is the piezoelectric coefficient, *T* is the applied stress, *ε* is the electric permittivity and $E_c$ is the electric field strength. PVDF (Polyvinylidene fluoride) film sensors have high voltage output ten times higher than piezo ceramics for the same input force. They also have the advantages of being thin and flexible and have wide frequency response, and good linearity.

WSPs are impregnated with bromophenol blue solution, which as a result of the impact of the droplets, stains are recorded on them. The papers are mounted on plant targets or on special stands. After spraying and drying, they are collected and digital images are prepared. Then, they are analyzed using image processing techniques. Volume Median Diameter (VMD) refers to the midpoint droplet size, where half of the spray volume is in droplets smaller, and half of the volume is in droplets larger than the mean. The spray deposition can be estimated by computing the volume of all droplets per unit area (*Matthews, 2008*).

Support Vector Machine (SVM) first introduced by Vapnik and Chervonenkis in 1971, is a machine learning algorithm based on statistical learning theory and is a kind of structural risk minimization based algorithms and a supervised learning model. It is optimized overall and is used today as a robust and reliable classification tool. The nature of the SVM could be of two types, either linearly separated data with the largest distance, or by using nonlinear kernel functions map data into a high dimensional space to seek a separate hyperplane. Then it can perform classification by using the constructed N-dimensional hyperplane that optimally separates data (*Vapnik, 1998*).

In this study, by using the approach of droplet impaction to surfaces and detecting the minor forces originated by impactions, vibration signals were acquired, filtered and processed. By extracting the features from the signals and implementing machine learning techniques, the classification of the sprays was performed in terms of the spray characteristics. The main objective is to provide a method or tool to evaluate the spraying characteristics for different nozzle status.

## MATERIALS AND METHODS

The main part of electronic setup is comprised of a piezoelectric polymer (PVDF) sensor model LDT1-028K manufactured by Measurement Specialties Inc. which formed a cantilever beam by using of two jaw holders (Fig. 1). The sensor specifications are listed in Table1.

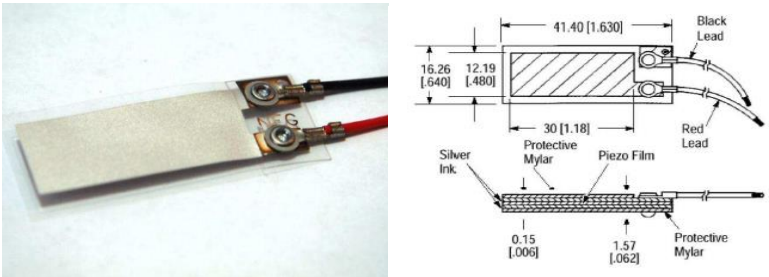


**Fig. 1 - LDT01-28K film sensor and its dimensions in mm [inches]**

**Table 1**

**LDT1-028K PVDF film sensor specifications**

| | |
|---|---|
| **Minimum Impedance** | 1MΩ |
| **Preferred Impedance** | 10MΩ and higher |
| **Output Voltage** | 10mV-100V depending on force and circuit impedance |
| **Storage Temperature** | -40℃ - +70℃[-40℉- 60℉] |
| **Operating Temperature** | 0℃ - +70℃[32℉-60℉] |

To increase the local resolution of the sensor, a sliding plastic plate with 10 x 10 $mm^2$ aperture was installed on sensor so that 1 $cm^2$ effective sensor surface is created in order to decrease the number of spray droplets impact or avoid multiple impacts. It relatively ensures that each sensor signal will be produced from one droplet. An ARDUINO board was used as an analog to digital converter and microcontroller. Signal amplifier module was designed using Proteus Pro 8.8 software and after it was built, it was mounted on the ARDUINO board (Fig.2).

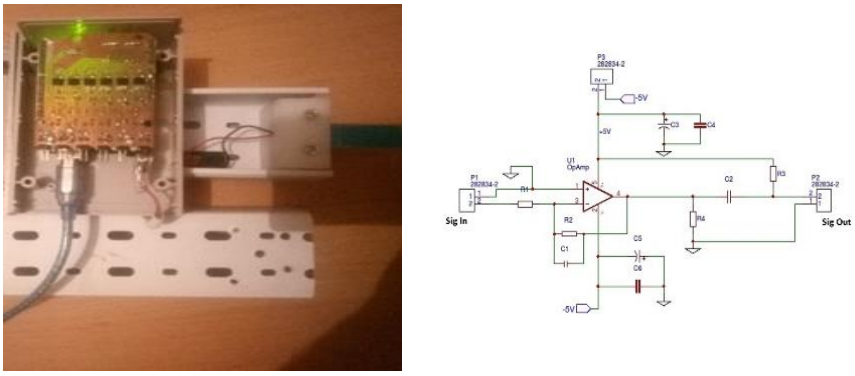


**Fig. 2 - Amplifying module on board and its circuit**

LM358A operational amplifiers were used to amplify the signals. The data acquisition system was developed using the ARDUINO and serial communication script on the board side, as well as the Excel Macro on the laptop computer side, which could handle sampling frequency about 600 Hz. To reduce the noise effects on the signals, a shielded cable was used to transmit the signal, and a USB shielded cable was used to connect the board to the laptop computer.

Despite the development of new atomization and spraying techniques such as centrifugal and air-assisted techniques, hydraulic nozzles are used in most countries for spraying. The size and distribution of the droplets in these nozzles is very non-uniform and the application rate is very high. Hollow cone nozzles are classified into three types of spiral, axial whirl and tangential whirl, and the first type is mostly used in the agricultural applications (Fig.3).


**Fig. 3 - Three types of hollow cone nozzles**

To perform the spraying tests, a laboratory spraying setup was provided including a tank, centrifugal pump, barometer, and adjustable lance equipped with a hollow cone nozzle. By twisting Lance handle, five spraying status were determined including I, II, III, IV and V. The tap water was used as the spray liquid and performed primary tests using WSPs as droplet sampling surfaces and sensor system as a means of sensing vibration signals. To control the spraying time length, a metal base frame was provided with a sliding plastic plate as a barrier. The frame was located closer to the nozzle and in front of it. For sampling with WSPs and Sensor, barrier plate was raised and released. All spraying tests were carried out in the same spraying condition. The samples of vibration signals due to droplets impaction are shown in Fig.4.

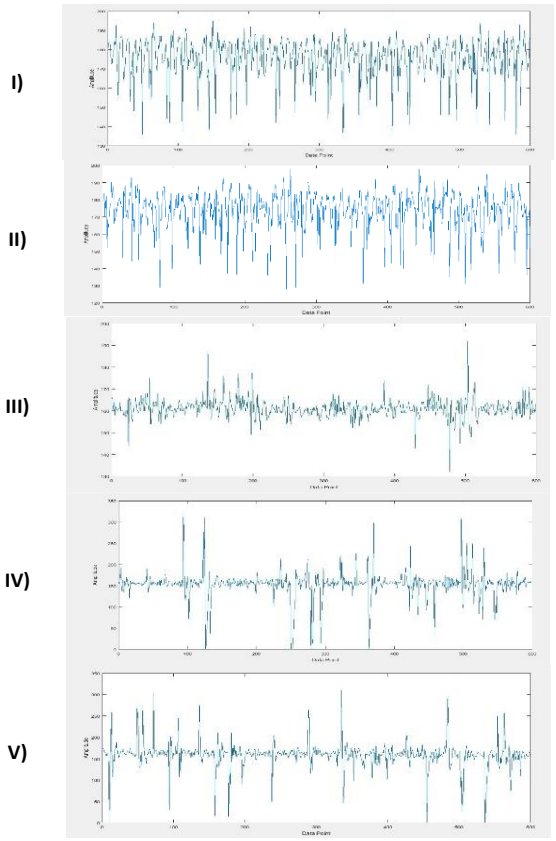


**Fig. 4 - Samples of vibration signals for five spraying status**

Spray droplets were sampled by WSP with 30 replications for each spray status. The papers were scanned and digital images were obtained (Fig.5). By using image processing algorithm developed by coding in MATLAB environment it was able to identify objects and their properties by performing low-level and mid-level processing with segmentation and labelling functions (Poorvousooghi Gargari, 2013). By analyzing the papers, the five spray classes were separated in terms of VMD and spray deposition. These classes were used as SVM targets.

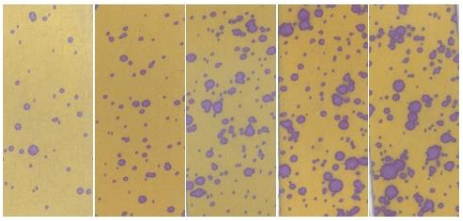

**Fig. 5 - Digital images of water sensitive papers**

Signal processing includes signal conditioning and extraction of features from the signals. Initially, by applying the moving average filter and the band-stop filter, the signals were smoothed and filtered. Ninety signals with one second duration were selected for each spraying status. Twenty six features were extracted using a developed algorithm that includes peak detection functions, statistics and vibration features computing functions. By means of peak analysis, these features were extracted:
Mean of Peak values is the central value of a discrete set of values (Eq.2).

$$\mu_p = \frac{\sum_{m=1}^{M} p_m}{M} \quad (2)$$

Median of Peak values is the value separating the higher half from the lower half of samples (Eq.3).

$$median_p = l + \frac{h}{f}\left(\frac{M}{2} - c\right) \quad (3)$$

Where:

$l$ is lower class boundary of median class, $h$ is size of median class, $f$ is frequency corresponding to the median class, $M$ is sum of frequencies and *c* is cumulative frequency preceding median class.

Mode of peak values is the value that appears most often (Eq.4).

$$mode_p = l + h\left(\frac{f_m - f_1}{2f_m - f_1 - f_2}\right) \quad (4)$$

Where:

$l$ is lower class boundary of modal class, $h$ is size of modal class, $f_m$ is frequency corresponding to the modal class, $f_1$ is frequency proceeding the modal class and $f_2$ is frequency proceeding the modal class.

Some important statistical and vibration features extracted from the signals and their equations are listed in Table 2.

**Table 2**

**Some important features extracted from signals**

| Feature | Equation | Feature | Equation |
|---|---|---|---|
| **Mean** | $\mu = \frac{\sum_{n=1}^{N} x_n}{N}$ | **Mean Deviation** | $MD = \frac{\sum_{n=1}^{N} \lvert x_n - \mu \rvert}{N}$ |
| **Root Mean Square** | $RMS = \sqrt{\frac{\sum_{n=1}^{N} (x_n)^2}{N}}$ | **Moment (order i)** | $Mom_i = \frac{\sum_{n=1}^{N} (x_n - \mu)^i}{N}$ |
| **Kurtosis** | $Ku = \frac{\sum_{n=1}^{N} (x_n - \mu)^4}{(N-1)(STD)^4}$ | **Impulse Factor** | $IF = \frac{Max(x_n)}{\frac{1}{N}\sum_{n=1}^{N} \lvert x_n \rvert}$ |

By means of reducing the volume of SVM inputs, the processing speed can be increased, which reduces the time required for modeling and increases precision. To dimensionality reduction of the features, Correlation-based Feature Subset Evaluation algorithm and Best First method in Weka software were used. More efficient and main features were selected including mean, median, mode of peak values, root mean square, mean deviation and impulse factor of signals. The features matrix was created and 70% of the data were considered as training data and 30% as test data. In other words from 90*6 features for each spraying Status, 63*6 were used as training data and 27*6 as test data.

Classification was implemented using the SVM classifier and by cross validation method in MATLAB software. The learning process was performed using SVM classifier with different kernel functions on the training data, the models were tested using test data and two most accurate learning models were extracted. The confusion matrix was used to analyze the classifier performance. In this matrix, the criteria such as Accuracy, Sensitivity, Specificity and Precision were used as the overall evaluation of the classifiers. The equations of these criteria are as follows:

$$Accuracy = \frac{TP+TN}{TP+FN+FP+TN} \quad (5)$$

$$Sensitivity = \frac{TP}{TP+FN} \quad (6)$$

$$Specificity = \frac{TN}{FN+TN} \quad (7)$$

$$\text{Precision} = \frac{TP}{TP+FP} \quad (8)$$

Where:

*TP* is the number of true positive instances, *TN* is the number of true negative instances, *FP* is the number of false positive instances and *FN* is the number of false negative instances.

Cohen's kappa coefficient is used as criterion for further evaluation of classifier performance and indicates the degree of agreement between predicted and actual instances for all classes (Eq.9).

$$\mathbb{K} = \frac{P_0 - P_e}{1 - P_e} \quad (9)$$

Where:

$P_0$ is the observed relative agreement among actual values and prediction values and $P_e$ is the hypothetical probability of chance agreement or probability that both prediction and actual values are positive or negative. Interpretation of Kappa coefficient is presented in Table 3.

**Table 3**

**Kappa interpretation guidelines of Landis and Koch (1977)**

| Kappa statistic | Strength of Agreement |
|---|---|
| <0 | Poor |
| 0.01-0.20 | Slight |
| 0.21-0.40 | Fair |
| 0.41-0.60 | Moderate |
| 0.61-0.80 | Substantial |
| 0.81-1.00 | Almost Perfect |

## RESULTS

The analysis of water sensitive papers indicated that the averaged VMD for the five spraying status were estimated to be 580, 621, 719, 903 and 1267 µm. Also, the averaged spray depositions were 0.52, 0.65, 1.26, 1.47 and 4.07 µl/cm$^2$. This points out that wisting the lance handle changes the nozzle status and thus increases the droplet size and the spray deposition. It is clear that the increase in droplet size has a slight slope in three first statuses and is evident in status IV and is sharp in status V. In the case of spray deposition, since the volume is theoretically directly related to the third power of the diameter, the slope of the increase is very significant. These results show that five spray classes were separable by using image processing technique including A,B,C,D and E. These classes were used for SVM classifier targets. Table 4 presents spray classes and their specifications.

**Table 4**

**Spray classes and their specifications**

| Nozzle status | Averaged VMD | Averaged Deposition | Spray Class |
|---|---|---|---|
| I | 580 | 0.52 | A |
| II | 621 | 0.65 | B |
| III | 719 | 1.26 | C |
| IV | 903 | 1.47 | D |
| V | 1267 | 4.07 | E |

Signal processing, feature extraction and finally feature selection provide data for use as SVM inputs. The averaged features of signals for each nozzle status are presented in Table 5.

**Table 5**

**The averaged features of Signals**

| Nozzle status | $\mu_p$ | $median_p$ | $mode_p$ | $RMS$ | $MD$ | $IF$ |
|---|---|---|---|---|---|---|
| I | 193.47 | 193.38 | 188.10 | 189.15 | 2.59 | 1.06 |
| II | 192.19 | 192.05 | 186.92 | 187.75 | 2.66 | 1.07 |
| III | 179.77 | 179.10 | 177 | 177.66 | 1.74 | 1.09 |
| IV | 181.14 | 175.64 | 170.50 | 171.88 | 9.61 | 1.60 |
| V | 189.12 | 182.88 | 177.04 | 177.88 | 9.69 | 1.62 |

The result of SVM classifier implementation shows that the overall accuracy of classifier with Linear, Quadratic, Cubic, Fine Gaussian, Medium Gaussian and Coarse Gaussian kernel functions are 94.6, 91.1, 90.5, 91.7, 94.3 and 89.2%, respectively. Linear and Medium Gaussian have the highest performance accuracy in training and was further investigated. The prediction models were obtained and tested with test data.

The overall evaluation criteria of the SVM classifier with linear and medium Gaussian kernels are presented in Table 6.

**Table 6**

**The overall evaluation criteria of the SVM classifiers**

| | Data | Accuracy | Sensitivity | Specificity | Precision | Kappa |
|---|---|---|---|---|---|---|
| **Linear kernel** | Training | 94.60 | 94.60 | 98.65 | 94.63 | 0.83 |
| | Test | 92.59 | 92.59 | 98.15 | 92.58 | 0.77 |
| **Gaussian kernel** | Training | 94.29 | 94.29 | 98.57 | 94.31 | 0.82 |
| | Test | 90.37 | 90.37 | 97.59 | 90.56 | 0.70 |

Based on data from table 6, overall 92.58 percent of the cases classified by the linear model are accurate. Overall precision of classifier for predicting is 92.58%. SVM with linear kernel has performed better on training data and the evaluation criteria are great, SVM with Gaussian kernel performed much better in the training process but predicting with the obtained model has been weaker. The values of kappa coefficient are within the range of 0.61-0.80 that indicate the overall substantial agreement between the predicted and the target instances and validate classifier performance. These values for training show almost perfect agreement.

However, the values of the overall classification criteria are desirable and acceptable. Therefore, the selected features can be used as SVM inputs to reduce the computational load of the processor and reduce the prediction time. The classification error using the linear kernel is up to 7.41%. Table 7 presents the sensitivity and precision of the linear classifier for each spray class.

**Table 7**

**The Sensitivity and Precision of classifier for each class**

| Class | Sensitivity | | Precision | |
|---|---|---|---|---|
| | Training Data | Test Data | Training Data | Test Data |
| **A** | 96.83 | 96.30 | 96.83 | 92.86 |
| **B** | 93.65 | 92.59 | 95.16 | 92.59 |
| **C** | 92.06 | 85.19 | 93.55 | 92.00 |
| **D** | 93.65 | 92.59 | 90.76 | 92.59 |
| **E** | 96.83 | 96.30 | 96.83 | 92.86 |

The linear SVM model is less sensitive to class C separation but in separation of class A and E is very sensitive. Miss rate (False Negative Rate) of linear SVM model in separation of class C from other 4 classes is highest (approximately 8% for training data and 15% for test data). Precision of classifier model is higher than 92% for all class separation. Low precision of classifier in separating class D from class C in training is due to its low accuracy in the separation of class C. ROC (Receiver Operating Characteristics) curves were obtained for test data that show that specificity is close to 100 in all classes and minimum sensitivity is 85% in Class C. Area Under Curve (AUC) for this class is within acceptable and good range (80-90) and classifying model is sufficiently reliable (Fig.6).

Although classification of spray droplet has not been reported so far, spraying quality evaluation has been investigated with often expensive techniques in several papers. Sun et. al. (2017) reported a relative system error less than 7.75% in a system that works based on solution conductivity compared with WSPs. Baijing and Li (2011) used spectral technique and regression models to predict droplet concentration with an average error of 6.41. The method proposed by *Yang Jun et. al.* (2017) using the LiDAR technique for detection of spray droplet distribution had relative error less than 7% compared with WSPs.

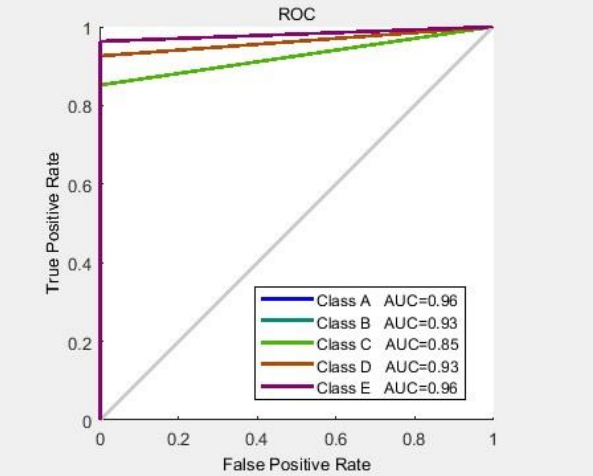


**Fig. 6 - ROC curves for all classes in training data**

## CONCLUSIONS

The research was conducted for the nozzle spraying characterization in agricultural activities. Analysis of vibration signals as a result of spray droplets impaction to the active sensor surface was considered. Spraying tests were carried out by using an adjustable nozzle. Spray droplets were sampled with water sensitive papers, and specifying characteristics were identified using image processing techniques. Feature extraction and selection algorithms were used for determination of effective signal features. The Support Vector Machine (SVM) classifier was implemented with various kernel functions for supervised classification and their performances were studied. As a consequence, the conclusion is summarized below:

1) Results of machine learning process showed that accuracy and precision of SVM models with various kernel functions were acceptable. Therefore, SVM models have high potential for classification of spraying status.
2) Linear SVM model has higher overall accuracy and precision than others. The model is capable of separating the spray classes with 92.59% overall accuracy. Kappa coefficient for the model was 0.77 which indicates substantial agreement in classification. Within class analysis, Precision of classifier model is higher than 92% for all class separation. The lowest sensitivity of model is related to class C. Miss rate for class C was the highest value (approximately 15%).
3) Due to the advantages such as low cost, real time outputs, easy set up and faster execution of the method, it can be uses as efficient and useful tool for the spray characterization in fields and testing centres. Manufacturer of nozzles and spraying equipment can also use it for preparation of nozzle instructions and guidelines.

## REFERENCES

[1] Baijing Q., Lei Y., (2011), Non-contact measurement of droplets concentration on the leaf based on Vis/NIR spectroscopy. *Fuzzy Systems and Knowledge Discovery (FSKD), Eighth International Conference;*

[2] Crowe T., Downey D., Giles D., (2005), Digital device and technique for sensing distribution of spray deposition. *Transactions of the ASAE,* vol.48(6), pp.2085-2093;

[3] Delele M. A., Nuyttens D., Duga A., Ambaw A., Lebeau F., Nicolai B., Verboven P., (2016), Predicting the dynamic impact behaviour of spray droplets on flat plant surfaces. *Soft Matter*, vol.12(34), pp.7195-7211;

[4] Dorr G.J., Kempthorne D.M., Mayo L.C., Forster W.A., Zabkiewicz J.A., McCue S.W., Hanan J., (2014), Towards a model of spray–canopy interactions: interception, shatter, bounce and retention of droplets on horizontal leaves. *Ecological Modeling,* vol.290, pp.94-101;

[5] FallahJeddi R., (2005), *Calibration of conventional sprayers in IRAN*. AREEO Pubs. Karaj. Iran, (in Farsi);

[6] Kesterson M.A., Luck J.D., Sama M.P., (2015), Development and Preliminary Evaluation of a Spray Deposition Sensing System for Improving Pesticide Application. *Sensors*, vol.15(12), pp.31965-31972;

[7] Koch H., Knewitz H., (2014), Methodology and sampling technique of spray deposit and distribution measurement in vineyards. *Nachrichtenbl. Deut. Pflanzenschutzd*, 60(2);

[8] Landis J.R.; Koch G.G., (1977), The measurement of observer agreement for categorical data. *Biometric*, vol.33(1), pp.159–174;
[9] Matthews G., (2008), Pesticide application methods: *John Wiley & Sons*.
[10] Maze R. C., Parekh K.T., (1993), Sensor for measuring low volume spray deposit. Paper presented at the *American Society of Agricultural Engineers Meeting* (USA);
[11] Measurement Specialties Inc., (2013), *Piezo Film Sensors*. Technical Manual;
[12] Minov S.V., Cointault F., Vangeyte J., Pieters J.G., Nuyttens D., (2016), Spray Droplet Characterization from a Single Nozzle by High Speed Image Analysis Using an In-Focus Droplet Criterion. *Sensors*, vol.16(2), p.218;
[13] Poorvousooghi Gargari H., (2013), *Study the Performance of Electrostatic Spraying System on Leaf Surfaces using Image Processing*. MSc Dissertation. Bu-Ali Sina University. IRAN. (in Farsi);
[14] Sun C., Qiu W., Ding W., Gu J., (2017), Design and Experiment of a Real-Time Droplet Accumulating Mass Measurement System. *Transactions of the ASABE,* vol.60(3), pp.615-624;
[15] Vapnik V., (1998), *Statistical Learning Theory*: John Wiley and Sons, New York;
[16] Wang P., Yu W., Ou M., Gong C., Jia W., (2019), Monitoring of the Pesticide Droplet Deposition with a Novel Capacitance Sensor. *Sensors,* vol.19(3), p.537;
[17] Yongjun Z., Shenghui Y., Lan Y., Hoffmann C., Chunjiang Z., Liping C., Yu T., (2017), A novel detection method of spray droplet distribution based on LIDARs. *International Journal of Agricultural and Biological Engineering,* vol.10(4), pp.54-65;
[18] Zhu H., Salyani M., Fox R.D., (2011), A portable scanning system for evaluation of spray deposit distribution. *Computers and Electronics in Agriculture*, vol.76(1), pp.38-43.

# DEVELOPMENT AND IMPLEMENTATION OF A MOBILE APPLICATION FOR THE MEASUREMENT OF TEMPERATURE AND RELATIVE HUMIDITY IN GREENHOUSE CROPS
# /
# *DESARROLLO E IMPLEMENTACIÓN DE UN APLICATIVO MÓVIL PARA LA MEDICIÓN DE TEMPERATURA Y HUMEDAD RELATIVA EN INVERNADEROS*

**Lina Marcela Rodríguez-Soto[1)], Arley Bejarano Martínez[1)], Iván Darío Arellano-Ramírez[1*)]**
[1)] Technological University of Pereira, Pereira, Colombia
*Tel: +57-6-313-7147; E-mail: arellano@utp.edu.co*
*DOI: 10.35633/INMATEH-59-18*

***Keywords:*** *agriculture innovation, greenhouse crop, mobile application, monitoring system, rural engineering.*

## ABSTRACT

*The tendency in recent years to improve worldwide agricultural production has opened the door to innovative research techniques to prevent diseases, pests, and negative consequences due to climate variations in crops. This study aims to develop an acquisition system using the embedded BeagleBone Black and the DHT 22 sensor, which allow measuring the physical parameters of temperature and relative humidity; these were registered in a database that was created in MySQL. The system was implemented within a greenhouse crop; additionally, a mobile application was developed, written in Kotlin language, to facilitate monitoring the physical parameters of temperature and relative humidity remotely, so that farmers can collect valuable information about their crops wherever they are. This development was carried out using a client-server structure, making use of free software and hardware, which makes for a low-cost, easily-implemented system for farmers. The monitoring system worked as expected, and the information obtained was reliable. The results show that the implementation is useful in greenhouse agriculture and that, through digital innovation, effective agricultural practices can be improved which could increase production and decrease costs, making use of modern technologies.*

## RESUMEN

*La tendencia en los últimos años de mejorar la producción agrícola a nivel mundial ha permitido desarrollar técnicas para prevenir los cultivos de enfermedades, plagas y de consecuencias negativas generadas por las variaciones climáticas. En este estudio, se presenta el desarrollo de un sistema de adquisición, utilizando la tarjeta de desarrollo BeagleBone Black y sensores, que permite medir las variables físicas de temperatura y humedad relativa dentro de un cultivo en invernadero para ser registradas en una base de datos, creada en Mysql; adicionalmente, se desarrolló un aplicativo móvil escrito en lenguaje Kotlin con el fin de que los campesinos puedan visualizar la información valiosa de manera remota acerca de sus cultivos. Todo este desarrollo se realizó con una estructura cliente-servidor, haciendo uso de software y hardware libre, lo que hace que el sistema sea de bajo costo y que se pueda implementar este tipo de tecnología en el campo. Los resultados muestran que la implementación es útil en invernaderos. Este estudio confirma que las prácticas agrícolas efectivas, que conducen a un aumento en la producción y una disminución en los costos, pueden ser impulsadas a través de la innovación digital.*

## INTRODUCTION

Agriculture is one of the oldest activities of the primary sector of the economy. Its origin dates to the Stone Age (year 7000 BC), when human societies went from nomadism to sedentary life, forming the first civilizations *(Tauger, 2010)*.

Today, agriculture continues to be an important activity in the worldwide economy, especially in developing countries. For example, in India, agriculture is one of the main sources of income for the population and contributes significantly to the economy of the country *(Channe et al., 2015)*. In Thailand, agriculture has driven the development of the rural economy, which is why Thai farmers have a sustainable system for small-farmer management based on basic principles such as the cost reduction of agricultural supplies and food security; furthermore, agriculture is adopted as a philosophy of life *(BCN, 2017; Tummarattananont et al., 2018)*.

In China, the level of modernization is still far behind compared to developed countries, even so, in recent years, technological developments have been increasing, placing China among one of the most productive agricultural countries in the world *(Zhang, 2018)*.

In African and Latin American countries, techniques must be developed in order to produce more, since there is more population to feed, and the amount of land and water is increasingly limited *(García et al., 2017)*. Colombia is a country with an excellent geographical location and great natural resources *(NRE, 2013)*, despite this, more and more farmers are leaving the countryside, since they do not have the necessary conditions to produce better, and higher quality crops, due to the high costs of supplies and transportation.

In recent years, crops have been affected worldwide by climatic variations, which are increasingly adverse *(Ortega et al., 2018)*. In such cases, technology plays an important role to generate more efficient production with a lower environmental impact. Precision agriculture has been a fundamental part of an agricultural tendency in recent years, as it has been at the root of the use of new technologies in agriculture that involve the use of sensors, wireless monitoring systems, devices for irrigation management, and geographic information systems in order to optimize resources such as water, energy, fertilizers, pesticides, etc. *(Atzberger, 2013; Satyanarayana and Mazaruddin, 2013; Aggarwal et al., 2013; Borges et al., 2014; Khriji et al., 2014; Li et al., 2018; Zhao et al., 2018; Dholu and Ghodinde, 2018)*.

Recently, the development of mobile applications has been a useful tool in agriculture, *(Suleman et al., 2018; Valiente et al., 2018; Alzarliani et al., 2019; Gómez-Chabla et al., 2019)*; also, mobile applications have been important in intelligent irrigation systems *(Aleotti et al., 2018; Barkunan et al., 2019; Joshi and Goudar, 2019; Muangprathub et al., 2019)*. An example of this implementation was carried out in Pune, India, in 2018. An electronic system that includes a node composed of temperature sensors, relative humidity and soil moisture was developed. This system collects data from these variables and, at the same time, exercises control over them, since the activation of the irrigation valve depends on said data. The data is stored in the cloud and visualized through a mobile application developed in Android. The hardware was made using MCU, a DHT11 sensor, and WiFi module *(Dholu and Ghodinde, 2018)*.

The concept of smart farm arises from the combination of IoT, Cloud computing, Big data and Mobile technology, which are known as an ICBM platform. A recent ICBM implementation was done in the Republic of Korea, in 2019. A management system was implemented to monitor environmental data from inside a greenhouse, and in turn, to control the crop. The collected data were analyzed in the cloud to improve quality and productivity *(Lee et al., 2019)*.

The cultivation of greenhouse crops has many advantages. Crops can be planted throughout the year and are protected from atmospheric phenomena, such as heavy rains, winds, hail falls and high temperatures. Moreover, it is possible to better control pests and diseases. Fertilizer products are used more efficiently. All these factors lead to higher productivity and savings on agricultural supplies. In Colombia, most farmers use greenhouse crops without knowing what happens inside them, because they do not keep records of the temperature and relative humidity, parameters that are fundamental for the development of the plants. When farmers cover crops with plastics, the temperature and relative humidity rise causing problems that affect production.

Therefore, the purpose of this article is to present the design, development, and implementation of a mobile application, which monitored the physical parameters of temperature and relative humidity of the greenhouse crop Horfrubella, located in the La Bella region in the city of Pereira, Colombia. Real-time monitoring allows farmers to obtain a data record, which facilitates decision making in order to increase production and prevent diseases and pests. To carry out this process, a two-phase system is proposed: hardware and software. The first phase refers to the acquisition system, where the DHT22 digital sensor and the BeagleBone Black card are used to record data and store it in the database. The second phase refers to the mobile application, created in Kotlin, where farmers can easily access information, as it has an easy-to-use graphical interface, which can be installed on any smart mobile device, now available to users, even in rural areas.

This article is structured as follows: first, the materials and methods used to carry out the implementation of the monitoring system are presented, detailing the development of the mobile application. Next, the results of its application in the Horfrubella greenhouse crop in the rural area of the city of Pereira, Colombia are reported. Finally, the main conclusions are presented, in which the reliability of the proposed system is emphasized.

## MATERIALS AND METHODS

The present methodology shows the development of the monitoring system of the greenhouse crop Horfrubella, which is divided in two stages: hardware and software (see Fig. 1). The first stage required the following for its implementation: an acquisition system, a telemetry system, an information system, and the interconnection of the telemetry system with the information system. For the software stage, the design and creation of the mobile application was necessary.

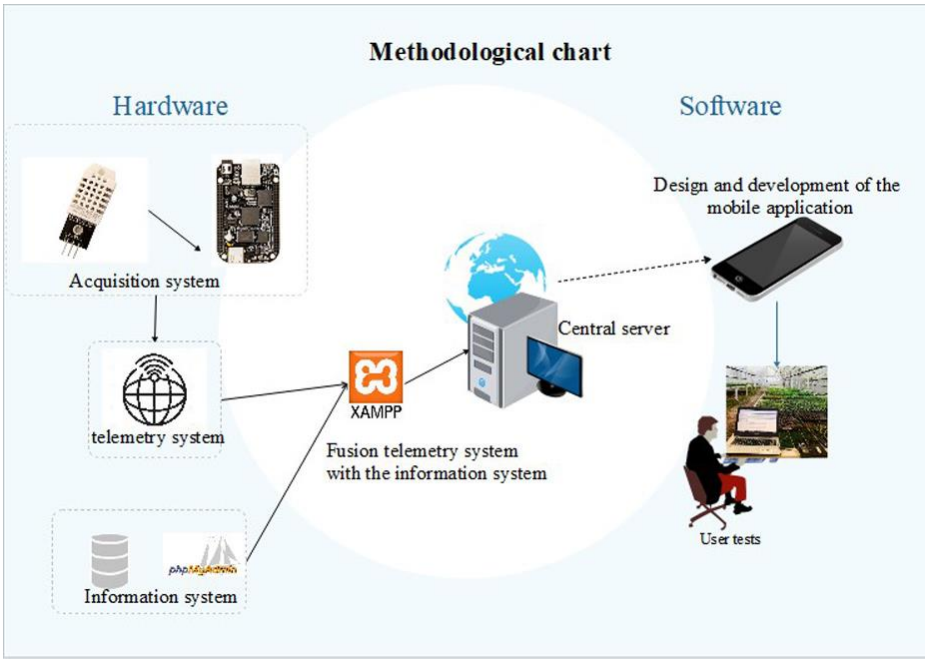


**Fig. 1 – The flowchart of the methodological development**

### *Hardware*

*Data Acquisition System*

In this step, the values of the physical magnitudes of temperature and relative humidity were captured. To carry out this process, the DHT22 digital sensor, which consists of a thermistor and a capacitive humidity sensor, was connected through one of the general purpose in/out ports of the embedded BeagleBone Black (BBB) system, which was chosen because of its functionality: its low cost; its low power consumption; and it performs well compared to other computer systems.

*Telemetry system*

Through the telemetry system, the information obtained in the previous step was sent to the central server. To carry this out, an algorithm was created in C ++. In the first phase of the program, the physical parameters of temperature and relative humidity were read using the libraries of Adafruit Industries. Then, the stored measurements were transmitted to the database using the client-server architecture. The free and open-source Apache server was used as a web server. The client, in this case, was the algorithm created, and is responsible for sending the request to the server, and the Apache server has the function of processing programs and ensuring communication.

*Information system*

The manager MySQL and the phpMyAdmin tool, a web application written in PHP, were used for the management of the database of the obtained information. Fig. 2 shows the database that was created through the tool phpMyAdmin. The table has four columns: the first corresponds to the Id, which is the number of the record; the second column stores the temperature value; the third stores the humidity variable; the last column records the date the information was collected.

*Interconnection of the information system with the telemetry system*

To store the collected values in the database, the free and open source cross platform XAMPP was used, using the modules Apache and MySQL. Fig. 3 shows the flowchart of the complete system. The first step corresponds to the initialization of the BBB, XAMPP and phpMyAdmin, followed by the execution of the algorithm in the BBB, where the sensor readings are included. Then the connection is established, and, finally, the values collected in the database are recorded.

***Software***

For the visualization stage, a mobile application was developed using the Kotlin programming language. This programming language is the new language for programming native applications for the Android operating system. In this phase, the database query was carried out through the Volley library. This Android library allows communication through port 80. The queries correspond to the search for the date on which the measurements were made. The same client-server structure is used at this stage, but instead of capturing data, a request of information to the server is made. Once the data are obtained, they are plotted to be easily visualized and to obtain data on the crop users want to observe. Finally, a simple and intuitive visual phase is proposed, with the aim to create a user-friendly application.

Estructura de tabla | Vista de relaciones

| # | Nombre | Tipo | Cotejamiento | Atributos | Nulo | Predeterminado | Comentarios | Extra | Acción |
|---|---|---|---|---|---|---|---|---|---|
| 1 | id | int(10) | | | No | *Ninguna* | | AUTO_INCREMENT | Cambiar Eliminar Más |
| 2 | temperatura | varchar(5) | latin1_spanish_ci | | No | *Ninguna* | | | Cambiar Eliminar Más |
| 3 | humedad | varchar(5) | latin1_spanish_ci | | No | *Ninguna* | | | Cambiar Eliminar Más |
| 4 | fecha | timestamp | | | No | CURRENT_TIMESTAMP | | | Cambiar Eliminar Más |

**Fig. 2 – Structure of the database**

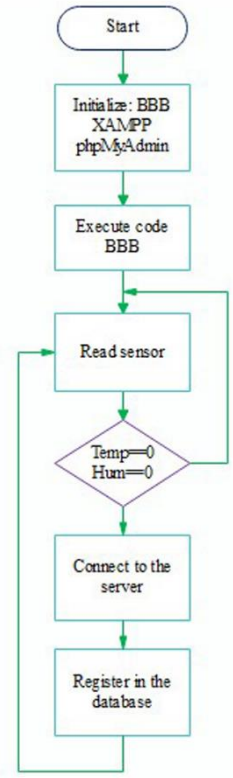


**Fig. 3 – Flowchart of the telemetry and information systems**

**RESULTS**

The graphic interface (GI) of the mobile application was designed in such a way that any farmer could easily use it, as it is user-friendly and easy to handle. Then, algorithms were created in order to visualize the data in the mobile application, and, finally, these algorithms were merged with the information system. The GI has 3 screens: the main menu, the desired query date selection panel, and the search results (Fig. 4).

In order to verify the correct functioning of the monitoring system of the physical parameters of temperature and relative humidity, several tests were carried out in three places with different characteristics. The first place was in the facilities of the Technological University of Pereira, where it was possible to verify that the acquisition and telemetry system worked as expected; the second place corresponded to a farm located in the rural area of Pereira city, where reliability tests were carried out on a tomato crop. The system captured data every five minutes. The data was taken during four days at different times evidencing that the system did not present dead times nor intermittence. Finally, the system was implemented in the La Bella region, in the Horfrubella greenhouse crop (see Fig. 5). In Horfrubella, they grow lettuce, tomatoes, onions, carrots, beets, beans and broccoli from seeds. When seedlings are developed, they are taken to low-income families to be transplanted in their gardens and, in this way, produce their food.

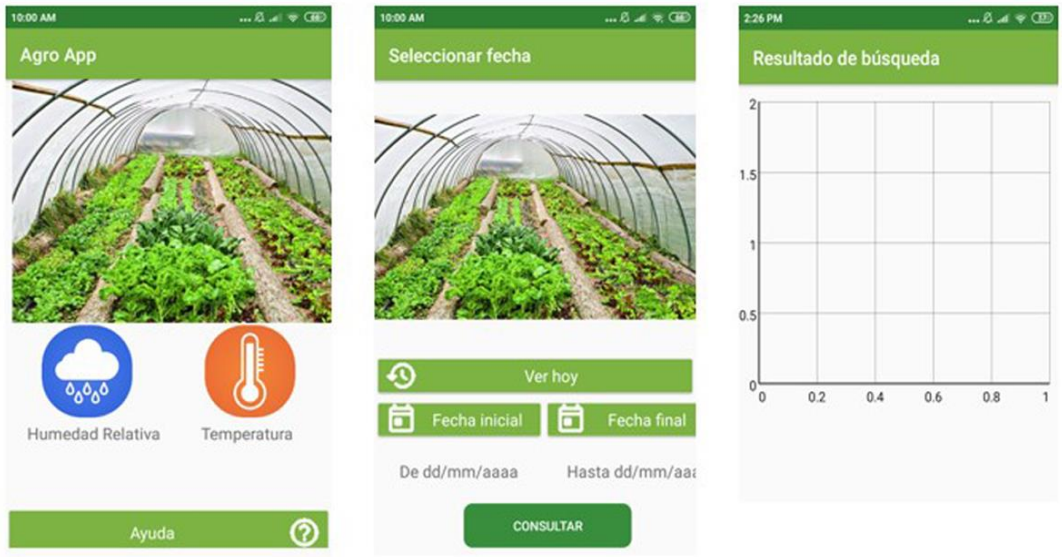


**Fig. 4 – Graphic interface of the mobile application**

**Fig. 5 – Physical implementation of the monitoring system in the greenhouse crop Horfrubella**

In Figure 6, you can see the database table created through phpMyAdmin. In the columns, it is possible so see the following variables: record number, temperature value in Celsius, relative humidity value, and date and time of the data collection.

The information collected through the DHT22 sensor can be consulted directly on the phpMyAdmin website. To do this, the XAMPP server must be open, enabling Apache and MySQL modules. Information can also be consulted through the developed mobile application. The data is displayed in an easy-to-interpret graphic. The search results yield a title corresponding to the magnitudes of temperature or relative humidity from which the information is to be obtained. For instance, in Fig. 7a the results of temperature are shown and in Fig. 7b, the relative humidity results are shown.

The results obtained showed that the proposed monitoring system worked properly, and that the information collected was reliable. In addition, more sensors could be added to the monitoring system in order to obtain more information, and, with it, implement a control system according to the needs of the greenhouse crop, increasing productivity.

| ←T→ | | id | temperatura | humedad | fecha |
|---|---|---|---|---|---|
| ☐ | Editar Copiar Borrar | 437 | 21.20 | 78.30 | 2019-03-20 08:51:31 |
| ☐ | Editar Copiar Borrar | 438 | 21.20 | 78.80 | 2019-03-20 08:56:31 |
| ☐ | Editar Copiar Borrar | 439 | 21.29 | 78.40 | 2019-03-20 09:01:32 |
| ☐ | Editar Copiar Borrar | 440 | 21.20 | 78.30 | 2019-03-20 09:06:32 |
| ☐ | Editar Copiar Borrar | 441 | 21.20 | 77.19 | 2019-03-20 09:11:33 |
| ☐ | Editar Copiar Borrar | 442 | 21.20 | 77.50 | 2019-03-20 09:16:34 |
| ☐ | Editar Copiar Borrar | 443 | 21.29 | 78.09 | 2019-03-20 09:21:34 |
| ☐ | Editar Copiar Borrar | 444 | 21.20 | 79.00 | 2019-03-20 09:26:35 |
| ☐ | Editar Copiar Borrar | 445 | 21.29 | 79.09 | 2019-03-20 09:31:35 |

**Fig. 6 – Database of the obtained values of the greenhouse crop**

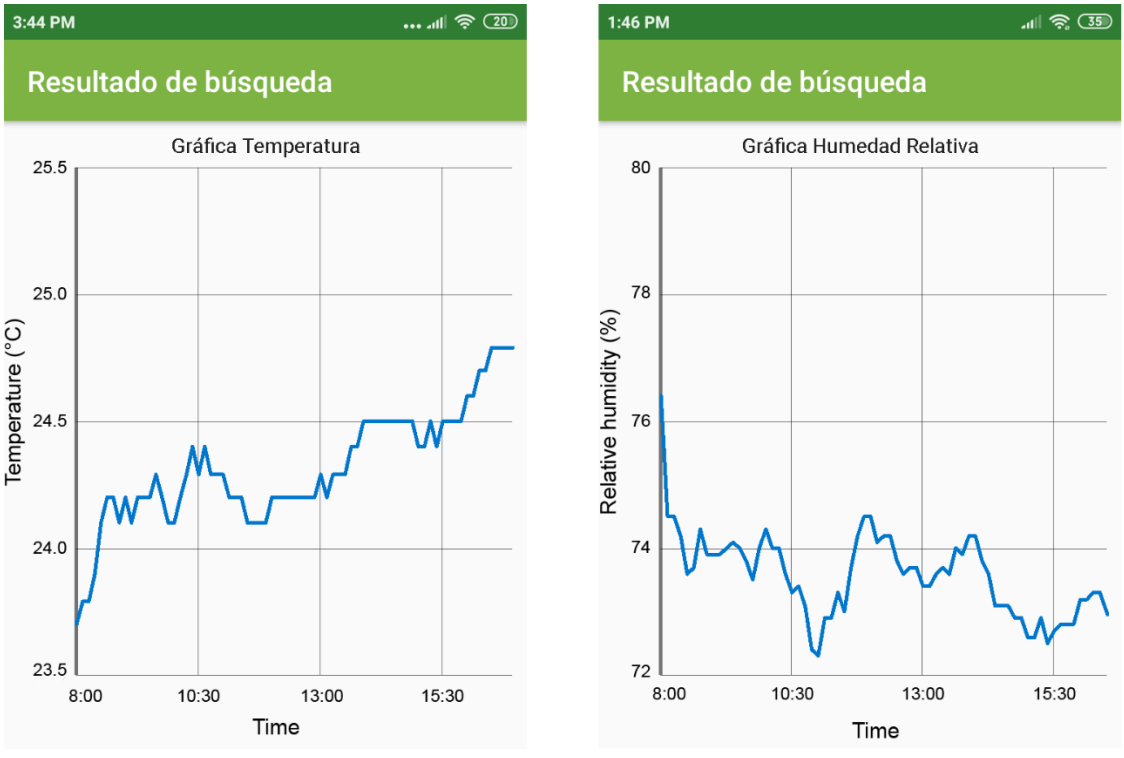


*a)* *b)*

**Fig. 7 – Search results of:**
*a) Temperature; b) Relative humidity*

## CONCLUSIONS

A mobile application was designed and applied in greenhouse crops to monitor temperature and relative humidity in order to improve crop yields, increase quality of products, and reduce production costs. The proposed system had two stages; the first was implemented using a BeagleBone Black and a DHT22 sensor through which the data acquisition was performed. In the second stage, the graphic interface was designed and implemented to visualize the information collected, which is used to make decisions to improve production and detect diseases or possible pests in crops. The monitoring system implemented was reliable, since in the tests carried out, it did not show intermittence, nor dead times, and the capture time was constant. The developed monitoring system was installed in the greenhouse crop Horfrubella in the rural region of La Bella, in the city of Pereira, Colombia. This system can be implemented to remotely and efficiently monitor greenhouse crops, helping farmers to acquire real-time, necessary information to help them make decisions that generate improvements to crops. This case study shows high potential for digital technology applications in agriculture.

## ACKNOWLEDGEMENTS

The authors would like to express their gratitude to the Horfrubella Association and the Faculty of Agricultural Sciences of the Technological University of Pereira, for allowing this research to be carried out at their facilities. We would also like to show our gratitude to the anonymous reviewers for the comments that improved the manuscript.

## REFERENCES

[1] Aggarwal C. C., Ashish N., Sheth A., (2013), The Internet of Things: A Survey from the Data-Centric Perspective. In: AGGARWAL, C. (eds.). *Managing and mining sensor data*, pp. 383-428, Springer, Boston, MA;

[2] Aleotti J., Amoretti M., Nicoli A. et al., (2018), A Smart Precision-Agriculture Platform for Linear Irrigation Systems, *26th International Conference on Software, Telecommunications and Computer Networks, SoftCOM, IEEE,* pp. 1-6, Split, Croatia;

[3] Alzarliani W. D., Arsyad M., Salam M. et al., (2019), Effect of App utilization on the agricultural efficiency of rural communities. *IOP Conference Series: Earth and Environmental Sciences*, Vol. 235, 012101, ISSN 1755-1315, IOP Publishing;

[4] Atzberger C., (2013), Advances in Remote Sensing of Agriculture: Context Description, Existing Operational Monitoring Systems and Major Information Needs, *Remote Sensing*, Vol. 5, Issue 2, ISSN 2072-4292, pp. 949-981; Basel, Switzerland.

[5] Barkunan S. R., Bhanumathi V., Sethuram J., (2019), Smart sensor for automatic drip irrigation system for paddy cultivation, *Computers and Electrical Engineering*, Vol. 73, ISSN 0045-7906, pp. 180-193;

[6] BCN, Biblioteca del Congreso Nacional de Chile, (2017), El sistema de agricultura sostenible en Tailandia que apunta a la seguridad laboral y alimentaria. Available at: < https://www.bcn.cl/observatorio/asiapacifico/noticias/sistema-agricultura-sostenible-tailandia>;

[7] Borges L. M., Velez F. J., Lebres A.S., (2014), Survey on the characterization and classification of wireless sensor network applications, *IEEE Communications Surveys & Tutorials*, Vol. 16, Issue 4, pp. 1860-1890;

[8] Channe H., Kothari S., Kadam D., (2015), Multidisciplinary Model for Smart Agriculture using Internet-of-Things (IoT), Sensors, Cloud-Computing, Mobile-Computing & Big-Data Analysis, *International Journal of Computer Technology & Applications*, Vol. 6, Issue 3, ISSN 2229-6093, pp. 374-382, India;

[9] Dholu M., Ghodinde K. A., (2018), Internet of things (IoT) for precision agriculture application, *2nd International Conference on Trends in Electronics and Informatics (ICOEI)*, *IEEE*, 339-342, Tirunelveli, India;

[10] García J. E., Chavez J., Jurado A. K., (2017), Modelado de una red de sensores y actuadores inalámbrica para aplicaciones en agricultura de precisión, *IEEE Mexican Humanitarian Technology Conference (MHTC)*, pp. 109-116, Puebla, Mexico;

[11] Gómez-Chabla R., Real-Avilés K., Calle K. et al., (2019), A Monitoring System for Lettuce Cultivation in an NFT Hydroponic System: A Case Study, *2nd International Conference on ICTs in Agronomy and Environment*, pp. 49-58, Guayaquil, Ecuador;

[12] Joshi V. B., Goudar R. H, (2019), IoT-based automated solution to irrigation: An approach to control electric motors through Android phones. *Recent Findings in Intelligent Computing Techniques*, pp. 323-330, Springer, Singapore.

[13] Khriji S., El Houssaini D., Jmal M. W. et al., (2014), Precision irrigation based on wireless sensor network, *IET Science, Measurement & Technology*, Vol. 8, Issue 3, pp. 98-106, The Institution of Engineering and Technology, England;

[14] Lee M., Kim H., Yoe H, (2019), ICBM-Based Smart Farm Environment Management System. In: Lee R. (eds.) Software Engineering, Artificial Intelligence, Networking and Parallel/Distributed Computing, *Studies in Computational Intelligence*, Vol. 790, pp. 42-56, Springer Cham.;

[15] Li B., Wang J., Chi Y.D., et al., (2018), Wireless measurement and control system of carbon dioxide using infrared sensor in greenhouse environment, *INMATEH-Agricultural Engineering*, Vol. 54, Issue 1, pp. 47-54, INMA, Bucharest, Romania.

[16] Muangprathub J., Boonnam N., Kajornkasirat S. et al., (2019), IoT and agriculture data analysis for smart farm, *Computers and Electronics in Agriculture*, Vol. 156, pp. 467-474, Elsevier, Netherlands;

[17] Ortega L. A., Paz L. P., Giraldo Mendez D. C. et. al., (2018), Implementación de Servicios Integrados Participativos de Clima para la Agricultura (PICSA) en el TESAC-Cauca Colombia, Research Program on Climate Change, *Agriculture and Food Security*. Available at: < https://cgspace.cgiar.org/bitstream/handle/10568/93424/SISTEMATIZACION_PICSA_TeSAC.pdf?sequence=8&isAllowed=y >

[18] Satyanarayana G. V., Mazaruddin S. D., (2013), Wireless sensor based remote monitoring system for agriculture using ZigBee and GPS, *Proceedings of the Conference on Advances in Communication and Control Systems*, ISSN 1951-6851, Atlantis Press;

[19] Suleman Y., Manurung R. V., Kurniawan D. et al., (2018), Development of precision farming using modular multi node sensor. *2018 International Conference on Radar, Antenna, Microwave, Electronics, and Telecommunications (ICRAMET)*, *IEEE*, pp. 99-103, Serpong, Indonesia;

[20] Tauger M.B., (2010), *Agriculture in world history*. Routledge, Taylor & Francis Group, ISBN 0415773873, First edition;

[21] Tummarattananont P., Suntiwichaya S., Chunwijitra S. et al., (2018), Agricultural Social Application for Adaptive Planning on Crop Cycle Model Based on Plant Area, ECTI-CON 2018 - *15th International Conference on Electrical Engineering/Electronics, Computer, Telecommunications and Information Technology*, 225-228, Chiang Rai, Thailand;

[22] Valiente F. L., Garcia R. G., Domingo E. J. A. et. al., (2018), Internet of Things (IOT) - Based mobile application for monitoring of automated aquaponics system, *2018 IEEE 10th International Conference on Humanoid, Nanotechnology, Information Technology, Communication and Control, Environment and Management (HNICEM),* pp. 1-6, Baguio City, Philippines;

[23] Zhang X., (2018), Application of Internet of Things Technology in Agricultural Production, *Proceedings of the International Symposium on Big Data and Artificial Intelligence*, pp. 269-274, Hong Kong;

[24] Zhao K., Chang J., Ma X., et al., (2018), Drought monitoring and forecasting method based on Google cloud computing service platform, *INMATEH-Agricultural Engineering*, Vol. 55, Issue 2, pp. 151-160, INMA, Bucharest, Romania;

[25] ***NRE, Natural Resource Extraction, (2013), Three countries, three different trajectories, *Americas Quarterly, 2013,* Available at: <http://americasquarterly.org/charticles/natural-resource-extraction-chile-peru-colombia/pdf/COLOMBIA.pdf>.

# DESIGN AND VALIDATION OF A SURFACE PROFILING APPARATUS FOR AGRICULTURAL TERRAIN ROUGHNESS MEASUREMENTS

/

# 农田地面不平度测试装置的设计与验证

**Jianguo Yan, Chunguang Wang*), Shengshi Xie, Lijuan Wang [1]**
College of Mechanical and Electrical Engineering, Inner Mongolia Agricultural University, Hohhot 010018, China
*Tel: +86 13624713647; E-mail: nmndwcg@126.com*
*DOI: 10.35633/INMATEH-59-19*

***Keywords:*** *agricultural terrain profiles, field surface roughness, profiling apparatus, profiling validation*

## ABSTRACT

*How to accurately and efficiently measure the profiles of the terrain on which agricultural machines operate has been an ongoing research topic. In this study, a surface profiling apparatus (profiler) was developed to measure agricultural terrain profiles along parallel tracks. The profiler is mainly composed of sensor frames, an RTK-GNSS system (Real Time Kinematics-Global Navigation Satellite Systems), laser sensors, an Inertial Measurement Unit (IMU) sensor and a data acquisition system. Along with a full description of how the terrain profiles were produced, a methodology to compensate for the tractor motion was included in the sensor data analysis. In field profiling validation, two trapezoidal bumps with known dimensions were used to assess the ability of the terrain profiler to reproduce the vertical profiles of the bumps, resulting in root mean square error (RMSE) of 3.6-4.7 mm and 4.5-5.1 mm with profiling speeds of 1.02 and 2.56 km/h, respectively. In addition, a validation test was also conducted on an asphalt road by profiling a flat road with the measuring wheels of the profiler rolling on the flat section but with the tractor wheels driving over a trapezoidal bump to excite the tractor pitch and roll motion. The measured profiles then also exhibited a flat road, which showed the ability of the profiler to remove the tractor motion from the profiling measurements.*

## 摘要

*如何准确、高效地测量农业机械所接触的农田地面不平度一直是研究者们关注的问题。本文设计了一种可并排测量农田地面不平度的装置，主要由传感器架、RTK-GNSS 系统、激光传感器、IMU 传感器和数据采集系统等部分组成。在数据分析中，除了对地面不平度的生成进行了完整描述外，提出了一种补偿拖拉机运动的方法。农田试验中，利用两个尺寸已知的梯形凸台检验不平度测试装置再现凸台垂直剖面的性能，当测试速度分别为 1.02 和 2.56 km/h 时，不平度均方根误差范围分别为 3.6-4.7 mm 和 4.5-5.1 mm。另外，在沥青路面上也开展了验证试验，方法是对平坦沥青路面进行不平度测试，使不平度测试装置的地轮在平坦路面上滚动，而拖拉机车轮经过一个梯形凸台，以激励其产生俯仰和侧倾运动。测量的不平度结果依然反映的是一条平坦的路面，证明了不平度测试装置从测量值中去除拖拉机运动成分的有效性。*

## INTRODUCTION

Agricultural tractors and implements usually operate on very rough terrain and are vibrated by the displacement of the field profiles acting on each wheel during operation in an agricultural field. The vibration restricts the work efficiency and operation quality of the agricultural machinery (*Ren Wentao et al., 2009; Zhao Manquan et al., 2012*), which also causes parts of the agricultural machines to bear a great dynamic load (*Clijmans L. et al., 1998*), and seriously endangers the health of the driver (*Liang X. C. et al., 2018; Niu P. et al., 2017*). To study the dynamic response characteristics of agricultural machinery caused by terrain roughness, terrain profiles should be investigated. This arises a problem that is how to accurately and efficiently measure the agricultural terrain profiles that agricultural machines operate on.

Profiling instruments have become the standard tools for investigating road roughness.

[1] *Jianguo Yan, As. Ph.D. Stud. Eng.; Chunguang Wang, Prof. Ph.D. Eng.; Shengshi Xie, Lect. Ph.D. Eng.; Lijuan Wang, Lect. M.S. Eng.*

However, these instruments are not suitable for measuring agriculture-related profiles due to the large unevenness of fields and the impact of weeds or crop stubble on the profiling results. There are mainly two types of profiling instruments developed for achieving the agricultural terrain roughness measurement: static profiling apparatus and dynamic profiling apparatus (*Sayers M. W. et al., 1998*). The rod and level are familiar static measuring tools. This method is referred to as “static” because the instruments are stationary when the profile elevation measures are taken. A micro laser relief meter, a static profiler, was designed to measure soil profiles with the maximum test distance of 1 meter at a time (*Lu Z. X. et al., 2005*). Obviously, it is very time consuming and resource intensive to measure hundreds of meters of terrain profiles.

Dynamic profiling instruments are preferred and make highly efficient profiling possible for investigating the roughness of agricultural terrain. The first attempt to build a high-speed profiler was made by Spangler (*Spangler E.B. et al., 1966*). Accelerometers were commonly used to characterize road roughness based on vehicle responses such as spindle acceleration and load (*González A. et al., 2008*). These inertial profilers relying on accelerometers to measure the vertical position suffer at low host vehicle speeds due to their limited accelerometer bandwidth (*Walker R.S. et al., 2006*). Because modern measurements require high resolution and large vertical dynamic measuring ranges, terrain measurement technology has progressed from inertial profilers to optical techniques such as laser distance-measuring instruments for field profile measurement (*Paraforos D.S. et al., 2016*). Vision acquisition has also been incorporated for characterizing the surface roughness of different terrains (*Howard A. et al., 2001*).

With the aim of measuring agricultural-related profiles, a profiling apparatus was developed with the following capabilities: producing high profiling efficiency, avoiding the impact of weeds or crop stubble on the profiling results and effectively removing the tractor motion from the profiling measurements.

## MATERIALS AND METHODS

### *Instrumentation*

As shown in Fig. 1, the profiler was mounted on the front counterweight of a tractor, which makes it easy to further analyse the coupling vibration between the tractor and the field ground because the profiles measured are the ones that will vibrate the tractor when the tractor wheels roll on the profile path. The profiler comprises two sensor frames mounted on the front counterweight of a tractor, two laser sensors (Banner LT3NU W/30, USA) for measuring the distance from the sensor frame *1* to a metal plate mounted on each wheel, a RTK-GNSS system (Trimble AgGPS 542 RTK-GNSS, USA) for providing geo-reference of the measured data, an IMU (LMRK 20 AHRS, USA) for providing real-time tilt (roll-pitch-yaw) information of the tractor, and a data acquisition system for receiving and saving all sensor data in parallel.


**Fig. 1 - Profiling apparatus mounted on the front counterweight of a tractor**

The schematic diagram of the sensor frame 1 is illustrated in Fig. 2.

The frame was mounted on the front counterweight of a tractor via two connecting rods under a connecting seat and was fixed by fastening nuts. The sensor frame was supported by two road-following wheels with widths of 125 mm and diameters of 200 mm. A suitable wheel material, such as nylon, was chosen to maintain a low wheel mass and reduce the vibration from the wheels to the frame. To prevent soil compaction while maintaining contact with the profiled surface, stainless steel square tubes with transverse dimensions of 40*40*2.5 mm were utilized to minimize the mass of the sensor frame. The static load of each wheel on the ground surface was measured to be 32 N. Therefore, it can be approximated that the wheels do not change the elevations of the ground surface and the field surface roughness can be effectively reflected by the up-and-down motions of the wheels. Additionally, springs, in which the preload can be adjusted by nuts, were added to push the wheels towards the surface ground.

Referring to Fig. 2, two parallelogram linkages in the profiler, which are connected to the two wheels, ensure that the metal plates move up and down and the motion of each plate is always “parallel” to the ground. Each parallelogram linkage comprises an upper hinged plate, a lower hinged plate, a wheel guided rod, a sleeve guided rod and two adjusting sleeves. The parallelogram linkages and supported wheels were driven by two drag beams that were rotatably mounted to connecting seat by a pin shaft.

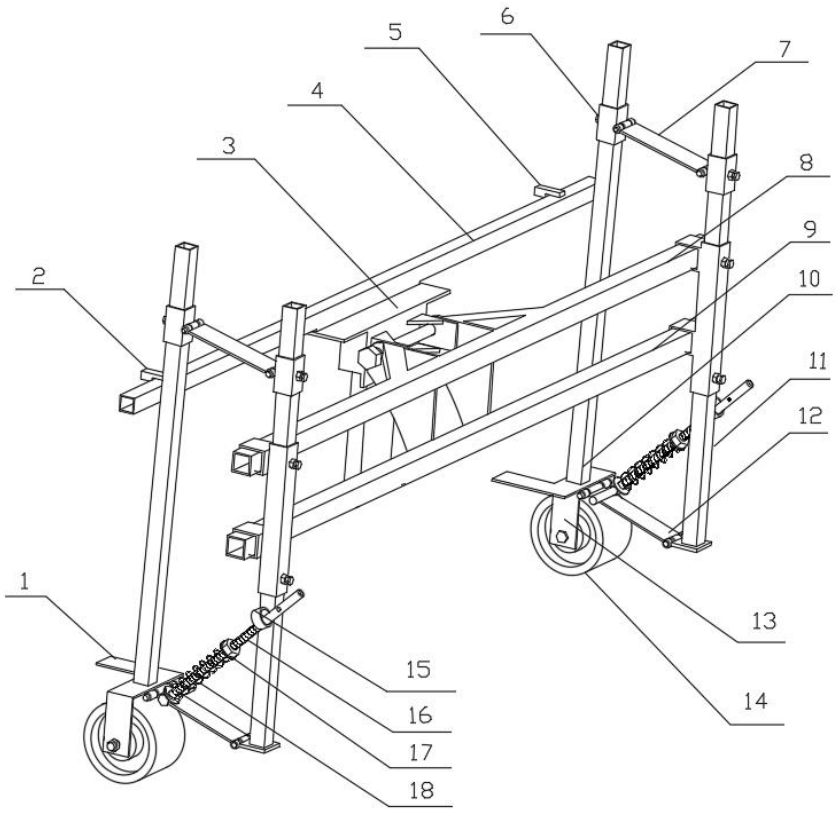


**Fig. 2 - Schematic diagram of the sensor frame 1 of the profiler**

*1- Metal plate; 2-Laser sensor 1; 3-Connecting seat; 4-Sensor beam; 5-Laser sensor 2; 6-Adjusting sleeve; 7-Upper hinged plate; 8-Drag beam 1; 9-Drag beam 2; 10-Wheel guide rod; 11-Sleeve guide rod; 12-Lower hinged plate; 13-Wheel axle; 14-Road-following wheel; 15-Inclined hole; 16-Threaded rod; 17-Nut; 18-Spring*

The IMU and GNSS antenna were attached on sensor frame 2, which was mounted on the front counterweight of the tractor to ensure that the IMU and GNSS antenna align on the longitudinal centre plane of the tractor.

Two laser sensors with measuring distances of 0.3-5 m were attached on a sensor beam and symmetrical to the longitudinal centre plane of the tractor. To avoid the impact of weeds or crop stubble on the field surface profiling, the relative vertical distances from the sensor beam to the metal plates mounted on each wheel axle were measured with two laser sensors. The positions of the road-following wheels and the laser sensors were adjustable so that surface profiles of the parallel tracks with different widths could be measured. The road-following wheels could also be adjusted to 30 cm high from the ground surface after the profile measurement, which did not affect the normal operation of the tractor.

Data acquisition software was developed in LabVIEW for acquiring and recording all sensor data in parallel, as shown in Fig. 3. A computer and a virtual instrument were necessary to acquire the signals and readings obtained from the measuring sensors carried on the profiler and its driving vehicle. This data acquisition system could also be extended to synchronously measure the field terrain surface profiles and dynamic responses of the tractor-caused by the surface roughness, which provides a possibility for further study regarding the coupling vibration characteristics of terrain roughness and vehicle dynamics.


**Fig. 3 – Software interface of profiling data acquisition system**

***Profiling validation test***

The location of the profiling validation test was situated at 40.21°N latitude and 111.34°E longitude in Hohhot, China, and the test was completed on October 5, 2019.

The validation test took place in a harvested corn field to provide close to real-world operating conditions, as shown in Fig. 4.

**Fig. 4 - Field profiling validation test**

Two trapezoidal bumps with known dimensions were used to verify the ability of the terrain profiler to reproduce the vertical profiles of the bumps. In addition, a validation test was also conducted on an asphalt road by profiling a flat road with the road-following wheels of the profiler rolling on the flat section but with the tractor wheels on one side driving over a bump to excite tractor pitch and roll motion, as shown in Fig. 5.


**Fig. 5 - Asphalt road profiling validation test**

The laser and positioning systems were also evaluated concurrently with digital signal processing techniques to compensate for vehicle body motion. Whether the measured results always reflect a flat road could indicate the ability of the profiler to remove the tractor motion from the laser measurements. During all validation tests, the tractor was maintained at two constant forward speeds of 1.02 and 2.56 km/h. The tire pressure of the tractor was 230 kPa in the front and 200 kPa in the rear.

The two trapezoidal bumps were made of wood, and their dimensions are shown in Fig. 6. Such bumps are commonly used for road profile validation (*Becker C.M. et al, 2014; Smith H. et al, 2010*). A 0.7-metre bump was used on the left track, while a 0.9-metre bump was used on the right track with the road-following wheels of the profiler rolling over the bumps in the field validation test. A 0.7-metre bump was used on the left track to excite the tractor pitch and roll motion in the asphalt road validation test.

The difference between the measured profile and the actual profile of the bump can be expressed quantitatively as the root mean square error (*RMSE*) using equation (1) below:

$$RMSE = \sqrt{\frac{\sum_{i=1}^{n}(Z_{mi} - Z_{ai})^2}{n}} \quad (1)$$

where: $Z_{mi}$ is the measured profile of the bump for time instance $i$;

$Z_{ai}$ is the actual profile of the bump for time instance $i$;

$n$ is the number of measured points for the bump profile.

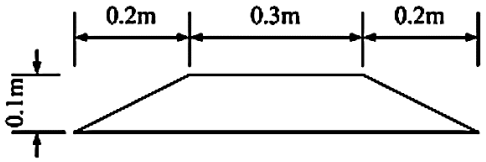


(a)

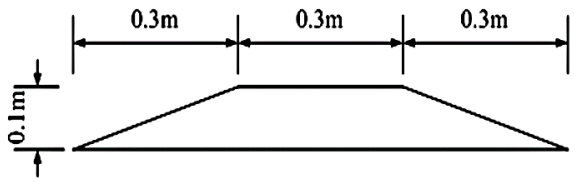


(b)

**Fig. 6 - Trapezoidal bump dimensions**
*(a) 0.7-meter bump (b) 0.9-meter bump*

**THEORY**

The tractor as a carrying vehicle influences the built sensor frame. Especially in agricultural terrains, potholes and bumps are common and even sudden changes in the terrain inclination. In this way, the motion of the tractor is combined with the motion of the terrain in the laser measurements. Thus, the laser movement caused by the roll and pitch motion of the tractor needs to be deducted from the profiling measurements. In this study, along with a full description of how the terrain profiles were being produced, a methodology to compensate for the tractor motion was included in the sensor data analysis.

***Coordinate transformation***

An RTK-GNSS was used to provide absolute geo-referenced coordinates of the measured data. Using the real-time dynamic tilt information (roll-pitch-yaw) provided by the IMU, the motion of the lasers on the sensor frame could be calculated through coordinate transformation.

The position data obtained directly through RTK-GNSS receiver are the latitude $\varphi$, longitude $\lambda$ and altitude $h$, which are expressed in WGS-84 (World Geodetic System-1984) coordinates. The output data from the IMU, such as the angles of roll $\psi$, pitch $\theta$, and yaw $\phi$, are based on vehicle body coordinates. To integrate the data acquired from the RTK-GNSS and the IMU, it is necessary to convert the GNSS data coordinates into vehicle body coordinates. This procedure requires that the RTK-GNSS data be converted to the Earth-Centered Earth-Fixed (ECEF) coordinates, then to the NED coordinates, and finally to the vehicle body coordinates.

If $P_E = \left[X_E, Y_E, Z_E\right]^T$ is the position in ECEF coordinates, the conversion from the WGS-84 coordinates to the ECEF coordinates can be performed using the following equations (*Farrell J. et al, 1999*):

$$X_{\mathrm{E}} = (N(\varphi)+h)\cos(\varphi)\cos(\lambda) \tag{2}$$

$$Y_{\mathrm{E}} = (N(\varphi)+h)\cos(\varphi)\sin(\lambda) \tag{3}$$

$$Z_{\mathrm{E}} = \left[N(\varphi)(1-e^2)+h\right]\sin(\varphi) \tag{4}$$

where:

$e = 0.0818$ is the first numerical eccentricity of the earth ellipsoid;

$N$ is the distance from earth's surface to the Z-axis along the ellipsoid normal given by:

$$N = \frac{a}{\sqrt{1-e^2\sin^2\varphi}} \tag{5}$$

where:

$a = 6378137$ m is the semi-major axis length of the earth.

If $P_N = \left[X_N, Y_N, Z_N\right]^T$ is the position in the local NED coordinates, the conversion from the ECEF coordinates to the NED coordinates is

$$P_{\mathrm{N}} = R_{\mathrm{N/E}} \cdot P_{\mathrm{E}} \tag{6}$$

where:

$R_{N/E}$ is the transformation matrix from the ECEF coordinates to the NED coordinates.

$$R_{\mathrm{N/E}} = \begin{bmatrix} -\sin\varphi\cos\lambda & -\sin\varphi\sin\lambda & \cos\varphi \\ -\sin\lambda & \cos\lambda & 0 \\ -\cos\varphi\cos\lambda & -\cos\varphi\sin\lambda & -\sin\varphi \end{bmatrix} \tag{7}$$

If $P_B = \left[X_B, Y_B, Z_B\right]^T$ is the position in the vehicle body coordinates, the conversion from the NED coordinates to the vehicle body coordinates is

$$P_{\mathrm{B}} = R_{\mathrm{B/N}} \cdot P_{\mathrm{N}} \tag{8}$$

where:

$R_{B/N}$ is the transformation matrix from the NED coordinates to the vehicle body coordinates (*Farrell J. et al., 1999*):

$$R_{B/N} = \begin{bmatrix} \cos\theta\cos\psi & \cos\theta\sin\psi & -\sin\theta \\ \sin\phi\sin\theta\cos\psi - \cos\phi\sin\psi & \sin\phi\sin\theta\sin\psi + \cos\phi\cos\psi & \sin\phi\cos\theta \\ \cos\phi\sin\theta\cos\psi + \sin\phi\sin\psi & \cos\phi\sin\theta\sin\psi - \sin\phi\cos\psi & \cos\phi\cos\theta \end{bmatrix} \quad (9)$$

***Measured profile calculation***

The parallel profiles were calculated using the known dimensions of the sensor frame and the measured distances provided by the two laser sensors. With compensation for the tractor motion, the motion of the lasers on the sensor frame was deducted from the profiling measurements.


**Fig. 7 - Coordinates of x (Roll), y (Pitch) and Z (Yaw) on the IMU**

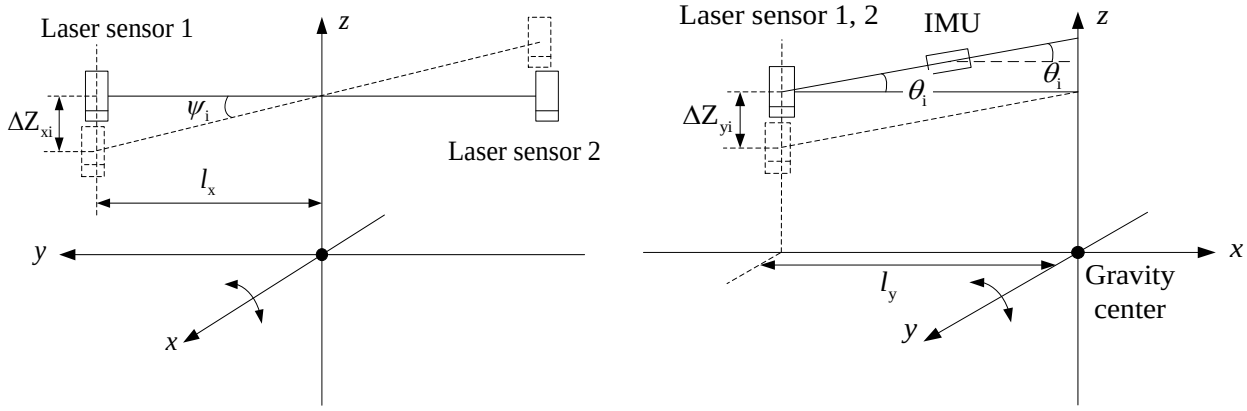


a) b)

**Fig. 8 - Vertical displacement change of the laser sensors caused by tractor motion**

*(a) Roll motion (b) Pitch motion*

The coordinates of X (roll), Y (pitch) and Z (yaw) on the IMU are shown in Fig. 7. The attachment of the IMU could ensure that the X-axis of the IMU was on the longitudinal centre plane of the tractor. In relation to the tractor body, the positive directions of the axes are X - backward, Y - left and Z - upward. The roll-pitch-yaw angle values of the IMU comply with the right-hand rule. Fig. 8 shows the vertical displacement change in the laser sensors caused by the roll and pitch motion of the tractor.

With compensation for the tractor motion, the expression of the measured profile is as follows:

$$Z_m = -(Z_i - Z_0 \pm \Delta Z_{xi} + \Delta Z_{yi}) \quad (10)$$

where:

$Z_m (m=0,1,\ldots, N-1)$ are the measured surface roughness heights of each profile;

$Z_i$ is the vertical distance the laser sensor measured for time instance $i$;

$Z_0$ is the vertical distance from laser sensor to the metal plate when the tractor is placed horizontally (Fig. 2).

$\Delta Z_{xi} = l_x \tan\psi_i$ is the vertical displacement change of the laser sensors caused by the roll motion of the tractor at the $i$ th measuring point, seen as Fig. 8 (a). For laser sensor 1, the value is taken as $+\Delta Z_{xi}$, while for laser sensor 2, the value is taken as $-\Delta Z_{xi}$. The parameter $l_x$ is the distance from a laser sensor to the longitudinal centre plane of the tractor, and $\psi_i$ is the tractor roll angle for time instance $i$.

$\Delta Z_{yi} = l_y \tan\theta_i$ is the vertical displacement change of the laser sensors caused by the pitch motion of the tractor at the $i$ th measuring point, as shown in Fig. 8 (b). The parameter $l_y$ is the longitudinal distance from a laser sensor to the gravity centre of the tractor, and $\theta_i$ is the tractor pitch angle for time instance $i$.

Assume the $Z_m (m=0,1,\ldots, N-1)$ are measured at equally spaced intervals $\Delta x$, then the measured surface profile roughness $Z(l)$ which is the $Z_m$ as a function of longitudinal distance $l=m\Delta x$ could be fixed.

## RESULTS

### *Field profiling validation results*

The profiles measured while traversing two trapezoidal bumps in the harvested corn field in one of the validation tests with a profiling speed of 1.02 km/h are presented in Fig. 9. The accuracy of the profiler could be evaluated by comparing the actual profile of the bump to the profile as measured by the laser. The error between these signals was evaluated using the *RMSE* calculated by the equation (1).

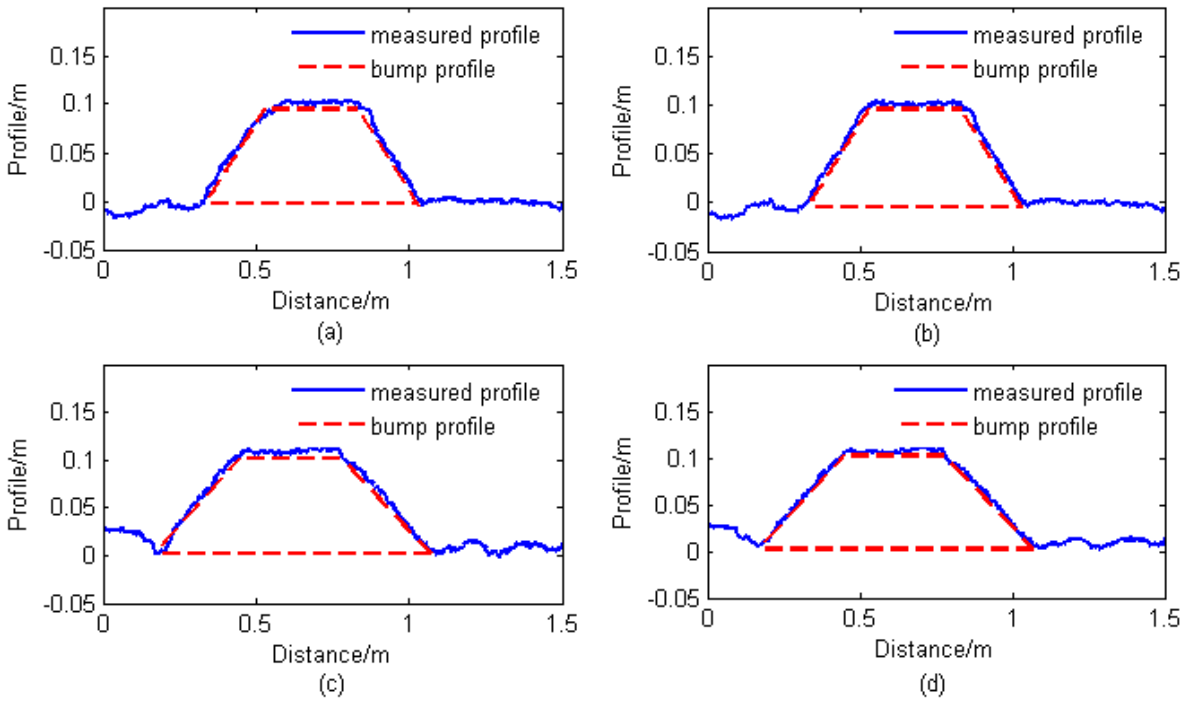


**Fig. 9 - Measured profiles in one of the field profiling validation tests**

*(a) Measured profile of a 0.7-metre bump; (b) measured profile of a 0.7-metre bump with compensation for the tractor motion; (c) measured profile of a 0.9-metre bump; and (d) measured profile of a 0.9-metre bump with compensation for the tractor motion*

It can also be seen from Fig. 9 that the measured profiles could reflect the elevations of the trapezoidal bumps. The overall agreement between the measured profiles and the actual profiles of the bumps was improved by compensating for the tractor motion. In Fig. 9, using equation (1), the *RMSE* values were calculated to be 5.8 mm and 5.2 mm for the left and right tracks, respectively, while they were reduced to 4.3 mm and 3.9 mm with compensation for the tractor motion.

The *RMSE* values in the field profiling validation tests were calculated and summarized in Table 1.

**Table 1**

**Field profiling validation results**

| Test code | Left track bump profile | | Right track bump profile | |
|---|---|---|---|---|
| | ***RMSE* value with no compensation [mm]** | ***RMSE* value with compensation [mm]** | ***RMSE* value with no compensation [mm]** | ***RMSE* value with compensation [mm]** |
| A1 | 5.8 | 4.3 | 5.2 | 3.9 |
| A2 | 5.6 | 4.7 | 5.4 | 4.6 |
| A3 | 5.1 | 3.6 | 4.9 | 3.8 |
| B1 | 6.0 | 5.1 | 6.2 | 4.9 |
| B2 | 6.1 | 4.8 | 5.8 | 4.7 |
| B3 | 6.4 | 4.9 | 5.7 | 4.5 |

*The test code letters A and B indicate validation tests with profiling speeds of 1.02 and 2.56 km/h, respectively. Different numbers (1, 2, 3) indicate three repeated treatments of each test.*

In Table 1, the *RMSE* values ranged from 4.9 mm to 5.8 mm and from 5.7 mm to 6.4 mm, when the profiling speed was maintained at 1.02 km/h and 2.56 km/h, respectively. With compensation for the tractor motion, the *RMSE* values reduced to range from 3.6 mm to 4.7 mm and from 4.4 mm to 5.1 mm for profiling speeds of 1.02 km/h and 2.56 km/h, respectively.

According to Table 1, the comparison of the measured profile values is shown in Fig. 10.

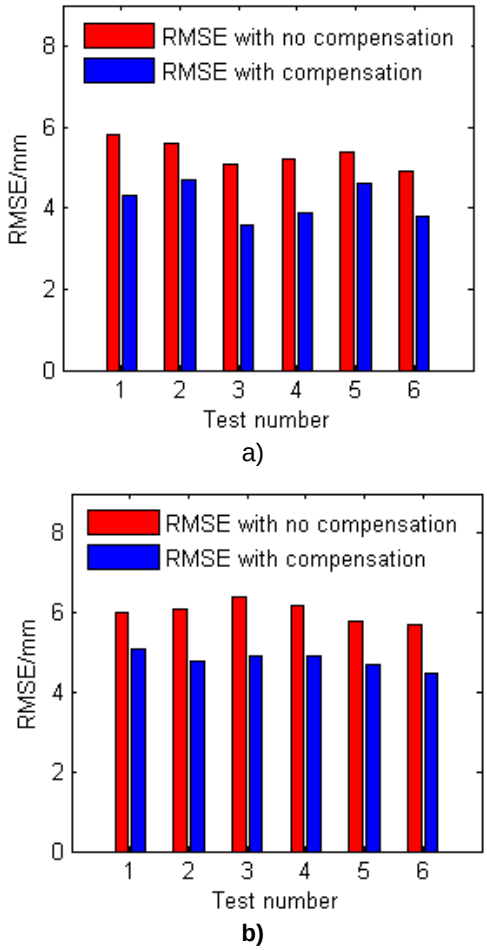


**Fig. 10 - *RMSE* values of the field profiling validation results**
*(a) Profiling speed of 1.02 km/h; (b) Profiling speed of 2.56 km/h*

As shown in Fig. 10, the RMSE values of the field profiling validation results decreased noticeably with compensation for the tractor motion.

***Asphalt road profiling validation results***

The profiles measured in one asphalt road validation test with a profiling speed of 1.02 km/h are presented in Fig. 11.

Fig. 11 (a) and (c) show that the measured profiles were significantly affected by the tractor body roll and pitch motion (4-8 m section) when the front and rear wheels on one side of the tractor passed through the bump. The profiling results calculated by equation (10) are shown in Fig. 11 (b) and (d). With compensation for the tractor motion, the measured profiles basically reflected a flat road, which could indicate the ability of the profiler to remove the tractor motion from the laser measurements.

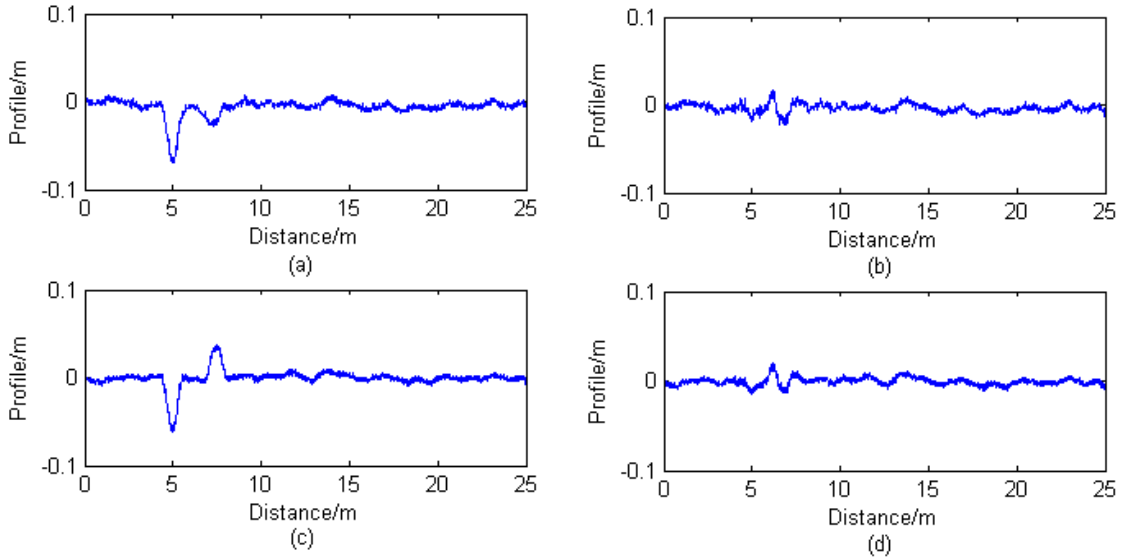


**Fig. 11 - Measured profiles in one of the asphalt road validation tests**

*(a) Measured profile of the left track; (b) measured profile of the left track with compensation for the tractor motion; (c) measured profile of the right track; and (d) measured profile of the right track with compensation for the tractor motion*

In Table 2, the $RMS_{4\text{-}8}$ values ranged from 24.3 mm to 28.1 mm and from 27.7 mm to 29.8 mm when the profiling speed was maintained at 1.02 km/h and 2.56 km/h, respectively. With compensation for the tractor motion, the $RMS_{4\text{-}8}$ values reduced to a range from 5.7 mm to 6.1 mm and from 6.1 mm to 6.8 mm for profiling speeds of 1.02 km/h and 2.56 km/h, respectively. The *RMS* values of the measured profiles on the whole test section of a flat asphalt road ranged from 5.5 mm to 5.8 mm and from 5.5 mm to 5.9 mm for profiling speeds of 1.02 km/h and 2.56 km/h, respectively.

The *RMS* values in the asphalt road profiling validation were calculated and summarized in Table 2.

**Table 2**

**Asphalt road profiling validation results**

| Test code | Left track profile | | | Right track profile | | |
|---|---|---|---|---|---|---|
| | $RMS_{4\text{-}8}$ value with no compensation [mm] | $RMS_{4\text{-}8}$ value with compensation [mm] | *RMS* value with compensation [mm] | $RMS_{4\text{-}8}$ value with no compensation [mm] | $RMS_{4\text{-}8}$ value with compensation [mm] | *RMS* value with compensation [mm] |
| A1 | 27.7 | 5.9 | 5.7 | 24.3 | 5.7 | 5.6 |
| A2 | 28.1 | 5.8 | 5.5 | 24.6 | 5.9 | 5.7 |
| A3 | 27.4 | 6.1 | 5.6 | 25.2 | 6.0 | 5.8 |
| B1 | 29.5 | 6.6 | 5.8 | 27.7 | 6.6 | 5.9 |
| B2 | 29.3 | 6.8 | 5.6 | 28.5 | 6.1 | 5.5 |
| B3 | 29.8 | 6.4 | 5.6 | 29.1 | 6.2 | 5.8 |

*The test code letters A and B indicate validation tests with profiling speeds of 1.02 and 2.56 km/h, respectively. Different numbers (1, 2, 3) indicate three repeated treatments of each test. $RMS_{4\text{-}8}$ represents the root mean square value of the measured profile on 4-8 m test sections, on which the tractor wheels on one side passed through a bump to excite pitch and roll motion. RMS represents the root mean square value of the measured profile on the whole test section of a flat asphalt road.*

According to Table 2, the comparison of the measured profile values is shown in Fig. 12.

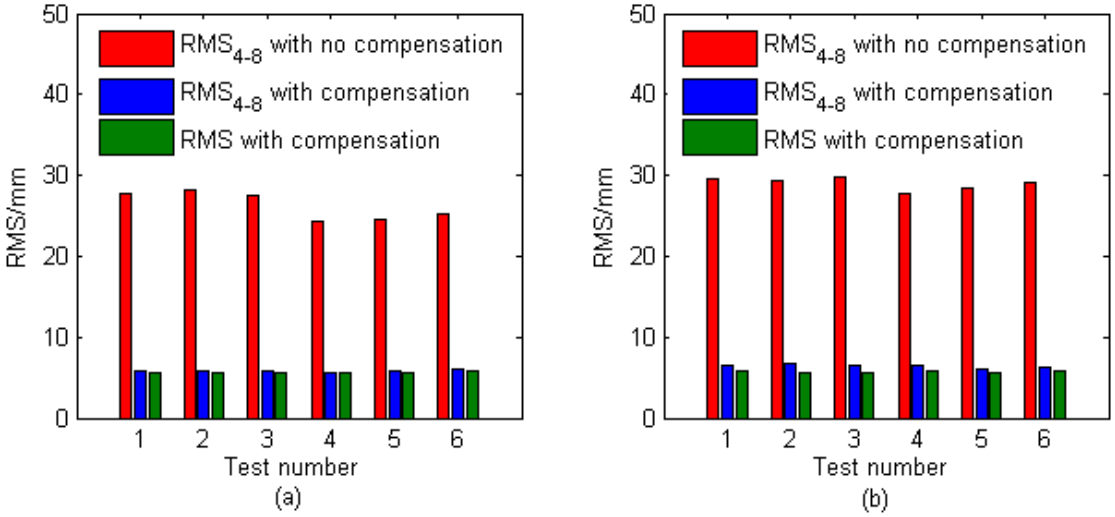


**Fig. 12 - *RMS* values of the asphalt road profiling validation results**

*(a) Profiling speed of 1.02 km/h and (b) profiling speed of 2.56 km / h*

From Fig. 12, comparing with no compensation for the tractor motion, the $RMS_{4-8}$ values with compensation for the tractor motion were significantly reduced, and they were close to the *RMS* values of the measured profiles on the whole test section of a flat asphalt road.

These results indicate that the laser movement caused by the roll and pitch motion of the tractor can be effectively deducted from the profiling measurements and that the accuracy of the profiler is reliable.

## CONCLUSIONS

The surface profiling apparatus (profiler) was designed to measure agricultural terrain profiles along parallel tracks. A methodology of how the terrain profiles were calculated and how to remove the tractor motion from the laser measurements was presented in the data analysis. To assess the accuracy of the developed profiler, profiling validation tests were carried out in a harvested corn field and on an asphalt road. Based on the profiling validation results and the analyses presented above, the following conclusions can be drawn:

(1) Using the developed profiler and the presented methodology, the agricultural terrain profiles on which the tractor was moving could be measured. The overall accuracy of the profiler, expressed by the root mean square error (RMSE) value, was 3.6-4.7 mm and 4.5-5.1 mm with profiling speeds of 1.02 km/h and 2.56 km/h, respectively. Considering the large size of the agricultural machinery tires, the resulting accuracy is regarded as adequate. With compensation for the vehicle body motion, the laser movement induced by the tractor roll and pitch motion could be effectively subtracted from the profiling measurements.

(2) The accuracy of the developed profiler was improved as the profiling speed was decreased. Thus, if very rough terrain is profiled, the most accurate profile will be obtained by profiling the terrain as slowly as possible.

## ACKNOWLEDGEMENT

Special thanks are due to the Research Program of Science and Technology at Universities of Inner Mongolia Autonomous Region (NJZY20046), the National Natural Science Foundation of China (31901409), and the Natural Science Foundation of Inner Mongolia Autonomous Region (2019BS05012) for supporting authors' research.

## REFERENCES

[1] Becker C.M., Els P.S., (2014), Profiling of rough terrain, *International Journal of Vehicle Mechanics and Mobility*, Vol. 64, Issue 2-4, pp. 240-261;

[2] Clijmans L., Ramon H., Baerdemaeker J. D., (1998), Structural modification effects on the dynamic behavior of an agricultural tractor, *Transactions of the ASABE*, Vol.41, Issue 1, pp.5-10;

[3] Farrell J., Barth M., (1999), The global positioning system & inertial navigation. McGraw-Hill Publishers, New York/U.S.A.;
[4] González A., O'Brien E. J., Li Y. Y., Cashell K., (2008), The use of vehicle acceleration measurements to estimate road roughness, *International Journal of Vehicle Mechanics and Mobility*, Vol. 46, Issue 6, pp. 483-499;
[5] Howard A., Seraji H., (2001), Vision-based terrain characterization and traversability assessment, *Journal of Robotic Systems*, Vol. 18, Issue 10, pp. 577-587;
[6] Liang X. C., Chen J., Wang Z., (2018), Research on the vibration of mini tiller, *INMATEH Agriculture Engineering*, vol. 56, issue 3, pp. 17-24;
[7] Lu Z. X., Nan C., Perdok U. D., Hoogmoed W. B., (2005), Characterisation of soil profile roughness, *Biosystems Engineering*, Vol. 91, Issue 3, pp.369-377;
[8] Niu P., Yang M. J., Chen J., Yang L., Xie S. Y., Chen X. B., (2017), Structural optimization of a handheld tiller handrail by vibration modal analysis, *INMATEH Agriculture Engineering*, vol. 52, issue 2, pp. 91-98;
[9] Paraforos D. S., Griepentrog H. W., Vougioukas S. G., (2016), Country road and field surface profiles acquisition, modelling and synthetic realisation for evaluating fatigue life of agricultural machinery, *Journal of Terramechanics*, Vol. 63, Issue 2, pp. 1-12;
[10] Ren Wentao, Lu Xiaorong, Zhang Benhua, (2009), Dynamic response of taped type rice direct seeding machine for field surface roughness, Transactions of the Chinese Society for Agricultural Machinery, Vol. 40, Issue 8, pp. 58-61;
[11] Sayers M. W., Karamihas S. M., (1998), *The little book of profiling-basic information about measuring and interpreting road profiles*, 100 p., University of Michigan Publishers, Michigan/U.S.A.;
[12] Spangler E. B., Kelly W. J., (1966), GMR road profilometer - a method for measuring road profile, *Highway Research Board*, Vol. 121, Issue 3, pp.27-54;
[13] Smith H., Ferris J. B., (2010), Calibration surface design and validation for terrain measurement systems, *Journal of Testing and Evaluation*, Vol. 38, Issue 4, pp. 431-438;
[14] Walker R. S., Becker E., (2006), Collecting stop and go inertial profile measurements, *Pavement Management Systems*, Vol. 20, Issue 2, pp. 56-65;
[15] Zhao Manquan, Hu Yongwen, (2012), Measurement and analysis on vibration characteristics of pneumatic seed metering device of no-till seeder. *Transactions of the Chinese Society of Agricultural Engineering*, Vol. 28, Issue 2, pp.78-83.

# DEVELOPMENT OF MECHATRONIC MODULE FOR THE SEEDING CONTROL SYSTEM
# /
# РОЗРОБКА МЕХАТРОННОГО МОДУЛЯ ДЛЯ СИСТЕМИ УПРАВЛІННЯ ВИСІВОМ

**Aulin V. V., Pankov A. O., Zamota T. M., Lyashuk O. L., Hrynkiv A. V., Tykhyi A. A., Kuzyk A. V.** [1]
Central Ukrainian National Technical University / Ukraine
*Tel: +380950396372; E-mail: andrei.pankov73@gmail.com*
*DOI: 10.35633/INMATEH-59-20*

***Keywords:*** *automation, control, structure, mechatronics, module, sowing.*

**ABSTRACT**

*Existing control systems of sowing machines are intricate and not reliable enough. In these systems, devices are connected by a variety of signal and power wires. This leads to a "problem of interfaces" and a decrease in the efficiency of the control process. The solution to this problem is based on the mechatronic approach or combining elements and control units into mechatronic modules. They are characterized by reliability, compact design and lower cost. The improvement of functional and structural integration of the control system components by their integration into the mechatronic module is considered. The module of regulation of seeding rate on the basis of software and hardware platform Arduino is developed. The work of the proposed control system when changing the seeding rate in the seeding system is studied.*

**АНОТАЦІЯ**

*Існуючі системи управління роботою посівних машин складні і недостатньо надійні. В цих системах пристрої з'єднуються безліччю сигнальних і силових проводів. Це призводить до «проблеми інтерфейсів» і зниження ефективності процесу управління. Рішення даної проблеми засноване на мехатронному підході, або на об'єднанні елементів і блоків системи управління в мехатронні модулі. Вони характеризуються надійністю, компактністю, меншою вартістю. Розглянуто поліпшення функціонально-структурної інтеграції компонентів системи управління їх об'єднанням в мехатронний модуль. Розроблено модуль регулювання норми висіву на основі програмно-апаратної платформи Arduino. Досліджено роботу запропонованої системи управління при зміні норми висіву у висівній системі.*

## INTRODUCTION

The structural complexity of the system is determined by the number of elements and the intensity of the links between them. Analysis of existing automation and control systems (*Boyko A. I., Sviren M. O., 2006; Parkhomenko Yu.M. et. al., 2014; Sivak I. M., 2012; Aniskevich L. V., Popovich A. N., 2014*) establish that numerous interfaces connect devices of different physical nature (mechanical, electronic and informational). This determines the design and hardware-software complexity of the systems. In the traditional design of control systems for communication devices there is the need to connect dozens of signal and power wires. Experience of such systems' operation shows that up to 70% of the problems in their work are associated with unreliable connections. This is a wire break and poor contact in the connections, which causes failures and false positives (*Poduraev Yu.V., 2006*). An example of a traditional system is a block diagram of seeding control (Fig. 1) (*Boyko A. I., Sviren M. O., 2006*). It is implemented on traditional electric and hydraulic actuators with program control and includes the following elements:

- coordinate sensor with global positioning system (GPS) antenna to obtain information about the location of the machine in the field;
- on-Board computer to regulate the seeding rate based on the information about the place of the machine and the given seeding rate;
- matching device - information-electrical Converter that implements the transmission of the control signal from the computer to the power actuator;

[1] *Aulin V. V., Prof. D.Sc. Eng.; Pankov A. O., D.Sc. Eng.; Zamota T. M., D.Sc. Eng.; Lyashuk O. L., D.Sc. Eng.; Hrynkiv A. V., Ph.D. Eng.; Tykhyi A. A., Ph.D. Eng.; Kuzyk A. V., Ph.D. Eng.*

– force actuator (electric motor driven), which performs electromechanical conversion, to control the operation of the seeding system;

– a device that implements a given control movement or working body that interacts with external objects — seeding system of seeder;

– feedback device. It is a seeding control sensor that gives information about the intensity of the seed flow;

– interface devices, indicated in Fig. 1 by the arrows.

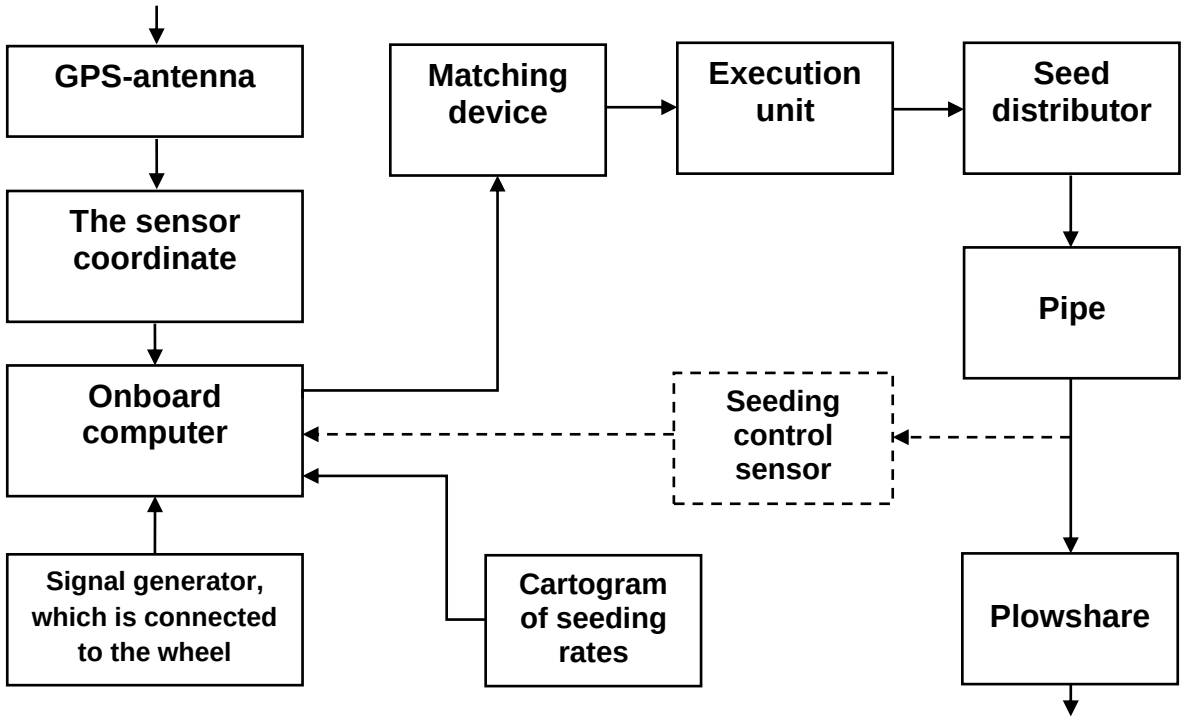


**Fig. 1 – Structural model of the traditional system of sowing control**

In the process of analyzing the model in Fig.1 by Poduraev's method *(Poduraev Yu. V., 2006*) it is established that there are six functional transformations in it: informational, mechanical, information-electrical, electromechanical, as well as electro-informational and mechanical-informational in feedback circuits (*Aulin V. V. et. al., 2017*). This complicates the seeding control system and reduces the reliability of its operation.

Currently, there is a trend of development of controls based on a new, mechatronic approach (*Teryaev E. D. et. al. In 2009; Antoshenkov R. V., Kovalev R. Yu., 2011*). Its essence is to combine elements and components into integrated modules, which solves the "problem of interfaces". The structural complexity of the control systems is reduced and their efficiency is increased.

The advantage of mechatronic modules (MM) consists in reliability, accuracy of movements, compactness of structures and ease of programming. Such solutions are cost-effective, as the service of the machine is simplified and its suitability for repair is improved (*Poduraev Yu.V., 2006; Aulin V., Hrinkiv A. et. al., 2018*). In (*Kosik P. O., 2009; Pastukhov V. I. et. al., 2015; Antoshenkov R. V., Kovalev R. Yu., 2011*) shows the advantages of mechatronic approach due to the durability, speed and almost trouble-free operation of mechatronic modules.

A feature of the modern stage of mechatronics development is the creation of a new generation of mechatronic modules - intelligent mechatronic modules (IMM). In comparison with the existing mechatronic modules, computer devices and power electronic converters are additionally integrated into the design of the IMM. This allows the IMM to perform manipulations on its own, without having to access the upper level of control.

The implementation of the hardware and software part of the IMM should be based on structural solutions that are open to development and have a hierarchical structure (*Poduraev Yu.V., 2006; Aulin V., Arifa W. et. al., 2016; Aulin V., Lyashuk O. et. al., 2018*). Arduino is a tool for developing devices that interact with the physical environment.

It is an open hardware and software platform for working with physical objects. Arduino is a Board with microcontroller and development environment to create software. The platform has built-in elements for programming and integration with other devices and circuits.

Therefore, the Arduino platform is the basis for research in the field of mechatronics (Omelchenko *E. Ya. et. al., 2013*). Arduino simplifies the work with microcontrollers and provides the following advantages: low cost, cross-platform, the use of additional modules for automation, control and control of various physical processes and functions.

The aim of the research is to develop and test a seeding control system with a minimum number of structural elements combined in the mechatronic module.

Research problem:

- to analyse functional and structural schemes of seeding control systems;
- on the basis of mechatronic approach, combining structural blocks and reducing the number of interfaces to develop a new seed control system;
- to select the hardware and software platform for the new seeding control system;
- to test the developed control system of seeding.

## MATERIALS AND METHODS

Study of control system with mechatronic module for the sowing system with fluidics elements, proposed by *Pankov A. A. et. al. (Pankov A.A. et. al., 2016)* and *Aulin V.V. et. al., (Aulin V.V. et. al., 2017*) was carried out at the stand, which includes the devices and equipment presented in Fig. 2.

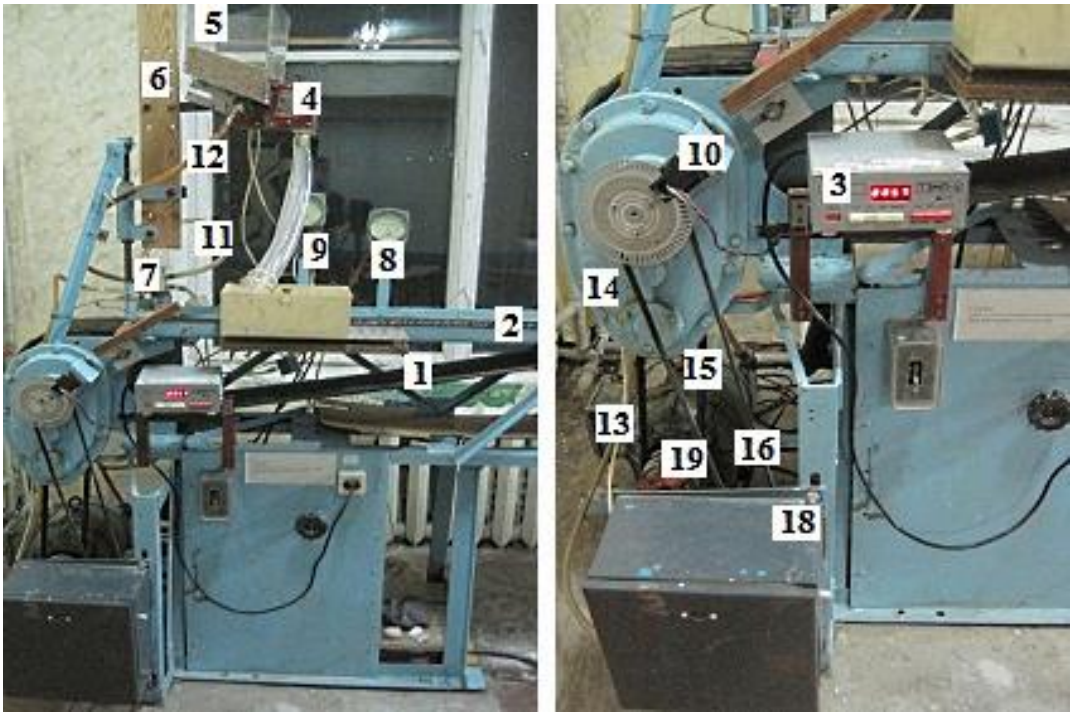


**Fig. 2 – General view of the test bench:**

*1 – conveyor with a length of 6.5 m and a width of 0.2 m; 2 – dimensional grid; 3 – pulse recorder TEMP-4 (measurement error ± 1,0%); 4 – sowing system; 5 – hopper; 6 – tripod; 7 – switch; 8, 9 – pressure measuring devices; 10 – photo sensor; 11, 12 – air ducts; 13 – signal tube; 14 – gearbox; 15, 16 – belt drive; 17 – valve; 18 – control unit with developed mechatronic module; 19 – DC motor P-21, power 1.5 kW.*

Seeding rate depends on the number of pneumatic pulses supplied to the seeding machine. The number of pulses is set by the computing device of the mechatronic module in the control unit *18*. The control unit *18* is connected to the shaft of the reducer *14* by a belt drive *16*. The control unit *18* includes: perforated disc, speed sensor, jet elements, pneumatic pulse delay line (*Pankov A. A. et. al., 2016; Aulin V. V. et. al., 2016*). When the conveyor belt moves *1* rotation is transmitted to the perforated disk in the control unit. The perforated disc speed sensor generates pneumatic pulses. Then the pneumatic pulses through the signal tube *13* through the switch *7* enter the sowing system *4*. The air pressure in the pneumatic sowing system 4 is measured by devices *8* and *9*.

Bench tests of the developed control system with mechatronic module are to determine the seeding rate when the servo motor is rotated by an angle corresponding to the location of the pneumatic switch nozzles (Fig. 5). From the vertical (neutral) position, the servo motor rotates at fixed angles (30, 90, 150, 210, 2800). This changes the number of supplied pneumatic pulses and seeding rate in the seeding system.

The experiment begins with the installation of the required seeding rate. Conveyor drive is switched on; its belt begins to move. The seeding system starts and seeding is performed on the moving belt. After sowing the seeds on the tape length section, the seed supply stops.

To determine the number of pneumatic pulses, pulse recorder *3* is used. To find the mass of seeds sown per meter of movement (seeding rate), the sown seeds were collected from the conveyor *1* and weighed. According to the results of measurements, graphical dependences were built.

## RESULTS AND DISCUSSION

The purpose of the control system integration elements is the exclusion of intermediate interfaces. In the original model (Fig. 1) structural blocks are combined and interfaces are excluded. This preserves the functional transformation performed by the resulting mechatronic module.

Therefore, the traditional structural model (Fig. 1) it is proposed to replace the improved structural model of seeding control with a mechatronic module (Fig. 3). The developed mechatronic module is more compact and assembled from common elements and assemblies, which reduces its cost.

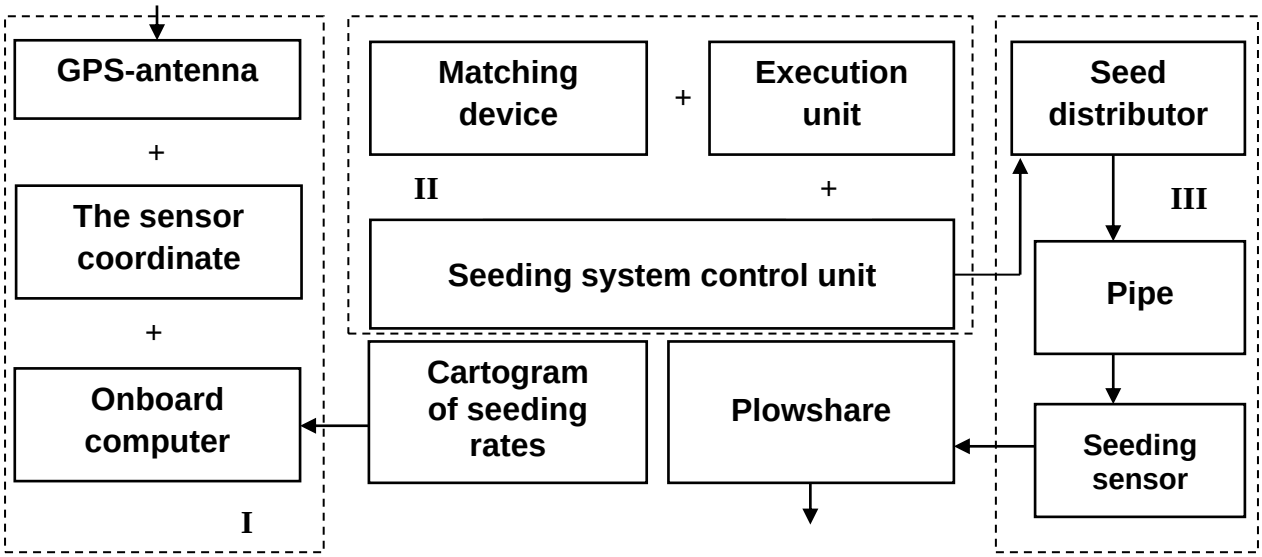


**Fig. 3 – The structural model with the mechatronic control module sowing for seeding apparatus and devices with fluidic elements:**
*I – calculator; II – mechatronic module; III – sowing system*

In the structural model with mechatronic module, the coordinate sensor with the GPS antenna and the on-Board computer are combined in one module – a smartphone or a tablet. The matching device and the executive device when combined form a mechatronic module. It is located in the control unit 18 of the seeding system (Fig. 2). The sensor of the seeding control is the wired interface which transmits the data via wireless communication. The total number of interfaces is reduced.

Compare the model with the mechatronic module (Fig. 3) and the traditional model (Fig. 1). It can be concluded that the number of blocks and interfaces in the traditional model is greater than in the developed model. Therefore, there is a structural redundancy of the system in Fig. 1.

Proposed in Fig. 3, the model with mechatronic module contains two information inputs (program of work and information feedback) and one output - impact on the sowing system. Therefore, the structural model with mechatronic module (Fig. 3) can be built as an information-pneumatic-mechanical Converter or intelligent mechatronic module. In it, functional transformations are concentrated in a single structural element (Fig. 4).

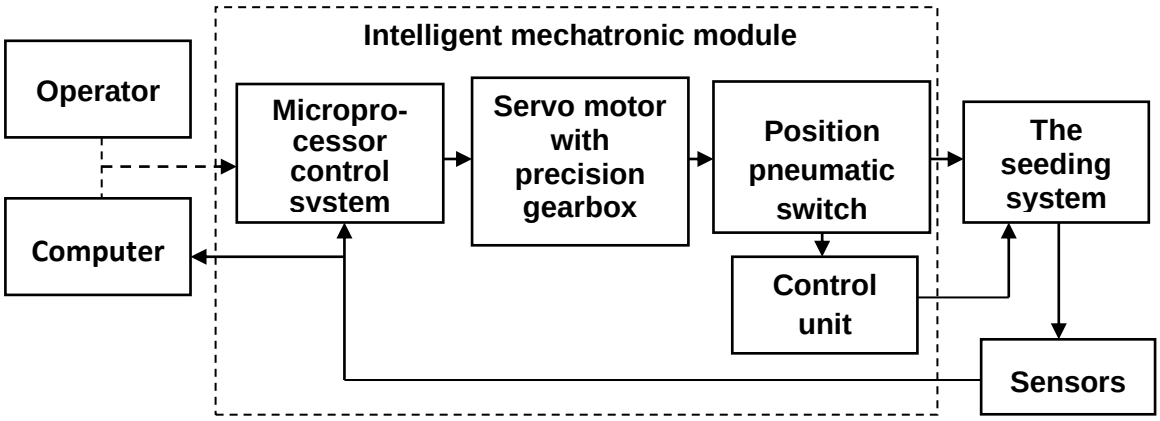


**Fig. 4 - Block diagram of intelligent mechatronic module**

Based on the diagram (Fig. 4), obtained as a result of functional and structural analysis and application of the hardware platform Arduino, a schematic diagram of the hardware-software complex regulation of the seeding rate (HSC RSR) with mechatronic module (Fig. 5) was developed.

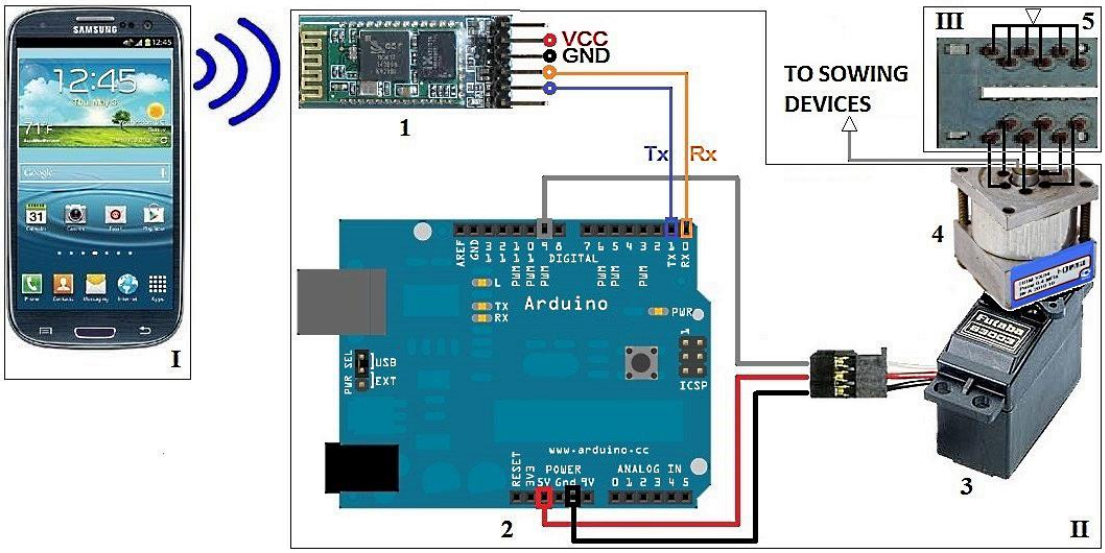


**Fig. 5. – Schematic diagram of HSC RSR:**

*I – computer; II – mechatronic module; III – control unit of the sowing system; 1 – bluetooth module; 2 – Arduino platform; 3 – servo motor; 4 – pneumatic multi-position switch; 5 – speed sensor; VCC - plus power; GND - minus power; Tx, Rx – control signals*

HSC RSR working. The seeding rate is set in the computing device *I*, transmitted to the bluetooth-module *1* and in the form of a control signal interacts with the program in the memory of Arduino *2*. From the Arduino *2*, the control action is transmitted to the servo motor *3*, which rotates the pneumatic switch *4* at a certain angle. Thus, the corresponding channels of the speed sensor *5* in the control unit III of the sowing system are connected. The number of seeds sown by the devices changes as the frequency of impulses changes. This is how the seeding rate is adjusted.

On the basis of structural and schematic diagrams (Fig. 4 and Fig. 5) the HSC RSR layout with the mechatronic module for the power control operation of the seeding system (Fig. 6), was designed.

The software of the mechatronic module consists of two parts. The first part is the Arduino *5* interaction program (Fig. 6) with actuator (servo 4) and computing device *1*. The second part is the seeding rate management application, which is designed for computing device *1*.

The Arduino interaction program with the servo drive and computing device is created in the Arduino IDE development environment. After debugging, the program is loaded into the Arduino memory to regulate the seeding rate in offline mode.

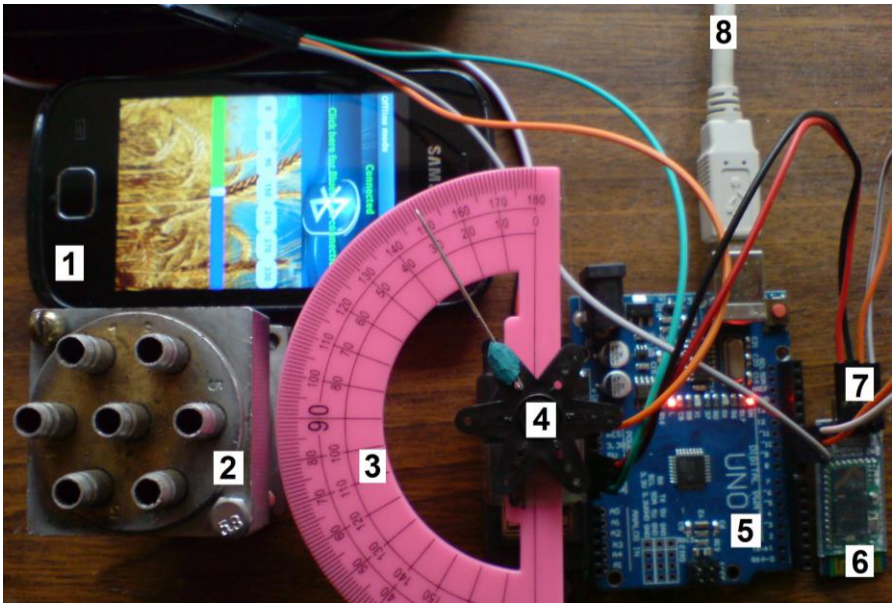


**Fig. 6 - Mechatronic module HSC RSR:**

*1 – computing device (smartphone GT-S5660); 2 – multi-position pneumatic switch (it forms one node with servo motor, but for clarity shown separately); 3 – protractor; 4 – servo motor Futaba S3003; 5 – Arduino UNO; 6 – bluetooth module HC-0,5; 7 – complete set of connecting cables; 8 – power supply Seekwood*

Operator application in the computing device to control the seeding rate was created in the programming environment MIT_app. inventor. After debugging, the application is downloaded and installed on the mobile computing device.

The developed mechatronic module is located in the control unit 18 (Fig. 2). The smartphone controls the position of the servomotor that move the pneumatic switch of the mechatronic module. For this purpose, a special program has been developed and installed on the smartphone. Then the number of pneumatic pulses per meter of the test bench conveyor movement was recorded. The results are presented in table. 1.

**Table 1**

**The number of pneumatic pulses of the control unit of the meter movement**

| Position belt's on the pulleys drive's control unit *18* (Fig. 2) | Position of multi-position pneumatic switch of mechatronic module | | | | | |
|---|---|---|---|---|---|---|
| | 1 | 2 | 3 | 4 | 5 | 6 |
| 1 | 0.51 | 1.00 | 2.05 | 4.03 | 5.55 | 6.08 |
| 2 | 0.61 | 1.21 | 2.46 | 4.82 | 6.84 | 7.28 |
| 3 | 0.74 | 1.46 | 2.97 | 5.83 | 8.03 | 8.80 |
| 4 | 0.88 | 1.76 | 3.56 | 7.00 | 9.84 | 10.56 |

Depending on the weight of the seeds sown in one pneumatic pulse, it is possible to determine the seeding rate per meter of movement of the machine. The resulting value of the seeding rate is equal to the mass of seeds sown per meter of conveyor length (Fig. 2). The graph of seeding rates for wheat seeds is shown in Fig. 7.

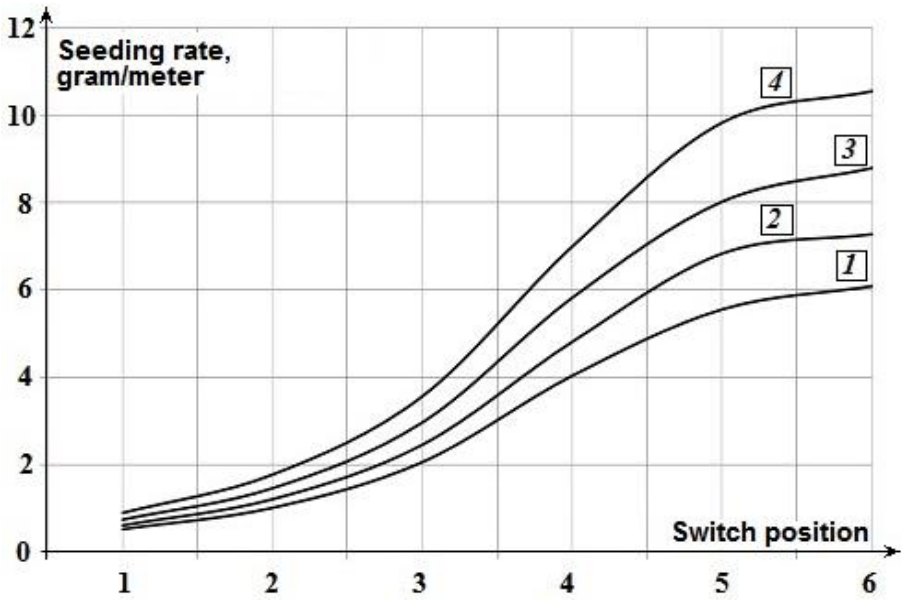


**Fig. 7 – Change in wheat seeding rate:**
*1...4 – position of the timing belt on the pulleys of the drive control unit*

According to Fig. 7 it is established that the regulation function of the seeding rate has the form of a cubic dependence. To regulate the seeding rate, it is rational to use a linear portion of the cubic dependence with increased frequencies of pneumatic pulses at the positions of the switch 3...5. This is necessary to improve the uniformity of the distribution of seeds in a row.

## CONCLUSIONS

It is established that traditional automation and control systems have an excessive structure. The presence of redundant units and interfaces leads to a decrease in the reliability of control systems, the deterioration of their mass, size and cost indicators.

It is shown that the solution of the problem of interfaces is possible with the mechatronic approach in the development of automation and control systems of seeding. The essence of the mechatronic approach is to combine elements into integrated modules and eliminate unnecessary interfaces. Thus, the performance of control systems is improved.

It is proved that the development of software and hardware automation and control systems with mechatronic approach can be based on the Arduino platform.

## REFERENCES

[1] Aniskevich L.V., Popovich A.N., (2014), Principles of construction of sowing systems in precision agriculture (Принципы построения высевающих систем в точном земледелии), *proceedings of the International scientific and technical conference «Scientific and technical progress in agricultural production»*, vol.2, pp.32–26, Minsk/Belarus;

[2] Antoshenkov R.V., Kovalev R.Yu., (2011), Mechatronic information system of machine-tractor unit (Мехатронна інформаційна система машино-тракторного агрегату), *Bulletin of KhNTUA «Mechanization of agricultural production*, Vol. 107/2, pp.110–113, Kharkiv/Ukraine;

[3] Aulin V., Hrinkiv A., Dykha A., Chernovol M., Lyashuk O., Lysenko S., (2018), Substantiation of diagnostic parameters for determining the technical condition of transmission assemblies in trucks, *Eastern-European Journal of Enterprise Technologies,* № 2 (1-92), pp.4-13, Kharkiv/Ukraine;

[4] Aulin V., Lyashuk O., Tykhyi A., Karpushyn S., Denysiuk N., (2018), Influence of rheological properties of a soil layer adjacent to the working body cutting element on the mechanism of soil cultivation, *Acta Technologica Agriculturae,* № 21/4, pp.153-159, Warsaw/Poland;

[5] Aulin V., Arifa W., Lysenko S., Kuzyk A., (2016), Improving of the wear resistance of working parts agricultural machinery by the implementation of the effect of self-sharpening. *International Journal of Engineering and Technology,* Vol.5/4, pp.126-130, Abu Dhabi/UAE;

[6] Aulin V.V., Chernovol M.I., Pankov A.A., (2017), Functional and structural analysis of the control system of seeding rate in the information system of agriculture (Функционально-структурный анализ системы управления нормой высева в информационной системе земледелия), *Collection of scientific articles of the International scientific-practical conference «Technical support of innovative technologies in agriculture*, pp.72–74, Minsk/Belarus;

[7] Aulin V.V., Chernovol M.I., Pankov A.O., Zamota T.M., Panayotov K.K. (2017), Sowing machines and systems based on the elements of fluidics, *INMATEH-Agricultural Engineering.* Vol. 53/3, pp.21–28, Bucharest/Romania;

[8] Aulin V.V., Pankov A.A., Stahorskaya A.G., (2016), Flow-program regulation of operating parameters of mobile technological machines, *MOTROL. Commission of Motorization and Energetics in Agriculture,* Vol. 18/2, pp.25–32, Lublin/Poland;

[9] Boyko A. I., Sviren M.O., (2006), Model of functioning of pneumatic sowing system for precision farming technologies (Модель функціонування пневматичної висівної системи для технологій точного землеробства), *Design, production and operation of agricultural machinery,* № 36, pp.13–18, Kirovograd/Ukraine;

[10] Kosik P.O., (2009), Mechatronic systems on agricultural mobile units (Мехатронні системи на сільськогосподарських мобільних агрегатах), *Mechanization and electrification of agriculture*, № 93, pp.464–468, Glevaha/Ukraine;

[11] Omelchenko E.Ya., Tanich V.O., Maklakov A.S., Karyakina E.A., (2013), Brief overview and prospects of application of Arduino microprocessor platform (Краткий обзор и перспективы применения микропроцессорной платформы Arduino), *Electrical systems and complexes*, № 21, pp.28–33, Magnitogorsk/Russia;

[12] Pankov A.A., Aulin V.V., Chernovol M.I., (2016), Technical means of the seeding process on the basis of fluidics elements (Технические средства процесса высева на основе элементов пневмоники), *Monograph*, 232p., Kirovograd/Ukraine;

[13] Parkhomenko Yu.M., Parkhomenko M.D., Likkey M.O., (2014), Automating the process of seeding row crops by the drill SUPN-8 technology of precision agriculture (Автоматизація процесу висіву просапних культур сівалкою СУПН-8 за технологією точного землеробства), *Collection of scientific works of Kirovograd national technical University,* Vol. 27, pp.251-259, Kirovograd/Ukraine;

[14] Pastukhov V.I., Bakum, N.V., Mikhailov A.D., Kirichenko R.V., (2015), Development of mechatronic systems for sowing machines (Розробка мехатронних систем посівних машин), *Bulletin of the Kharkiv national technical University of agriculture named after Peter Vasilenko*, №156, pp.156–162, Kharkiv/Ukraine;

[15] Poduraev Yu.V., (2006), *Mechatronics: fundamentals, methods, application (Мехатроника: основы, методы, применение)*, Ed. Engineering, 256p., Moscow/Russia;

[16] Sivak I.M., (2012), Mathematical reliability processes control system's model of dosing and redistribution of mineral fertilizers in technologies of controlled agriculture (Математична модель системи надійності керуванням процесами дозування і перерозподілу мінеральних добрив в технологіях керованого землеробства), *Bulletin of the Kharkiv national technical University of agriculture named after Peter Vasilenko*, № 128, pp.309–314, Kharkiv/Ukraine;

[17] Teryaev E.D., Filimonov N.B., Petrin K.V., (2009), Mechatronics as a computing paradigm for the development of technical cybernetics (Мехатроника как компьютерная парадигма развития технической кибернетики), *Mechatronics, automation, control*, № 6, pp.2–10, Moscow/Russia.

# SWEET SORGHUM BIOMASS QUANTITATIVE AND QUALITATIVE CHARACTERISTIC DEPENDING ON HYBRID AND TYPE OF SOIL

/

# КІЛЬКІСНА ТА ЯКІСНА ХАРАКТЕРИСТИКА БІОМАСИ ЦУКРОВОГО СОРГО ЗАЛЕЖНО ВІД ГІБРИДІВ ТА ТИПУ ҐРУНТУ

**Kharytonov M.M. [1], Martynova N.V. [2], Tokar A.V. [1], Rula I.V. [1], Babenko M.G. [1], Bagorka M.O. [1] [1]**

[1] Dnipro State Agrarian and Economics University, Faculty of Agronomy / Ukraine;

[2] Oles Honchar National University, Botany Garden, Dnipro, Ukraine

*Tel: +38-0504844773; E-mail: envteam@ukr.net*

*DOI: 10.35633/INMATEH-59-21*

***Keywords*:** *sweet sorghum, reclaimed lands, thermogravimetry, lignin structure*

**ABSTRACT**

*Ukrainian and American sweet sorghum hybrids were studied as raw material under reclaimed lands conditions in the southeast Ukraine. Among the cultivars in the range of hemicellulose destruction the highest reactivity was recorded for American hybrids, whereas the process of cellulose decomposition was most active in Ukrainian hybrids. Thermogravimetry (TG) curves of Ukrainian hybrids were more differed for plants grown on loess like loam comparative with American hybrids. The molecular structure of sweet sorghum lignin is represented by the spatially hindered hydroxyl groups of alcohol and phenolic type with the strength hydrogen bonding between some other structural fragments of macromolecules, ordinary carbon-oxygen bonds of metoxyl groups, and double carbon-carbon bonds.*

**РЕЗЮМЕ**

*Українські та американські гібриди цукрового сорго вивчалися як сировина в умовах рекультивованих земель південного Сходу України. Стадія випаровування води і видалення летких компонентів у біомасі американських гібридів проходила в інтервалі більш високих температур. Криві ТG українських гібридів різнились більше у рослинах, що були вирощені на лесоподібному суглинку, порівняно з американськими гібридами. Молекулярна структура лігніну цукрового сорго представлена просторово ускладненими гідроксильними групами спиртового і фенольного типу з міцним водневим зв'язком між деякими іншими структурними фрагментами макромолекул, звичайними вуглець - кисневими зв'язками метоксильних груп і подвійними вуглець - вуглецевими зв'язками*

## INTRODUCTION

It is known that sorghum has highly efficient C4 photosynthesis, high water use efficiency, and high tolerance to drought, salt, high or low temperature, and poor or low soil fertility (*Taylor et al., 2010; Wang et al., 2012*). Large - scale planting on marginal lands would require improved varieties with optimized biofuel-related traits and tolerance to biotic and abiotic stresses (*Mathur et al., 2017*). In fact, sweet sorghum ability to adapt to marginal growing conditions is main pre-requisite to provide significant amounts of feed stuff and energy (*Cavalaris et al., 2017*). A novel approach for the bio-refining of sweet sorghum stem is application where biodegradable material is required (*Yu et al., 2012*). In the recent years, sweet sorghum residues have been considered as lignocellulosic material that could serve as feedstock for second generation biofuels (*Anfinrud et al., 2013; Kumar et al., 2008; Zolotovs'ka et al., 2016*). Currently in Ukraine there are more than 1.1 million hectares of degraded, unproductive and technologically polluted lands (*Fileccia et al., 2014*). Among the sources of destructive environmental impact, one of the first places is occupied by mining enterprises. In the process of their production activity, the natural initial relief is disturbed, and lands on which mineral resources are directly mined, as well as areas for storing waste rocks, are withdrawn from agricultural use.

[1] *Kharytonov M.M, Prof. Ph.D. Agri.Sci.; Martynova N.V., Senior Sci. Ph.D. Bio.; Tokar A.V., Lect.. Ph.D. Chem.; Rula I.V., Lect. Chem.; Babenko M.G., Senior Sci. Ph.D. Agri.Sci.; Bagorka M.O., Lect. Manag. Ph.D.*

During open-cast mining, rocks of past geological epochs are carried onto the earth's surface, and, when interacting with the atmosphere, are exposed to intensive weathering (*Sheoran et al., 2010; Menendez and Loredo, 2018*). Substrates formed in this way significantly differ from zonal soils by the level of fertility, physical, physicochemical, agrochemical and other ecologically important characteristics. Even after prolonged reclamation, such lands are unproductive and may contain phytotoxic compounds (*Boruvka et al., 2005; Navarro et al., 2008*). Sweet sorghum is genetically diverse and variations exist for characteristics such as juice sucrose concentration, total stalk sugar yield, fresh stalk yield, biomass yield and others indicating potential for improvement (*Regassa et al., 2014*). It was possible to provide a selection process to obtain sweet sorghum hybrids with high cellulose and hemicellulose content (*Zhao et al., 2009*).

The main objective was to give sweet sorghum biomass quantitative and qualitative characteristic depending on sweet sorghum hybrid and type of soil.

## MATERIALS AND METHODS

Field experiments were carried out for two years (2017 and 2018) in Dnipropetrovsk province situated in the south-eastern part of steppe zone of Ukraine and particularly in the Pokrov land reclamation station of Dnipro State Agrarian and Economic University. In recent years, there has been a gradual increase in the average monthly air temperature with a simultaneous decrease in the amount of precipitation during the vegetation period. Eight sweet sorghum hybrids of Ukrainian and American selection *(Medove, Zubr, Pokrovske, Silosne-42, SS506, Sioux, Mohawk, G1990)* were investigated in the field experiments. Experiments were carried out in two versions. In the first case the plants were grown on long-term plant meliorated loess-like loam (LLL), in the second - on the black soil (BS) mass taken in stockpiling. The pH was 7.4 -7.6. The humus content in the loess-like loam is about 1.1%, while in the black soil it is 3.3. The experimental design was a randomized complete block with 3 replications. Sorghum seeds were sown in early May.

Sweet sorghum lignin structure was studied with methods of IR absorption spectroscopy. The IR absorption spectra of lignin were recorded with a SPECTRUM ONE (PerkinElmer) instrument. The samples for recording were prepared using the standard procedure with KBr (*Smith et al.,1987*). The quantum-chemical calculations have been carried out with the help of Gaussian 03, Revision E.01 package of programs (*Frisch et al., 200*4) at the *DFT*-PBE1PBE/6-311++G(d,p) level of theory. The spectral characteristics of located stationary points have been achieved by using the harmonic vibrational frequency approximation. The thermal analysis of plant biomass was carried out using the derivatograph Q-1500D of the “F. Paulik-J. Paulik-L. Erdey” system. Differential mass loss and heating effects were recorded (*Carrier et al., 2011; Wróblewski and Ceran, 2016*). The results of the measurements were processed with the software package supplied with the device. Samples of biomass were analyzed dynamically at a heating rate of 10°C/min in an air atmosphere. The mass of samples was 100 mg. The reference substance was aluminum oxide. All the results obtained were treated by statistical methods using the StatGraphics Plus5 software package at significance level of 0.95 % (P-value < 0.05).

## RESULTS

It was revealed that thermolysis of biomass passed in the temperature range from 20-50$^{o}$C to 530-590$^{o}$C and consisted of two periods. The first period was represented by one stage, at which the water evaporation and the active removal of volatile components took place. This process was accompanied by an expressive endothermic effect. Depending upon the sorghum cultivar and type of substrate, the temperature interval of this stage was within 20°C-150°C for Ukrainian hybrids, and within 40°C-190°C for American hybrids (Table 1 and fig.1).

The analysis of the rate of change in mass showed a single peak in this region. In samples grown on the black soil, the mass loss varied within 6.1-10.1%. In samples grown on loess-like loam, the mass loss was lower, in the range of 3.2-7.5%, with the exception of Silosne - 42 (20.4%). The rate of destruction at this stage was small and did not exceed 15%/min. However, in the samples of the Silosne - 42 taken on loess-like loam, the rate of decomposition was significantly higher (23.2%/min), indicating a high content of volatile components in biomass of plants growing on this substrate.

The second period embraced three stages which were represented by the thermal reactions sum of decomposition of individual constituents: hemicellulose, cellulose and lignin.

At the same time, the intervals of these components destruction partially overlapped. The temperature of 150°C-160°C was the beginning of the exothermic reactions passing.

The main process of hemicellulose and cellulose decomposition passed in the temperature interval 180°C-734,00°F, implied two stages and was characterized by one or two peaks in this range (Fig.2). In this temperature range, a small fraction of the lignin also decomposed, but without expressed peaks. The stage of hemicellulose and cellulose destruction was accompanied by the greatest mass loss (55-67%).

**Table 1**

**Data of Ukrainian and American hybrids of sweet sorghum biomass thermal degradation.**

| Type | Temperature interval [°C](temperature of maximum rate of decomposition [°C] Mass loss [%] | | | | The share of residual mass [ %] |
|---|---|---|---|---|---|
| **Zubr** | | | | | |
| **S** | 40–140 (100) 6.8 | 140–220 (190) 17.0 | 220–390 (280) 40.6 | 390–570 (430) 30.4 | 5.2 |
| **LL** | 30–120 (90) 3.2 | 120–250 (220) 35.2 | 250–380 (270) 31.8 | 380–530 (410) 19.8 | 10.0 |
| **Medove** | | | | | |
| **S** | 40–140 (110) 8.6 | 140–220 (190) 13.6 | 220–380 (270) 47.4 | 380–550 (430) 24.0 | 6.4 |
| **LL** | 30–130 (90) 6.4 | 130–210 (180) 14.2 | 210–390 (270) 50.2 | 390–540 (440) 20.4 | 8.8 |
| **Pokrovske** | | | | | |
| **S** | 50–130 (110) 6.4 | 130–200 (150) 9.2 | 200–350 (270) 47.6 | 350–570 (390) 27.2 | 9.6 |
| **LL** | 30–130 (90) 4.4 | 130–230 (200) 17.6 | 230–360 (270) 44.0 | 360–550 (430) 26.8 | 7.2 |
| **Silosne - 42** | | | | | |
| **S** | 20–130 (100) 7.0 | 130–220 (190) 15.6 | 220–380 (270) 46.6 | 380–560 (430) 24.4 | 6.4 |
| **LL** | 30–140 (80) 20.4 | 140–230 (190) 25.2 | 230–330 (270) 31.8 | 330–420 (340) 12.6 | 10.0 |
| **Mohawk** | | | | | |
| **S** | 50–180 (110) 6.87 | 180–300 (290) 24.24 | 300–390 (320) 33.73 | 390–590 (460) 28.89 | 6.27 |
| **LL** | 50–160 (110) 6.87 | 160–400 (280) 58.98 | | 400–560 (420) 25.25 | 8.9 |
| **SS506** | | | | | |
| **S** | 50–160 (100) 7.4 | 160–390 (290) 58.2 | | 390–560 (430) 24.8 | 9.6 |
| **LL** | 50–180 (100) 7.47 | 180–300 (280) 31.11 | 300–390 (310) 27.27 | 390–550 (450) 26.87 | 7.28 |
| **G1990** | | | | | |
| **S** | 40–190 (100) 10.1 | 190–380 (310) 54.94 | | 380–550 (440) 25.86 | 9.1 |
| **LL** | 40–180 (100) 7.19 | 180–300 (280) 28.97 | 300–390 (310) 26.86 | 390–570 (540) 25.46 | 11.52 |
| **Sioux** | | | | | |
| **S** | 40–180 (100) 6.08 | 180–390 (280) 55.52 | | 390–570 (410) 23.6 | 14.8 |
| **LL** | 50–180 (90) 7.2 | 180–290 (280) 22.2 | 290–380 (310) 33.6 | 380–550 (440) 25.4 | 11.6 |

Among the cultivars in the range of hemicellulose destruction the highest reactivity was recorded for American hybrids, whereas the process of cellulose decomposition was most active in Ukrainian hybrids.

During the last stage of thermolysis (360°C-590°C) thermal decomposition of cellulose and lignin is completed, the carbonated residue combusts as well. At this stage, the most pronounced exothermic effect emerged.

The weight loss was 23.6-30.4% (black soil) and 12.6-26.9% (loess-like loam). TG curves of Ukrainian hybrids were more differed for plants grown in loess like loam comparative with American hybrids.

The rate of decomposition was small for all cultivars and substrates and varied from 6.2 %/min to 11.4 %/min. G1990, Zubr and Pokrovske had higher reactivity than others hybrids. The most complete combustion of biomass (except for the Pokrovske, SS506 and Sioux) was observed on black soil.

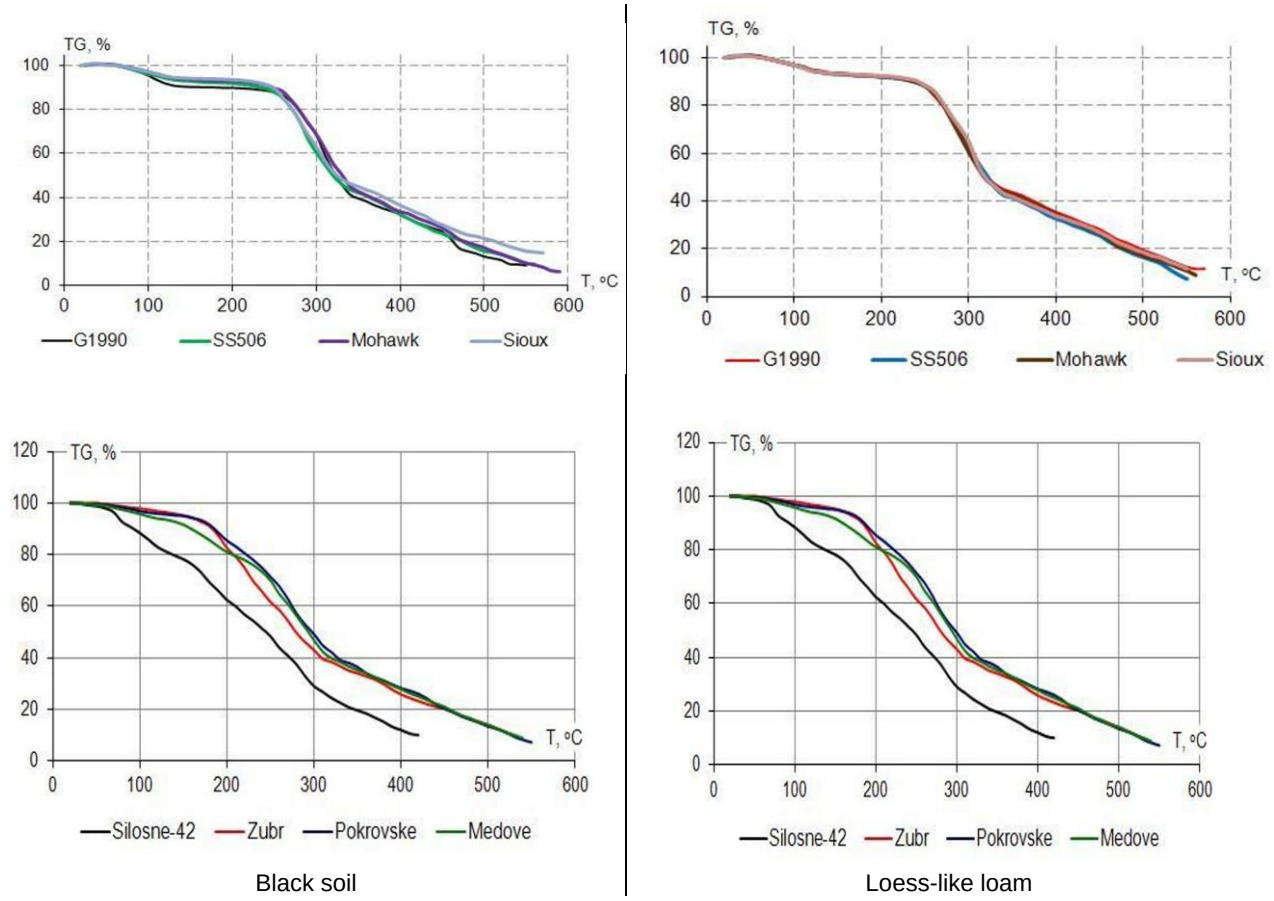


**Fig. 1 - TG curves of sorghum biomass thermal destruction**

The activation energy of thermal-oxidative degradation is a universal sensitive criterion for assessing the thermal stability of biomass. Based on the calculation of the kinetic parameters of different stages of biomass thermal decomposition, it was found that the thermal stability of various sorghum samples is somewhat different. The values of the activation energy of the American and Ukrainian hybrids did not differ significantly and were in the range of 55.0-66.2 kJ $mol^{-1}$on black soil at the stage of volatile components removal. At the stage of hemicellulose and cellulose decomposition, the activation energy indices in American hybrids practically did not change, while in Ukrainian hybrids they decreased almost twice and varied within 28.5-31.9 kJ $mol^{-1}$ (Table 2). Thus, for the destruction of molecular bonds at this stage, it is required to apply a greater amount of energy to the biomass of American hybrids than for the Ukrainian ones, which indicates a higher rate of thermal stability of their biomass. It is revealed that the type of substrate can affect the thermal stability of biomass. In American hybrids G1990 and Mohawk, a decrease in activation energy (by 5.5-10.9%) was observed at both stages of biomass decomposition, and vice versa, in hybrids SS506 and Sioux, this indicator increased by 5.6-11.4%. In all Ukrainian hybrids, at the first stage, a medium (12.2-19.5%) and significant (32.1 - 42.5%) decrease in the activation energy value was noted. At the second stage, the activation energy of the hybrids Pokrovske and Zubr was higher than at the first stage by 10.4% and 22.3%, respectively, and lower by 3% and 27.8% in the hybrids Medove and Silosne-42.

It is known that sorghum feedstock has a high volatile content while a low fixed carbon ratio that indicates a lower lignin composition in the biomass (*Dhyani et al., 2017*). According to data in sweet sorghum bagasse average content of cellulose, hemicelluloses and lignin are 34-45%, 15-25%, and 12-18% respectively (*Bakeer et al., 2013*). Lignin is known to impede conversion of plant biomass to pulp or biofuels.

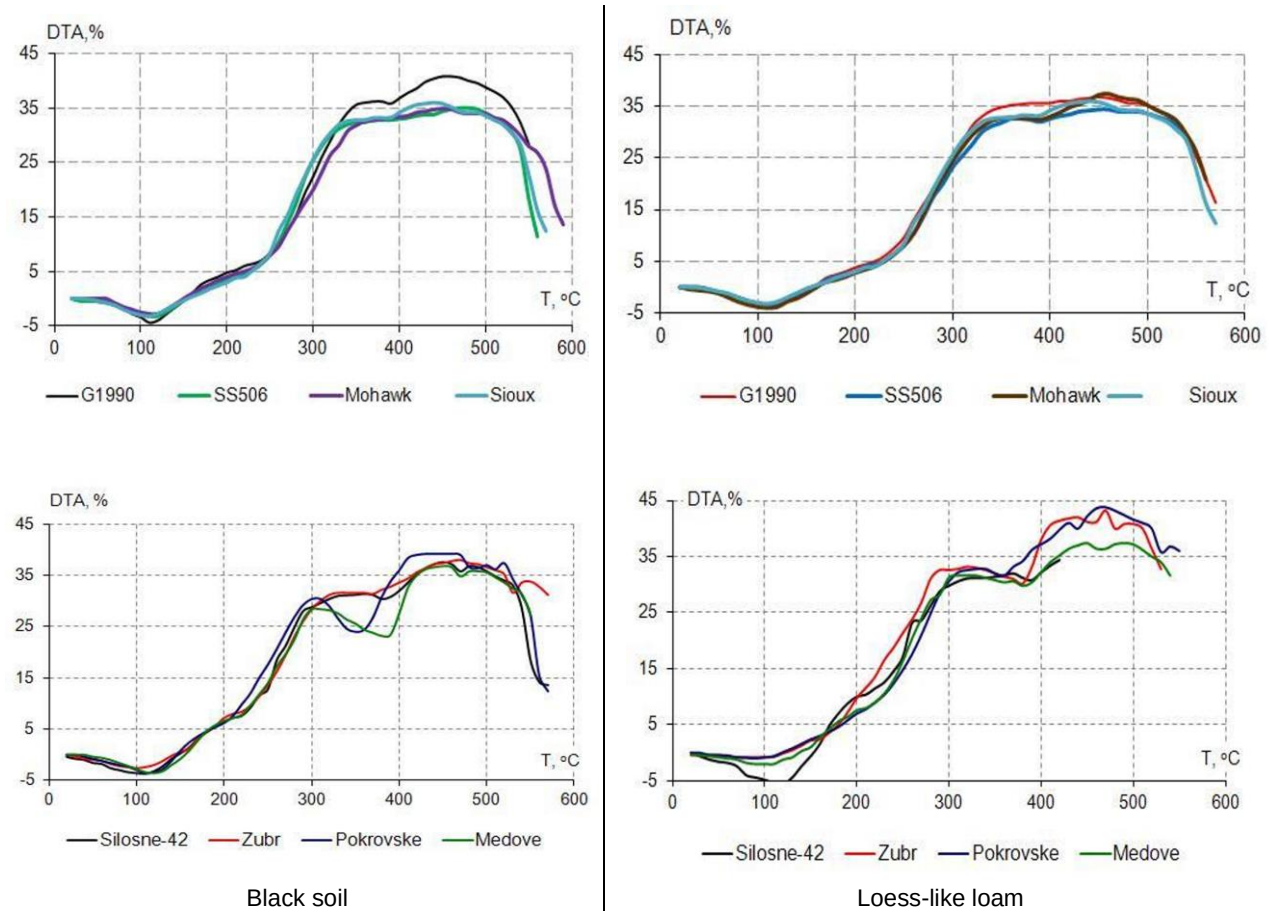


Black soil Loess-like loam

**Fig. 2 - DTA curves of sorghum biomass thermal destruction**

**Table 2**

**The kinetic characteristics of sorghum biomass thermal - oxidative degradation**

| Sorghum hybrid | Stage of biomass decomposition | Black soil | | Loess-like loam | |
|---|---|---|---|---|---|
| | | Approximation dependence, (correlation coefficient R) | Activation energy [kJ mol$^{-1}$] | Approximation dependence, (correlation coefficient R) | Activation energy [kJ mol$^{-1}$] |
| **Mohawk** | I* | -2.6375x + 4.0095 (R=0.99) | 65.84 | -2.446x + 3.7291 (R=0.98) | 60.22 |
| | II | -0.7663x - 0.9664 (R= 0.91) | 63.60 | -0.8727x - 0.646 (R=0.95) | 60.07 |
| **SS506** | I* | -2.4769x + 3.8082 (R=0.99) | 55.03 | -2.5468x + 3.9102(R=0.97) | 61.30 |
| | II | -0.7575x - 0.8531 (R= 0.94) | 57.52 | -0.8181x - 0.741 (R= 0.96) | 57.87 |
| **G1990** | I* | -2.5954x + 4.0259 (R =0.98) | 63.93 | -2.3516x + 3.5436 (R=0.99) | 59.58 |
| | II | 0.4706x - 1.2099 (R=0.87) | 66.24 | -0.8659x - 0.6674 (R=0.98) | 59.04 |
| **Sioux** | I* | -2.1499x + 3.2183 (R=0.99) | 64.41 | -2.2165x + 3.3902 R=0.99) | 67.37 |
| | II | -0.5949x - 1.4405 ($R^2$ = 0.93) | 63.36 | -0.681x - 1.0866 (R=0.97) | 59.78 |
| **Zubr** | I* | -2.4123x + 3.8734 (R=0.98) | 60.25 | -2.0001x + 3.2684 (R=0.99) | 48.47 |
| | II | -1.7493x + 1.5718 (R=0.94) | 28.25 | -2.7913x + 3.6333 (R =0.99) | 34.53 |
| **Medove** | I* | -2.2985x + 3.7155 (R=0.98) | 56.45 | -2.1829x + 3.5084 (R=0.98) | 38.35 |
| | I | -2.6237x + 3.9057 (R=0.96) | 29.75 | -2.4449x + 3.4016 (R=0.96) | 28.89 |
| **Pokrovske** | I* | -2.1553x + 3.418 (R= 0.99) | 66.18 | -2.3482x + 3.744 (R=0.98) | 38.02 |
| | II | -3.343x + 5.5522 (R=0.99) | 31.86 | -1.5993x + 0.8747 (R=0.97) | 35.16 |
| **Silosne-42** | I* | -2.4598x + 3.9316 (R=0.98) | 61.18 | -2.1706x + 3.9713 (R=0.99) | 53.69 |
| | II | -1.8765x + 1.9653 (R=0.95) | 29.85 | -1.8565x + 3.0096 (R=0.98) | 21.52 |

**I - stage of volatile components removal, II - stage of hemicellulose and cellulose decomposition*

The removal of lignin from plant biomass is a costly process; hence, research efforts are now aimed at designing genotypes that either deposit less lignin or produce lignin that are more amenable to chemical degradation (*Sticklen, 2006*). Lignins are characterized by the extreme complexity of the chemical structure, heterogeneity in the monomeric composition and types of intermonomeric links.

Unlike cellulose, which has the same structure for all plants, there are no identical lignins in nature (*Davin and Lewis, 2005; Vanholme et al., 2010*). The main building blocks of lignin are the hydroxycinnamyl alcohols (or monolignols) coniferyl alcohol and sinapyl alcohol, with typically minor amounts of p-coumaryl alcohol (*Rippert et al., 2009*). To study the sweet sorghum lignin macromolecules by method of IR absorption spectroscopy, some model structures have been chosen as the typical building blocks such as p-coumaryl (A), coniferyl (B) and sinapyl (C) alcohols with trans-configuration of double carbon-carbon bond in these molecules. Some final geometries have been located at DFT-PBE1PBE/6-311++G (d,p) level of theory. The relatively uniform nature of the overestimation of quantum-chemical harmonic vibrational frequencies for a particular theoretical procedure allows the application of generic frequency scale factors, which in the case of PBE approximation are 0.9904 and 0.9944 for basis sets 6-31+G(d,p) and 6-311+G (d,p), respectively (*Merrick et al., 2007*). The results of calculations as well as some experimental parameters of IR absorption spectra are in Table 3 and Figure 3.

**Table 3**

**Some harmonic vibrational frequencies [$cm^{-1}$], obtained experimentally as well as calculated at PBE1PBE/6-311++G(d,p) level of theory**

| Intensity, band shape[1] | Theoretical model | | | Experiment | Interpretation |
|---|---|---|---|---|---|
| | A | B | C | | |
| **v. s., wd.** | 3879 | 3878 | 3877 | 3417–3438 | $\nu_{(OH)}$ of alcohol groups, capacity of moisture |
| | 3871 | 3801 | 3793 | | $\nu_{(OH)}$ of phenolic groups, capacity of moisture |
| **av.** | – | 3084<br>3016 | 3087<br>3017 | 2917–2938 | $\nu_{(CH3)}$ of methoxyl groups |
| **w.** | 3016<br>2971 | 3015<br>2970 | 3016<br>2970 | 2833–2854 | $\nu_{(CH2)}$ of hydroxymethyl groups |
| **w.** | 1729 | 1728 | 1729 | 1719–1729 | $\nu_{(CC)}$ of carbon-carbon double bonds |
| **av.** | 1674<br>1552 | 1671<br>1559 | 1661<br>1555 | 1615–1625<br>1480–1510 | $\nu_{(CC)}$ of benzene rings |
| **w.** | – | 1499<br>1461 | 1497<br>1453 | 1408–1427<br>1365–1378 | $\delta_{(CH3)}$ of methoxyl groups |
| **w.** | 1384 | 1329 | 1363 | 1245–1250 | $\delta_{(CC)}$ with $\delta_{(CH)}$ of benzene rings |
| **v. s.** | 1063 | 1064 | 1064 | 1041–1052 | $\nu_{(CO)}$ of methoxyl with hydroxymethyl groups |

*Symbols explanation: s. – strong, av. – average intensity, w. – weak, wd. – wide, v. – very; ν – stretching vibrations, δ – bending vibrations*.

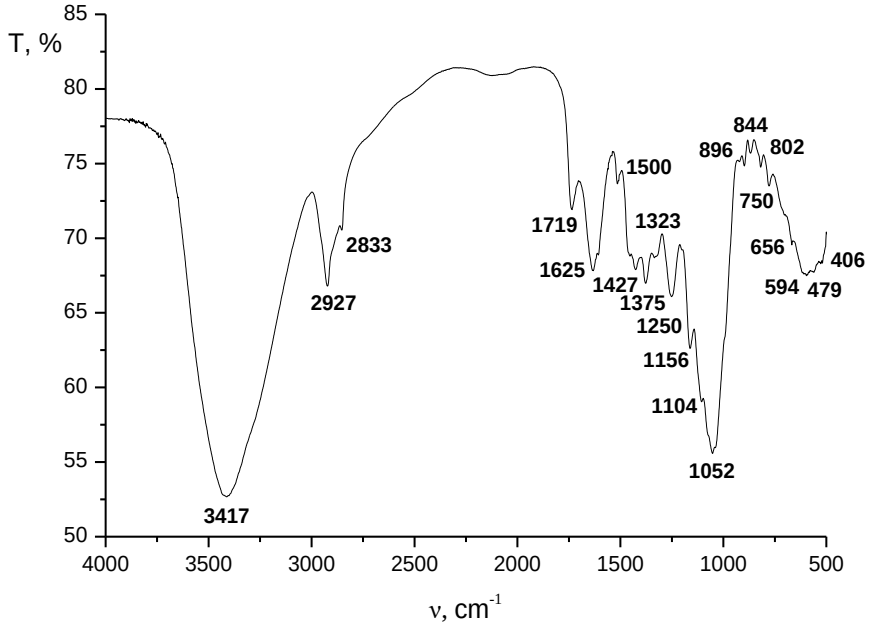


**Fig. 3 - The typical IR absorption spectrum of native lignin material derived from saccharine sorghum**

Analysis of the results showed that the most intensive absorption bends are in area 3417–3438 and 1041–1052 $cm^{-1}$. For the first one, mainly deals with the stretching vibrations of spatially hindered hydroxyl groups of alcohol or phenolic type with the strength hydrogen bonding between some other structural fragments of macromolecules.

For the second one, some intensive stretching vibrations of ordinary carbon-oxygen bond of metoxyl groups have the main contribution with predominance of intra-molecular hydrogen bonding effects, which occur at the distances about 2.050–2.070 Å. There are also two typical stretching vibrations of benzene rings at 1625 and 1500 $cm^{-1}$. As to the area 1719–1729 $cm^{-1}$, there is only one not very intensive fringe giving by the stretching vibrations of double carbon-carbon bonds. However, this band may be interpreted as a conjugated carbonyl group's signal. In fact, such type structural fragments usually have much more intensive bands with shifting in area ~1750 $cm^{-1}$. Finally, some average sets of theoretical versa experimental wave numbers, which are shown below correlate to each other:

$$\nu,\delta(\text{expt.}) = (124.82 \pm 54.09) + (0.89 \pm 0.02) * \nu,\delta\ (\text{theor.});$$

$$r=0.997;\ s_0=74.58;\ n=13.$$

The proposed theoretical models are validated in reflection of spectral and energetic parameters for investigating systems.

**ACKNOWLEDGEMENT**

The work has been funded by the Ukrainian Ministry of Education and Science.

**CONCLUSIONS**

Thermolysis of dry sorghum biomass took place in the temperature range from 20-50°C to 530-590°C. The stage of water evaporation and removal of volatile components passed in the interval of higher temperatures in the biomass of American hybrids. Among the cultivars in the range of hemicellulose destruction the highest reactivity was recorded for American hybrids, whereas the process of cellulose decomposition was most active in Ukrainian hybrids. TG curves of Ukrainian hybrids were more differed for plants grown on loess like loam comparative with American hybrids. It is required to apply a greater amount of energy for the destruction of molecular bonds at stage of main components degradation to the biomass of American hybrids than for the Ukrainian ones, which indicates a higher thermal stability of their biomass. The most complete combustion of biomass (except for the Pokrovske, SS506 and Sioux) was observed on black soil. The molecular structure of sweet sorghum lignin is represented by the spatially hindered hydroxyl groups of alcohol and phenolic type with the strength hydrogen bonding between some other structural fragments of macromolecules, ordinary carbon-oxygen bonds of metoxyl groups, and double carbon-carbon bonds.

**REFERENCES**

[1] Anfinrud R., Cihacek L., Johnson B. L., Ji Y., Berti M. T., (2013), Sorghum and kenaf biomass yield and quality response to nitrogen fertilization in the Northern Great Plains of the USA*. Industrial Crops and Products,* vol. 50, pp.59-165. https://doi.org/10.1016/j.indcrop.2013.07.022;

[2] Bakeer B., Taha I., El - Mously H., Shehata S.A., (2013), On the characterisation of structure and properties of sorghum stalks. *Ain Shams Engineering Journal*, vol. 4, pp.265–271. http://dx.doi.org/10.1016/j.asej.2012.08.001;

[3] Borůvka L., Vacek O., Jehlička J., (2005), Principal component analysis as a tool to indicate the origin of potentially toxic elements in soils. *Geoderma*, vol. 128 (3–4), pp. 289-300. https://doi.org/10.1016/j.geoderma.2005.04.010;

[4] Carrier M. Loppinet-Serani A., Denux D., Lasnier J.M., Ham-Pichavant F., Cansell F., Aymonier C., (2011), Thermogravimetric analysis as a new method to determine the lignocellulosic composition of biomass. *Biomass and Bioenergy*, vol.35, pp.298-307. https://doi.org/10.1016/j.biombioe.2010.08.067;

[5] Cavalaris C., Merkouris O., Karamoutis C., Akademir S., Mamma D., Kekos D., Gemtos T., (2017), Effects of Row Spacing on Growth, Yield and Quality Parameters of Sweet Sorghum. *Journal of Agricultural Faculty of Gaziosmanpasa University.* Vol.34(1). P.229–237. doi:10.13002/ jafag4215;

[6] Davin L.B., Lewis N.G., (2005), Lignin primary structures and dirigent sites. *Current Opinion in Biotechnology*, vol. 16(4), pp.407-415. https://doi.org/10.1016/j.copbio.2005.06.011;

[7] Dhyani V., Kumar J., Bhaskar T., (2017), Thermal decomposition kinetics of sorghum straw via thermogravimetric analysis. *Bioresource Technology*, vol. 245, pp. 1122-1129. http://dx.doi.org/10.1016/j.biortech.2017.08.189;

[8] Fileccia T., Guadagni M., Hovhera V., Bernoux M., (2014), Ukraine: Soil fertility to strengthen climate resilience Preliminary assessment of the potential benefits of conservation agriculture FAO Investment Centre. Report №9.79p., Rome/ Italy;

[9] Frisch M. J., Trucks G. W., Schlegel H. B. et al., (2004), Gaussian 03, Revision E.01 [*Computer software*]. Gaussian, Inc.: Wallingford CT;

[10] Kumar A., Wang L., Dzenis Y.A., Jones D.D., Hanna M., (2008), Thermogravimetric characterization of corn stover as gasification and pyrolysis feedstock. *Biomass and Bioenergy*, vol. 32(5), pp.460-467. doi:10.1016/ j.biombioe.2007.11.004;

[11] Mathur S., Umakanth A.V., Tonapi V.A., Sharma R., Sharma M.K., (2017), Sweet sorghum as biofuel feedstock: recent advances and available resources. *Biotechnol Biofuels,* vol. 10: 146, pp. 1-19. https://doi.org/10.1186/s13068-017-0834-9;

[12] Menéndez, J.,Loredo J., (2018), Reclamation of Degraded Landscape due to Open Pit Coal Mining: Biomass for Renewable Power Plants**.** *WSEAS Transactions on Environment and Development*, 14, 251–255. http://www.wseas.org/multimedia/journals/environment/2018/a505915-aav.php;

[13] Merrick J. P., Moran D., Radom L., (2007), An Evaluation of Harmonic Vibrational Frequency Scale Factors. *Journal Physical Chemistry A.*, vol.111 (45), pp.11683-11700. https://doi.org/10.1021/jp073974n;

[14] Navarro, M.C., Pérez-Sirvent, C., Martínez-Sánchez, M.J., Vidal, J., Tovar, P.J., Bech, J., (2008), Abandoned mine sites as a source of contamination by heavy metals: A case study in a semi-arid zone. *Journal of Geochemical Exploration*, 96(2–3), 183-193;

[15] Regassa T.H., Wortmann C.S., (2014), Sweet sorghum as a bioenergy crop: literature review. *Biomass Bioenergy*. Vol.64. P.348–355. https://doi.org/ 10.1016/j.biombioe.2014.03.052;

[16] Rippert P., Puyaubert J., Grisollet D., Derrier L., Matringe M., (2009), Tyrosine and phenylalanine are synthesized within the plastids in Arabidopsis. *Plant Physiology,* vol.149, pp.1251-260;

[17] Sheoran V., Sheoran A.S., Poonia P., (2010), Soil reclamation of abandoned mine land by re-vegetation: a review. *International Journal of Soil, Sediment and Water,* 3(2), Art.13;

[18] Smith G.A., Bagby M.O., Lewellan R.T., Doney D.L., Moore P.H., Hills F.J., Campbell L.G., Hogaboam G.J., Coe G.E., Freeman K., (1987), Evaluation of Sweet Sorghum for Fermentable Sugar Production Potential. *Crop Science,* vol. 27(4), pp. *788-793.* doi:10.2135/cropsci1987.0011183X002700040037x;

[19] Sticklen M. (2006) Plant genetic engineering to improve biomass characteristics for biofuels. *Curr Opin Biotechnol*. 2006,17(3):315-319DOI: 10.1016/j.copbio.2006.05.003;

[20] Taylor S. H., Hulme S. P., Rees M., Ripley B., Wooward F. I., Osborne C. P., (2010), Ecophysiological Traits in C3 and C4 Grasses: A Phylogenetically Controlled Screening Experiment, *New Phytologist*, Vol. 185, No. 3, pp. 780-791. doi:10.1111/j.1469-8137.2009.03102.x;

[21] Vanholme R., Demedts B., Morreel K., Ralph J., Boerjan W., (2010), Lignin Biosynthesis and Structure. *Plant Physiology,* vol.153, pp. 895-905. https://doi.org/10.1104/pp.110.155119;

[22] Wang M., Xin Z., Tonnis B., Farrell G., Pinnow D., Chen Z., Davis J., Yu J., Hung Y, Pederson G.A., (2012), Evaluation of sweet sorghum as a feedstock by multiple harvests for sustainable bioenergy production. *Journal of Sustainable Bioenergy Systems*, vol. 2, pp. 122-137;

[23] Wróblewski R., Ceran B., (2016), Thermogravimetric analysis in the study of solid fuels. *E3S Web of Conferences*, 10, 00109 (2016), pp.1-6. DOI: 10.1051/ e3sconf/20161000109;

[24] Zhao Y.L., Dolat A., Steinberger Y., Wang X., Osman A., Xie G.H., (2009), Biomass yield and changes in chemical composition of sweet sorghum cultivars grown for biofuel. *Field Crops Research*, vol. 111 (1-2), pp. 55-64. https://doi.org/10.1016/j.fcr.2008.10.006;

[25] Yu J., Zhang T., Zhong J., Zhang X., Tan T., (2012), Biorefinery of sweet sorghum stem. *Biotechnology Advances*, vol. 30(4), pp.811-816. https://doi.org/10.1016/j.biotechadv.2012.01.014;

[26] Zolotovs'ka O.V., Kharytonov M**.,** Onyshchenko O., (2016), Agricultural residues gasification, dependency of main operational parameters of the process on feedstock characteristics. *INMATEH, Agricultural Engineering*, Vol.50, No.3.pp.119-126, Bucharest/Romania.

# OPTICAL SIMULATION OF A SOLAR PARABOLIC COLLECTOR AND CAVITY RECEIVERS USING RAY-TRACING SOFTWARE TRACEPRO WITH NATIVE CONDITIONS OF IRAN FOR SOLAR DRYERS

**/**

شبیه سازی نوری کلکتور بشقابی به وسیله دریافت کننده های استوانه ای و کروی بهینه *شده با استفاده از نرم افزار* ***TRACEPRO*** *با شرایط بومی ایران برای خشک های خوردشیدی*

**Hosseinzadeh J. [1], Mohhebi A.*[1], Loni R.[2] [1]**

[1] Urmia University, Department of Mechanical Engineering of Biosystems / Iran;

[2] Tarbiat Modarres University, Department of Mechanical Engineering of Biosystems / Tehran

*Tel: +98 914 441 2042; E-mail: arash.mech@gmail.com, a.mohebbi@urmia.ac.ir*

*DOI: 10.35633/INMATEH-59-22*

***Keywords:*** *Parabolic dish collector, ray-tracing simulation, TracePro software, Monte Carlo method*

## ABSTRACT

*This paper proposes the design and optical evaluation of a solar dish collector with changeable structure using TracePro software with native conditions of Iran for solar dryers. The designed dish concentrator has a diameter of 1.5m. TracePro's goal is to design and evaluate complex optical systems. Modeling a parabolic concentrator in TracePro can be achieved using several methods. All segments of dish collectors are made of glass (perfect parabolic mirror with a reflection coefficient of 95%). In the ray-tracing simulations, the two cavity receiver model (cylindrical and semi-sphere) is added to study the influence of physical parameters of the cavity. The simulation result shows that semi-spherical receiver is better and it has got better optical performance. Thereby it is highly recommended for various types of solar dryers such as direct drying (solar box dryer), or indirect drying (solar cabinet dryer).*

چکیده:

این مقاله طراحی و شبیه سازی اپتیکی یک کلکتور بشقابی خورشیدی با ساختار متغیر را با استفده از نرم افزار *TracePro* برای شاریط بومی ایران برای استفاده در خشک کن های خورشیدی ارائه می نماید.قطر بشقاب بررسی شده 1.5 متر می باشد. هدف نرم افزار *TracePro* مدل سازی اپتیکی سیستم های پیچیده برای سامانه های خورشیدی وآنالیزس نوری آنها می باشد. روشهای مختلفی می توان برای مدل سازی کلکتور بشقابی در نرم افزار *TrcePro* استفاده کرد. در این مقاله شبیه سازی های نوری واحد کلکتور بشقابی پارابولیک با استفاده از نرم افزار پرتوی ردیابی *TracePro* ارائه شده است. بخش های کوچکی از کلکتور بشقابی پارابولیک از شیشه ساخته شده اند (آینه پارابولیک کامل با ضریب بازتاب 95٪). دو مدل گیرنده (استوانه ای و نیمه کروی) به منظور بررسی تأثیر پارامترهای فیزیکی حفره در شبیه سازی های ردیابی پرتویی اضافه شده است. نتیجه شبیه حاکی از این می باشدکه گیرنده نیمه کروی بهتر است و عملکرد نوری بهتری دارد. بدین ترتیب برای انواع مختلفی از خشک کن های خورشیدی مانند خشک کردن مستقیم (خشک کن جعبه خورشیدی) ، خشک کردن غیرمستقیم (خشک کن کابین خورشیدی) بسیار توصیه می شود.

## INTRODUCTION

As the primary source of energy, solar energy is one of the best alternatives to fossil fuels because it is green, it is environmentally-friendly and it can be used in systems requiring minimal maintenance and operating costs. Solar energy use is critical to tackle recent energy problems such as global warming, the fossil fuel depletion and high electricity prices *(Stijepovic M.Z., Papadopoulos A.I. et al., 2017)*. The abundance is the key advantages of solar energy *(Jamil and Akhtar, 2017)* and possibility of direct heat conversion *(Kasaeian A., Daneshazarian R. et al., 2017)*. The production of solar thermal energy can be carried out with concentrating technologies such as parabolic trough collectors, linear Fresnel reflectors, solar plates and solar towers *(Kaushika N. and Reddy K., 2000)*.

In tropical and semi-tropical areas, the use of solar energy for thermal applications such as cooking, heating and drying is well established *(Bal L.M., Satya S. et al., 2010)*. In Iran, conventionally, open sun drying (OSD) is used to dry agricultural products. The disadvantage of OSD is the uncontrolled heat transfer to the product and slow drying rate. As a result, the quality of the products is very poor and they aren't able to compete on the international market.

[1] *Hosseinzadeh J., Ph.D. Stud. Eng.; Mohhebi A., Lect. Ph.D. Eng.; Loni R., Lect. Ph.D.*

To improve the product quality, drying should be performed in controlled conditions in order to maintain a constant temperature and a low relative humidity. It can be done by means of hot air (produced either using electric energy or biomass), or by means of infrared radiation.

Such methods, however, require a lot of investment and also consume a lot of energy. One of the cleanest and simplest options is to dry using renewable energy sources.

Karthikeyan and Murugavelh have developed a solar tunnel dryer for turmeric drying integrated with a solar flat plate collector. They conducted drying kinetics experiments and found that the Verma model is best suited to represent the drying behaviour of turmeric *(Karthikeyan A. and Murugavelh S., 2018)*.

José Vásquez et al., proposed a novel solar dryer for agricultural products with thermal energy storage system. The dryer's mathematical model included three stages: a solar panel, a solar accumulator and a drying chamber *(Vásquez J, Reyes R. et al., 2019)*. Kumar et al. modeled a greenhouse dryer with modifications to define temperature distribution with wind speed variability. They reported a better drying rate for forced circulation compared to natural convection in accordance with the available experimental results *(Kumar R., Gupta V. et al. 2017)*. Compared to linear technologies, solar dishes have high concentration ratios and are therefore promising for high-temperature applications. In recent years, substantial theoretical and experimental work has been carried out on solar dish concentrators for a wide range of industrial applications *(Reddy K. and Kumar N.S., 2009; Wang M. and Siddiqui K., 2010; Wu Xiao et al., 2010; Wu Xiao et al., 2010; Wu Z., Caliot C et al., 2010; Li Tang et al., 2011; Lovegrove K., Burgess G. et al., 2011)*. In solar collectors, the receiver plays the most important role in improving the efficiency of the solar system and it must be designed to result in high optical efficiency and low heat loss.

In the literature, the shape and dimensions of the receivers have been investigated to achieve a design that absorbs as much solar energy as possible while having a low external area to reduce heat loss. In past years, a lot of research has centered on solar collectors as compact technologies that can generate heat at high temperatures and also different absorber shapes, such as conical, cylindrical and rectangular, have been investigated. Roux et al. designed a rectangular absorber for solar thermal Brayton cycle in which the air was used as working fluid. They suggested a method for determining temperatures of the receiver surface and performance of various cavity receiver *(Le Roux W.G., Bello-Ochende T. et al. 2014)*. Thirunavukkarasu and Venkatachalam performed an experimental analysis on the thermal efficiency of the cavity receiver with specific aspect ratios. They found that the temperature of the receiver's surface was decreased by increasing the aspect ratio *(Venkatachalam T. and Cheralathan M., 2019)*.

Evangelos Bellos et al. investigated different cavity receivers (cylindrical, rectangular, spherical, conical and cylindrical-conical) under different operating temperature levels. They reported that cylindrical-conical shape receiver has the best optical, thermal and exergy efficiency *(Bellos E., Bousi E. et al., 2019)*. Song Yang et al. suggested a new model of a heat-pipe cavity receiver for a two-stage dish concentrator. They found that improved dish concentrator configuration shows superior performance compared to the conventional one, especially in terms of compact structure, flux and temperature distribution uniformity, and solar to thermal efficiency. Moreover they stated that there are fewer scale limitations such as weight and volume on the new receiver with overlapped configuration *(Yang S., Wang J. et al., 2018)*.

ZhouSi-Quan et al., created a three-dimensional model to investigate the spherical cavity receiver's optical and thermodynamic performance. They found that when the spherical receiver moves away either positively or negatively from the focal plane, the distribution of the radiation flux is more uniform *(Si-Quan Z., Xin-Feng L. et al., 2019)*. Sara Soltani et al. experimentally and theoretically studied a helically baffled cylindrical cavity receiver and they investigated the effect of certain mathematical, structural and functional parameters on the thermal performance of the system. Their results showed that the optimal selection of the above parameters could improve the system's thermal performance by up to 65% *(Soltani S., Bonyadi M. et al. 2019)*. Huang et al., suggested a novel method to optimize the system to provide maximum solar energy for net heat output under typical conditions for specific optical errors *(Huang W., Huang F. et al. 2013)*.

A revised hybrid computational approach was proposed by Li Zhang et al. to investigate the thermal performance of the steady-state three-dimensional molten salt cavity models. They found that when only the lengths of the back walls next to the side walls were raised, the thermal efficiency first decreased and then increased as the depth decreased *(Zhang L., Fang J. et al., 2017)*.

Huairui Li et al. suggested an experimental approach for predicting the performance of a solar concentrator with a cavity receiver. They found that a non-window cavity receiver is favoured if the optical error is less than 4 mrad and the ideal geometric concentration ratio is more than 3000 and if the optical error

is larger than 4 mrad, a windowed cavity receiver with an optimal geometric concentration below 1200 is preferred *(Li H, Huang W. et al. 2013)*.

Steinfeld and Schubnell described a semi-empirical method for determining the optimum aperture size and the optimum operating temperature of a solar cavity receiver with maximum energy conversion efficiency *(Steinfeld A. and Schubnell M., 1993)*. Wu et al. performed a three-dimensional numerical analysis to determine the cumulative heat loss from the cavity receiver under various inclinations of the receiver. Results showed that natural convection heat loss Nusselt number is sensitive to the tilt angle and aperture size, except at 90° tilt angle, no matter how other parameters change at this point, the natural convection heat loss Nusselt number always fluctuates in a small value *(Wu S., Guo et al., 2014)*.

Qiu et al., studied numerically and experimentally a cavity receiver dish collector. They found that the cavity receiver's performance is better with up-flows than down-flows *(Qiu K., Yan L. et al. 2015)*. The rectangular and cylindrical cavity receivers were investigated as the heat source of the organic cycle of the Rankine by *Loni et al*. The various parameters of the cavity receivers are designed to achieve higher collector performance and higher overall thermal efficiency *(Loni R., Kasaeian A. et al. 2016, Loni R, Kasaeian A. et al. 2016)*. The thermal performance of the Fuzzy Focal Solar Parabolic Dish Concentrator with modified cavity receiver was experimentally and theoretically analyzed by Reddy et al., for different operating conditions. It has been found that the collector's performance has been improved by increasing volume flow rates *(Reddy K., Natarajan S.K. et al. 2015)*.

## MATERIALS AND METHODS

### MODEL DESIGN AND METHODOLOGY

The factors that contribute to the receiver wall's temperature profile and net heat transfer rate can be divided into two components: geometry-dependent factors and temperature-dependent factors. The geometry-dependent factors include: tracking error, reflectance, spillage and shadowing *(Loni R., Kasaeian A. et al., 2016)*.

TracePro *software* can measure the effects of geometry-dependent factors. Temperature-dependent factors include external radiation heat loss, inner cavity wall irradiation, convection heat loss, and heat loss from conduction. These factors depend on the different parts of the receiver's surface temperatures *(Le Roux W.G., Bello-Ochende T. et al., 2014).*

The present parabolic collector was entirely designed in SolidWorks 2016 SP5 Premium and to optimize the solar energy output from the reflective surfaces to the heat collecting component, the mirrors on a parabolic concentrator need to be precisely aligned. To achieve maximum efficiency, multiple parameters of system can be varied, including the mirror and receiver positions. A major parameter of the dish solar collector system is the solar flux distribution on the absorber. In order to know above mentioned parameters, the flux peaks and the local slope errors must be introduced in the ray tracing code, not the total concentration error. Then the behaviour of each of these light rays is determined, taking into consideration multiple factors that reduce the total energy entering the receiver. Atmospheric attenuation causes a ray's power to decrease as it passes through air and is modeled by a mathematical function in this simulation. In this paper, two important factors have been added to the existing model, which affect the efficiency of a solar parabolic collector. The first was the shape of the sun, referring to the fact that the sun is not a point source and does not emit parallel light rays. In this method, the shape of the sun was determined by a Gaussian function describing the possibility of a ray coming from a certain position on the sun and thus having a certain angle usual with the curved surface. Optical error was the second factor considered in this paper. This can be broken down into two parts: slope and specular error. Slope error is associated with the parabolic mirror's macroscopic shape and occurs when the reflective mirror is not perfectly parabolic, but slightly rough with small parabolic mirror surface imperfections. Specular error is related to the heliostat surfaces microscopic roughness, surface parabolic reflectors, parabolic troughs, etc.

The following equation was used to integrate the two sources of error:

$$\sigma_{tot} = \sqrt{\sigma_{slope}^2 + \sigma_{specular}^2 + \sigma_{sun}^2} \quad (1)$$

Where the $\sigma_{total}$ was then used to describe a single Gaussian distribution representing the probability of a reflected ray leaving a surface mirror with a certain angle of deviation from the predicted light *(Pavlovic S., Stefanovic V. et al., 2014)*.

## FOCAL RECEIVER

The modeling of the open-cavity receivers is shown in Fig.1.

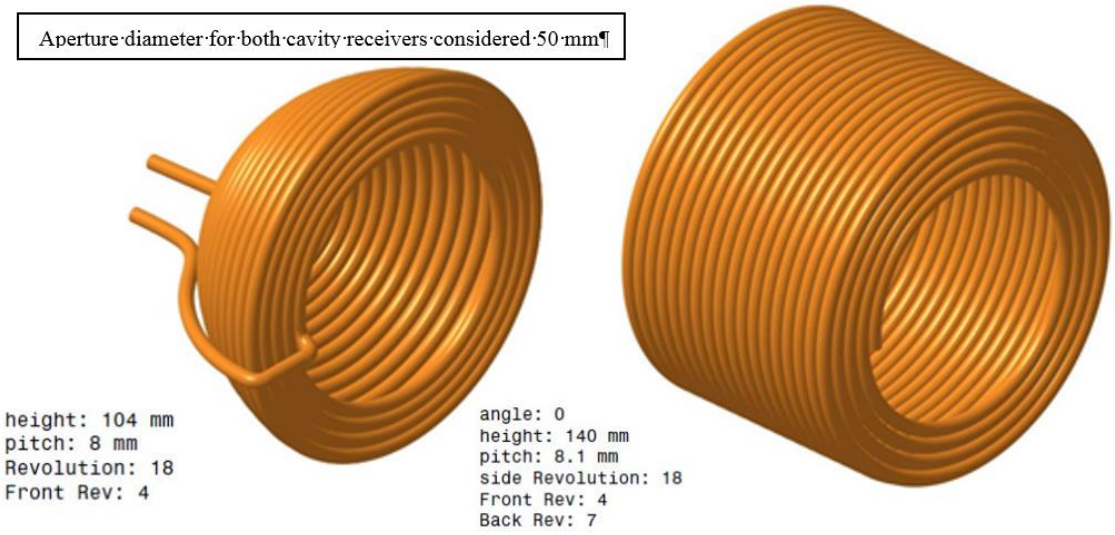


**Fig. 1 - A rectangular open-cavity solar receiver and optimized semi-spherical cavity receiver**

In a subsequent step, the focal absorber absorbs the concentrated solar radiation and converts it into thermal energy *(Kaushika N. and Reddy K., 2000)*. A receiver's basic feature is to absorb the maximum amount of solar energy reflected and transfer it to the working fluid as heat, with minimal losses. To achieve this purpose, a cavity receiver is used. The position of the cavity receiver should be varying to achieve the preferred performance of collector in different setups. The receiver is covered with insulation (Fig. 2).

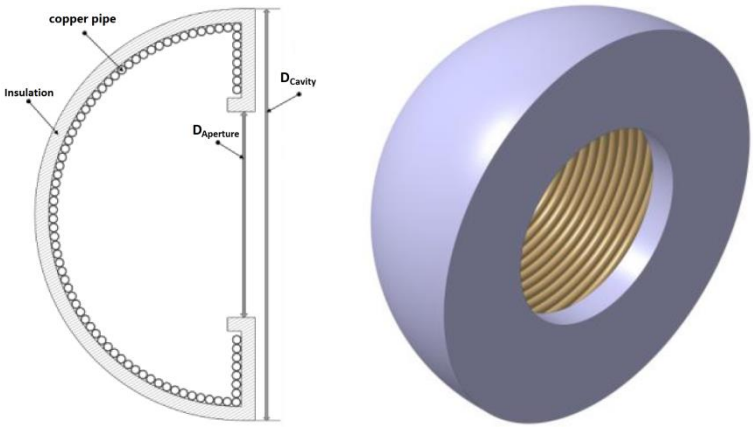


**Fig. 2 - Insulated cavity receiver**

## BASIC FEATURES OF THE CONCENTRATING SOL AR COLLECTOR

In this part, the design of the solar collector is viewed with an emphasis on the design of the reflector. This design dramatically reduces the cost of the system, while allowing high concentration ratios for medium and high temperature applications. Table 1 shows the design parameters of the Solar Parabolic Dish Concentrator (SPDC). The table gives the values of different parameters because the built model has many geometric features.

**Table 1**

**Changeable characteristics of the SDC and achieved results**

| | |
|---|---|
| **Concentrator diameter (m)** | 1.5 |
| **Focal distance (mm)** | 1004.46 |
| **Paraboloid rim angle** | 25.25 |
| **Collector aperture area ($m^2$)** | 1.767146 |
| **Cavity tube outer diameter (mm)** | 8 |
| **Cavity tube inner diameter (mm)** | 6 |
| **Number of tube coils** | 18 |
| **Cylindrical Cavity inner diameter, Din (m)** | 0.13 |
| **Cylindrical Cavity outer diameter, Dout (m)** | 0.14 |
| **Semi-spherical cavity receiver inner diameter, Din (m)** | 0.13 |
| **Semi-spherical cavity receiver outer diameter, Dout (m)** | 0.14 |
| **Height of the cavity receiver, h (m)** | 0.18 |
| **Solar beam irradiations, Isun($W/m^2$)** | 700 |
| **Average wind speed (m/s)** | 5 |
| **Ambient temperature (°C)** | 22 |
| **Volumetric flow rate, V (ml/s** | 100 |
| **Working fluid (Water/Oil)** | water |
| **Reflectivity of segments** | 95%. |
| **CRg** | 114.8542 |
| **Number of mirrors** | 200 |
| **Fs/Diam** | 00.67 |

A common SPDC consists mainly of a parabola with an absorber placed at the focal position by some arms.

A reflector in a nacelle can be rotated around two axes: the horizontal axis (angle of elevation) of the mast support and the vertical axis (angle of azimuth) of the mast support.

The SPDC is placed on the ground and is made from small elementary square mirrors. Its novelty is the changeable characteristics of the SPDC (dish opening diameter, dish depth, and Focal distance).

Such ranges are adequate for comprehensive applications such as research on heat and electricity generation, etc.

In Fig.3, a pilot model of the assembled SPDC illustrates the arrangement of 200 mirrors on main frame with 1500 mm dish aperture diameter, 1004.46 mm focal distance and 150 mm dish depth.

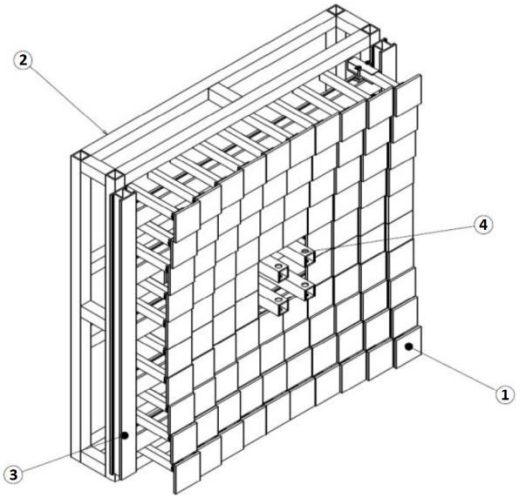


**Fig. 3 - Pilot model of changeable collector**

*(Feizolahzadeh M., Motlagh A.M. et al. 2017)*

*1-optical unit; 2-main frame; 3-aluminium profile; 4-receiver joints*

The dimensions of the reflective surfaces in the solar dish concentrator are determined by the desired power at the maximum insolation and collector conversion efficiency levels.

The parabolic concentrator's mathematical representation is a paraboloid that can be represented as a surface obtained by rotating parabola around the axis shown in Fig.4.

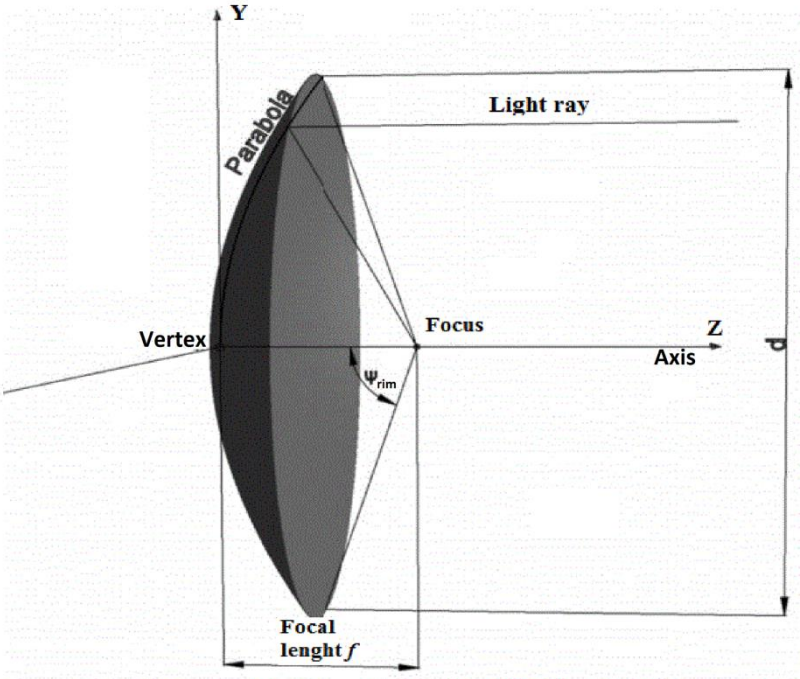


**Fig. 4 - Ideal shape of parabolic solar concentrator**

*(Pavlovic S., Stefanovic V. et al. 2014)*

Parabolic dish solar mathematical equations: the ratio of geometric concentration can be defined as the area of the collector aperture $A_{app}$ divided by the receiver surface area $A_{rec}$ and it can be calculated by Eq.(2):

$$CR_g = (sin^2\theta_a)^{-1} = A_c A_r^{-1} = \frac{A_{app}}{A_{rec}} \quad (2)$$

The geometric concentration ratio of the designed solar parabolic concentrator is CR = 114.8542.

The solar parabolic concentrator's mechanical model is designed in SolidWorks 2016 SP5 Premium.

For selected points, the parabolic shape of the solar concentrator is obtained by entering X and Y coordinates. Parabola Calculator 2.0 is used to calculate the necessary points that define parabola. Table.2 shows the calculated coordinates (X and Y) for the designed parabola.

**Table 2**

**Coordinates of designed parabola**

| X(mm) | Y(mm) | X(mm) | Y(mm) | X(mm) | Y(mm) | X(mm) | Y(mm) | X(mm) | Y(mm) | X(mm) | Y(mm) |
|---|---|---|---|---|---|---|---|---|---|---|---|
| -750 | 140 | -525 | 68.6 | -300 | 22.4 | -75 | 1.4 | 150 | 5.6 | 375 | 35 |
| -742.5 | 137.214 | -517.5 | 66.654 | -292.5 | 21.294 | -67.5 | 1.134 | 157.5 | 6.174 | 382.5 | 36.414 |
| -735 | 134.456 | -510 | 64.736 | -285 | 20.216 | -60 | 0.896 | 165 | 6.776 | 390 | 37.856 |
| -727.5 | 131.726 | -502.5 | 62.846 | -277.5 | 19.166 | -52.5 | 0.686 | 172.5 | 7.406 | 397.5 | 39.326 |
| -720 | 129.024 | -495 | 60.984 | -270 | 18.144 | -45 | 0.504 | 180 | 8.064 | 405 | 40.824 |
| -712.5 | 126.35 | -487.5 | 59.15 | -262.5 | 17.15 | -37.5 | 0.35 | 187.5 | 8.75 | 412.5 | 42.35 |
| -705 | 123.704 | -480 | 57.344 | -255 | 16.184 | -30 | 0.224 | 195 | 9.464 | 420 | 43.904 |
| -697.5 | 121.086 | -472.5 | 55.566 | -247.5 | 15.246 | -22.5 | 0.126 | 202.5 | 10.206 | 427.5 | 45.486 |
| -690 | 118.496 | -465 | 53.816 | -240 | 14.336 | -15 | 0.056 | 210 | 10.976 | 435 | 47.096 |
| -682.5 | 115.934 | -457.5 | 52.094 | -232.5 | 13.454 | -7.5 | 0.014 | 217.5 | 11.774 | 442.5 | 48.734 |
| -675 | 113.4 | -450 | 50.4 | -225 | 12.6 | 0 | 0 | 225 | 12.6 | 450 | 50.4 |
| -667.5 | 110.894 | -442.5 | 48.734 | -217.5 | 11.774 | 7.5 | 0.014 | 232.5 | 13.454 | 457.5 | 52.094 |
| -660 | 108.416 | -435 | 47.096 | -210 | 10.976 | 15 | 0.056 | 240 | 14.336 | 465 | 53.816 |
| -652.5 | 105.966 | -427.5 | 45.486 | -202.5 | 10.206 | 22.5 | 0.126 | 247.5 | 15.246 | 472.5 | 55.566 |
| -645 | 103.544 | -420 | 43.904 | -195 | 9.464 | 30 | 0.224 | 255 | 16.184 | 480 | 57.344 |
| -637.5 | 101.15 | -412.5 | 42.35 | -187.5 | 8.75 | 37.5 | 0.35 | 262.5 | 17.15 | 487.5 | 59.15 |
| -630 | 98.784 | -405 | 40.824 | -180 | 8.064 | 45 | 0.504 | 270 | 18.144 | 495 | 60.984 |
| -622.5 | 96.446 | -397.5 | 39.326 | -172.5 | 7.406 | 52.5 | 0.686 | 277.5 | 19.166 | 502.5 | 62.846 |
| -615 | 94.136 | -390 | 37.856 | -165 | 6.776 | 60 | 0.896 | 285 | 20.216 | 510 | 64.736 |
| -607.5 | 91.854 | -382.5 | 36.414 | -157.5 | 6.174 | 67.5 | 1.134 | 292.5 | 21.294 | 517.5 | 66.654 |
| -600 | 89.6 | -375 | 35 | -150 | 5.6 | 75 | 1.4 | 300 | 22.4 | 525 | 68.6 |
| -592.5 | 87.374 | -367.5 | 33.614 | -142.5 | 5.054 | 82.5 | 1.694 | 307.5 | 23.534 | 532.5 | 70.574 |
| -585 | 85.176 | -360 | 32.256 | -135 | 4.536 | 90 | 2.016 | 315 | 24.696 | 540 | 72.576 |
| -577.5 | 83.006 | -352.5 | 30.926 | -127.5 | 4.046 | 97.5 | 2.366 | 322.5 | 25.886 | 547.5 | 74.606 |
| -570 | 80.864 | -345 | 29.624 | -120 | 3.584 | 105 | 2.744 | 330 | 27.104 | 555 | 76.664 |
| -562.5 | 78.75 | -337.5 | 28.35 | -112.5 | 3.15 | 112.5 | 3.15 | 337.5 | 28.35 | 562.5 | 78.75 |
| -555 | 76.664 | -330 | 27.104 | -105 | 2.744 | 120 | 3.584 | 345 | 29.624 | 570 | 80.864 |
| -547.5 | 74.606 | -322.5 | 25.886 | -97.5 | 2.366 | 127.5 | 4.046 | 352.5 | 30.926 | 577.5 | 83.006 |
| -540 | 72.576 | -315 | 24.696 | -90 | 2.016 | 135 | 4.536 | 360 | 32.256 | 585 | 85.176 |
| -532.5 | 70.574 | -307.5 | 23.534 | -82.5 | 1.694 | 142.5 | 5.054 | 367.5 | 33.614 | 592.5 | 87.374 |
| 600 | 89.6 | 630 | 98.784 | 660 | 108.416 | 690 | 118.496 | 720 | 129.024 | 750 | 140 |
| 607.5 | 91.854 | 637.5 | 101.15 | 667.5 | 110.894 | 697.5 | 121.086 | 727.5 | 131.726 | | |
| 615 | 94.136 | 645 | 103.544 | 675 | 113.4 | 705 | 123.704 | 735 | 134.456 | | |
| 622.5 | 96.446 | 652.5 | 105.966 | 682.5 | 115.934 | 712.5 | 126.35 | 742.5 | 137.214 | | |

## EXPERIMENTAL SETUP

The parabolic dish collector system's changeable parameters are as follows: focal length of the dish ($f$), aperture diameter of dish ($D$), dish rim angle ($\varphi$), area of the receiver ($A$) and concentration ratio ($C$). The Experimental SPDC's main components are: the solar concentrator, the cavity receiver, the solar heat exchanger, the drying chamber, as shown in Fig.5.

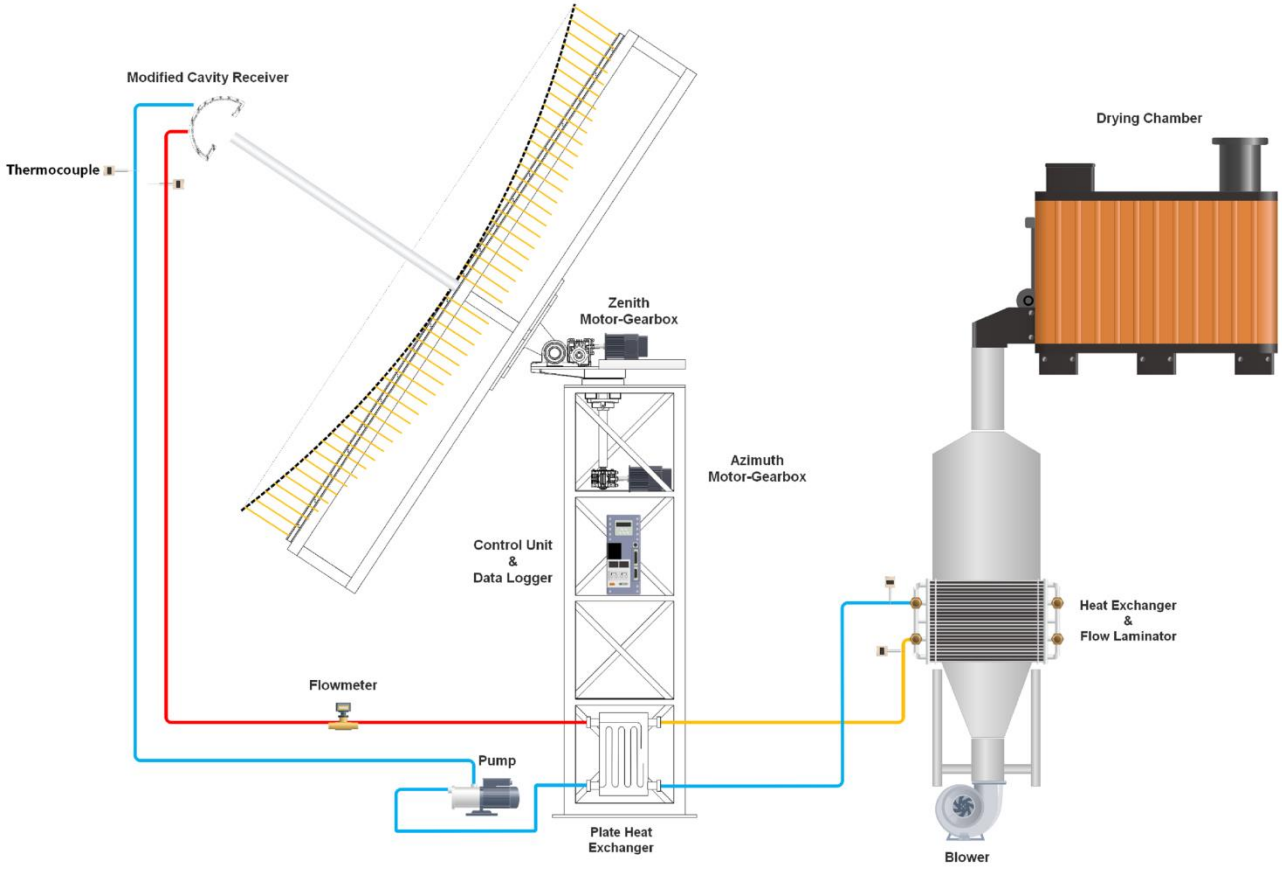


**Fig. 5 - Schematic of experimental setup of a solar drying apparatus with changeable solar dish collector**

## SIMULATION OF THE MODEL

TracePro software, Lamda Research Corporation, USA, is used for optical analysis of the solar parabolic thermal concentrator. All material properties are assigned in TracePro. Concentrator segments are defined as standard reflective-coated mirrors with the reflection coefficient of 95%.

Cavity receivers have been placed in different distances from vertex of dish concentrator (At the concentrator's focal point and below the focal length). The internal surface of the cavity receiver was considered to be a perfect absorber.

The source of radiation was considered to be circular with a diameter equal to the parabolic dish diameter (1,500 mm).

The radiation source was placed 4,000 mm from the vertex of the parabolic dish and had a circular grid pattern for Monte Carlo ray tracing to generate 120,000 rays.

The spatial profile of the rays produced was random and solar radiation was the angular profile.

According to experiential value, the solar irradiation for the city of Urmia in Iran is between 450 W/m$^2$ and 950 W/m$^2$.

Then for optical analysis, the solar irradiance was considered 750 W/m$^2$.

Fig.6 shows the optical system for the traced-ray solar parabolic concentrator.

The process of optical concentration consists of three objects: solar parabolic dish reflector, radiation source and cavity receiver (at the concentrator's focal point and below the focal length).

Optical analyses are performed by generating and calculating Monte Carlo ray trace for 120,000 rays.

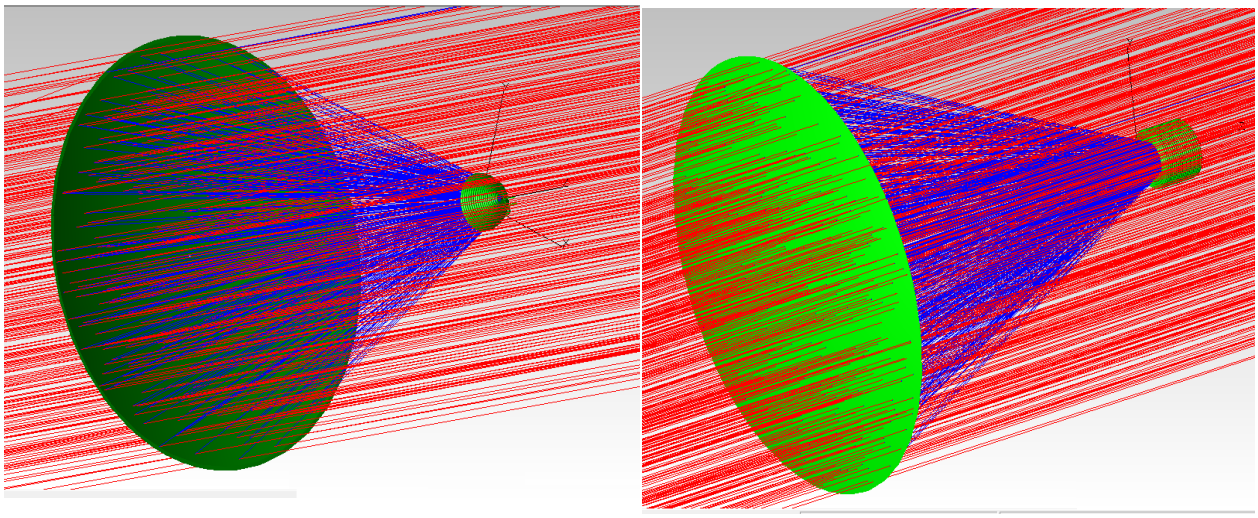

**Fig. 6 - Optical system of solar parabolic concentrator with cylindrical and semi-spherical receivers**

Based on simulation results for cylindrical cavity receiver from all emitted rays 113,251 rays reached the absorber surface, which is 94.37% of the rays emitted. Total map of irradiance for absorbed flux on receiver is shown in Fig.7.

The total cavity receiver flux was 990.23 W. It can be seen from Fig.7 that calculated values for total irradiance are in compliance with the theoretical values. The irradiance in the receiver ranges from 5.177× $10^{-8}$ W/m$^2$ to 2.917× $10^5$W/m$^2$ and at the receiver periphery the irradiance varies from 6.012 to 3.88 × $10^4$ W/m$^2$. The maximum irradiance occurs in a circle with diameter of 40 mm (from -20 mm to 20 mm).

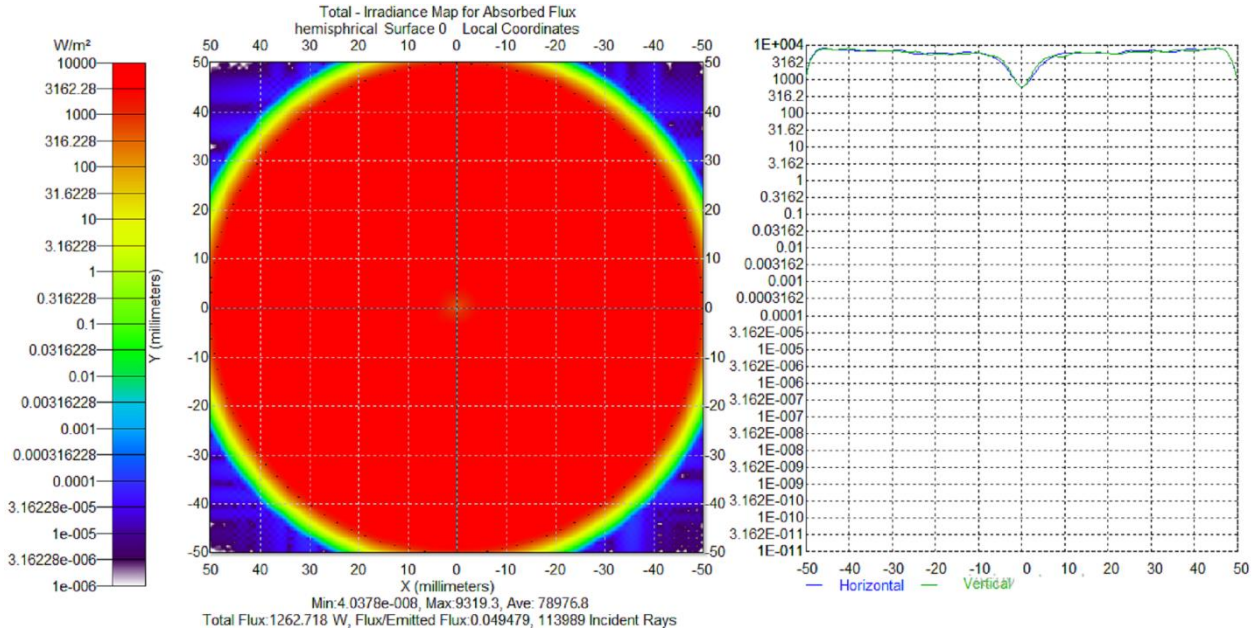


**Fig. 7 - Irradiance Map for absorbed flux on cylindrical receiver**

For semi-spherical cavity receiver from all emitted rays 113,989 rays reached the absorber surface, which is 94.9% of the rays emitted. Total map of irradiance for absorbed flux on receiver is shown in Fig. 8. The total cavity receiver flux was 1262.718 W. It can be seen from Fig.8 that the calculated values for total irradiance match to the theoretical values. The irradiance in the receiver ranges from 4.037× 10-8 W/m$^2$ to 3.162×105 W/m$^2$ and at the receiver periphery the irradiance varies from 264.6 to 2.025 × 104 W/m$^2$. The maximum irradiance occurs in a circle with diameter of 50 mm (from -25 mm to 25 mm).

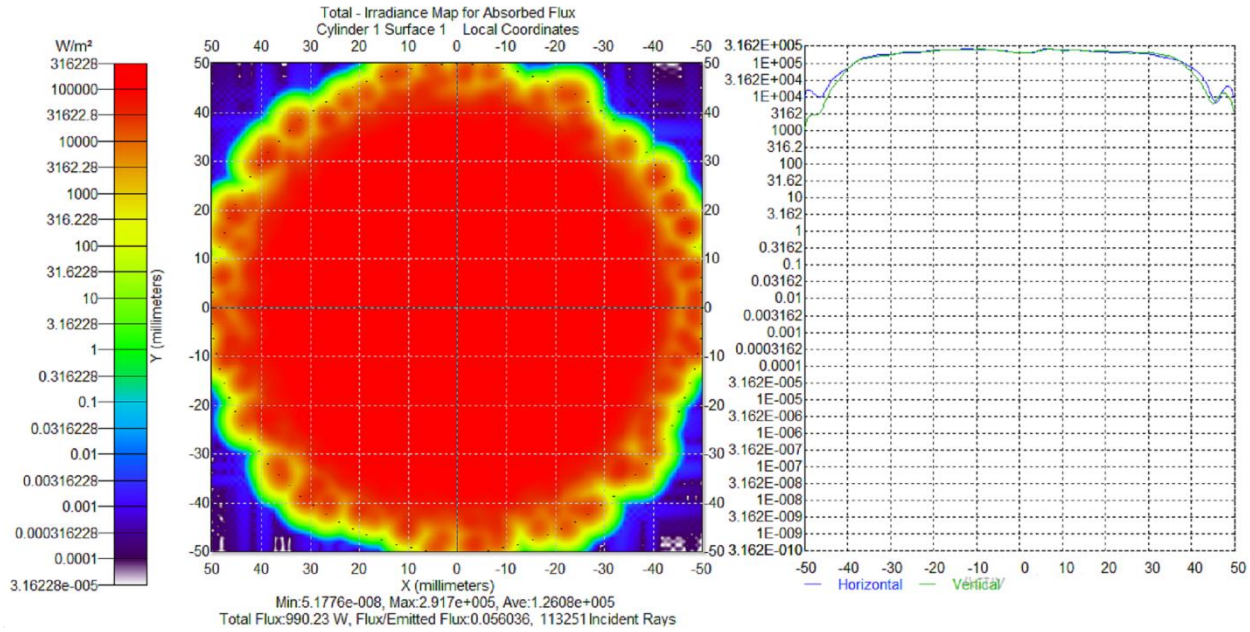


**Fig. 8 - Irradiance Map for absorbed flux on semi-spherical receiver**

Considering the total area of the receivers, this assessment can be made: the uniformity of irradiance in semi-spherical receiver is better and it has got better optical performance.

## APPLICATION OF SOLAR ENERGY TO DRY CROPS AND GRAINS

During the conventional open-air drying process, a large percentage of agricultural produce is spoiled. Using the solar drying process, crops will dry faster than open sun drying in the field with the added advantage of protecting against birds, insects and worms. Sun drying is still the most common method used to preserve agricultural products in most of Iran. Temperature required for drying is 60°- 70°C. Solar concentrating parabolic dish collector is used to get this temperature.

The temperature at receiver is up to 125°C; the receiver has water as working fluid and a circulating pump passes it through the heat exchanger. Heat from hot fluid is extracted by supplying cold air through heat exchanger. Then the hot air is blown by a pump inside the cabin where crops are placed as shown in Fig.9.

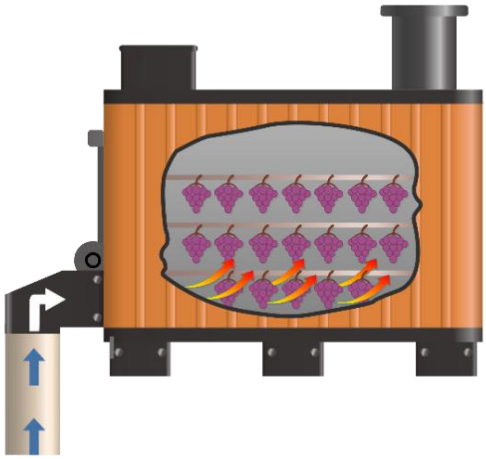

**Fig. 9 - Schematic diagram of drying chamber**

The objective of this work is to simulate and optimize Solar Parabolic Collector and cavity receivers which can be used in a solar drying apparatus and increase the performance of the solar drying apparatus. The result shows that semi-spherical receiver is better and it has got better optical performance. Thereby, it is highly recommended for different types of solar dryers, such as direct drying (solar box dryer), or indirect drying (solar cabinet dryer).

As shown in Fig.9, the drying cabinet temperature with a width of 0.55 m and a length of 0.65 m, equipped with 3 drying trays mounted inside the drying cabinet, can be controlled using the designed collector. Fresh air flows into the heat exchanger via the air inlet and the heated air exits the heat exchanger. Then the heat exchanger's heated air is passed over the drying material that is horizontally stacked on the 3 thin layers. As simulation results show, the temperature obtained through the semi-spherical receiver is higher than through the cylindrical receiver. So, the designed Solar Parabolic Collector and cavity receivers need less time for drying compared to other collectors.

## CONCLUSIONS

This paper presents optical simulations of an innovative solar dish reflector and cavity receivers using the ray-tracing software. In the ray-tracing simulations, a receiver model is introduced to test the effect of physical parameters of the cavity. This type of cavity enables a homogeneous distribution of solar flux on the absorber and increases the efficiency of the cavity receiver. The advantage of TracePro software is that when sufficient rays are used, the Monte Carlo method gives reliable results. In many applications, this solar collector can be used, from domestic hot water applications to industrial processes. The model is designed in SolidWorks 2016 SP5 Premium and then analyzed optically. This method of optimization will enable optimum geometric and optical parameters to be found for the different types of solar parabolic dish concentrators as well as for the geometric, optical and thermal parameters of the cavity receivers. The result shows that semi-spherical receiver is better and it has got better optical performance. Therefore, it can be recommended for different types of solar dryers, such as direct drying (solar box dryer), or indirect drying (solar cabinet dryer).

## REFERENCES

[1] Bal L.M., Satya S. and Naik S., (2010), Solar dryer with thermal energy storage systems for drying agricultural food products: A review. *Renewable and Sustainable Energy Reviews,* 14(8): 2298-2314;

[2] Bellos E., Bousi E., Tzivanidis C. and Pavlovic S., (2019), Optical and thermal analysis of different cavity receiver designs for solar dish concentrators. *Energy Conversion and Management*: X: 100013;

[3] Feizolahzadeh M., Motlagh A.M. and Banakar A., (2017), Experimental setup of solar dish collector with changeable structure. *INMATEH-Agricultural Engineering*, 53(3): 103-112;

[4] Huang W., Huang F., Hu P. and Chen Z., (2013), Prediction and optimization of the performance of parabolic solar dish concentrator with sphere receiver using analytical function. *Renewable energy,* 53: 18-26.

[5] Jamil B. and Akhtar N., (2017), Comparative analysis of diffuse solar radiation models based on sky-clearness index and sunshine period for humid-subtropical climatic region of India: A case study. *Renewable and Sustainable Energy Reviews*, 78: 329-355.

[6] Karthikeyan A. and Murugavelh S., (2018), Thin layer drying kinetics and exergy analysis of turmeric (Curcuma longa) in a mixed mode forced convection solar tunnel dryer. *Renewable energy*, 128: 305-312;

[7] Kasaeian A., Daneshazarian R., Rezaei R., Pourfayaz F. and Kasaeian G., (2017), Experimental investigation on the thermal behaviour of nanofluid direct absorption in a trough collector. *Journal of Cleaner Production,* 158: 276-284;

[8] Kaushika N. and Reddy K., (2000), Performance of a low cost solar paraboloidal dish steam generating system. *Energy conversion and management*, 41(7): 713-726;

[9] Kumar R., Gupta V. and Varshney R., (2017), Numerical simulation of solar greenhouse dryer using computational fluid dynamics. *International Journal of Research and Scientific Innovation* IV (Issue VIS): 111-115;

[10] Le Roux W.G., Bello-Ochende T. and Meyer J.P., (2014), The efficiency of an open-cavity tubular solar receiver for a small-scale solar thermal Brayton cycle. *Energy Conversion and Management*, 84: 457-470;

[11] Li H., Huang W., Huang F., Hu P. and Chen Z., (2013), Optical analysis and optimization of parabolic dish solar concentrator with a cavity receiver. *Solar energy*, 92: 288-297;

[12] Li Z., Tang D., Du J. and Li T., (2011), Study on the radiation flux and temperature distributions of the concentrator–receiver system in a solar dish/Stirling power facility. *Applied Thermal Engineering* 31(10): 1780-1789;

[13] Loni R., Kasaeian A., Asli-Ardeh E.A. and Ghobadian B., (2016), Optimizing the efficiency of a solar receiver with tubular cylindrical cavity for a solar-powered organic Rankine cycle. *Energy*, 112: 1259-1272;
[14] Loni R., Kasaeian A., Asli-Ardeh E.A., Ghobadian B. and Le Roux W., (2016), Performance study of a solar-assisted organic Rankine cycle using a dish-mounted rectangular-cavity tubular solar receiver. *Applied Thermal Engineering*, 108: 1298-1309;
[15] Lovegrove K., Burgess G. and Pye J., (2011), A new 500 $m^2$ paraboloidal dish solar concentrator. *Solar Energy,* 85(4): 620-626;
[16] Pavlovic S., Stefanovic V. and Bojic M., (2014), Optical simulation of a solar parabolic collector using ray-tracing software Trace Pro. Hong Kong, China: 211-218;
[17] Qiu K., Yan L., Ni M., Wang C., Xiao G., Luo Z. and Cen K., (2015), Simulation and experimental study of an air tube-cavity solar receiver. *Energy conversion and management*, 103: 847-858;
[18] Reddy K. and Kumar N.S., (2009), An improved model for natural convection heat loss from modified cavity receiver of solar dish concentrator. *Solar Energy*, 83(10): 1884-1892;
[19] Reddy K., Natarajan S.K. and Veershetty G., (2015), Experimental performance investigation of modified cavity receiver with fuzzy focal solar dish concentrator. *Renewable Energy,* 74: 148-157;
[20] Si-Quan Z., Xin-Feng L., Liu D., Qing-Song M., (2019), A numerical study on optical and thermodynamic characteristics of a spherical cavity receiver. *Applied Thermal Engineering*, 149: 11-21;
[21] Soltani S., Bonyadi M. and Avargani V. M., (2019), A novel optical-thermal modeling of a parabolic dish collector with a helically baffled cylindrical cavity receiver. *Energy*, 168: 88-98;
[22] Steinfeld A., Schubnell M., (1993), Optimum aperture size and operating temperature of a solar cavity-receiver. *Solar Energy,* 50(1): 19-25;
[23] Stijepovic M.Z., Papadopoulos A.I., Linke P., Stijepovic V., Grujic A.S., Kijevčanin M. and. Seferlis P., (2017), Organic Rankine Cycle system performance targeting and design for multiple heat sources with simultaneous working fluid selection. *Journal of cleaner production*, 142: 1950-1970;
[24] Vásquez J., Reyes A. and Pailahueque N., (2019), Modeling, simulation and experimental validation of a solar dryer for agro-products with thermal energy storage system. *Renewable energy*, 139: 1375-1390;
[25] Venkatachalam T., Cheralathan M., (2019), Effect of aspect ratio on thermal performance of cavity receiver for solar parabolic dish concentrator: An experimental study. *Renewable energy,* 139: 573-581;
[26] Wang M., Siddiqui K., (2010), The impact of geometrical parameters on the thermal performance of a solar receiver of dish-type concentrated solar energy system. *Renewable Energy,* 35(11): 2501-2513;
[27] Wu S.Y., Guo F.H. and Xiao L., (2014), Numerical investigation on combined natural convection and radiation heat losses in one side open cylindrical cavity with constant heat flux. *International Journal of Heat and Mass Transfer*, 71: 573-584;
[28] Wu S.Y., Xiao L., Cao Y. and Li Y.R., (2010), Convection heat loss from cavity receiver in parabolic dish solar thermal power system: A review. *Solar energy*, 84(8): 1342-1355;
[29] Wu S.Y., Xiao L., Cao Y., Li Y.R., (2010), A parabolic dish/AMTEC solar thermal power system and its performance evaluation. *Applied Energy*, 87(2): 452-462;
[30] Wu Z., Caliot C., Bai F., Flamant G., Wang Z., Zhang J. and Tian C., (2010), Experimental and numerical studies of the pressure drop in ceramic foams for volumetric solar receiver applications. *Applied Energy*, 87(2): 504-513;
[31] Yang S., Wang J., Lund P.D., Jiang C., Huang B., (2018), Design and performance evaluation of a high-temperature cavity receiver for a 2-stage dish concentrator. *Solar Energy* 174: 1126-1132;
[32] Zhang L., Fang J., Wei J., Yang G., (2017), Numerical investigation on the thermal performance of molten salt cavity receivers with different structures. *Applied energy,* 204: 966-978.

# SEGMENTATION OF APPLE POINT CLOUDS BASED ON ROI IN RGB IMAGES
/
# 基于彩色图像中感兴趣区域的苹果点云分割方法

**Yuanxi Zhang[1)], Ye Tian[1)], Change Zheng*[2)], Dong Zhao[1)], Po Gao[1)], Ke Duan[1)]**
[1)]School of Technology, Beijing Forestry University, Beijing, 100083/China,
[2)]Key Lab of State Forestry Administration on Forestry Equipment Automation, School of Technology,
Beijing Forestry University, Beijing, 100083/China;
*Tel: +8618601224519; E-mail: zhengchange@bjfu.edu.cn*
*DOI: 10.35633/INMATEH-59-23*

***Keywords:*** *Faster-RCNN, segmentation, apple tree, point clouds, unstructured scenes, ROI*

**ABSTRACT**

*Autonomous harvesting and evaluation of apples reduce the labour cost. Segmentation of apple point clouds from consumer-grade RGB-D camera is the most important and challenging step in the harvesting process due to the complex structure of apple trees. This paper put forward a segmentation method of apple point clouds based on regions of interest (ROI) in RGB images. Firstly, an annotated RGB dataset of apple trees was built and applied to train the optimized Faster R-CNN to locate ROI containing apples in RGB images. Secondly, the relationship between RGB images and depth images was built to roughly segment the apple point clouds by ROI. Finally, the quality control procedure (QCP) was proposed to improve the quality of segmented apple point clouds. Images for training mainly included two lighting condition, two colours and three apple varieties in orchard, making this method more suitable for practical applications. QCP performed well in filtering noise points and achieved Purity as 96.7% and 96.2% for red and green apples, respectively. Through the comparison method, experimental results indicated that the segmentation method based on ROI is more effective and accurate for red and green apples in orchard. The segmentation method of point clouds based on ROI has great potential for segmentation of point clouds in unstructured scenes.*

**摘要**

*苹果的自动采摘和评估降低了劳动成本。在采摘过程中由于苹果树的复杂结构，分割消费级 RGB-D 相机获得的苹果点云是最重要且具有挑战性的一步。本文提出基于彩色图像中感兴趣区域的点云分割方法。首先制作了一个用来训练优化过的 Faster-RCNN 的苹果树数据集，定位出彩色图像中包含有苹果的感兴趣区域。然后，构建了彩色图与深度图之间的关系量，依照此关系量使用感兴趣区域对点云进行快速的粗分割。最后，针对粗分割的点云特征提出质量控制程序，提升苹果点云的分割质量。用来训练的彩色图像主要包含了果园中的两种光照条件以及三个品种、两种颜色的苹果，提升了此方法在实际场景中的适用性。质量控制程序的处理效果理想，对于红绿两色苹果分别得到了 96.7%和 96.2%的纯净度。通过对比实验，结果证明了基于彩色图像中感兴趣区域的苹果点云分割方法对于果园中红绿两色的苹果均有更高的效率和准确率，在非结构化场景中具有非常大的应用前景*

## INTRODUCTION

Harvesting and evaluation of apples is a labour-intensive task in a short period. In the task of reducing the labour cost, automatic system is of great value to agriculture (*Kitamura S. and Oka K., 2006; English A. et al., 2014; Bac CW et al., 2015*). The key of automatic system is the apple detection based on segmentation of point clouds. Since the point clouds is one of the most intuitive formats for a machine to perceive the world (*Charles RQ et al., 2017; Li Y et al., 2018; Pas AT and Platt R, 2015*), much more information such as the optimized end-effector pose and the position of apples can be obtained. Therefore, it is highly desirable to analyse the features (e.g., surface fitting and calculate the normal vector distribution) from segmented point clouds of apples. In structured scenes like buildings or other objects that contain neat planes and lines (*Yamauchi H et al., 2005; Himmelsbach M et al., 2010 Xu Y et al., 2018*;) achieved a good result of segmentation using geometry features, William R. introduced normal distribution feature representation to segment indoor point clouds. Moreover (*Green WR and Grobler H, 2015*), Huijun Y proposed an algorithm for segmenting fruit from background by converting octree cell into a splat and approximating its local surface with MLS (*Huijun Y, 2011*). However, when these methods were used for real apple trees, the accuracy was not satisfactory.

The segmentation of apple point clouds is of considerable difficulty due to the limited size of apples, meanwhile, the occlusions from leaves or branches brought more difficulty for segmentation in unstructured scenes. Additionally, apples have different colours (such as red and green), making it difficult to segment the point clouds only based on colour information. Nguyen TT segmented the 3D information belonging to the red or bicolored apples from backgrounds (*Nguyen TT et al., 2014*). Combining Gaussian processes and a Gibbs-sampler with Euclidean distance between colours, Soria PR et al. segmented clusters of apples and estimated the centroids of red apples (*Soria PR et al., 2017*). Tao Y et al. adopted HSI to segment apple point clouds (*Tao Y et al., 2017*). Meanwhile, Bayesian discriminant method based on RGB model was performed on classing fruits (*Blasco J et al., 2003*). Linker R and Kelman E proposed detection of apples in night-time tree images by converting RGB to gray-level (*Linker R and Kelman E, 2015*). However, when it comes to the different colour condition like green apples in green leaves, the performance of above-mentioned methods is not satisfactory. Paulus et al. segmented point clouds of plant organs using an accurate laser scanner. But this paper got a poor result on apple point clouds using a consumer-grade RGB-D camera (*Paulus et al., 2013; Wahabzada M et al., 2015*). A support vector machine optimized by genetic algorithm (GA-SVM) classifier was constructed by Tao et al. to recognize apples. However, the GA-SVM didn't work well in different orchard scenes. Although there was some impressive progress in 3D deep convolutional neural networks trained by 3D datasets demanding great expense such as S3DIS and Scannet (*Wang W et al., 2017; Dai A et al., 2017*), it is too difficult to build a 3D point clouds dataset of real apple trees for this paper due to the complexity of the unstructured apple tree point clouds. 2D dataset, by contrast, is relatively easier to build, thus 2D deep learning has been widely adopted for many tasks like crops detection. Hasan MM et al. performed accurate detection of wheat spikes using Faster R-CNN and counted wheat spikes for yield estimation (*Hasan MM et al., 2018*).

This paper focuses on segmentation of apple point clouds in order to make full use of 3D data. The main contribution of this paper is using the optimized Faster R-CNN to segment apple point clouds, making segmentation effective and accurate. In this process, we built an apple dataset including 5660 images of different-colour apples in green leaves under different lighting conditions, 4810 images were labelled manually in standard format. Therefore, the dataset can be used for other works. Moreover, we proposed a quality control procedure (QCP) for filtering noise points, improving the quality of point clouds obviously.

## MATERIALS AND METHODS

In this study, a new method for segmentation was proposed for apple tree point clouds. The Kinect V2 was used to obtain RGB-D information of apple trees as shown in Fig. 2. At the same time, a manually annotated RGB dataset, which contained the RGB images, was built and applied to train the optimized Faster R-CNN to locate the ROI containing apples in RGB images, and then, the relationship between RGB images and depth images was established by defining a variable called $IDX$, which was used to segment the point clouds. After roughly segmenting point clouds based on the ROI and $IDX$, QCP was put forward to ensure an accurate result. The main works and methods are shown in Fig. 1. In order to evaluate the performance of segmentation, the improved method based on Pixel Colour (MBPC) was introduced as comparison experiments.

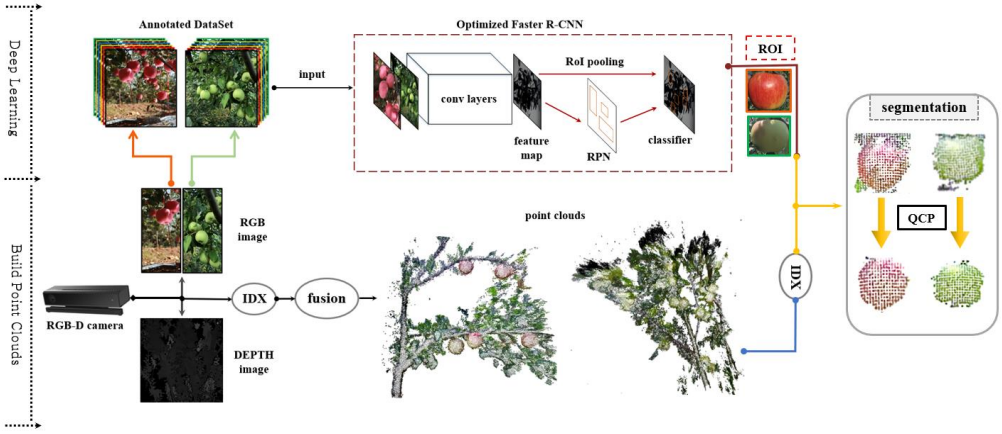


**Fig. 1 - Flowchart of segmentation method using optimized Faster R-CNN and RGB-D camera. RGB images were used to train the optimized Faster R-CNN and fuse into point clouds. Combining ROI with $IDX$, the segmentation of raw apple point clouds was achieved, and the quality of segmentation was improved by QCP**

**Fig. 2 - Images of different apple trees in RGB dataset obtained on different lighting conditions (sunshine and shadow)**

- **Dataset**

Apples have different colours, among them, the red and green apples are the most common colours, the apple varieties in RGB dataset included Fuji, Qinyang and Liaofu, which were collected in Heze and Jinan, Shandong province, China. These raw images were obtained by the Kinect V2 RGB sensor in two kinds of lighting conditions as shown in Fig. 2. The basic task in this paper is to detect the apples in RGB images; therefore, the apples in RGB images were manually labelled. In addition, the distance between the camera and the target was about 1-1.5m similar with practical harvesting applications. The Kinect V2 depth sensor uses a structured light technique to acquire the depth information of the apple trees, which is able to extract a set of discrete point clouds of apple trees. The resolution of each sensor is shown in Table 1.

**Table 1**

**Main parameters of sensors used in data collection**

| Sensor | Resolution | Range of Detection |
|---|---|---|
| RGB | 1920*1080 | ✗ |
| Depth | 512*424 | 0.5m~4.5m |

The image annotations were manually labelled and saved in XML files in PASCAL VOC format. The annotations included two categories: red apple (RA) and green apple (GA), and the bounding boxes (bbox).

In order to reduce the possibility of over-fitting in training process (*Grinblat GL et al., 2016*), horizontal flip processing was used as data enhancement. Specifically, by performing horizontal symmetry processing on all RGB images, the amount of data was doubled. The enhanced RGB dataset contains a total of 5660 pictures in two categories: Red Apples in Green Leaves (RAGL) and Green Apples in Green Leaves (GAGL). Before training the optimized Faster R-CNN, 15% of the images from each category were randomly selected as validation set. The details of the RGB dataset are shown in Table 2. After the validation set was reserved, the apple tree point clouds were generated by using the RGB images aligned with the depth information, and then the Ground Truth (GT) dataset of apple point clouds was manually segmented according to the RGB images, as shown in Fig. 3. The remained RGB images were used as a training set of the optimized Faster R-CNN, the details of GT dataset are shown in Table 3.

**Table 2**

**Number of images from RGB dataset for training and testing (Augmentation-performed)**

| Image | RAGL | | GAGL | |
|---|---|---|---|---|
| Training | 2000 | bbox | 2810 | bbox |
| | | 12640 | | 18304 |
| Validation | 300 | ✗ | 550 | ✗ |
| Total | 2300 | | 3360 | |

**Fig. 3 - Examples of GT dataset corresponding to the validation set. (Two colours)**

**Table 3**

**Details of GT dataset**

| GT | RA | GA |
|---|---|---|
| GT Num (piece) | 1717 | 2350 |
| Point Num (million) | 1.88 | 2.29 |

- **The optimized Faster R-CNN**

Regions with convolutional neural networks (R-CNN) are widely used in object detection, using selective search methods to detect ROI, and then using CNN to classify these regions (*Girshick R et al., 2013*). After that, Fast R-CNN uses the ROI pooling to extract fixed-length feature vectors from the feature map, and backpropagates all network weights in training (*Girshick R, 2015*). When Faster R-CNN is proposed, the efficiency is further improved to 10ms for generating the candidate regions of an image by using the Region Proposal Networks (RPN) (*Ren S et al., 2015*).

In this paper, RGB images were used to detect apple regions, and the implementation of the RPN is the key work of this model. In addition, the sliding scan is performed by using the 3×3 sliding window on the 120×67 feature map of the fifth layer extracted by ZF network structure (*Zeiler MD and Fergus R, 2013*); then the optimized Faster R-CNN performs a convolution with a 1×1 kernel. As a result, a 256-dimensional feature vector was obtained. In addition, RPN relies on the anchor mechanism to generate candidate regions, then the R-CNN is used to perform apple detection and fine adjustment of the ROI. At the end, the apples in the image can be located by ROI.

For each ROI in RGB images detected by optimized Faster R-CNN, we provide a confidence C ∈ [0,1], 0 is for the lowest confidence and 1 is for the highest confidence. In the detection, the confidence thresholds were set to 0.5 for RAGL and 0.55 for GAGL, which were proved by experiments in both categories. More importantly, since training Faster R-CNN with RGB images is independent of point clouds, once the optimized Faster R-CNN is successfully trained for other objects, this model can be extended to more practice than apple.

- **Segmentation method based on ROI**

In this paper, the point clouds without colour were obtained from depth images as first step as follows: $\mathbf{V(u)} = D(\mathbf{u})\mathbf{K}^{-1}\mathbf{[u,1]}$, where $\mathbf{u} = (u, v)$ is a separate pixel in a depth image, $D(\mathbf{u})$ is the depth value of $\mathbf{u}$ and $\mathbf{K}$ is the intrinsic calibration matrix of the Kinect depth camera. As a result, a specific depth measurement as a 3D vertex $\mathbf{V(u)}$ in the camera's coordinate space was obtained. Moreover, to get coloured point clouds, for each pixel $\mathbf{m} = (m_c, v_c)$ in RGB image, we used $\mathbf{[m,1]} = \mathbf{CTV(u)}^*$ to search the corresponding 3D vertex to fuse coloured point clouds based on the pixel colour in RGB image, where $\mathbf{C}$ is the intrinsic calibration matrix of RGB camera, $\mathbf{T}$ is the external calibration matrix between two cameras and $\mathbf{V(u)}^* = \mathbf{V(u)} / D(\mathbf{u})$.

The second step in segmentation method based on ROI is to search the points in all the apple tree point clouds corresponding to coloured pixel in ROI. To avoid complex computation, the $IDX$ containing constant relationship between RGB images and point clouds was defined as Equation (1), where $w(C)$ and $h(C)$ are the width and height of the RGB pixels respectively. Therefore, the $IDX$ is the real number mapping each RGB pixel to its 3D vertex as well as a link between 2D RGB information and 3D point clouds information.

$$IDX = m_c w(C) + n_c, 1 < m_c < w(C), 1 < n_c < h(C) \quad (1)$$

As a result, the point clouds corresponding to colour pixels in ROI can be rapidly segmented by a series of $IDX$. In other words, based on $IDX$ and the ROI output by the optimized Faster R-CNN in the RGB images, the point clouds of ROI were roughly segmented.

- **Quality control procedure (QCP).**

The ROI output from RGB images are a series of boxes. However, since the outline of an apple is a rough circle, a small amount of background will also be contained in the box, as shown in Fig. 4. Therefore, a few noise points were included in the apple point clouds, which will bring great negative effects to practical applications demanding precise shape of apple, such as evaluating size, quality and yield. In addition, when using the robotic arm to pick apples, the normal vectors of the apple surface is critical to the pose of the arm, while the noise points are of great risk to lead to failure in apple grasping task, thus the noise points have to be filtered out to refine the point clouds. QCP was based on estimating surface normal vector and curvature using region growing method. Before this, we computed, using the cross product between two neighbouring vertices, whole corresponding normal vectors using Equation (2),

$$\mathbf{N(u)} = \left[\mathbf{n(V}(u+1,v)-\mathbf{V}(u,v))\times(\mathbf{V}(u,v+1)-\mathbf{V}(u,v))\right] \quad (2)$$

where $\mathbf{n(a)} = \mathbf{a} / \|\mathbf{a}\|_2$

After computing all surface normal vectors, through analyzing the apple point clouds, the $D(\mathbf{u})$ of noise points will have an obvious "drop" separating the noise point from the apple point clouds like the red lines shown in Fig. 4. In addition, the size of an apple is about 0.07m. So, given two vertices $\mathbf{V(u_1)}$ and $\mathbf{V(u_2)}$, we introduced the Euclidean Distance Score ( $EDS \in [0,1]$) as shown in Equation (3) and validity distance $d_N$ = 0.01m,

$$EDS(\mathbf{V(u_1)}, \mathbf{V(u_2)}) = (d_N - \|\mathbf{V(u_2)} - \mathbf{V(u_1)}\|_2) / d_N \quad (3)$$

In addition, the curvature of vertex $\mathbf{v(u_1)}$ is approximately equal to

$$c(\mathbf{V(u_1)}, \mathbf{V(u_2)}) = \left|\cos^{-1}(\mathbf{N(u_1)} \bullet \mathbf{N(u_2)} / \|\mathbf{N(u_2)}\|_2 \|\mathbf{N(u_1)}\|_2) / \|\mathbf{V(u_2)} - \mathbf{V(u_1)}\|_2\right|$$

The Curvature Score ( $CS(\mathbf{V(u_1)}, \mathbf{V(u_2)}) \in [0,1]$) was defined as Equation (4) and the validity radius is $r_N$ = 0.06m

$$CS(\mathbf{V(u_1)}, \mathbf{V(u_2)}) = 1 - \left|1 - 1 / r_N c(\mathbf{V(u_1)}, \mathbf{V(u_2)})\right| \quad (4)$$

More importantly, through data statistics, we finally defined a QCP mask $M(\mathbf{V(u_1)}, \mathbf{V(u_2)}) \in [0,1]$ for a vertex $\mathbf{V(u_1)}$, combining surface normal vector with curvature to filter noise points with a threshold of 0.77 as shown in Equation (5): $M(\mathbf{V(u_1)}, \mathbf{V(u_2)}) \geq 0.77$ is for a point is valid, otherwise, the point is to be filtered when $M(\mathbf{V(u_1)}, \mathbf{V(u_2)}) < 0.77$.

$$M(\mathbf{V(u_1)}, \mathbf{V(u_2)}) = 0.65EDS + 0.35CS \quad (5)$$

By using QCP on roughly segmented apple point clouds, most of noise points can be filtered out.

The arithmetic logic of QCP is briefly showed in Algorithm 1.

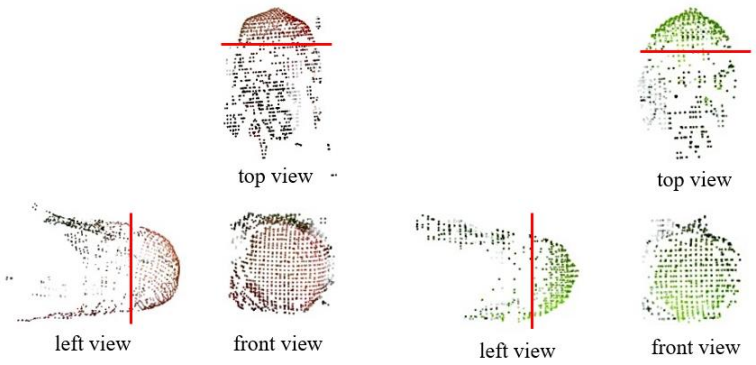


(a) (b)

**Fig. 4 - Two instances of the 'drop' in raw point clouds segmented by method based on ROI**

- **Comparison methods**

Although the colour information has been extracted into the point clouds, it is saved in the RGB model. The Excessive Green Index (ExG) was successfully used to segment red Fuji apple (*Bulanon DM et al., 2002*). The ExG-ExR with zero threshold was proved to be 55% higher than the performance of others in segmenting green crops (*Meyer GE and Neto JC, 2008*). In this paper, ExG was used to segment point clouds of RAGL and ExG-ExR was used to segment point clouds of GAGL.

The detail of indices is shown in the Table 4.

**Table 4**

**Segmentation algorithms for point colour detection**

| Colour indices | Formula |
|---|---|
| ExG | 2G-R-B |
| ExG-ExR | 3G-2.4R-B |

**Algorithm 1: QCP**

- *While* $\{PtClouds\}$ is not empty *do*
  - $Current\{valid\} \leftarrow \varnothing$
  - $Current\{seeds\} \leftarrow \varnothing$
  - Point at the centre of ROI in $\{PtClouds\} \rightarrow d_c$
  - $\{valid\} \leftarrow d_c$
  - $\{seed\} \leftarrow d_c$
  - *for* i = 0 to size $(\{seeds\})$ *do*
    - *Freshfind* 4 nearest neighbours of current seed point $\{Nr\} \leftarrow \{N_4 seed(i)\}$
    - *for* j = 0 to size $\{Nr\}$ *do*
      - Current neighbour point $P_j \leftarrow N_r\{j\}$
      - Compute EDS$\{j\}$ & CS$\{j\}$ & M$\{j\}$
        - *If* M$\{j\} \geq 0.77$
        - $\{valid\} \leftarrow \{valid\} \bigcup P_j$
        - $\{Nextseeds\} \leftarrow P_j$
          - *If* M$\{j\} < 0.77$
            - $\{PtClouds\} \leftarrow \{PtClouds\} \setminus P_j$
          - end *If*
        - end *If*
    - end *for*
  - end *for*
  - $\{seeds\} \cap \varnothing \leftarrow \{Nextseeds\}$
- end *While*
- *return* R

- **Evaluation methods**

We evaluate the above-mentioned methods by comparing the Apple Point Clouds (APtC) from segmentation with each manually-segmented sample defined as $GT^*$ in GT dataset. An intersection between $GT^*$ and APtC segmented by the method based on ROI, is named $\mathbb{S}$, as shown in Equation (6),

$$\mathbb{S} = APtC \cap GT^* \tag{6}$$

conversely, there is a point set that does not belong to $GT^*$ (NBGT). Due to the difference in size of apple, the number of points is also different. For this reason, the Overlap is defined as shown in Equation (7),

$$Overlap = \frac{\mathbb{S}}{GT^*} \tag{7}$$

which is the important criterion for measuring the segmentation effect. Given the influence of NBGT on the segmentation is also significant, Inaccuracy is defined as shown in Equation (8),

$$Inaccuracy = \frac{NBGT}{GT^*} \tag{8}$$

more importantly, the Purity is introduced here as shown in Equation (9), and the quality of Segmentation is evaluated by both $\mathbb{S}$ and NBGT.

$$Purity = \frac{\mathbb{S}}{APtC} \tag{9}$$

In addition, although training optimized Faster R-CNN is the first step of segmenting point clouds, the effect of training directly affects the result of segmentation of point clouds. If the accuracy of training effect can be improved, the result of segmentation will also be enhanced. Therefore, an evaluation of the training effect was introduced here.

Since the optimized Faster R-CNN used in this task will output a series of bounding boxes, and we hope that these boxes contain all the apples in an image that meet the requirements. Denoting boxes as apple or non-apple can yield three potential results, with the latter two being sources of error: true positive (TP)-Correctly classifying a region as an apple; false positive (FP)-Incorrectly classifying a background region as an apple or multiple detection of the same apple; false negative (FN)-Incorrectly classifying an apple as a background region. In contrast, true negative (TN)-Correct classification of background is not required in this binary classification problem where foreground is always determined for object detection. In order to quantify our training effect, three parameters are introduced as shown in Equation (10) *(Hasan MM et al., 2018*).

$$\begin{cases} precision = \dfrac{TP}{TP + FP} \\ recall = \dfrac{TP}{TP + FN} \\ F1\,score = 2\dfrac{precision * recall}{precision + recall} \end{cases} \quad (10)$$

## RESULTS

- **Results of Segmentation method based on ROI**

In the testing process, since there are a large number of annotated apples, the validation set was divided into several groups in order to ensure the objectivity and robustness of the results, each group included 10 images for testing. When testing the performance of the model, 10 groups were randomly picked out. The recognition result of each group and the overall evaluation are shown in Table 5 and Table 6.

**Table 5**

**Evaluation of RAGL/GAGL detection results of the optimized Faster R-CNN model**

| Group | | Selected | | Detection | | TP | | FP | | FN | |
|---|---|---|---|---|---|---|---|---|---|---|---|
| RA | GA | RA | GA | RA | GA | RA | GA | RA | GA | RA | GA |
| r03 | g01 | 65 | 70 | 62 | 68 | 60 | 67 | 2 | 1 | 5 | 3 |
| r05 | g05 | 61 | 73 | 60 | 69 | 59 | 68 | 1 | 1 | 2 | 5 |
| r10 | g09 | 52 | 65 | 50 | 64 | 49 | 62 | 1 | 2 | 3 | 3 |
| r11 | g15 | 69 | 67 | 65 | 64 | 65 | 61 | 0 | 3 | 4 | 6 |
| r17 | g16 | 40 | 74 | 38 | 71 | 38 | 71 | 0 | 0 | 2 | 3 |
| r20 | g23 | 70 | 64 | 66 | 63 | 66 | 62 | 0 | 1 | 4 | 2 |
| r25 | g29 | 55 | 73 | 54 | 70 | 53 | 70 | 1 | 0 | 2 | 3 |
| r26 | g30 | 54 | 50 | 53 | 48 | 52 | 48 | 1 | 0 | 2 | 2 |
| r27 | g40 | 67 | 69 | 65 | 68 | 65 | 66 | 0 | 2 | 2 | 3 |
| r30 | g51 | 30 | 66 | 30 | 63 | 30 | 63 | 0 | 0 | 0 | 3 |

**Table 6**

**Confusion matrix of the optimized Faster R-CNN model**

| Category | Predicted group | | | | Precision (%) | Recall (%) | F1 score |
|---|---|---|---|---|---|---|---|
| | RAGL | Background | GAGL | Background | | | |
| RAGL | 537 | 26 | - | - | 98.9 | 93.4 | 96.1 |
| Background | 6 | ✗ | - | - | | | |
| GAGL | - | - | 638 | 33 | 98.5 | 95.1 | 96.8 |
| Background | - | - | 10 | ✗ | | | |

As the confusion matrix can be seen in Table 6, the optimized Faster R-CNN model trained with enhanced RGB dataset got precision over 98% and recall over 93% for recognizing both RAGL and GAGL data. The results of F1 score indicated that the optimized Faster R-CNN had great robustness in this task.

Based on this step, the point clouds data was segmented by combining the RGB-D mapping relationship with ROI output from the Faster R-CNN. The overall evaluation is shown in Table 7.

The Overlap can directly reflect the effect of segmentation of point clouds. Without QCP, the Overlap achieved by RAGL and GAGL represented satisfactory results of segmentation based on the optimized Faster R-CNN. Among them, RAGL's Overlap was lower. Through data analysis, in the recognition process using the Faster R-CNN model, a small number of red apples that were partially occluded by green leaves were not recognized as the TP results. Thus, the APtC correspondingly missed some points overlapping with $GT^*$, then the RAGL's Overlap was reduced. In fact, the evaluation of the APtC was consistent with the result of apple detection by the Faster R-CNN. Moreover, Inaccuracy of RAGL and GAGL were both more than 40%, reflecting that a lot of noise points corresponding to the corners of ROI existed in APtC. Therefore, both Purity of RAGL and GAGL were not satisfactory at all without QCP.

More importantly, Purity can directly reflect the performance of QCP, and QCP algorithm is the key of high Purity. Table 7 shows that the Purity (QCP performed) of RAGL and GAGL much better than the Purity without QCP. Even though QCP-performed Overlap was slightly reduced, the Inaccuracy was reduced by more than 40%, indicating that QCP is of great value. The detail of QCP's effect is shown in Fig. 5. A set of experimental results of the method based on ROI is shown in Fig. 6.

**Table 7**

**Evaluation of RAGL/GAGL segmentation**

| Method | Category | Evaluation | | |
|---|---|---|---|---|
| | | Overlap (%) | Inaccuracy (%) | Purity (%) |
| RGB ROI | RAGL | 95.1 | 48.7 | 66.1 |
| | GAGL | 95.7 | 44.8 | 68.1 |
| RGB ROI (QCP-performed) | RAGL | 93.5 | 3.2 | 96.7 |
| | GAGL | 94.5 | 3.7 | 96.2 |
| MBPC | RAGL | 96.8 | 3.8 | 96.2 |
| | GAGL | 97.2 | 236.3 | 29.1 |

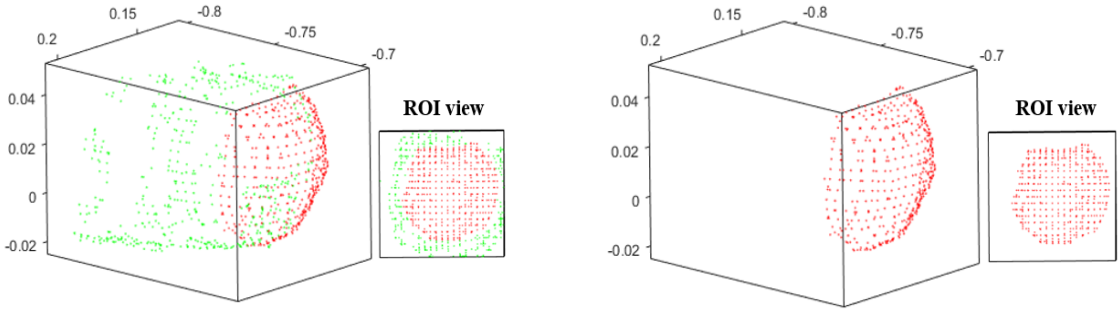


**Fig. 5 - Effect of QCP-performed apple point clouds**

*(a) Raw apple point clouds segmented by RGB ROI, green points are noise that will be filtered by QCP, red points are target points of the apple. (b) QCP-performed apple point clouds of the side facing the camera*

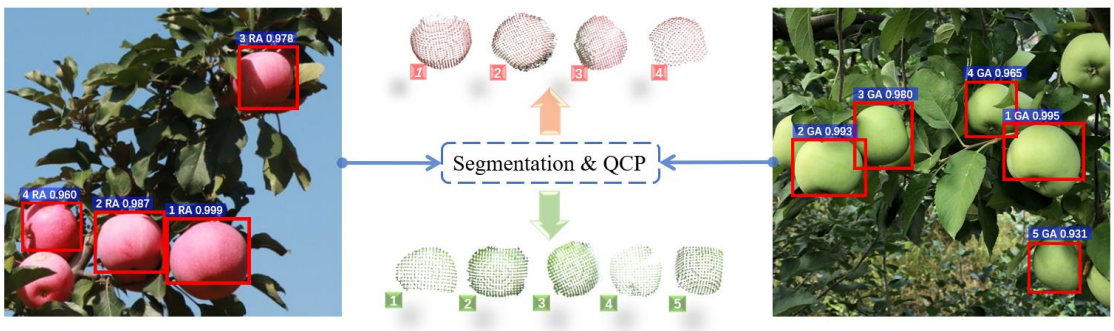


**Fig. 6 - A group of results from the method based on ROI**

- **Results of comparison methods**

At last, in the results of the MBPC, the segmentation of RAGL point clouds achieved excellent results due to the obvious colour difference between red apples and green leaves. As shown in Table 7, the Overlap of RAGL was even better than the method based on ROI without QCP, and MBPC achieved a great Inaccuracy. ExG can segment RAGL point clouds well, as shown in Fig. 7(a-b). In addition, Purity of RAGL using MBPC was much higher than the method based on ROI before QCP was performed. However, the QCP-performed Purity of the method based on ROI was the best result in segmentation.

When the GAGL was segmented, the Greenness difference between the leaves and the apples was not enough, making the result of segmentation unsatisfactory, the Inaccuracy is over 250%. It shows that points in NBGL were much more than the apple points. Therefore, the score of segmentation was very poor in Purity. As shown in the Fig. 7(c-d), lots of green points of apples and leaves both existed, and the segmentation of GAGL was not completed.

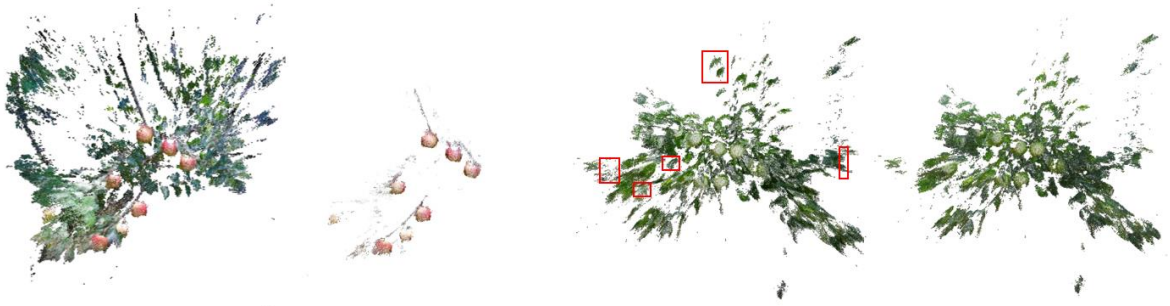

(a) (b) (c) (d)

**Fig. 7 - Results of the segmentation of MBPC**

*(a) Raw data of RAGL. (b) Results of RAGL data (c) Raw data of GAGL. (d) Results of GAGL data, except for the red marks, MBPC recognizes other parts as apple point clouds, the segmentation effect is bad*

## CONCLUSIONS

This paper put forward the segmentation method of apple point clouds based on ROI. An annotated RGB dataset of apple trees was built to train Faster-R-CNN to locate ROI in RGB images, which made this method robust in practical application. And then apple point clouds were roughly segmented by the relationship between point clouds and RGB images, and QCP was proposed to refine the apple point clouds. Some conclusions can be reached from the comparison experiments by the MBPC:

(1) The segmentation method based on ROI is simplified by combining the smart Faster R-CNN with the point clouds from consumer-grade RGB-D camera.

(2) QCP can greatly improve the quality of apple point clouds roughly segmented by ROI. Purity is raised from 66.1% to 96.7% for RAGL and from 68.1% to 96.2% for GAGL.

(3) The segmentation method based on ROI is effective for small-size point clouds in unstructured scenes.

## ACKNOWLEDGEMENT

This study was supported by National Natural Science Foundation of China [31971668] and Beijing Natural Science Foundation [2182045].

## REFERENCES

[1] Bac CW., Henten EJV., Hemming J., Edan Y., (2015), Harvesting Robots for High-value Crops: State-of-the-art Review and Challenges Ahead. *Journal of Field Robotics,* Vol.31, pp. 888-911, Ed.Wiley, USA;

[2] Blasco J. et al., (2003), Machine Vision System for Automatic Quality Grading of Fruit. *Biosystems Engineering,* Ed. Elsevier, pp.415-423, London/U.K.;

[3] Bulanon DM., Kataoka T., Ota Y. et al., (2002), AE-Automation and Emerging Technologies: A Segmentation Algorithm for the Automatic Recognition of Fuji Apples at Harvest., *Biosystems Engineering,* Ed. Elsevier, pp. 405-412, London/U.K.;

[4] Charles RQ., Hao S., Mo K., Guibas LJ., (2017), PointNet: Deep Learning on Point Sets for 3D Classification and Segmentation, *IEEE Conference on CVPR,* Ed. IEEE, pp. 77-85, PR/US;

[5] Dai A. et al., (2017), ScanNet: Richly-annotated 3D Reconstructions of Indoor Scenes, IEEE Conference on Computer Vision and Pattern Recognition, Ed. IEEE, pp. 2432-2443.;
[6] English A., Ross P., Ball D., (2003), Vision based guidance for robot navigation in agriculture., *IEEE International Conference on Robotics & Automation.*, pp. 1693-1698, Ed. IEEE, Hong Kong/China;
[7] Girshick R., et al., (2014), Rich feature hierarchies for accurate object detection and semantic segmentation, *IEEE Conference on Computer Vision and Pattern Recognition*, Ed. IEEE, pp. 580-587
[8] Girshick R., (2015), Fast R-CNN. Computer Science., *IEEE International Conference on Computer Vision,* Ed. IEEE, pp.1440-1448;
[9] Green WR., Grobler H., (2015), Normal distribution transform graph-based point cloud segmentation, *Pattern Recognition Association of South Africa & Robotics & Mechatronics International Conference*, Ed. IEEE, pp.54–59, Port Elizabeth / South Africa;
[10] Grinblat GL. et al., (2016), Deep learning for plant identification using vein morphological patterns. *Computers & Electronics in Agriculture.* Ed. Elsevier, pp.418-424., London/U.K.;
[11] Hasan MM. et al., (2018) Detection and analysis of wheat spikes using Convolutional Neural Networks, *Plant Methods,* Vol.14, Ed. BMC, Melbourne/Australia.;
[12] Himmelsbach M., Hundelshausen FV., Wuensche HJ., (2010), Fast Segmentation of 3D Point Clouds for Ground Vehicles, *Intelligent Vehicles Symposium*, Ed. IEEE, pp.560–565, California/US;
[13] Huijun Y., (2011), A Novel Algorithm for Segmenting Fruit from Unorganized Point Clouds, *International Conference on Virtual Reality Continuum & Its Applications in Industry,* Ed. ACM, pp.379-382, Hong Kong/China;
[14] Kitamura S., Oka K., (2006), Recognition and cutting system of sweet pepper for picking robot in greenhouse horticulture., *Mechatronics & Automation, IEEE International Conference*, Ed. IEEE, pp.1807-1812, Niagara Falls/Canada;
[15] Linker R., Kelman E., (2015), Apple detection in night-time tree images using the geometry of light patches around highlights. *Computers & Electronics in Agriculture.,* Ed. Elsevier, pp.154-162., London/U.K.;
[16] Li Y., Rui B., Sun M., Chen B., (2018), PointCNN, Shan Dong University/China;
[17] Meyer GE., Neto JC., (2002), Verification of colour vegetation indices for automated crop imaging applications., *Computers & Electronics in Agriculture.,* Ed. Elsevier, pp. 282-293, London/U.K.;
[18] Nguyen TT., et al., (2013), Apple detection algorithm for robotic harvesting using a RGB-D camera*, Computer Methods in Applied Mechanics & Engineering*, pp.06-10, Zurich/Swit;
[19] Pas AT., Platt R., (2018), Using Geometry to Detect Grasp Poses in 3D Point Clouds, *Robotics Research.*, pp. 307-324, Ed. Springer, Boston/US;
[20] Paulus et al., (2013), Surface feature based on classification of plant organs from 3D laser scanned point clouds for plant phenotyping, *BMC Bioinformatics,* Vol.14, Issue 1, pp.1-14, Ed. Springer Nature;
[21] Ren S., He K., Girshick R., Jian S., (2015), Faster R-CNN: Towards Real-Time Object Detection with Region Proposal Networks., *IEEE Transactions on Pattern Analysis and Machine Intelligence,* Ed. IEEE, pp.1137-1449;
[22] Soria PR., et al., (2017), Multi-view Probabilistic Segmentation of Pome Fruit with a Low-Cost RGB-D Camera, *Iberian Robotics Conference*, Sevilla/Spain;
[23] Tao Y., Zhou J., (2017), An Automatic Segmentation and Recognition Method of Apple Tree Point clouds in the Real Scene Based on the Fusion of Colour and 3D Feature, *ASABE Meeting,* Michigan/US;
[24] Zeiler MD., Fergus R., (2014), Visualizing and Understanding Convolutional Networks., *Lecture Notes in Computer Science*, Ed. Springer, pp.818-833.;
[25] Wahabzada M., et al., (2015), Automated interpretation of 3D laser scanned point clouds for plant organ segmentation, *BMC Bioinformatics,* Vol.16, Issue 1, pp. 248-258, Ed. Springer Nature;
[26] Wang W. et al., (2017) SGPN: Similarity Group Proposal Network for 3D Point Cloud Instance Segmentation, *Computer science,* Ed. Cornell University. New York/US.;
[27] Xu Y. et al., (2018), Unsupervised Segmentation of Point Clouds from Buildings Using Hierarchical Clustering Based on Gestalt Principles*, IEEE Journal of Selected Topics in Applied Earth Observations & Remote Sensing,* Ed. IEEE, pp.1-17;
Yamauchi H. et al., (2005), Feature Sensitive Mesh Segmentation with Mean Shift., *International Conference on Shape Modeling & Applications*, Ed. IEEE, London/UK.

# EXPERIMENTAL PULSE GENERATOR COMBINED WITH THE MILKING MACHINE COLLECTOR
# /
# ЕКСПЕРИМЕНТАЛЬНИЙ ГЕНЕРАТОР ІМПУЛЬСІВ СУМІЩЕНИЙ ІЗ КОЛЕКТОРОМ ДОЇЛЬНОГО АПАРАТА

**Dmytriv V.T.*), Dmytriv I.V., Yatsunskyi P.P.** [1]
Lviv Polytechnic National University, Lviv / Ukraine
*E-mail: Dmytriv_V@ukr.net*
*DOI: 10.35633/INMATEH-59-24*

***Keywords:*** *pulse generator, pneumatic-electromagnetic pulsator-collector, vacuum, pulsation frequency, regression model*

## ABSTRACT

*Factors affecting the milk ejection intensity and power consumption of the pulse generator combined with the milking machine collector have been analyzed. The main factors and limits of their variation, as well as the results of experimental studies are given. The matrices of a multivariate planned experimental study of a pulse generator with a combined collector (pneumatic-electromagnetic pulsator-collector) have been developed. According to the results of experimental studies, the coded and natural values of the regression equation are derived. The equations characterize the dependence of the milk ejection intensity on the pulsation frequency, the ratio between the strokes and the vacuum pressure in the under teats space of the teat cup. The dependence of the power consumption of the pulse generator on the pulse rate and the ratio between the strokes are derived. Graphical models of interpretation of regression dependencies according to the experimental data are constructed. Student's t-test, Fisher and Cochran criteria are calculated. These indicators show the adequacy and reproducibility of the models obtained during the studies using an experimental pulse generator combined with a milking machine collector.*

## РЕЗЮМЕ

*Проаналізовано фактори, які впливають на інтенсивність молоковіддачі і споживану потужність генератора імпульсів із суміщеним колектором доїльного апарата. Наведено основні фактори і межі їх варіювання, розроблено матриці багатофакторного планованого експерименту генератора імпульсів суміщеного із колектором (пневмоелектромагнітний пульсоколектор), а також результати експериментальних досліджень. За результатами експериментальних досліджень виведено рівняння регресії у кодованих і натуральних значеннях, які характеризують залежність інтенсивності молоковіддачі від частоти пульсації, співвідношення між тактами та вакуумметричного тиску у піддійковому просторі доїльного стакана, та залежність споживаної потужності генератора імпульсів від частоти пульсації і співвідношення між тактами. Побудовано графічні моделі інтерпретації регресійних залежностей за експериментальними даними. Розраховано t-критерій Стьюдента, критерії Фішера і Кохрена, які показують адекватність і відтворюваність отриманих моделей технологічного процесу з використанням експериментального генератора імпульсів суміщеного із колектором доїльного апарата.*

## INTRODUCTION

Robotization of the milking process provides a complete adaptation of the technical system to the physiology of the cow and is an urgent task of today. The automatic milking system is a technology of labour saving *(Floridi et al., 2013)*. Today's ensuring of adaptive milking is one of the major innovations of dairy farms worldwide *(De Koning, 2010)*.

However, attention should be paid to the automation of individual milking operations, which is part of the overall milking system. Automatic milking is quite favourable for the cow (*Pastell et al., 2006*). The design and its components are the main elements that influence the servicing characteristics of the milking machine (*Spencer et al., 2004*). There are many factors that determine the quality of the process. However, it is important to observe the appropriate operating parameters, as not adjusting the unit to a particular animal may result in injury and disease to the udder of the cow.

[1] *Dmytriv V.T.,' Prof. Dr.Sc.Eng.; Dmytriv I.V., Ph.D.Eng., Yatsunskyi P.P., PhD Stud.*

Pulse rate and vacuum also affect the cow's adaptation of the system and determine the softness and speed of milking (*Penry et al., 2016*). Changing the ratio between strokes from 50:50 to 70:30 with a steady pulse rate of 60 pulses/min and the 42 kPa vacuum pressure level in the system reduces the duration of the milking time to 25%, but at the 51 kPa vacuum pressure in the system the milking time is reduced by only 5% (*Thomas et al., 1993*). The results of research by scientists (*Spencer et al., 2007*) showed that the maximum amount of milk was at the vacuum pressure of 43.9 kPa.

This confirms that the level of vacuum, the frequency of pulsations and the stroke ratio create a dominant influence on the intensity of milk production (*Mein Graeme et al., 2007*).

Therefore, the development and research of an adaptive pulse generator combined with a collector is relevant.

## MATERIALS AND METHODS

The purpose of the work was to study the characteristics of an experimental pulse generator combined with the milking machine collector, depending on the parameters of the process of machine milking of cows. The general view and scheme of the experimental pulse generator combined with the milking machine collector is shown in Fig. 1.

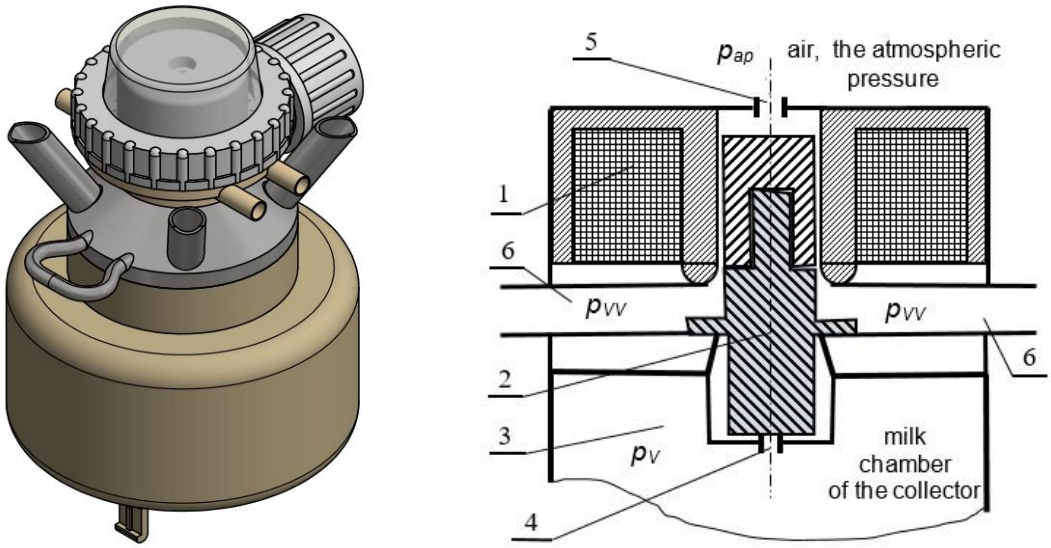


**a)** **b)**

**Fig. 1 - The general view (a) and scheme (b) of experimental pulse generator combined with milking machine collector**

*1 – electromagnet; 2 – keeper (armature) valve; 3 – milk chamber of collector; 4 – drain port of vacuum pressure; 5 – drain port of atmospheric pressure; 6 – chamber of variable pressure (engaging the inter wall chamber of teat cups)*

An experimental pulse generator combined with a collector (Fig. 1b) ensures the movement of the (2) armature valve by electric current feed with a given frequency to the (1) electromagnet. The (2) armature valve moves and with a given frequency closes the (4) and (5) drain ports by turn. When an electric current is applied to the electromagnet (1), the electromagnetic force arises and raises the (2) armature valve upwards and closes the (5) drain ports of the atmospheric pressure access. Then, through the drain ports of (4), the vacuum pressure $p_v$ from the (3) collector milk chamber enters into the (6) chamber of variable vacuum pressure, from where the $p_{vv}$ variable vacuum pressure enters into the inter wall chamber of teat cups. It is a stroke of sucking. In the absence of electric current on the (1) electromagnet, the armature valve moves down, closes the (4) drain port and opens the drain port of (5). Then, through the (5) drain port, the atmospheric pressure $p_{ap}$ enters into the (6) chamber of variable pressure, from where the $p_{vv}$ atmospheric pressure enters into the inter wall chamber of teat cups. This corresponds to a compression stroke.

The nature of the armature valve switching and the influence on this process of technological operation parameters of the milking machine with the experimental pulse generator combined with the collector were investigated using a full-scale planned experiment. The technique of the experiment was taken as the basis of (*Dmytriv et al., 2019*), taking into account the weight of each factor and decoding the elements of the regression dependence into the coefficients of the equation for the natural values of the factors.

The general view of connection of the pulse generator combined with the collector is shown in Fig. 2. To measure the pressures (Fig. 2) in the inter wall chamber of teat cups, in the under teats space and milk chamber of artificial udder of the cow (3) the intelligent pressure sensors are activated for (4), (5) and (6) respectively. To simulate the diagram of the cow's milk ejection the milk ejection intensity simulator, developed by the authors, was used (*Dmytriv V. T. and Dmytriv I. V., 2013*).

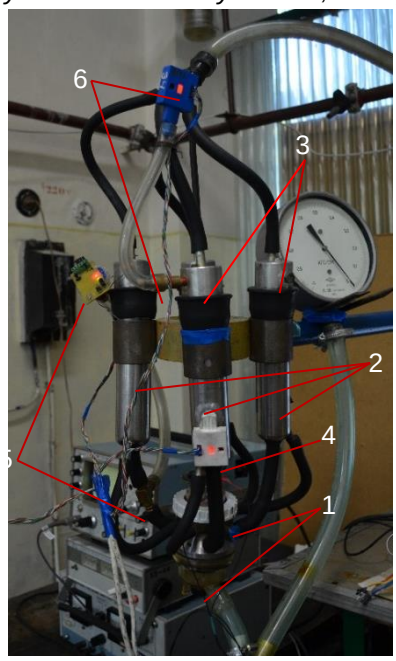


**Fig. 2 - The general view of connection of experimental pulse generator combined with collector**

*1 – pulse generator combined with collector; 2 – teat cups; 3 – artificial udder of cow;*
*4 – sensor of pressure of the inter wall chamber of teat cup; 5 – sensor of pressure of under teat space of the teat cup;*
*6 – sensor of pressure in "milk chamber" of artificial udder of cow*

Response criteria were the *q* [g/sec] intensity of milk ejection and *N* [W] power consumption. The factors were the ripple frequency of *n* [imp./min] – $x_1$, the ratio between the strokes of *t/T* – $x_2$ and the vacuum gauge pressure in the under teat space of the teat cup of $p_n$ [kPa] – $x_3$. The values of the vacuum gauge pressure in the under teat space of the teat cup were 26, 32 and 38 kPa, the *n* ripple frequency was at levels of 40, 60 and 80 imp/min, and the ratio between the strokes was 40:60, 60:40 and 70:30.

The coding factors, according to the theory of experiment planning, are given in Table. 1.

**Table 1**

**Levels of variation of factors and their code values in the planned experiment**

| Factors | Designation | Dimension | Levels of factors | | | Variation interval |
|---|---|---|---|---|---|---|
| | | | upper | null | lower | |
| | | | Code values | | | |
| | | | + 1 | 0 | - 1 | |
| Ripple frequency, *n* | $x_1$ | [imp./min]<br>[Hz] | 40<br>0.67 | 60<br>1.0 | 80<br>1.33 | 20<br>0.33 |
| Ratio between the strokes, *t/T* | $x_2$ | | 40:60<br>= 0.667 | 60:40<br>= 1.5 | 70:30<br>= 2.333 | 0.833 |
| Vacuum gauge pressure in the under teat space of the teat cup, $p_n$ | $x_3$ | [kPa] | 26 | 32 | 38 | 6 |

## RESULTS

Taking into account the real operational modes mentioned above, we have applied a second-order polynomial, which is easily systematized and investigated as to the extremum. To make the planned experiment of the milk ejection dependence on the following factors - the ripple frequency, the ratio between the stroke and the vacuum pressure in the under teat space of the teat cup we have selected an orthogonal central composite plan (Table 2). Such factors correspond to the technological parameters of the milking machine. Column 11 is an orthogonal matrix of the planning, and column 12 is the value of the experiment response criterion.

The values of the factors for the planned experiment of the study of power consumption by an experimental pulse generator combined with a collector are given in Table. 3. The main factors were the ripple frequency and the ratio between the strokes. The pressure was constant during the planned experiment.

**Table 2**

**Extended matrix of orthogonal experiment planning for a three-factor model of the second order for milk ejection dependence on factors**

| Experiment № | $x_1$ | $x_2$ | $x_3$ | $x_1 \cdot x_2$ | $x_1 \cdot x_3$ | $x_2 \cdot x_3$ | $\left(x_1^{/}\right)^2$ | $\left(x_2^{/}\right)^2$ | $\left(x_3^{/}\right)^2$ | $x_1 \cdot x_2 \cdot x_3$ | $y$ ($q$), [g/sec] |
|---|---|---|---|---|---|---|---|---|---|---|---|
| 1 | +1 | +1 | +1 | +1 | +1 | +1 | 0.3333 | 0.3333 | 0.3333 | +1 | 40 |
| 2 | 0 | +1 | +1 | 0 | 0 | +1 | -0.6667 | 0.3333 | 0.3333 | 0 | 46.110 |
| 3 | -1 | +1 | +1 | -1 | -1 | +1 | 0.3333 | 0.3333 | 0.3333 | -1 | 47.333 |
| 4 | +1 | +1 | -1 | +1 | -1 | -1 | 0.3333 | 0.3333 | 0.3333 | -1 | 42.443 |
| 5 | 0 | +1 | -1 | 0 | 0 | -1 | -0.6667 | 0.3333 | 0.3333 | 0 | 43.333 |
| 6 | -1 | +1 | -1 | -1 | +1 | -1 | 0.3333 | 0.3333 | 0.3333 | +1 | 43.333 |
| 7 | +1 | +1 | 0 | +1 | 0 | 0 | 0.3333 | 0.3333 | -0.6667 | 0 | 40 |
| 8 | 0 | +1 | 0 | 0 | 0 | 0 | -0.6667 | 0.3333 | -0.6667 | 0 | 39.553 |
| 9 | -1 | +1 | 0 | -1 | 0 | 0 | 0.3333 | 0.3333 | -0.6667 | 0 | 41.553 |
| 10 | +1 | -1 | +1 | -1 | +1 | -1 | 0.3333 | 0.3333 | 0.3333 | -1 | 38 |
| 11 | 0 | -1 | +1 | 0 | 0 | -1 | -0.6667 | 0.3333 | 0.3333 | 0 | 38.667 |
| 12 | -1 | -1 | +1 | +1 | -1 | -1 | 0.3333 | 0.3333 | 0.3333 | +1 | 36.557 |
| 13 | +1 | -1 | -1 | -1 | -1 | +1 | 0.3333 | 0.3333 | 0.3333 | +1 | 23.330 |
| 14 | 0 | -1 | -1 | 0 | 0 | +1 | -0.6667 | 0.3333 | 0.3333 | 0 | 25.443 |
| 15 | -1 | -1 | -1 | +1 | +1 | +1 | 0.3333 | 0.3333 | 0.3333 | -1 | 26.447 |
| 16 | +1 | -1 | 0 | -1 | 0 | 0 | 0.3333 | 0.3333 | -0.6667 | 0 | 37.667 |
| 17 | 0 | -1 | 0 | 0 | 0 | 0 | -0.6667 | 0.3333 | -0.6667 | 0 | 40.890 |
| 18 | -1 | -1 | 0 | +1 | 0 | 0 | 0.3333 | 0.3333 | -0.6667 | 0 | 39.777 |
| 19 | +1 | 0 | +1 | 0 | +1 | 0 | 0.3333 | -0.6667 | 0.3333 | 0 | 42.667 |
| 20 | 0 | 0 | +1 | 0 | 0 | 0 | -0.6667 | -0.6667 | 0.3333 | 0 | 44.447 |
| 21 | -1 | 0 | +1 | 0 | -1 | 0 | 0.3333 | -0.6667 | 0.3333 | 0 | 43.777 |
| 22 | +1 | 0 | -1 | 0 | -1 | 0 | 0.3333 | -0.6667 | 0.3333 | 0 | 26.223 |
| 23 | 0 | 0 | -1 | 0 | 0 | 0 | -0.6667 | -0.6667 | 0.3333 | 0 | 30 |
| 24 | -1 | 0 | -1 | 0 | +1 | 0 | 0.3333 | -0.6667 | 0.3333 | 0 | 32.557 |
| 25 | +1 | 0 | 0 | 0 | 0 | 0 | 0.3333 | -0.6667 | -0.6667 | 0 | 40 |
| 26 | 0 | 0 | 0 | 0 | 0 | 0 | -0.6667 | -0.6667 | -0.6667 | 0 | 41.557 |
| 27 | -1 | 0 | 0 | 0 | 0 | 0 | 0.3333 | -0.6667 | -0.6667 | 0 | 40.667 |
| ∑ | 18 | 18 | 18 | 12 | 12 | 12 | - | - | - | 8 | - |

**Table 3**

**Extended matrix of orthogonal experiment planning for a two-factor model of the second order for power consumption dependence on factors**

| Experiment № | $x_1$ | $x_2$ | $x_1 \cdot x_2$ | $\left(x_1^{/}\right)^2$ | $\left(x_2^{/}\right)^2$ | $y$ ($N$), [W] |
|---|---|---|---|---|---|---|
| 1 | +1 | +1 | +1 | 0.3333 | 0.3333 | 3.51 |
| 2 | 0 | +1 | 0 | -0.6667 | 0.3333 | 4.60 |
| 3 | -1 | +1 | -1 | 0.3333 | 0.3333 | 6.77 |
| 4 | +1 | -1 | -1 | 0.3333 | 0.3333 | 2.09 |
| 5 | 0 | -1 | 0 | -0.6667 | 0.3333 | 2.7 |
| 6 | -1 | -1 | +1 | 0.3333 | 0.3333 | 3.743 |
| 7 | +1 | 0 | 0 | 0.3333 | -0.6667 | 3.13 |
| 8 | 0 | 0 | 0 | -0.6667 | -0.6667 | 3.98 |
| 9 | -1 | 0 | 0 | 0.3333 | -0.6667 | 5.77 |
| ∑ | 6 | 6 | 4 | - | - | - |

According to the data in table 2 as to the established procedure (*Dmytriv et al., 2019*), the results of calculations of the coded and natural values of the regression equation coefficients are given in Table 4, and for the data in the Table 3 results of calculations of the coded and natural values of the regression equation coefficients are given in Table 5.

**Table 4**

**Results of calculating the coefficients of the regression equation of the milk ejection dependence on factors**

| Coefficient of the regression equation | Coded coefficient | Real coefficient |
|---|---|---|
| $b_0$ | 40.593 | -78.231 |
| $b_1$ | -1.204 | -30.726 |
| $b_2$ | 4.271 | -3.771 |
| $b_3$ | 4.691 | 6.360 |
| $b_{12}$ | -0.499 | 26.67 |
| $b_{13}$ | 0.278 | 1.508 |
| $b_{23}$ | -2.806 | 0.289 |
| $b_{11}$ | -0.982 | -8.837 |
| $b_{22}$ | 0.369 | 0.536 |
| $b_{33}$ | -2.926 | -0.097 |
| $b_{123}$ | -1.375 | -0.904 |

The regression equation that models the change in the intensity of cow's milk ejection in natural factors will look like:

$$q = -78.231 - 30.726 \cdot n - 3.771 \cdot (t/T) + 6.360 \cdot p_n + 26.67 \cdot n \cdot (t/T) + 1.508 \cdot n \cdot p_{II} + \\ + 0.289 \cdot (t/T) \cdot p_n - 8.837 \cdot n^2 + 0.536 \cdot (t/T)^2 - 0.097 \cdot p_{II}^2 - 0.904 \cdot n \cdot (t/T) \cdot p_{II} \quad (1)$$

where $q$ – the milk ejection. [g/sec];

$n$ – the ripple frequency. [Hz];

$t/T$ – the ratio of strokes (compression stroke to suction stroke);

$p_n$ – the vacuum gauge pressure in the under teat space of the teat cup. [kPa];

The graphical representation of (1) dependence is shown in Fig. 3.

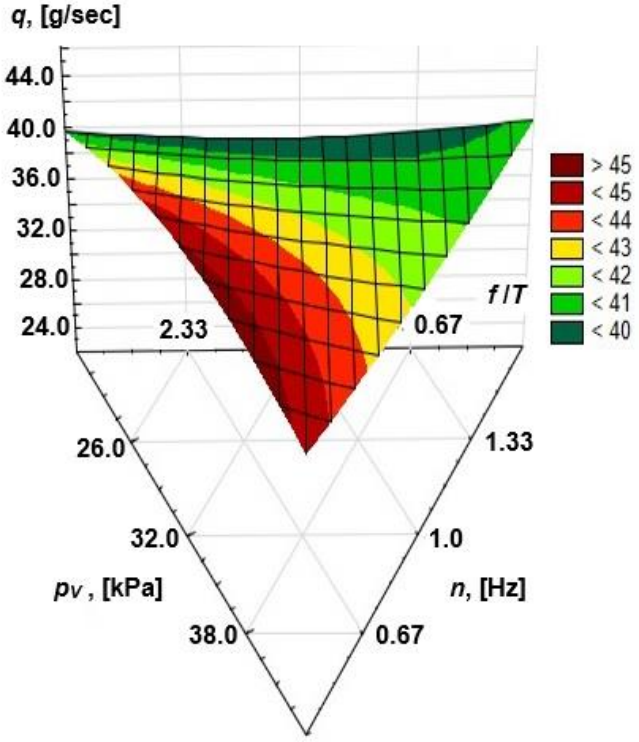


**Fig. 3 - The dependence of the $q$ intensity of the milking machine milk ejection on the technological process parameters**

*n – the ripple frequency; t/T – the ratio between strokes; $p_v$ - the vacuum gauge pressure in the under teat space of the teat cup*

**Table 5**

**Results of calculating the regression equation coefficients of the power consumption by factors**

| Coefficient of the regression equation | Coded coefficient | Real coefficient |
|---|---|---|
| $b_0$ | 4.02 | 6.205 |
| $b_1$ | -0.839 | -9.12 |
| $b_2$ | 0.706 | 4.434 |
| $b_{12}$ | -0.403 | -1.47 |
| $b_{11}$ | 0.409 | 3.755 |
| $b_{22}$ | -0.388 | -0.563 |

The regression equation that models the change in the *N* power consumption in natural factors will look like:

$$N = 6.205 - 9.12 \cdot n + 4.434 \cdot \left(\frac{t}{T}\right) - 1.47 \cdot n \cdot \left(\frac{t}{T}\right) + 3.755 \cdot n^2 - 0.563 \left(\frac{t}{T}\right)^2 \quad (2)$$

The graphical representation of (2) dependence is shown in Fig. 4.

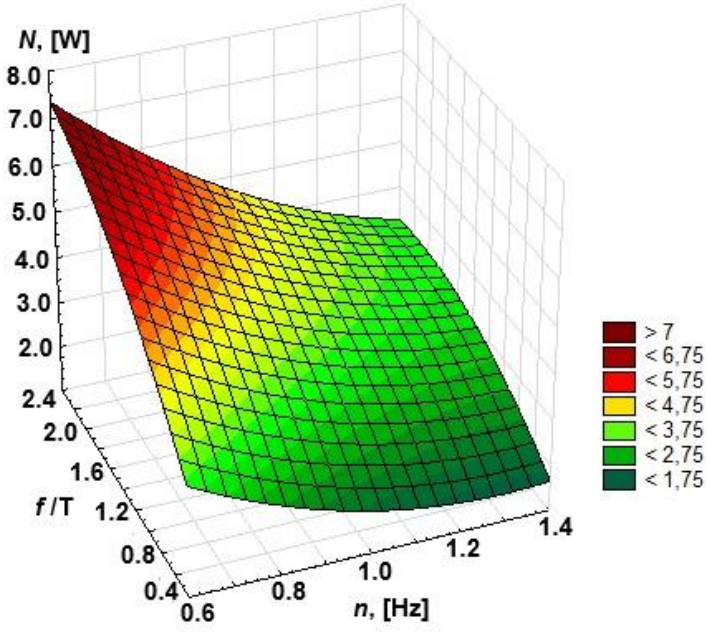


**Fig. 4 - The dependence of the *N* power consumption by the experimental pulse generator combined with a collector on the technological process parameters**

*n – the ripple frequency; t/T – the ratio between strokes*

The results of the analysis of the experimental data on the reproducibility of the experiments by the Cochran criterion, on the significance of the regression equations' coefficients by the Student's *t*-test and on the evaluation of the models adequacy by the Fisher *F*-test showed the following.

To confirm the reproducibility of the experiments (measurements) according to the (1) dependence of the milk ejection intensity, the calculated value of the Cochran criterion is 0.1136, being less than the table value, which is 0.198.

To estimate the significance of the regression coefficients the mean variance of $S^2$ was determined as $S^2$ = 523.019/27 = 19.371.

The variance in the determination of the regression coefficients *(Dmytriv et al., 2019*) is calculated by the dependence:

$$S_A^2 = S^2/(k \cdot m_k) \quad (3)$$

where *k* – the number of experiments; $m_k$ - the number of reinvestigation.

$$S_A^2 = \frac{19.371}{27 \cdot 3} = 0.239$$

To compare each regression coefficient with the $S_A \cdot t$ expression, the Student's *t*-test is determined for the significance level of 0.95, so the degree of freedom is calculated by the dependence:

$$fn = k \cdot (m_k - 1). \quad (4)$$

$$fn = 27 \cdot (3 - 1) = 54.$$

Accordingly, the tabular value of the *t*-criterion is $t = 2.004$.

The value of the $S_A^2 \cdot t = 0.479$ expression is compared with the coefficients of (1) equation. The $|b_i| > S_A^2 \cdot t$ condition is fulfilled except the coefficients of $b_{23}$ and $b_{33}$. We can conclude that the other coefficients of (1) equation are significant.

The suitability of the (1) regression equation for a characteristic description of the optimization criterion dependence on factors by the known method (*Dmytriv et al., 2019*) is checked and the Fisher criterion (*F*-criterion) is determined.

The $S_{a\partial}^2$ variance of adequacy and the calculated value of the *F*-criterion $F_p$ are $S_{a\partial}^2 = 29.057$ and respectively $F_p = 1.5$.

The table value of the *F*-criterion is $F_т = 1.95$ for the calculated degrees of freedom of the main variance of $f_1 = 18$ and the variance of adequacy of $f_n = 54$.

The model adequacy is estimated by the $F_p \leq F_T$ condition, respectively at the $1.5 \leq 1.95$ the model described by (1) equation is adequate.

To confirm the reproducibility of the experiments according to the (2) dependence of the power consumption, the calculated value of the Cochran criterion is 0.32, being less than the table value, which is 0.4775.

To estimate the significance of the regression coefficients the $S^2$ mean variance was determined as $S^2 = 0.53954/9 = 0.05995$.

The variance in the determination of the regression coefficients (*Dmytriv V.T. et al., 2019*) is calculated by the (3) formula:

$$S_{\text{A}}^2 = \frac{0.05995}{9 \cdot 3} = 0.00222$$

To compare each regression coefficient with the $S_A \cdot t$ expression, the Student's *t*-test is determined for the significance level of 0.95, so the degree of freedom is calculated by the (4) formula:

$$fn = 9 \cdot (3 - 1) = 18$$

Accordingly, the tabular value of the *t*-criterion is $t = 2.10$.

The value of the $S_A^2 \cdot t = 4.663 \cdot 10^{-3}$ expression is compared with the coefficients of (2) equation. The $|b_i| > S_A^2 \cdot t$ condition is fulfilled. We can conclude that all coefficients of (2) equation are significant.

The suitability of the (2) regression equation for a characteristic description of the optimization criterion dependence on factors is checked by the known method (*Dmytriv et al., 2019*) and the Fisher criterion (*F*-criterion) is determined.

The $S_{a\partial}^2$ variance of adequacy and the calculated value of the *F*-criterion $F_p$ are $S_{a\partial}^2 = 0.1798$ and respectively $F_p = 3$.

The table value of the *F*-criterion is $F_т = 4.58$ for the calculated degrees of freedom of the main variance of $f_1 = 3$ and the variance of adequacy of $f_n = 18$.

The model adequacy is estimated by the $F_p \leq F_T$ condition, respectively at the $3 \leq 4.58$ the model described by (2) equation is adequate.

## CONCLUSIONS

The regression model of studied factors (the dependence of the milk ejection intensity from the pulsation frequency, the ratio between the stroke and the vacuum pressure) approaches to linear form. With the increase of the vacuum gauge pressure and the ratio between strokes and the pulse rate decrease, the milking machine intensity of milking was increased. The maximum milk ejection is 49 g/sec at a vacuum gauge pressure of 38 kPa, a ripple frequency of 0.67 Hz and the 2.33 ratio between the suction and compression strokes.

With increasing the ripple frequency and decreasing the duration of the suction stroke, the power consumption decreased. The maximum power consumption is 7 W at a ripple frequency of 0.67 Hz and the 2.33 ratio between the suction and compression strokes accordingly.

**REFERENCES**


[1] De Koning C.J.A.M.., (2010), Automatic Milking - Common Practice on Dairy Farms. *Proceedings of the 1st First North American Conference on Precision Dairy Management. 2-5 March*, pp. 52-67, Toronto / Canada;

[2] Dmytriv V.T., Dmytriv I.V., Yatsunskyi P.P., (2019), Study of the pneumatic electromagnetic pulse collector of the milking machine by the planned experiment method (Дослідження пневмоелектромагнітного пульсоколектора доїльного апарата методом планованого експерименту). *The scientific journal "Engineering of Nature Management" (Науковий журнал "Інженерія природокористування"*). Kharkiv National Technical University of Agriculture. Petr Vasilenko, vol. 2(12), pp. 66-720, Kharkiv / Ukraine;

[3] Dmytriv V.T., Dmytriv I.V., (2013), Simulator of milk ejection intensity in experimental studies of milking machines (Імітатор інтенсивності молоковіддачі при експериментальних дослідженнях доїльних апаратів). *Bulletin of Lviv National Agrarian University. Agroengineering Research* (*Вісник Львівського національного аграрного університету. Агроінженерні дослідження*). Lviv National Agrarian University, vol. 17, pp.124-129, Lviv / Ukraine;

[4] Floridi M., Bartolini F., Peerlings J., Polman N., Viaggi D., (2013), Modelling the adoption of automatic milking systems in Noord-Holland. *Bio-based and Applied Economics,* vol. 2(1), pp. 73-90;

[5] Mein A.Graeme, Reinemann J.D., (2007), Making the most of machine-on time: what happens when the cups are on ? . [Electronic resource] . Mode of access : http://citeseerx.ist.psu.edu/viewdoc/summary?doi=10.1.1.394.2868. Date of call: 16.01.2019;

[6] Pastell M., Takko H., Grohn H., Hautala M., Poikalainen V., Praks J., Veermae I., Kujala M., Ahokas J., (2006), Assessing Cows' Welfare: weighing the Cow in a Milking Robot. *Biosystems Engineering*, vol. 93, pp. 81–87;

[7] Penry J.F., Leonardi S., Upton J., Thompson P.D., Reinemann D.J., (2016), Assessing liner performance using on-farm milk meters. *Journal of Dairy Science*, vol. 99, pp, 6609–6618;

[8] Spencer S.B., Shin J.W., Rogers G.W., Cooper J.B., (2007), Short Communication: Effect of Vacuum and Ratio on the Performance of a Monoblock Silicone Milking Liner. *Journal of Dairy Science*, vol. 90, pp. 1725-1728;

[9] Spencer S.B., Rogers G.W., (2004), Optimization of milking-machine liners. *100 Years with Liners and Pulsators in Machine Milking*. *International Dairy Federation*. IDF Bull. No. 388, pp. 507-514. Brussels / Belgium;

[10] Thomas C.V., Bray D. R., Delorenzo M.A., (1993), Evaluation of 50/50 and 70/30 pulsation ratios in a large commercial dairy herd. *Journal of Dairy Science*, vol. 76, pp.1298–1304.

# STUDY ON TENSILE MECHANICAL PROPERTY AND MICROSTRUCTURE OF FRUIT AND VEGETABLE PEELS

/

# 果蔬果皮拉伸力学性质与微观结构的研究

**Juxia Wang [1)], Decong Zheng [*1)], Qingliang Cui [1)], Shuanghua Xu [2)], Bingyao Jiang [1)] [1]**
[1)] College of Engineering, Shanxi Agriculture University, Taigu/China
[2)] Organization Department, Shanxi Agricultural University, Taigu/China
*Tel: +86-0354-6289686; E-mail: wangjuxia79@163.com*
*DOI: 10.35633/INMATEH-59-25*

**Keywords:** *fruit and vegetable peel, tensile mechanical properties, curve fitting, microstructure*

## ABSTRACT

*Fruit and vegetable peels exert a protective effect on fruits as constituent parts of the outermost tissue and their properties are of great importance to reducing fruit and vegetable mechanical injury. Four kinds of fruit and vegetable peels such as Nagafu apple, Crisp pear, Tainong mango and long eggplant were chosen to perform longitudinal and transverse tests of tensile property by means of electronic universal testing machine. Stress-strain curve, tensile strength, elastic modulus and fracture strain of peels were obtained; and the microstructures of four kinds of peels were scanned using an electron microscope (SEM). The results indicated that cubic polynomials proved superior for quantifying the stress-strain non-linear relationship of peels and the fitting error of tensile strength is less than 10 parts per thousand. Tensile strength, elastic modulus and fracture strain of peels were different in the case of different fruits and vegetables cultivated and different parts of the same peel; fruit and vegetable peels belong to anisotropic heterogeneous materials and have certain strength. The mean values of tensile strength and fracture strain of the long eggplant peel are the biggest in four kinds of peels and that of elastic modulus of Nagafu apple peel is the largest; long eggplant and Nagafu apple peels had better resistance to damage sensibility than Crisp pear peel. The bearing capacity of the peels depends on the number, width and distribution of microcracks on the surface, and the shape of the epidermal cells and fruit dot on peels; the number of microcracks is bigger and the width of microcracks is wider, the tensile strength is smaller and the elastic modulus of peel is bigger with the slippage increase of epidermis cells. This study provides basic technical parameters for mechanical equipment design for fruit and vegetable during harvesting, processing, packaging, storing and transporting and builds the correlations between macro-mechanics properties and microstructures of fruit and vegetable peels.*

## 摘要

*果蔬果皮作为果实最外层的组成部分，对果实起到保护作用，降低果蔬果实的机械损伤。在微机控制的电子万能试验机上对长富苹果、酥梨、台农芒果和长茄子果皮进行了拉伸力学性能试验，获得果皮拉伸应力—应变曲线、抗拉强度、弹性模量、断裂应变；采用扫描电子显微镜观测果皮微观组织结构。试验结果表明：不同果蔬品种及同种果蔬果皮不同部位间，果皮的力学性能均有差异，果蔬果皮属各项异性材料，具有一定的强度；4 种果蔬果皮的抗拉强度、断裂应变平均值均以长茄子的为最大，酥梨的为最小，而弹性模量则以长富苹果的为最大，芒果的为最小，反映出长茄子、长富苹果果皮对损伤敏感性低于酥梨果皮；果皮承载能力取决于表皮上微裂纹的数量、宽度及分布状态、表皮细胞及果点的形状等。研究结果为苹果、酥梨、台农芒果和长茄子果皮力学模型的建立及 4 种果蔬采收、加工、包装等机械装备的设计提供力学参数，构建果皮宏观力学性质与微观组织结构的联系。*

## INTRODUCTION

As important sources of human dietary nutrition *(Wang et al., 2013; Pan et al., 2008)*, fruits and vegetables have already become the second largest pillar industry of China's agriculture *(Shan, 2010;)*, but

[1] *Juxia Wang, A.P. Ph.D. Eng.; Decong Zheng, Prof. M.S. Eng.; Qingliang Cui, Prof. Ph.D. Eng.; Shuanghua Xu, Ph.D. Stud. Eng.; Bingyao Jiang, Ph.D. Stud. Eng.*

fruit deformation, peel and pulp fracture can be easily caused, thus forming injury, by external loads in the storage and transportation process *(Veringă et al., 2015; Veringă et al., 2018)*.

Fruit and vegetable peels can exert a protective effect on fruits as constituent parts of the outermost tissue and properties are of great importance to reduce fruit and vegetable mechanical injury. Meanwhile, peels can also keep fruits fresh and their microstructures can effectively characterize related fruit qualities *(Homutová et al., 2006; Zamorskyi, 2007; Deng et al., 1995; Liu et al., 2012)*.

At present, domestic and foreign scholars have carried out studies on mechanical properties of fruit and vegetable peels and found that their mechanical properties generated effects on fruit harvest, processing, storage and transportation quality. *Hetzronia et al. (2011)* selected tomato peels of different varieties for tensile test and puncture test, force-displacement curves, tensile strength and elasticity modulus of peels were obtained through the tensile test and the analysis of test data variance indicated that varieties of low tensile strength and elasticity modulus were suitable for industrial processing. Whether each tomato variety was suitable for mechanical harvest could be determined via rupture force and puncture stiffness obtained through the puncture test.

The researches on tomatoes by *Amots et al. (2011)* and *Allende et al. (2004)* showed that the mechanical properties of peels decided economic value of entire fruit processing and storage. *Krishna et al. (2006)* conducted tensile test and shear test of orange peels after picking, and the results indicated that rupture force, tensile strength and elasticity modulus in the peel tensile test and shear strength and shear energy in peel shear test presented declining tendencies with the storage time under whatever environment. *Wang et al. (2004)* carried out a tensile test of grape peel and tomato peel, obtained their elasticity modulus and breaking strength and pointed out critical importance of their mechanical properties to the analysis of mechanical injury. The mechanical property test was implemented and found that susceptibilities of peels of different varieties to injury were different *(Wang et al., 2015; Wang et al., 2016; Wang et al., 2017)*. Fruit and vegetable microstructures are polymerized by many complicated cells. Microscopic features like cell shape, size and gap are closely related to macro-chemical properties of fruits and vegetables, so many scholars explained fruit and vegetable differences in their macro-chemical properties through their microscopic features *(Oey et al., 2007; Alamar et al., 2008)*. Structural characteristics of peels, which are natural “packages” on edible parts of fruits and vegetables, have a great influence on fruit and vegetable qualities *(Homutová et al., 2006; Sivakumar et al., 2008)*.

Tensile test was performed for Nagafu apple, crisp pear, Tainong mango and long eggplant peels on a microcomputer controlled electronic universal testing machine, their elasticity modulus, tensile strength and fracture strain were obtained, followed by the corresponding analysis. Microstructures of the peels were observed, and the correlations between macro-mechanical properties and microstructures of fruit and vegetable peels were established. Mechanical quantities obtained through the test provided technical parameters for mechanical equipment design for fruits and vegetables, e.g. harvest, processing and packaging, so as to provide a basis for establishing a nonlinear model of fruit and vegetable peel materials.

## MATERIALS AND METHODS

### Materials and Instruments

The test materials were Nagafu apple, crisp pear, Tainong mango and long eggplant. Nagafu apple, crisp pear and long eggplant were purchased from Pomology Institute, Shanxi Academy of Agricultural Sciences in September 2018. Tainong mango was bought from Tianyang, Guangxi in June 2018. The test was completed within 2 days after the fruits were transported to the laboratory. In order to reduce the loss of fruit moisture and other nutritional ingredients, they were placed in a refrigerator at 3～5℃. Fruits with regular shape, no disease or insect pest or mechanical injury were selected in the test.

A microcomputer controlled electronic universal testing machine (INSTRON-5544) was used to measure mechanical parameters of the peels with load range of 0～2 kN. It could dynamically display measured values of stress, strain, load and displacement and related curves and automatically collect and save test data. The grating thickness gauge (JC010-1, China) was utilized to measure peel thickness with a measurement range of 0～10 mm and measurement accuracy of 0.001mm. Original gauge lengths of the samples were measured in the tensile test using a digital display Vernier caliper with measurement accuracy of 0.01 mm.

**Tensile test samples**

In order to obtain the differences of peel materials in various mechanical properties, Nagafu apple, crisp pear, Tainong mango and long eggplant peel samples were taken along longitudinal and transverse directions under indoor temperature (Fig. 1a). Peels were taken off from fruits using a blade and then placed on a smooth and flat rubber blanket, and pulp parts of the peels were gently scraped off under a microscope to ensure that no injury occurred to peel samples. To avoid stress concentration of the tensile test samples, peels were fabricated into 40 mm×15 mm× t mm (t is peel sample thickness) long strips as shown in Fig. 1b. Sample sizes in the longitudinal and transverse peel tests were both 6. Thickness ranges of Nagafu apple, crisp pear, Tainong mango and long eggplant peel samples were 0.215±0.004 mm, 0.321±0.028 mm, 0.211±0.015 mm and 0.242±0.022 mm, respectively. To prevent moisture loss of the samples, peel samples were immediately tested on the wedge-shaped fixture of the testing machine (Fig. 1c), original gauge length of the samples was 10.00 mm±0.03, samples which ruptured between two fixtures were regarded as valid samples and those rupturing at the fixture root were invalid samples. Loading rate of tensile test was 1 mm/min, which was kept unchanged in the whole test process.

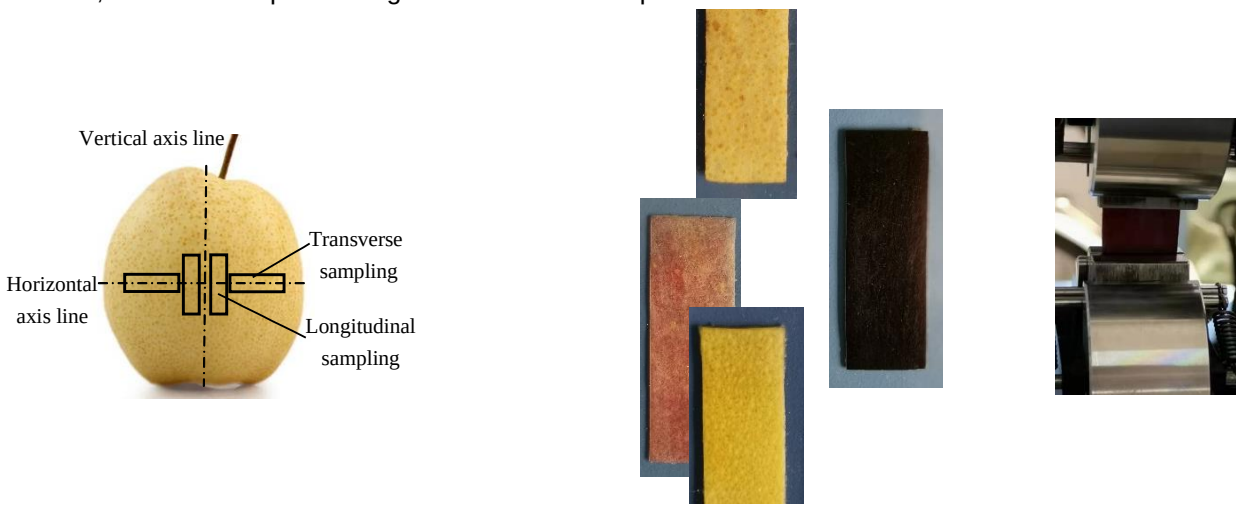


*a. Sampling directions* *b. Tensile samples* *c. Tensile test*

**Fig. 1 - Samples direction, tensile samples and test of fruit and vegetable peel**

**SEM sample observation**

5 samples of Nagafu apple, crisp pear, Tainong mango and long eggplant were respectively collected. Samples were collected from peels and cut into proper small segments for standby use. The collected samples were rapidly placed into 3% glutaraldehyde fixative (prepared using 0.1 mol/L and pH=7.2 phosphate buffer), air exhaust was performed using a vacuum pump so that materials submerged, and then they were fixed at 0~4ºC for 2 d. The samples were rinsed using the same buffer solution for 3 times (15 min each time), dehydrated using 30%, 50%, 70%, 80%, 90% and 95% ethanol by stages (20 min each time), the solution was replaced by tert-Butyl alcohol, they were frozen and dried in JEOL JFD-320, and dried materials were adhered to the sample table using a conductive adhesive and plated with platinum using JEOL JFC-1600 ion sputtering coating apparatus. Platinum plated materials were placed under JEOL JEM-6490 LV SEM for morphological observation.

**Data analysis**

In order to obtain a mathematical model of tensile stress-strain curves of the samples, SAS (SAS Institute, Cary, NC, USA) software was utilized to conduct curve fitting for nonlinear regression analysis of test data points. For a comparison of differences between longitudinal and transverse directions of fruit and vegetable peels and between different fruit and vegetable varieties in the aspects of tensile strength, elasticity modulus and fracture strain, significance analysis was performed through ANOVA program in SAS. Meanwhile, peel microstructural indicators were determined via image processing program in MatLAB software.

## RESULTS

### Tensile test of the peels

Tensile stress-strain curves of longitudinal and transverse samples of Nagafu apple, crisp pear, Tainong mango and long eggplant are shown in Fig. 2. Stress presented a nonlinear relation with strain in their tensile test, and curves of the 4 peels had no obvious bioyield points (Fig. 2), which were similar to stress-strain curves obtained through the peel tensile test of grape, tomato and apple *(Wang et al., 2004; Wang et al., 20017)*. Tensile test was performed for Nagafu apple, crisp pear, Tainong mango and lon [12,14]. Nagafu apple, crisp pear, Tainong mango and long eggplant fruits were quite nonplanar, especially Nagafu apple fruit was similar to spherical shape and when the peel was not stretched, peel samples presented severe micro-buckling state, which led to nonuniform stress distribution in the tensile stress-strain curves of the peels in the initial phase, and the strain increased faster than stress. As peel samples were gradually stretched and extended, stress distribution tended to be uniform until the stress reached the maximum value, and then peel samples started rupturing. However, stress didn't rapidly turn into zero, but instead, it rapidly declined to zero only after a transitional period with gentle reduction.

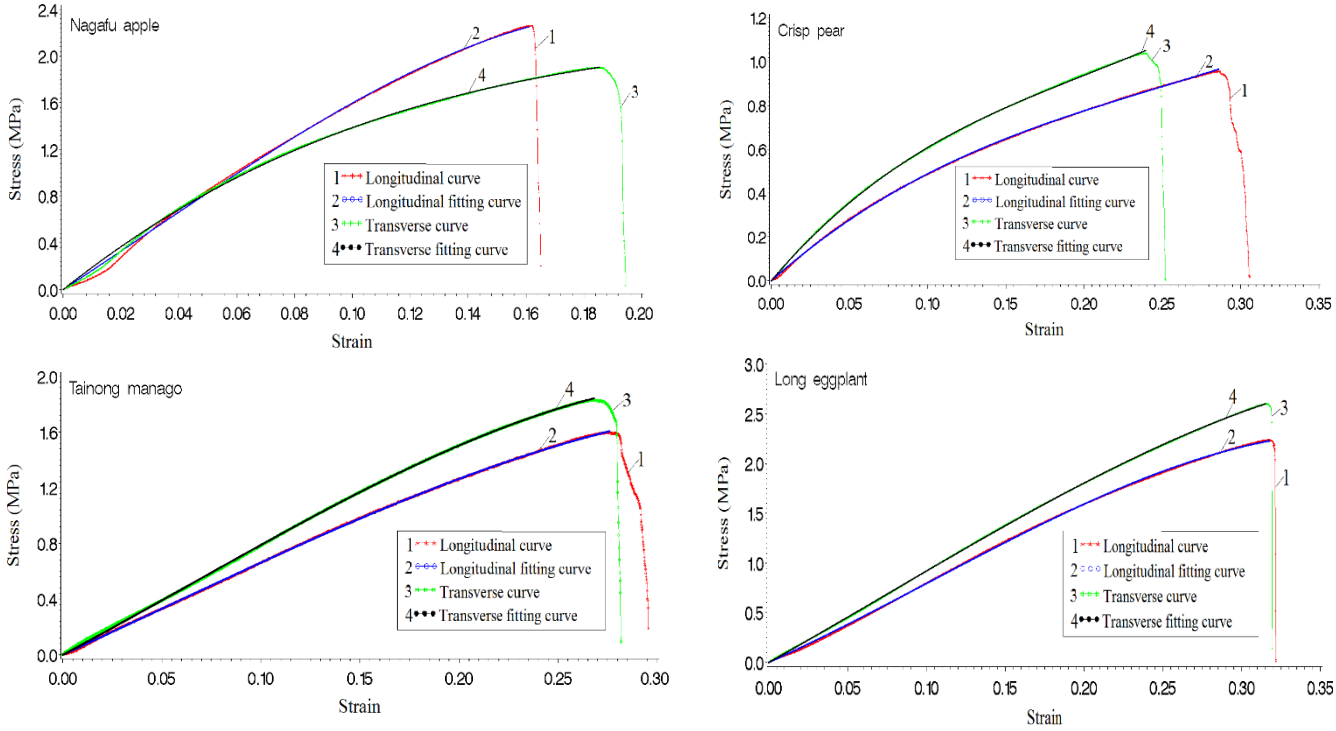


**Fig. 2 - The polynomial fitting curves of peel tensile stress-strain of fruit and vegetable**

### Relationship between elasticity modulus and deformation of the peels

Mechanical property indicators like elasticity modulus and tensile strength of peels as the outmost layer of fruit, decide mechanical injury degrees of fruits and vegetables in the harvest, packaging, storage and transportation processes to a great extent *(Allende et al., 2004; Desmet et al.2002; Krishna et al., 2006)*, and peel elastoplasticity has an influence on fruit and vegetable quality *(Wang et al., 2004)*. As an important index used to measure difficulty level of elastic deformation of peels, elasticity modulus can be characterized by the material stress-strain relation. In comparison with common metallic materials, stress-strain relation of peels, which belong to soft biological microstructures, doesn't follow Hooke's law, but instead, it is a nonlinear relation. In order to obtain elasticity modulus values of peels under different deformation degrees, the least square method of curve fitting was used to conduct cubic polynomial fitting of test data of peels when they started rupturing and before their rupture. Curve fitting results of longitudinal and transverse samples of the 4 kinds of peels are shown in Fig. 2.

The cubic fitting polynomial is:

$$\sigma = \alpha_1 \varepsilon^3 + \alpha_2 \varepsilon^2 + \alpha_3 \varepsilon \quad (1)$$

where: $\sigma$ is tensile stress, [MPa]; $\alpha_1$ is cubic coefficient of the fitting polynomial;

$\alpha_2$ is quadratic coefficient of the fitting polynomial;

$\alpha_3$ is linear term coefficient of the fitting polynomial; $\varepsilon$ is tensile strain;

The elasticity modulus E of each peel can be acquired through the cubic fitting polynomial as:

$$E = d_\sigma / d_\varepsilon = 3\alpha_1\varepsilon^2 + 2\alpha_2\varepsilon + \alpha_3 \quad (2)$$

Elasticity modulus of corresponding point can be solved with known deformation value using equation (2). Coefficients of polynomial fitted tensile stress-strain curves of the fruit and vegetable peels are shown in Table 1. Tensile strength, elasticity modulus, fracture strain, fitted value and fitting error obtained through the test are shown in Table 2.

**Tensile property analysis**

It can be seen from Table 1 that, fitting coefficients of cubic stress-strain curves of longitudinal and transverse fruit and vegetable peel samples of different varieties are different and as shown in Table 2, fitting errors k of their tensile strength are all lower than 10‰, indicating that the cubic polynomial fitted curve can be used to describe nonlinear tensile stress-strain relations of the 4 kinds of fruits and vegetables very well.

**Table 1**

**Curve fitting coefficients of fruit and vegetable peels under tensile loading**

| Variety | Sample number | Longitudinal fitting coefficients | | | Transverse fitting coefficients | | |
|---|---|---|---|---|---|---|---|
| | | $\alpha_1$ | $\alpha_2$ | $\alpha_3$ | $\alpha_1$ | $\alpha_2$ | $\alpha_3$ |
| Nagafu apple | 1 | 187.75 | 16.19 | 16.25 | -187.43 | 24.58 | 13.22 |
| | 2 | -356.11 | 51.41 | 14.53 | -325.30 | 46.27 | 12.33 |
| | 3 | -723.65 | 132.58 | 10.01 | -679.09 | 108.24 | 10.75 |
| | 4 | -274.25 | 13.53 | 18.89 | -153.34 | -0.54 | 16.20 |
| | 5 | -969.40 | 163.02 | 11.27 | -403.07 | 32.74 | 14.40 |
| | 6 | -479.31 | 48.54 | 17.11 | 86.34 | -66.81 | 19.70 |
| Crisp pear | 1 | 7.94 | -12.49 | 7.38 | -10.73 | -3.68 | 5.73 |
| | 2 | 60.89 | -35.03 | 8.87 | 147.21 | -61.19 | 11.86 |
| | 3 | 58.78 | -35.24 | 9.61 | 48.68 | -34.46 | 11.29 |
| | 4 | 22.64 | -16.83 | 6.34 | 45.92 | -27.69 | 8.39 |
| | 5 | 72.95 | -41.35 | 10.33 | 13.86 | -20.20 | 9.00 |
| | 6 | 36.64 | -25.19 | 8.20 | 30.99 | -26.44 | 9.25 |
| Tainong mango | 1 | -25.10 | 5.61 | 6.06 | -11.77 | 1.96 | 6.61 |
| | 2 | -27.94 | 5.05 | 7.27 | -20.24 | 4.56 | 6.61 |
| | 3 | -20.31 | 3.08 | 6.52 | -8.14 | -6.47 | 9.68 |
| | 4 | -9.85 | 3.62 | 8.19 | -21.97 | -8.02 | 8.98 |
| | 5 | -94.33 | 22.42 | 6.90 | -33.99 | 6.45 | 7.59 |
| | 6 | -30.51 | 5.46 | 6.99 | -29.89 | 2.80 | 7.90 |
| Long eggplant | 1 | 13.16 | -15.49 | 10.69 | -9.62 | 8.14 | 8.19 |
| | 2 | 8.41 | -15.10 | 12.23 | -34.87 | 14.38 | 9.81 |
| | 3 | -38.17 | 11.72 | 7.15 | -23.29 | 5.34 | 8.89 |
| | 4 | -0.81 | -1.98 | 6.92 | -20.59 | 6.79 | 10.10 |
| | 5 | 10.25 | -15.17 | 12.12 | -18.79 | 8.00 | 10.71 |
| | 6 | 7.33 | -9.60 | 9.42 | -21.43 | 9.58 | 9.54 |

**Table 2**

**Mean value of property parameters and fitted error of fruit and vegetable peels under tensile loading**

| Variety | | Fracture strain | Tensile strength/MPa | | | Elastic modulus /MPa |
|---|---|---|---|---|---|---|
| | | | Experimental value | Fitted value | Fitting error $k$ | |
| Nagafu apple | Longitudinal | 0.15±0.01a | 2.16±0.08a | 2.13±0.09 | 0.0042 | 20.75±1.94a |
| | Transverse | 0.17±0.02a | 1.90±0.20b | 1.86±0.20 | 0.0049 | 18.16±1.25b |
| Crisp pear | Longitudinal | 0.28±0.03a | 1.12±0.15a | 1.13±0.15 | 0.0016 | 7.68±1.02a |
| | Transverse | 0.24±0.03b | 1.16±0.17a | 1.15±0.18 | 0.0026 | 8.89±1.41a |
| Tainong mango | Longitudinal | 0.27±0.04a | 1.69±0.10a | 1.69±0.09 | 0.0011 | 7.60±0. 75a |
| | Transverse | 0.29±0.05a | 1.84±0.24a | 1.83±0.24 | 0.0023 | 7. 85±0.82a |
| Long eggplant | Longitudinal | 0.47±0.09a | 3.09±0.48b | 3.10±0.49 | 0.0010 | 9.25±1.36b |
| | Transverse | 0.44±0.09a | 4.19±1.00a | 4.17±1.00 | 0.0022 | 11.48±1.23a |

*Note: Fitting error of tensile strength indicated the relative error of tensile strength of peel between fitted values and experimental values.*

As shown in Table 2, tensile strength, elasticity modulus and fracture strain were different in longitudinal and transverse parts of the same peel variety. Average tensile strength and elasticity modulus of crisp pear, Tainong mango and long eggplant peels were all maximum in their transverse parts, while they were the maximum in longitudinal part of Nagafu apple peel. Average transverse fracture strains of Nagafu apple and Tainong mango peels were both greater than their average longitudinal fracture strains, and average transverse rupture strains of crisp pear and long eggplant peels were both smaller than their average longitudinal rupture strains. Independent-samples *t* test was performed for transverse and longitudinal tensile strength, elasticity modulus and rupture strain of the same peel variety, and the results showed that no significant differences existed between longitudinal and transverse tensile strength and elasticity modulus of crisp pear and Tainong mango peels, but significant differences existed between those of Nagafu apple and long eggplant ($p<0.05$). Longitudinal rupture strain of crisp pear was significantly different from transverse rupture strain ($p<0.05$), and differences between longitudinal and transverse ruptures of other varieties were insignificant.

Tensile mechanical property parameters of different fruit and vegetable varieties are compared as shown in Fig. 3. Mechanical property parameters of peels, which are the outmost microstructures of fruit and vegetable fruits, exert a very important effect on the abilities of fruit and vegetable peels of different varieties to resist cracks and mechanical injury *(Wang et al., 2004; Wang et al., 2016; Grimm et al., 2012)*. Fruit and vegetable peels of different varieties were different in tensile strength, elasticity modulus and fracture strain (Fig. 3). For the four cultivars, average tensile strength of eggplant was the maximum, being 3.64 MPa, crisp pear had the minimum average tensile strength (1.14 MPa), and those of Nagafu apple and Tainong mango were 2.03 MPa and 1.76 MPa, respectively. Tensile strength of long eggplant was remarkedly different from those of Nagafu apple, crisp pear and Tainong mango ($p<0.001$), average elasticity modulus of Nagafu apple was the maximum, being 19.46 MPa, that of crisp pear presented an extremely significant difference from those of Nagafu apple and Tainong mango, that of Tainong mango was the minimum (7.72 MPa) and those of long eggplant and crisp pear were 10.36 MPa and 8.29 MPa, respectively. Elasticity modulus of long eggplant was extremely significantly different from those of crisp pear, Tainong mango and long eggplant ($p<0.001$) , the difference between long eggplant and Tainong mango in this aspect was rather notable and that between long eggplant and crisp pear was significant, but that between crisp pear and Tainong mango was insignificant. Long eggplant had the maximum average fracture strain (0.46), Nagafu apple had the minimum average fracture strain (0.16) and those of long eggplant and crisp pear were 0.28 and 0.26, respectively. Long eggplant had extremely significant differences from Nagafu apple, crisp pear and Tainong mango in fracture strain ($p<0.001$), Nagafu apple was also extremely significantly different from crisp pear and Tainong mango in fracture strain, and the difference between crisp pear and Tainong mango was insignificant.

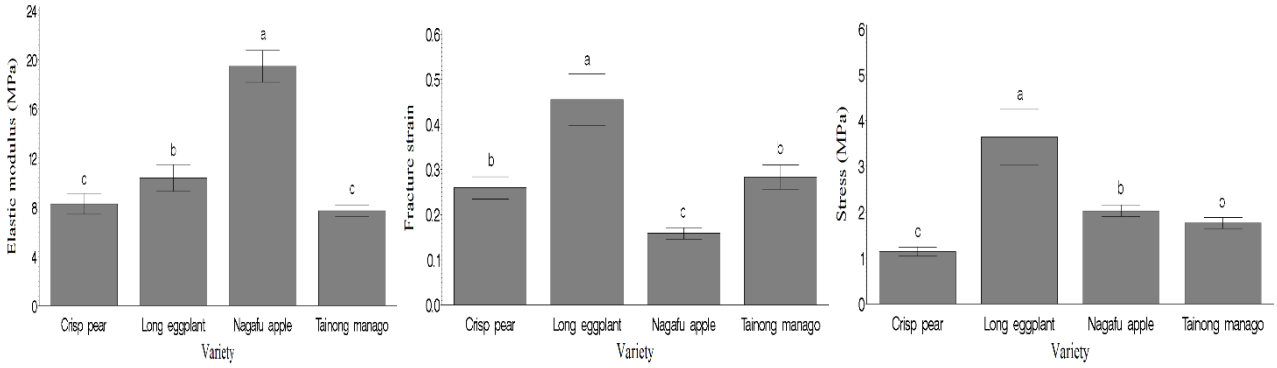


**Fig. 3 - Comparison of peel tensile mechanical parameters of different fruit and vegetable varieties**

## Peel image analysis

Fruit and vegetable microstructures have a direct impact on their macroscopic texture features *(Cai et al., 2015; Wei et al., 2016)*.

For a deeper understanding of differences between Nagafu apple, crisp pear, Tainong mango and long eggplant peels in their macro-chemical properties, peel microstructures were investigated.

Peel surface microstructures. Fig. 4 shows surface microstructures of fruit and vegetable peels. Epithelial cells in Nagafu apple peel presented pentagonal shape or hexagonal with microcracks on the surface, which presented parallel arrangement, and fracture surfaces of which were disorderly. Small hill-like protuberances appeared on the crisp pear peel surface, so epithelial cell shape could not be identified, and moreover, there was a large quantity of microcracks which were under net-shaped distribution with orderly fracture surfaces. Tainong mango peel was rough surface with horny patterns and formed a number of microcracks under irregular distribution. No microcracks appeared on the long eggplant peel surface, epithelial cells presented long strip shape under regular distribution. Microcracks appearing in the structural chart obtained through SEM were measured via MatLAB program, and the microcrack width range of four kinds of peel smaples is shown in Table 3. The average width range of microcracks for Nagafu apple, crisp pear and Tainong mango was 7.28μm, 4.34μm and 5.86μm, respectively. Based on the above results, microcracks on peel surfaces were formed due to fruit development and expansion during the fruit growth process *(Veraverbake et al., 2001)*, there were a large quantity of microcracks on rough peel surfaces *(Knoche et al., 2008)*, and the quantity of microcracks on the peel surface had an effect on tensile strength of peels of different fruit and vegetable varieties *(Wang et al., 2015; Wang, et al., 2017)*.

As the above results showed, because microcracks exist on fruit and vegetable surfaces, average tensile strength values of Nagafu apple, crisp pear and Tainong mango peels were lower than that of long eggplant peel. The quantity, width and distribution of microcracks on the peel surface would all generate an effect on tensile strength of fruit and vegetable peels: the larger the quantity of microcracks, the smaller the tensile strength. Epithelial cell shape on the peel surface would impact its elasticity modulus, and slippage of epithelial cells which were pentagonal or hexagonal in the tensile process was greater than that of long strip-shaped epithelial cells, which might be one of the reasons for large elasticity modulus of Nagafu apple peel.

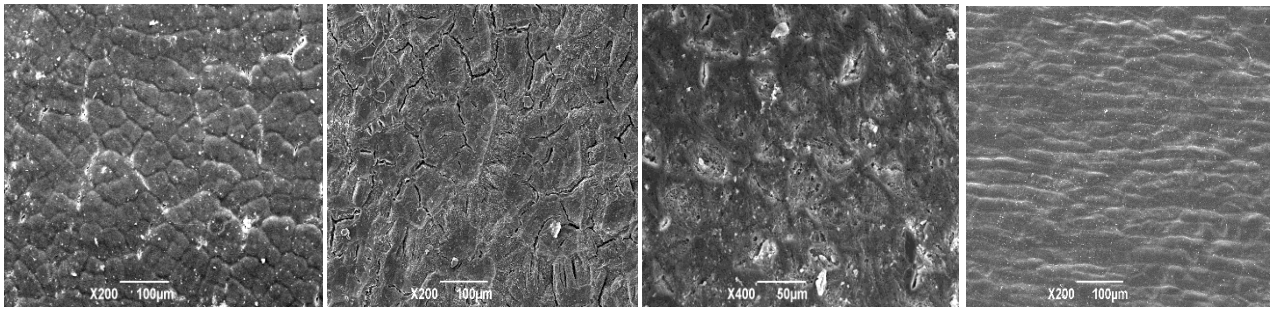


*a. Nagafu apple* *b. Crisp pear* *c. Tainong mango* *d. Long eggplant*

**Fig. 4 - The surface microstructure of fruit and vegetable peels**

**Table 3**

**Width range of microcracks on t fruit and vegetable peels**

| Variety | Peel micro crack width/μm |
|---|---|
| | Mean value ( min-max ) |
| **Nagafu apple** | 7.28 (2.88-17.02) |
| **Crisp pear** | 4.34 (1.12-15.42) |
| **Tainong mango** | 5.86 (1.41 ~ 13.54) |
| **Long eggplant** | 0 |

Fruit dot microstructures. Fruit dots were formed by young fruit epidermis pores that act as the channel for substance exchange of fruits with the outside environment in the early fruit development phase, and the fruit dots are filled by phellem tissue during the fruit maturing period (*Yu et al., 2002; Li, et al., 2009*), therefore the fruit spots were considered the stress concentration points in the process of peel tensile (*Wang et al., 2015*).

Fig. 5 shows fruit dot microstructures of fruit and vegetable peels. Fruit dots on fruit and vegetable peels of different varieties were differently shaped: fruit dots of Nagafu apple were polygonal and included the angle between edges that was sharp, crisp pear fruit dots were circular and smooth and could be approximated to round shape, but tissues at its edges were discontinuous with slightly protuberant tissues in the center. Fruit dots on Tainong mango peel were round with sunken tissues in the center. Fruit dots on long eggplant peel were approximately elliptical with smooth transition, indicating stress concentration degree of fruit dots in the tensile process of long eggplant peel was lower than those of other varieties, and tensile strength of long eggplant peel was great. Stress concentration degree at fruit dots in the tensile process of Nagafu apple peel was quite severe, it might be ruptured in advance due to severe stress concentration of fruit dots before it reached the real tensile strength, so tensile strength of its peel was relatively small.

Fruit shape made a difference in mechanical properties of longitudinal and transverse peel samples. Nagafu apple fruit was approximately spherical, so its peel was extended greatly in transverse direction in the growth process and average tensile strength of transverse sample was lower than that of longitudinal sample in the tensile process. Fruits of crisp pear, Tainong mango and long eggplant were approximately cylindrical, long oval shape and long round oval shape, respectively. Longitudinal extension of peels during the fruit growth process was large, so average tensile strength of transverse sample was higher than that of longitudinal sample.

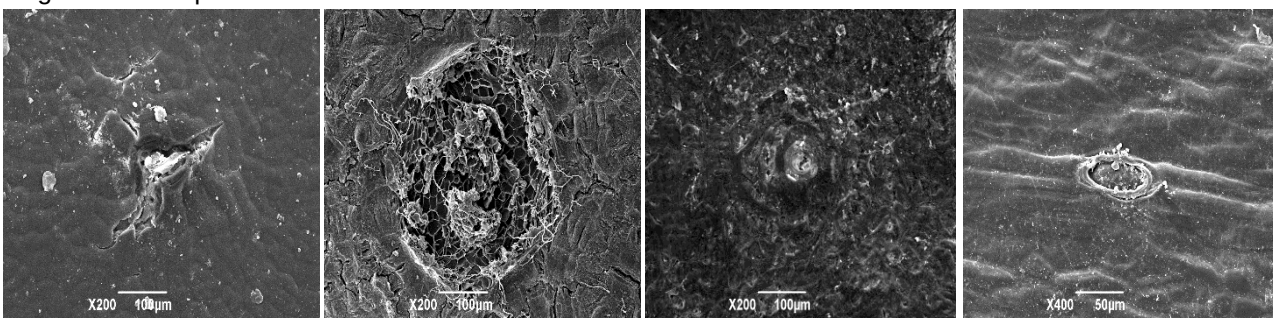


*a. Nagafu apple* *b. Crisp pear* *c. Tainong mango* *d. Long eggplant*

**Fig. 5 - The fruit dot microstructure on the peels**

## CONCLUSIONS

(1) Stress and strain present a nonlinear relation in the tensile process of the 4 fruit and vegetable varieties. There are no obvious bioyield points in their stress-strain curves. The tensile stress-strain curves of longitudinal and transverse peel samples are fitted using a cubic polynomial. Fitting coefficients of the fitted curves are not the same and fitting errors k of tensile strength are all lower than 10‰, showing that the cubic polynomial can describe nonlinear relations in the tensile process of the 4 peels very well and provide a reference basis for establishing the nonlinear model for peel materials.

(2) Longitudinal and transverse samples of the same fruit and vegetable variety are different in elasticity modulus, so fruit and vegetable peels are anisotropic materials. Elasticity modulus of fruit and vegetable peels can characterize the material ability to resist against deformation, and Nagafu apple has the maximum elasticity modulus, Tainong mango has the minimum value. Nagafu apple is extremely significantly different from crisp pear, Tainong mango and long eggplant in the aspect of elasticity modulus ($p$<0.001), indicating that Nagafu apple has the strongest ability to resist against deformation, followed by long eggplant.

(3) Average tensile strength of long eggplant is the maximum and over 3.2 times of that of crisp pear which has the minimum average tensile strength. Long eggplant is extremely significantly different from Nagafu apple, crisp pear and Tainong mango in tensile strength ($p$<0.001). Tensile strength of peel is an important index used to evaluate fruit injury or destruction. Crisp pear peel has higher susceptibility to injury than other 3 peels in the harvest, transportation and storage processes, followed by Tainong mango peel. Average tensile strength values of transverse peel samples of crisp pear, Tainong mango and long eggplant are all greater than those of their longitudinal samples, average tensile strength of longitudinal Nagafu apple peel sample is larger than that of transverse one, so the difference of the optimal clamping direction between different fruit and vegetable varieties should be considered in the design of recovery machinery.

(4) Average fracture strain of long eggplant is the maximum, followed by Tainong mango, crisp pear and Nagafu apple in succession, and the maximum value is over 2.9 times of that of minimum value. Long eggplant is extremely significantly different from Nagafu apple, crisp pear and Tainong mango in fracture strain ($p$<0.001). Average fracture strain of transverse Nagafu apple and Tainong mango peel samples are both greater than those of their longitudinal samples, but the case is the opposite for crisp pear and long eggplant peels, demonstrating that extensibility of transverse Nagafu apple peel sample and that of longitudinal crisp pear and long eggplant peel samples are strong.

(5) Macro-mechanical properties of fruit and vegetable peels, which are polymerized by complex cells, vary from microstructures. Mechanical properties of fruit and vegetable peels mainly depend on quantity, width and distribution state of microcracks on the peel surface, shapes of epithelial cells and fruit dots, etc. Peel strength is reduced with increasing quantity and width of microcracks on the peel surface, but its elasticity modulus will increase with the slippage of epithelial cells.

Therefore, the effects of different directions of peels of different fruit and vegetable varieties should be taken into consideration in the design of harvesting machinery and processing, storage and transportation equipment following the harvest. Susceptibilities of long eggplant and Nagafu apple peels to the injury are lower than those of other two peels, and Nagafu apple has the most powerful ability to resist against penetration of blunt parts. Storage endurance of different fruit and vegetable varieties is not only closely related to microstructures of their outmost peels but has also a high correlation with their pulp qualities.

**ACKNOWLEDGEMENT**

This research, titled 'STUDY ON TENSILE MECHANICAL PROPERTY AND MICROSTRUCTURE OF FRUIT AND VEGETABLE PEELS', was funded by the National Natural Science Foundation of China (11802167), the applied basic research of Shanxi Province (201801D221297), the Doctor Scientific Research Foundation of Shanxi Agricultural University (2017YJ15) and the Excellent Doctor Scientific Research Foundation the Excellent Doctor Foundation of Work Reward for Shanxi Province (SXYBKY201754). The authors are grateful and honoured to have obtained support from the Key Laboratory of Biomechanics.

**REFERENCES**

[1] Alamar M.C., (2008), Micromechanical behaviour of apple tissue in tensile and compression tests: Storage conditions and cultivar effect [J]. *Journal of Food Engineering*, Vol. 86, Issue 3, pp. 324－333, Oxford/England;

[2] Allende A., (2004), Micromechanical and geometrical properties of tomato skin related to differences in puncture injury susceptibility. *Postharvest Biology and Technology*, Vol. 59, Issue 1, pp. 80－84, Amsterdam/Netherlands;

[3] Cai J.R., (2015), Three-dimensional imaging of morphological changes of potato slices during drying. *Transactions of the Chinese Society of Agricultural Engineering*, Vol. 35, Issue 1, pp. 278－284, Beijing/P.R.C.;

[4] Deng J.G., (1995), Investigation on the Organization Structure of Apple Fruits. *Journal of fruit trees*, Vol. 12, Issue 2, pp. 71－74, Zhengzhou/P.R.C.;

[5] Desmet M., (2002), Mechanical Properties of Tomatoes as Related to Puncture Injury Susceptibility. *Journal of Texture Studies*, Vol.33, Issue 33, pp. 415－429, Malden/U.S.A.;

[6] Grimm E., (2012), Structural and physiological changes associated with the skin spot disorder in apple. *Postharvest Biology and Technology*, Vol. 64, Issue 1, pp. 111－118, Amsterdam/Netherlands;

[7] Hetzronia A., (2011), Biomechanical characteristics of tomato fruit peels. *Postharvest Biology and Technology*, Vol. 59, Issue 1, pp. 80－84, Amsterdam/Netherlands;

[8] Homutová I., (2006), Differences in fruit skin thickness between selected apple (Malus domestica Borkh.) cultivars assessed by histological and sensory methods. *Horticultural Science*, Vol. 33, Issue 3, pp. 108－113, Prague/Czech Republic;

[9] Knoche M., (2008), Surface moisture induces microcracks in the cuticle of 'Golden Delicious' apple. *Horticultural Science*, Vol. 43, Issue 6, pp. 1929–1931, Prague/Czech Republic;

[10] Krishna K.S., (2006), Post-Harvest Physico-Mechanical Properties of Orange Peel and Fruit. *Journal of Food Engineering*, Vol. 73, Issue 2, pp. 112－120, Oxford/England;

[11] Li H.J., (2009), Apple Fruit Varieties Different Organizational Structure Research. *Chinese Fruit Trees*, Issue 3, pp. 13－17, Xingcheng/P.R.C.;

[12] Liu G.C., (2012), Research on the Change of ‘Hanfu’ Apple Fruit Anatomic Structure and Quality During Storage. *Transactions of the Chinese Society of Agricultural Engineering*, Issue 15, pp. 1－4, Haerbin/P.R.C.;

[13] Oey M.L., (2007), Effect of turgor on micromechanical and structural properties of apple tissue: A quantitative analysis. *Postharvest Biology and Technology*, Vol. 44, Issue 3, pp. 240 － 247, Amsterdam/Netherlands;

[14] Pan L.G., (2008), Review on non-destructive deternination technology for agricutural prodcuct quality. *Transactions of the Chinese Society of Agricultural Engineering*, Vol. 24, Issue 1, pp. 325－330, Beijing/P.R.C.;

[15] Shan Y., (2010) Current Situation and Development Strategic Consideration of the Fruits and Vegetables Processing Industry in China. *Journal of Chinese Institute of Food Science and Technology*, Vol. 10, Issue 1, pp. 1－9, Beijing/P.R.C.;

[16] Singh K.K., (2006), Post-harvest physico-mechanical properties of orange peel and fruit. *Journal of Food Engineering*, Vol. 73, Issue 2, pp. 112－120, Oxford /England;

[17] Sivakumar D., (2008), Volatile compounds, quality attributes, mineral composition and pericarp structure of South African litchi export cultivars Mauritius and McLean’s Red. *Journal of the Science of Food and Agriculture*, Vol. 88, Issue 6, pp. 1074－1081, Chichester/England;

[18] Veraverbake E.A., (2001), Non destructive analysis of the wax layer off apple (Malus domestica Borkh.) by means of confocal laser scanning microscopy. *Planta*, Issue 213, pp. 525–533, Berlin/Germany;

[19] Veringă D., (2015), Determination of the Relaxation Time at Static Compression of Idared Apples Variety. *INMATEH-Agricultural Engineering*, Vol. 47, Issue 3, pp. 75-80, Bucharest/Romania;

[20] Veringă D., (2018), Determination of the Relaxation Period at Static Compression of Golden Delicios Apples Variety. *INMATEH-Agricultural Engineering*, Vol. 48, Issue 1, pp. 61-66, Bucharest/Romania;

[21] Wang J.X., (2015). Experimental Research on Mechanical Properties of Apple Peels. *Journal of Engineering and Technology Science*, Vol. 47, Issue 6, pp. 688－705, Bandung/Indonesia;

[22] Wang J.X., (2016), Evaluation on peels texture of different apple cultivars based on rheological properties. *Transactions of the Chinese Society of Agricultural Engineering*, Vol. 32, Issue 21, pp. 305-314, Beijing/P.R.C.;

[23] Wang J.X., (2017), Mechanical Properties and Microstructure of Apple Peels during Storage. *International Journal of Food Properties*, Vol. 2017, Issue 20, pp. 1159-1173, Philadelphia/U.S.A.;

[24] Wang M.L., (2013), Progress in Research on Effect of Different Processing and Storage Methods for Changes of Nutritious and Antioxidant Activities. *Modern Food Science and Technology*, Vol. 29, Issue 1, pp. 629－697, Guangzhou/P.R.C.;

[25] Wang R., (2004), Determination of macromechanic parameters of grapes and tomatoes. *Transactions of the Chinese Society of Agricultural Engineering*, Vol. 20, Issue 2, pp. 54－57, Beijing/P.R.C.;

[26] Wei Y.L., (2016), Effect of hot air drying temperature on microstructure of Chinese jujube. *Transactions of the Chinese Society of Agricultural Engineering*, Vol. 32, Issue 7, pp. 244－251, Beijing/P.R.C.;

[27] Yu H., (2002), Anatomical Observation on Process of Pear Fruitlet Stomata Changing to Fruit Dots. *Journal of fruit trees*, Vol. 12, Issue 1, pp. 62－63, Zhengzhou/P.R.C.;

[28] Zamorskyi V., (2007), The role of the anatomical structure of apple fruits as fresh cut produce. *Acta Horticulturae*, Issue 746, pp. 509－512, Leuven/Belgium.

# HANDLING COMFORT ANALYSIS OF ELECTRIC MINI-TILLER UNDER DIFFERENT CONDITIONS
/
# 电动微耕机不同工况下的操作舒适性分析

**Liang X.C. *), Zhao J. D.**
Southwest University, College of Engineering and Technology, Chongqing Key Laboratory of Agricultural Equipment for Hilly and Mountainous Regions / P. R. China
*Tel: 86-02368251265; E-mail:dylb1978@swu.edu.cn*
*DOI: 10.35633/INMATEH-59-26*

***Keywords:*** *Electric mini-tiller, vibration, handling comfort, frequency spectrum*

**ABSTRACT**

*The electric mini-tiller can produce extra vibration during tilling, shortening the span life of components and undermining manipulator's body. Therefore, sensors are set in the electric motor and armrest, and field experiments under different conditions have been accomplished. Test data show that some of the vibration frequency bands of electric mini-tiller are sensitive to the human, imposing great harm on people's health. So redesigning the electric one to lessen or cut off the vibration transmission is an urgent engineering problem.*

**摘要**

*电动微耕机在作业过程中会产生较为明显的振动，既缩短了零部件的寿命，也给操纵者的健康带了巨大的伤害。在微耕机的电动机和扶手处设置了传感器，进行了不同工况下的田间实验。数据表明微耕机部分振动频率接近人体的敏感频段，因而对人体的影响较大。因此，如何对微耕机的结构进行全新设计，进一步减小和切断电动机和刀具的振动传递是亟待解决的工程问题。*

## INTRODUCTION

The mini-tiller is powered by a gasoline or diesel engine of 1.0-7.5 kW and weighs 50-150 kg. It can achieve a tilling depth of 10-16 cm and efficiency of 220-540 $m^2$/h *(Chen J. et al, 2014)*. In the mountainous regions, the use of large and middle sized mechanical equipment is restricted, so such tillers are popular.

Although the progress of technology can improve mini-tillers, the problems are still significant. Firstly, intense vibration is common for most agriculture equipment. In the case of the mini-tiller, nearly all the assembly is connected in a rigid rack, which creates unacceptable vibration during the tilling process. Vibrations caused by engines and rotary blades, will transfer to the handlebar which is directly in contact with the operator's body, causing body organs disorders and neurological disease *(Range L. et al,1999; Tewari V. K. et al, 2009)*. Secondly, high fuel consumption means that it is difficult to meet the severe environmental requirements of less pollution, especially in high value-added equipment in agriculture. Thirdly, being short of protecting measures, the rotary blades are exposed and can easily injure the manipulator who is fatigued and absent-minded after walking on the furrow for a distance of approximately 15 to 20 km *(Mehta C. R. et al, 1997)*, especially in mountainous and hilly regions. If mini-tillers cannot offer satisfactory properties including handling comfort and safety, then severe accidents will occur.

There are many reports in the literature of studies trying to improve the mini-tiller. In order to reduce the vibration level, biodiesel and biodiesel-diesel have been tried to replace traditional fuel for engines *(Heidary B., et al, 2013; Taghizadeh-Alisaraei A. et al, 2012)*. Vibration is a complicated action process involving several factors, including firmness of the soil, tilling speed, the geography of the blade, moisture content of the soil, material type, depth of tilling, etc. In these papers the relationship between vibration and contributing factors is explored *(Niu P. et al, 2017; Zhang Y. H. et al, 2016)*. Statistics indicates that most agricultural equipment do not contain elastic components, in particular tilling instruments. Hence, assemblies installed in a flexible way may improve the handling comfort, as reported in the literature *(Hao K. Y. et al, 2011; Caffaro F. et al, 2016)*. In addition, some new methods are used to settle vibration reduction *(Fabbri A., et al, 2017; Cutini M., et al, 2016)*.

Some factors, including light, temperature, moisture, should be considered to analyse the vibration effect *(Deboli R. et al, 2017)*. Furthermore, it is beneficial to investigate some accidents to enhance the performance of tillers *(Mattetti M. et al., 2017)*.

Compared with the traditional mini-tiller, the electric one has vast advantages on environmental friendliness, lower noise and controlling convenience. Unluckily, few papers focused on the dynamic character have been published. Considering distinct difference of driving condition between electric vehicles and new type of mini-tillers, the features of thermal and span life for lithium battery are still unknown and should have been analysed, although such mechanisms have been researched in the domain of electric vehicles.

## MATERIALS AND METHODS

The prototype used in this study is the electric mini-tiller 1WG0.75-70DD-ZC, which is developed by Hesheng Co., Ltd., Chongqing. The firmness of soil is a significant factor to test outcomes, which has been measured several times and then the average value was obtained. The prototype of the tiller is shown in Figure 1, and the coordinate direction is also signified at the same time. Besides, the parameters of this tiller are listed in Table 1. It must be pointed out that the capacity of battery and the power of electric motor are both smaller than those computing outcome, verifying the feasibility of prototype.

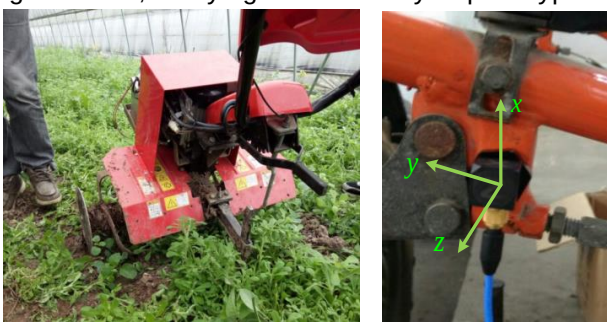


**Fig. 1 - Electric elementary prototype and battery box**

**Table 1**

**The parameters of electric mini-tiller**

| Properties of mini-tiller | parameters |
|---|---|
| **Rated power [kW]** | 0.75 |
| **Dimension （L×W×H[mm]** | 1750×700×920 |
| **Pure weight [kg]** | <65 |
| **Tilling width [mm]** | 70 |
| **Tilling depth [mm]** | 10-16 |
| **Working speed [m/s]** | 0.1-0.3 |
| **Roller rotational speed [r/mm]** | 150(h),130(m),110(l) |
| **Efficiency [hm²/h·m]** | ≥0.04 |

Supplementary instruction is listed here. Collecting data program is compiled by LabVIEW software, and the three-dimensional acceleration sensor is 356A16, produced by the PCB Company in the US. The frequency scope is 0.3~6 kHz and measured range is -50~50g. In addition, the sensitivity of the instrument in x-, y- and z- coordinate directions is 98.2, 101.0 and 98.5 mV/g, respectively. The acquisition card is NI 9234, made in NI Company in the US, the input voltage is -5~5V and the rate of digital signal is 51.2 kHz.

The test location was situated at 29.3° N latitude and 106.3° E longitude, and the experimental date was on March 19, 2017. The air temperature was 17.5°C, and the soil texture was sandy loam. The soil was covered with grass and the moisture was 30.5%. In addition, the average firmness was 0.26-0.31mm/MPa.

Commonly a vibration signal is expressed as a time domain and frequency domain. The advantage of time domain is that the relationship between time and vibration magnitude is distinct, while the influencing frequency elements are vacant. Instead, it is easy to determine specific frequency spectra, but time signals are vague. Therefore, two methods to describe the vibration process will be used, which are signified by the formula below:

$$\begin{cases} S(f) = \int_{-\infty}^{\infty} s(t) e^{-j2\pi ft} dt \\ s(t) = \int_{-\infty}^{\infty} S(f) e^{j2\pi ft} df \end{cases} \quad (1)$$

Where:

$s(t)$ is time signal, and $t$ is time, [$s$];

$S(f)$ is frequency spectrum, and $f$ is frequency, [$Hz$].

In a strict sense, the output signal of a mini-tiller is a non-stationary random signal, and two formulas cannot be used directly. Simplifying study course, it is common to assume that the vibration signal within infinitesimal time is stationary in engineering field, so the formula can then be applied. Furthermore, the precision of the calculations is dependent on the length of time the signal collected, and 5100 vibration accelerations are gathered for each time point in this study.

The tilling process of the mini-tiller is difficult to be described, but can be depicted as follows based on how the vibration is generated and transmitted in Figure 2. Part of the vibration is generated by the electric motor, and the armrest is the only part of the mini-tiller touching human body. Transducers have been installed on the cover of the motor and the end of each handlebar using 502 glue.

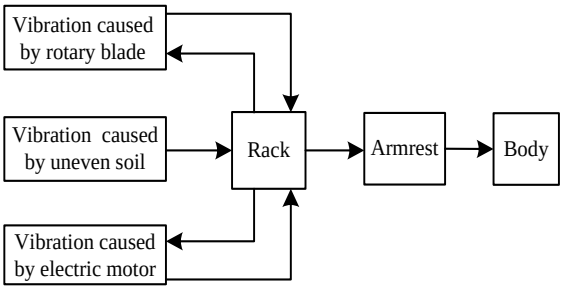


**Fig. 2 - The process of producing and transmitting vibrations**

Theoretical analysis and field experiments can be used to determine the properties of the electric mini-tiller. In order to investigate the range of performance of the tiller, different operational conditions, including reverse gear, essential in minimizing the turning radius of the mini-tiller, are designed.

## RESULTS

Figure 3 shows that vibration signals are similar over a time span of less than four gears. However, in the frequency domain, there are more frequency peaks and troughs under low and middle gears than in other gears. In each gear, the acceleration vibration peak in tri-axle directions is unique. Besides, the faster the electric motor runs, the more wave peaks are generated.

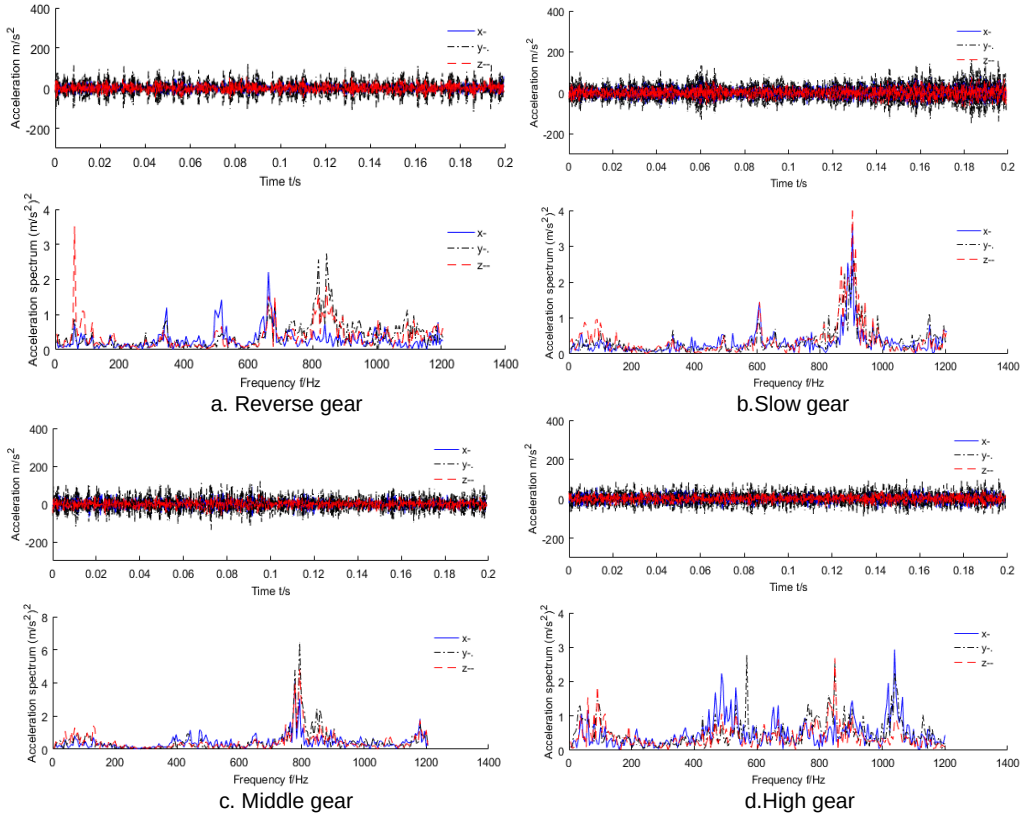


**Fig. 3 - Vibration signal of electric motor during movement**

In the same way, the vibration signal of armrest can be disposed in Figure 4.

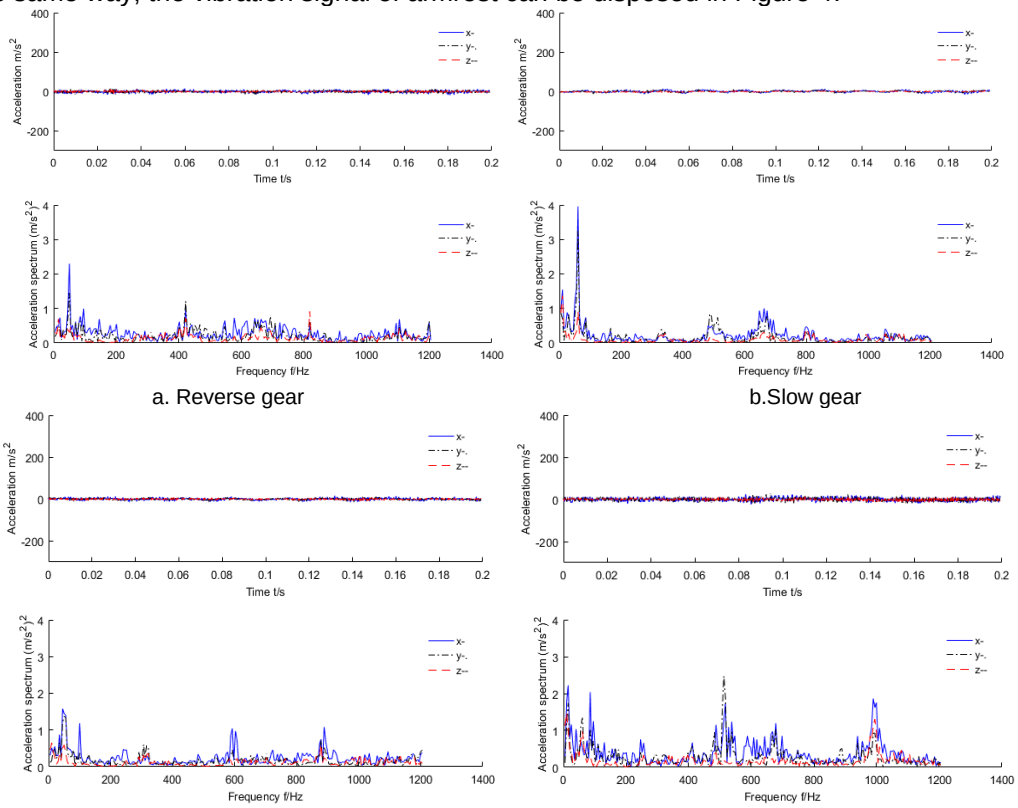


a. Reverse gear b.Slow gear

c. Middle gear d.High gear

**Fig. 4 - Vibration signal of armrest during movement**

From Figure 4, it is easy to discern the vibration amplitude in the armrest is significantly weaker than that of the covering of motor, being absorbed by the soil. Moreover, the variation trend of acceleration is similar to that in Figure 3. Identically, vibration signals can be expressed in Figure 5 and Figure 6 during working.

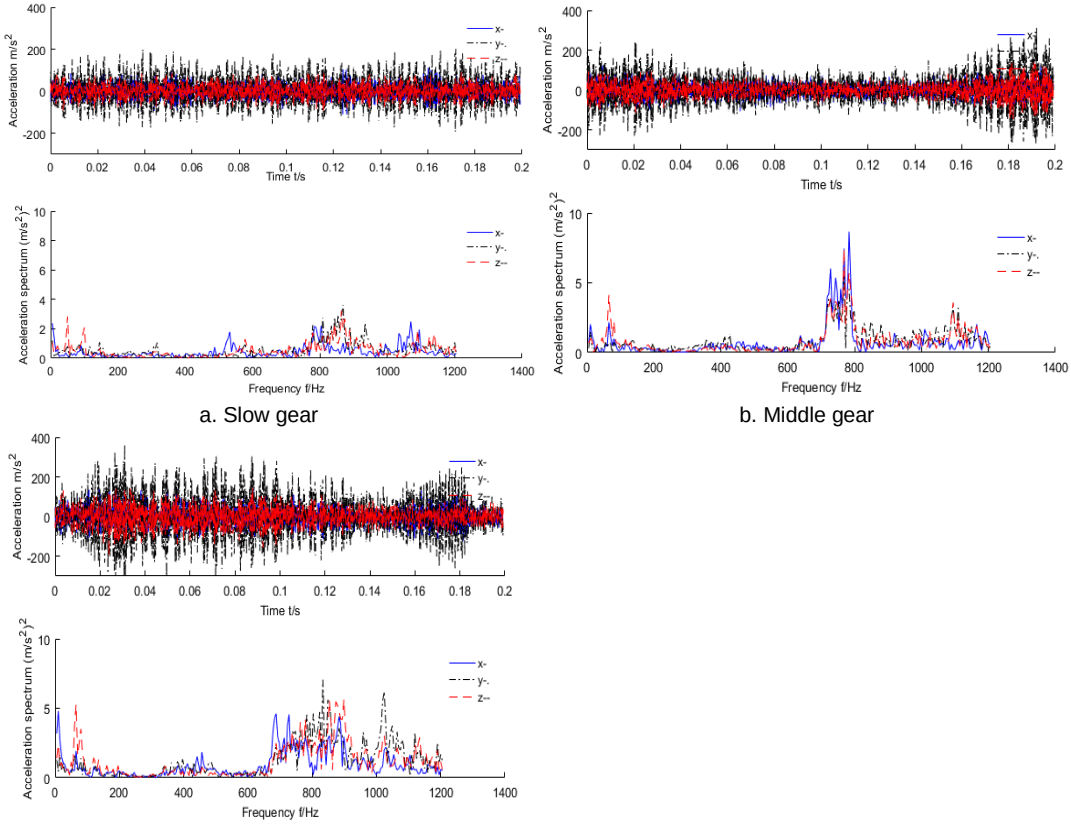


a. Slow gear b. Middle gear

c. High gear

**Fig. 5 - Vibration signal of electric motor during tilling**

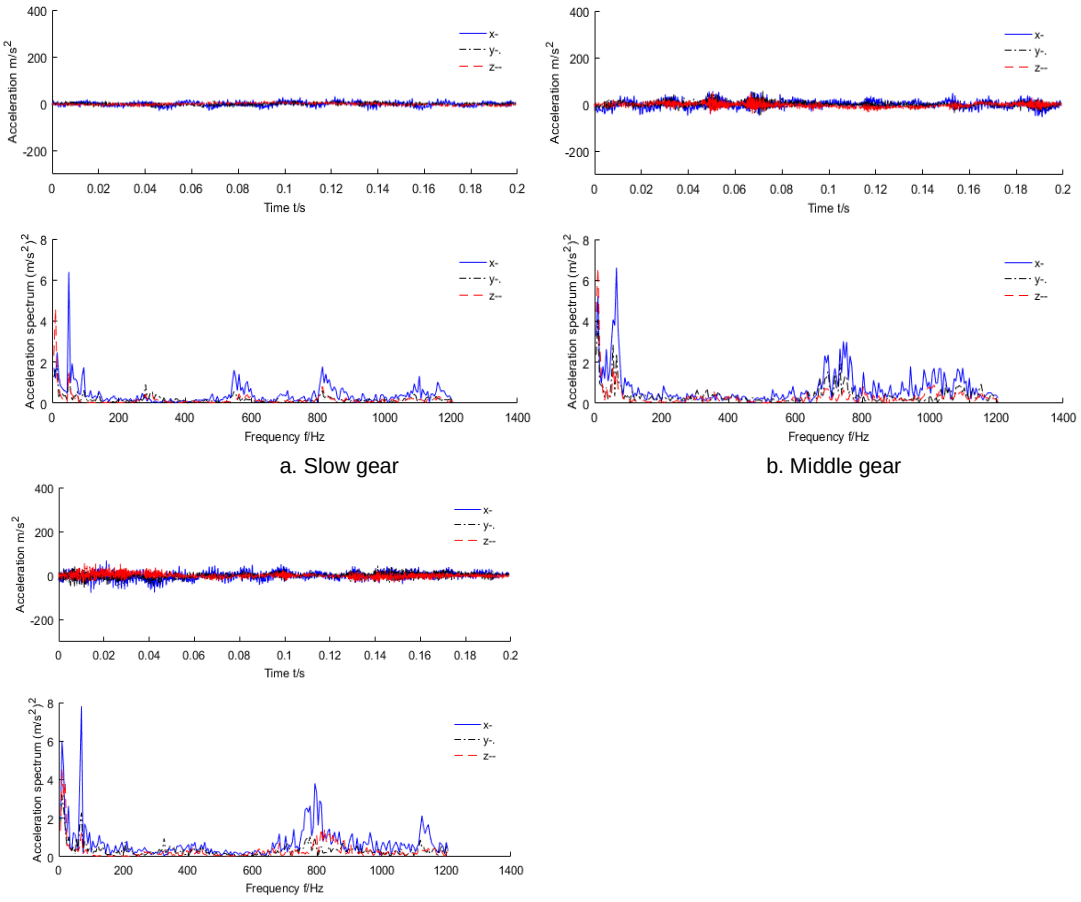


a. Slow gear

b. Middle gear

c. High gear

**Fig. 6 - Vibration signal of armrest during tilling**

Obviously, the vibration acceleration is much greater in Figure 5 than that in Figure 4; the same conclusion is also drawn from Figure 4 and Figure 6. During movement, the weight of mini-tiller is supported by the blades, resulting in a lower tilling depth. While tilling the working depth is greater than 10 mm, which means large force must be output to cut the clod into pieces, bringing about vibration intensity being measured either in time domain or frequency domain. When the mini-tiller is walking in the reverse gear, the less cutting force is needed and the vibration acceleration can be neglected, so such case has not been analyzed in Figure 5 and Figure 6. In addition, there is a distinct vibration peak of x-coordination direction in Figure 6, which is different from that in Figure 4, and by such phenomenon can be explained that the shape of rotary blade plays a crucial role *(Liang X.C. et al, 2018)*. This is easy to be demonstrated when the rotary blade is replaced by the new rotary blade with the different shape. Briefly, in Figure 5 and Figure 6, the intensity of vibration is increased in time and frequency domains, which would lead to the handling comfort of the mini-tiller to deteriorate quickly. During the process of tilling, most time is spent in tilling mode and the time spent moving is very short. Consequently, it is rational to ignore the mini-tiller walking in the reverse gear during tilling.

The reaction of the human body to the vibration is determined by the average acceleration, although every vibration frequency can give rise to different effect, so it is necessary to compute the root mean square (RMS) acceleration and evaluate the handling comfort of the electric mini-tiller. Formula (2) is used to calculate RMS acceleration, and results are shown in Figure 7.

$$a_{rms} = \sqrt{\left(\sum_{i=1}^{n} a_i^2\right) / n} \tag{2}$$

Where:

$a_i$ is an arbitrary acceleration, [ms$^{-2}$];

$n$ is the number of collected vibration signal;

$a_{rms}$ is the RMS acceleration, [ms$^{-2}$].

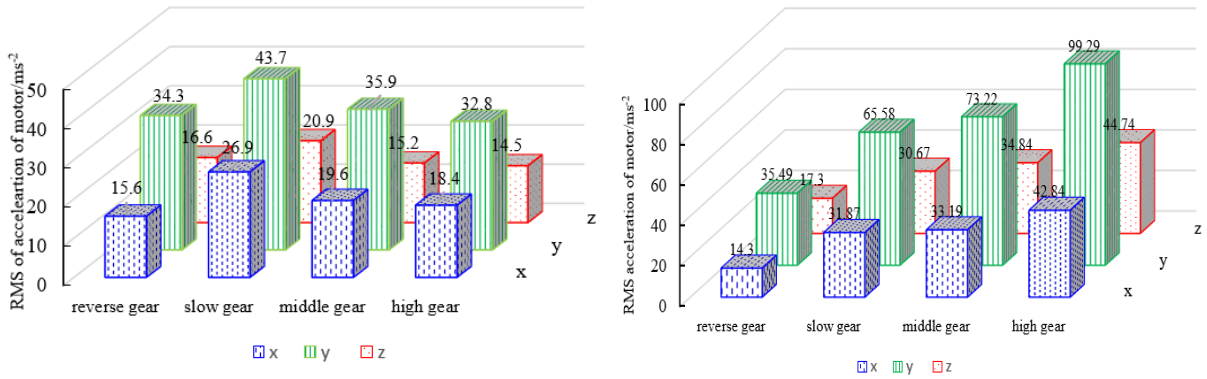


a. Moving mode b. Tilling mode

**Fig. 7 - RMS acceleration of electric motor under different modes and gears**

The acceleration in the moving mode is smaller than that in tilling mode, and acceleration in y- axis is much greater than the value in other axis directions, which could be caused by the geometry of the rotary blades, but needs to be further verified by experiment. Meanwhile, the variation tendency of RMS acceleration, shown in Figure 7a, is initially increasing and then decreasing. While in Figure 7b, it is uniformly increasing for three coordinate directions.

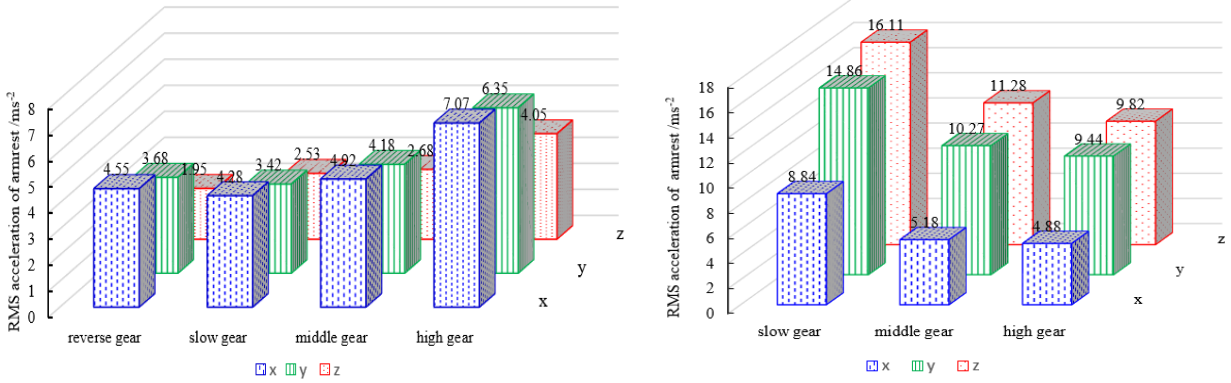


a. Moving mode b. Tilling mode

**Fig. 8 - RMS acceleration of armrest under different modes and gears**

Figure 8 shows a similar outcome, and thus the acceleration of vibration in the moving mode is smaller than that in the tilling mode, which may be explained that the rotary blade in moving mode cuts the soil at a shallower level. The significant difference about the variation tendency of RMS acceleration is inverse. Besides, RMS acceleration in x- coordinate direction is the greatest for all axis directions in Figure 8a, while it is the smallest for all axis directions in Figure 8b. However, acceleration in the high gear has the least vibration in Figure 8b. This paradox may be explained by the higher the electric motor runs, the less each bite accomplishes, so the acceleration is decreased slightly. Moreover, not all of the vibrational energy of the electric motor is transmitted to the handlebars. Though the reaction to vibration is different for each person, when the vibration acceleration is larger than 2ms$^{-2}$, the handling comfort is hard to sustain for over half an hour for most of people. In a word, the handling comfort of electric mini-tiller is not wanted, in particular for an intelligent agriculture era.

It is not always possible to describe the reaction to vibration with three different accelerations. In a common scenario, the acceleration in an axis direction is large, while in the other directions is small. In order to depict the vibration level, a total weighted acceleration is calculated based on the ISO2631-1:1997(E)

$$a_V = [(1.4a_{xw})^2 + (1.4a_{yw})^2 + a_{zw}^2]^{0.5} \quad (3)$$

Where:

$a_V$ is the total weighted acceleration, [ms$^{-2}$];
$a_{xw}$ is the acceleration in x- coordinate direction, [ms$^{-2}$];
$a_{yw}$ is the acceleration in y- coordinate direction, [ms$^{-2}$];
$a_{zw}$ is the acceleration in z- coordinate direction, [ms$^{-2}$].

For this study, almost all accelerations in Figures 7 and Figure 8 are greater than $2ms^{-2}$, so the weighted accelerations must be bigger than 2 $ms^{-2}$, and thus the results are similar to the outcome computed by the formula (2) as well.

It is noted that a frequency band of 1~2Hz in the horizontal direction and 4~8Hz in the vertical direction are very uncomfortable to the most of human. Therefore, a distribution of vibration frequency has also been analyzed, and is shown in Table 2 and Table 3.

**Table 2**

**Frequency distribution of armrest in each axis direction under moving and tilling modes**

| Item | | $a_x$ | | $a_y$ | | $a_z$ | |
|---|---|---|---|---|---|---|---|
| | | f [Hz] | A [$ms^{-2}$] | f [Hz] | A [$ms^{-2}$] | f [Hz] | A [$ms^{-2}$] |
| Moving | r | 60 | 3.96 | 60 | 3.25 | 10 | 1.37 |
| | s | 45 | 1.58 | 50 | 1.37 | 10 | 0.65 |
| | m | 50 | 2.3 | 50 | 1.46 | 818 | 0.92 |
| | h | 15 | 2.22 | 512 | 2.47 | 10 | 1.48 |
| Tilling | s | 50 | 6.39 | 15 | 1.7 | 10 | 4.6 |
| | m | 65 | 6.61 | 10 | 4.1 | 10 | 6.58 |
| | h | 70 | 7.8 | 10 | 3.23 | 10 | 4.5 |

**Table 3**

**Frequency distribution of motor in each axis direction under moving and tilling modes**

| Item | | $a_x$ | | $a_y$ | | $a_z$ | |
|---|---|---|---|---|---|---|---|
| | | f[Hz] | A[$ms^{-2}$] | f[Hz] | A[$ms^{-2}$] | f[Hz] | A[$ms^{-2}$] |
| Moving | r | 666 | 2.2 | 844 | 2.7 | 60 | 3.5 |
| | s | 904 | 3.6 | 909 | 2.6 | 904 | 4.1 |
| | m | 778 | 4.1 | 793 | 6.4 | 793 | 4.8 |
| | h | 1038 | 2.9 | 567 | 2.8 | 849 | 2.7 |
| Tilling | r | 10 | 3.5 | 795 | 2.6 | 10 | 1.7 |
| | s | 1069 | 2.5 | 868 | 3.6 | 863 | 3.2 |
| | m | 783 | 8.7 | 768 | 5.6 | 768 | 7.4 |
| | h | 10 | 4.8 | 833 | 7.1 | 898 | 5.6 |

Symbols in Tables 2 and Table 3 such as r, s, m and h represent reverse gear, low gear, middle gear and high gear, respectively. Table 2 shows that all except two maxima accelerations in x-, y- and z- coordinate directions are smaller than 100Hz, and the peak distribution is not regular. It is necessary to acknowledge that there are some differences between the coordinate system used in this study and the coordinate system in the ISO criterion. Namely, $a_x$ in this study is equivalent to $a_z$ in ISO norm, etc. There are eight peaks at 10Hz, with 75% distributed in the z- coordinate direction, which is close to the sensitive frequency of the human body. Furthermore, over 50% of vibrational amplitudes are greater than $2ms^{-2}$, nearly three times greater than the ISO standard, which will disturb the operator's body and tilling quality.

In Table 3, most frequency peaks are larger than 600Hz, and the maximum acceleration is $8.7ms^{-2}$, which is four times the ISO norm. Observed from Figure 7, Figure 8, Table 2 and Table 3, the vibrational amplitude of the electric motor is greater than the values in the armrest. Two conclusions can be drawn. Firstly, the working environment of the electric motor is unsatisfactory. Secondly, not all of the vibrational energy of the electric motor is transmitted to the armrest. Although these peaks are not within the sensitive frequency bands of the human body, additional vibration amplitudes harm the service life of the components of the mini-tiller. Therefore, to minimize the vibrational energy of the motor is the key to improving the performance of the electric mini-tiller.

## CONCLUSIONS

- The structure of the electric mini-tiller is not superior because no elastic components are used in its assembly, causing vibrations to be transmitted throughout the machine. Therefore, redesigning of the structure for a new tiller rather than partly modify a conventional mini-tiller, is probably the best option.
- It is not always possible to enhance the properties of the mini-tiller through the optimization of the structure. The terrain is diverse in mountainous and hilly regions, and certain aspects of the mini-tiller are not suitable for all terrains. Designing a suspension system in the tiller could be more feasible.

**ACKNOWLEDGEMENT**

This paper is financially supported by the Fundamental Research Funds for the Central Universities (No. XDJK2016B025) and the Doctoral Fund of Southwest University (No.SWU115022).

**REFERENCES**

[1] Caffaro F., Cremasco M., M., Preti C. et al, (2016), Ergonomic analysis of the effects of a telehandler's active suspended cab on whole body vibration level and operator comfort, *International Journal of Industrial Ergonomics*, vol.53, pp.19-26;

[2] Chen J., Chen C., Chen H., (2014), Three new challenges micro tillers face in southwest China and study of countermeasures (西南地区微耕机面临的三大挑战及对策探讨), *Journal of Agricultural Mechanization Research*, vol.10, pp.245-248;

[3] Cutini M., Costa C., Bisaglia C., (2016), Development of a simplified method for evaluating agricultural tractor's operation whole body vibration, *Journal of Terramechanics*, vol. 63, pp.23-32;

[4] Deboli R., Calvo A., Preti C., (2017), Whole-body vibration: Measurement of horizontal and vertical transmissibility of an agricultural tractor seat, *International Journal of Industrial Ergonomics*, vol. 58, pp. 69-78;

[5] Fabbri A., Cevoli C., Cantalupo G., (2017), A method for handlebars ballast calculation in order to reduce vibration transmissibility in walk behind tractors, *Journal of agricultural engineering*, vol. 599, pp.1-82;

[6] Hao K. Y., Ean O. L., Rapine Z. M., (2011), The design and development of suspended handles for reducing hand-arm vibration in petrol driven grass trimmer, *International Journal of Industrial Ergonomics*, vol. 41, pp. 459-470;

[7] Heidary B., Hassan-beygi S. R., Ghobadian B., (2013), Investigating a power tiller vibration transmissibility using diesel-biodiesel fuel blends on stationary conditions, *Journal of mechanical Engineering and Technology*, vol. 5, issue 1, pp. 9-31;

[8] Liang X. C., Chen J., Wang Z., (2018), Research on the vibration of mini-tiller, *INMATEH Agriculture Engineering*, vol. 56, issue 3, pp. 17-24;

[9] Mattetti M., Molari G., Serreni E., (2017), Damage evaluation of driving events for agricultural tractors, *Computers and Electronics in Agriculture*, vol. 135, pp. 328-337;

[10] Mehta C.R., Tiwari P. S., Varshney A. C., (1997), Ride vibration on a 7.5 kW rotary tiller, *Journal of Agricultural Engineering Research*, vol. 66, pp. 169-176;

[11] Niu P., Yang M. J., Chen J. et al, (2017), Structural optimization of a handheld tiller handrail by vibration modal analysis, *INMATEH Agriculture Engineering*, vol. 52, issue 2, pp. 91-98;

[12] Range L., Vasalini G., Xu F. et al, (1999), Vibration and noise of small implements for soil tillage, *Journal of Agricultural Engineering Research*, vol. 74, issue 4, pp. 403-409;

[13] Taghizadeh-Alisaraei A., Ghobadian B., Tavakoli-Hashjin T., (2012), Vibration analysis of a diesel engine using biodiesel and petro-diesel fuel blends, *Fuel*, vol. 102, pp.414-422;

[14] Tewari V. K., Dewangan K. N., (2009), Effect of vibration isolators in reduction of work stress during field operation of hand tractor, *Biosystems Engineering*, vol. 103, issue 2, pp. 146-158;

[15] Zhang Y. H., Yang L., Niu P. et al, (2016), Study on the scoop angle characteristics of a handheld tiller's rotary blade, *INMATEH Agriculture Engineering*, vol. 49, issue 2, pp. 5-12.

# FIELD TESTING OF COMPACTION CHARACTERISTICS FOR FARM TRACTOR UNIVERSAL 445
# /
# *TESTAREA ÎN CÂMP A CARACTERISTICILOR DE COMPACTARE PENTRU TRACTORUL AGRICOL UNIVERSAL 445*

**Cujbescu D.[1)], Ungureanu N.[2)], Vlăduț V.[1)], Persu C.[1)], Oprescu M.R.[1)], Gheorghiță N.E.[2)] [1]**
[1)] National Institute for Research–Development of Machines and Installations Designed for Agriculture and Food Industry - INMA Bucharest / Romania
[2)] Politehnica University of Bucharest, Faculty of Biotechnical Systems Engineering / Romania;
*E-mail: dcujbescu@yahoo.com*
*DOI: 10.35633/INMATEH-59-27*

***Keywords:*** *soil, tractor, compaction, pressure, contact area*

## ABSTRACT

*In the past few decades, size and weight of agricultural machinery have increased significantly, and as a consequence, the severity and depth to which the stress is transmitted into agricultural soil have increased. The objective of experimental determinations was to study the influence of some factors characteristic to compaction: tire inflation pressure, wheel load and contact pressure on the contact area between tire and soil, as well as 2D and 3D mapping of pressure distribution in the footprint. The front tire of the U445 Romanian agricultural tractor was tested at five tire inflation pressures: 100, 150, 200, 250 and 300 kPa, obtaining contact areas between 0.0252 – 0.0349 m² and contact pressures between 98 - 136 kPa.*

## REZUMAT

*În ultimele decenii, mărimea și greutatea mașinilor agricole au crescut în mod semnificativ și, în consecință, au crescut severitatea și adâncimea la care se propagă tensiunile în solul agricol. Obiectivul determinărilor experimentale îl constituie studiul influenței unor factori caracteristici ai compactării, precum: presiunea din pneu, încărcarea pe roată și presiunea de contact asupra ariei de contact dintre pneu și sol, precum și obținerea hărților 2D și 3D ale distribuției presiunilor în pata de contact. S-a testat pneul față al tractorului agricol romanesc U445, la cinci presiuni în pneu: 100, 150, 200, 250 și 300 kPa, obținându-se suprafețe de contact între 0.0252 – 0.0349 m² si presiuni de contact intre 98 - 136 kPa.*

## INTRODUCTION

Worldwide, soil compaction has become a concern and is recognized as one of the major problems in modern agriculture associated with soil degradation. Soil compaction is an increase of soil wet density, and it occurs mostly when a vehicle operates on soil with increased soil moisture or due to improperly dimensioned running gear of heavy field machinery, though loaded and inflated according to manufacturers' technical instructions (*Grecenko and Prikner, 2014*).

Soil compaction due to external mechanical stress applied by wheeling deforms the pore space, which affects soil aeration, water and solute transport, nutrient availability (*de Pue and Cornelis, 2019*), it reduces fertiliser use efficiency, increases the risk of run-off and erosion and reduces crop productivity (*Bluett et al., 2019*), it reduces pesticide decomposition and increases pesticide leaching into groundwater, it accelerates the potential pollution of surface water by organic waste.

Soil compaction under the wheels of agricultural field vehicles such as tractors with mounted or trailed implements is of special concern (*de Lima et al, 2018*), because of demand for mechanization, hence increased field traffic under predominantly all-weather operations.

In European agriculture, tractor weight increased from 3 tons (in 1940) to 7 tons (in 1998) respectively 20 tons (at present). Although with the increasing adoption of precision agriculture that can confine the traffic, modern tractors are heavier, their available power and load carrying/pulling capacity is greater, so current field machines have the potential to cause much more site disturbance and damage (*Mohsenimanesh and Ward, 2010*).

[1] *Cujbescu D., PhD.Eng.; Ungureanu N., PhD.Eng.; Vlăduț V.N., PhD.Eng.; Persu C., PhD.Stud.Eng.; Oprescu M.R., PhD.Stud.Eng.; Gheorghiță N.E., PhD.Stud.Eng.*

Soil compaction due to the traffic of agricultural machinery on fields is observed as sinkage at soil surface, which is the cumulative effect of deformation beneath soil surface (*Elaoud and Chehaibi, 2011*).

The vulnerability of soil to become compacted has been observed as an interaction of numerous factors, including soil moisture, soil organic matter, soil type, wheel load, size and shape of the footprint area formed between the tire and soil, tire inflation pressure, contact pressure, number of passes of agricultural machinery, tillage system, machine speed and even the treading of animals on pastures.

In contact with the soil, the tire of agricultural machinery forms a footprint whose shape and size depend on several categories of factors: the type of soil and its physical characteristics, the type of tire (rigidity, tread pattern), tire inflation pressure, wheel load. The contact area is the part of the tire that comes into contact with the soil and is calculated as the ratio between the wheel load and the tire inflation pressure. Static contact area is the contact area between the tire and a rigid or deformable surface when the tire is statically loaded without movement (*Wulfsohn D., 2009*). The contact area between has a major influence on the distribution of stress in the soil. The increase in the contact area does not necessarily lead to the decrease of the stress in the soil, but to the limitation of the distribution of the large stresses in the depth, respectively to their extension in horizons close to soil surface. The problem of deep distribution of large stress can be solved by adopting double-drive wheels for which the contact area doubles.

Tire inflation pressure is, along with soil moisture, one of the most important factors influencing soil compaction (*Batey T., 2009*) because it influences the contact area and the contact pressure at the soil-tire interface for a given wheel load (*Xia K., 2011*). By lowering the tire inflation pressure, soil-tire interaction can be modified by altering soil-tire interface pressure, tire performance and rutting effect (*Pytka, 2005*).

Contact pressure can be determined as ratio between wheel load and the contact area between the wheel and the soil. Contact pressure causes topsoil compaction, while high wheel load leads to subsoil compaction. The contact pressure at the soil-tire interface is a good indicator of the potential for compaction of agricultural soils. In order to reduce the contact pressure and therefore to reduce the artificial compaction, it is recommended to use machines and agricultural equipment fitted with tracks or tires higher than the standard ones and with low tire inflation pressures (radial tires) (*Ziyaee and Roshani, 2012*). As the vertical contact pressure is distributed over the contact area unevenly, the vertical resultant reaction force tends to shift toward the leading edge (*El-Sayegh et al, 2018*). One of the approaches to reduce the risk of soil compaction is to reduce tire pressure on soil either by decreasing axle load and/or increasing the contact area of wheels on the soil (*Kenarsari et al, 2017*).

Studying the tire-soil interaction in agricultural soil is important because the vertical deformation of soil (as a deformable material) is sometimes larger than tire deflection (*Farhadi et al, 2018*). Soil-tire interaction is complex and difficult to quantify by direct measurements and also by modeling.

Knowledge of stress distribution in the soil is important for understanding soil compaction due to vehicle traffic (*Keller et al, 2018*). To obtain a precise definition of the extent of compacted layers of soil, it is important to determine its vertical and horizontal spatial distribution (*Lamandé and Schjønning, 2011*). For example, it was found that in coarse-textured soils, wheel load gives stresses distributed in vertical direction, while in fine-textured soils, stress distribution would be multidirectional (*Shah et al, 2016*). Understanding the stresses at the soil–tire interface would provide insight into the current state of tire traction development, data for soil–tire interface discrete and finite element models, and information for future tire designs (*Roth and Darr, 2011*).

## MATERIALS AND METHODS

Experimental research was carried out at the National Research - Development Institute for Machines and Installations Designed to Agriculture and Food Industry – INMA Bucharest.

Initial characterization of the tested plot of soil resulted in the following characteristics: the upper layer of soil (0-20 cm deep) is loamy clay with glomerular rugged structure, medium and fine texture, moderately plastic and adhesive, 2.49 g/cm$^3$ density, 1.22 g/cm$^3$ bulk density and 51 % total porosity; between 20-35 cm deep, the soil is clayey loam, with high angular glomerular structure and fine texture, is moderately compact, plastic and adhesive, with total porosity of 46 %; between 35-80 cm the soil is clayey loam, with medium prismatic structure and fine texture, compact, plastic, adhesive and dry, 2.69 g/cm$^3$ density, 1.75 g/cm$^3$ bulk density and 36 % total porosity.

At the time of experiments, the plot of soil was cultivated with red basil. It was tested the pressure distribution under the left front wheel of the Universal 445 tractor (Fig. 1), which is a small agricultural tractor equipped with a 33 kW engine. On the front axle, the tires are type Danubiana Superfront Tractor, size 6.00-16, profile F-2.

The weight of the Universal 445 tractor, determined by the electronic weighing platform type RW-10PRF, was 2041 kg, of which 700 kg were distributed on the front axle (350 kg or 3.43 kN on each front wheel) and 1341 kg on the rear axle (670.5 kg or 6.57 kN on each rear wheel).

**Fig. 1 – Universal 445 Romanian tractor**

The pressure at the interface between the agricultural soil and the front wheel of the tractor and the sizes of contact area were established by interpolating between the two elements a Tekscan Industrial Sensing sensor for measuring the pressure distribution (sensor size: 600 x 500 mm).

After calibration, the pressure sensor was coupled to the VersaTek Handle electronic data acquisition system (Fig. 2) and to a laptop.

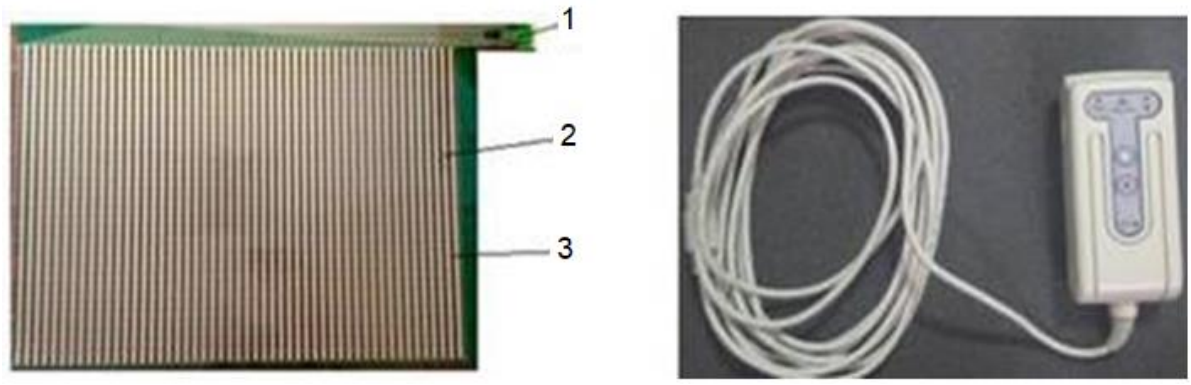


**Fig. 2 – Tekscan pressure sensor and VersaTek Handle data acquisition system**
*1 – connection to the data acquisition system; 2 – sensitive elements;*
*3 – connecting threads between sensitive elements*

Data acquisition was done in the I-Scan software, which displays the 2D and 3D pressure distribution in the contact area, as well as the values and variations in time of some parameters such as contact area, contact pressure, maximum pressure, force on the soil, etc.

During the experiments, tire inflation pressure values were varied five times and measured with the aid of the compressor and the pressure gauge: 100 kPa, 150 kPa, 200 kPa, 250 kPa and 300 kPa.

**Fig. 3 – Variation of tire inflation pressure**

Figure 4 shows the under-wheel placing of the mesh-type pressure sensor and the profile of the front tire of the U445 tractor at the minimum tested tire inflation pressure of 100 kPa.

**Fig. 4 – Front tire at minimum inflation pressure (100 kPa)**

## RESULTS

The experimental data for both the input and output parameters monitored and analyzed are presented in Table 1.

**Table 1**

**Compaction characteristics under the front wheel of U445 tractor**

| Wheel load Q [kN] | Tire inflation pressure $p_i$ [kPa] | Size of contact area A [$m^2$] | Contact pressure $p_c$ [kPa] | Footprint length $l_c$ [m] | Footprint width $l_w$ [m] |
|---|---|---|---|---|---|
| 3.43 | 100 | 0.0349 | 98 | 0.241 | 0.179 |
| | 150 | 0.0314 | 109 | 0.214 | 0.170 |
| | 200 | 0.0298 | 115 | 0.246 | 0.161 |
| | 250 | 0.0290 | 118 | 0.223 | 0.165 |
| | 300 | 0.0252 | 136 | 0.212 | 0.162 |

As it can be seen from Table 1, by varying the tire inflation pressure from 100 kPa to 300 kPa, contact areas ranging from 0.0252 - 0.0349 $m^2$ were obtained, with the corresponding contact pressures varying between 98 kPa and 136 kPa.

Studies in the literature mention that the agricultural soil is compacted if the contact pressure exceeds 85 kPa. Considering that, it can be said that in all tested situations, compaction would mainly affect the arable layer of soil, but its negative effects can usually be alleviated by moldboard or chisel plowing.

However, repeated passes of the tractor on the same traffic lanes would intensify the effects of compaction, and stresses could affect the subsoil. Subsoil compaction persists for longer periods and the compacted layers are difficult to alleviate, resulting in increased fuel consumption and reduced crop yields.

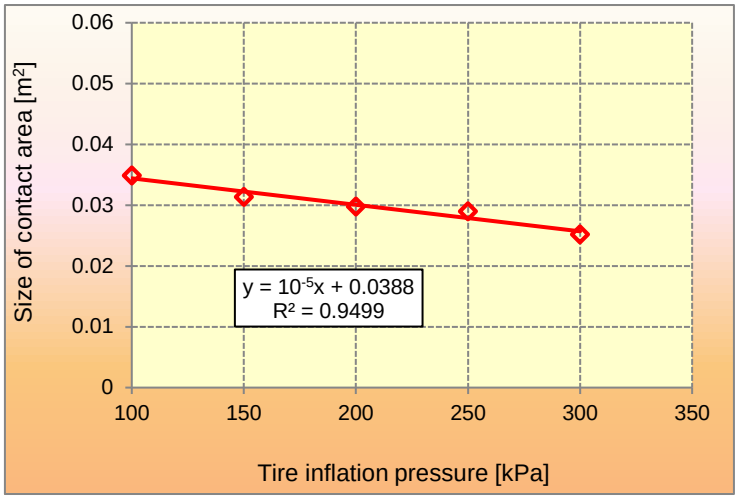


**Fig. 6 – Influence of tire inflation pressure on the contact area of the U445 tractor**

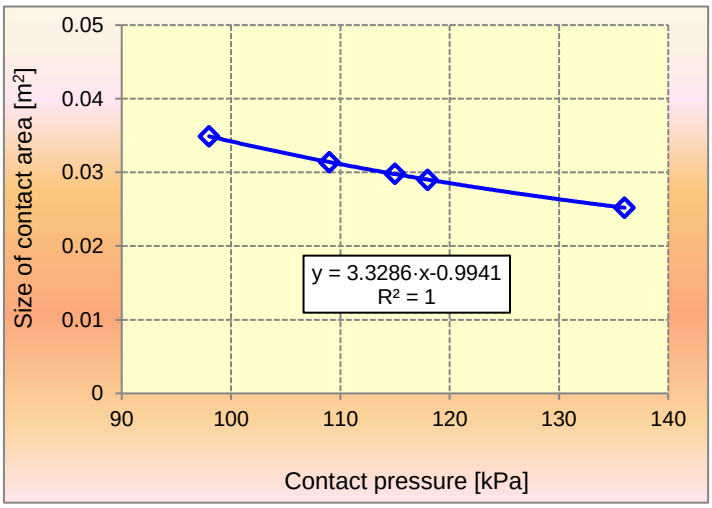


**Fig. 7 – Influence of contact pressure on the contact area of the U445 tractor**

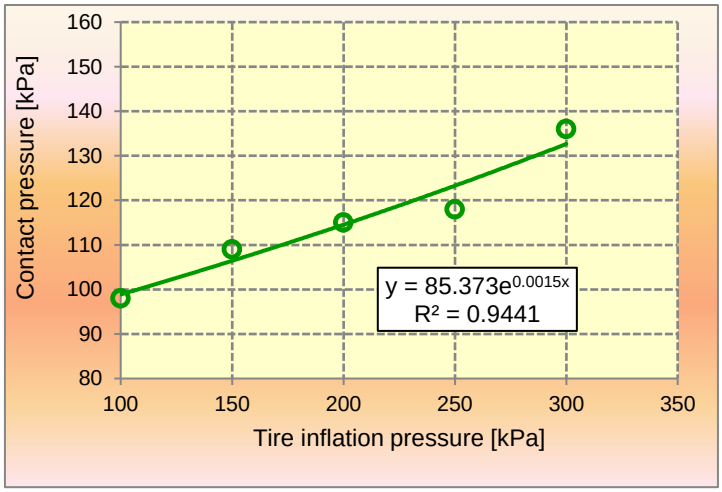


**Fig. 8 – Influence of tire inflation pressure on the contact pressure of the U445 tractor**

With the I-Scan software were recorded the 2-D and 3-D distribution maps of contact pressures at the tire-soil interface. It should be noted that the value of the contact pressure indicated by the data acquisition software represents an average of the pressure recorded on each sensitive element of the Tekscan Industrial Sensing Pressure Sensor which was in contact with the tire of the Universal 445 tractor during testing.

Thus, for the front wheel of the U445 tractor (wheel load Q = 3.43 kN), were obtained the pressure distributions in the contact area shown in Figure 9 and Figure 10.

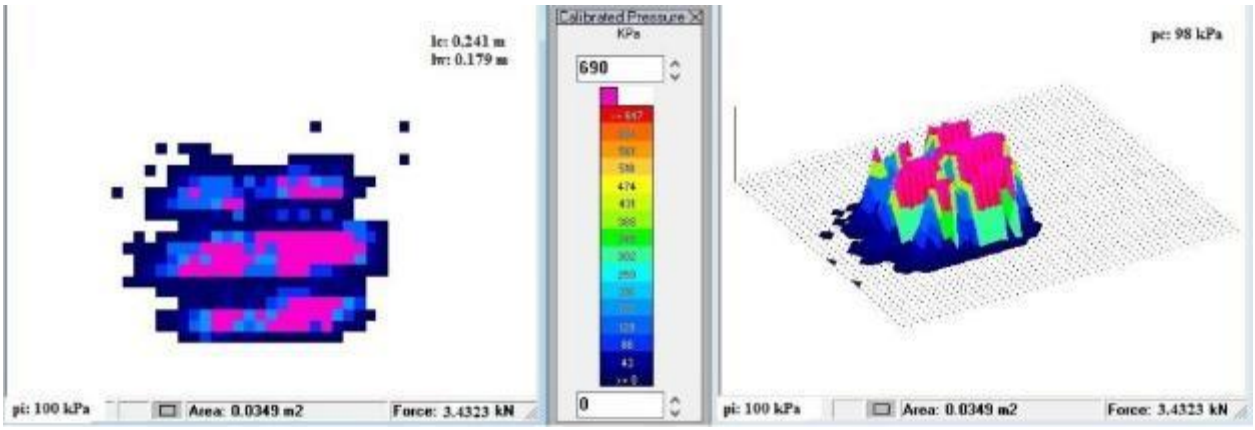


a)

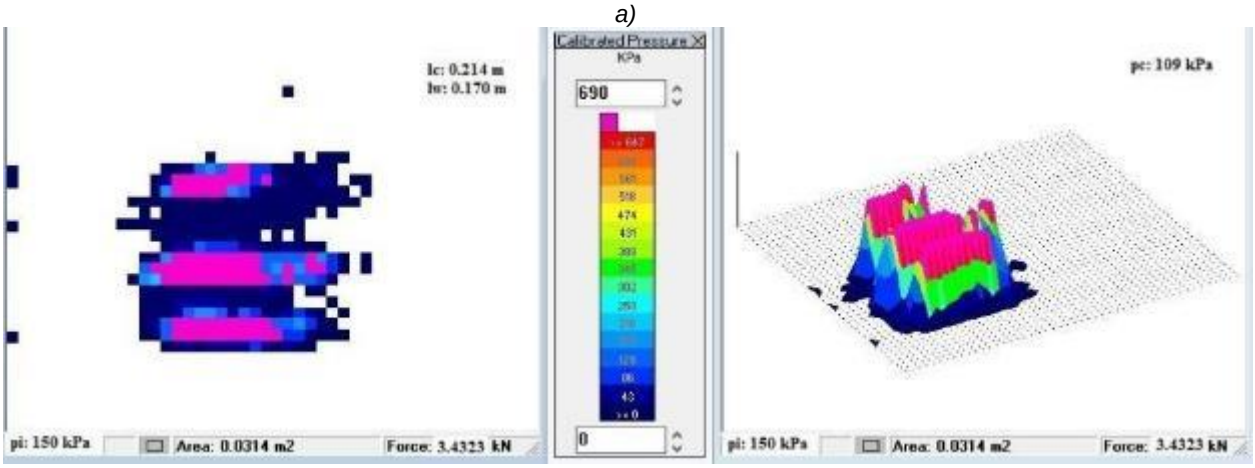


b)

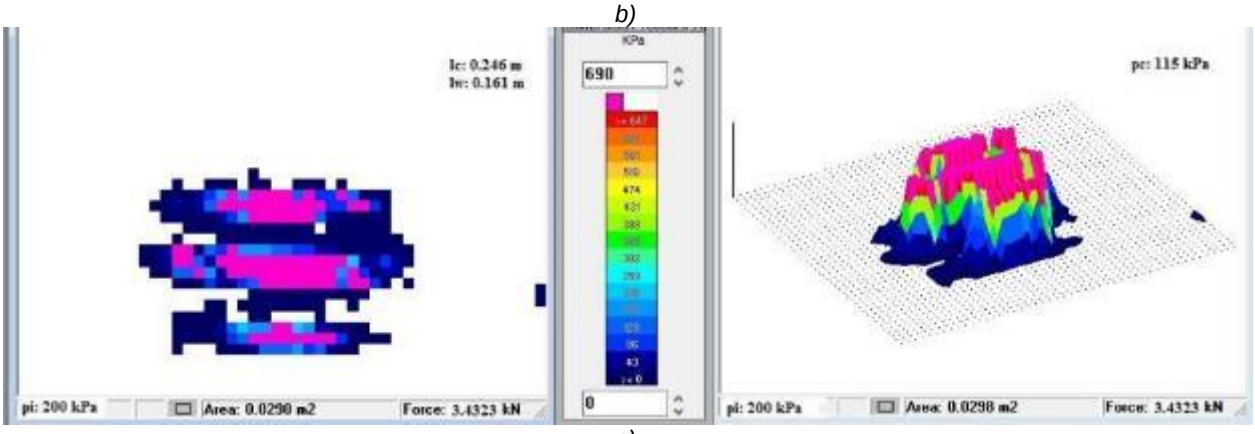


c)

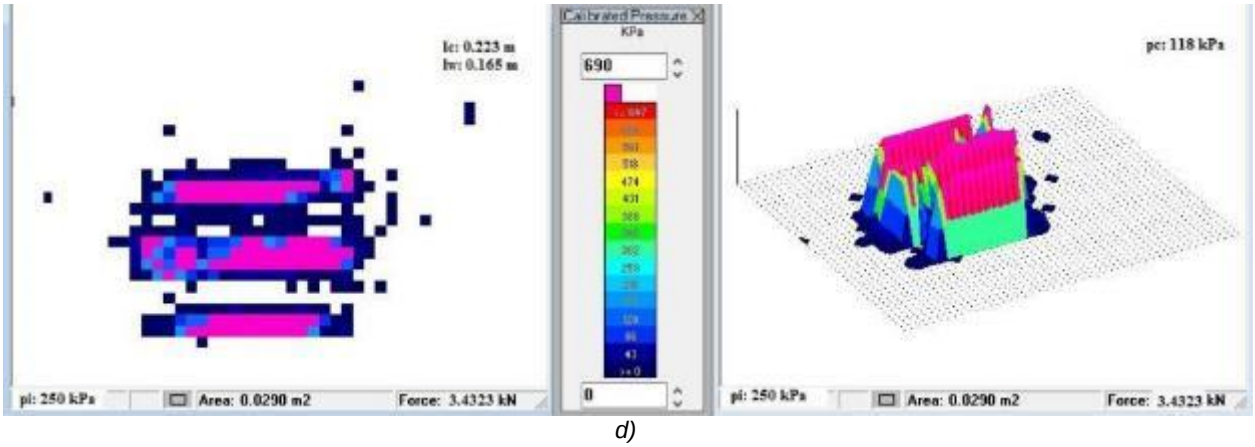


d)

**Fig. 9 – Maps of pressure distribution in the contact area, at 3.43 kN wheel load and tire inflation pressures:**
*a) 100 kPa; b) 150kPa; c) 200 kPa;*

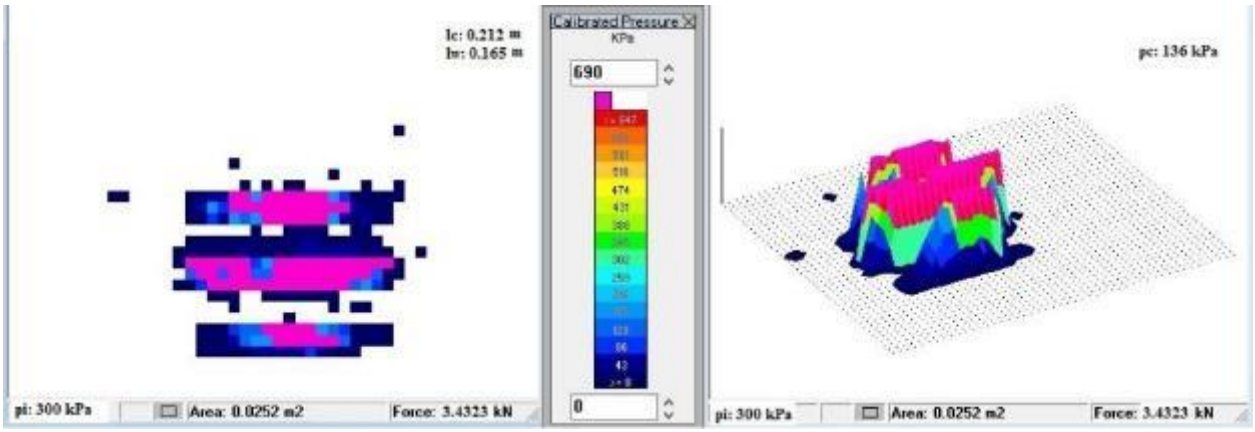


*a)*

**Fig. 10 – Maps of pressure distribution in the contact area, at 3.43 kN wheel load and tire inflation pressures:** *300kPa*

As it can be seen from Figure 9 and Figure 10, the shape and size of the tire-soil contact have changed in the tested conditions. Under the influence of tire pressure and wheel load, the tire deforms both longitudinally and transversally and the contact area tends to have a rectangular shape with rounded corners (more or less) and less towards an elliptical shape.

## CONCLUSIONS

The shape and size of the tire-soil contact contour changed with tire inflation pressure which in turn affects the soil-tire interface pressures across the surface of the tire. The benefits of low inflation pressure of farm tractor tires may include decreased soil-tire interface pressures, increased tire performance, and decreased soil compaction and a smoother ride.

Compaction in the plow layer is largely related to contact pressure of the tire on the soil. Compaction below the plow layer is related to total wheel load. Considering that the agricultural soil is compacted if the contact pressure exceeds 85 kPa, it can be said that in all tested situations, compaction would mainly affect the upper soil layer, but its negative effects can usually be alleviated by moldboard or chisel plowing.

Proper tractor and machine set up and operation can minimize the effect of compaction, but improved management of agricultural works is the best solution for addressing compaction.

## ACKNOWLEDGEMENT

This work has been funded by Politehnica University of Bucharest, through the “Excellence Research Grants” Program, UPB–GEX2017, Ctr. No. 61/25.09.2017, internal number IS 25.17.03/2017 (COMPSOL)”.

## REFERENCES

[1] Batey T., (2009), Soil compaction and soil management – a review, *Soil Use and Management*, Vol. 25, pp. 335–345;

[2] Bluett T., Tullberg J.N., McPhee J.E., Antille D.L., (2019), Soil and Tillage Research: Why still focus on soil compaction? *Soil and Tillage Research*, Vol. 194, 104282;

[3] De Lima R.P., Da Silva A.P., Giarola N. F.B., Da Silva A. R., Rolim M.M., (2017), Changes in soil compaction indicators in response to agricultural field traffic, *Biosystems Engineering*, Vol. 162, pp. 1–10;

[4] De Pue J., Cornelis W.M., (2019), DEM simulation of stress transmission under agricultural traffic Part 1: Comparison with continuum model and parametric study, *Soil and Tillage Research*, Vol. 195, 104408;

[5] Elaoud A., Chehaibi S., (2011), Soil compaction due to tractor traffic, *J Fail. Anal. and Preven*., Vol. 11, pp. 539–545;

[6] El-Sayegh Z., El-Gindy M., Johansson I., Öijer F., (2018), Improved tire-soil interaction model using FEA-SPH simulation, *Journal of Terramechanics*, Vol. 78, pp. 53–62;

[7] Farhadi P., Golmohammadi A., Sharifi A., Shahgholi G., (2018), Potential of three-dimensional footprint mold in investigating the effect of tractor tire contact volume changes on rolling resistance, *Journal of Terramechanics*, Vol. 78, pp. 63–72;

[8] Grecenko A., Prikner P., (2014), Tire rating based on soil compaction capacity, *Journal of Terramechanics*, Vol. 52, pp. 77–92;
[9] Keller T., Lamandé M., Naderi-Boldaji M., de Lima R.P., (2018), Approaches towards understanding soil compaction processes, Novel methods and results of landscape research in Europe, Central Asia and Siberia, Vol. II, Understanding and Monitoring Processes in Soils and Water Bodies, Chapter 6.4 Soil Compaction, pp. 274–279;
[10] Kenarsari A.E., Vitton S.J., Beard J.E., (2017), Creating 3D models of tractor tire footprints using close-range digital photogrammetry, *Journal of Terramechanics*, Vol. 74, pp. 1–11;
[11] Lamandé M., Schjønning P., (2011), Transmission of vertical stress in a real soil profile. Part III: effect of soil water content, *Soil & Tillage Research*, Vol. 114, pp. 78–85;
[12] Mohsenimanesh A., Ward S.M., (2010), Estimation of a three-dimensional tyre footprint using dynamic soil–tyre contact pressures, *Journal of Terramechanics*, Vol. 47, pp. 415–421;
[13] Pytka J., (2005), Effects of repeated rolling of agricultural tractors on soil stress and deformation state in sand and loess, *Soil and Tillage Research*, Vol. 82, pp. 77–88;
[14] Roth J., Darr M., (2011), Data acquisition system for soil–tire interface stress measurement, *Computers and Electronics in Agriculture*, Vol. 78, pp. 162–166;
[15] Shah A.N., Tanveer M., Shahzad B., Yang G., Fahad S., Ali S., Bukhari M.A., Tung S.A., Hafeez A., Souliyanonh B., (2017), Soil compaction effects on soil health and crop productivity: an overview, *Environ Sci Pollut Res*. *Int.*, Vol. 24, Issue 11, pp. 10056–10067;
[16] Wulfsohn D., (2009), Soil - tire contact area, *Advances in Soil Dynamics*. ASABE, Vol. 3, pp. 59–84;
[17] Xia K., (2011), Finite element modeling of tire/terrain interaction: Application to predicting soil compaction and tire mobility, *Journal of Terramechanics*, Vol. 48, pp. 113–123;
[18] Ziyaee A., Roshani M.R., (2012), A survey study on soil compaction problems for new methods in agriculture, *Intl. Res. J. Appl. Basic. Sci*., Vol. 3, Issue 9, pp. 1787–1801.

# GENERAL STRUCTURE OF TILLAGE DRAFT FORCE. CONSEQUENCES IN EXPERIMENTAL AND APPLICATIVE RESEARCHES

## I

# STRUCTURA GENERALA A FORŢEI DE TRACŢIUNE, CONSECINŢE ÎN CERCETĂRILE EXPERIMENTALE ŞI APLICATIVE

**Cardei P., Muraru S.L., Sfiru R., Muraru V.** [1]
National Institute of Research and Development for Machines and Installations for Agriculture and Food Industry – INMA Bucharest/Romania
*Tel: +726142837; E-mail: petru_cardei@yahoo.com*
*DOI: 10.35633/INMATEH-59-28*

***Keywords:*** *soil, tillage, formulas, structure, applications*

**ABSTRACT**

*The empirical and theoretical estimation of the draft force of agricultural machinery for soil tillage, has been the target of scientific research for about one hundred years. The results obtained so far may seem contradictory or divergent. The article presents the results of some research on the usual calculation formulas of the draft force of agricultural machines for soil tillage. Although apparently these formulas are different, analyzing the structure of the formula, we find cohesion and coherence embodied in a simple generalization and easy to use both theoretical and experimental. Moreover, the formulas are convertible between them, the two languages used for their definition (the mechanics of deformable solids and that of the phenomenological description), are only different forms of expression for the same phenomenon. Another problem that is addressed in the research whose results are presented in this article is that of highlighting the dependence of the draft force on the tool speed (in the field) of the soil tillage machine. Exposure is complemented by an algorithm that highlights the dependence of the draft force on the tillage tool speed. Also like a consequences of the draft tillage force structure, finally, a third problem addressed in these researches and whose results and perspectives are given in this paper is that of optimizing the working processes of agricultural machinery for soil tillage. The treatment of the problem starts from the hypothesis of the most general formula of the traction resistance force and proposes some ways to solve the optimal problem.*

**REZUMAT**

*Estimarea empirică și teoretică a forței de tracțiune a mașinilor agricole pentru prelucrarea solului a fost in atenția cercetării științifice timp de aproximativ o sută de ani. Rezultatele obținute până acum pot părea contradictorii sau divergente. Articolul prezintă rezultatele unor cercetări privind formulele obișnuite de calcul al forței de tracțiune a mașinilor agricole pentru prelucrarea solului. Deși aparent aceste formule sunt diferite, analizând structura formulei, găsim coeziune și coerență integrate într-o generalizare simplă și ușor de folosit, atât teoretic cât și experimental. Mai mult decât atât, formulele sunt convertibile între ele, cele două limbaje utilizate pentru definirea lor (mecanica solidelor deformabile și cea a descrierii fenomenologice) sunt doar forme diferite de exprimare pentru același fenomen. O altă problemă abordată în cadrul cercetării, ale cărei rezultate sunt prezentate în acest articol, este aceea a evidențierii dependenței forței de tracțiune de viteza in câmp a organului de lucru montat pe mașina de prelucrare a solului. Expunerea este completată de un algoritm care evidențiază dependența forței de tracțiune asupra vitezei instrumentului de prelucrare. De asemenea, ca o consecință a structurii forței de tracțiune, în final, a treia problemă abordată în aceste cercetări și a cărei rezultate și perspective sunt prezentate în lucrare este cea a optimizării proceselor de lucru ale mașinilor agricole pentru prelucrarea solului. Abordarea problemei pornește de la ipoteza celei mai generale formule a forței de rezistență la tracțiune și propune câteva modalități de rezolvare optimala a problemei.*

[1] *Cardei P., Math; Muraru S.L., Sfiru R., Eng; Muraru V., PhD. Eng.*

## INTRODUCTION

The specialists considered that the working speed, does not influence the draft force or its influence, is insignificant compared to the static component of the same force. Among the formulas that take into account only the static component, one can notice the formulations based on soil mechanics (*McKyes, 1985),* developed especially for tools working in soil (agricultural machines or machines used in land or civil engineering or mining) at a low speed. The influence of the working speed is considered in many papers, *(Letosnev, 1959; ASAE, 2003; Toma et al., 1978; Sandru et al., 1983; Tecusan and Ionescu, 1982; Scripnic and Babiciu, 1979; Gill and Vanden, 1968).* In some of the last mentioned papers, the authors also consider reduced formulas, particular cases of general formulas that contain the working speed and which can be used also in the absence of terms that contain the speed of work.

An interesting separation can be made between the views of two schools with profound contributions to the development of formulas for the estimation of the traction draft force of the soil tillage machines: North American school (USA and Canada) and Russian (Soviet) school, but whose results have been used successfully throughout the Eastern European. The results of the American school are represented in the works (*McKyes, 1985; Owen, 1989; Larson, 1964*; *Gill and Vanden, 1968*; *Ibarra, 2001*; *Fielke, 1994; Sharifat, 1999).* The results of the Russian school are represented by (*Letosnev, 1959; Krasnicenko, 1964; (Asmolovsky and Nosnikov, 2014)* and in Romania, by (*Toma et al., 1978; Sandru et al., 1983; Tecusan and Ionescu, 1982; Scripnic and Babiciu, 1979; Sandru et al., 1982).*

The proposed calculation formulas differ in form, as sense of terms and factors, in part. However, a simple analysis shows that all formulas converge and that terms are convertible from one formula to another. Moreover, there is a generalizing formula from which is obtained all other formulae, by customization.

The structure of the draft force formulas has profound implications in the experimental plan and in the theoretical and experimental plan of identifying possible optimal working regimes of agricultural machinery for soil tillage. The two issues are briefly discussed in this paper.

## MATERIALS AND METHODS

The most general form of the draft force of tools for the soil tillage machinery is, according to (*ASAE, 2003)*:

$$F = A + B \cdot v + C \cdot v^2 \tag{1}$$

where the parameters in the formula are explained in Table 1.

**Table 1**

**Parameters of the interaction process between soil and the soil tillage machinery: notations, significance and units of measure**

| Notation | Name | Unit [2] |
|---|---|---|
| *F* | Draft force | N |
| *A* | The static coefficient of term of the draft force | N |
| *B* | The coefficient of the term that depends on the working speed of the draft force | Kg/s |
| *C* | The coefficient of the term that depends on the square of the working speed, of the draft force | Kg/m |
| $F_i$ | Dimensionless factor describing the influence of soil texture: i = 1 fine , i = 2 average, and i = 3 coarse . | - |
| *K* | Parameter specific of the tillage machine | MPa |
| *D* | Parameter specific of the tillage machine | $Kgm^{-2}s^{-1}$ |
| *E* | Parameter specific of the tillage machine | $kg/m^3$ |
| *v* | Working speed | m/s |
| *b* | Working width | m |
| *a* | Working depth | m |
| *k* | Coefficient that characterizes specific soil deformation resistance | MPa |
| $\varepsilon$ | Coefficient which depends on the shape of the active surface of the body and the soil properties[3] | $kg/m^3$ |
| $\delta$ | Angle of friction between tillage tools and soil | rad |

[2] *For ease of computation and comparisons, as well as for unification of language, we have transformed the measurement units of all authors into the international system (SI) of measurement units.*

[3] *The coefficient $\varepsilon$, according to (Letosnev, 1959), has the unit $kgf \cdot s^2/m^4$, which by simplification returns to the mass density unit.*

| Notation | Name | Unit [2] |
|---|---|---|
| $f$ | Coefficient analogous to friction coefficient | - |
| $G$ | Plough weight | N |
| $g$ | Gravitational acceleration | m/s$^2$ |
| $\rho$ | Soil mass density | Kg/m$^3$ |
| $C_o$ | The apparent cohesion of the soil | MPa |
| $C_a$ | Adhesion of the soil to the surface of the tool | MPa |
| $\mu$ | Angle of friction between soil and metal | rad |
| $q$ | Overpressure acting vertically on the surface of the soil | MPa |
| $N_\rho$ | Factor depends on soil friction resistance, tool geometry and soil properties. | - |
| $N_c$ | Factor depends on soil friction resistance, tool geometry and soil properties. | - |
| $N_{ca}$ | Factor depends on soil friction resistance, tool geometry and soil properties. | - |
| $N_q$ | Factor depends on soil friction resistance, tool geometry and soil properties. | - |
| $N_a$ | Factor depends on soil friction resistance, tool geometry and soil properties. | |
| $\phi$ | Angle of internal soil friction | rad |
| $\alpha$ | Horizontal blade angle (rake angle) | rad |

The general formula (1) for the draft force is a theoretical mathematical model of this force. For the calculation of coefficients or model parameters experimental data can be used. This procedure customizes the formula for different types of tillage tools and environmental conditions (soil type, humidity, etc.).

Another category of mathematical models of the draft force is that of the statistical models, based on experimental data subjected to the regression analysis.

Finally, another category of mathematical models for traction resistance force is form by the formulas obtained through dimensional analysis. Generating formulas through this method requires the use of experimental data, and consequently involvs the customization of machine-based formulas and environmental conditions.

## RESULTS

*Particular structures, general formula*

In formula (1), the parameters A, B, C can be explained by various expressions, obtaining particular forms commonly used in the literature and in the design and exploitation of machines for soil works.

**Table 2**

**The coefficients from the formula (1) of the draft force, for four particular reference cases, and generalization**

| Formula | *A* | *B* | *C* |
|---|---|---|---|
| Goreacikin* , (*Letosnev, 1959)* | $fG+kab$ | 0 | $\varepsilon ab$ |
| The USA Standard**, (*ASAE, 2003*) | $F_i Kab$ | $F_i Dab$ | $F_i Eab$ |
| Reece (1965)***, (*McKyes, 1985)* | $\left(\rho gaN_\rho + C\cdot N_c + q\cdot N_q\right)\cdot a\cdot b$ | 0 | 0 |
| Simplified formula****, (*Sandru et al., 1983*) | $K_b\cdot b$ | 0 | 0 |
| (*Owen, 1989; Al-Neama and Hertzilius, 2017*) | $\left(\rho gaN_\rho + C_o N_c + C_a N_{ca} + qN_q\right)ab$ | 0 | $\rho N_a ab$ |
| Generalizations, (*Owen, 1989; Al-Neama and Hertzilius, 2017*) | $\left(\rho gaN_\rho + C_o N_c + C_a N_{ca} + qN_q\right)ab$ | $Dab$ | $\rho N_a ab$ |

* The coefficients *f* and *ε* are given, for example in (*Letosnev, 1959),* for different types of soil or general and the coefficient *k*, is tabled for different types of soils.

** The coefficients $F_i, K, D, E$ are given in (*ASAE, 2003),* for every usual agricultural machine or equipment in American agriculture.

*** The coefficients $N_\rho, N_c, N_q$ ,and $N_{ca}$ are given in formula (2).

**** The coefficients $K_b$ are tabulated, in the works where the formula is used, by categories of agricultural machines (*Toma et al., 1978*), for example.

$$N_\rho = \frac{1}{2}\left(1+\sin\phi\right)\left(1+\frac{tg\phi}{tg\mu}\right), N_c = \left[\left(\frac{1+\sin\phi}{1-\sin\phi}\right)-1\right]ctg\phi, N_q = \frac{1+\sin\phi}{1-\sin\phi},$$
$$N_{ca} = \frac{1-ctg\alpha ctg\left(\beta+\phi\right)}{\cos\left(\alpha+\delta\right)+\sin\left(\alpha+\delta\right)ctg\left(\beta+\phi\right)} \quad (2)$$

By coefficients (2), which depend on soil characteristics (internal friction angle, angle of friction between soil and tool steel and soil density), traction force depends implicitly on the soil moisture, texture and physico-chemical properties of the soil. If the influence of humidity is partly known and quantifiable, the influences of soil texture and its physico-chemical composition, are difficult to quantify.

It can also be observed that in the formulas in *(McKyes, 1985; Owen, 1989; Al-Neama and Hertzilius, 2017*), there is a term which dependend by the square of the working depth, in the static term, which can often be neglected in relation to the other components of the same static term.

*Variation of draft force with working speed of the soil tillage machine*

Taking into consideration the general shape of the draft force (1) and the numerous theoretical, experimental or mixed studies dealing with the influence of the working speed on the draft force, this subchapter attempts to give some indications to those interested about a way to address of this issue. First of all, it should be remembered that the working speed for some agricultural works is limited by the proper quality of the work: sowing, spraying, phytosanitary treatments, possibly soil tillage, etc. The most important result of this chapter is that it is possible to estimate the working speed that an agricultural aggregate needs to achieve in order for the load-dependent component of the draft force to be significant in relation to the component static.

To calculate the critical work speed at which the component that depends on the speed of the traction resistance equals the static component of the same force, the next second degree equation must be solved:

$$Bv + Cv^2 = A \tag{3}$$

Taking into account that all the coefficients *A, B, C* are positive (see Table 1), it follows that if *C* is not null, the only acceptable root is the positive one:

$$v_{cr} = \frac{\sqrt{B^2 + 4AC} - B}{2C}, C > 0 \tag{4}$$

Solution (4) is valid for those forces of traction resistance that depend on the square of velocity. For the cases where the draft force depends only linearly on the working speed (concrete cases are given in the American standard (*ASAE, 2003*), ie *C* is null and *B* is non null, there is another critical speed given by the formula:

$$v_{cr} = \frac{A}{B}, C = 0, B > 0 \tag{5}$$

For draft force formulas that do not depend on the working speed or the dependence is insignificant, the critical speed value does not exist. The expressions of the critical working speed at which the dynamic component of the draft force become equal to the static component are calculated for the models considered in Table 2 and are written in Table 3.

**Table 3**

**The critical speeds of the variants of the draft forces given in Table 2**

| Formula | $v_{cr}$ |
|---|---|
| Goriacikin*, (*Letosnev, 1959)* | $\sqrt{\frac{k}{\varepsilon} + \frac{fG}{ab} \cdot \frac{1}{\varepsilon}}$ |
| USA Standard**, (*ASAE, 2003)* | $\sqrt{\frac{K}{E} + \frac{D^2}{4E}} - \frac{D}{2E}, if\ E \neq 0\ and\ \frac{K}{D}\ if\ E = 0\ and\ D \neq 0$ |
| (*Owen, 1989; Al-Neama and Hertzilius, 2017*) | $v_{cr} = \sqrt{ag\frac{N_\rho}{N_a} + \frac{C_o}{\rho} \cdot \frac{N_c}{N_a} + \frac{C_a}{\rho} \cdot \frac{N_{ca}}{N_a} + \frac{q}{\rho} \cdot \frac{N_q}{N_a}}, N_a \neq 0$ |
| Generalization (*Owen, 1989; Al-Neama and Hertzilius, 2017)* | $v_{cr} = \sqrt{ag\frac{N_\rho}{N_a} + \frac{C_o}{\rho} \cdot \frac{N_c}{N_a} + \frac{C_a}{\rho} \cdot \frac{N_{ca}}{N_a} + \frac{q}{\rho} \cdot \frac{N_q}{N_a} + \frac{D^2}{4\rho^2 N_a^2}} - \frac{D}{2\rho N_a}, N_a \neq 0$ |

For the draft force formula given in (*Letosnev, 1959*), according to the data in this paper, the minimum critical speed is 2.13 m / s, or 7.7 km / h (for light or very light soils). For the machines included in the American Standard (*ASAE, 2003*), the critical speed varies between 11.07 and 20.53 km / h or between 3.07 and 5.7 m / s.

It is noted that in general the critical speed calculation formulas, starting from which the component that depends on the working speed, of the draft force exceeds the static one, are of the same nature as the formula of the speed of movement of some types of waves in the soil. According to data from (*Obrzud and Truty, 2012; Kezdi, 1974; Prat et al., 1995*), the speeds of the elastic waves in the ground start at 15 km / h, reaching values above 1500 km / h. This specification is made because there is the possibility of breaking or pre - breaking compacted areas using mechanical waves produced by special plows. By producing suitable mechanical waves (whose velocity, wavelength and frequency depend on the humidity and soil structure), some resonances became possible to appear that produce remarkable cracks in the soil before the tillage tool, which would reduce the effort of cutting and of friction.

In the Table 4 critical speeds are calculated, according to the American standard (*ASAE, 2003*) and the formulas from Table 3.

**Table 4**

**Critical speed for the american standard machinery** *(ASAE, 2003)*

| ***Implement*** | ***K*** | ***D*** | ***E*** | ***critical speed, m/s*** |
|---|---|---|---|---|
| MAJOR TILLAGE TOOLS Subsoiler/Manure Injector narrow point | 22600 | 0 | 2332.8 | 3.11 |
| 30 cm winged point | 29400 | 0 | 3110.4 | 3.07 |
| Moldboard Plow | 65200 | 0 | 6609.6 | 3.14 |
| Chisel Plow 5 cm straight point | 9100 | 1944 | 0 | 4.68 |
| 7.5 cm shovel/35 cm sweep | 10700 | 2268 | 0 | 4.72 |
| 10 cm twisted shovel | 12300 | 2628 | 0 | 4.68 |
| Sweep Plow primary tillage | 39000 | 6840 | 0 | 5.70 |
| secondary tillage | 27300 | 4788 | 0 | 5.70 |
| Disk Harrow, Tandem primary tillage | 30900 | 5760 | 0 | 5.36 |
| secondary tillage | 21600 | 4032 | 0 | 5.36 |
| Disk Harrow, Offset primary tillage | 36400 | 6768 | 0 | 5.37 |
| secondary tillage | 25400 | 4752 | 0 | 5.34 |
| Disk Gang, Single primary tillage | 12400 | 2304 | 0 | 5.38 |
| secondary tillage | 8600 | 1620 | 0 | 5.31 |
| Coulters smooth or ripple | 5500 | 972 | 0 | 5.65 |
| bubble or flute | 6600 | 1188 | 0 | 5.55 |
| Field Cultivator primary tillage | 4600 | 1008 | 0 | 4.56 |
| secondary tillage | 3200 | 684 | 0 | 4.68 |
| Row Crop Cultivator S-tine | 14000 | 2520 | 0 | 5.55 |
| C-shank | 26000 | 4680 | 0 | 5.55 |
| No-till | 43500 | 7848 | 0 | 5.54 |
| Rod Weeder | 21000 | 3852 | 0 | 5.45 |
| Disk-Bedder | 18500 | 3420 | 0 | 5.41 |

*The effects of the structure of the draft force on the optimal problem of the working process of the machines for the soil tillage*

The optimization of the working processes of the agricultural machinery for the soil tillage has two main types of objective functions: the functions related to the economic performances (energy consumption, the working capacity) and the functions related to the quality of the soil tillage performed. Less commonly used objetive functions, are related to the wear of tillage tools or to the quantity of pollutant emissions in the environment (although these are implicitly considered by the reduction of energy consumption, the separate considerations being directed to the use of green from renewable sources). The objective functions that reflect the quality of the tillage done are difficult to consider as they require a very high number of experiences and, on this way, depend by many specified factors. However, the beginnings of broader approaches, have already emerged, (*Al-Suhaibani and Ghaly, 2010; Deshpande and Shriwal, 2017*). As a result, taking into account the subject of this paper, the first category of objective functions is only refered to.

The objective functions aimed at economical performance (reducing consumption, increasing productivity, decreasing specific consumption, etc.) are based almost invariably on the draft force and

continuing with the power consumed, the energy consumed on the surface unit worked, etc. Some of the more complex models also consider the traction tool skating function. This article does not take into account skating, because it does not have as a specific objective the optimization of agricultural aggregates for soil tillage.

The draft force (1), which is a continuous and differentiable function in report to the working speed (second degree function of the working speed), has positive coefficients *A*, *B* and *C*. This can be seen in Table 2. It can be seen that the coefficients $N_{\rho,}\, N_{c,}\, N_{ca,}\, N_{q,}$ are positive from their definition formulas given in (*McKyes, 1985*). For the coefficient $N_a$ , the are no information from (*Owen, 1989; Al-Neama and Hertzilius, 2017)*, but there is no physical reason to consider it negative. As a result of these considerations, it seems that the traction resistance force has a minimum point relative to the working speed, but the value of this speed that minimizes the draft force, is negative. This result has no physical meaning for the modeled work process, so that in the usual working range, the draft force is rising monotonously. Likewise, it turns out that the power required to overcome traction resistance has optimal positive speeds.

One possibility to obtain an optimal (potential[4]) point of the soil tillage process is to consider the objective function called the *traction resistance force specific to the unit of productivity*[5],, defined as the ratio between two process parameters:

$$H(v) = \frac{F(v)}{bv} = \frac{A + Bv + Cv^2}{bv} \tag{6}$$

The *H* function, defined by (6), has a positive minimum of coordinates:

$$v_{\min} = \sqrt{\frac{A}{C}}, H_{\min} = \frac{2\sqrt{AC} + B}{b} \tag{7}$$

Obviously, the optimal point with coordinates (6) and (7) exists only for machines for which the draft force depend by the square of working speed, that is $C \neq 0$ . The expressions of the resistance to traction and productivity given in (8) are obtained:

$$F_{opt} = F(v_{\min}) = B\sqrt{\frac{A}{C}} + 2A, W_{opt} = b \cdot v_{\min} = b\sqrt{\frac{A}{C}} \tag{8}$$

According to the data from (*ASAE, 2003*) only three equipment in the US standard list show optimal points of type (7) - (8). The values of the coordinates of these points and the performance of the equipment for these optimal working regimes are given in Table 5. I underline once again that, according to (*ASAE, 2003*), the coordinates of the critical speed of the optimal point, do not depend on the ground, the width and the working depth or the number of working organs.

**Table 5**

**Coordinates of optimal points and aggregate performance in this case, calculated after (*ASAE, 2003*)**

| *Implement* | *Optimal speed m/s* | *Draft force per productivity unit N/m²* | *Pt. prod, ha/h* | *Optimal draft, kN* |
|---|---|---|---|---|
| MAJOR TILLAGE TOOLS Subsoiler/Manure Injector narrow point | 3.11 | 13.45 | 1.68 | 94.92 |
| 30 cm winged point | 3.07 | 132.82 | 1.66 | 123.48 |
| Moldboard Plow | 3.14 | 57.66 | 1.70 | 273.84 |

*Note 1*: The critical speed (4) is equal to the optimal speed (7), if B = 0 (cases C = 0 or A = 0 being uninteresting). Like the critical point (4) - (5), the optimal point given by (8) must be validated experimentally. Experiences are not simple and should start from near the theoretically predicted speed, whether critical or optimal.

*Note 2*: The general problem of optimization of the draft force consider not only in the working speed of agricultural aggregates for soil tillage, but also in terms of the geometric parameters of the tools, geometric parameters (rake angle, friction angle between the metal surface of the tools and soil) and parameters

[4] The optimal point is obtained theoretically and, for the time being, it is not validated experimentally.

[5] Only effective productivity is considered, so no account is taken of the returns at the ends of the plot and no technological breaks.

describing the soil's internal properties (cohesion, adhesion and the internal friction angle of the cohesive or non-cohesive soil, eventually in relation with humidity). Obviously, at the higher level of optimization of the entire working process, the parameters of the traction means, especially skating, adherence, etc., will be taken into account.

*Note 3*: The formulas of the draft force written in Table 2 are not fully equivalent, even though, mathematically, the transformations of one of the formulas into another are relatively simple. This is mainly due to the limits of the validity of formulas. The limits of validity refer especially to the working depth. For example, the k-values of the Goriacikin model are tabulated in (*Letosnev, 1959*) only for depths of up to 15-20 cm.

**Techniques for identifying the dependence of the draft force on the working speed**

In order to estimate the coefficients of the function given in the formula (1) for the draft force, based on experimental data, a relatively simple calculation method is proposed in this chapter.

Suppose we have the experimental data $(F_i, v_i), i = 1...n_v$, that forms a coordinate string, the first being the draft force measured, and the second corresponding working speed. The hypothesis that helps to solve the problem is that the draft force is of the form (1). Therefore, it is assumed that, with some approximation, the next relations are valid:

$$F_i = A + B \cdot v_i + C \cdot v_i^{\,2}, i = 1,...,n_v . \tag{9}$$

The three constants can be directly determined by the least squares method. In this paper another method will be given, based on the form (9) of the function sought.

The next matrix is constructed by defintion of the elements:

$$\Delta F_{i,j} = F_i - F_j, i, j = 1,...,n_v, v_i > v_j . \tag{10}$$

Assuming that the draft force of the experimental data behaviour with satisfactory approximation, according to formula (9), results the relations:

$$\Delta F_{i,j} = F_i - F_j = B(v_i - v_j) + C(v_i^2 - v_j^2), i, j = 1,...,n_v, v_i > v_j . \tag{11}$$

The matrix with the elements is built:

$$\Delta R_{i,j} = \frac{\Delta F_{i,j}}{v_i - v_j} = B + C(v_i + v_j), i, j = 1,...,n_v, v_i > v_j . \tag{12}$$

Whether matrix:

$$Sv_{i,j} = v_i + v_j, i, j = 1,...,n_v, . \tag{13}$$

From relations (12) and (13), the next relationship is obtained:

$$R_{i,j} = B + C \cdot Sv_{i,j}, i, j = 1,...,n_v, . \tag{14}$$

In order to conform to the usual computational algorithms in experimental data processing programs, the *R* and *Sv* matrices are transformed into vectors by line readings, with the exception of null elements. Then, obviously using the relations (14) for the resulting vector pair, the coefficient *B* is determined as the draft force value for the zero working speed ("intercept" in the usual software language), and *C* is the slope of the right line ("slope", in the languages common software). The coefficient *A* is found by differences or by averaging differences between experimental data:

$$A = \frac{\sum_{i=1}^{n_v} F_i - B \cdot v_i - C \cdot v_i^{\,2}}{n_v} \tag{15}$$

**CONCLUSIONS**

Although, apparently, the calculation of the draft forces is made in many variants, following the study, there is a form that integrates all these variants. Two visible centers in which mathematical models of draft force have been developed are the North American (US and Canada), respectively the East European, with the center in Soviet Russia (USSR). Both proposals are found in the generalized form of the American Standard.

The dependence of the force of draft force by the square of the working speed is found in most of the literature. In the formulas where the working speed does not appear, it is often neglected. The negligence of the traction resistance-dependent component is due to its low value compared to the static component value (under normal operating conditions, ie low operating speeds compared to critical speeds). This situation is found both experimentally and theoretically, from the proposed formulas.

American specialist literature prefer the introduction of the static component of draft force as the sum of terms imposed by soil properties (density, cohesion, adhesion, internal friction, vertical loading, so, in the terms of soil mechanics, convertible into the terms of the mechanics of continuous media) and the impact characteristics between the ground and the tool (friction between tool steel and ground, rake angle, general geometry of the tool). Eastern European literature uses global, phenomenological coefficients, directly defined, on concrete or general soils (*k*, *f*). As for the dynamic term (depending on the working speed), the situation, although seemingly the same as for the static term, is basically absolutely convergent, the soil density being one of the most important parameters that give the coefficient of the dynamic component. Although in Soviet literature the main coefficient giving the term dynamics is introduced as having its own meaning, the authors then show that its main component is, also, the soil density. In what concerns the first-degree coefficients in the working speed, the information is very few. In any case, the American standard gives a number of agricultural machines to which the coefficient of the first degree term in the travel speed is nonzero.

The general structure of the draft force, (1) together with the detailed formulas, especially for the static component (Table 1), allow the binding of the draft force, and the mechanical characteristics of the soil (given in terms of the classical mechanics of the continuous media), of the soil-tool interaction data, width, work depth, and working speed. In addition, knowing the humidity dependence of soil mechanical parameters and tool - to - soil interaction parameters, the soil moisture parameter can become an argument of the draft force function. This specification of factors that influence the strength of traction resistance also leads to the idea of multi parametric optimization of the work process.

As far as the optimization of the traction force is concerned, it has very little chance of having optimal points within the range of variables of the function. Minimum or maximum points for draft force are only found on the border of the variance range of the function variables. The static term generally has no extremum points within the usual multidimensional range, except for one more complicated model than that is given in Table 1, the case of the cohesive soil with the rough surface, isolated case, for which an experimental confirmation is difficult. Under these conditions, the optimization of the working process is sought by trying to use other functions involved in the modeling process or by minimizing some combinations of draft force and other functions describing the working process of the soil tillage machines (eg productivity). By any theoretical way optimal points that define an optimal working regime would be obtained, these results should be validated experimentally. Until a satisfactory experimental validation, theoretical outcomes remain within the hypothesis.

An alternative solution is the optimization in relation to parameters of the quality of the work, but this variant is very expensive (it requires a large amount of experimental research), the results having a low generality. Another more complex variant may consider the skidding of the traction means, and compaction of the soil, but this is also very demanding in terms of experimental costs, whether for validation only.

Attempts to obtain better performance formulas for traction resistance force using theoretical-empirical methods based on experimental data have the chance to make estimates slightly more accurate than the analytical formulas in Table 2. However, these attempts to introduce such formulas (theoretically empirical: of the polynomial form, in the form of products of factors at different powers), are affected by the following disadvantages:

- have a profoundly particular character: they are only correct for the soils and the climate in which the experiences whose results have been used, have been conducted. For any other estimate in another geographic area, experiences must be resumed. Experiences should cover the full season as fully as possible, the state of the land being different in different seasons (soil moisture, vegetal remains, crop roots, etc.).
- the physical explanation of the coefficients introduced in the formulas (measurement units and their actual measurement) is deficient, especially in the polytropic functions, where even coefficients with unacceptable dimension, resulting from calculation, can occur.

As a first consequence, it is recommended to use the combinations of dimensional correct parameters in the theoretical - empirical analysis. A second consequence is the continuation of the use of the analytical formulas in various variants, even though some corrections should be made, but they can be easily applied to the coefficients that physically represent the currently used parameters of the soil: cohesion, adhesion, angle of internal friction, soil-steel friction angle, humidity, density etc.

A set of problems are left for study and clarification: the comparative study of the performances of the various formulas for calculating the tensile strength for a particular machine or category of machines, the optimal framework for the characteristics of the whole aggregate for the soil works, the estimation of the conditions in which the American standard can be applied in Europe and many more.

In conclusion, once again it is underlined that the theoretical formulas for estimating the draft force of the soil tillage machinery are consistent and convergent. Their architecture represents a natural development integrated into the physics of the deformable solid. The representative differences are given by the typical ways of describing used by the contemporary physics: the phenomenological approach (*https://en.wikipedia.org/wiki/Phenomenological_model*) (predominantly in early Russian school, subsequently used also in American school) and the theoretical approach (starting from principles and theoretical models of higher rank, preponderant in early American school). The two models converge to the same overall final shape was showned. The differences between them are minor and are based on the local and random structure of the soil and climate. In fact, viewed from the perspective of these categories of models, the formula in the American standard is a phenomenological description, just like the classical formula of the Russian school. However, by identifying it is concluded that the phenomenological coefficients can be expressed in terms of the mechanics of soil, regarded as a deformable solid (continous media). Thus, it is possible to pass from the choice of coefficients in formulas by soil types (light, medium, heavy, etc.), in phenomenological terms, to the characterization of these coefficients by precise soil characteristics (also used in the field of civil constructions, etc.): cohesion, adhesion , angle of internal friction. Formulas thus get a form closer to a theoretical model. In addition to the last parameters of soil moisture and its composition, they allow the introduction of these characteristics into the calculation of estimation and search for optimal working regimes.

As far as possible, it is recommended that all users use all of the traction force computation formulas, even if the data for some of them is computed by conversion, using for example conversion relationships. Particular attention will be paid to the suitabillity of soil characteristics within experimentally admitted limits. Full equivalence through the control and validation of draft force calculation formulas remains a basic objective for the broader work to follow. In these papers, any corrections or adjustments should be studied to harmonize the results of the formulas in Table 2 for each major category of agricultural machinery for soil tillage.

**ACHNOWLEDGEMENTS**

This work was supported by a grant of the Romanian Research and Innovation Ministry, through Programme 1 – Development of the national research-development system, subprogram 1.2 – Institutional performance – Projects for financing excellence in RDI, contract no. 16PFE, and was done by “NUCLEU” Programme, developed with the support of the Romanian Research and Innovation Ministry, project PN 19 10 01 02.

**REFERENCES**

[1] Asmolovsky M.K., Nosnikov V.V., (2014*), Mechanization of forestry work. course design, (Механизация лесохозяйственных работ. курсовое проектирование),* Educational establishment “Belarusian State Technological University", (“Белорусский государственный технологический университет”) Minsk/ Belarus;

[2] Al-Neama A.K.A., Hertzilius T., (2017), Draft forces prediction model for standard single tines by using principles of soil mechanics and soil profile evaluation, *Landtechnik* 72(3), pp. 157–164, Germany;

[3] Al-Suhaibani S.A, Ghaly A.E., (2010), Effect of Plowing Depth of Tillage and Forward Speed on the Performance of a Medium Size Chisel Plow Operating in a Sandy Soil, *American Journal of Agricultural and Biological Sciences,* vol. 5, Issue 3, Science Publications, ISSN Print: 1557-4989, ISSN Online: 1557-4997, pp. 247-255, India;

[4] Deshpande Sh., Shriwal S., Effect of Operational Parameters of Selected Tillage Tools in Soil Bin, *International Journal of Current Microbiology and Applied Sciences,* Vol. 6, no. 6, Excellent Publishers, ISSN: 2319-7706, pp. 1051-1061, India;
[5] Fielke J.M., (1994), Interactions of cutting edge of tillage implements with soil, PhD Thesis, *The University of Adelaide, Waite Agricultural Research Institute*, Glen Osmond/South Australia;
[6] Gill W.R., Vanden Berg G.E., (1968), Soil Dynamics in Tillage and Traction, Agriculture Handbook, no. 316, *U.S. Government Printing Office*, Agricultural Research Service, United States Department of Agriculture (USDA), pp. 14 – 114, Washington/USA;
[7] Ibarra S.Y., (2001), *A model of stress distribution and cracking in cohesive soils produced by simple tillage implements*, PhD Thesis, McGill University Montreal, Canada;
[8] Kezdi, A. (1974). Handbook of Soil Mechanics, vol. 1, Elsevier, ISBN: 9630500884, Amsterdam/ Netherlands;
[9] Krasnicenko A. V., (1964), *Farm Machinery Builder Manual* (*Manualul constructorului de masini agricole)*, Technical Publishing House (Editura Tehnica) Bucuresti / Romania;
[10] Larson L.W., (1964), *Predicting draft forces using model moldboard, plows in agricultural soils*, Retrospective Theses and Dissertations. Iowa State University of Science and Technology, USA;
[11] Letosnev M.N., (1959), *Farm Machinery (Masini Agricole)*, Ministry of Agriculture and Forestry (Ministerul Agriculturii si Silviculturii), State Agro-Forestry Publishing House (Editura Agro-Silvica de Stat) Bucuresti / Romania;
[12] McKyes E., (1985), *Soil Cutting and Tillage*, vol. 7, Elsevier Science, eBook ISBN: 9780444601049;
[13] Obrzud R., Truty, *A, (*revised 31.01.2012), *The hardening soil model - a practical guidebook Z Soil. PC 100701 report,* Switzerland*;*
[14] Owen G.T., (1989), *Subsoiling forces and tool speed in compact soils*, vol. 31, Issue 1, Canadian Society for Bioengineering, Canada;
[15] Prat M., Bisch E., Millard A., Mestat P., Cabot G., (1995), *The modeling of the structures (La modelisation des ouvrages),* Hermes Publishing House (Maison d'édition Hermes), Paris / France;
[16] Sandru A., Badescu M., Sandru L., (1982), *Reduce energy consumption by rational use of agricultural aggregates (Reducerea consumului de energie prin folosirea rationala a agregatelor agricole)* Romanian Writing Publishing House (Editura Scrisul Romanesc), Craiova / Romania;
[17] Sandru A., Popescu S., Cristea I., Neculaiasa V., (1983), *Agricultural machinery exploitation* (*Exploatarea utilajelor agricole)*, Educational and Pedagogical Publishing House (Editura Didactica si Pedagogica), Bucuresti / Romania;
[18] Scripnic V., Babiciu P., (1979), *Agricultural machines* (*Masini agricole)*, Ceres Publishing House (Editura Ceres), Bucuresti / Romania;
[19] Sharifat K., (1999), *Soil Translocation with Tillage Tools*, PhD Thesis, University of Saskatchewan, Canada;
[20] Tecusan N., Ionescu E., (1982), *Tractors and automobiles* (*Tractoare si automobile)*, Educational and Pedagogical Publishing House (Editura Didactica si Pedagogica), Bucuresti / Romania;
[21] Toma D., Neagu T., Florescu I., Lepsi S., (1978), *Agricultural tractors* (*Tractoare agricole)*, Educational and Pedagogical Publishing House, Bucuresti / Romania;
[22] *** ASAE American Society of Agricultural Engineers, (2017), *Agricultural machinery management data*, *ASAE standards*, D497.4, 2017, pp. 373-380, St. Joseph, USA;
[23] *** https://en.wikipedia.org/wiki/Phenomenological_model.

# EXPERIMENTAL RESEARCH ON THE KNIFE BLADES USED TO CUTTING AND SHREDDING FIBROUS FODDER

# *CERCETĂRI EXPERIMENTALE ASUPRA ORGANELOR DE TĂIERE-MĂRUNŢIRE A FURAJELOR FIBROASE*

**Caba I.L.*[1)], Laza E.A.[1)], Constantinescu M.[2)], Radu O.D.[1)], Boiu-Sicuia O.A.[3)], Popescu C.[4)]**
[1)]INMA Bucharest / Romania; [2)]SC INTERMANAGEMENT CONSULTING SRL / Romania; [3)]ICDPP Bucharest / Romania;
[4)]S.C. HOFIGAL Export Import S.A. / Romania
*E-mail: inmatm_caba@yahoo.com*
*DOI: 10.35633/INMATEH-59-29*

***Keywords:*** *cutting shredding organs*

**ABSTRACT**

*In the process of harvesting fibrous fodder an important and negligible requirement is the appropriate shredding of the fiber feed directly or indirectly into the composition of animal feed, whether it be fresh fodder, high moisture or fodder feed or even dried. The degree of comminution of feeding stuffs decisively influences the speed of assimilation by animals of the administered feed, implicitly their weight gain, the profitability of the respective cattle farm and not only. In the paper are presented the possibilities of technically obtaining a finest shredding of fibrous fodder, especially by using multirow knives in the feed channel of self-loading hay trailer. However, these technical solutions also have certain disadvantages in the daily operation of such machines.*

**REZUMAT**

*În procesul de recoltare a furajelor fibroase o cerinţă importantă şi de loc de neglijat este mărunţirea corespunzătoare a furajelor fibroase care intră direct sau indirect în componenţa hranei animalelor, indiferent dacă este vorba de furaje fibroase proaspete, cu un grad de umiditate ridicat sau despre furaje vestejite sau chiar uscate. Gradul de mărunţire a furajelor influenţează în mod hotărâtor viteza de asimilare de către animale a nutreţului administrat, implicit sporul în greutate al acestora, rentabilitatea de funcţionare a fermei respective de bovine şi nu numai. În lucrare se prezintă posibilităţile de a obţine tehnic o mărunţire cât mai bună a furajelor fibroase, cu precădere prin utilizarea a cuţitelor multiple aşezate pe mai multe rânduri în canalul de alimentare ale remorcilor autoîncărcătoare fân. Aceste soluţii tehnice însă prezintă şi anumite dezavantaje în exploatare de zi cu zi ale utilajelor de acest gen.*

## INTRODUCTION

In order to counteract all these shortcomings presented above, we carried out some theoretical research, resulting in a universal knife profile, which has the advantage of general usability.

Its profile is thus conceived from the design stage to meet the requirements of cutting - shredding of all types of green fodder feed used in animal feed in zootechnics, regardless of their degree of humidity.

In the experimental researches we performed a series of cutting - shredding tests on different types and kinds of fibrous feeds in order to establish the correctness regarding the results of the experimental research and the actual shape of the knife obtained from the researches.

For this purpose, we designed and executed a cutting bench at the laboratory, where we used different forms of knives to determine the specific energy needed to cut different types of fibrous feed (*Caba I., 2006; Babinszky L., Halas V., 2019).*

## MATERIALS AND METHODS

In order to carry out experimental laboratory tests to ascertain the usefulness and viability of the projected knife profile, it was necessary to design and execute a test stand where successive, repeated cuts with different shapes and sharpening angles could be performed, where the section of the test samples fodder feed remained constant and measurable at all times (*Ciocârdia C., 1999; Dănilă I., 1981; Neculăiasa V., Dănilă I., 1995*). The actual operation scheme is shown in Figure 1.

Another requirement was ease, simplicity and last but not least the safety of clamping of different shapes of their edges. The basic element of the experimental laboratory tests was the Charpy pendulum (*Dutton A. and Mines R., 2002; Truşculescu M., 2016*), for which we designed and built a special support device for easy gripping of the knives and samples. This support allowed the knives to snap and loosen easily and ensured that they were hardened during the laboratory experiment. The clamping-fastening device of the knife is made up of a metal plate identical in shape to the pendulum profile. Stiffening of this plate (the knife holder) to the pendulum profile was accomplished by the application of four fastening heels welded to the surface of the plate. On the surface of the disc, I have reinforced with electric arc welding four clamping clamps, which serve to stiffen the cutting and grinding blade during the measurements, but also allow for a slight change of the clamp.

Balancing the accessories applied to the surface of the pendulum profile was done with great care, while recording these values. The weight of the initial hammer arm of 2074 g was reached after the knife fastening device was mounted at 2530 g, but the balancing was so carefully chosen that it did not significantly change the center of gravity of the knife.

Another urgent necessity has also been to provide a certain distance between the knife and the hammer, failure to meet this requirement, and the removal of the detached part by cutting from the length of the specimen automatically led to the locking of the cutting knife in the feed material used as the test samples. In order to achieve a proper grip of the feed material specimen and to ensure a constant cutting section throughout the measurements, we designed and made a simple clamping vice, with three rigid walls and a fourth movable. Thus, we ensured a cross section of the constant and measurable specimen. The vise movable wall was operated with a press screw, and the vise supply was possible by completely detaching the movable wall and its support bracket into stiffening screws.

The drawings of the Charpy hammer pendulum are shown in Figure 2, which allows us to easily determine the specific energy consumed in the cutting of the fibrous feed specimen and the technical data related to this device used in the experimental determinations made in the laboratory are as follows:

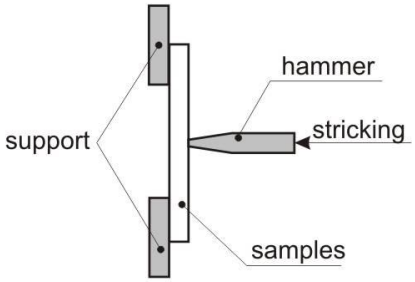


**Fig. 1 - The principle of the test**

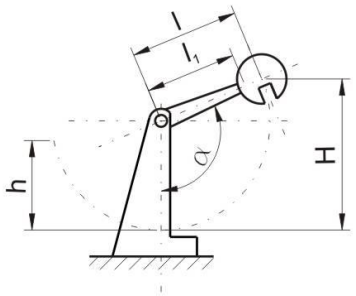


**Fig. 2 - Scheme of Charpy hammer operation**

where:

$l$ - the distance from the axis of rotation - the suspension at the cutting center of the knife blades, in this case $l$ = 0.380 m;

$l_1$ - distance from rotation axis - suspension at the center of gravity, having the following value $l_1$ = 0.335 m;

$d$ - angle of hammer launch, in the present case $\alpha = 130^0$;

$\beta$ - the angle of maximum hammer position after cutting of the specimen, read on the graduated screen of the appliance;

$H$ - the hammer launch height;

$h$ - the height at which the hammer is lifted after cutting the specimen

In the case mentioned above for the equilibrium position of the pendulum hammer, the condition is that:

$$Gl \neq G_1 l_1 \quad (1)$$

where: $G_1$ - the weight of the hammer;

$G$ - the weight of the hammer reduced in the percussion center.

The energy consumed when cutting a fiber feed specimen is determined by calculating the difference between potential potentials of the Charpy pendulum hammer in the initial and final position.

By calculating the heights $H$ and $h$ we obtain:

$$H = l_1 + l_1 \sin(\alpha - 90^0) = l_1 (1 - \cos \alpha) \quad (2)$$

$$h = l_1 - l_1 \cos \beta = l_1 (1 - \cos \beta) \quad (3)$$

of these two relationships, the value of the energy $W$ consumed at the cutting of the fibrous feed specimen results:

$$W = G_1 l_1 (\cos \beta - \cos \alpha) \quad (4)$$

With this cut-off energy calculated with the above relationship, we can easily determine the value of the specific energy used to cut the surface unit:

$$W_S = W/S_O \quad (5)$$

where: $S_O$ - surface area of the fibrous feed material specimen.

Knowing the angular values, the hammer weight and the length from the axis of rotation to the cutting center (values determined in the laboratory experiments), we can obtain the specific energy and cutting energy values for each cut. These calculated and tilted values can also be graphical.

The working procedure in the Charpy hammer-pendulum experiments and the fibrous feed samples were practically carried out as follows:

1. place the indicator needle at zero on the dial with the hammer left in the static equilibrium position;
2. raise the hammer and fasten it to the heel, place the knife in the holder;
3. place the test samples of the fibrous feed material on the support of the apparatus so that one end of it is locked in the vise and the other end is free, measure the dimensions of the samples by means of a caliper, make adjustments with the central screw if it is applicable;
4. the fall occurs;
5. after cutting the samples, stop the hammer and read the values indicated by the needle from the dial;
6. collect the comminuted feed material by repeated cuts into the capsules to determine the moisture content of the samples used.

These tests have been repeatedly carried out for cutters having the cutting angle between $0^0$, $20^0$, $25^0$ and $30^0$ and the cutting edge angle of $20^0$. The sliding cutting angle represents the angular cutting tangent and had the values k = 0.57 for $\alpha = 30^0$; k = 0.46 for $\alpha = 25^0$ and k = 0.36 for $\alpha = 20^0$ (*Krasznicsenko A., 1965; Letoşnev M., 1969*).

The laboratory experiment was performed on samples of fibrous feed material, which is used mainly in livestock breeding for livestock feed. $S_o$ we used lucerne, in the two versions available at the moment, corn - stalk, sunflower and freshly harvested lolium pasture grass and we also made some attempts on dried wheat straw. After each cut, we collected the detached material and proceeded to determine the moisture content of the specimen (*Nosov V., 1988; Szendro P., 2000; Bellus Z., Fenyvesi L., 2016)*.

The fibrous feed material, detached by cutting the knife, was placed in crucibles, weighed, dried in the oven, and then weighed again (*Zaman A., Sagar M., 2018*). The data thus obtained were tabulated. Also in these tables are the values indicated by the needle on the graduated dial, whenever cuts are made. Several determinations were made with each knife profile, precisely to ensure accuracy in the processing and interpretation of the results obtained from experimental laboratory tests.

**RESULTS**

Following experimental laboratory determinations carried out using the Charpy hammer pendulum simulating the actual cutting of the fibrous feeds made by the grinding knives of the furrow-gathering machines during its exploitation, we find that an almost perfect simulation of the phenomena what is happening in reality.

Here, I refer to the grinding process - cutting which is made by knives, existing in a larger or smaller number, inside the feed channel, constructive part of self-loading hay trailers, cutting knives of different types, in function the type of feed, the way of feeding the feed furnace at the moment of penetration into the feed channel, its degree of humidity, the way of laying the knives in the groove, the profile of their cutting line, the angle of sharpening, the material used to make the knife, the frequency sharpening, s.o. Keeping the sharpening angle at $20^0$, we try blades with different angles of bend in order to determine the specific energy when cutting (*Csulak A. and Stoica A., 1968; Gainov N.S., 1985*).

These experimental laboratory tests should indicate the ideal profile of a knife that if we have correctly calculated it should be similar to the one we obtained from the calculations.The fodder materials used for the test specimens are as follows: freshly harvested lucerne; semy dry lucerne; lolium; dry wheat straw; corn stalk; sunflower stem.The results obtained are shown in the tables as follows:

**Table 1**

***Cutting the fresh lucerne samples. Cutting angle knife $0^0$, sharpening angle $20^0$***

| Nr. crt. | Test-bar size (mm /mm) | Angle indicator ($^0$) | Energy needed to cut (J) | Specific energy to cut (J/cm$^2$) | Observation |
|---|---|---|---|---|---|
| 1 | 27*27 | 117 | 1.57 | 0.58 | Tip of the stem with leaves |
| 2 | 27*27 | 117 | 1.57 | 0.58 | |
| 3 | 27*27 | 116 | 1.70 | 0.63 | |
| 4 | 27*27 | 114 | 1.96 | 0.73 | Rods and leaves |
| 5 | 27*27 | 112 | 2.23 | 0.82 | |
| 6 | 27*27 | 113 | 2.09 | 0.78 | |
| 7 | 27*27 | 113 | 2.09 | 0.78 | Rods at the harvesting level |
| 8 | 27*27 | 109 | 2.64 | 0.98 | |
| 9 | 27*27 | 109 | 2.64 | 0.98 | |

**Table 2**

***Cutting the fresh lucerne samples. Cutting angle knife $0^0$, sharpening angle $25^0$***

| Test-bar size (mm /mm) | Angle indicator ($^0$) | Energy needed to cut (J) | Specific energy to cut (J/cm$^2$) | Observation |
|---|---|---|---|---|
| 27*27 | 112 | 2.23 | 0.82 | Tip of the stem with leaves |
| 27*27 | 112 | 2.23 | 0.82 | |
| 27*27 | 111 | 2.36 | 0.87 | |
| 27*27 | 110 | 2.50 | 0.93 | Rods and leaves |
| 27*27 | 110 | 2.50 | 0.93 | |
| 27*27 | 109 | 2.64 | 0.98 | |
| 27*27 | 105 | 3.19 | 1.18 | Rods at the harvesting level |
| 27*27 | 103 | 3.47 | 1.29 | |
| 27*27 | 101 | 3.76 | 1.31 | |

**Table 3**

***Cutting the fresh lucerne samples. Cutting angle knife $0^0$, angle of sharpening $30^0$***

| Nr. crt. | Test-bar size (mm /mm) | Angle indicator ($^0$) | Energy needed to cut (J) | Specific energy to cut (J/cm$^2$) | Obser-vation |
|---|---|---|---|---|---|
| 1 | 27*27 | 104 | 3.33 | 1.23 | Tip of the stem with leaves |
| 2 | 27*27 | 103 | 3.47 | 1.29 | |
| 3 | 27*27 | 103 | 3.47 | 1.29 | |
| 4 | 27*27 | 99 | 4.04 | 1.50 | Rods and leaves |
| 5 | 27*27 | 97 | 4.33 | 1.60 | |
| 6 | 27*27 | 95 | 4.62 | 1.71 | |
| 7 | 27*27 | 94 | 4.62 | 1.76 | Rods at the harvesting level |
| 8 | 27*27 | 94 | 4.62 | 1.76 | |
| 9 | 27*27 | 92 | 5.05 | 1.87 | |

**Table 4**

***Cutting the lucerne lucerne samples. Cutting angle knife $0^0$, sharpening angle $20^0$***

| Test-bar size (mm /mm) | Angle indicator ($^0$) | Energy needed to cut (J) | Specific energy to cut (J/cm$^2$) | Obser-vation |
|---|---|---|---|---|
| 27*27 | 105 | 3.19 | 1.18 | Tip with leaves |
| 27*27 | 104 | 3.33 | 1.23 | |
| 27*27 | 104 | 3.33 | 1.23 | |
| 27*27 | 101 | 3.76 | 1.39 | Rods and leaves |
| 27*27 | 101 | 3.76 | 1.39 | |
| 27*27 | 100 | 3.90 | 1.44 | |
| 27*27 | 98 | 4.19 | 1.55 | Rods at the harvesting level |
| 27*27 | 98 | 4.19 | 1.55 | |
| 27*27 | 96 | 4.19 | 1.66 | |

**Table 5**

***Cutting the semy dry lucerne samples. Cutting angle knife $0^0$, sharpening angle $25^0$***

| Nr. crt. | Test-bar size (mm /mm) | Angle indicator ($^0$) | Energy needed to cut (J) | Specific energy to cut (J/cm$^2$) | Obser-vation |
|---|---|---|---|---|---|
| 1 | 27*27 | 100 | 3.90 | 1.44 | Tip with leaves |
| 2 | 27*27 | 98 | 4.19 | 1.55 | |
| 3 | 27*27 | 99 | 4.04 | 1.50 | |
| 4 | 27*27 | 95 | 4.62 | 1.71 | Strains with leaves |
| 5 | 27*27 | 95 | 4.62 | 1.71 | |
| 6 | 27*27 | 93 | 4.90 | 1.82 | |
| 7 | 27*27 | 92 | 5.05 | 1.87 | Rods at the harvesting level |
| 8 | 27*27 | 90 | 5.34 | 1.98 | |
| 9 | 27*27 | 89 | 5.49 | 2.03 | |

**Table 6**

***Cutting the semy dry lucerne samples. Cutting angle knife $0^0$, angle of sharpening $30^0$***

| Test-bar size (mm /mm) | Angle indicator ($^0$) | Energy needed to cut (J) | Specific energy to cut (J/cm$^2$) | Obser-vation |
|---|---|---|---|---|
| 27*27 | 94 | 4.76 | 1.76 | Tip with leaves |
| 27*27 | 93 | 4.90 | 1.82 | |
| 27*27 | 93 | 4.90 | 1.82 | |
| 27*27 | 92 | 5.05 | 1.87 | Strains with leaves |
| 27*27 | 90 | 5.34 | 1.98 | |
| 27*27 | 90 | 5.34 | 1.98 | |
| 27*27 | 88 | 5.63 | 2.09 | Rods at the harvesting level |
| 27*27 | 88 | 5.63 | 2.09 | |
| 27*27 | 88 | 5.63 | 2.09 | |

**Table 7**

***Cutting the wheat straw samples. Cutting angle knife $0^0$, sharpening angle $20^0$***

| Nr. crt. | Test-bar size (mm /mm) | Angle indicator ($^0$) | Energy needed to cut (J) | Specific energy to cut (J/cm$^2$) | Obser-vation |
|---|---|---|---|---|---|
| 1 | 27*27 | 90 | 5.34 | 1.98 | Rods |
| 2 | 27*27 | 89 | 5.49 | 2.03 | |
| 3 | 27*27 | 89 | 5.49 | 2.03 | |
| 4 | 27*27 | 87 | 5.78 | 2.14 | Rods |
| 5 | 27*27 | 85 | 6.07 | 2.25 | |
| 6 | 27*27 | 86 | 5.92 | 2.19 | |
| 7 | 27*27 | 84 | 6.21 | 2.30 | Rods |
| 8 | 27*27 | 84 | 6.21 | 2.30 | |
| 9 | 27*27 | 82 | 6.50 | 2.41 | |

**Table 8**

***Cutting the wheat straw samples. Cutting angle knife $0^0$, sharpening angle $25^0$***

| Test-bar size (mm /mm) | Angle indicator ($^0$) | Energy needed to cut (J) | Specific energy to cut (J/cm$^2$) | Obser-vation |
|---|---|---|---|---|
| 27*27 | 88 | 5.63 | 2.09 | Rods |
| 27*27 | 86 | 5.92 | 2.19 | |
| 27*27 | 86 | 5.92 | 2.19 | |
| 27*27 | 83 | 6.36 | 2.35 | Rods |
| 27*27 | 82 | 6.50 | 2.41 | |
| 27*27 | 80 | 6.79 | 2.51 | |
| 27*27 | 79 | 6.93 | 2.57 | Rods |
| 27*27 | 79 | 6.93 | 2.57 | |
| 27*27 | 79 | 6.93 | 2.57 | |

**Table 9**

***Cutting the wheat straw samples. Cutting angle knife $0^0$, angle of sharpening $30^0$***

| Nr. crt. | Test-bar size (mm /mm) | Angle indicator ($^0$) | Energy needed to cut (J) | Specific energy to cut (J/cm$^2$) | Obser-vation |
|---|---|---|---|---|---|
| 1 | 27*27 | 83 | 6.36 | 2.35 | Rods |
| 2 | 27*27 | 82 | 6.50 | 2.41 | |
| 3 | 27*27 | 83 | 6.36 | 2.35 | |
| 4 | 27*27 | 81 | 6.64 | 2.46 | Rods |
| 5 | 27*27 | 80 | 6.69 | 2.51 | |
| 6 | 27*27 | 79 | 6.93 | 2.57 | |
| 7 | 27*27 | 79 | 6.93 | 2.57 | Rods |
| 8 | 27*27 | 75 | 7.50 | 2.78 | |
| 9 | 27*27 | 75 | 7.50 | 2.78 | |

**Table 10**

***Cutting the lolium samples. Cutting angle knife $0^o$, sharpening angle $20^0$***

| Test-bar size (mm /mm) | Angle indicator ($^0$) | Energy needed to cut (J) | Specific energy to cut (J/cm$^2$) | Obser-vation |
|---|---|---|---|---|
| 27*27 | 98 | 4.19 | 1.55 | Strains and leaves |
| 27*27 | 97 | 4.33 | 1.60 | |
| 27*27 | 96 | 4.47 | 1.66 | |
| 27*27 | 95 | 4.62 | 1.71 | Strains and leaves |
| 27*27 | 93 | 4.90 | 1.82 | |
| 27*27 | 91 | 5.20 | 1.92 | |
| 27*27 | 89 | 5.49 | 2.03 | Strains and leaves |
| 27*27 | 89 | 5.49 | 2.03 | |
| 27*27 | 88 | 5.63 | 2.09 | |

**Table 11**

***Cutting the lolium samples. Cutting angle knife $0^0$, sharpening angle $25^0$***

| Nr. crt. | Test-bar size (mm /mm) | Angle indicator ($^0$) | Energy needed to cut (J) | Specific energy to cut (J/cm$^2$) | Obser-vation |
|---|---|---|---|---|---|
| 1 | 27*27 | 27*27 | 5.20 | 1.92 | Strains and leaves |
| 2 | 27*27 | 27*27 | 5.49 | 2.03 | |
| 3 | 27*27 | 27*27 | 5.49 | 2.03 | |
| 4 | 27*27 | 27*27 | 5.78 | 2.14 | Strains and leaves |
| 5 | 27*27 | 27*27 | 5.78 | 2.14 | |
| 6 | 27*27 | 27*27 | 5.78 | 2.14 | |
| 7 | 27*27 | 27*27 | 5.92 | 2.19 | Strains and leaves |
| 8 | 27*27 | 27*27 | 5.92 | 2.19 | |
| 9 | 27*27 | 27*27 | 6.07 | 2.25 | |

**Table 12**

***Cutting the lolium samples. Cutting angle knife $0^0$, angle of sharpening $30^0$***

| Test-bar size (mm /mm) | Angle indicator ($^0$) | Energy needed to cut (J) | Specific energy to cut (J/cm$^2$) | Obser-vation |
|---|---|---|---|---|
| 27*27 | 87 | 5.78 | 2.14 | Rods and leaves |
| 27*27 | 85 | 6.07 | 2.25 | |
| 27*27 | 86 | 5.92 | 2.19 | |
| 27*27 | 84 | 6.21 | 2.30 | Rods and leaves |
| 27*27 | 84 | 6.21 | 2.30 | |
| 27*27 | 83 | 6.36 | 2.35 | |
| 27*27 | 82 | 6.50 | 2.41 | Rods and leaves |
| 27*27 | 82 | 6.50 | 2.41 | |
| 27*27 | 82 | 6.50 | 2.41 | |

**Table 13**

***Cutting the fresh corn stalk samples. Cutting angle knife $0^0$, sharpening angle $20^0$***

| Nr. crt. | Test-bar size (mm /mm) | Angle indicator ($^0$) | Energy needed to cut (J) | Specific energy to cut (J/cm$^2$) | Observation |
|---|---|---|---|---|---|
| 1 | 27*27 | 109 | 2.64 | 0.98 | Rods and leaves |
| 2 | 27*27 | 108 | 2.77 | 1.03 | |
| 3 | 27*27 | 108 | 2.77 | 1.03 | |
| 4 | 27*27 | 106 | 3.05 | 1.13 | Rods and leaves |
| 5 | 27*27 | 105 | 3.19 | 1.18 | |
| 6 | 27*27 | 105 | 3.19 | 1.18 | |
| 7 | 27*27 | 101 | 3.76 | 1.39 | Rods and leaves |
| 8 | 27*27 | 100 | 3.90 | 1.44 | |
| 9 | 27*27 | 99 | 4.04 | 1.50 | |

**Table 14**

***Cutting the fresh corn stalk samples. Cutting angle knife $0^0$, sharpening angle $25^0$***

| Test-bar size (mm /mm) | Angle indicator ($^0$) | Energy needed to cut (J) | Specific energy to cut (J/cm$^2$) | Observation |
|---|---|---|---|---|
| 27*27 | 102 | 3.61 | 1.34 | Rods and leaves |
| 27*27 | 101 | 3.77 | 1.39 | |
| 27*27 | 101 | 3.77 | 1.39 | |
| 27*27 | 99 | 4.04 | 1.50 | Rods and leaves |
| 27*27 | 98 | 4.19 | 1.55 | |
| 27*27 | 99 | 4.04 | 1.50 | |
| 27*27 | 98 | 4.19 | 1.55 | Rods and leaves |
| 27*27 | 97 | 4.33 | 1.60 | |
| 27*27 | 97 | 4.33 | 1.60 | |

**Table 15**

***Cutting the fresh corn stalk samples. Cutting angle knife $0^0$, angle of sharpening $30^0$***

| Nr. crt. | Test-bar size (mm /mm) | Angle indicator ($^0$) | Energy needed to cut (J) | Specific energy to cut (J/cm$^2$) | Observation |
|---|---|---|---|---|---|
| 1 | 27*27 | 101 | 3.76 | 1.39 | Rods and leaves |
| 2 | 27*27 | 99 | 4.04 | 1.50 | |
| 3 | 27*27 | 99 | 4.04 | 1.50 | |
| 4 | 27*27 | 97 | 4.33 | 1.60 | Rods and leaves |
| 5 | 27*27 | 96 | 4.47 | 1.66 | |
| 6 | 27*27 | 96 | 4.47 | 1.66 | |
| 7 | 27*27 | 93 | 4.90 | 1.82 | Rods and leaves |
| 8 | 27*27 | 94 | 4.76 | 1.76 | |
| 9 | 27*27 | 93 | 4.90 | 1.82 | |

**Table 16**

***Cutting the fresh sunflower samples. Cutting angle knife $0^0$, sharpening angle $20^0$***

| Test-bar size (mm /mm) | Angle indicator ($^0$) | Energy needed to cut (J) | Specific energy to cut (J/cm$^2$) | Observation |
|---|---|---|---|---|
| 27*27 | 105 | 3.19 | 1.82 | Especially rods and sloppy leaves |
| 27*27 | 103 | 3.47 | 1.29 | |
| 27*27 | 104 | 3.33 | 1.23 | |
| 27*27 | 100 | 3.90 | 1.44 | Especially rods and sloppy leaves |
| 27*27 | 100 | 3.90 | 1.44 | |
| 27*27 | 99 | 4.04 | 1.50 | |
| 27*27 | 98 | 4.19 | 1.55 | Especially rods and sloppy leaves |
| 27*27 | 98 | 4.19 | 1.55 | |
| 27*27 | 95 | 4.62 | 1.71 | |

**Table 17**

***Cutting the fresh sunflower samples. Cutting angle knife $0^0$, sharpening angle $25^0$***

| Nr. crt. | Test-bar size (mm /mm) | Angle indicator($^0$) | Energy needed to cut (J) | Specific energy to cut (J/cm$^2$) | Observation |
|---|---|---|---|---|---|
| 1 | 27*27 | 97 | 4.33 | 1.60 | Especially rods and sloppy leaves |
| 2 | 27*27 | 95 | 4.62 | 1.71 | |
| 3 | 27*27 | 96 | 4.47 | 1.66 | |
| 4 | 27*27 | 95 | 4.62 | 1.71 | Especially rods and sloppy leaves |
| 5 | 27*27 | 94 | 4.76 | 1.76 | |
| 6 | 27*27 | 93 | 4.90 | 1.82 | |
| 7 | 27*27 | 94 | 4.76 | 1.76 | Especially rods and sloppy leaves |
| 8 | 27*27 | 93 | 4.90 | 1.82 | |
| 9 | 27*27 | 91 | 5.20 | 1.92 | |

**Table 18**

***Cutting the fresh sunflower samples. Cutting angle knife $0^0$, angle of sharpening $30^0$***

| Test-bar size (mm /mm) | Angle indicator($^0$) | Energy needed to cut (J) | Specific energy to cut (J/cm$^2$) | Observation |
|---|---|---|---|---|
| 27*27 | 93 | 4.90 | 1.82 | Especially rods and sloppy leaves |
| 27*27 | 92 | 5.05 | 1.87 | |
| 27*27 | 92 | 5.05 | 1.87 | |
| 27*27 | 89 | 5.49 | 2.03 | Especially rods and sloppy leaves |
| 27*27 | 88 | 5.63 | 2.09 | |
| 27*27 | 86 | 5.92 | 2.19 | |
| 27*27 | 87 | 5.78 | 2.14 | Especially rods and sloppy leaves |
| 27*27 | 87 | 5.78 | 2.14 | |
| 27*27 | 85 | 6.07 | 2.25 | |

From the above, it appears that the best results in terms of energy consumption required for the cutting of the fibrous feed samples were made using the blades with a sharpening angle of $20^0$, and in cases where we increased the angle of sharpening at $25^0$ and $30^0$, respectively, we had business with a significant increase in energy consumption when cutting samples.

Next, we retain the most convenient sharpening value obtained by the laboratory tests, the sharpen angle remains at $20^0$, and alter the tilting angle of the knife so as to achieve a truly sliding cutting process. In the same manner as before, we will proceed to the cutting of samples from fibrous feed materials, with the difference that the angle of inclination of the cutting knife changes, taking successive values of $20^0$, $25^0$ or $30^0$. Applying the above, we obtain the following experimental values:

**Table 19**

***Cutting the fresh lucerne samples. Knife with cutting angle $20^0$, sharpening angle $20^0$***

| Nr. crt. | Test-bar size (mm /mm) | Angle indicator($^0$) | Energy needed to cut (J) | Specific energy to cut (J/cm$^2$) | Obser-vation |
|---|---|---|---|---|---|
| 1 | 27*27 | 116 | 1.70 | 0.63 | Tip of the stem with leaves |
| 2 | 27*27 | 114 | 1.96 | 0.73 | |
| 3 | 27*27 | 114 | 1.96 | 0.73 | |
| 4 | 27*27 | 110 | 2.50 | 0.93 | Rods and leaves |
| 5 | 27*27 | 109 | 2.64 | 0.98 | |
| 6 | 27*27 | 104 | 3.33 | 1.23 | |
| 7 | 27*27 | 102 | 3.61 | 1.34 | Rods at the harvesting level |
| 8 | 27*27 | 98 | 4.19 | 1.55 | |
| 9 | 27*27 | 97 | 4.33 | 1.60 | |

**Table 20**

***Cutting the fresh lucerne samples. Cutting angle knife $25^0$, sharpening angle $20^0$***

| Test-bar size (mm /mm) | Angle indicator($^0$) | Energy needed to cut (J) | Specific energy to cut (J/cm$^2$) | Obser-vation |
|---|---|---|---|---|
| 27*27 | 117 | 1.57 | 0.58 | Tip of the stem with leaves |
| 27*27 | 116 | 1.70 | 0.63 | |
| 27*27 | 116 | 1.70 | 0.63 | |
| 27*27 | 111 | 2.36 | 0.87 | Rods and leaves |
| 27*27 | 112 | 2.23 | 0.82 | |
| 27*27 | 110 | 2.50 | 0.93 | |
| 27*27 | 109 | 2.64 | 0.98 | Rods at the harvesting level |
| 27*27 | 107 | 2.91 | 1.08 | |
| 27*27 | 107 | 2.91 | 1.08 | |

**Table 21**

***Cutting the fresh lucerne samples. Knife with cutting angle $30^0$, sharpening angle $20^0$***

| Nr. crt. | Test-bar size (mm /mm) | Angle indicator($^0$) | Energy needed to cut (J) | Specific energy to cut (J/cm$^2$) | Obser-vation |
|---|---|---|---|---|---|
| 1 | 27*27 | 119 | 1.31 | 0.49 | Tip of the stem with leaves |
| 2 | 27*27 | 118 | 1.44 | 0.53 | |
| 3 | 27*27 | 116 | 1.70 | 0.63 | |
| 4 | 27*27 | 115 | 1.83 | 0.68 | Rods and leaves |
| 5 | 27*27 | 115 | 1.83 | 0.68 | |
| 6 | 27*27 | 112 | 2.23 | 0.82 | |
| 7 | 27*27 | 111 | 2.36 | 0.87 | Rods at the harvesting level |
| 8 | 27*27 | 109 | 2.64 | 0.98 | |
| 9 | 27*27 | 109 | 2.64 | 0.98 | |

**Table 22**

***Cutting the lucerne lucerne samples. Knife with cutting angle $20^0$, sharpening angle $20^0$***

| Test-bar size (mm /mm) | Angle indicator ($^0$) | Energy needed to cut (J) | Specific energy to cut (J/cm$^2$) | Obser-vation |
|---|---|---|---|---|
| 27*27 | 106 | 3.05 | 1.13 | Tip of the stem with leaves |
| 27*27 | 105 | 3.19 | 1.18 | |
| 27*27 | 103 | 3.47 | 1.29 | |
| 27*27 | 102 | 3.61 | 1.34 | Rods and leaves |
| 27*27 | 102 | 3.61 | 1.34 | |
| 27*27 | 99 | 4.04 | 1.50 | |
| 27*27 | 98 | 4.19 | 1.55 | Rods at the harvesting level |
| 27*27 | 99 | 4.04 | 1.50 | |
| 27*27 | 98 | 4.19 | 1.55 | |

**Table 23**

***Cutting the lucerne lucerne samples. Cutting angle knife $25^0$, sharpening angle $20^0$***

| Nr. crt. | Test-bar size (mm /mm) | Angle indicator($^0$) | Energy needed to cut (J) | Specific energy to cut (J/cm$^2$) | Obser-vation |
|---|---|---|---|---|---|
| 1 | 27*27 | 108 | 2.77 | 1.03 | Tip of the stem with leaves |
| 2 | 27*27 | 107 | 2.91 | 1.08 | |
| 3 | 27*27 | 106 | 3.05 | 1.13 | |
| 4 | 27*27 | 105 | 3.19 | 1.18 | Rods and leaves |
| 5 | 27*27 | 103 | 3.47 | 1.29 | |
| 6 | 27*27 | 102 | 3.61 | 1.34 | |
| 7 | 27*27 | 100 | 3.90 | 1.44 | Rods at the harvesting level |
| 8 | 27*27 | 98 | 4.19 | 1.55 | |
| 9 | 27*27 | 98 | 4.19 | 1.55 | |

**Table 24**

***Cutting the lucerne lucerne samples. Knife with cutting angle $30^0$, sharpening angle $20^0$***

| Test-bar size (mm /mm) | Angle indicator ($^0$) | Energy needed to cut (J) | Specific energy to cut (J/cm$^2$) | Observation |
|---|---|---|---|---|
| 27*27 | 110 | 2.50 | 0.93 | Tip of the stem with leaves |
| 27*27 | 110 | 2.50 | 0.93 | |
| 27*27 | 108 | 2.77 | 1.03 | |
| 27*27 | 107 | 2.77 | 1.08 | Rods and leaves |
| 27*27 | 104 | 3.33 | 1.23 | |
| 27*27 | 104 | 3.33 | 1.23 | |
| 27*27 | 102 | 3.61 | 1.34 | Rods at the harvesting level |
| 27*27 | 99 | 4.04 | 1.50 | |
| 27*27 | 99 | 4.04 | 1.50 | |

**Table 25**

***Cutting the wheat straw samples. Knife with cutting angle $20^0$, sharpening angle $20^0$***

| Nr. crt. | Test-bar size (mm /mm) | Angle indicator ($^0$) | Energy needed to cut (J) | Specific energy to cut (J/cm$^2$) | Obser-vation |
|---|---|---|---|---|---|
| 1 | 27*27 | 95 | 4.62 | 1.71 | Rods |
| 2 | 27*27 | 94 | 4.76 | 1.76 | |
| 3 | 27*27 | 91 | 5.20 | 1.92 | |
| 4 | 27*27 | 92 | 5.05 | 1.87 | Rods |
| 5 | 27*27 | 90 | 5.34 | 1.98 | |
| 6 | 27*27 | 88 | 5.63 | 2.09 | |
| 7 | 27*27 | 87 | 5.78 | 2.14 | Rods |
| 8 | 27*27 | 87 | 5.78 | 2.14 | |
| 9 | 27*27 | 87 | 5.78 | 2.14 | |

**Table 26**

***Cutting the wheat straw samples. Cutting angle knife $25^0$, sharpening angle $20^0$***

| Test-bar size (mm /mm) | Angle indicator ($^0$) | Energy needed to cut (J) | Specific energy to cut (J/cm$^2$) | Obser-vation |
|---|---|---|---|---|
| 27*27 | 97 | 4.33 | 1.60 | Rods |
| 27*27 | 97 | 4.33 | 1.60 | |
| 27*27 | 95 | 4.62 | 1.71 | |
| 27*27 | 94 | 4.76 | 1.76 | Rods |
| 27*27 | 94 | 4.76 | 1.76 | |
| 27*27 | 93 | 4.90 | 1.82 | |
| 27*27 | 90 | 5.34 | 1.98 | Rods |
| 27*27 | 91 | 5.20 | 1.92 | |
| 27*27 | 90 | 5.34 | 1.98 | |

**Table 27**

***Cutting the wheat straw samples. Knife with cutting angle $30^0$, sharpening angle $20^0$***

| Nr. crt. | Test-bar size (mm /mm) | Angle indicator ($^0$) | Energy needed to cut (J) | Specific energy to cut (J/cm$^2$) | Obser-vation |
|---|---|---|---|---|---|
| 1 | 27*27 | 99 | 4.04 | 1.50 | Rods |
| 2 | 27*27 | 98 | 4.19 | 1.55 | |
| 3 | 27*27 | 97 | 4.33 | 1.60 | |
| 4 | 27*27 | 97 | 4.33 | 1.60 | Rods |
| 5 | 27*27 | 94 | 4.76 | 1.76 | |
| 6 | 27*27 | 94 | 4.76 | 1.76 | |
| 7 | 27*27 | 93 | 4.90 | 1.82 | Rods |
| 8 | 27*27 | 92 | 5.05 | 1.87 | |
| 9 | 27*27 | 92 | 5.05 | 1.87 | |

**Table 28**

***Cutting the fresh corn stalk samples. Knife with cutting angle $20^0$, sharpening angle $20^0$***

| Test-bar size (mm /mm) | Angle indicator ($^0$) | Energy needed to cut (J) | Specific energy to cut (J/cm$^2$) | Obser-vation |
|---|---|---|---|---|
| 27*27 | 110 | 2.50 | 0.93 | Rods and leaves |
| 27*27 | 109 | 2.63 | 0.98 | |
| 27*27 | 108 | 2.77 | 1.03 | |
| 27*27 | 108 | 2.77 | 1.03 | Rods and leaves |
| 27*27 | 105 | 3.19 | 1.18 | |
| 27*27 | 102 | 3.61 | 1.34 | |
| 27*27 | 100 | 3.90 | 1.44 | Rods and leaves |
| 27*27 | 99 | 4.04 | 1.50 | |
| 27*27 | 97 | 4.33 | 1.60 | |

**Table 29**

***Cutting the fresh corn stalk samples. Cutting angle knife $25^0$, sharpening angle $20^0$***

| Nr. crt. | Test-bar size (mm /mm) | Angle indicator ($^0$) | Energy needed to cut (J) | Specific energy to cut (J/cm$^2$) | Observation |
|---|---|---|---|---|---|
| 1 | 27*27 | 111 | 2.36 | 0.87 | Rods and leaves |
| 2 | 27*27 | 110 | 2.50 | 0.93 | |
| 3 | 27*27 | 109 | 2.63 | 0.98 | |
| 4 | 27*27 | 109 | 2.63 | 0.98 | Rods and leaves |
| 5 | 27*27 | 107 | 2.91 | 1.08 | |
| 6 | 27*27 | 106 | 3.05 | 1.13 | |
| 7 | 27*27 | 103 | 3.47 | 1.29 | Rods and leaves |
| 8 | 27*27 | 100 | 3.90 | 1.44 | |
| 9 | 27*27 | 99 | 4.04 | 1.50 | |

**Table 30**

***Cutting the fresh corn stalk samples. Knife with cutting angle $30^0$, sharpening angle $20^0$***

| Test-bar size (mm /mm) | Angle indicator ($^0$) | Energy needed to cut (J) | Specific energy to cut (J/cm$^2$) | Observation |
|---|---|---|---|---|
| 27*27 | 116 | 1.70 | 0.63 | Rods and leaves |
| 27*27 | 114 | 1.96 | 0.73 | |
| 27*27 | 114 | 1.96 | 0.73 | |
| 27*27 | 112 | 2.23 | 0.82 | Rods and leaves |
| 27*27 | 111 | 2.36 | 0.87 | |
| 27*27 | 107 | 2.91 | 1.08 | |
| 27*27 | 105 | 3.19 | 1.18 | Rods and leaves |
| 27*27 | 101 | 3.76 | 1.39 | |
| 27*27 | 100 | 3.90 | 1.44 | |

**Table 31**

***Cutting the fresh sunflower samples. Knife with cutting angle $20^0$, sharpening angle $20^0$***

| Nr. crt. | Test-bar size (mm /mm) | Angle indicator ($^0$) | Energy needed to cut (J) | Specific energy to cut (J/cm$^2$) | Observation |
|---|---|---|---|---|---|
| 1 | 27*27 | 107 | 2.91 | 1.08 | Especially rods and sloppy leaves |
| 2 | 27*27 | 105 | 3.19 | 1.18 | |
| 3 | 27*27 | 103 | 3.47 | 1.29 | |
| 4 | 27*27 | 101 | 3.76 | 1.39 | Especially rods and sloppy leaves |
| 5 | 27*27 | 100 | 3.90 | 1.44 | |
| 6 | 27*27 | 97 | 4.33 | 1.60 | |
| 7 | 27*27 | 97 | 4.33 | 1.60 | Especially rods and sloppy leaves |
| 8 | 27*27 | 95 | 4.62 | 1.71 | |
| 9 | 27*27 | 94 | 4.76 | 1.76 | |

**Table 32**

***Cutting the fresh sunflower samples. Cutting angle knife $25^0$, sharpening angle $20^0$***

| Test-bar size (mm /mm) | Angle indicator ($^0$) | Energy needed to cut (J) | Specific energy to cut (J/cm$^2$) | Observation |
|---|---|---|---|---|
| 27*27 | 110 | 2.50 | 0.93 | Especially rods and sloppy leaves |
| 27*27 | 108 | 2.77 | 1.03 | |
| 27*27 | 109 | 2.63 | 0.97 | |
| 27*27 | 106 | 3.05 | 1.13 | Especially rods and sloppy leaves |
| 27*27 | 105 | 3.19 | 1.18 | |
| 27*27 | 103 | 3.47 | 1.29 | |
| 27*27 | 102 | 3.61 | 1.34 | Especially rods and sloppy leaves |
| 27*27 | 99 | 4.04 | 1.50 | |
| 27*27 | 96 | 4.47 | 1.66 | |

**Table 33**

***Cutting the fresh sunflower samples. Knife with cutting angle 20⁰, sharpening angle 20⁰***

| Nr. crt. | Test-bar size (mm /mm) | Angle indicator (⁰) | Energy needed to cut (J) | Specific energy to cut (J/cm²) | Observation |
|---|---|---|---|---|---|
| 1 | 27*27 | 112 | 2.23 | 0.82 | Especially rods and sloppy leaves |
| 2 | 27*27 | 110 | 2.50 | 0.93 | |
| 3 | 27*27 | 109 | 2.63 | 0.98 | |
| 4 | 27*27 | 109 | 2.63 | 0.98 | Especially rods and sloppy leaves |
| 5 | 27*27 | 106 | 3.05 | 1.13 | |
| 6 | 27*27 | 104 | 3.33 | 1.23 | |
| 7 | 27*27 | 101 | 3.76 | 1.39 | Especially rods and sloppy leaves |
| 8 | 27*27 | 99 | 4.04 | 1.50 | |
| 9 | 27*27 | 99 | 4.04 | 1.50 | |

**Table 34**

***Cutting the fresh sunflower samples. Cutting angle knife 25⁰, sharpening angle 20⁰***

| Test-bar size (mm /mm) | Angle indicator (⁰) | Energy needed to cut (J) | Specific energy to cut (J/cm²) | Observation |
|---|---|---|---|---|
| 27*27 | 104 | 3.33 | 1.23 | Strains and leaves |
| 27*27 | 103 | 3.47 | 1.29 | |
| 27*27 | 102 | 3.61 | 1.34 | |
| 27*27 | 102 | 3.61 | 1.34 | Strains and leaves |
| 27*27 | 99 | 4.04 | 1.50 | |
| 27*27 | 99 | 4.04 | 1.50 | |
| 27*27 | 98 | 4.19 | 1.55 | Strains and leaves |
| 27*27 | 97 | 4.33 | 1.60 | |
| 27*27 | 95 | 4.62 | 1.71 | |

**Table 35**

***Cutting the lolium samples. Cutting angle knife 25⁰, sharpening angle 20⁰***

| Nr. crt. | Test-bar size (mm /mm) | Angle indicator (⁰) | Energy needed to cut (J) | Specific energy to cut (J/cm²) | Observation |
|---|---|---|---|---|---|
| 1 | 27*27 | 107 | 2.91 | 1.08 | Strains and leaves |
| 2 | 27*27 | 105 | 3.19 | 1.18 | |
| 3 | 27*27 | 105 | 3.19 | 1.18 | |
| 4 | 27*27 | 104 | 3.33 | 1.23 | Strains and leaves |
| 5 | 27*27 | 103 | 3.47 | 1.29 | |
| 6 | 27*27 | 100 | 3.90 | 1.44 | |
| 7 | 27*27 | 100 | 3.90 | 1.44 | Strains and leaves |
| 8 | 27*27 | 99 | 4.04 | 1.50 | |
| 9 | 27*27 | 98 | 4.19 | 1.55 | |

**Table 36**

***Cutting the lolium samples. Knife with cutting angle 30⁰, sharpening angle 20⁰***

| Test-bar size (mm /mm) | Angle indicator (⁰) | Energy needed to cut (J) | Specific energy to cut (J/cm²) | Observation |
|---|---|---|---|---|
| 27*27 | 109 | 2.64 | 0.98 | Strains and leaves |
| 27*27 | 109 | 2.64 | 0.98 | |
| 27*27 | 107 | 2.91 | 1.08 | |
| 27*27 | 106 | 3.05 | 1.13 | Strains and leaves |
| 27*27 | 105 | 3.19 | 1.18 | |
| 27*27 | 103 | 3.47 | 1.29 | |
| 27*27 | 103 | 3.47 | 1.29 | Strains and leaves |
| 27*27 | 101 | 3.76 | 1.39 | |
| 27*27 | 100 | 3.90 | 1.44 | |

After a simple analysis, it can be noticed that the specific cutting energy values vary not only depending on the humidity or origin and type of the feed material samples used during the experimental laboratory determinations, but also according to the place where the cutting along the rod the knife sharpening angle, and the degree of inclination of the knife used for cutting, as well as a number of other factors that are not considered in this research phase.

There is a decrease, in some cases even significant, of the value of the specific cutting energy, starting from the base of the stem, to the tip of the stem. This is represented in the graphs below, grouping the values of the specific cutting energy into three value groups, while taking into account the constructive angles of the knife.

The first group is the specific energy values for cutting in the upper area of the feed material rods used as test samples, where the rods are mostly thin, with many leaves, the relative humidity of this part is higher and, last but not least, the rods contain tissues young, soft. In this first group, we can analyze a constructive variant, which is the straight knife variant, where only the angle of sharpening $i_c$ changes, but the angle of inclination of the alpha knife is equal to zero; $\alpha = 0$. Under these conditions, we obtain according to Figure 3. a slow increase in the specific cutting energy values due to the gradual increase in sharpen angle values. In fact, this phenomenon occurs when using uncut knives, blunted due to a high workload. There is also a well-known phenomenon, namely the increase of the specific energy in the cutting of fodder materials with a low humidity, such as the grinding of wheat straw, where the humidity determined during the laboratory experiments did not exceed 6%.

At high relative humidity levels of plants, in the case of semy dry lucerne or corn and sunflower, the cutting-specific energy gets lower values, cuts can be made easier, and hence a number of functional exploitation advantages, lower costs accounted for per kg of harvested forage.

We must also remember that it is very important to choose the material from which the knife is made. Good materials, quality steels are more expensive but resist over time, keep the angle of sharpening longer, their wear is reduced. Poor quality steels cost less, but their use is limited precisely because of repeated regrinding and their premature exit from use (*Caba I. 2006*).

These losses also have to be added to the losses suffered by the company through the non-use, the stagnation of the machinery, mostly due to the increased working capacity with these knives.

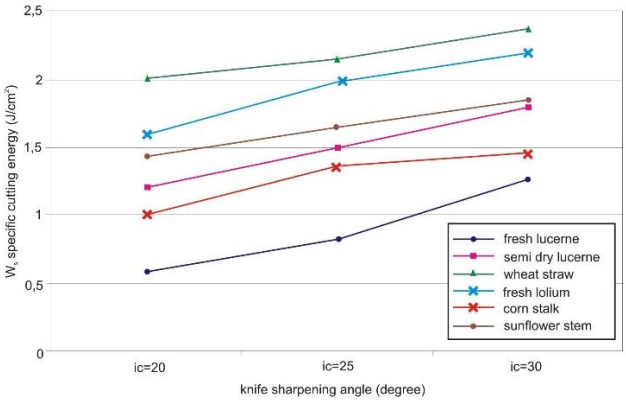


**Fig. 3 - Variation of the specific cutting energy according to the angle of the knife sharpening. The samples contain leaves and rods at the top**

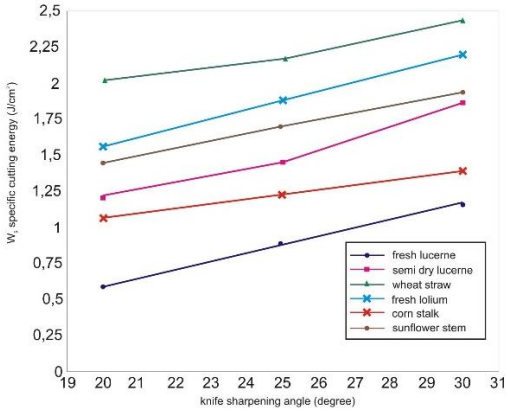


**Fig. 4 - Variation of the specific cutting energy processed according to the angle of the knife sharpening. The samples contain leaves and rods at the top**

Processing the experimental data represented graphically in Figure 3. obtained in laboratory conditions, using the statistics applied in mathematics, we traced the real curves, obtaining some straight lines related to the cuts made on the fodder samples made from different feeds, according to the legend of the Figure 4, with strictly linear variations, has confirmed the initial assumption, that is, the increase in the sharpness values of the cutting-chopping knife, entails increasing the values of the specific energies at cutting, resulting in extreme cases at forces so large that no cutting actually takes place, breaking the samples material, or even stopping the knife in the material of the test specimen used.

The second group, represented by Figure 5, signifies the specific cutting energy values from the middle of the length of the samples, the area where the fiber feed samples has, besides many rods and leaves, in most cases this ratio is substantially equal.

There is a noticeable increase in the specific energy required to cut samples from feed materials to the values recorded at the cutting of samples formed from foliage and stems at the tip of the plants.

This increase is due to the decrease of the foliage and the increase in the number of rods, which have a more pronounced lignin structure in this area of plants. The increase in specific cutting energy expressed as a percentage represents approximately 10-15%, copying the percentage increase expressed as a sharp increase in the knife sharpening angle.

Applying identically, as in the previous case, the statistical processing of the experimental values obtained in the laboratory determinations on fodder samples and graphs, a linear variation, represented in Figure 6 was also obtained. And in the third group, represented by Figure 7. the values of the specific cutting energy in the lower area of the plants near the harvest area, which have been used as cutting material, are found.

This area is rich in lignite, aging, and low-moisture tissue, with a marked lack of leaves. Rods are ubiquitous in this type of samples, the cross section of the stems is much higher compared to the cross section of the stems at the tips, they are characterized by the high resistance to penetration of the knife blade.

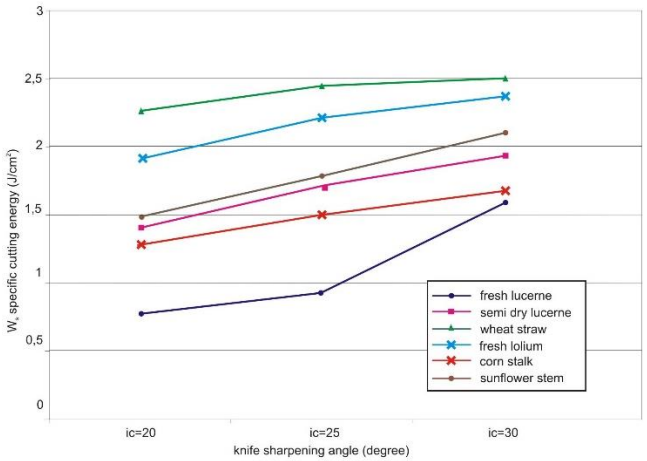


**Fig. 5 - The specific cutting energy variation according to the angle of the knife sharpening. The samples contain leaves and rods at the top**

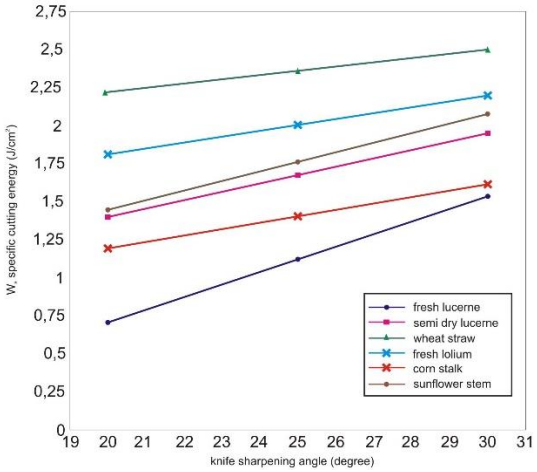


**Fig. 6 - The specific cutting energy variation processed statisticaly according to angle of the knife sharpening. The samples contain leaves and rods at the top**

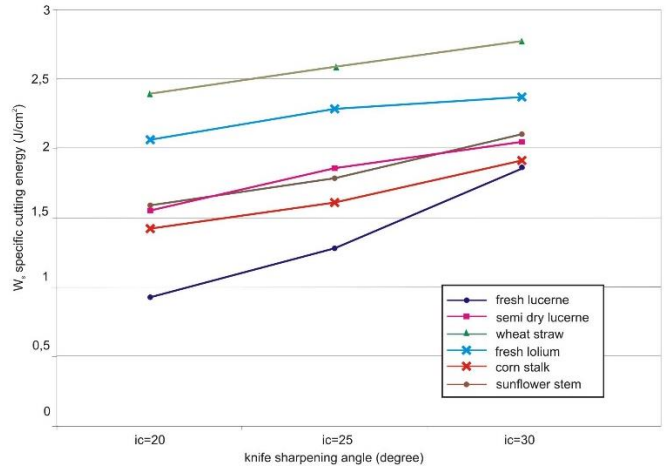


**Fig. 7 - The specific cutting energy variation according to the angle of the knife sharpening. The samples contain leaves and rods at the top**

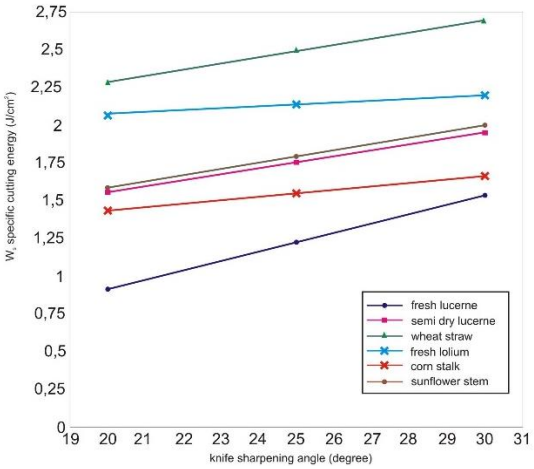


**Fig. 8 - The specific cutting energy variation processed according to the angle of the knife sharpening. The samples contain leaves and rods at the top**

After the statistical processing of the values obtained in the laboratory tests at the cutting of samples from feed materials, we obtain, according to expectations, also a linear variation, but with higher values than in the other two studied cases, phenomenon explained by taking into account the increased resistance of the strains aged, ligninous, with a relatively lower moisture content as compared to the stem tips.

The sharpening and tilting angles of the knife also play an important role in modifying the specific cutting energy values, their correct choice depending on the material of the samples, its moisture content and other factors, may lead to a a significant decrease in the specific energy consumed in the cutting of the feed material used to make the daily feed of livestock from zootechnical farms.

This also results from the laboratory determinations performed on feed specimen specimens, where we modified only the angle of inclination alpha of the knife, while keeping the most convenient angle of sharpening, determined by the experimental tests performed, being $i_c = 20^0$. The specimen in this case, it mostly contains leaves and thin rods from the tip of the forage plant, from which it can be concluded that the cutting is carried out with a lower energy effort, according to Figure 9, we have values that gradually decrease with increasing the angle of inclination of the knife .

This decrease is not very spectacular and cannot be achieved to extreme values because of some conditions of exploitation and design of the shape of the knife and its resistance to daily exploitation. An inclination of more than $30^0$ of the cutting-grinding knife in the laboratory experiment has made it technically impossible for the knife to be executed and used with the projector.

After performing the statistical processing of the obtained experimental data, we can see that this time a linear variation of the specific cutting energies was obtained, according to Figure 10.

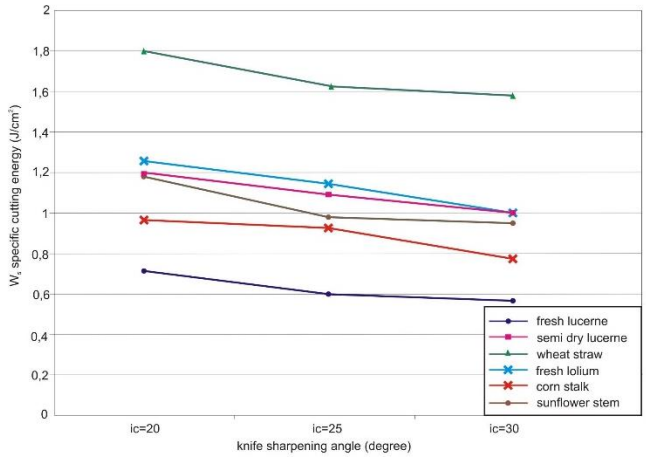


**Fig. 9 - Specific energy variation when cutting the feed material samples from leaves and rods at the plant tip according to the angle of the knife sharpen at $20^0$**

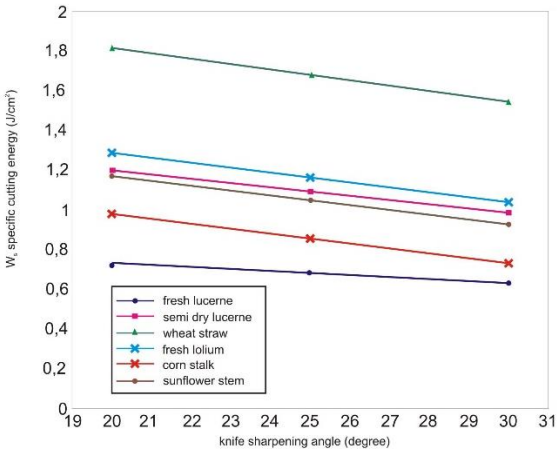


**Fig. 10 - Specific energy variation processed statisticaly when cutting the feed material samples from leaves and rods at the plant tip according to the angle of the knife sharpen at $20^0$**

If the angle of sharpening of the knife $i_c = 20^0$ is maintained, but we vary the angle of inclination, using high-feed feed samples in rods and leaves harvested from the middle of the forage plants where the ratio of rods and leaves is substantially equal, values represented in Figure 11.

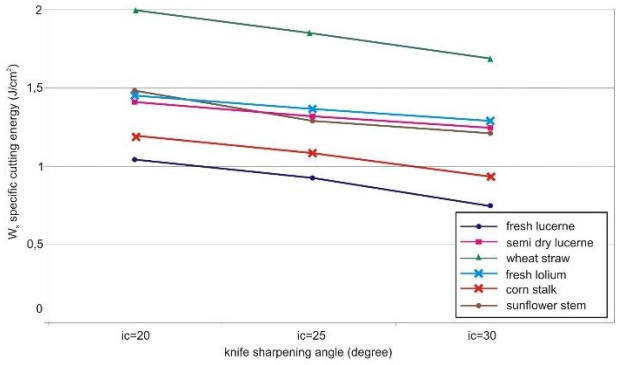


**Fig. 11 - Specific energy variation when cutting the samples feed material with a rod content and leaves in the middle of the plant according to the inclination of the knife $20^0$**

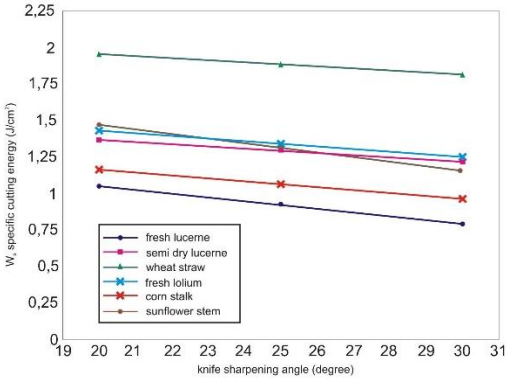


**Fig. 12 - Specific energy variation processed statisticaly when cutting the samples feed material with a rod content and leaves in the middle of the plant according to the inclination of the knife $20^0$**

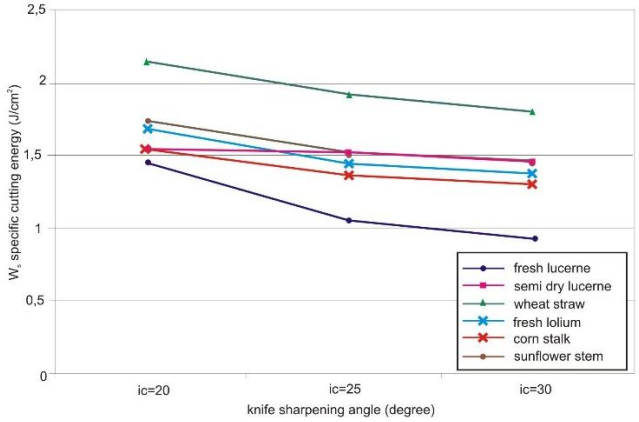


**Fig. 13 - The specific energy variation when cutting the feed material specimen with a high rod content, depending on the inclination of the knife $20^0$**

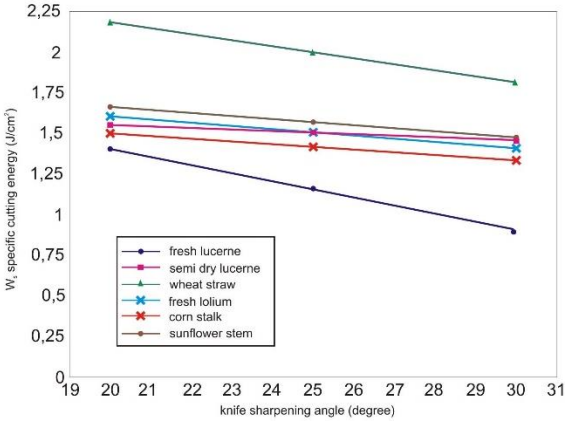


**Fig. 14 - The specific energy variation processed statisticaly when cutting the feed material specimen with a high rod content, depending on the inclination of the knife $20^0$**

As can be seen, a linear decrease in the specific energy required to perform the cutting of the samples was obtained in this case, which is shown in Figure 12.

The last evaluation of the specific cutting energy represented by Figure 13. which is carried out in the case of cuts made on samples of feed materials mainly made of rods with a high content of hard tissues, and in these determinations the value of the angle of sharpening the knife at $i_c$ = $20^0$, but altering the tilting of the knife, alpha, in those three previously known steps, previously described.

After the statistical processing of the experimental data obtained from the cutting of samples of feed materials with a high content of rods and this time a linear variation of the values of the specific cutting energies according to Figure 14 was obtained. There is a relative increase of these values compared to those obtained in the experiments performed on specimens with high leaf or mixed samples (leaves and rods) but after a realistic analysis it was found that this increase is justified by changing the structure of the stems, which are lighter, less water content, and last but not least we notice the total absence or low presence of leaves.

## CONCLUSIONS

Starting from the experimental results obtained from the laboratory research on the fibrous fodder organs, we obtained conclusive results which, after their processing, proved the veracity of the theory presented in the above chapters regarding the design of a cutting knife that is universally usable to the cutting-off of a variety of assortment of fibrous feed, irrespective of the maturity status or the time elapsed since harvesting.

In the first part of the experiments, straight knives were used and we only varied their angles of sharpening, from $20^0$ to $25^0$ or $30^0$, thus obtaining a permanent increase in the specific cutting energy (*Neculăiasa V., Dănilă I. 1995*). In the second part of the experiments carried out in the research laboratory, the angle of the most convenient knife sharpening angle of $20^0$ was chosen, at which the specific cutting energy values were the lowest and we varied this time the angle of inclination of the knife $20^0$, $25^0$ and $30^0$ to the corresponding cutting factor k = 0,36; k = 0.46 and k = 0.57.

Conclusions on the results obtained are as follows:

1) plant humidity significantly influences the consumption of the specific energy of cutting fodder plants;

2) specific cutting energy consumption varies according to the place where the cutting is done, higher at the base of the plants and gradually decreases towards the top of the plant;

3) the angle of sharpening of the knives has an important role in establishing the energy balance at the cutting-shredding of the plants, a small angle of sharpening leads to a specific consumption of low cutting energy, and if the angle of rotation increases, we have a significant increase in the specific energy of cutting;

4) sharpen angle of less than $20^0$ leads to rapid knife cut, resulting in an increase in cutting-specific energy, knife rewind stops, machine productivity decreases, increases operating cost;

5) a solution to this problem is the use of knives made of special materials which do not require repeated re-drilling, but the cost of the special knives would be too high and their equally fragile, which would lead to their frequent change with repeated stops, the loss of precious harvest time;

6) the sharpening angle of more than $30^0$ causes an excessive energy consumption of excessive cutting, especially in the case of drier fodders, because the actual cutting is partially replaced by the breaking of the fibrous feed material, vibrations occur during the cutting and even the clogging of the cutter;

7) a specific energy consumption of balanced cutting and at the same time a minimal wear of the blade cutting edge during the work we obtained at the angle of sharpening of the knife $25^0$, even with a material not recommended for making the knife;

8) while keeping the knife sharpening angle at $20^0$, where the specific cutting energy values were the smallest, we varied the tilting angle of the knife by which we obtained the sliding cut, the cutter energy values gradually decreasing with the increase of the inclination angle knife;

9) the highest cut-off energy values were recorded for the cutting angle $20^0$ and the tilting angle of the knife $20^0$ as well, and the lowest specific cutting energy values for the sharpen angle of $20^0$ and the angle of inclination of the knife of $30^0$;

10) passing over these values causes some knife execution problems, and in extreme cases slipping the material on the cut.

**REFERENCES**


[1] Babinszky L., Halas V., (2019), Innovative feeding, (Innovatív takarmányozás), *Academic Publisher Budapest, Hungary, Online Publication,* ISBN (13) 978-963-454-057-1;

[2] Bellus Z., Fenyvesi L., (2016), *Fodder Production Procedures and Equipment, (A takarmánygyártás eljárásai és berendezései)*, year LVII, nr.2, pp 30-33, Hungary Agricultural Engineering, NAIK MGI, Gödöllő/Hungary;

[3] Caba I., (2006), *Research regarding the improvement of the constructive and functional parameters of the working organs of the self-loading machines of tight and transported fibrous fodder*, Brumar Publishing House, Timişoara / Romania, ISBN (13) 978-976-602-233-3;

[4] Ciocârdia C., (1999), *Basis of experimental research in machine building technology; (Bazele cercetării experimentale în tehnologia construcţiilor de maşini)*, Technique and Pedagogical Pub. House Bucharest /Romania;

[5] Csulak A., Stoica A., (1968), *Contributions to the study of cutting machines with straight drum and knives; (Contribuţii la studiul aparatelor de tocare cu tobă şi cuţite drepte),* Studies and Research of Agricultural Mechanics, Scientific publication, Bucharest/Romania;

[6] Dănilă I., (1981), *Contributions to the analysis of the working process of two-knife cutters (Contribuţii la analiza procesului de lucru al aparatelor de tăiere cu două cuţite),* Scientific publication I. P. Timişoara/Romania*;*

[7] Dutton A., Mines R., (2002), *Analysis of the Hopkinson presure bar loaded instrumeted Charpy test using an inertial modelling tehnique*, A. S. T. M., Philadelphia/USA;

[8] Gainov N.S., (1985), *Determination of elasticity properties of agricultural plants (Determinarea proprietăţilor de elasticitate a plantelor agricole)*, Meh. Ielek. Sot. Sel. P. H. nr.6, Moskow/Russia;

[9] Krasznicsenko A., (1965), *Manual of the of agricultural machinery manufacturer; (Mezogazdasagi gepszerkesztok kezikonyve),* (translation from Russian), Akademiai Publishing House, Budapest /Hungary*;*

[10] Letoşnev M., (1969), *Agricultural machinery, (Maşini agricole),* Agrosilvică P. H. Bucharest/Romania;

[11] Neculăiasa V., Dănilă I., (1995), *Working processes and agricultural machinery for harvesting, (Procese de lucru şi maşini agricole de recoltat)*, A92 Publishing House Iaşi/Romania;

[12] Nosov V., (1988), Researching the working process of thick stem plants (Cercetarea procesului de tăiere a tulpinelor groase), *Traktor i selhozmasinie nr.9. Publishing House, Moskow/Russia*;

[13] Szendro P., (2000), *The examination of the process of chopping, based on the analysis of the slag length distribution (Apritasi folyamat vizsgalata, a szecskahosszusag eloszlasanak elemzese alapjan*), Szent Istvan Agricultural University Publishing House, Godollo/Hungary;

[14] Truşculescu M., (2016), *Study materials. Analyzes and researches. (Studiul materialelor. Analize şi cercetări)*, Litografia Publishing House U. P. Timişoara / Romania.

[15] Zaman A., Sagar M. (2018), *Cutting Edge Technology for Agricultural Sustainability*, New India Publishing Agency- NIPA/India, ISBN-(13) 978-938-797-328-2.

# TARGET DETECTION AND ANALYSIS OF INTELLIGENT AGRICULTURAL VEHICLE MOVEMENT OBSTACLE BASED ON PANORAMIC VISION

/

# 基于全景视觉的智能农用车运动障碍物目标检测与分析

**Wu Weibing** [1]
School of Electrical Engineering, Tongling University, Anhui, Tongling, 244061 / China
*Tel: 15756263199; E-mail: wwb11109@163.com*
*DOI: 10.35633/INMATEH-59-30*

***Keywords:*** *panoramic vision, intelligent agricultural vehicle, motion disorder, watershed algorithm*

## ABSTRACT

*Agricultural automation and intelligence have a wide range of connotations, involving navigation, image, model, strategy and other engineering disciplines. With the development of modern agriculture, intelligent agricultural vehicles are applied in many engineering areas. The operating environment of agricultural vehicles is very complex, especially as they often face obstacles, affecting the intelligent operation of agricultural vehicles. The traditional obstacle detection mostly uses the limited detection algorithm, in the case of which it is difficult to achieve the moving target detection of panoramic vision. In this paper, mean shift algorithm is selected to detect the moving obstacles of intelligent agricultural vehicles, and adaptive colour fusion is introduced to optimize the algorithm to solve the problems of mean shift. In order to verify the effect of the improvement and application of the algorithm, the video image obtained by the intelligent agricultural vehicle is selected for the simulation experiment, and the best combination (- 0.8.0.2) is obtained for the unequal spacing sampling method. In the process of colour selection, the coefficient needs to be adjusted continuously to improve the tracking accuracy of the algorithm. Further it can be seen that when using a variety of different quantitative methods for comparative analysis, the quantitative method of HIS-360 level is determined.*

## 摘要

*农业的自动化和智能化内涵十分广泛，涉及到了导航、图像、模型、策略等多个工程学科，随着现代农业的发展，智能农用车的应用越来越多，由于农用车的运行环境非常复杂，特别是会经常面临障碍物，影响到农用车的智能运行。传统的障碍物目标检测大多采用的是具有局限性的检测算法，难以实现全景视觉的运动的目标检测。此次选取 Mean-Shift 算法来实现智能农用车运动障碍物的目标检测，并引入自适应色彩融合来进行算法优化改进来解决单纯 Meant-Shift 存在的问题。为了验证该算法改进和应用的效果，此次选取智能农用车获取的图像视频进行仿真实验，针对不等间距采样方法得到了最佳组合为（-0.8.0.2），在进行色彩选取时，需要不断调整系数从而提高算法的跟踪准确率。进一步分析可以看出，在采用多种不同量化方式对比分析时，确定了采用 HIS-360 等级的量化方式。*

## INTRODUCTION

With the development of modern science and technology and the progress of industrial technology, the degree of industrialization of agricultural production activities is getting higher and higher. China has a vast territory and a vast agricultural planting area, and also attaches great importance to the development of agricultural machinery industrialization *(Casimero V. et al, 2001)*. However, due to the backward development of China's economy and science and technology, compared with the developed countries, the industrialization level of domestic agricultural machinery is also relatively backward. Among these agricultural machinery tools, agricultural vehicles are one of the most widely used and basic equipment, so they are also the key objects in the research of agricultural mechanization industry in various countries *(Guo-Qing D.U, 2013)*. With the rapid development of computer technology and information technology, people began to combine it with agricultural vehicles. In combination with computer technology and information technology, reasonable algorithm and mechanical operation are used to replace a large number of simple and repeated manual operations, so as to better reduce human demand and effectively improve

[1] *Wu Weibing, As. Lec.*

agricultural work efficiency *(Hou M. et al, 2000)*.

At present, the research on agricultural vehicles mainly focuses on the detection of moving obstacle target of agricultural vehicles, which is one of the key factors for agricultural vehicles to have intelligent automatic driving function. After the automatic driving of agricultural vehicles is realized, the work efficiency of agricultural vehicles can be improved again, and the demand for manpower can be reduced, which is also the key factor for the improvement of agricultural production efficiency in the future *(Huang Y. et al, 1995)*. However, limited by the performance of the technical algorithm, at present, the detection and analysis of the obstacles in the movement of agricultural vehicles is still in the early stage of experimental testing, and the practical application of this technology needs to be further studied.

The Mean-Shift algorithm selected in this paper is an automatic tracking method that can be applied to target dynamic tracking detection. Using this method, we can get the histogram distribution of search window under the weighted values of calculation Kernel function, and use this method to calculate the corresponding window histogram distribution of the current frame. According to the principle of the maximum similarity of the two distributions, along the direction of the maximum increase of search density, we can move to the real location. Through the optimization of the algorithm, we can achieve more efficient, fast and more accurate dynamic target tracking detection.

The main innovations of this paper are as follows: (1) based on panoramic vision, this paper analyses the detection technology of moving obstacle of intelligent agricultural vehicles from multiple angles, uses the unique technical advantages of panoramic vision to comprehensively improve the detection ability of moving obstacle of agricultural vehicles, and optimizes the detection technology, and demonstrates the results (2) based on the mean shift algorithm, the optimization and improvement can effectively solve the problem that the target is easily lost when the background colour and pixel colour are similar, making the target more prominent.

There are four parts in this paper, the second part is about the analysis of the research status of the intelligent agricultural vehicle full view obstacle detection and target tracking detection methods at home and abroad; the third part is to analyse the principle and shortcomings of mean shift algorithm, and improve the shortcomings of the algorithm, considering the background colour and colour fusion, colour space, etc.; the fourth part is to put this algorithm into consideration. The algorithm is applied to the panoramic vision system of obstacle detection of intelligent agricultural vehicles, and the effectiveness and practicability of the algorithm are known through simulation analysis.

**State of the art**

Proposing a method of moving target detection and tracking for autonomous navigation of agricultural vehicles. Using panoramic vision for target tracking detection has the advantage of no blind area detection, and effectively solves the problem of overlapping in the process of target tracking. The specific operation is to first collect multiple images for panoramic evaluation, and automatically detect and track moving objects based on the kernel function algorithm of segmented image. Through application analysis and research, it can be seen that the memory consumption of the improved algorithm is reduced by 66% compared with the traditional kernel function algorithm, and the algorithm speed is increased by 35% *(Khalil S.M.S. et al, 2006)*. Aiming at the inertial navigation error of agricultural machinery, accurate modeling and compensation were made, thus extending the positioning working time and building the dynamic model of agricultural machinery *(Li Q. et al, 2010)*. Putting forward a method of obstacle detection and avoidance of AGV based on binocular vision. In the process of obstacle detection, put forward an algorithm of obstacle information acquisition based on frame subtraction, so as to realize the dynamic and static detection of obstacles. The result shows that the algorithm has good reliability, relatively small error, and further introduces fuzzy Algorithm, which verifies the feasibility and effectiveness of this method *(Min W. et al, 1999)*. Proposing a general method and framework for vehicle and pedestrian detection and tracking based on deep learning, which makes full use of depth information sources and local patterns to generate robust road vehicle and pedestrian recognition and detection. The algorithm has good robust performance and can identify the possible vehicles and pedestrian obstacles on the road *(Noguchi N, 2018)*. Based on the unsupervised deep learning method, *Rozsa et al*. proposed the problem of urban scene monitoring and obstacle tracking. They designed an innovative hybrid encoder and further proposed an effective method of obstacle location estimation and tracking based on scene density *(Rozsa Z. et al, 2018)*. *Teng Z.Q. et al.* fully considered the specific conditions of the road and reduced the workload of test data and preparation as much as possible, and designed an automatic hypothesis assistant system based

on stereo vision algorithm *(Teng Z.Q. et al, 2009)*.

*Tiemin Z. et al* proposed a road obstacle detection method based on light insensitive features, conducted experiments using image sequences collected under different light conditions, and verified the effectiveness of the method *(Tiemin Z. et al, 2015)*.

The detection and analysis technology of agricultural vehicle moving obstacle has developed to the present and a large number of excellent research results have appeared. The detection and analysis technology of agricultural vehicle moving obstacle has been improved for several generations, but after all, the detection and analysis technology of agricultural vehicle moving obstacle is a new product, in the background of rapid development, it also needs rapid development. To carry out the development of agricultural vehicles, how to improve the detection and analysis technology of moving obstacles of agricultural vehicles is an urgent matter *(Wang L. et al, 2015)*. Only further research on the detection and analysis technology of moving obstacles of agricultural vehicles can provide a solid foundation for the development of agricultural vehicles and meet the basic requirements of modern agricultural production demand *(Wang L. et al, 2019)*. Therefore, based on panoramic vision, this paper analyses the moving obstacle detection of intelligent agricultural vehicles, improves the moving obstacle detection and analysis technology of agricultural vehicles, comprehensively improves the working efficiency of agricultural vehicles, and improves the moving obstacle detection and analysis technology of agricultural vehicles.

## MATERIALS AND METHODS

### Mean shift algorithm

Mean shift algorithm is a common algorithm in semi-automatic tracking algorithm, which needs to determine the search window w manually in order to determine the moving target. Its specific working principle is to calculate the distribution of W histogram under the weight of kernel function, and move it to the real position of target along the maximum direction of density increase according to the principle of maximum distribution similarity. When the probability density function is used to detect moving objects, it is difficult to estimate the continuous point density function effectively based on the sample observation method in the small area of continuous points. If we set the dimension $d$ of a space and there is a point $x$ in the current space, then we can calculate the estimated density probability value of this point:

$$\hat{f}(x)=\frac{1}{n}\sum_{i=1}^{n}K_H(x-x_i) \tag{1}$$

$$K_H(x)=|H|^{-\frac{1}{2}}K\left(|H|^{-\frac{1}{2}}x\right) \tag{2}$$

In the above formula, $d\times d$ broadband matrix is represented by $H$, the use of this matrix can greatly improve the flexibility of estimation and ensure that it has different width, but it will become more complex. In this case, it is necessary to consider that the broadband matrix is modified to the form of proportional unit matrix, i.e. $H=h^2I$, and the formula (1) is modified to:

$$\hat{f}(x)=\frac{1}{nh^d}\sum_{i=1}^{n}K\left(\frac{x-x_i}{h}\right) \tag{3}$$

In Figure 1, the real ink point in the centre is the centre of the kernel function. The white dots around the centre are all sample points. The offset of the centre point is indicated by arrows. The average offset will point towards the direction with higher sample point density, which is the gradient direction of the function. It can be seen that the direction of mean shift vector offset is the direction of density gradient. The closer it is to the centre of kernel function, the more important the estimation characteristics of sampling points are.

After the mean shift vector is introduced, the central point of kernel function will gradually converge to the point with the highest density, and the estimated density of this point is 0. The mean shift vector step size will be larger in the region of no interest features, and smaller in the region of interest, so the step size will

decrease with the reduction of the distance from the maximum density, which shows that the mean shift algorithm belongs to an adaptive gradient rise algorithm.

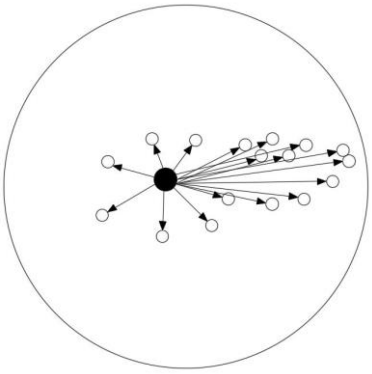

**Fig. 1 - Mean shift vector diagram**

Through further analysis, we can see that there are many factors that affect the convergence speed of mean shift algorithm. If the division of gray level is more detailed, the calculation speed of the algorithm is slower, but the corresponding anti-interference ability and tracking effect are better. If the gray level is not divided in detail, its anti-interference ability and tracking effect will also be reduced. The size of the window will also have an impact on the tracker broadband *(Zhang J. et al, 2013)*. Without considering the time-consuming factor, the larger the window, the slower the calculation speed, but the larger the tracking broadband. It can be seen from the comprehensive analysis that the mean shift algorithm has a great advantage in application, and its calculation is relatively low, so it can be used for real-time tracking when the target area is known. In addition, it is more convenient to be integrated as other algorithms and a single module, even if there is rotation, deformation and edge occlusion of the target, it also has low sensitivity.

However, mean shift algorithm has many shortcomings in application. If the moving speed of the target in the detection environment is faster, there may be overlapping areas between two adjacent frames, and the target may be converged to the background with similar colour distribution, not in the scene. On the other hand, mean shift algorithm is mainly used to select colour features for analysis, which is insensitive to deformation and rotation *(Zhong D. et al, 2014)*. Although the introduction of unimodal kernel function can make the pixels far away from the centre give smaller weight, so it can have better robustness. However, when the area of the target is occluded in a large proportion, it will lead to the failure of mean shift algorithm, which cannot track the target.

**Optimization and improvement of mean shift algorithm**

In view of the problem of operation speed in mean shift algorithm, we can see that, when collecting data information in the moving target area, is the speed can be easily limited to the local ashing degree, which needs to be improved. If the gray level is set to m, the m value directly affects the speed and tracking effect of the whole algorithm. If the gray space only considers the colour, then the brightness change will make the whole algorithm very sensitive to it. All experiments must be based on the condition that the brightness condition is stable. There will be loss of colour information in the process of converting RGB to gray space, so it is necessary to optimize and improve on the original basis and adopt RGB three primary colours quantization. After quantizing the RGB three primary colours collected in panoramic image, the target eigenvalues of three colour components are calculated, and the weighted average value is calculated. Although this method will affect the calculation speed to a certain extent due to the calculation of three target characteristics, it can significantly improve the tracking efficiency. When RGB quantization and grayscale quantization are used for colour quantization, the colour space contains colour information and brightness information, and the change of brightness will directly affect the colour. For the same target, when its brightness changes, the target characteristics will change correspondingly. This kind of change has little influence on the target features with big difference between the target colour and background colour, but has great influence on the tracking results with small difference between the background colour and the target colour. To solve this problem, this colour space model should be introduced to improve colour quantization. $H$ represents chromaticity and does not contain brightness information in target features, so it can deal with the above problems well.

For the target with unbalanced length and width, if the selected template is elliptical, if the target is rotated, it will inevitably lead to the failure of target tracking due to the introduction of background area in the template area. Therefore, it is necessary to propose a tracking method based on the statistical characteristics of the target. Unlike the conventional method, it uses the horizontal and vertical second-order target. The rotation and tracking of the target are realized by the relationship between the moment and the angle of its axis of symmetry. Although this method can effectively solve the adverse effect of target rotation, it has a high requirement for target shape combination. It is required that the target shape must be symmetrical, so this method is limited in application. All are shown in Figure 2 and 3.

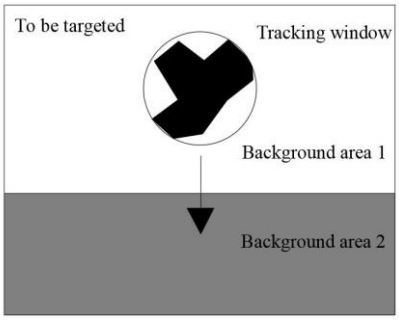


**Fig. 2 - Irregular shape target tracking graph**

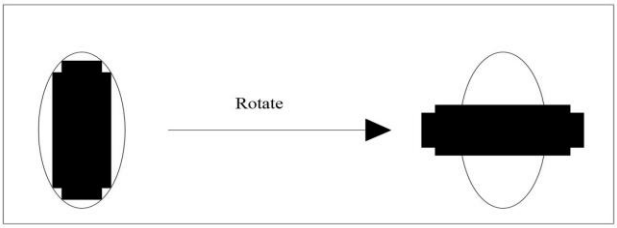


**Fig. 3 - Long and wide unbalanced target tracking**

## RESULTS

### The effect of obstacle target tracking in the process of intelligent agricultural vehicle movement

In order to verify the application effect of the proposed adaptive colour fusion mean shift algorithm in intelligent agricultural vehicles, the images and videos obtained by intelligent agricultural vehicles are selected for simulation experiments. The whole image in the target area of the image is taken as the background. In order to reduce the computation, the unequal interval sampling method based on the large background is adopted. The polar coordinates of the central point of the target are constructed to represent the image sampling process, and the target area of three times is taken as the boundary. The polar radius in this area is three-pixel step-by-step, while the polar radius outside the area is nine-pixel step-by-step. The sampling angle is 0.1rad step. See Figure 3, figure 4 and figure 5 for the core histogram after the fusion of $H$ and $S$ weights, where $S$ stands for saturation.

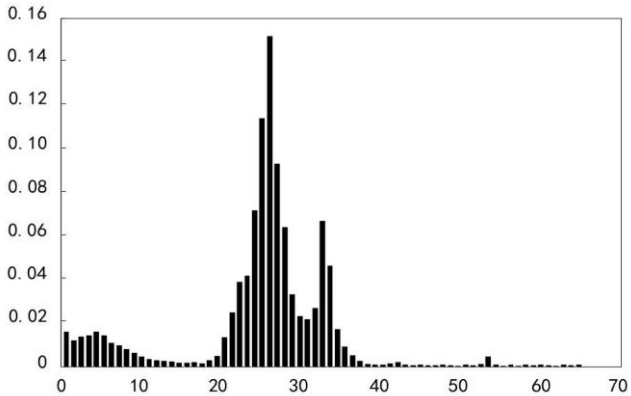


**Fig. 4 - Background full sampling histogram**

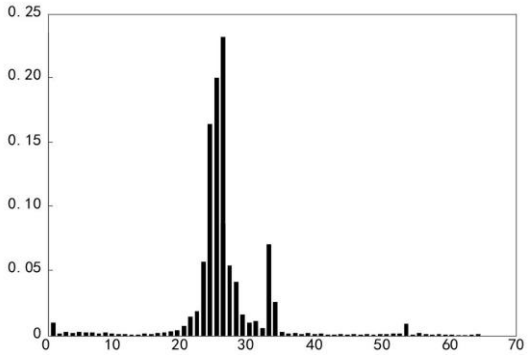


**Fig. 5 - Three times target area histogram**

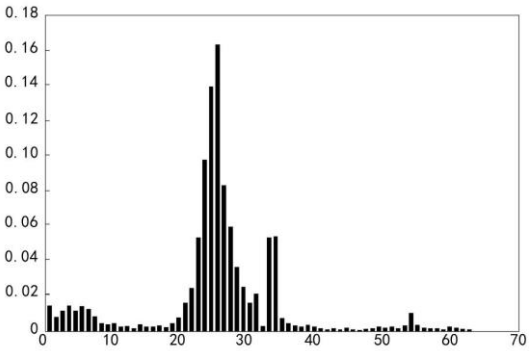


**Fig. 6 - Sampling histogram with unequal spacing**

From the analysis in the figure, it can be seen that the sampling method with unequal spacing can take into account the global characteristics of the image; on the other hand, it can also reflect the near-range colour characteristics around the target, which shows that this method can effectively obtain the colour characteristics around the target. Further processing with this method can calculate the BH value of each group of coefficients. The specific results are shown in Table 1. It can be seen from table 1 that the best combination is (- 0.8, 0.2).

**Table 1**

**Better fusion coefficient and HH value**

| **BH** | 1 | 2 |
|---|---|---|
| **0.362154** | -0.8 | 0.2 |
| **0.365487** | -0.8 | 0.1 |
| **0.367854** | -0.7 | 0.1 |
| **0.367458** | -0.9 | 0.3 |

It can be seen from the process of colour selection that the target and background can be distinguished better within the background range of feature selection. With the change of time, the background is also changing. The best colour fusion weight initially selected may not be suitable for the current frame, which requires adjustment of the weight. Using the above method to recalculate the BH value of all coefficient combinations will not only take longer time, but also seriously affect the real-time performance of the tracking algorithm. Therefore, it is necessary to adjust the coefficients to improve the accuracy of tracking. A coefficient adaptive adjustment neighbourhood method is proposed.

**Panoramic application effect of improved mean shift algorithm**

For a set of colour fusion coefficients $\omega_1, \omega_2$ , set the step size to 0.1, and the corresponding combination of colour fusion coefficients and a group of fusion coefficients adaptively adjust the neighbourhood L. When tracking the initial frame, a group of fusion coefficients which can distinguish the tracking target and the background region of the target are selected by the method of colour fusion. With similar objects approaching or background changing, the original fusion coefficient may not be the best fusion coefficient.

Table 2 shows the optimal colour fusion coefficient and corresponding BH coefficient of 7 consecutive frames obtained by an intelligent agricultural vehicle.

**Table 2**

**Optimal Image Fusion coefficient and BH coefficient in Video sequence**

| BH | $\omega_1$ | $\omega_2$ |
|---|---|---|
| **0.063254** | 0.3 | 0.8 |
| **0.062456** | 0.2 | 0.9 |
| **0.075842** | 0.2 | 0.8 |
| **0.125147** | 0.2 | 0.8 |
| **0.127654** | 0.3 | 0.8 |
| **0.114875** | 0.2 | 0.9 |
| **0.090424** | 0.1 | 0.9 |

From the data in the table, it can be seen that the optimal fusion coefficient of continuous images in a group of video sequences obtained by intelligent agricultural vehicles is mutual domain. The reason is that if the background changes slowly, then the optimal fusion coefficient will not jump in this case, and the original fusion coefficient can be adaptively adjusted to be searchable in the domain. Firstly, the target is selected, the optimal colour fusion coefficient corresponding to the initial frame is calculated, then the next frame image is collected, and the latest target position is obtained after the target is automatically tracked by mean shift algorithm. After calculating the BH coefficient of the adaptive colour fusion domain element of the new target, the core histogram of the target is obtained and the next image is collected. It has many advantages to choose the domain as the adaptive adjustment range. It changes continuously in the process of target and background tracking. This change is not sudden. The domain of the previous frame as the search range can better suppress the feature drift. From the further analysis in Table 3, it can be seen that the experimental results obtained by using the adaptive adjustment in the field are very reasonable.

In order to achieve better tracking efficiency, we set up a variety of different quantization methods to find the best one. We compare and analyse the time consumed by tracking operation and tracking results, as shown in the following table:

**Table 3**

**Comparison Table of tracking results under different quantitative methods**

| **Quantization method** | HIS 360 | HIS 60 | RGB 32 | Gray 64 | Degree 16 |
|---|---|---|---|---|---|
| **Operation time (ms)** | 91.8 | 90.4 | 88.7 | 87.2 | 85.3 |
| **Tracking rate (%)** | 31.18 | 28.47 | 35.22 | 32.19 | 26.14 |

From the analysis in the table, it can be seen that the higher the level of quantization method is, the higher the tracking rate is, but the lower the operation speed is. The colour space quantization method of HIS-360 can achieve better operation speed and target tracking effect, so in the process of moving target tracking, it is best to use the quantization method of his360 level.

## CONCLUSION

In the running process of intelligent agricultural vehicles, the tracking and detection of all kinds of targets is a dynamic process. The traditional static image tracking and detection algorithm is difficult to meet the use needs. This time, based on the mean shift tracking algorithm for optimization and improvement, first from the colour space to get different colour space differences, analysis of the mathematical principle of mean shift vector is made. Since there are many problems in the tracking algorithm, especially the problem that the target colour is similar to the background colour, which is easy to cause the target loss, an improved algorithm based on adaptive colour fusion is proposed. This method of target tracking considering background will analyse and study the background of target area, so as to highlight the target and effectively solve the problem of similar colour. In order to verify the

related performance of the algorithm, the images collected by the intelligent agricultural vehicle in the process of operation are selected for simulation verification and analysis. Through this analysis, the accuracy, real-time and rapidity of the improved algorithm are verified. In this study, the optimization of mean shift algorithm is improved, which can be applied to the detection of obstacles in intelligent agricultural vehicles, but there are still some deficiencies in the detection of obstacles in panoramic vision.

**ACKNOWLEDGEMENT**

The work was financially supported by Key project of Natural Science Research in 2017 Anhui Province Department of Education "Research on New Dynamic Voltage Restorer Based on Flywheel Energy Storage", Project approval number (KJ2017A474); and Demonstration project of massive online open course (MOOC) in 2018 Anhui Provincial Department of Education provincial-level quality engineering "Analog electronic technology foundation", Project approval number (2018mooc012).

**REFERENCES**

[1] Casimero V., Nakasuji F., Fujisaki K., (2001), The influences of larval and adult food quality on the calling rate and pre-calling period of females of the cotton bollworm, Helicoverpa armigera Huebner (Lepidoptera: Noctuidae). *Applied Entomology & Zoology,* Vol.36, Issue 1, Japan, pp.33-40;

[2] Guo-Qing D.U., (2013), Discussion on New Sensor Technology for Automatic Monitoring of Bridge Structure Deflection. *Transportation Standardization,* Issue 6, Beijing/China, pp.28;

[3] Hou M., Sheng C., (2000), Effects of adult feeding on reproduction of the cotton bollworm female moth. *Acta Ecologica Sinica,* Vol.20, Issue 4, Beijing/China, pp.601-605;

[4] Huang Y., Zhou Z., Dang D., (1995), Studies on the male sex pheromone of cotton bollworm, Heliothis armigera. IV. The EAG response of cotton bollworm to female and male sex pheromone components. *Journal of Hunan Agricultural University*, Vol.21, Issue 5, Hunan/China, pp.458-463;

[5] Khalil S.M.S., Anspaugh D.D., Roe R.M., (2006), Role of juvenile hormone esterase and epoxide hydrolase in reproduction of the cotton bollworm, Helicoverpa zea. *Journal of Insect Physiology,* Vol.52, Issue 7, USA, pp.669-678;

[6] Li Q., Wang X., Zhang Q., (2010), Remote Wireless of Sensor Networks Technology Applying in Intelligence Irrigation Monitoring. *Journal of Agricultural Mechanization Research*, Vol. 3, Heilongjiang/China, pp.182-188;

[7] Min W., Jin C., Kangde Y., (1999), Application of grey theory in predicting methotrexate loaded nanocapsules long period release in vitro. *Chinese pharmaceutical journal,* Issue 9, China, p.12;

[8] Noguchi N., (2018), Agricultural vehicle robot. *Journal of Robotics and Mechatronics,* Vol.30, Issue 2, Japan, pp.165-172;

[9] Rozsa Z., Sziranyi T., (2018), Obstacle prediction for automated guided vehicles based on point clouds measured by a tilted LIDAR sensor. *IEEE Transactions on Intelligent Transportation Systems,* Vol.19, Issue 8, USA, pp.2708-2720;

[10] Teng Z.Q., Zhang Q.W., (2009), Determinants of male ejaculate investment in the cotton bollworm Helicoverpa armigera: mating history, female body size and male age. *Physiological Entomology,* Vol.34, Issue 4, England, pp.338-344;

[11] Tiemin Z., Huihui L., Dawei C., (2015), Agricultural vehicle path tracking navigation system based on information fusion of multi-source sensor. *Transactions of the Chinese Society for Agricultural Machinery,* Vol.46, Issue 3, China, pp.37-42;

[12] Wang L., Chen Y., Ma W.H., (2015), Effects of Methoprene on Female Reproduction, Longevity and F1 Progeny Development in the Cotton Bollworm Moth Helicoverpa armigera (Hübner) (Lepidoptera: Noctuidae). *African Entomology,* Vol.23, Issue 1, South Africa, pp.157-165;

[13] Wang L., Lan Y., Zhang Y., (2019), Applications and Prospects of Agricultural Unmanned Aerial Vehicle Obstacle Avoidance Technology in China. *Sensors,* Vol.19, Issue 3, Switzerland, pp.642;

[14] Zhang J., Ji-Hong M.A, Yang-Cheng X.U., (2013), Migration behaviour of cotton bollworm in Xinjiang of Northwest China based on the ovarian development characteristics of adult females. *Chinese Journal of Ecology,* Issue 6, Liaoning/China, pp.9;

[15] Zhong D., Tong X., (2014), Application research on hydraulic coke cutting monitoring system based on optical fibre sensing technology. *Transactions of the Chinese Society for Agricultural Machinery,* Vol.4, Issue 2, China, pp.147-151.

# MODELLING AND MEASUREMENT OF A PHOTOVOLTAIC CELL ARRAY MAXIMUM POWER POINT TRACKING SYSTEM FOR GREENHOUSE
# /
# 用于大棚光伏电池矩阵的最大功率点跟踪建模与测量

**Liming Wei[1)], Jinxin Luo[1)], Boheng Li[1)], Xiujuan Guo[1)], Bin Li* [1, 2 )1]**
[1)] Institute of Electrical & Computer, Jilin Jianzhu University, Changchun 130012, P.R. China;
[2)] College of Computer Science and Technology, Jilin University, Changchun 130012, P.R. China
*Tel: +86-043184566184; E-mail: 870731919@qq.com*
*DOI: 10.35633/INMATEH-59-31*

***Keywords:*** *PV cell array, MPPT, power prediction algorithm, fuzzy control algorithm*

**ABSTRACT**

*Maximum power point tracking (MPPT) strategy has been performed by experimental simulation and measurement in order to minimize the energy loss for photovoltaic greenhouse projects. Calculations and simulation of power prediction algorithm were carried out for obtaining the suitable parameters and duty cycle of the fuzzy control algorithm, to modulate output power in real-time. Experiments were carried out to evaluate the performance by using simulation and measurement involving corresponding circuits. Results of experiments demonstrate that the proposed method in this paper can achieve quicker response and less power loss than traditional method. The proposed algorithm can be adopted and optimized by carrying out further experiments for increasing the efficiency of solar energy utilization.*

**摘要**

*为了使光伏温室项目的能量损失最小化,通过实验仿真和测量来实现最大功率点跟踪策略。研究中采用了功率预测算法和模糊控制算法相结合的方法。为能实时调节输出功率，进行功率预测计算和仿真，得到模糊控制算法的合理参数并输出合适的占空比，以实现功率最大化。并通过对相应电路的仿真和测量，对其性能进行实验评价。实验结果表明，本文提出的方法比传统方法具有更快的响应时间和更小的功耗。为提高太阳能利用效率，本文提出的算法可以通过进一步的实验加以采用和优化。*

## INTRODUCTION

The development and utilization of photo-voltaic (PV) power generation in agricultural greenhouse is a trend in recent years. The solar energy can provide suitable temperature and environment for crops and it is also a supplement to electricity consumption in agricultural greenhouse *(Maher A., 2016; Dinesh H., 2016; Hassan G.E., 2016)*. For example, the electric quantity required by the ventilation and heating in the greenhouse, the illumination in the shed and the electricity utilization of the crop irrigation can be powered by solar electricity. The distribution of the electric energy obtained by the photo-voltaic power generation is carried out also realizing circular ecological agriculture, with high efficiency of science and technology *(Li C., 2017; Rubio-Aliaga A., 2019; Ju YT., 2019; Jones M., 2015)*.

Photo-voltaic cell is usually composed of photo-voltaic arrays. Since the material of the photo-voltaic cell is generally crystalline silicon, the power generation efficiency can only reach about 18% *(Bechouat M., 2019; Joshi P., 2018)*. This is due to the strong nonlinear characteristics of photo-voltaic cells. The output of photo-voltaic cells is affected by many environmental factors, such as temperature and light intensity. Therefore, the power output is not stable and there is a certain loss of oscillation.

MPPT (Maximum Power Point Tracking) algorithm is applied to achieve less power waste and is widely researched in recent years *(Yilmaza U., 2019; Murtaza AF., 2019)*. MPPT algorithm maintains the power output in the maximum state, which can be applied to solar photo-voltaic array to improve its power generation efficiency.

In this paper, a photo-voltaic power generation system with MPPT device is modeled and is measured to evaluate the performance. Power prediction algorithm and fuzzy control algorithm are adopted in this modelling process. The results have been tested by using corresponding circuits. Based on the proposed methods, less output power wasted can be achieved due to the advantages including fast response time, high efficiency and high robustness.

[1] *Liming Wei, Prof.; Jinxin Luo, Stud.; Boheng Li, Stud.; Xiujuan Guo, Prof.; Bin Li, PhD.*

## SYSTEM STRUCTURE AND THEORY

### System structure

The functional block diagram of the MPPT adopted PV cell array system and is shown in Figure 1. In this figure, the complete set of photovoltaic power generation system includes PV cell array, Boost converter, MPPT device, DC load, AC load, inverter and battery *(Reddy, J., 2018; Mishra, AK., 2018)*. The photovoltaic cell array receives solar illumination and outputs electrical energy. The output voltage is raised to a certain level by the Boost circuit in order to drive DC load, AC load or charge batteries. The system can also be connected with an inverter to convert DC to AC for supplying AC loads. And the MPPT device is used for monitoring the voltage and current generated by the photovoltaic cell in real time to determine the working point and the maximum power point of the current system. By adopting MPPT algorithm, the MPPT device produces the corresponding adjusting signals. After the pulse modulation process, the switch ratio of the boost converter can be adjusted by the generated PWM signal which is determined by the MPPT algorithm. The internal resistance of photovoltaic cell array can be matched with the load impedance by changing the duty cycle. Thus, the photovoltaic array can always be adjusted in real time to output at the maximum power point.

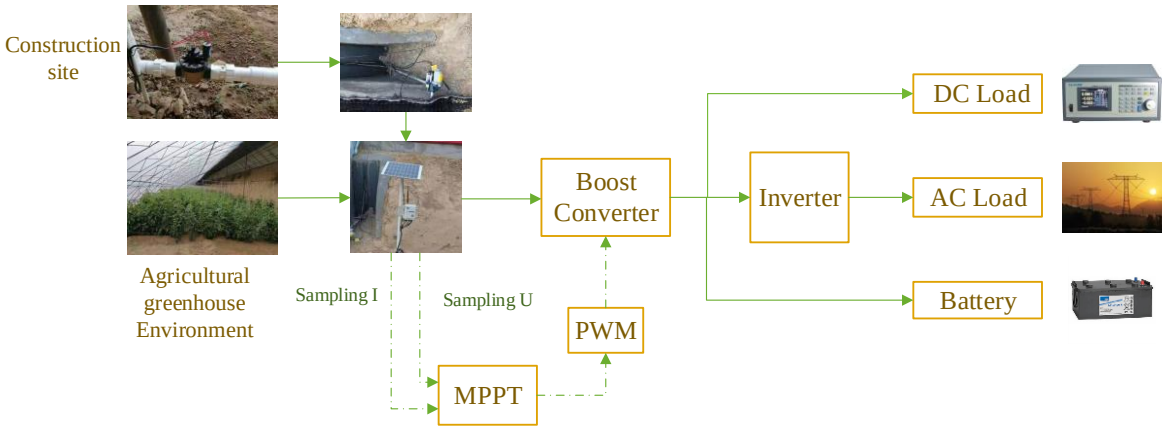


**Fig. 1 - Block diagram of the MPPT adopted PV cell array system**

### MPPT Theory

The MPPT theory is adopted in this PV cell array system, which has features including nonlinear, asymmetry and mono-pole, in order to achieve the target that the output power of the system can be maintained constant at its maximum power as the environment changes. The general MPPT algorithm modes can be divided into three categories, which are direct sampling control mode, indirect approximate control mode and intelligent control mode. Intelligent control mode has been developed rapidly by many researchers in recent years because of highly self-adoption and fast processing speed *(Boutabba T., 2018; Chekired, F., 2011; Nabipour M., 2019)*.

Fuzzy control method is one of intelligent control methods and the applied fuzzy control algorithm is shown in Figure 2 *(Abdourraziq M.A., 2018; Blaifi S.A., 2018; Eltawil M.A., 2013)*. The fuzzy controller has two input ports and the inputs will be processed separately. Then, the operation of fuzzy controller is carried out through the database, the knowledge base and the rule base. The final output is duty cycle and can be shortened as D.

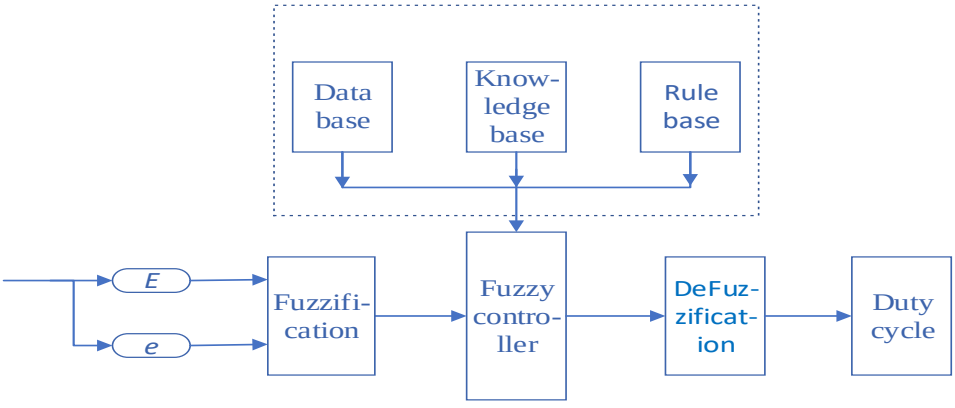


**Fig. 2 - Applied Fuzzy control method in the system**

Power prediction algorithm is widely adopted in applications involving system misjudgement *(Xie Y., 2013; Osorio, G.J., 2015)*. Misjudgement is generally due to the fact that the samples measured by the system come from different characteristic curves. For instance, the initial voltage and power are $U_1$ and $P_1$ as shown in Figure 3. While the voltage is increasing, the raised output power is $P_2$ according to the initial curve. However, the final output is $P_3$, which is not equal to the predicted output power of $P_2$, due to the influence of the environmental change. In this way, the misjudgement is produced. To avoid this misjudgement, sampling of system factors should be added in the process and the predicted power can be obtained by calculation.

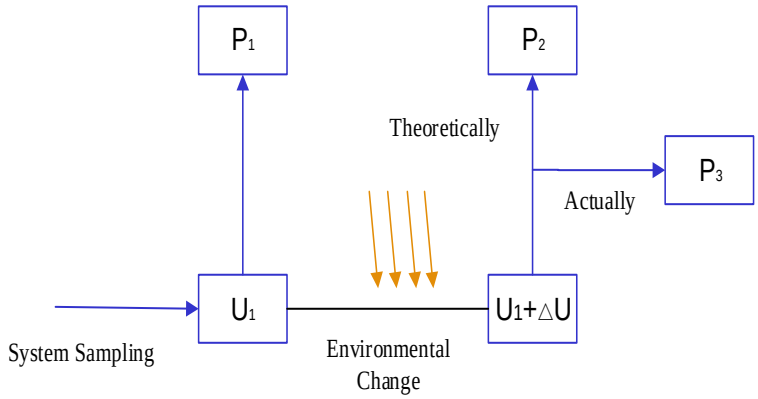


**Fig. 3 - Misjudgement analysis diagram for power prediction**

In this paper, the power difference obtained by the formula of power prediction method is applied to the fuzzy controller to get D (duty cycle). The combination of the two algorithms can minimize the error of system judgment. Before the fuzzy control calculation, the power prediction process can result in an optimized output power. Therefore, the system can reach maximum power point more quickly by adopting the power prediction and fuzzy control algorithm.

## MATERIALS AND METHODS

### Simulation of power prediction algorithm

Hypothesis at $kT$ time the output power of photovoltaic cell is $P_{(k)}$. By adding one sample at $(k+1/2)T$ times, the power value can be obtained as Equation (1).

$$P'_{(k)} = 2P_{(k+1/2)} - P_{(k)} \tag{1}$$

Continue the sampling process, the system obtains $P_{(k+1)}$ in the period of time of $(k+1)T$ According to the power prediction theory, $P_{(k+1)}$ is same as $P'_{(k)}$. Therefore, the difference between output power at $(k+1)T$ and at $kT$ is:

$$dP = P'_{(k)} - P_{(k)} = 2[P_{(k+1/2)} - P_{(k)}] \tag{2}$$

Based on the above equations, the relationship between real-time power and predicted power can be calculated by designing a fuzzy controller using Simulink as shown in Figure 4. In this designed module, two input factors are voltage and current of the PV cell array and the power prediction process is performed. The final output is D which is the duty cycle and it will be applied as input to the fuzzy control algorithm.

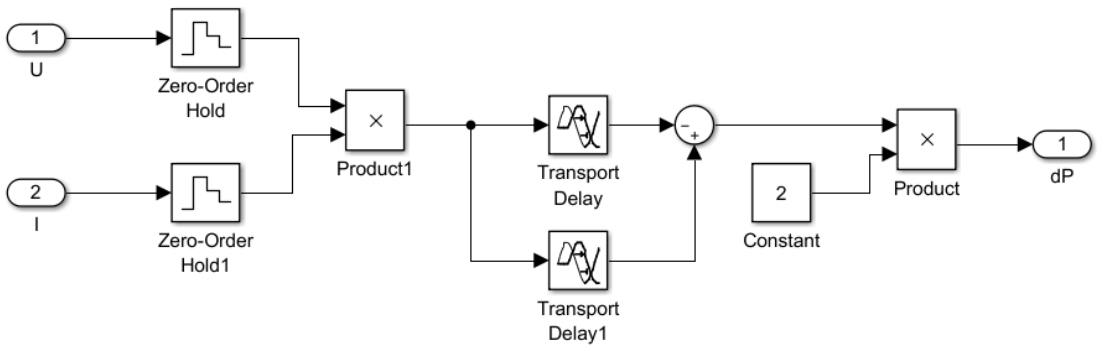


**Fig. 4 - Sub-module of the power prediction simulation module**

**Simulation of fuzzy control algorithm**

The fuzzy control algorithm uses the power prediction calculation's output, which is the duty cycle D, as its input. The input of fuzzy control method for power prediction is represented as $E_1$ and $e_1$ as shown in Equation (3). The input of the traditional fuzzy control method is represented as $E_2$ and $e_2$ as shown in Equation (4).

$$E_1 = \frac{dP}{U_{k+1} - U_k}, \quad e_1 = E_{1(k+1)} - E_{1(k)} \tag{3}$$

$$E_2 = \frac{P_{(k+1)} - P_k}{U_{k+1} - U_k}, \quad e_2 = E_{2(k)} - E_{2(k-1)} \tag{4}$$

The fuzzy subsets of $E_1$, $e_1$, $E_2$, $e_2$ and $D$ are represented in {NB, NM, NS, Z, PS, PM, PB} as shown in Table 1. In this assembly, NB is Negative Big, NM is negative middle, NS is negative small, Z is zero, PS is positive small, PM is the positive middle, PB is positive big. The fuzzy domain of $E_1$ and $E_2$ is [-5, 5], $e_1$, $e_2$ and $D$ is [-1, 1]. Fuzzy rules as follows are made by IF $A$ and $B$ then $C$. The above information is essential for the fuzzy controller and has been filled in the designed module as shown in Figure 5(a).

**Table 1**

**Fuzzy Control Decision Table**

| $E_1$, $E_2$ / $e_1$, $e_2$ | NB | NM | NS | Z | PS | PM | PB |
|---|---|---|---|---|---|---|---|
| NB | PB | PB | PB | PS | NS | NB | NB |
| NM | PB | PB | PM | PS | NS | NB | NS |
| NS | PB | PM | PS | PS | NS | NM | NS |
| Z | PM | PS | PS | Z | NS | NS | NM |
| PS | PS | PS | Z | NS | NS | NS | NB |
| PM | PS | PS | Z | NS | NS | NM | NS |
| PB | Z | Z | Z | NS | NM | NB | NB |

Finally, the decision module is obtained by using the above assembly and parameters as shown in Figure 5 (b) and (c). In this simulation module, the temperature is set as 25°C, the luminous intensity is set as 1000 W/m², and the time duration is 1 s. The obtained coefficient surface is shown in Figure 5 (d) In order to illustrate the performance of this algorithm, the traditional fuzzy control algorithm is compared with the fuzzy control algorithm of power prediction in the experimental results section.

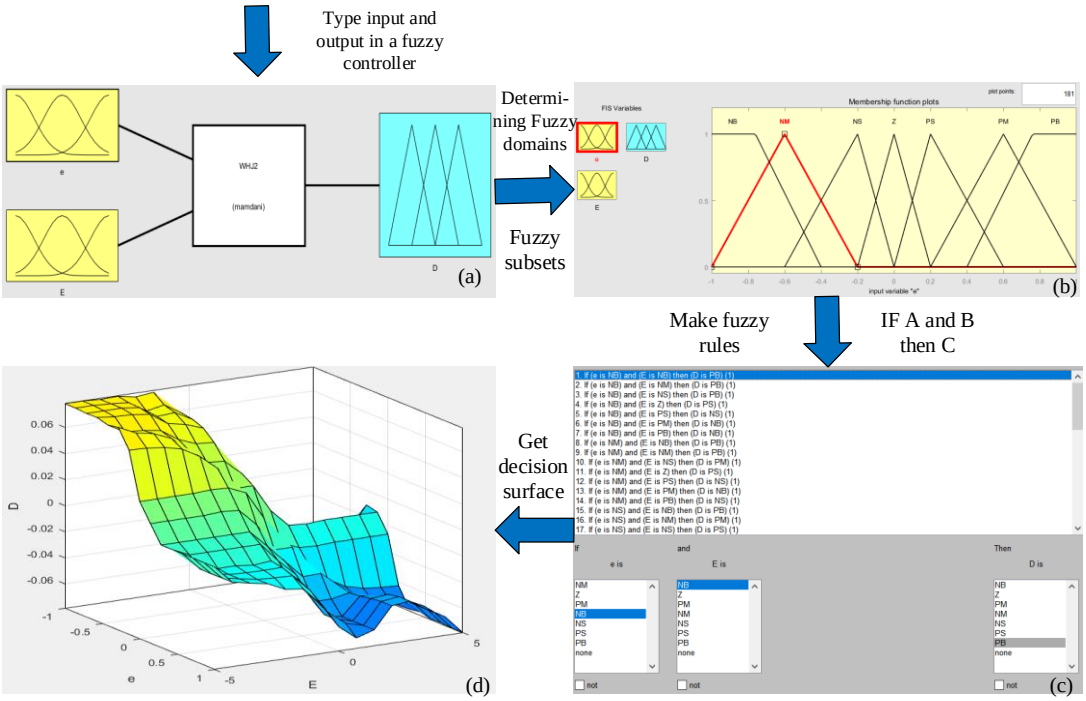


**Fig. 5 - Working flowchart of the fuzzy control simulation module**

**Experimental circuits**

The schematic diagram of the proposed MPPT circuit is shown in Figure 6. The output current and voltage of the PV cell array is measured in real time in order to perform the power prediction and fuzzy control algorithm. The current detection circuit converts current to voltage for its following ADC (analog-to-digital converter). And the output voltage of the PV cell array can be measured by the ADC circuit as well. The main controller board has multiple functions including ADC, UART (Universal Asynchronous Receiver/Transmitter), and PWM generation. The output PWM is generated by the main controller board for controlling the working status of the boost circuit. In addition, the power supply voltage for these boards is unified as 5V and is supplied by a low ripple linear power circuit.

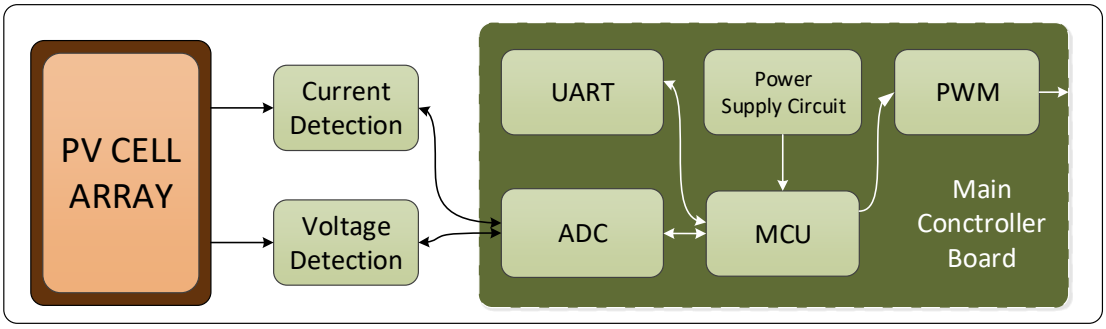


**Fig. 6 - Schematic diagram of the MPPT circuit in this system**

The applied circuits have been tested separated and are shown in Figure 7. The current detection circuit, which is shown in Figure 7 (a), has a maximum detection range from -5 A to 5 A. It converts current to voltage by using a ratio of 185 mV/A and the output voltage is linked to the ADC input port. The main controller board, which is shown in Figure 7 (b), is a highly integrated circuit with many functions. The main controller chip is STC15W4K56S4 that has 4 KB integrated RAM and 56 KB Flash. It has 8 ADC channels with 10 bit converting accuracy. In addition, the PWM generator is also integrated in this chip which is determined by the adopted algorithm for controlling the boost circuit. The boost converter circuit has a wide range of output voltage from 10V to 120V and is shown in Figure 7 (c). Considering the high output voltage, it also has a numeric display module to show the output voltage to avoid safety issues. The working frequency can be adjusted by the main controller board in order to drive loads or batteries.

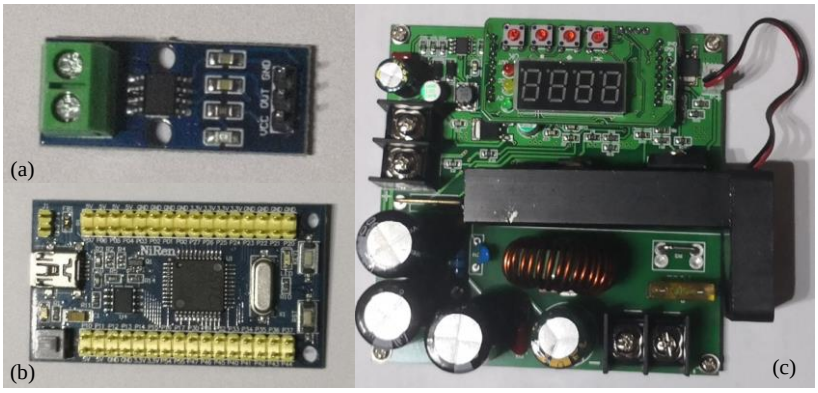


**Fig. 7 - Current detection circuit (a), main control board (b) and Boost converter circuit for PV cell array system**

**RESTULTS AND DISCUSSION**

- **Results**

**Simulation results**

In combination with the condition of the simulation setting in the previous section, the model is established in MATLAB/Simulink and the results are shown in Figure 8. Two curves of the proposed fuzzy control algorithm and the traditional fuzzy algorithm of the power prediction can be obtained as shown in Figure 8. It can be seen that the power prediction combined fuzzy control algorithm reaches MPP at 0.15 s and the traditional fuzzy control algorithm reaches MPP at 0.28 s. This result suggests that PV cell array system adopting the proposed fuzzy control algorithm can reach peak output power quicker and has less power waste comparing with the traditional fuzzy control algorithm.

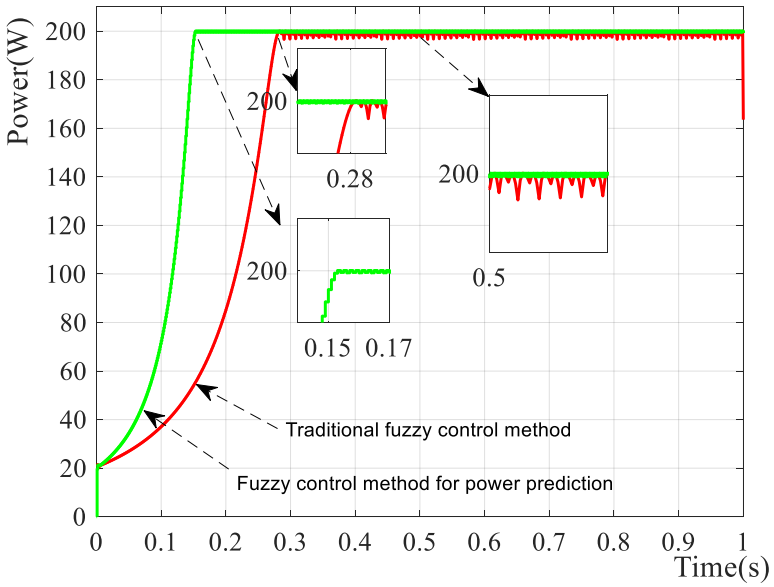


**Fig. 8 - Comparison between the proposed and traditional fuzzy control algorithm**

**Robust test**

A robust test of the simulated system adopting fuzzy control algorithm was carried out to investigate its performance in condition of environment factors varies. For instance, the luminous intensity drops from 1000 W/m$^2$ to 800 W/m$^2$ and the comparison curves are plotted in Figure 9. It can be seen that the curve of the proposed fuzzy control algorithm has a shorter response time the traditional fuzzy control algorithm. This also results in less power waste suggesting effectiveness of the proposed algorithm.

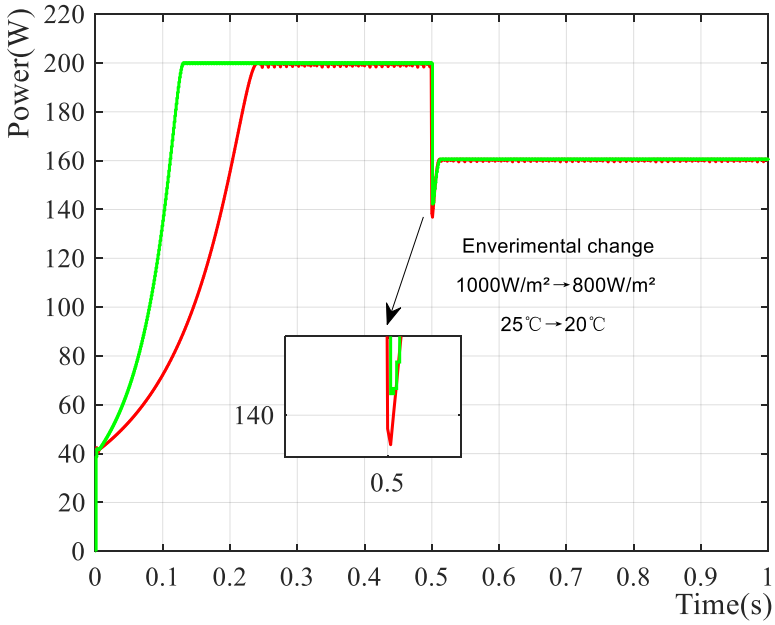


**Fig. 9 - Contrast curves under the condition of environmental factors varies**

**Experimental results**

Experiments were carried out to investigate the performance of the proposed algorithm by using the circuits demonstrated in the last section. The measured curves are shown in Figure 10. It can be seen that the red curve, which is the proposed fuzzy control algorithm combined with power prediction method, reaches its peak output voltage quickly when the system was powered on. The response time is much shorter than the black curve, which is the traditional fuzzy control method, though it was optimized to direct output without algorithm control. The experimental measurement shows the effectiveness of the proposed method.

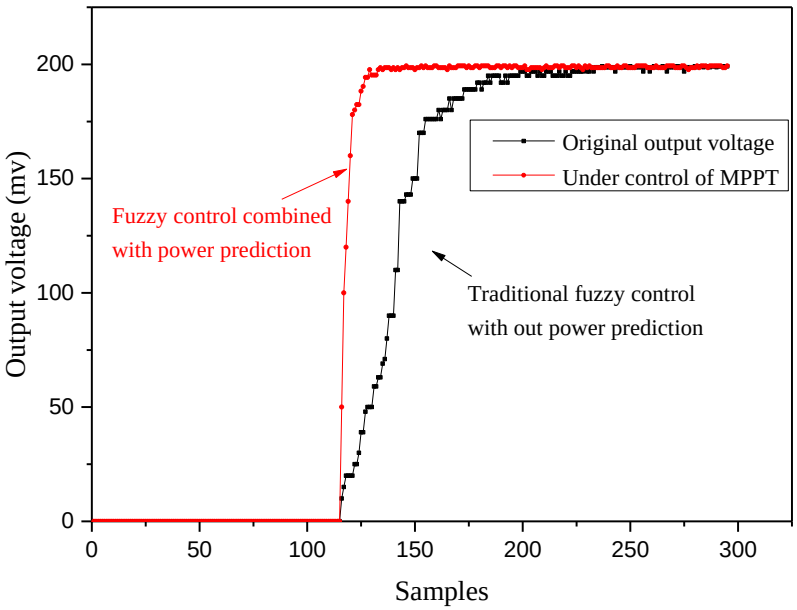


**Fig. 10 - Response speed comparison**

**Discussion**

The proposed algorithm has been verified by performing simulation and experimental measurement in above sections. For the agricultural greenhouse photovoltaic project demonstrated in this paper, MPPT algorithm is used to maximize the output power of the system. As shown in Figure 5, the power obtained by the fuzzy control algorithm using power prediction is 199.7~200.1 W, and the power loss is 0.2%. In this way, the proposed algorithm is capable to reduce power loss. The power obtained by using the traditional fuzzy control algorithm is 199.3~199.9W and the power loss is 0.4%. In the case of environmental change in Figure 6, the strain ability of the proposed algorithm is more efficient than the traditional method. In addition, the measured waveform displayed in the oscilloscope also demonstrated the effectiveness of the experiment.

## CONCLUSIONS

In this paper, modulation and measurement has been carried out to minimize the energy loss in a photovoltaic cell array system. Fuzzy control algorithm and power prediction algorithm has been adopted and calculated. In this process, models have been established and relative parameters have been obtained experimentally. The duty cycle, which is shorted as D, is obtained by the model of power prediction algorithm and it is essential for the fuzzy control algorithm as its input. The PWM signal can be modified according to the environmental change based on the proposed method. In this way, the output power can reach its peak value quicker than traditional method and the power loss can also be minimized. Therefore, the photovoltaic cell array system can be optimized to generate more electricity. In the future, further experiments will be carried out to optimize the performance of the system in order to increase the efficiency of solar energy utilization.

## ACKNOWLEDGEMENT

The authors wish to express their gratitude to the State Administration of Work Safety (2012-127), Jilin Jianzhu University (201810191114), the National Key Technology R&D Program of the Ministry of Science and Technology of China, Province of China and the Education Department of Jilin Province of China (JJKH20180573KJ, JJKH20170240KJ) the Science and Technology Department of Jilin (20180201052SF, 20180201063SF, 20190303114SF), for the generous support of this work.

## REFERENCES

[1] Abdourraziq M.A., Abdourraziq S., Maaroufi M., (2018), Efficiency optimisation of a microcontroller-based PV system employing a single sensor fuzzy-logic controller. *IET Power Electronics*, Vol. 11, pp. 539-547, Rabat/Morocco;

[2] Bechouat M., Sedraoui M., Feraga C.E. et al., (2019). Modeling and fuzzy MPPT controller design for photovoltaic module equipped with a closed-loop cooling system. *Journal of Electronic Materials*. Vol. 48, pp. 5471-5480, Guelma/Algeria;
[3] Blaifi S.A., Moulahoum S., Benkercha R. et al, (2018), M5p model tree based fast fuzzy maximum power point tracker, *Solar Energy*, Vol. 163, pp. 405-424, Medea/ Algeria;
[4] Boutabba T., Drid S., Chrifi-Alaoui L., (2018), A New Implementation of Maximum Power Point Tracking Based on Fuzzy Logic Algorithm for Solar Photovoltaic System, *International Journal of Engineering*, Vol. 31, pp. 580-587, Algeria;
[5] Chekired F., Larbes C., Rekioua D., et al, (2011), Implementation of a MPPT fuzzy controller for photovoltaic systems on FPGA circuit. *Energy Procedia*, Vol. 6, pp.541-549, Alger / Algeria;
[6] Dinesh H., Pearce J.M., (2016), The potential of agrivoltaic systems, *Renewable and Sustainable Energy Reviews*, Vol. 54, pp.299-308, Michigan/U.S.A.;
[7] Eltawil M.A., Zhao Z., (2013), MPPT techniques for photovoltaic applications, *Renewable and Sustainable Energy Reviews*, Vol. 25, pp.793-813, Saudi Arabia;
[8] Hassan G.E., Salah A.H., Fath H. et al., (2016), Optimum operational performance of a new stand-alone agricultural greenhouse with integrated-TPV solar panels. *Solar Energy*, Vol. 136, pp. 303-316, Alexandria/Egypt;
[9] Ju YT., Jin MX., Wang JK., (2019), Research on Optimal Dispatching Strategy for Micro-Energy-Grid of Protected Agriculture, *Applied Sciences-Basel*, Vol. 9, Beijing/China;
[10] Jones M., (2015), Systems modelling and economic analysis of photovoltaic (PV) powered water pumping and brackish water desalination for agriculture, *Dissertations & Theses – Gradworks*, Logan/Utah;
[11] Joshi P., Arora S., (2017), Maximum power point tracking methodologies for solar PV systems – a review. *Renewable and Sustainable Energy Reviews*, Vol. 70, pp.1154-1177, Guelma/ Algeria;
[12] Li C., Wang H., Miao H. et al., (2017), The economic and social performance of integrated photovoltaic and agricultural greenhouses systems: case study in China. *Applied Energy*, Vol. 190, pp.204-212, China;
[13] Murtaza AF., Ahmad R, (2019), Optical isolation mechanism based MPPT for PV array under partial shading condition, *Solar energy*, Vol. 185, pp..516-524, Lahore/Pakistan;
[14] Mishra A.K., Singh B., (2018), Design of solar-powered agriculture pump using new configuration of dual-output buck-boost converter, *IET Renewable Power Generation*, Vol. 12, pp.1640-1650, New Delhi/India;
[15] Maher A., Kamel E., Enrico F. et al., (2016), An intelligent system for the climate control and energy savings in agricultural greenhouses, *Energy Efficiency*, Vol. 6, pp.1241-1255, Tunis/Tunisia;
[16] Nabipour M., Razaz M., Seifossadat S.GH et al., (2019), A new MPPT scheme based on a novel fuzzy approach, *Renewable & Sustainable Energy Reviews*, Vol. 74, pp. 1147-1169, Ahwaz/ Iran;
[17] Osrio G.J., Matias J.C.O., Catalão. J.P.S., (2015), Short-term wind power forecasting using adaptive neuro-fuzzy inference system combined with evolutionary particle swarm optimization, wavelet transform and mutual information, *Renewable Energy*, Vol. 75, pp.301-307, Covilha/Portugal;
[18] Reddy J., Natarajan S., (2018), Control and Analysis of MPPT Techniques for Standalone PV System with High Voltage Gain Interleaved Boost Converter, *Gazi University Journal of Science*, Vol. 31, pp.515-530, Ankala/Turkey;
[19] Rubio-Aliaga A., Molina-Garcia A., Garcia-Cascales M.S. et al., (2019), Net-Metering and Self-Consumption Analysis for Direct PV Groundwater Pumping in Agriculture: *A Spanish Case Study*, Vol. 8, Cartagena/Spain;
[20] Sun C., Wang Y., (2016), Research of kind of variable step size perturbation and observation MPPT based on power prediction, *2016 IEEE International Conference on Mechatronics and Automation*, IEEE. Harbin/China;
[21] Xie Y., Wu Q., Wang Y. et al., (2013), A variable step MPPT optimized algorithm based on power prediction, *Control Conference*, China;
[22] Yilmaza U., Turksoy O., Tekec A., (2019), Improved MPPT method to increase accuracy and speed in photovoltaic systems under variable atmospheric conditions, *Electrical Power and Energy Systems*, Vol. 113, pp.634-651, Turkey.

# STABILITY ANALYSIS OF EQUILIBRIUM FOR TROMBE WALL SOLAR CHICK BROODER
# /
# *NYOCHA ỊMATA MA AJA TROMB NA ỤLỌ EBE Ọ DỊ A GA-ENWE IKE INYE ỤMỤ ỌKỤKỌ ABỤRỤ ỌHỤRỤ EKPOMỌKỤ GA-ADIGIDE*

**Ohagwu C. J.[1)], Okonkwo W. I.[1)], Akubuo C. O.[1)], Mbah G. C.E.[2)], Njoku H. O.[3 )1]**
[1)]Department of Agricultural and Bioresources Engineering, [2)]Department of Mathematics,
[3)]Department of Mechanical Engineering, University of Nigeria, Nsukka

*Corresponding Author name: Chukwuemeka Jude Ohagwu*
*Corresponding Author Tel:+2348063507144*
*Email address: chukwuemeka.ohagwu@unn.edu.ng*
*DOI: 10.35633/INMATEH-59-32*

***Keywords***: *Equilibrium Analysis, Stability, Trombe wall solar brooder, optimal brooding*

## ABSTRACT

*Trombe wall solar chick brooder was developed for 150-200 birds' capacity. System evaluation as well as stability and equilibrium analysis were carried out. A set of linear differential equations were formulated that described the dynamic modeling of Trombe wall solar chick brooder for optimal poultry production. The descriptive models were referred to as system control. The model was transformed into Jacobian matrix and solved for stability and equilibrium. Further tests for stability using Routh-Hurwitz criterion were conducted. The solved Jacobian matrix had negative eigenvalues and as such was locally stable. Routh-Hurwitz criterion affirmed that the system model was stable. It implied, the system supported brooding of 200 birds for the 28 days of brooding operation at temperature range of 25-39$^{o}$C of the brooding room.*

## ỤMỊ EDEMEDE

*Aja tromb dị n'ụlọ si n'anyanwụ adọta ike bụ nke e wubere iji were nwee ike ịzụpụta ụmụ ọkụkọ dị 150-200 n'ọnụ ọgụgụ. Emere nnyocha sistem ya nakwa nnyocha ndigide ekpomọkụ na ndaba ụlọ ahụ iji were hụ na ọrụrụ ọrụ ka o si were kwesị. Ewepụtara usoro mgbakọ na mwepụ kọwara maka ịrụaja Tromb iji were zụọ ụmụ ọkụkọ nke ga-eme ka enwee ike na-azụpụta ọkụkọ nke ọma. Mgbakọ na mwepụ emere bụ nke ahụrụ dịkaịlekọta sistem. Emeghaṛịṛị mgbakọ na mwepụ a na matris Jacob were hụ ndigide ekpomọkụ na ndaba ụlọ ahụ iji were nye ihe a chọrọ. E ji Routh-Hurwitz were mee nnyocha banyere ndigide ekpomọkụ a. Matris Jacob ewepụtara nwere mpụtara dị negetiv nke gosiri na ọdabara. Usoro Routh-Hurwitz wepụtara gosikwara na ọdabara. O na-egosi na usoro a kwadoroịzụ ụmụ ọkụkọ 200 na mkpụrụ ụbọchị 28 n'ogo okpomọkụ ụlọ dị 25-39$^{o}$C.*

## INTRODUCTION

Poultry industry is one the subsectors of the Agricultural sector that is contributing immensely to the economy of any nation. It requires sectorial synergy in energy supply in the value chain. Energy is required in different unit of operations (such as hatching, brooding, defeathering, etc.) in poultry production. Due to energy need in the value chain of production especially during brooding of day-old chicks, solar energy utilization technologies were most suitable. Due to obvious enormous benefits like its renewability, cheap energy source etc. These technologies as an appropriate technology were required to achieve optimal poultry brooding operation *(Okoye J.A.O, 1992).* This was essential to maximize animal health and husbandry production and it contributed to good performances. The most essential performance index/ brooding parameter to control was the chick body temperature because day old chicks were unable to regulate their body temperature post hatched *(Obioha F.C., 1992)*. The quest to proffer solution in this regard necessitated the development of Trombe wall solar chick brooder for optimal poultry production *(Echiegu E.A, 1993; 1986, Okonkwo W.I., 1993, Okonkwo W.I. and Akubuo C.O., 2001; Okonkwo W.I and Agunwamba J.C., 1997; Okonkwo W.I., Anazodo*

[1] *Ohagwu C. J., Ph.D., M.Eng., B.Eng.; Okonkwo W. I., Prof. Ph.D., M.Eng., B.Eng.;Akubuo C. O., Prof., Ph.D., M.Eng., B.Eng.; Mbah G. C.E.[2)], Prof., Ph.D., M.Sc., B.Sc.; Njoku H. O., Ph.D., M.Eng., B.Eng.*

*G.U.N, Akubuo C.O., Echiegu E.A., Iloeje O.C.,1992; Okonkwo W.I. and Akubuo C.O., 2007).* Experimental studies on the viability of the system have been proven *(Odo L.O., 2016)*. Perennial problems associated with poultry day-old chick brooding were solved with the aid of solar systems. Further studies have been carried out in mathematical modeling of Trombe wall solar chick brooder for optimal poultry production *(Ohagwu et.al, 2017).* The model was simulated and validated with measured data. Thus the need to examine the system further numerically for stability and equilibrium analysis was imperative. The study had shown trade-off between physically built brooder and modeled brooder (*Maria A. and Zhang C., 1997).* Therefore, modeled brooder has now become the platform for further studies.

## MATERIALS AND METHODS

Passive Trombe wall solar chick brooder was developed with brooding capacity of one hundred and fifty two hundred birds (150-200) per batch as seen fig.1.0. The system adopted deep litter system of chicken brooding. The thermophysical properties, materials and dimensions of the Trombe wall solar chick brooder were shown in table 1.

## PHYSICAL DESCRIPTIVE MODEL/ PARAMETRIC CONSIDERATIONS

The physical Trombe wall *(Trombe et.al., 1977)* solar chick brooder was dimensioned (3m x 2.2m x 3m) with brooding area as 6.6m$^2$ *(Okonkwo W.I., Akubuo C.O., 2007)* The building materials used for the construction were materials accessed locally in the tropics, namely: solid cement blocks, acrylic transparent glazing, ceiling board, zinc, pebble stone (limestone chippings), black paint and wooden door. The physical component model of the Trombe wall solar chick brooder studied is shown in Figure 1 and was segmented into components namely: (a) solar energy collector (vented)-the Trombe wall (b) pebble bed collector (vented)-pebble bed bin (c) thermal heat storage wall (vented)-Trombe wall and pebble bed bin (d) Air Chimney (e) poultry brooding room (f) sensible heat from the birds stocked and exit of heat and water vapour transmission in the poultry room through the chimney. But the basic component parts were shown below.

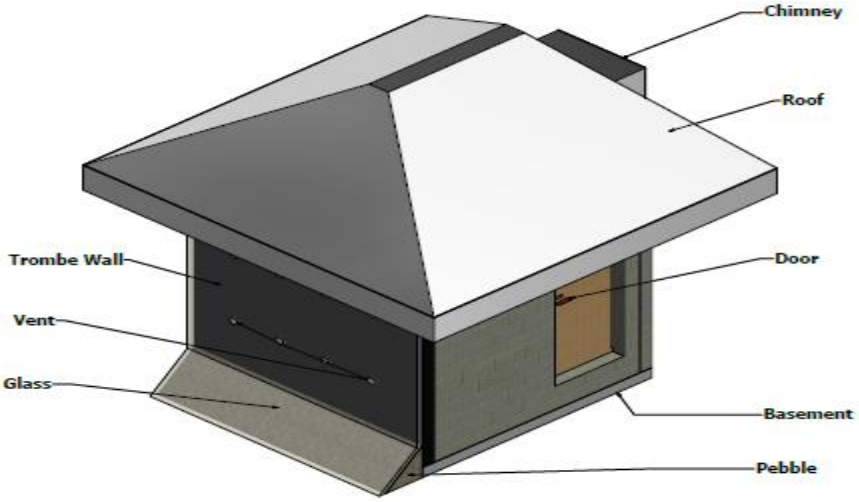


**Fig. 1 - Three Dimensional View of Trombe Wall Solar Chick Brooder with the Component Parts**

The effect of solar radiation incidence and utilization on the physical model - solar collector component is illustrated in figure 2. The structure is oriented facing due south. During the sunrise of the day, radiant energy from the sun is absorbed, stored and concentrated on the collector surface through the glaze. This energy is converted to heat energy which was absorbed on the surface. The absorbed energy caused an increase in the internal energy of the Trombe wall thereby increasing the temperature of the collector. The energy got stored and by conduction (assumed-one directional) transported to inner surface of the Trombe wall. Factors that determined solar radiation intensity received by the Trombe wall included *(Duffie J.A. and Beckmann W.A., 1991)*: Earth-sun distance ($G_{sn}$) which depended on the number of the day(n) in a year (Jan1=1, Dec.31=365), Air mass (m), insolation (H), total/global solar radiation (beam and diffuse radiation), sometimes, reflected radiation and is measured against horizontal surface, solar altitude angle (m),solar time and solar angle($\theta$) which is dependent on latitude $\phi$, declination $\delta$, slope, $\beta$ solar hour angle $\omega$ , angle of incidence $\theta$, zenith angle $\theta_z$, solar altitude angle $\alpha_s$, surface azimuth angle $\gamma$, solar azimuth angle $\gamma_s$. These factors were used in determining the quantity of heat energy from the sun used for brooding operation.

**Table 1**

**Thermo-physical Properties, Materials and Dimensional parts of Trombe wall Solar Brooder**

| **Trombe wall glaze (perplex)** | Units |
|---|---|
| Emissivity | 1180 |
| Absorptivity | 0.05 |
| Specific heat capacity (J/kg/K) | 1470 |
| Transmissivity | 0.75 |
| Thickness(m) | 0.003 |
| Height (m) | 3 |
| Width | 3 |
| **Trombe wall (Masonry wall)** | |
| Emissivity | 0.86 |
| Absorptivity | 0.95 |
| Thickness (m) | 0.40 |
| Radius of vents | 0.015 |
| Width and width of the air gap | 3 |
| Sunspace width ($D_{gap}$) | 0.003 |
| Thermal diffusivity | $K_{Tw}/(\rho_{Tw}Cp_{Tw}T)$ |
| Height (m) and height of the air gap (m) | 3 |
| Thermal Conductivity (K) (W/m$^2$) | 0.1 |
| Specific heat capacity (J/Kg/ $^0$C) | 920 |
| Density (Kg/m$^3$) | 2240 |
| **Pebble bed bin** | |
| Emissivity | 0.88 |
| Absorptivity | 0.95 |
| Height between inlet and outlet | 0.5 |
| **Brooder (Deep litter)** | |
| Overall heat loss (J/Kg/Kg) | 30 |
| Width (m) | 2.2 |
| Length of door | 1.83 |
| Width of door | 0.3 |
| Thermal conductivity of door | 0.16 |
| Door thickness (m) | 0.15 |
| Area | $A_{Tw}$ x (4) |
| Area of the chimney outlet vent | 0.0009 |
| Discharge | 0.62 |
| Air | |
| Specific heat capacity (K/Kg/Kg) | 1005 |
| Viscosity (Kg/m$^3$) | 1.857 |
| Density (Kg/m$^3$) | 1.177 |
| Prandtl Number | 0.713 |
| Thermal conductivity (W/m/K) | 0.02544 |
| Thermal diffusivity (m$^2$/s) | 2.213 x10$^{-5}$ |

## MATHEMATICAL FLOW MODEL OF TROMBE WALL SOLAR ENERGY BROODER SYSTEM

This numerically described the energy trend flow across the system component of the brooder. The energy transport and transformation across the component parts are as follows: global solar radiation, glaze of Trombe wall and pebble bed bin, Trombe wall, pebble bed bin, brooding room, chicks and other sources of heat losses such as roof, walls, chimney and door. The global solar radiation component regarded as diffused radiation is part of the heat losses such as reflected rays(r) and ground reflected rays (gr) are part of radiant energy considered in the model. Neglecting the initial temperature of the brooding room before the birds were stocked with respect to heat gain from the Trombe wall and pebble bed bin, the system process models were explained thus: solar radiation intensity (sun) incident on the vertical glaze ($G_1$) of the Trombe wall from sunrise to sunset, transmitted heat energy to the Trombe wall ($T_w$). Also solar radiation was incident on the inclined glaze ($G_2$) of the pebble bed bin (Pb) from sunrise to sunset, transmitted heat energy to the pebble bed bin.

Of course, solar radiations are characterized by losses due to reflection(r) and ground reflected rays (gr) as well as solar flux incident on the collector (beam and diffused radiation). These heat energy/flux were stored on Trombe wall ($T_w$) and were convectionally released the heat to the brooding room where day old chicks were stocked through the upper and lower vents and that of the lower vents of the pebble bed bin and conductively across the wall. The heat energy stored on Trombe wall ($T_w$) and pebble bed bin exchanged heat to each other via conduction and convection by thermo-circulation. There were thermal interactions between Trombe wall ($T_w$), pebble bed bin (Pb) and N-chicks, other heat losses were through chimney, other walls, roof etc. Fig. 2 showed the flow diagram of the mathematical model equations formulated.

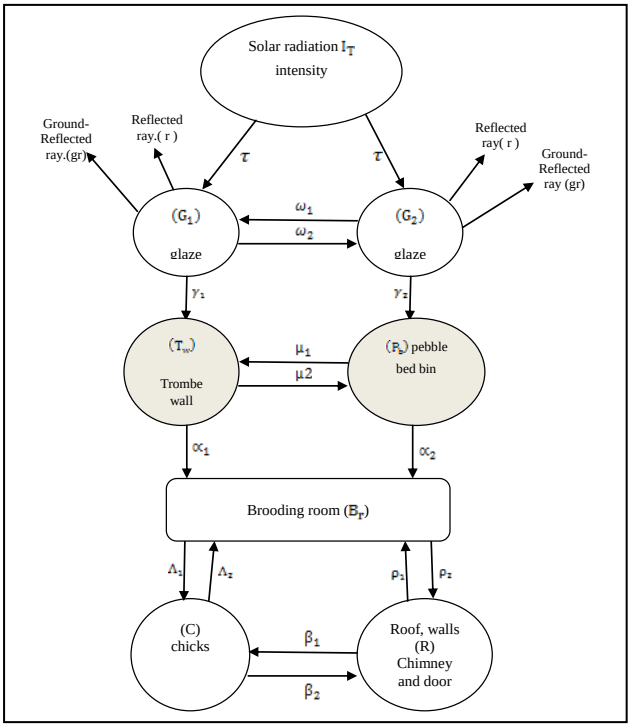


**Fig. 2 - Mathematical Flow Model Diagram of Trombe wall Solar Energy Chick Brooder**

As a result of thermo-circulation and thermal losses in and across the brooding room, and in order to maintain optimal energy balance in the brooding room, temperature of the brooding room must be greater than the ambient temperature or heat gained through the roof (R). If the ambient temperature (Ta) of the surroundings were greater than the brooding room temperature ($T_{Br}$) then heat losses occurred through the other walls, roof and other orifices. If the temperature of the brooding room was greater than the temperature of the walls, in other words, other walls absorbed the temperature gradient. Temperature fluctuation/swing between the environment and the brooding room was such that the overall objectives were to provide optimal heat (temperature) required for brooding of chicks within the environmental atmospheric pressure. The quantity of heat gained /lost $Q_{G1,}Q_{G2}, Q_{Tw}, Q_{Pb}, Q_{Br}, and\ Q_R$ across the system to the brooding room and exit through the chimney created potential brooding energy for the birds. From the mathematical flow model diagram in fig. 2, at any given time, heat gains were expressed additively while heat losses were by subtraction. Therefore, to determine the quantity of heat gain across the Trombe wall glaze at any given time (t), the model equation was given as:

$$\frac{dQ_{G1}}{dt} = \tau I_T + \omega_1 dQ_{G2} - \gamma_1 dQ_{G1} - rdQ_{G1} - grdQ_{G1} - \omega_2 dQ_{G1} \quad (1)$$

*where* $dQ_{G1}$ *is the differential heat loss from the glaze.*

Also, to determine the quantity of heat gain across the pebble bed bin glaze at any given time (time), the model equation was given as:

$$\frac{dQ_{G2}}{dt} = \tau dI_T + \omega_2 dQ_{G1} - \omega_1 dQ_{G2} - \gamma_2 dQ_{G2} - rdQ_{G2} + grdQ_{G2} \quad (2)$$

For the quantity of heat gain at any time (t) on the Trombe wall, we have the model equation as:

$$\frac{dQ_{TW}}{dt} = \gamma_1 dQ_{G1} + \mu_1 dQ_{Pb} - \mu_2 dQ_{TW} - \alpha_1 dQ_{TW} \quad (3)$$

For the quantity of heat gain at any time (t) on the pebble bed bin storage, we have the model equation as:

$$\frac{dQ_{Pb}}{dt} = \gamma_2 dQ_{G2} + \mu_2 dQ_{TW} - \mu_1 dQ_{Pb} - \alpha_2 dQ_{Pb} \quad (4)$$

To determine the temperature of the chick at any time (t) in the brooding room, we have the model equation as:

$$\frac{dT_C}{dt} = \lambda_1 dT_{Br} + \beta_1 dT_R - \lambda_2 dT_C - \beta_2 dT_C \quad (5)$$

Temperature of the chick can only be maintained, if $dQ_{Br} > dT_A$ where $dT_A$= ambient temperature, then $\lambda_2 = \beta_1 = 0$, $dT_C$ = change in temperature of the chicks and $dQ_R$ = change in quantity of the heat or temperature of the roof, n-walls and door.

To determine the quantity of heat loss from the roof, walls, chimney and door at any time (t) of the brooding room, we have the model equation as:

$$\frac{dQ_R}{dt} = \rho_2 dQ_{Br} + \beta_2 dT_C - \rho_1 dQ_R - \beta_1 dQ_R \quad (6)$$

Meanwhile, to determine the quantity of heat in the brooding room at any time (t) to keep the chicks warm, we have the model equation as:

$$\frac{dQ_{Br}}{dt} = \alpha_1 dQ_{TW} + \alpha_2 dQ_{pb} + \lambda_2 dT_C + \rho_1 dQ_R - \lambda_1 dQ_{Br} - \rho_2 dQ_{Br} \quad (7)$$

Equation (7) holds, if $\lambda_1 = 0\ if dQ_{Br} > dT_C and \rho_2 = 0, if dQ_{Br} > dT_A$

- **EQUILIBRIUM STATE ANALYSIS OF THE SYSTEM MODEL**

For the system model to achieve stability among the heat contributing component factors affecting thermal transport/the operation of the brooding process (maintaining optimal temperature for chick brooding), the factors like the change in the temperatures of the Trombe wall glazing, pebble bed bin glazing, Trombe wall, pebble bed bin, brooding room, and chicks with respect to time, neglecting heat losses via roof, walls, chimney and door supported the brooding operation. Therefore, the Equilibrium State Analysis of the System Model was given in equation (8)

$$\frac{dT_{TW}}{dt} = \frac{dT_C}{dt} = \frac{dT_{Br}}{dt} = \frac{dT_{pb}}{dt} = \frac{dT_{G1}}{dt} = \frac{dT_{G2}}{dt} = \frac{dT_R}{dt} = 0 \quad (8)$$

Ultimately, for the system to be in equilibrium, the system component parts that provide the enthalpy must be equal such that: change in temperature of the Trombe wall is equal to change in temperature of the chicks and is equal to change in temperature of the brooding room and is equal to change in temperature of pebble bed bin and is equal to change in temperatures of glazing of the Trombe wall and pebble bed bin as well as change in the temperatures of the roof, chimney, walls and door. Relying on equations (1) to (7) to derive the equilibrium stability of each system component parts that contributes to these processes, we have the following expressions:

For Trombe wall temperature, referring to equation (3), it is expressed as:

$$\frac{\partial T_{TW}}{\partial t} \xrightarrow{yields} 0, \Longrightarrow \gamma_1 dT_{G1} + \mu_1 dT_{Pb} - \mu_2 dT_{TW} - \alpha_1 dT_{Tw} = 0$$

$$\gamma_1 dT_{G1} + \mu_1 dT_{Pb} - (\mu_2 + \alpha_1) dT_{Tw} = 0 \Rightarrow dT_{TW} = \frac{\gamma_1 dT_{G1} + \mu_1 dT_{Pb}}{\alpha_1 + \mu_2} \quad (9)$$

Heat gained by the system, even if heat supply from Trombe wall yielded as low as zero, equation (9) still supported the system to brood the chicks.

For temperature of *N* chicks, refer to equation (5), it is expressed as:

$$\frac{dT_C}{dt} \xrightarrow{yields} 0, \quad \Longrightarrow \lambda_1 dT_{Br} + \beta_1 dT_R - \lambda_2 dT_C - \beta_2 dT_C = 0 \qquad \text{see the fig.2.}$$

$$\lambda_1 dT_{Br} + \beta_1 dT_R - (\lambda_2 + \beta_2) dT_C = 0 \Rightarrow (\lambda_2 + \beta_2) dT_C = \lambda_1 dT_{Br} + \beta_1 dT_R$$

$$\Rightarrow dT_C = \frac{\lambda_1 dT_{Br} + \beta_1 dT_R}{(\lambda_2 + \beta_2)} \quad (10)$$

Heat gained by the system, even if heat supply from chicks yielded as low as zero, equation (10) still supported the system to brood the chicks.

For temperature of brooding room, referring to equation (7), it is expressed as:

$$\frac{\partial T_{Br}}{\partial t} = \xrightarrow{yields} 0, \Longrightarrow \alpha_1 dT_{TW} + \alpha_2 dT_{pb} + \lambda_2 dT_C + \rho_1 dT_R - \lambda_1 dT_{Br} - \rho_2 dT_{Br} = 0$$

$$\alpha_1 dT_{TW} + \alpha_2 dT_{pb} + \lambda_2 dT_C + \rho_1 dT_R - (\lambda_1 + \rho_2) dT_{Br} = 0 \Rightarrow (\lambda_1 + \rho_2) dT_{Br} = \alpha_1 dT_{TW} + \alpha_2 dT_{pb} + \lambda_2 dT_C + \rho_1 dT_R$$

$$dT_{Br} = \frac{\alpha_1 dT_{TW} + \alpha_2 dT_{pb} + \lambda_2 dT_C + \rho_1 dT_R}{\lambda_1 + \rho_2} \quad (11)$$

Heat gained by the system, even if heat supply from brooder yielded as low as zero, equation (11) still supported the system to brood the chicks.

For temperature of pebble bed bin, referring to equation (4), it is expressed as:

$$\frac{dT_{Pb}}{dt} = \xrightarrow{yields} 0, \Rightarrow \gamma_2 dT_{G2} + \mu_2 dT_{TW} - \mu_1 dT_{Pb} - \alpha_2 dT_{Pb} = 0$$

$$\gamma_2 dT_{G2} + \mu_2 dT_{TW} - (\mu_1 + \alpha_2) dT_{Pb} = 0 \Rightarrow (\mu_1 + \alpha_2) dT_{Pb} = \gamma_2 dT_{G2} + \mu_2 dT_{TW} \Rightarrow dT_{pb} = \frac{\gamma_2 dT_{G2} + \mu_2 dT_{TW}}{(\mu_1 + \alpha_2)} \quad (12)$$

Heat gained by the system, even if heat supply from pebble bed yielded as low as zero, equation (12) still supported the system to brood the chicks.

For temperature of Trombe wall glazing, referring to equation (1), it is expressed as:

$$\frac{dT_{G1}}{dt} = \xrightarrow{yields} 0, \Rightarrow \tau dI_T + \omega_1 dT_{G2} - \gamma_1 dT_{G2} - \gamma_1 dT_{G1} - r dT_{G1} - gr dT_{G1} - \omega_2 dT_{G1} = 0$$

$$\tau dI_T + (\omega_1 - \gamma_1) dT_{G2} - (\gamma_1 + r + gr + \omega_2) dT_{G1} = 0$$

$$\frac{\tau dI_T + (\omega_1 - \gamma_1) dT_{G2}}{(\gamma_1 + r + gr + \omega_2)} = dT_{G1} \quad (13)$$

For temperature of pebble bed bin glazing, referring to equation (2), it is expressed as:

$$\frac{dT_{G2}}{dt} = \xrightarrow{yields} 0, \Rightarrow \tau dI_T + \omega_2 dT_{G1} - \omega_1 dT_{G2} - \gamma_2 dT_{G2} - r dT_{G2} + gr dT_{G2} = 0$$

$$\tau dI_T + \omega_2 dT_{G1} - (\omega_1 + \gamma_2 + -gr) dT_{G2} = 0 \Rightarrow dT_{G2} = \frac{\tau dI_T + \omega_2 dT_{G1}}{(\omega_1 + \gamma_2 + r - gr)} \quad (14)$$

For temperature of roof, walls, chimney and door refer to equation (6), it is expressed as:

$$\frac{dT_R}{dt} = 0, \Rightarrow \rho_2 dT_{Br} + \beta_2 dT_C - \rho_1 dT_R - \beta_1 dT_R = 0$$

$$\rho_2 dT_{Br} + \beta_2 dT_C - (\rho_1 + \beta_1) dT_R = 0$$

$$dT_R = \frac{\rho_2 dT_{Br} + \beta_2 dT_C}{(\rho_1 + \beta_1)} \quad (15)$$

## STABILITY/STEADY STATE ANALYSIS OF THE SYSTEM MODEL

From the derived model equations (1) to (7), the stability/steady state of the components parts that contribute heat/ temperature change to the brooding system can be mathematically presented in a matrix form given as:

$$\begin{pmatrix} T_{G1} & T_{G2} & T_{TW} & T_{pb} & T_{Br} & T_C & T_R \\ -(\omega_2 + \gamma_1 + r + gr) & \omega_1 & 0 & 0 & 0 & 0 & 0 \\ \omega_2 & -(\omega_1 + \gamma_2 + r + gr) & 0 & 0 & 0 & 0 & 0 \\ \gamma_1 & 0 & -(\alpha_1 + \mu_1) & \mu_2 & 0 & 0 & 0 \\ 0 & \gamma_2 & +\mu_2 & -(\alpha_1 + \mu_2) & 0 & 0 & 0 \\ 0 & 0 & \alpha_1 & +\alpha_2 & -(\lambda_1 + \rho_2) & \lambda_2 & -\rho_1 \\ 0 & 0 & 0 & 0 & +\lambda_1 & -(\lambda_2 + \beta_2) & +\beta_1 \\ 0 & 0 & 0 & 0 & +\rho_2 & +\beta_2 & -(\rho_1 + \beta_1) \end{pmatrix}$$

The matrix above is transformed to Jacobian matrix; solving this equation might be difficult, but test for the stability condition is stated as follows: we only need the sign of the eigenvalues. The steady state point is stable if Re ($\lambda$) < 0 for all $\lambda$: The stability condition is established by the following Routh-Hurwitz criteria.

Given the characteristic equation

$$\lambda^k + a_1 \lambda^{k-1} + a_2 \lambda^{k-2} + \cdots + a_k = 0$$

From the following k Hurwitz matrices:

$$H_1 = (a_1) \quad ; H_2 = \begin{pmatrix} a_1 & 1 \\ a_3 & a_2 \end{pmatrix} \quad ;$$

$$H_3 = \begin{pmatrix} a_1 & 1 & 0 \\ a_3 & a_2 & a_1 \\ a_5 & a_4 & a_3 \end{pmatrix} \quad ; \ldots \; ; \; H_3 = \begin{pmatrix} a_1 & 1 & 0 & \ldots & 0 \\ a_3 & a_2 & a_1 & \cdots & 0 \\ \vdots & \vdots & \vdots & \vdots & \vdots \\ 0 & 0 & 0 & \cdots & a_k \end{pmatrix}$$

The steady state is stable that is $Re(\lambda) < 0 \; for \; all \; \lambda$ if $det \; H_j \geq 0 \; for \; all \; j = 1,2, \ldots, k$ If the eigenvalues of J all have real parts less than zero, then the steady state is stable.

- If at least one of the eigenvalues of J has real part greater than zero, then the steady state is unstable.
- If at least one of the eigenvalues of J has real part equal to zero then no conclusion can be made from the linear analysis. We have a borderline case between stability and instability. In these cases, nonlinear terms need to be considered *(Nazim M. and Hazrat M.D, 2018)*.

**RESULTS AND DISCUSSIONS**

The results for stability were presented as:

$$J = \begin{pmatrix} -(\omega_2 + y_1 + r + gr) & \omega_1 & 0 & 0 & 0 & 0 & 0 \\ \omega_2 & -\omega_2 + y_2 + r + gr & 0 & 0 & 0 & 0 & 0 \\ \gamma_1 & 0 & -(\mu_2 + \alpha_1) & \mu_1 & 0 & 0 & 0 \\ 0 & \gamma_2 & \mu_2 & -(\mu_1 + \alpha_2) & 0 & 0 & 0 \\ 0 & 0 & \alpha_1 & \alpha_2 & \lambda_2 & \lambda_2 & \rho_1 \\ 0 & 0 & 0 & 0 & -(\lambda_2+\beta_2) & -(\lambda_2+\beta_2) & \beta_1 \\ 0 & 0 & 0 & 0 & \beta_2 & \beta_2 & -(\rho_1 + \beta_1) \end{pmatrix} = 0$$

Neglecting 7th column of the matrix since it is heat gain from the roof $T_R$ , which is minor; the matrix is reduced to 7x6 matrices given as:

$$J = \begin{pmatrix} -(\omega_2 + y_1 + r + gr) & \omega_1 & 0 & 0 & 0 & 0 \\ \omega_2 & -\omega_2 + y_2 + r + gr & 0 & 0 & 0 & 0 \\ \gamma_1 & 0 & -(\mu_2 + \alpha_1) & \mu_1 & 0 & 0 \\ 0 & \gamma_2 & \mu_2 & -(\mu_1 + \alpha_2) & 0 & 0 \\ 0 & 0 & \alpha_1 & \alpha_2 & \lambda_2 & \lambda_2 \\ 0 & 0 & 0 & 0 & -(\lambda_2+\beta_2) & -(\lambda_2+\beta_2) \\ 0 & 0 & 0 & 0 & \beta_2 & \beta_2 \end{pmatrix} = 0$$

$A_1 = \omega_2 + \gamma_1 + r + gr, \; A_2 = \omega_1 + \gamma_2 + r + gr,$

$A_3 = \mu_2 + \alpha_2, A_4 = \mu_1 + \alpha_2, A_5 = \lambda_1 + \rho_2 ,$

$$A_6 = \lambda_1 \lambda_2 + \lambda_2 \beta_2 (\lambda^* + A_1)(\lambda^* + A_2)(\lambda^* + A_3)(\lambda^* + A_4)(\lambda^* + A_5)(\lambda^* + A_6) = 0$$

$\Rightarrow \lambda^{*6} + \beta_1 \lambda^{*5} + \beta_2 \lambda^{*4} + \beta_3 \lambda^{*3} + \beta_4 \lambda^{*2} + \beta_5 \lambda^* + \beta_6 = 0$ but, $B_1 = A_1 + A_2 + A_3 + A_4 + A_5 + A_6$

$$B_2 = A_6(A_1 + A_2 + A_3 + A_5) + A_5(A_1 + A_2 + A_3 + A_4) + A_4(A_1 + A_2 + A_3) + A_3(A_1 + A_2) + A_1 + A_2$$

$$B_3 = A_6(A_1A_2 + A_1A_3 + A_1A_4 + A_1A_5 + A_2A_3 + A_2A_4 + A_2A_5 + A_3A_4 + A_3A_5 + A_4A_5) + A_5(A_1A_2 + A_1A_3 + A_1A_4 + A_2A_3 + A_2A_4 + A_3A_4) + A_1A_2 + A_1A_2A_3 + A_2A_3A_4$$

$$B_4 = A_6(A_1A_2A_3 + A_1A_2 + A_1A_2A_5 + A_1A_3A_4A_5 + A_1A_3A_5 + A_1A_4A_5 + A_2A_3A_4 + A_2A_3A_5 + A_2A_4A_5 + A_3A_4A_5) + A_5(A_1A_2 + A_1A_2A_3 + A_1A_3A_4 + A_2A_3A_4) + A_1A_2A_3A_4$$

$$B_5 = A_6(A_2A_3A_4A_5 + A_1A_3A_4A_5 + A_1A_3A_4A_5 + A_1A_2A_5 + A_1A_2A_3A_5 + A_1A_2A_3A_4) + A_5(A_1A_2A_3A_4)B_6 = A_1A_2A_3A_4A_5A_6$$

Now we find the eigenvalues by forming the characteristics equation given by $|A - \lambda I| = 0$, where *A* is replaced with *J*.

Therefore, the eigenvalues are:

$$\lambda_1^* = -(\omega_2 + \gamma_1 + r + gr), \lambda_2^* = -(\omega_1 + \gamma_2 + r + gr), \lambda_3^* = -(\mu_2 + \alpha_1), \lambda_4^* = -(\mu_1 + \alpha_2),$$
$$\lambda_5^* = -(\lambda_1 + \rho_2), \quad \lambda_6^* = -(\lambda_2 + \beta_2), \lambda_7^* = -(\rho_1 + \beta_1)$$

Since, all the eigenvalues are negative; we can conclude that the stability of equilibrium state of the model is locally stable. Further prove of stability using Routh-Hurwitz criteria, given the polynomial $H(\lambda) = \lambda^n +$

$\beta_1\lambda^{n-1} + \beta_{n-1} + \beta_n$. where the coefficients $\beta_i$ are real constants $i = 1, \ldots, n,$ define the n Hurwitz (T) matrices using coefficients $\beta_i$of the characteristic polynomial.

$$\begin{vmatrix} -(\omega_2 + y_1 + r + gr) & \omega_1 & 0 & 0 & 0 & 0 & 0 \\ \omega_2 & -\omega_2 + y_2 + r + gr & 0 & 0 & 0 & 0 & 0 \\ \gamma_1 & 0 & -(\mu_2 + \alpha_1) & \mu_1 & 0 & 0 & 0 \\ 0 & \gamma_2 & \mu_2 & -(\mu_1 + \alpha_2) & 0 & 0 & 0 \\ 0 & 0 & \alpha_1 & \alpha_2 & \lambda_2 & \lambda_2 & \rho_1 \\ 0 & 0 & 0 & 0 & -(\lambda_2+\beta_2) & -(\lambda_2+\beta_2) & \beta_1 \\ 0 & 0 & 0 & 0 & \beta_2 & \beta_2 & -(\rho_1 + \beta_1) \end{vmatrix} = 0$$

$$(\omega_2 + \gamma_1 + r + gr + \lambda^*)(\omega_1 + \gamma_2 + r + gr + \lambda^*)(\mu_2 + \alpha_1 + \lambda^*)(\mu_1 + \alpha_2 + \lambda^*)(\lambda_1+\rho_2 + \lambda^*)(\lambda_2+\beta_2 + \lambda^*)(\lambda_1\lambda_2) = 0$$

$$T_n = \begin{vmatrix} B_1 & 1 & 0 & 0 & 0 & \cdots & 0 \\ B_3 & B_2 & B_1 & 1 & 1 & \cdots & 0 \\ B_5 & B_4 & B_3 & B_2 & B_1 & \cdots & 0 \\ B_7 & B_6 & B_5 & B_4 & B_3 & \cdots & 0 \\ \vdots & \vdots & \vdots & \vdots & \vdots & \cdots & \vdots \\ \vdots & \vdots & \vdots & \vdots & \vdots & \cdots & \vdots \\ 0 & 0 & 0 & 0 & 0 & \cdots & B_n \end{vmatrix}$$

Where $B_i = 0$ if j > n. all the roots of the polynomial H ($\lambda$) are negative or have negative real parts if and only if the determinants of all Hurwitz matrices are positive. $det\,(T_j) > 0, j = 1, 2, \cdots, n.$

For the characteristics polynomial in (*), when n = 6, the Routh – Hurwitz criteria (*Negrean I., 2015*) are: $B_1 > 0,\ B_2 > 0,\ B_3 > 0,\ B_4 > 0,\ B_5 > 0, B_6 > 0 det\,(T_1) = B_1 > 0. det\,(T_2) = \begin{pmatrix} B_1 & 1 \\ B_3 & B_2 \end{pmatrix} = B_1B_2 > 0 det\,(T_3) = \begin{pmatrix} B_1 & 1 & 0 \\ B_3 & B_2 & B_1 \\ B_5 & B_4 & B_3 \end{pmatrix} = B_1B_2B_3 - {B_3}^2 > 0 \Rightarrow B_1B_2 - B_3 > 0$

$$B_1\left(B_1B_3B_4 - {B_2}^2B_5 - B_1{B_4}^5 - B_1B_2B_6 + 2B_4B_5 - B_3B_6\right) \det(T_4) = \begin{pmatrix} B_1 & 1 & 0 & 0 \\ B_3 & B_2B_1 & 1 \\ B_5 & B_4B_3 & B_2 \\ 0 & B_6B_5 & B_4 \end{pmatrix} =$$

$$-B_3\left(B_3B_4 - B_2B_5\right) - {B_2}^2 > 0$$

$$\det(T_5) = \begin{pmatrix} B_1 & 1 & 0 & 0 & 0 \\ B_3 & B_2 & B_1 & 1 & 0 \\ B_5 & B_4 & B_3B_2 & B_1 \\ 0 & B_6 & B_5B_4 & B_3 \\ 0 & 0 & 0 & 6 & B_5 \end{pmatrix}$$

$$= B_1\left(B_2B_3B_4B_5 - B_2{B_3}^2B_6 - {B_2}^2{B_5}^2 + B_1B_2B_5B_6 + B_1{B_4}^2B_5 + B_1B_3B_4B_6 + B_1B_2B_5B_6 - {B_1}^2{B_6}^2 + B_4{B_5}^2 - 2B_3B_5B_6 + B_4{B_5}^2\right) - \left({B_3}^2B_4B_5 + {B_3}^3B_6 + B_2B_3{B_5}^2 - B_3{B_5}^2B_6\right) > 0$$

$$det\,(T_5) = \begin{pmatrix} B_1 & 1 & 0 & 0 & 0 & 0 \\ B_3 & \beta_2 & B_1 & 1 & 0 & 0 \\ B_5 & B_4 & B_3B_2 & B_1 & 1 \\ 0 & B_6 & B_5B_4 & B_5 & B_2 \\ 0 & 0 & 0 & B_6 & B_5 & B_4 \\ 0 & 0 & 0 & 0 & 0 & B_6 \end{pmatrix}$$

$$= B_1\left(B_2B_3B_4B_5 - B_2{B_3}^2{B_6}^2 - {B_2}^2{B_5}^2 + B_1B_2B_5B_6 + B_1B_2B_5{B_6}^2 - B_1{B_4}^2B_5B_6 + B_1B_3{B_4}^2{B_6}^2 + B_1B_2B_5{B_6}^2 - B_1{B_6}^3 + 2B_4{B_5}^2B_6 - 2B_3B_5{B_6}^2\right) - \left({B_3}^2B_4B_5B_6 - {B_3}^3{B_6}^2 - B_2B_3{B_5}^2B_6 + {B_5}^3B_6\right) > 0$$

From the above solutions, all the determinants of the Routh-Hurwitz matrices are positive, this implies that all the eigenvalues of the Jacobian matrices have negative real part to which further validate earlier result. The model equations above were simulated and validated using measured data. Fig.3: showed graph of measured and predicted data of the temperatures of the Trombe wall inner surface and the brooding room temperature of the Trombe wall solar chick brooder. The graph (fig.3) showed that the temperature varies with definite pattern (sinusoidal) for both measured and predicted for the days simulated with minimum average temperature difference of less than 3$^o$C. The graph validates the mathematical matrix model of the system.

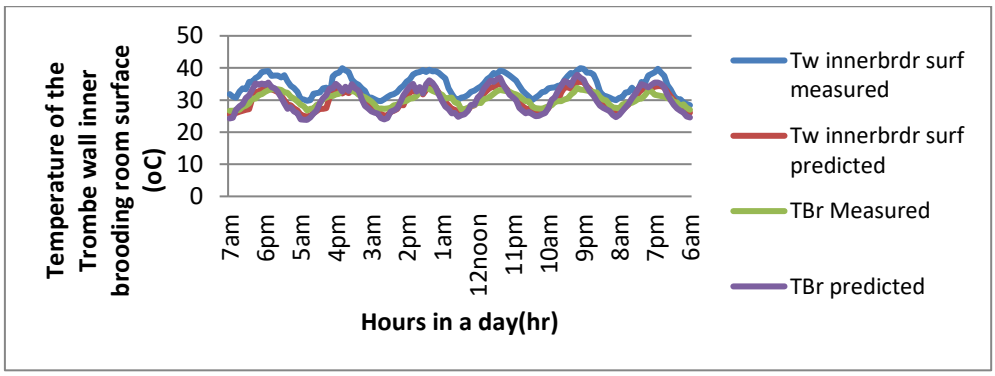


**Fig. 3 - The relationship between Measured and Predicted Temperature of the brooding room and Trombe wall inner brooding surface Temperature**

Therefore, the stability of equilibrium of the model is locally stable. Optimal chick stocking capacity is a function of chicks' metabolism and growth rate/age, ultimately to avoid overcrowding which may lead to cannibalism, heat stroke, disease outbreak etc. (*Harris G.C.1976*). For these reasons, the effects of stocking capacity (200birds) were studied for 28 days. Fig. 4: showed the graphical relationship between the temperature of the brooding room and Trombe wall room surface for 200 birds. The graph was broadened in Figure 5 and 6 to show the relationship for first two days and last two days of simulation (28 days). For the first two days of brooding, the system temperature in the morning (around 6-7 am) was 24.5 - 25$^{o}$C (room temperature), and also there was an interaction (heat energy release) between the temperatures of the Trombe wall room surface and the temperature of the brooding room with 200 birds stocked whereby the Trombe wall room surface releases heat energy required for brooding in the brooding room from 5pm to 10-11am (off- pick period). This was the pattern of energy release throughout the brooding period. The system provided variation of minimum temperature swing average of 25.5$^{o}$C and maximum of 39$^{o}$C based on solar radiation and environmental temperature of brooding. However, the Trombe wall and pebble bed bin were storing and dissipating heat energy in the day time of solar radiation.

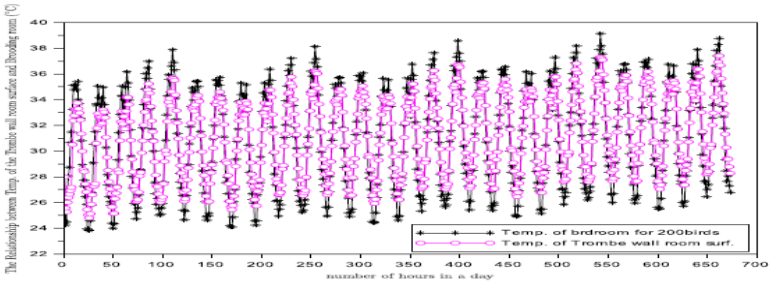


**Fig. 4 - The relationship between Temperature of the Brooding room and Trombe wall room surface for 200 birds in 28 days**

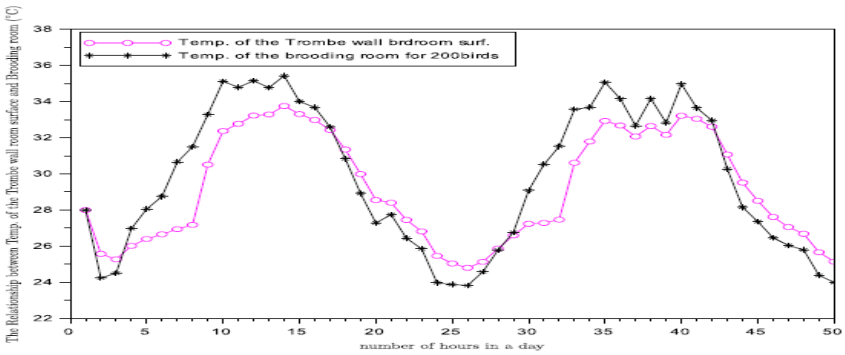


**Fig. 5 - The relationship between Temperature of the Brooding room and Trombe wall room surface for 48 hours in day 2 (two) of 28 days of brooding**

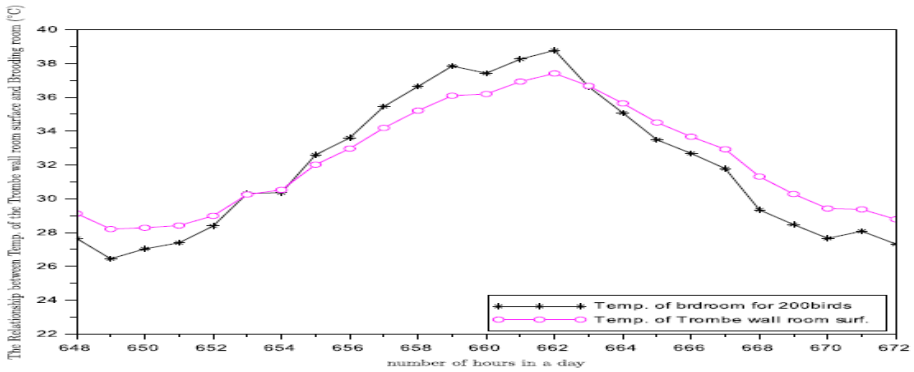


**Fig. 6 - The relationship between Temperature of the Brooding room and Trombe wall room surface for 24 hours in day 28 (twenty-eight) of 28 days of brooding**

These validate the component models that showed the brooder ability of the system model.

## CONCLUSIONS

This work has established solar energy utilization in poultry chick brooding operation (production) with the development stability and equilibrium analysis of the Trombe wall solar chick brooder. The mathematical models formulated that describe the system model were in equilibrium with the system component model that makes up the developed model of the Trombe wall solar chick brooder. The models were locally stable at the instance of solving the Jacobian matrix of the Trombe wall solar chick brooder. It was proven further using the Routh-Hurwitz criteria for steady state stability which showed that the model was stable. The model supported the brooding of 200 birds given the dimension of the brooder.

## REFERENCES

[1] Duffie J.A., Beckman W. A, (1991), *Solar Engineering of Thermal Processes*, Wiley;
[2] Echiegu E.A, (1986), The Development and Testing of a Passive Solar Energy Heated Poultry Brooder, *unpublished M. Eng., thesis, Dept. of Agricultural Engineering,* University of Nigeria, Nsukka;
[3] Echiegu E.A., (1993), Application of Solar Heat to Chicken Brooding", *Workshop paper, solar drying technologies for Agric. and Industries*, Energy Research Centre, University of Nigeria, Nsukka;
[4] Harris G.C., (1976), Limited Space Brooding in Optimum Brooding Conditions physio. *Bioenergetics Study Group* vol.12, pp.102-109;
[5] Maria A., Zhang L., (1997), Probability Distributions, Version 1.0 July 1997 Monograph, *Department of Systems Science and Industrial Engineering, SUNP at Binghamto*n, Binghamton, NY13902;
[6] Nazim M. Hazrat, A. Md (2018), A New Algorithm to Control Dynamic Stability of Higher-Order Systems, *Control System Computing and Engineering (ICCSCE 2018) 8th IEEE International Conference on*, pp. 53-58;
[7] Negrean I., (2015), Energies of Acceleration in Advanced Robotics Dynamics. *Applied Mechanics and Materials,* vol. 762, pp.67-73, Trans Tech publications;
[8] Obioha F.C. (1992). A Guide to Poultry Production in the Tropics, ACENA Publishers Enugu, Nigeria;
[9] Odo L.O (2016), Design, Construction and Performance Evaluation of a Passive solar Energy Heated Poultry Chick Brooder for Education, power and Employment for changing communities, *Journal of qualitative Education* Vol. 12, pp. 91-98;
[10] Ohagwu C.J., (2017), Mathematical Modeling of Trombe Wall Solar Chick Brooder for Optimal Poultry Production, *ABE, UNN, PhD. thesis* Research Work;
[11] Okonkwo W.I., (1993), Performance Evaluation of a Medium Scale Passive Solar Energy Brooding System, *Nigerian Journal of Solar Energy,* vol.12, pp.51-60;
[12] Okonkwo W.I. and Akubuo, C.O., (2001), Thermal Analysis and Evaluation of Heat Requirement of a Passive Solar Energy Poultry Chick Brooder. *Proceedings of the NIAE*.Vol.23 pp. 374-385.
[13] Okonkwo W.I. and Akubuo, C.O., (2007), Trombe Wall System for Poultry Brooding. *International Journal of Poultry Science,* vol. 6(2), pp. 125-130;
[14] Okonkwo W.I., AgunwambA J.C., (1997), Socio-Economic Impact of Solar Brooding System, *Proceedings International Conf. on Power Systems Operation and Planning* Abidjan;

[15] Okonkwo W.I., Anazodo G.U.N, Akubuo C.O., Echiegu E.A.,Iloeje, O.C (1992). The UNN Passive Solar Poultry Chick Brooder - Further Improvement and Preliminary Test" *Nig. J. Solar Energy*, vol.11, pp.32-40;

[16] Okoye J.A.O, (1992), Poultry Production in Nigeria, Prospects and Challenges. In: *Book of Proceedings. Workshop on improved disease diagnosis, health, nutrition and risk management practices in Poultry Production Efficiency (WIDRP)*, Ahmadu Bello University, Zaria, Nigeria, pp. 22-34;

[17] Trombe F., Robert J.F., Cabanat M., Sesolis B., (1977), Concrete Walls to Collect and Hold Heat. *Solar energy* 2 (8) 13-19.

# WRITING NORMS

## Article Types

Three types of manuscripts may be submitted:

1. **Regular articles:** These should describe new and carefully confirmed findings, and experimental procedures should be given in sufficient detail for others to verify the work. The length of a full paper should be the minimum required to describe and interpret the work clearly (max.10 pages, even number);
2. **Short Communications:** A Short Communication is suitable for recording the results of complete small investigations or giving details of new models or hypotheses, innovative methods, techniques or apparatus. The style of main sections has not necessarily to be in accordance with that of full-length papers (max. 6 pages, even number);
3. **Reviews:** Submissions of reviews and perspectives covering topics of current interest are welcome and encouraged (max.10 pages, even number).

Manuscripts should be written in English (American or British usage is accepted, but not a mixture of these) and submitted **electronically** at the following e-mail addresses: ***inmatehjournal@gmail.com***
Please be sure to include your full affiliation and e-mail address (see Sample manuscript)
The authors are responsible for the accuracy of the whole paper and references.
There are allowed 2 papers by each first author.
The text layout should be in single-column format. To avoid unnecessary errors it is strongly advised to use the "spell-check" and "grammar check" functions of your word processor.

## Review Process

All manuscripts are reviewed by 2 members of the Scientifically Review Office. Decisions will be made as rapidly as possible and the journal strives to return reviewers' comments to authors in approx.3 weeks.
The editorial board will re-review manuscripts that are accepted pending revision.

## NOTE:

Submission of a manuscript implies: that the work described has not been published before (excepting as an abstract or as part of a published lecture or thesis) that it is not under consideration for publication elsewhere.

## 1. REGULAR ARTICLES

- Manuscripts should be concise, in ***1.15 line spacing***, and should have 2 cm all over margins. The font should be ***Arial 10 pt.*** Ensure that each new paragraph is clearly indicated, using **TAB at 1 cm**.
- Title will be ***Arial 12 pt***. and explicit figures will be ***Arial 9 pt***.
- Text will be written in English.
- Chapters' titles are written by ***Arial 10 pt, Bold, Uppercase*** (e.g. **INTRODUCTION, MATERIALS AND METHODS**), between chapters is left a space for 10 pt. At the beginning of each paragraph, TAB of 1 cm.
- The paper body will be written in ***Arial 10 pt., Justify alignment***.

**TITLE** ***Arial 12 pt., Uppercase, Bold, Center*** *(in English language)* and ***Bold Italic*** *(in native language).*
Should be a brief phrase describing the contents of the paper. Avoid long titles; a running title of no more than 100 characters is encouraged (without spaces).

**AUTHORS** ***ARIAL 9, Bold, Centre alignment***
Under the paper's title, after a space (enter) 9 pt., write ***authors' names*** and ***affiliations (Arial 8 pt.-Regular)***
When the paper has more than one author, their name will be followed by a mark (Arabic numeral) as superscript if their affiliation is different. Less than 6 authors.
*Corresponding author's name* (next row), ***(Arial 8 pt.)***. Should be added also: phone, fax and e-mail information, for the paper corresponding author (***font: 8 pt., Italic***).

**KEYWORDS** ***(In English)*** about 4 to 7 words that will provide indexing references should be listed (title: ***Arial 10pt, bold italic,*** text ***Arial 10 pt., italic***).

A list of non-standard *Abbreviations* should be added. In general, non-standard abbreviations should be used only when the full term is very long and used often. Each abbreviation should be spelled out and introduced in parentheses the first time it is used in the text. Standard abbreviations (such as ATP and DNA) need not to be defined.
**ABSTRACT** ***(in English and Native language, Arial 10 pt.)***, the title *bold*; the text of abstract: *italic*) should be informative and completely self-explanatory, briefly present the topic, state the scope of the experiments, indicate significant data, and point out major findings and conclusions. The Abstract should be max.250 words. Complete sentences, active verbs, and the third person should be used, and the abstract should be written in the past tense. Standard nomenclature should be used and abbreviations should be avoided. No literature should be cited.

**INTRODUCTION** (***Arial 10 pt.)*** should provide a clear statement of the problem, the relevant literature on the subject, and the proposed approach or solution. It should be understandable to colleagues from a broad range of scientific subjects. We should refer to the current stage of researches performed in the field of the paper to be published, by quoting up-to-date specialty studies, preferably published after 2006, excepting certain referential specialty books/studies, especially papers issued in magazines/journals/conferences/ISI quoted symposia or in other international data bases, which are well known and available.

**MATERIALS AND METHODS** (***Arial 10 pt.)*** should be complete enough to allow experiments to be reproduced. However, only truly new procedures should be described in detail; previously published procedures should be cited, and important modifications of published procedures should be mentioned briefly. Methods in general use need not be described in detail.

**RESULTS** (***Arial 10 pt.)*** should be clarity presented. The results should be written in the past tense when describing findings in the authors' experiments. Results should be explained, but largely, without referring to the literature. Discussion, speculation and detailed interpretation of data should not be included in the Results, but should be put into the Conclusions section.

**CONCLUSIONS** (***Arial 10 pt.)*** The main conclusions drawn from results should be presented in a short Conclusions section. Do not include citations in this section.

***Formulae, symbols and abbreviations:*** Formulae will be typeset in Italics (preferable with the Equation Editor of Microsoft Office 2003) and should be written or marked as such in the manuscript, unless they require a different styling. They should be referred to in the text as Equation (4) or e.g. (4). The formulae should be numbered on the right side, between brackets ***(Arial 10 pt.)***:

$$P = F \cdot v \quad (1)$$

Terms of the equation and the unit measure should be explained, e.g.

*P* is the power, [W];
*F* – force, [N];
*v* – speed, [m/s]

SI units must be used throughout.

***Tables*** should be self-explanatory without reference to the text. The details of the methods used in the experiments should preferably be described in the legend instead of in the text. The same data should not be presented both in table and graph form or repeated in the text.
Table's title will be typed***Arial 9 pt, Bold, Centered***
In the table, each row will be written Arial 9 pt, single-spaced throughout, including headings and footnotes.
The table should be numbered on the right side, between brackets ***(Arial 10 pt)***:

***Figure (Arial 9 pt., Bold, Center)***should be typed in numerical order (Arabic numerals). Graphics should be high resolution (e.g.JPEG).Figure number is followed by what represent the figure or graph e.g.:

**Fig.1 – Test stand**

***Legend:*** ***Arial 8 pt, Italic, Center,*** e.g.

*1 - plansifter compartments; 2- break rolls; 3 – semolina machines; 4 – reduction rolls; 5 – flour*

**ACKNOWLEDGMENTS** (***Arial 10 pt.)*** of people, grants, funds etc should be brief (*if necessarily*).

**REFERENCES** (***Arial 10 pt.)***

*(In alphabetical order, in English and in the original publication language).*
*Minimum 10 references, last 10 years, minimum 3 references from the last 2 years*

References must be from all over the world, not only from the authors' country.
It can be used"*References*" tool from the *Word Editor*.
References should be cited in the text in brackets as in the following examples:

*(Babiciu P., Scripnic V., 2000)*

All references must be provided in English with a specification of original language in round brackets.
**Authors are fully responsible for the accuracy of the references.**
References should be alphabetically, with complete details, as follows:
Examples:
**Books:**Names and initials of authors, year (between brackets), title of the book (Italic), volume number, publisher, place, pages number or chapter, ISSN/ISBN:

[1] Vlădut V., (2009), *Study of threshing process in axial flow apparatus (Studiul procesului de treier la aparatele cu flux axial),* vol.1, ISSN/ISBN ……., "Terra Nostra" Publishing House, Iaşi/Romania;

**Journal Article:** Names and initials of authors, year (between brackets), full title of the paper, full name of the journal (Italic), volume number, publisher, place, ISSN, page numbers:

[1] Lizhi Wu, Yan Di., (2005), Demonstrational study on the land consolidation and rehabilitation (LCR) project of saline-alkali soil in arid areas: a case study of Lubotan LCR project in Pucheng County, Shaanxi Province(干旱区盐碱化土地整理工程实证研究-以陕西蒲城县卤泊滩土地整理项目为例), *Transactions of the Chinese Society of Agricultural Engineering*,vol.21, no.1, pp.179-182, Madison/Wisconsin;

[2] Leonov I.P., (1973), Basic machine theory for tobacco stringing. Post-harvest care of tobacco and rustic tobacco (Основы теории машин для закрепления табака на шнуры. Послеуборочная обработка табака и махорки), *Collection of scientific articles (сборник научно-исследовательских работ)*, pp.37-45;

**Conference or Symposium:** Names and initials of authors, year (between brackets), full title of the paper (Regular), full name of the conference/symposium (Italic), volume number, publisher, place, ISSN, page numbers

[1] Bungescu S., Stahli W., Biriş S., Vlăduţ V.,Imbrea F., Petroman C., (2009), Cosmos program used for the strength calculus of the nozzles from the sprayers (Program Cosmos folosit pentru calculul de rezistență la zgomot al aparatelor de distribuție), *Proceedings of the 35 International Symposium on Agricultural Engineering "Actual Tasks on Agricultural Engineering",* pp.177-184, Opatija / Croatia;

**Dissertation / Thesis:**Names and initials of authors, year (between brackets), full name of the thesis (Italic), specification (PhD Thesis, MSc Thesis), institution, place;

[1] Popa L., (2004), *Research on the influence of structural and functional parameters of the braking system on the braking performance of agricultural trailers (Cercetări privind influența caracteristicilor constructive şi funcționale ale sistemelor de frânare asupra performanțelor de frânare ale remorcilor agricole)*, PhD dissertation, Transylvania University of Braşov, Braşov / Romania.

**Patents:** Names and initials of authors, year (between brackets), patent title (Italic), patent number, country:

[1] Grant P., (1989), *Device for Elementary Analyses*. Patent, No.123456, USA.

**Legal regulations and laws, organizations:** Abbreviated name, year (between brackets), full name of the referred text, document title/type (Italic), author, place:

[1] *** EC Directive, (2000), Directive 2000/76/EC of the European Parliament and of the Council of 4 December 2000, on the incineration of waste, Annex V, *Official Journal of the European Communities*, L332/91, 28.12.2000, Brussels.

**Web references**: The full URL should be given in text as a citation, if no other data are known. If the authors, year, and title of the documents are known and the reference is taken from a website, the URL address has to be mentioned after these data:

*The title of the book, journal and conference must be written in Italic, the title of the article, chapter of the book, must be written Regular.*

**Citation in text**

Please ensure that every reference cited in the text is also present in the reference list (and vice versa). Do not cite references in the abstract and conclusions. Unpublished results, personal communications as well as URL addresses are not recommended in the references list.

Making personal quotations (one, at most) should not be allowed, unless the paper proposed to be published is a sequel of the cited paper. Articles in preparation or articles submitted for publication, unpublished, personal communications etc. should not be included in the references list.

***Citations style***

***Text:*** All citations in the text may be made directly (or parenthetically) and should refer to:

- ***single author:*** the author's name (without initials, unless there is ambiguity) and the year of publication:
  "as previously demonstrated *(Brown, 2010)*".
- ***two authors:*** both authors' names and the year of publication: *(Adam and Brown, 2008; Smith and Hansel, 2006; Stern and Lars, 2009)*
- ***three or more authors:*** first author's name followed by "et al." and the year of publication: "As has recently been shown *(Werner et al., 2005; Kramer et al., 2000)* have recently shown ...."

**Citations of groups of references should be listed first alphabetically, then chronologically**.

**Units, Abbreviations, Acronyms**

- Units should be metric, generally SI, and expressed in standard abbreviated form.
- Acronyms may be acceptable, but must be defined at first usage.

**Edited by: INMA Bucharest**
6 Ion Ionescu de la Brad Blvd., sect. 1, Bucharest, ROMANIA
Tel: +4021.269.32.60; Fax: +4021.269.32.73
http://www.inmateh.eu
e-mail: ***inmatehjournal@gmail.com***